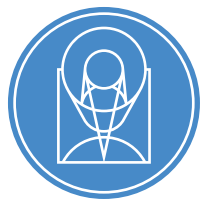

Version 12.0
December 2019

Wide Field Camera 3 Instrument Handbook for Cycle 28



STScI | SPACE TELESCOPE
SCIENCE INSTITUTE

3700 San Martin Drive
Baltimore, Maryland 21218
help@stsci.edu

WFC3 Instrument Handbook	5
Acknowledgments	7
Chapter 1: Introduction to WFC3	11
1.1 New for Cycle 28	12
1.2. Overview	13
1.3 Key Features of WFC3	14
1.4 WFC3 Quick Reference Guide	15
1.5 Special Considerations for Cycle 28	16
1.6 Sources of Further Information	18
1.7 The WFC3 Instrument Team at STScI	19
Chapter 2: WFC3 Instrument Description	20
2.1 Optical Design and Detectors	21
2.2 Field of View and Geometric Distortions	23
2.3 Spectral Elements	26
2.4 Detector Read-Out Modes and Dithering	30
Chapter 3: Choosing the Optimum HST Instrument	31
3.1 Overview	32
3.2 Choosing Between Instruments	33
3.3 Comparison of WFC3 with Other HST Imaging Instruments	
Chapter 4: Designing a Phase I WFC3 Proposal	42
4.1 Phase I and Phase II Proposals	43
4.2 Preparing a Phase I Proposal	44
Chapter 5: WFC3 Detector Characteristics and Performance	48
5.1 Overview of this Chapter	49
5.2 The WFC3 UVIS Channel CCD Detectors	51
5.3 WFC3 CCD Readout Formats	54
5.4 WFC3 CCD Characteristics and Performance	56
5.5 The WFC3 IR Channel Detector	83
5.6 WFC3 IR Readout Formats	88
5.7 IR Detector Characteristics and Performance	92
Chapter 6: UVIS Imaging with WFC3	105
6.1 WFC3 UVIS Imaging	106
6.2 Specifying a UVIS Observation	107
6.3 UVIS Channel Characteristics	108
6.4 UVIS Field Geometry	109
6.5 UVIS Spectral Elements	118
6.6 UVIS Optical Performance	137
6.7 UVIS Exposure and Readout	149
6.8 UVIS Sensitivity	153
6.9 Charge Transfer Efficiency	154
6.10 Photometric Calibration	164
6.11 Other Considerations for UVIS Imaging	165
6.12 UVIS Observing Strategies	169
Chapter 7: IR Imaging with WFC3	177
7.1 WFC3 IR Imaging	178
7.2 Specifying an IR Observation	179
7.3 IR Channel Characteristics	180
7.4 IR Field Geometry	181
7.5 IR Spectral Elements	186
7.6 IR Optical Performance	193
7.7 IR Exposure and Readout	203

7.8 IR Sensitivity	209
7.9 Other Considerations for IR Imaging	210
7.10 IR Observing Strategies	221
Chapter 8: Slitless Spectroscopy with WFC3	229
8.1 Grism Overview	230
8.2 Slitless Spectroscopy with the UVIS G280 Grism	231
8.3 Slitless Spectroscopy with the IR G102 and G141 Grisms	236
8.4 Sensitivities and Exposure-Time Estimation	242
8.5 Extraction and Calibration of Spectra	243
8.6 Slitless Spectroscopy with Spatial Scanning	247
Chapter 9: WFC3 Exposure-Time Calculation	251
9.1 Overview	252
9.2 The WFC3 Exposure Time Calculator - ETC	253
9.3 Calculating Sensitivities from Tabulated Data	255
9.4 Count Rates: Imaging	262
9.5 Count Rates: Slitless Spectroscopy	265
9.6 Estimating Exposure Times	266
9.7 Sky Background	268
9.8 Interstellar Extinction	276
9.9 Exposure-Time Calculation Examples	277
Chapter 10: Overheads and Orbit Time Determinations	281
10.1 Overview	282
10.2 Observatory Overheads	283
10.3 Instrument Overheads	285
10.4 Orbit Use Examples	289
Appendix A: WFC3 Filter Throughputs	294
A.1 Introduction	296
A.2 Throughputs and Signal-to-Noise Ratio Data	297
UVIS F200LP	299
UVIS F218W	303
UVIS F225W	307
UVIS F275W	311
UVIS F280N	315
UVIS F300X	319
UVIS F336W	323
UVIS F343N	327
UVIS F350LP	331
UVIS F373N	335
UVIS F390M	339
UVIS F390W	343
UVIS F395N	347
UVIS F410M	351
UVIS F438W	355
UVIS F467M	359
UVIS F469N	363
UVIS F475W	367
UVIS F475X	371
UVIS F487N	375
UVIS F502N	379
UVIS F547M	383
UVIS F555W	387

UVIS F600LP	391
UVIS F606W	395
UVIS F621M	399
UVIS F625W	403
UVIS F631N	407
UVIS F645N	411
UVIS F656N	415
UVIS F657N	419
UVIS F658N	423
UVIS F665N	427
UVIS F673N	431
UVIS F680N	435
UVIS F689M	439
UVIS F763M	443
UVIS F775W	447
UVIS F814W	451
UVIS F845M	455
UVIS F850LP	459
UVIS F953N	463
UVIS FQ232N	467
UVIS FQ243N	471
UVIS FQ378N	475
UVIS FQ387N	479
UVIS FQ422M	483
UVIS FQ436N	487
UVIS FQ437N	491
UVIS FQ492N	495
UVIS FQ508N	499
UVIS FQ575N	503
UVIS FQ619N	507
UVIS FQ634N	511
UVIS FQ672N	515
UVIS FQ674N	519
UVIS FQ727N	523
UVIS FQ750N	527
UVIS FQ889N	531
UVIS FQ906N	535
UVIS FQ924N	539
UVIS FQ937N	543
IR F098M	556
IR F105W	560
IR F110W	564
IR F125W	568
IR F126N	572
IR F127M	576
IR F128N	580
IR F130N	584
IR F132N	588
IR F139M	592
IR F140W	596
IR F153M	600

IR F160W	604
IR F164N	608
IR F167N	612
Appendix B: Geometric Distortion	625
B.1 Overview	626
B.2 UVIS Channel	628
B.3 IR Channel	631
B.4 IR Summary	634
Appendix C: Dithering and Mosaicking	635
C.1 Why Mosaicking and Dithering are Needed	636
C.2 WFC3 Patterns	637
Appendix D: Bright-Object Constraints and Image Persistence	643
D.1 UVIS Channel	644
D.2 IR Channel	645
Appendix E: Reduction and Calibration of WFC3 Data	650
E.1 The STScI Reduction and Calibration Pipeline	651
E.2 The SMOV Calibration Plan	655
E.3 The Cycle 17 Calibration Plan	658
E.4 The Cycle 18 Calibration Plan	661
E.5 The Cycle 19 Calibration Plan	663
E.6 The Cycle 20 Calibration Plan	666
E.7 The Cycle 21 Calibration Plan	668
E.8 The Cycle 22 Calibration Plan	670
E.9 The Cycle 23 Calibration Plan	672
E.10 The Cycle 24 Calibration Plan	674
E.11 The Cycle 25 Calibration Plan	676
E.12 The Cycle 26 Calibration Plan	678
E.13 The Cycle 27 Calibration Plan	680
Glossary	682

WFC3 Instrument Handbook

Version 12.0 – December 2019

[PDF version](#)

Wide Field Camera 3 Instrument Handbook for Cycle 28

User Support

Please contact the HST Help Desk for assistance. We encourage users to access the new web portal where you can submit your questions directly to the appropriate team of experts.

- Web: <http://hsthelp.stsci.edu>
- E-mail: help@stsci.edu

Additional Resources

Information and other resources are available from the STScI website:

- <http://www.stsci.edu/hst/instrumentation/wfc3>

Revision History

Version	Date	Editors
12.0	December 2019	Linda Dressel
11.0	January 2019	Linda Dressel
10.0	May 2018	Linda Dressel
9.0	January 2017	Linda Dressel
8.0	January 2016	Linda Dressel
7.0	January 2015	Linda Dressel
6.0	January 2014	Linda Dressel
5.0	December 2012	Linda Dressel
4.0	December 2011	Linda Dressel
3.0	December 2010	Linda Dressel
2.1	June 25, 2010	Linda Dressel, Michael H. Wong, Cheryl Pavlovsky, Knox S. Long
2.0	January 2010	Michael H. Wong, Cheryl Pavlovsky, Knox S. Long
1.0	December 2007	Howard E. Bond and Jessica Kim Quijano

Citation

In publications, refer to this document as

- Dressel, L., 2019. "Wide Field Camera 3 Instrument Handbook, Version 12.0" (Baltimore: STScI)

Acknowledgments

Contributors

Jay Anderson, Sylvia Baggett, Varun Bajaj, Bruce Balick, John Biretta, Howard Bond, Ray Boucarut, Matthew Bourque, Gabriel Brammer, Tom Brown, Howard Bushouse, Nicholas Collins, Colin Cox, Tomas Dahlen, Ilana Dashevsky, Tiffany Davis, Susana Deustua, Linda Dressel, Michael Dulude, Mario Gennaro, Mauro Giavalisco, Ron Gilliland, Heather Gunning, George Hartig, Bryan Hilbert, Robert J. Hill, Jason Kalirai, Diane Karakla, Harish Khandrika, Jessica Kim Quijano, Randy Kimble, Martin Kümmel, Harald Kuntschner, Janice Lee, Matt Lallo, Knox Long, Olivia Lupie, Jennifer Mack, John MacKenty, Eliot Malumuth, André Martel, Catherine Martlin, Peter McCullough, Brian McLean, Jennifer Medina, Ivelina Momcheva, Kai Noeske, Cheryl Pavlovsky, Larry Petro, Nor Pirzkal, Vera Kozhurina-Platais, Elizabeth Polidan, Manuel Quijada, Abhijith Rajan, Neill Reid, Adam Riess, Massimo Robberto, Barry Rothberg, Elena Sabbi, Kailash Sahu, Clare Shanahan, Kevin Stevenson, Massimo Stiavelli, Ben Sunquist, Randal Telfer, Alex Viana, Nolan Walborn, Jeremy Walsh, Allen Welty, Tom Wheeler, and Mike Wong.

The WFC3 Science Integrated Product Team (2019)

Jay Anderson
Sylvia Baggett (Team Lead)
Varun Bajaj
Annalisa Calamida
Michele DeLaPena
Susana Deustua
Linda Dressel
Julia Fowler
Mario Gennaro
Harish Khandrika
Vera Kozhurina-Platais
Benjamin Kuhn
Jennifer Mack
Catherine Martlin
Peter McCullough
Jennifer Medina
Heather Olszewski
Nor Pirzkal
Marc Rafelski
Adam Riess
Russell Ryan
Elena Sabbi
Kailash Sahu
Clare Shanahan
Kevin Stevenson
Ben Sunnquist

Past Science IPT Members

Elizabeth Barker
Wayne Baggett
John Biretta
Howard Bond
Matthew Bourque
Ariel Bowers
Gabriel Brammer
Howard Bushouse
Tom Brown
Laura Cawley
Ed Cheng (GSFC, now Conceptual Analytics)
Tomas Dahlen
Ilana Dashevsky
Tiffany Davis
Michael Dulude

Meredith Durbin
Michael Fall
Don Figer
Mauro Giavalisco
Ron Gilliland
Shireen Gonzaga
Catherine Gosemeyer
Heather Gunning
Derek Hammer
Christopher Hanley
George Hartig
Ron Henry
Bryan Hilbert
Robert Hill (GSFC)
Jason Kalirai
Jessica Kim Quijano
Randy Kimble (Instrument Scientist, GSFC)
Pat Knezek
Ray Kutina
Janice Lee
Casey Lisse
Knox Long
Olivia Lupie (GSFC)
John MacKenty
André Martel
Myles Mckay
Brian McLean
Ivelina Momcheva
Kai Noeske
Cheryl Pavlovsky
Larry Petro
Abhijith Rajan
Neill Reid
Massimo Robberto
Michael Robinson
Barry Rothberg
Megan Sosey
Massimo Stiavelli
Alex Viana
Mike Wong

The WFC3 Scientific Oversight Committee

Bruce Balick, University of Washington
Howard E. Bond, Space Telescope Science Institute
Daniela Calzetti, University of Massachusetts
C. Marcella Carollo, Institute of Astronomy, ETH, Zurich
Michael J. Disney, Cardiff University
Michael A. Dopita, Mt Stromlo and Siding Spring Observatories
Jay Frogel, AURA
Donald N. B. Hall, University of Hawaii
Jon A. Holtzman, New Mexico State University
Randy Kimble, NASA Goddard Space Flight Center (ex officio)
Gerard Luppino, University of Hawaii
Patrick J. McCarthy, Carnegie Observatories
John MacKenty, Space Telescope Science Institute (ex officio)
Robert W. O'Connell, University of Virginia (Chair)
Francesco Paresce, European Southern Observatory
Abhijit Saha, National Optical Astronomy Observatory
Joseph I. Silk, Oxford University
John T. Trauger, Jet Propulsion Laboratory
Alistair R. Walker, Cerro Tololo Interamerican Observatory
Bradley C. Whitmore, Space Telescope Science Institute
Rogier A. Windhorst, Arizona State University
Erick T. Young, University of Arizona

Thanks

The editor thanks Jay Anderson, Sylvia Baggett, Varun Bajaj, Jennifer Mack, Catherine Martlin, Jennifer Medina, Nor Pirzkal, and Clare Shanahan for providing information, contributions, and suggestions for improvements to support the editing of this edition. Contributions to earlier editions were made by past and present members of the Science IPT and by ECF scientists Martin Kümmel, Harald Kuntschner, and Jeremy Brett.

The contributions of Susan Rose (Senior Technical Editor) to the editing and production of this Instrument Handbook, as always, are greatly appreciated.

Chapter 1: Introduction to WFC3

Chapter Contents

- [1.1 New for Cycle 28](#)
- [1.2. Overview](#)
- [1.3 Key Features of WFC3](#)
- [1.4 WFC3 Quick Reference Guide](#)
- [1.5 Special Considerations for Cycle 28](#)
- [1.6 Sources of Further Information](#)
- [1.7 The WFC3 Instrument Team at STScI](#)

1.1 New for Cycle 28

We have made the following updates to the WFC3 Instrument Handbook for this cycle:

- We discuss recent results from studies of count rate non-linearity on the WFC3/IR detector ([Section 5.7.6](#)).
- We discuss the construction of focus-diverse PSF models for five commonly used UVIS broad-band filters and their relationship to HST focus ([Section 6.6.4](#)).
- We have extensively updated the description of photometric calibration ([Section 6.10](#)).
- We point out the existence of an offset between spatial scan images made in forward and reverse modes ([Section 6.12.3](#)).
- We update advice to observers using the spatial scan mode and demonstrate the advantage of monitoring UVIS system throughput with spatial scan data ([Section 6.12.3](#)).
- We state the increased drift rate associated with using a single guide star ([Section 6.12.4](#), [Section 7.10.4](#)).
- We summarize the results of recent studies of persistence on the WFC3/IR detector and advise the use of dither steps greater than 10 pixels for some photometric programs ([Section 7.9.4](#)).
- We note that the solar exclusion angle for HST observations has increased from 50 degrees to 55 degrees ([Section 7.9.5](#), [Section 9.7.1](#)).
- We provide new references to studies of the "blobs" in WFC3/IR images and discuss the date-dependent bad pixel tables that track the appearance of blobs ([Section 7.9.6](#)).
- We discuss the impending release of tools and a Jupyter notebook to assist users of the DASH mode to calibrate their observations ([Section 7.10.6](#)).
- We provide a more detailed discussion of the background in WFC3/IR grism exposures and illustrate the three components of the background (zodiacal light, He I airglow emission, and scattered light) in G102 and G141 images ([Section 8.5](#)).
- We confirm the stability of the geometric distortion solution for the WFC3/UVIS F606W filter and summarize the delivery of IDCTAB reference files for the WFC3/IR detector and the WFC3/UVIS detector ([Appendix B](#)).
- We have added a summary of the WFC3 calibration plan for the upcoming cycle in [Appendix E](#).

1.2. Overview

The **Wide Field Camera 3 (WFC3)** is a fourth-generation imaging instrument. It was installed in the *Hubble Space Telescope (HST)* during Servicing Mission 4 (SM4) in May 2009. WFC3 saw first light on June 24, 2009, following the cooling of its detectors. Servicing Mission 4 Observatory Verification (SMOV) activities were completed in late August 2009, and were followed by the Cycle 17 calibration and science programs.

This *WFC3 Instrument Handbook* has been prepared by the WFC3 team at STScI. It is the basic technical reference manual for WFC3 observers. The information in this Handbook is intended to be useful for Cycle 28 Phase I proposers, for the subsequently selected General Observers (GOs) as they prepare their Phase II specifications, and for those analyzing WFC3 data. The [*HST Primer*](#) and the [*HST Call for Proposals*](#) also contain valuable information for proposers, and the [*HST Call for Proposals*](#) is the final authority on *HST* policy.

This edition of the *WFC3 Instrument Handbook* (Version 12.0) was written during the execution of the Cycle 26 calibration plan. It supersedes Version 11.0. It includes results from analysis of most calibration programs executed through Cycle 26 and into Cycle 27. (See the [*Documents Archive*](#) for links to Instrument Handbooks from previous cycles.)

The WFC3 instrument occupies *HST*'s radial scientific-instrument bay, from where it obtains on-axis direct images. During SM4 the shuttle astronauts installed WFC3 in place of the long-serving Wide Field Planetary Camera 2 (WFPC2). WFPC2, in turn, was installed during SM1 in December 1993, to replace the original Wide Field/Planetary Camera (WF/PC1). WFC3, like WFPC2, contains optics that correct for the spherical aberration discovered in the *HST* primary mirror following launch of the telescope in April 1990.

WFC3 is designed to ensure that *HST* maintains its powerful imaging capabilities until the end of its mission, while at the same time advancing its survey and discovery capability through WFC3's combination of broad wavelength coverage, wide field of view, and high sensitivity. WFC3 also provides a good degree of redundancy for the Wide Field Channel of the Advanced Camera for Surveys (ACS) and has replaced some of the capabilities of the Near-Infrared Camera and Multi-Object Spectrometer (NICMOS) cameras.

A key feature of WFC3 is its panchromatic wavelength coverage. By combining two optical/ultraviolet CCDs with a near-infrared HgCdTe array, WFC3 is capable of direct, high-resolution imaging over the entire wavelength range from 200 to 1700 nm. Equipped with a comprehensive range of wide-, intermediate-, and narrow-band filters, WFC3 has broad applicability to a variety of new astrophysical investigations.

WFC3 is a facility instrument. It was developed, constructed, characterized, and calibrated by an Integrated Product Team (IPT) led by NASA's Goddard Space Flight Center (GSFC), and composed of staff astronomers and engineers from GSFC, STScI, Ball Aerospace & Technologies Corp., the Jet Propulsion Laboratory (JPL), and other industrial contractors.

A Scientific Oversight Committee (SOC), selected by NASA from the international astronomical community and appointed in 1998, provided scientific advice for the design and development of WFC3. The SOC's activities were in a range of areas, including: definition of the key scientific goals and success criteria for WFC3; participation in project reviews; recommending an optimum set of filters and grisms for the instrument and the pixel scale and field of view of the detectors; participation in the selection of flight detectors; and advice on technical trade-off decisions in the light of the scientific goals of the instrument.

1.3 Key Features of WFC3

The optical design of WFC3 features two independent channels, one sensitive at ultraviolet (UV) and optical wavelengths, approximately 200 to 1000 nm (the **UVIS channel**), and the other sensitive at near-infrared (near-IR) wavelengths, approximately 800 to 1700 nm (the **IR channel**). A channel-selection mirror directs on-axis light from the *HST* optical telescope assembly (OTA) to the IR channel, or the mirror can be removed from the beam to allow light to enter the **UVIS channel**. This means that *simultaneous* observations with the UVIS and IR detectors are not possible. However, both UVIS and IR observations can be made *sequentially*, even during the same *HST* orbit.

The extended wavelength range, combined with high sensitivity, high spatial resolution, large field of view, and a wide selection of spectral elements, makes WFC3 an extremely versatile instrument. Key features of WFC3 include:

- **UVIS channel:** two $2k \times 4k$ CCDs; pixel scale 0.04 arcsec/pix; field of view 162×162 arcsec; wavelength range 200-1000 nm; S/N=10 in a 10-hour exposure (F606W filter) for a point source with $V=29.2$ (ABMAG).
- **IR channel:** $1k \times 1k$ HgCdTe array; pixel scale 0.13 arcsec/pix; field of view 136×123 arcsec; wavelength range 800-1700 nm; S/N=10 in a 10-hour exposure (F160W) for a point source with $H=27.9$ (ABMAG).
- 62 wide-, medium-, and narrow-band filters in the UVIS channel.
- 15 wide-, medium-, and narrow-band filters in the IR channel.
- 1 grism in the UVIS channel, and 2 grisms in the IR channel.

A "White Paper," prepared by the SOC and the Science IPT, outlines some scientific areas that will especially benefit from the capabilities of WFC3. These include searches for galaxies at redshifts up to $z \sim 10$; studies of the physics of star formation in distant and nearby galaxies; investigations of resolved stellar populations down to faint levels in the UV, optical, and near-IR; and high-resolution imaging of objects in the solar system. WFC3's panchromatic capabilities allow investigations of the assembly and evolution of galaxies; star birth, evolution, and death and its relation to the interstellar medium; individual and collective properties of small solar system bodies; and aurorae and meteorology of the outer planets. The White Paper (Stiavelli, M., & O'Connell, R.W., eds., 2000, "*Hubble Space Telescope Wide Field Camera 3, Capabilities and Scientific Program*") can be found at:

<http://www.stsci.edu/~WFC3/resources/WFC3-WhitePaper-2001.pdf>

1.4 WFC3 Quick Reference Guide

The most important basic information about WFC3 can be found in this Handbook at the following locations:

- Table 5.1: Instrument Characteristics (field of view, pixel scale, detector parameters, etc.)
- Table 6.2: UVIS Channel Filters and Grism
- Figures 6.3-6.6: Plots of system throughput for UVIS Filters
- Table 7.2: IR Channel Filters and Grisms
- Figures 7.2-7.3: Plots of system throughput for IR Filter

1.5 Special Considerations for Cycle 28

- [1.5.1 Current Instrument Status](#)
- [1.5.2 Ongoing Calibration](#)
- [1.5.3 New Capabilities](#)

1.5.1 Current Instrument Status

WFC3 is operating as expected on *HST*, with its detectors at nominal setpoints of -83°C (UVIS) and -128°C (IR). There are no significant anomalies in its performance.

1.5.2 Ongoing Calibration

At the time of this writing, cycle 26 calibration observations have been completed and cycle 27 calibration observations have begun. Descriptions of the calibration plan for each cycle are given in [Appendix E](#) and at:

<http://www.stsci.edu/hst/instrumentation/wfc3/calibration>

Much of the analysis of the calibration programs from past cycles has already been documented in [WFC3 Instrument Science Reports](#) published on the [WFC3 website](#); documentation of the remaining analysis is on-going.

Proposers and users of WFC3 should monitor the Cycle 28 announcement website for the latest information:
<https://hst-docs.stsci.edu/display/HSP>

Additional information will be released as part of WFC3 Space Telescope Analysis Newsletters (STANs) and other updates posted directly to the [WFC3 website](#):

<http://www.stsci.edu/hst/instrumentation/wfc3/documentation/stsci-analysis-newsletter-stan>

Throughout this handbook, a special “” symbol indicates information that is especially likely to be updated on the WFC3 website.

1.5.3 New Capabilities

UVIS SHUTTER BLADE: The capability of commanding the UVIS shutter to use exclusively one of the two sides of the shutter blade in short exposures, resulting in less vibration and PSF smearing, was implemented early in cycle 21. This option will be made available to the observer when it is critical to the scientific success of a program. See [Section 6.11.4](#).

UVIS POST-FLASH: The major new capability of adding a flash at the end of a UVIS exposure (post-flash) was implemented for Cycle 20. APT began to issue diagnostic reports on exposures with inadequate or excessive flash in Cycle 23. Post-flash greatly increases the detection of faint sources in low background observations, where CTE losses would otherwise remove much or all of the flux from the sources. Most UVIS observers should consider using post-flash. It is useful for all UV, narrow band, and relatively short medium and broad band exposures where the detection of faint sources is required. It should replace Charge Injection in essentially all circumstances. (See [Section 6.9.2](#)) Those who are considering using Charge Injection rather than post-flash should consult STScI. See [Section 5.4.11](#), [Section 6.9](#), and the [WFC3 UVIS CTE](#) webpage for further information on CTE and post-flash.

SPATIAL SCANS: The observing technique of spatial scanning was introduced for WFC3 in cycle 19. (See Sections [6.12.3](#), [7.10.4](#), and [8.6](#).) Spatial scan mode was added to the ETC for UVIS and IR imaging and IR spectroscopy for cycle 24. This mode can be used to turn stars into well-defined streaks on the detector or to spread a stellar spectrum perpendicular to its dispersion. It is useful for:

- Observations requiring high temporal sampling and/or time resolution
- Observations requiring high temporal sampling and/or time resolution
- High precision relative astrometric observations
- Imaging and spectroscopy of brighter sources than previously possible



Information especially likely to be updated on the [WFC3 website](#) is indicated by this symbol.

1.6 Sources of Further Information

Table 1.1 provides a guide to online documents containing further information about HST, the proposal process, and data analysis.

Table 1.1: Useful documents

Purpose	Document or resource
General observatory information	HST Primer https://hst-docs.stsci.edu/display/HSP/The+Hubble+Space+Telescope+Primer+for+Cycle+28
Phase I proposals	Proposing Overview https://hst-docs.stsci.edu/display/HSP/HST+Proposal+Opportunities+and+Science+Policies Call for Proposals https://hst-docs.stsci.edu/display/HSP/Hubble+Space+Telescope+Call+for+Proposals+for+Cycle+28
Phase II programs	Phase II Proposal Instructions https://hst-docs.stsci.edu/display/HPIOM Astronomer's Proposal Tool (APT) for Phase I and II preparations http://apt.stsci.edu/
Data analysis and instrument characteristics	General WFC3 Information and Updates https://hst-docs.stsci.edu/display/WFC3IHB WFC3 Data Handbook https://hst-docs.stsci.edu/display/WFC3DHB DrizzlePac http://www.stsci.edu/scientific-community/software/drizzlepac Space Telescope Analysis Newsletter http://www.stsci.edu/hst/instrumentation/wfc3/documentation/stsci-analysis-newsletter-stan WFC3 Instrument Science Reports (ISRs) http://www.stsci.edu/hst/instrumentation/wfc3/documentation/instrument-science-reports-isrs Calibration and Pipeline Information http://www.stsci.edu/hst/observing/post-observation

Proposers who desire more detailed information about WFC3 capabilities should refer to the WFC3 Instrument Science Reports (ISRs; see link in [Table 1.1](#)), which contain extensive details about all aspects of the instrument. Proposers may also seek further assistance as described in the next section.

1.7 The WFC3 Instrument Team at STScI

STScI's team of scientific and technical staff support the design, development, operation, calibration, and documentation of WFC3. STScI also maintains a "Help Desk" to provide answers quickly to any WFC3 and HST related questions. Please refer all questions regarding WFC3 and HST to the Help Desk, as follows:

- Web portal: <http://hsthelp.stsci.edu>
- E-mail: help@stsci.edu

The Team Lead for WFC3 is Sylvia Baggett:

- E-mail: sbaggett@stsci.edu
- Phone: (410) 338-5054

Additional STScI contact info can be found in the *HST Call for Proposals*.

Chapter 2: WFC3 Instrument Description

Chapter Contents

- [2.1 Optical Design and Detectors](#)
- [2.2 Field of View and Geometric Distortions](#)
- [2.3 Spectral Elements](#)
- [2.4 Detector Read-Out Modes and Dithering](#)

2.1 Optical Design and Detectors

The optical design of WFC3 was driven by the need to provide a large field of view and high sensitivity over a broad wavelength range, excellent spatial resolution, and stable and accurate photometric performance. WFC3 features two independent imaging cameras: the **UV/Visible channel (UVIS)** and the **near-infrared channel (IR)**. [Figure 2.1](#) shows a schematic diagram of the instrument's optical and mechanical layout.

On-axis light coming from the *HST* optical telescope assembly (OTA) is intercepted by the flat 45° WFC3 pick-off mirror (POM) and is directed into the instrument. For IR observations, the channel select mechanism (CSM) then diverts the light into the IR channel; for UVIS observations, the CSM mirror is simply removed, which allows the light to enter the UVIS channel. Because of this design, only a single channel, either UVIS or IR, can be used at any one time, although it is possible to switch between them fairly quickly.

Optical elements in each channel (anamorphic aspherical correctors) correct separately for the ~1/2 wave spherical aberration of the HST primary mirror. Both channels also have internal flat-field illumination sources.

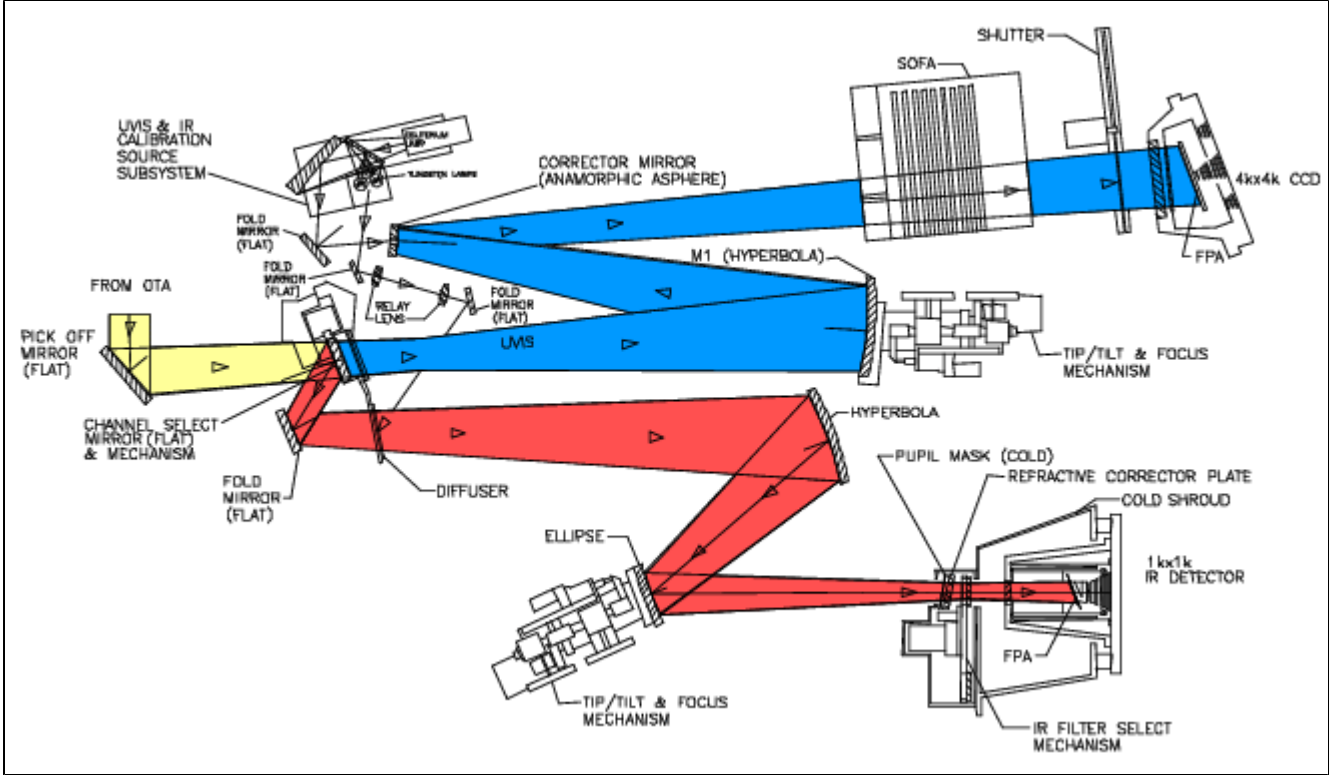
WFC3 uses two different types of detectors. The UVIS channel uses two butted 4096×2051 thinned, back-illuminated e2v Ltd. (formerly Marconi) CCD detectors to support imaging between 200 and 1000 nm. The IR channel uses a 1024×1024 Teledyne (formerly Rockwell Scientific) HgCdTe detector array, with the central 1014×1014 pixels useful for imaging, and covering the near-infrared between 800 and 1700 nm.

The primary characteristics of the two channels are summarized in [Table 2.1](#).

Table 2.1: Characteristics of the two WFC3 channels.

Channel	f-ratio	Detector type	Spectral range (nm)	Detector pixel format	Pixel scale (arcsec)	Field of view (arcsec)
UVIS	31	CCD	200-1000	$2 \times 2051 \times 4096$	0.0395×0.0395	162×162
IR	11	HgCdTe	800-1700	1014×1014	0.135×0.121	136×123

Figure 2.1: Schematic optical layout of the WFC3 instrument. Note that for schematic simplicity, the incoming OTA beam and POM have been rotated into the plane of the optical diagram.

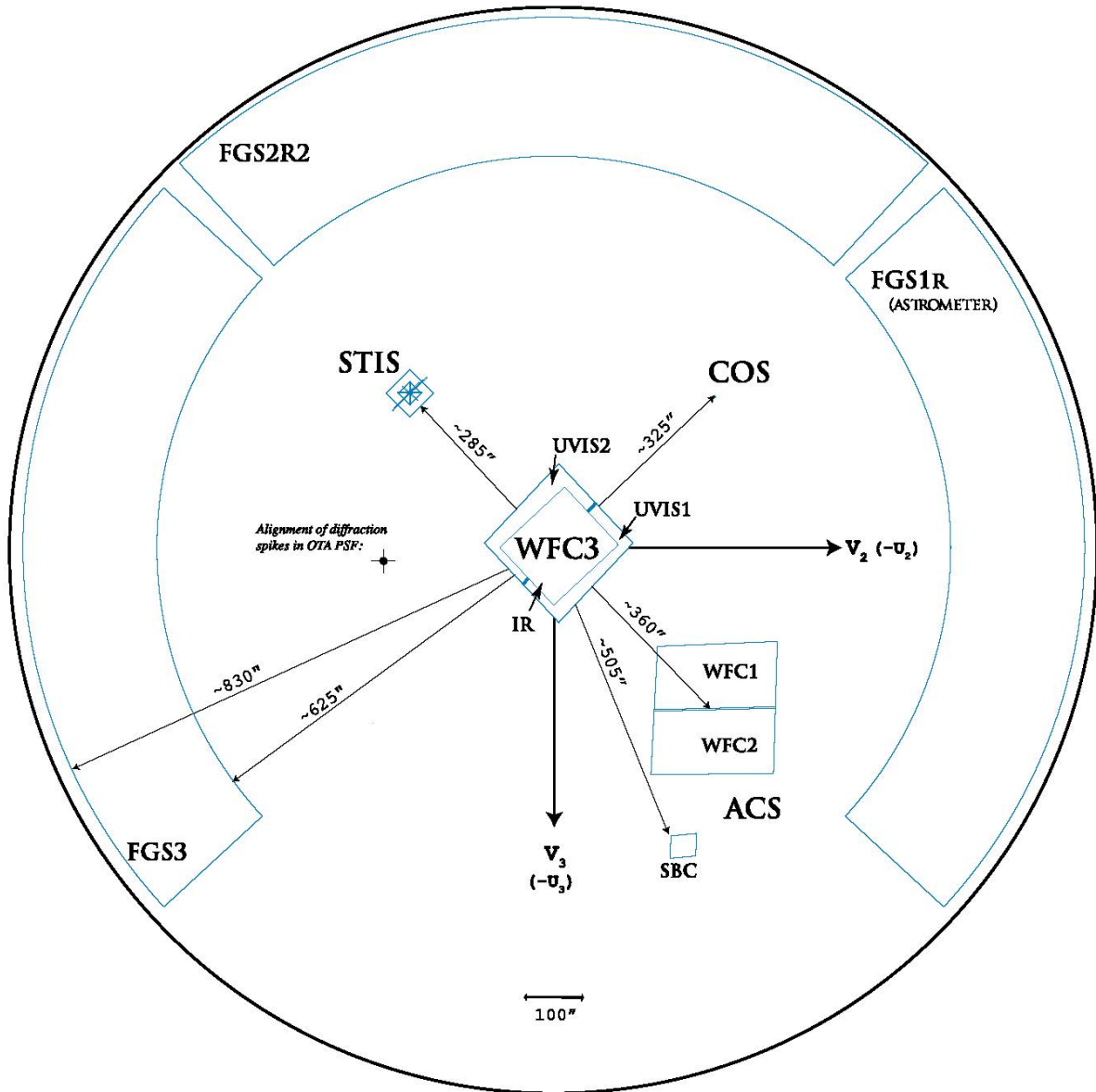


The actual incoming OTA beam direction is into the page and then reflected by the POM into the instrument. Yellow indicates light from the OTA, which is sent into the camera by the pick-off mirror. The Channel Select Mechanism then either allows light to pass into the UVIS channel (blue path), or directs light into the IR channel (red path). Mechanisms and optics in both channels allow for focus and alignment, and correct for the OTA spherical aberration. Filters and grisms are contained in the UVIS SOFA and the IR FSM. The UVIS channel has a mechanical shutter, while the IR channel is shuttered electronically by the detector. Light is detected by either the UVIS CCDs or the IR focal-plane array. A separate subsystem provides flat-field illumination for both channels.

2.2 Field of View and Geometric Distortions

WFC3 replaces WFPC2, *Hubble's* first large-area camera that included corrections for the spherical aberration of the *HST* primary mirror. The appearance of the *HST* focal plane following SM4 is shown in [Figure 2.2](#).

Figure 2.2: The *HST* focal-plane layout, showing the instrument complement following SM4.



Although the WFC3 IR and UVIS detectors appear co-aligned in this figure, IR alignment activities have confirmed that the two detector centers are actually offset by 4.8 arcsec. The diameter of the outer black circle, projected onto the sky, is about 28 arcminutes.

WFC3 images are subject to significant geometric distortions. These result primarily from the tilt of the focal plane relative to the optical axis (required for constant focus across the detectors; see [Figure 2.1](#)), which leads to a modest elongation of the field of view in both channels. In the UVIS detector, most of the distortion runs approximately parallel to the diagonal direction of the CCD, while in the IR channel the distortion is parallel to the sides of the detector. As a result, the UVIS field projected onto the sky is shaped like a rhombus, with an acute angle between the x- and y-axes of the detector of approximately 86.1°. The IR channel projected onto the sky is rectangular, with an aspect ratio of about 0.90. Individual pixels projected onto the sky have the same geometry; thus the UVIS pixels are rhombooidal, measuring 0.0395 arcsec on each side, while the IR pixels are rectangular, measuring 0.135×0.121 arcsec.

For further discussion of geometric distortions in WFC3, see [Appendix B](#).

2.3 Spectral Elements

- [2.3.1 The Filter Selection Process](#)
- [2.3.2 Filter and Grism Summaries](#)
- [2.3.3 Shutter Mechanism](#)

2.3.1 The Filter Selection Process

Both WFC3 channels are equipped with a broad selection of spectral elements. These elements were chosen on recommendation of the WFC3 SOC, following a lengthy process with wide scientific and community input. Initial community suggestions and advice were considered at the WFC3 Filter Selection Workshop, held at STScI on July 14, 1999. Other input came from the [WFC3 Science White Paper](#) (see [Section 1.3](#)), from a suite of SOC-developed test proposals representing a broad range of current astronomical investigations, and from statistics of historical filter use in previous *HST* imaging instruments. The filter sets were chosen to fully cover the wavelength regimes of both WFC3 channels with a range of bandwidths, while complementing the filter sets available in ACS and NICMOS.

Based upon the SOC recommendations, the WFC3 IPT (see [Section 1.2](#)) developed detailed specifications for the vendors who designed and manufactured the filters. The final flight spectral elements were fully characterized, evaluated by the IPT and SOC, approved for flight, and installed into the filter wheels.

2.3.2 Filter and Grism Summaries

The UVIS channel has a selectable optical filter assembly (SOFA) that contains a stack of 12 filter wheels housing a total of 48 elements: 42 full-frame filters, 5 quad filters, and 1 UV grism. Each wheel also has an open, or empty, slot. For UVIS observations, the appropriate wheel is rotated to place the chosen filter into the light path, and the other eleven wheels are rotated to place the open slot in the light path. Only a single filter can be used at a time. Since the simultaneous insertion of two filters would result in significant defocus, the ground system does not provide the capability of crossing two filters.

The IR channel has a single filter wheel (FSM, or Filter Select Mechanism) housing 17 elements: 15 filters and 2 grisms; an 18th slot contains an opaque element (or BLANK). For IR observations, the requested single element is rotated into the light beam. The FSM is a bidirectional wheel and always takes the shortest path to a new filter position. The filter wheel and all of its filters are housed, along with the HgCdTe detector package, in a cold shroud maintained at -30°C, a thermally-isolated enclosure which reduces the thermal loads and background emission onto the detector.

The filter sets in both channels include wide-, medium-, and narrow-band filters, as well as low-dispersion grisms (one in the UVIS channel, two in the IR channel) for slitless spectroscopy. The wide- and medium-band filters include popular passbands used in extragalactic, stellar, and solar-system astronomy, as well as passbands similar to those already used in other *HST* instruments for photometric consistency and continuity. The classical *UBVRJH*, Strömgren, and Washington systems are reproduced, along with the filters of the Sloan Digital Sky Survey (SDSS). In addition, several extremely wide-band filters have been included in both channels, for ultra-deep imaging.

There are also a total of 36 different narrow-band passbands in the UVIS channel, consisting of 16 full-field filters and 5 quad filters. Quad filters are 2×2 mosaics occupying a single filter slot; each one provides four different bandpasses, at the cost of each one covering only about 1/6 of the field of view. The narrow-band filters provide the capability for high-resolution emission-line imaging in many of the astrophysically important transitions, as well as the methane absorption bands seen in planets, cool stars, and brown dwarfs.

In addition to the wide-band filters, the IR channel includes six narrow-band filters, which likewise sample the most important planetary, stellar, and nebular spectral features in the near-IR.

Finally, wide-band filters with similar wavelength coverages to those of the grism dispersers are available. These allow direct images in the same spectral ranges covered by the grisms. They are used to accurately identify spectroscopic sources and for wavelength calibration. WFC3 contains no ramp filters or polarizers, unlike ACS or WFPC2.

Tables 6.2 and 7.2 provide a complete summary of the filters available for imaging with the UVIS and IR channels, respectively. Individual filter transmission curves as well as filter+WFC3+*HST* system throughput curves are presented in Appendix A. Graphical representations of the UVIS and IR filter wheels are shown in Figures 2.3, 2.4, and 3.2 shows the overall integrated system throughputs of WFC3 compared to other instruments.

Figure 2.3: UVIS Filter Wheels

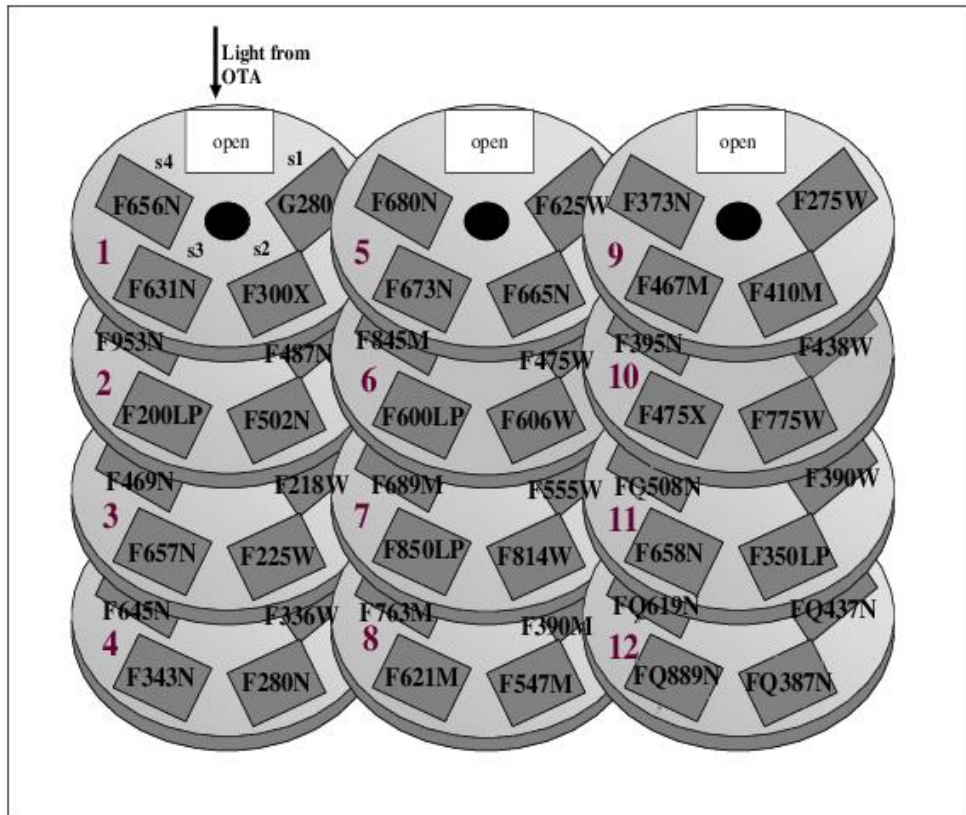
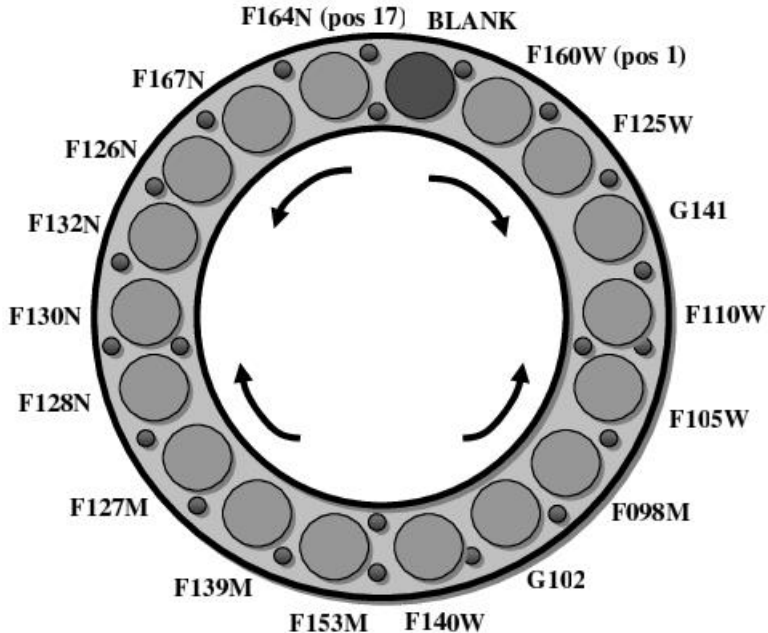


Figure 2.4: IR Filter Wheel



2.3.3 Shutter Mechanism

Integration times in the UVIS channel are controlled via a mechanical shutter blade very similar in design to the ACS/WFC shutter. Sitting directly behind the SOFA, the WFC3 UVIS shutter is a rotating disk about 12 inches in diameter; it is divided into four 90° quadrants, with alternating quadrants providing the blocking (i.e., there are two open and two closed positions). When the shutter is in the closed position initially, a commanded move of 90° places it into an open configuration; at the end of the exposure, another move of 90° places the shutter back into a closed position. Although the shutter can be operated in either a clockwise or counterclockwise direction, the current flight software always moves the blade in the same direction.

For very short exposure times in the UVIS channel, there are minor issues with exposure time non-uniformity ([Section 6.7.1](#)) and blurring due to shutter-induced vibration ([Section 6.11.4](#)).

There is no mechanical shutter in the IR channel; instead, the detector provides electronic shuttering. Dark-current measurements are obtained by using the BLANK, an opaque blocker in the filter wheel, which also is used to prevent the detector from viewing the Earth during occultations.

2.4 Detector Read-Out Modes and Dithering

The detectors in both channels offer subarray readout capability; see [Section 6.4.4](#) (UVIS) and [Section 7.4.4](#) (IR) for full details. The UVIS channel also allows 2×2 and 3×3 on-chip binning of full-frame images. Finally, a variety of dithering patterns can be requested using the Astronomer’s Proposal Tool ([APT](#)) software. Predefined patterns have been established to address common requirements, such as sub-pixel dithering to improve PSF sampling or dithering to achieve large areal coverage while also sampling the inter-chip gap ([Appendix C](#)). The post-observation pipeline software (see [Appendix E](#), the [WFC3 Data Handbook](#), and the [AstroDrizzle](#) documentation) carries out appropriate calibration of data taken in all of these configurations, and offers the option of reconstructing dithered images with a drizzling algorithm. A combination of software packages in [DrizzlePac](#) can be used to optimize the drizzling of images. If the dither pattern incorporates non-integer pixel offsets, it can effectively improve the sampling of the point-spread function (PSF). The software can also handle mosaicked images according to a set of rules or associations, rectifying them onto a cartesian pixel coordinate system.

Chapter 3: Choosing the Optimum HST Instrument

Chapter Contents

- [3.1 Overview](#)
- [3.2 Choosing Between Instruments](#)
- [3.3 Comparison of WFC3 with Other HST Imaging Instruments](#)

3.1 Overview

This chapter addresses the general questions that arise when observers choose between proposing to use WFC3 or one or more of the other imaging instruments that are available on *HST*. Following SM4, the observatory is at its highest level of capability: new instruments have been installed, and both STIS and ACS/WFC have been repaired.

In choosing between instruments for their particular projects, observers should carefully evaluate the capabilities of WFC3 and compare them to those of the other *HST* instruments, in the context of their own scientific goals. There is some intentional redundancy between WFC3, ACS, STIS, and COS to provide a degree of protection against degradation or failure of the instruments. However, the instruments largely complement one another, and therefore it is likely that one instrument will be preferred for any science program. Therefore, observers do need to give careful consideration to instrument capabilities in order to optimize their observations. They should refer to the [*HST Call for Proposals*](#) for any policy issues, and the [*HST Primer*](#) for additional comparison information.

3.2 Choosing Between Instruments

The primary factors to consider in choosing the preferred instrument are areal coverage, spatial resolution, wavelength coverage, sensitivity, and availability of specific spectral elements. [Table 3.1](#) lists the primary characteristics of the imaging instruments currently available on *HST*.

For some research programs, the instrument choice may be dictated by the need for a particular spectral element. In this regard, WFC3 offers considerable capability because of its broad complement of wide-, medium-, and narrow-band filters both at UV/optical and near-IR wavelengths, as well as one UV grism and two near-IR grisms for slitless spectroscopy.

For studies at optical wavelengths, the trade-offs to consider when deciding between WFC3/UVIS and ACS/WFC include pixel size, field of view and, to some extent, throughput. WFC3 is generally preferable when angular resolution has higher priority than field of view, because of its finer pixel size. On the other hand, ACS/WFC has higher throughput than WFC3 /UVIS at wavelengths longward of ~400 nm (see [Figure 3.2](#)), and hence may be the best choice when the highest possible sensitivity at such wavelengths is crucial. However, considerations of degraded charge transfer efficiency (CTE) should be kept in mind, since ACS has endured the high-radiation space environment for more than seven years longer than has WFC3.

At UV wavelengths, WFC3/UVIS is the only imager on *HST* to offer a large field of view combined with high throughput. However, its spectral coverage does not extend shortward of 200 nm, whereas ACS/SBC and STIS/FUV-MAMA both reach down to 115 nm (STIS/NUV-MAMA reaches 160 nm), and also offer finer spatial sampling (see [Section 3.3.3](#)). Thus, WFC3 will be the choice whenever both large field of view and coverage down to 200 nm are required (e.g., multi-wavelength surveys). However, if observations at extreme far-UV wavelengths are necessary, or if the highest available spatial sampling at UV wavelengths is a primary requirement, then ACS/SBC or the STIS UV channels should be considered. Because ACS/HRC could not be repaired during SM4, WFC3 offers imaging at the finest pixel scale of any *HST* instrument at optical wavelengths.

Table 3.1: Comparison of wavelength coverage, pixel scales, and fields of view of *HST*'s imaging instruments.

Instrument	Wavelength coverage (nm)	Pixel size (arcsec)	Field of View (arcsec)
WFC3 UVIS	200 – 1000	0.04	162 × 162
ACS WFC	370 – 1100	0.05	202 × 202
ACS SBC	115 – 170	0.032	34 × 31
STIS FUV-MAMA	115 – 170	0.024	25 × 25
STIS NUV-MAMA	165 – 310	0.024	25 × 25
STIS CCD	250 – 1100	0.05	52 × 52
WFC3 IR	800 – 1700	0.13	136 × 123

3.3 Comparison of WFC3 with Other HST Imaging Instruments

- [3.3.1 Wavelength Coverage](#)
- [3.3.2 Field of View](#)
- [3.3.3 Detector Performance](#)
- [3.3.4 System Throughputs and Discovery Efficiencies](#)

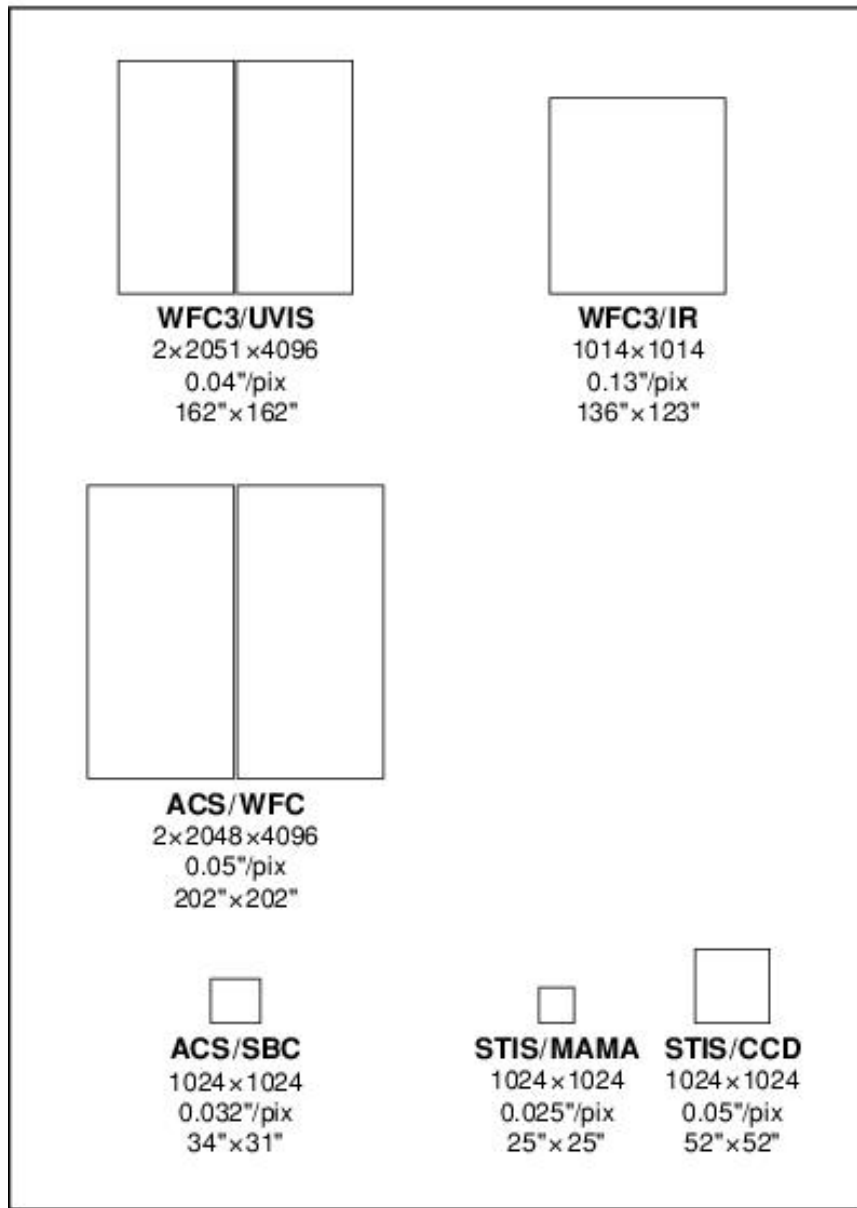
3.3.1 Wavelength Coverage

The WFC3 UVIS channel is similar in design to the Wide Field Channel (WFC) of the ACS. There are, however, a few differences. While ACS/WFC is blind at wavelengths shorter than about 370 nm (i.e., shortward of the *B* band), WFC3/UVIS has excellent sensitivity extending down to 200 nm. The design trade-offs adopted to achieve this extended UV wavelength coverage (primarily the CCD coating and the use of aluminum coatings for the reflective optics) lead to a reduced sensitivity of WFC3 at longer optical wavelengths compared to that of ACS/WFC. WFC3/UVIS has no sensitivity in the far-UV region below 200 nm. The far-UV is covered by three MAMA detectors in ACS and STIS.

3.3.2 Field of View

Figure 3.1 illustrates the fields of view, at the same scale, for all of the *HST* imaging instruments currently available on *HST*.

Figure 3.1: Schematic diagram comparing relative sizes of the fields of view for all available *HST* imaging instruments. Successive lines of text underneath each field of view give the field size in pixels, the pixel scale in arcsec/pixel, and the field size in arcsec. Detector footprints are rendered as rectangular in the diagram and thus do not include the effects of geometric distortion. For a more accurate depiction of detector footprints including geometric distortions and relative *HST* focal plane locations, see [Figure 2.2](#).



The pixel scale of the WFC3 UVIS channel is 20% finer in comparison to the ACS/WFC, obtained at the cost of covering only about 66% of the area of the ACS field of view.

[Table 3.1](#) presents a comparison of the wavelength coverage, pixel scale, and field of view of WFC3 and of the other *HST* imaging instruments that are currently available.

3.3.3 Detector Performance

Table 3.2 summarizes the on-orbit measurements of read-out noise and dark current for the WFC3 detectors, and compares them with the parameters for the other currently available *HST* imaging detectors. [Chapter 5](#) gives more detailed information about the detectors in both channels. [Chapter 9](#) discusses sensitivities, limiting magnitudes, and exposure times.

Table 3.2: Characteristics of *HST* CCD and HgCdTe imaging detectors currently available.

Detector	Read-out noise (e ⁻ rms)	Dark current (e ⁻ /pix/s)	Mean well Depth (e ⁻)
WFC3/UVIS	3.1–3.2	0.0020	63,000–72,000
ACS/WFC	4.8	0.0062	84,700
STIS/CCD	5.4 (gain=1), 7.7 (gain=4)	0.009	114,000
WFC3/IR	~12.0 ¹	0.05	77,900

¹ WFC3/IR read noise is for a 16-read linear fit. WFC3/IR double sampling read noise is 20.2–21.4 e⁻.

3.3.4 System Throughputs and Discovery Efficiencies

Figure 3.2 plots the measured on-orbit system throughputs of the two WFC3 channels as functions of wavelength, compared to those of ACS, NICMOS, and WFPC2. These curves include the throughput of the OTA, all of the optical elements of the instruments themselves, and the sensitivities of the detectors. Throughputs were calculated at the central wavelength (the “pivot wavelength”; see ³ to [Table 6.2](#)) of each wide-band filter of each instrument.

As [Figure 3.2](#) shows, WFC3 offers a unique combination of high sensitivity and wide spectral coverage ranging from the UV to the near-IR. WFC3 extends and complements, over a large field of view, the optical performance of ACS/WFC at wavelengths shorter than ~400 nm and longer than 1000 nm. The good degree of functional redundancy with ACS will help ensure that the unique scientific capabilities of *HST*, at optical wavelengths, will remain available until the end of its mission.

Another quantity that is useful when comparing different instruments, especially in the context of wide-angle surveys, is the “discovery efficiency,” defined as system throughput times area of the field of view as projected onto the sky. In [Figure 3.3](#) we plot the discovery efficiencies of the *HST* imaging instruments, again vs. wavelength. Note that the y-axis is now logarithmic. This figure dramatically illustrates the enormous gains that WFC3 offers, compared to current *HST* instruments, both in the optical/UV below 400 nm, and in the near-IR.

Finally, we present WFC3’s strengths by including detector noise and thus showing how its efficiency, wide wavelength coverage, and large field of view apply to general problems: the limiting point-source magnitude reached in 10 hours of

observing time ([Figure 3.4](#)); and the time needed to survey a sky area about 9 times larger than the Hubble Ultra Deep Field, to a limiting ABMAG of 26 ([Figure 3.5](#)).

Figure 3.2: System throughputs of optical/infrared imaging instruments on *HST* as functions of wavelength. The plotted quantities are end-to-end throughputs, including filter transmissions, calculated at the pivot wavelength of each wide-band filter of each camera.

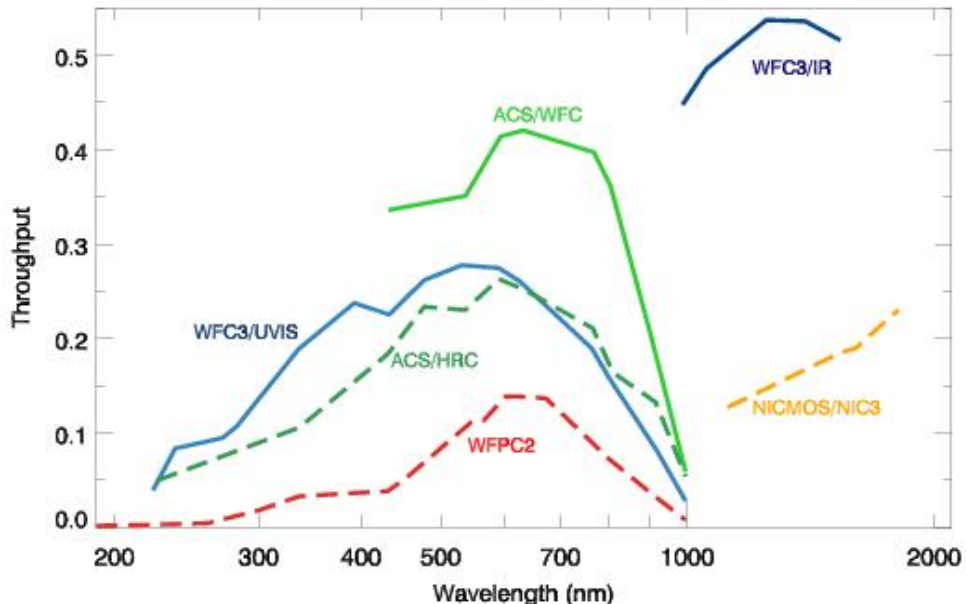


Figure 3.3: Discovery efficiencies of optical/infrared *HST* imaging instruments, including those verified on-orbit for WFC3. Discovery efficiency is defined as the system throughput (plotted in Figure 3.2) multiplied by the area of the field of view. Note that the y-axis is now logarithmic.

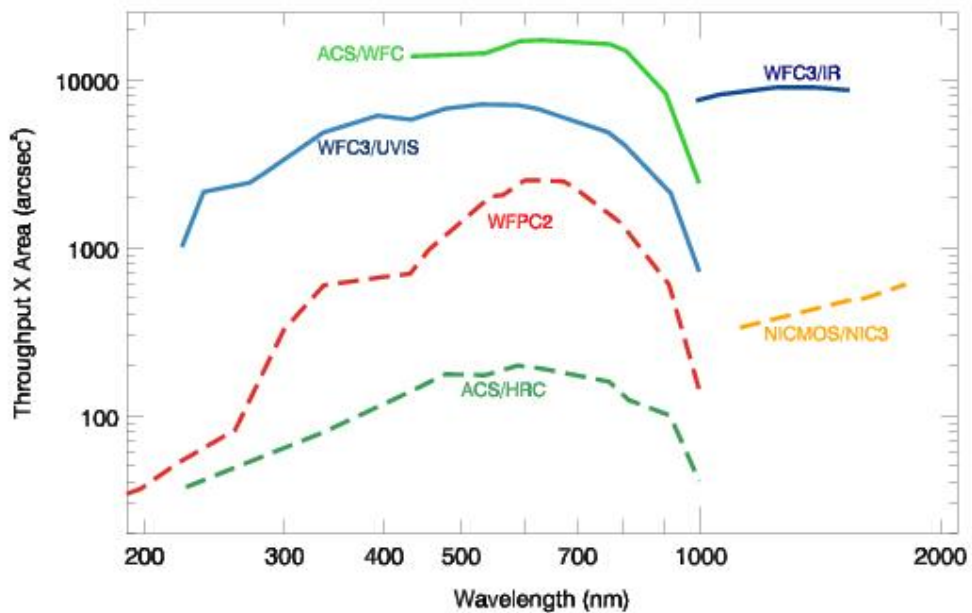


Figure 3.4: Limiting point-source magnitudes reached by optical/infrared *HST* imaging instruments in 10 hours. (WFC3/UVIS performance has declined slightly from the early on-orbit level shown here due to increasing CTE losses.)

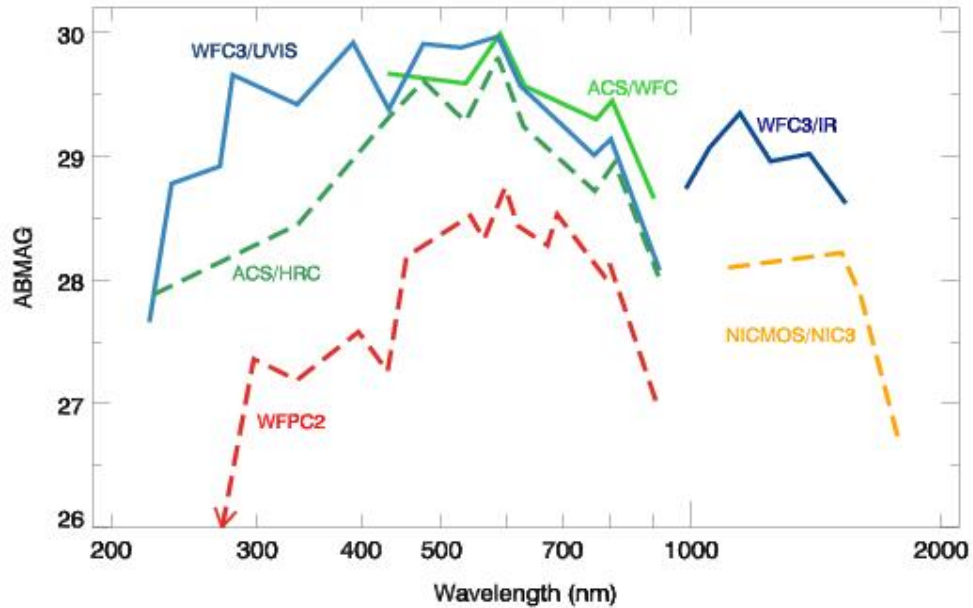
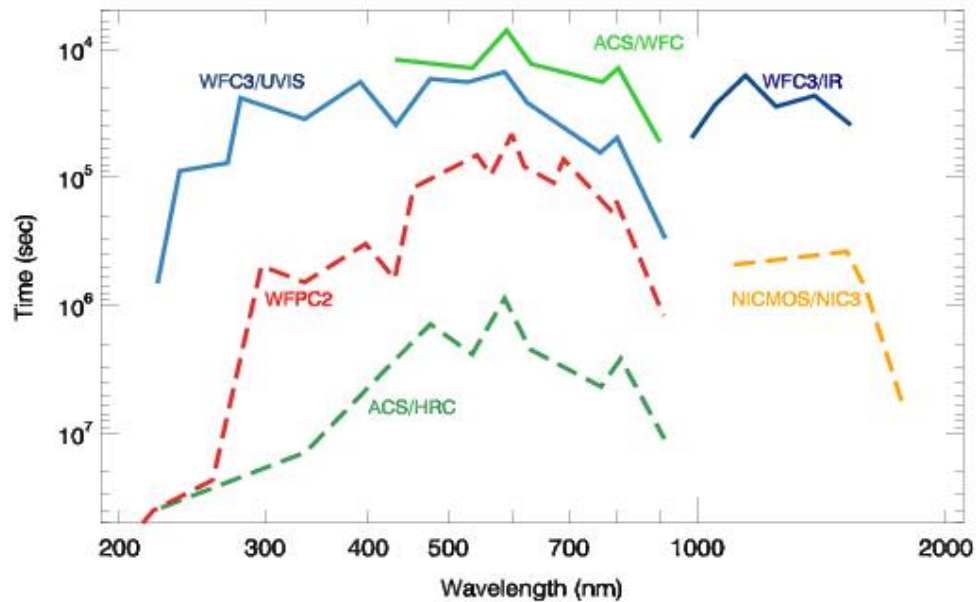


Figure 3.5: Time needed for optical/infrared *HST* imaging instruments to survey a wide sky area to a limiting extended (1 arcsec^2) ABMAG of 26. (WFC3/UVIS performance has declined slightly from the early on-orbit level shown here due to increasing CTE losses.)



Chapter 4: Designing a Phase I WFC3 Proposal

Chapter Contents

- [4.1 Phase I and Phase II Proposals](#)
- [4.2 Preparing a Phase I Proposal](#)

4.1 Phase I and Phase II Proposals

The first steps in preparing an *HST* program are to establish a set of science goals and to explore whether *HST* can be used to achieve those science goals (using the information provided in the *HST Call for Proposals*, the *HST Primer* and the instrument handbooks). Once an observer has decided that *HST* can achieve the science goals, they must prepare a formal proposal.

In this Chapter we give an overview of the steps that are taken in preparing an *HST* observing proposal that involves WFC3 observations. “**Phase I**” refers to the initial proposal that is reviewed by the Telescope Allocation Committee (TAC). The Phase I proposal presents the scientific justification for the project, lists the targets to be observed and the instrument(s) and spectral elements to be used, and includes a request for a specific number of spacecraft orbits. (See the *HST Call for Proposals* and *HST Primer* for a full discussion of all policy issues and additional guidance.)

The Phase I proposal does not contain many of the details that are actually required to carry out observations with *HST*. These are included in a “**Phase II**” proposal that will be needed if and after the proposal is recommended by the TAC and approved by the STScI Director. The *Phase II Proposal Instructions* are a vital resource at that time.

The actual submission of proposals in both Phase I and Phase II is accomplished using the **Astronomer’s Proposal Tool (APT)**; see <http://apt.stsci.edu>.

This Chapter focuses on the steps for assembling the information needed to prepare a Phase I WFC3 proposal for submission using APT.

4.2 Preparing a Phase I Proposal

- [4.2.1 Which WFC3 Channel\(s\) and Filter\(s\)?](#)
- [4.2.2 What Exposure Times?](#)
- [4.2.3 What Aperture or Subarray?](#)
- [4.2.4 What Overheads and How Many HST Orbits?](#)
- [4.2.5 Any Special Calibration Observations?](#)
- [4.2.6 What is the Total Orbit Request?](#)

An *HST* program is a set of exposures specified so as to achieve one or more scientific objectives. We can break down the development of a WFC3 observing program, imaging and/or spectroscopic, into a six-step process. Often there is not a unique way in which to achieve the scientific objectives, and you must assess the trade-offs and feasibilities of multiple approaches. Furthermore, you will wish to use *HST* and WFC3 efficiently, in order to obtain as much science within as small an orbit allocation as possible. Therefore, you may need to iterate these steps in order to achieve a final feasible program that is also optimal.

In this chapter we introduce issues that you may need to consider in designing your observations. Later chapters in this *Handbook* will present detailed information for your use. These six steps, and the considerations they entail, are described in the following subsections.

4.2.1 Which WFC3 Channel(s) and Filter(s)?

First, from your science requirements, determine the desired wavelength(s) of observation. Those requirements may include considerations of the spectral energy distribution (SED) of the target, or the required angular resolution, which also varies as a function of wavelength. Typically, if the wavelength of observation is less than 900 nm, then the WFC3 UVIS channel will be used; or if the wavelength is greater than 900 nm, then the WFC3 IR channel will be used. Your program may involve use of both channels.

The angular resolution, field of view, and sensitivity of the two channels differ appreciably, and may also influence your selection of the WFC3 channel(s) to use (see [Chapter 2](#) for an overview of the UVIS and IR channels). Features of interest in the target's SED can be matched to the spectral resolution of the observation by selecting appropriate filters (see [Chapter 6](#) for the UVIS channel, [Chapter 7](#) for the IR channel, and [Appendix A](#) for detailed filter passbands), or grisms (see [Chapter 8](#)).

To match continuum features, wide-, medium-, and/or narrow-band filters may be selected, presenting the possibility of a trade-off between detector signal and spectral resolution. Note that the UVIS quad filters limit the field of view to about one sixth of the full field.

4.2.2 What Exposure Times?

Second, you should determine the exposure time and exposure sequences needed to achieve the required signal-to-noise (S/N) with the chosen filter(s) or grism(s). A full discussion of exposure time calculation is presented in [Chapter 9](#), but, as mentioned in that chapter, in most cases you will use the online [Exposure Time Calculator \(ETC\)](#). The S/N depends upon the target's incident flux and the noise from the background and detector sources. These sources include zodiacal light, detector dark current, and stray light from both Earth and bright targets in the field of view.

Having determined the basic exposure time necessary to achieve the required S/N, you will in most cases find it necessary to achieve that total exposure time through a sequence of shorter exposures. For instance, if the exposure time is greater than the maximum orbital target visibility, it will be necessary to obtain a sequence of exposures. UVIS exposures exceeding 3,600 s require more than one exposure as do IR exposures greater than 2,800 s (see [Chapter 6](#) and [Chapter 7](#) for a fuller discussion).

Additional reasons to structure the total exposure time are described in the following paragraphs, as well as considerations peculiar to each of the two WFC3 channels.

Dithering and Mosaicking

A sequence of exposures obtained in a dither pattern of *HST* pointings will often be used to reduce the noise from flat-field calibration error, cosmic rays, and residual images. Including sub-pixel displacements in the dither pattern will allow better sampling of the point-spread function (PSF). You may design and specify a dither pattern, or use one of the pre-defined patterns already designed to sub-sample the PSF, to cover the UVIS inter-chip gap, or to mosaic a large field. The pre-defined sequences and information on designing your own patterns, are presented in [Appendix C](#) of this Handbook and in the [Phase II Proposal Instructions](#).

Bright Targets

For bright targets, a sequence of shorter exposures may be needed to avoid entering the non-linear or saturation regimes of the detectors (see Chapters 5, 6, and 7).

Bright objects do not cause safety concerns for either UVIS or IR observations with WFC3. Image persistence can be a concern for IR observations (as discussed in [Section 7.9.4](#) and [Appendix D](#)) but is not a problem with the UVIS channel.

UVIS Exposures

For UVIS observations, it will almost always be desirable to use multiple exposures to remove cosmic-ray impacts. Dithering is generally preferable to CR-SPLIT for the reasons discussed above under Dithering and Mosaicking. For observations with the UVIS channel of faint targets on low levels of background emission, the effects of charge transfer efficiency (CTE) during readout of the detector must be considered (see Sections [5.4.11](#) and [6.9](#)). Post-flash, implemented for Cycle 20, can greatly reduce CTE losses.

IR Exposures

For observations with the IR channel you must choose a readout method from the 12 available sample sequences, each of which may comprise from 1 to 15 non-destructive readouts. These include RAPID (linear), SPARS (linear), and STEP (linear-log-linear) sequences (see [Chapter 7](#)). The exposure time is dictated by the sequence chosen. The ability to remove cosmic-ray impacts will depend upon the sequence chosen.

4.2.3 What Aperture or Subarray?

Next, from considerations of the target's angular size and structure, and of data volume, you should determine the WFC3 aperture or subarray you will use. The available UVIS apertures and subarrays are presented in [Chapter 6](#), and those for the IR channel in [Chapter 7](#).

In some cases, correct placement of an extended target within an aperture may require you to specify a special *HST* pointing and possibly the orientation of the field of view (which is determined by the spacecraft roll angle). Additional considerations may include detector imperfections such as the UVIS inter-chip gap ([Chapter 5](#)), diffraction spikes ([Chapters 6 & 7](#)), filter ghost images (see [Chapters 6 & 7](#)), detector saturation (i.e., for bleeding in a UVIS image along a detector column; [Chapter 5](#)), detector charge transfer ([Chapter 5](#)), distortion of the image ([Appendix B](#)), or dispersion direction of the grism (see [Chapter 8](#)). However, most of these only need to be considered at the Phase II stage, unless they affect the number of orbits needed for the proposal.

Note that selection of a WFC3 aperture without specifying further constraints implicitly specifies: (1) the full image will be read out; (2) the target coordinates will be placed at a default location on the detector (see [Chapters 6 & 7](#); generally the target will be placed at the center of the chosen field of view); and (3) the telescope roll angle will be unspecified, as it will depend on the date the exposure is executed. You may override any of these defaults, however.

You can reduce the size of the image read out and thus the volume of data obtained by selecting a subarray. For the UVIS detector, on-chip binning of the pixels will also reduce the data volume, but at the expense of angular resolution (see [Chapters 5 & 6](#)). Reducing the data volume will reduce the overhead to read out and transfer images, which may be desirable in order to allow more images of the target of interest to be obtained during an *HST* orbit. During Phase II preparation, the location of the target can be specified with the POS TARG Special Requirement and the rotation of the image can be specified with the ORIENT Special Requirement (see [Chapters 6 & 7](#)). See Section 7.2.2 of the [Phase II Proposal Instructions](#), which gives detailed information on the relationship between detector coordinates, spacecraft coordinates, and ORIENT.

4.2.4 What Overheads and How Many *HST* Orbits?

Fourth, determine the overhead times required, in addition to the exposure times, in order to operate the spacecraft and the camera (see [Chapter 10](#)).

The spacecraft overhead includes the time needed for guide-star acquisition or re-acquisition at the beginning of each orbit. The camera overheads include time needed to change filters, change between the UVIS and IR channels, read out the exposure to the WFC3 data buffer, and transfer the images from the buffer to the *HST* science data storage. Note that overheads are especially severe for sequences of short exposures, but these can sometimes be mitigated by using small subarrays or by alternating short and long exposures. For Phase II proposals, the APT provides tools for detailed modeling of complete observation sequences.

Finally, you will add the overhead times to the exposure times to find the total time needed for your program, which is what you will request in your Phase I proposal.

This total time is expressed as the (integer) number of *HST* orbits required to obtain the observations.

4.2.5 Any Special Calibration Observations?

Most observers will not need to worry about special calibration observations. As a result of ground based and SMOV testing, WFC3 is fairly well-characterized as described in this Handbook and in more detail in [WFC3 Instrument Science Reports](#). Instrument characterization and calibration will be maintained and improved as part of the ongoing calibration program conducted by STScI ([Appendix E](#)).

The main reasons an observer would need to consider special observations are situations where a program requires greater precision than is provided through the standard calibration program. These additional observations must be justified in your Phase I proposal submission, and the orbits required to carry out the special observations must be included in the overall orbit allocation requested. Proposers are advised to discuss their need for special observations with the [helpdesk](#).

4.2.6 What is the Total Orbit Request?

Having determined the content of the science and supporting observations necessary to achieve your scientific objectives, you must finally determine the total amount of *HST* time to carry out those activities by including the appropriate amount of time for spacecraft and instrument overheads.

Detailed procedures for determining the total amount of time to request in your Phase I proposal are presented in [Chapter 10](#).

Chapter 5: WFC3 Detector Characteristics and Performance

Chapter Contents

- [5.1 Overview of this Chapter](#)
- [5.2 The WFC3 UVIS Channel CCD Detectors](#)
- [5.3 WFC3 CCD Readout Formats](#)
- [5.4 WFC3 CCD Characteristics and Performance](#)
- [5.5 The WFC3 IR Channel Detector](#)
- [5.6 WFC3 IR Readout Formats](#)
- [5.7 IR Detector Characteristics and Performance](#)

5.1 Overview of this Chapter

The science return on any data can typically be enhanced if observers acquire a basic understanding of how the detectors operate, and of their individual characteristics and limitations. For the most demanding observations, such as imaging very faint or extremely bright sources, or for exposures using non-default parameters, an even deeper understanding of the detectors and their operation may be required. This chapter aims to provide both basic and in-depth information on the detectors used in both WFC3 channels. Sections 5.2-5.4 discuss the CCD detectors used in the UVIS channel, and Sections 5.5-5.7 discuss the infrared detector used in the IR channel.

Table 5.1 summarizes the basic characteristics of the flight CCD and IR detectors. For the CCDs, the information is either an average for the two chips, or the range of values for both of them. Results are based on ground measurements as well as on-orbit data acquired during 2009 and 2010 after WFC3 was installed in *HST*.

Table 5.1: WFC3 Detector Characteristics

Characteristic	UVIS Channel CCDs	IR Channel Detector
Architecture	e2v CCD detectors. Thinned, backside illuminated, UV optimized, multi-phase pinned, buried/mini-channel, charge injection capability.	Teledyne HgCdTe infrared detector. MBE-grown, substrate removed, on Si CMOS Hawaii-1R multiplexer.
Wavelength Range	200 to 1000 nm	800 to 1700 nm
Pixel Format	2 butted 2051×4096 , 31-pixel gap (1.2")	1024×1024 (1014 \times 1014 active)
Pixel Size	$15 \mu\text{m} \times 15 \mu\text{m}$	$18 \mu\text{m} \times 18 \mu\text{m}$
Plate Scale	0.040"/pixel	0.13"/pixel
Field of View on Sky	Rhomboidal, $162'' \times 162''$	Rectangular, $136'' \times 123''$
Quantum Efficiency	50-59% @ 250 nm ¹ 68-69% @ 600 nm 47-52% @ 800 nm	77% @ 1000 nm 79% @ 1400 nm 79% @ 1650 nm
Dark Count	$\sim 9 \text{ e}^-/\text{hr/pixel}$ (median, projected to May 2019)	$0.048 \text{ e}^-/\text{s/pixel}$ (median)
Readout Noise	3.1-3.2 e^-	20.2-21.4 e^- (pair of reads) 12.0 e^- (16-read linear fit)
Full Well ²	63,000-72,000 e^-	77,900 e^- (mean saturation level)
Gain	$1.55 \text{ e}^-/\text{DN}$	$2.3 \text{ e}^-/\text{DN}$

ADC Maximum	65,535 DN	65,535 DN
Operating Temperature	-83°C	145 K

¹Quantum efficiency at 250 nm does not include multiple-electron events, which lead to larger apparent efficiency in e.g., [Figure 5.2](#).

²The IR full well value is based on fully-integrated instrument ground testing. Other CCD and IR parameters are derived from on-orbit data.

5.2 The WFC3 UVIS Channel CCD Detectors

5.2.1 Basics of CCD Operation

5.2.2 The WFC3 CCDs

5.2.1 Basics of CCD Operation

A charge-coupled device (CCD) is a silicon-based detector containing a two-dimensional array of summing wells called pixels, short for pixel elements. Each pixel accumulates electric charge in proportion to the number of photons striking that location on the detector. Physically, the summing wells are created by electric fields established at the depletion (charge-free) regions of the Si-SiO₂ metal-oxide-semiconductor (MOS) capacitors. In a typical three-phase CCD, the size of the depletion region is controlled by the voltage of three gates. The gates are arranged in parallel, with every third gate connected together.

At the end of an exposure, the voltages of the gates are changed with an appropriate clocking pattern, causing all charge packets to be sequentially transferred to the adjacent pixel, until they reach the readout circuitry at the detector's edge. The transfer of charges between pixels occurs in parallel, row by row, whereas the extraction of the "zeroth" row at the edge occurs along an external serial register, where each packet is serially transferred to an output amplifier at the detector corner.

5.2.2 The WFC3 CCDs

The WFC3 UVIS channel uses two CCD detectors fabricated by e2v Ltd. (formerly Marconi Applied Technologies Ltd.). Both CCDs are 2051 × 4096 devices with 15 × 15 μm square pixels. There are 2051 rows by 4096 columns, where the row/columns definition follows the convention of having the parallel direction first and the serial direction second. Having the serial register along the long (4096 pixel) edge reduces the number of transfers required to read out a charge packet.

The WFC3 CCDs are three-phase devices, thinned and back-illuminated (back-thinned) to improve the sensitivity to UV light. Thinning refers to the removal of the thick substrate on which the chip is originally built and is done to improve shorter-wavelength efficiency (only those electrons generated in the vicinity of the gate structure can be collected efficiently). Back-illumination means that photons are focussed on the back side of the chip, rather than having to pass through the opaque gate structures implanted on the front side.

Similar to ACS, the WFC3 CCDs also have buried channels and are operated in multi-pinned phase (MPP) mode. This buried channel, or mini-channel, improves CTE for targets with relatively low signal levels (~10K e⁻ or less) and reduces the dark current as well. The buried channels have the capability of injecting charges to fill in the traps and improve the CTE (but observers should see [Section 6.9.2](#)). Further details of these features are given in [Section 5.4.8](#).

The two WFC3 CCDs are butted together along their long dimension to create a 2×1 mosaic. [Figure 5.1](#) shows a picture of a CCD assembly similar to the flight detector. The butted configuration is equivalent to a 4102×4096 array, but with a gap of 31 ± 0.1 pixels between the two chips (1.2 arcsec on the sky).

The CCDs are cooled by a four-stage thermoelectric cooler (TEC) to a nominal temperature of -83° C. The detectors are packaged inside a cold enclosure, which is nearly identical to the one used for ACS, itself a scaled-up version of the STIS design. The package includes a second cooled window to reduce the radiative heat load.

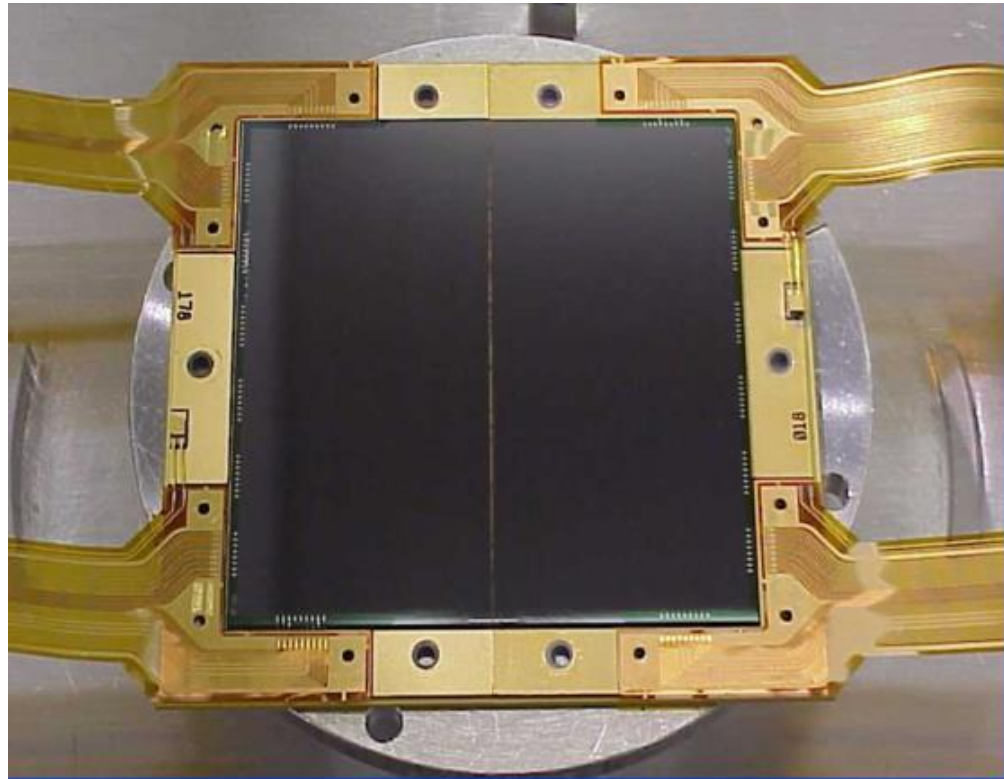
The CCD focal plane is assembled on a molybdenum (moly) base disk, which provides some shielding from cosmic rays and also serves as the thermal sink path from the hot side of the TEC stack to the heat pipes (which carry the heat to the external radiator). The “cover” with the external window is about 1 cm thick and is made of “alloy 42” steel; it provides some protection from CRs incident on the front side of the CCDs.

The WFC3 CCDs are quite similar to those used in the ACS Wide Field Channel (WFC). They have the same pixel size, nearly the same format (2051×4096 in WFC3, compared to 2048×4096 in ACS), the same orientation of the serial and parallel registers, similar technology (buried-channel, MPP operation), and nearly identical mechanical interfaces. The main differences of the WFC3 chips compared to those in ACS/WFC are:

- UV optimization of the WFC3 wavelength response
- Significantly lower readout noise for the WFC3 chips (~ $3.1\text{--}3.2\text{ e}^-$ compared to $3.9\text{--}4.6\text{ e}^-$)
- 2051 rows instead of 2048
- Charge-injection capability for mitigation of degradation in CTE due to on-orbit radiation damage (not generally available for science observations; see [Section 6.9.2](#))
- 31-pixel gap instead of 50
- Manufactured by e2V (formerly Marconi); ACS has Site devices.

An overview of the WFC3 CCD performance was given in [Table 5.1](#).

Figure 5.1: Detector package similar to the WFC3/UVIS flight detector. The size of the $4k \times 4k$ array is approximately 6×6 cm, and it consists of two butted 2051×4096 CCDs with a 31-pixel gap between them.



5.3 WFC3 CCD Readout Formats

- [5.3.1 Full-frame Readout](#)
- [5.3.2 Subarrays](#)
- [5.3.3 On-Chip Binning](#)

5.3.1 Full-frame Readout

The WFC3 UVIS channel contains two CCD chips, each of which has two readout amplifiers. The amplifiers on chip 1 are designated A and B, and those on chip 2 as C and D. Although a chip (or part of a chip) may be read out through a single amplifier, the default and fastest readout mode employs all four amplifiers simultaneously, such that each amplifier reads out half of a chip.

A full-frame UVIS exposure produces a single FITS file in which the data from each of the two chips are stored in separate image extensions, along with associated error and data quality arrays for each image. For consistency with ACS, the image data from CCD chip 2 are stored in SCI array 1 (FITS extension 1) and the image data from CCD chip 1 are stored in SCI array 2 (FITS extension 4). [Table 5.2](#) lists the chips, the associated amplifiers, and the FITS extensions of the science image data.

Each CCD chip contains 2051×4096 active pixels, but the raw images returned by the WFC3 electronics contain a larger number of pixels. This is due to the detector overscan: portions of the detector that are not exposed to light. Overscan regions are useful for characterizing detector electronics performance, and especially for measuring the bias level contained within an image. Serial overscan corresponds to a fixed number of unexposed pixels at each end of each serial shift register. Conversely, parallel overscan is generated by additional parallel shifting before or after all of the exposed rows of the detector have been read out. In principle, both serial and parallel overscan can be implemented either as physical overscan or virtual overscan. The physical overscan is a characteristic of the detector hardware, whereas virtual overscan is a software function, and the number of rows and columns of virtual overscan generated for an image is controllable via the readout timing pattern.

The WFC3 CCD overscan regions are described in more detail in [Section 6.7](#).

Table 5.2: WFC3 CCD Naming Conventions.

CCD Chip	Amplifiers	Science Image FITS File Extension	Error Array FITS File Extension	Data Quality Array FITS File Extension
1	A, B	[SCI,2]=[4]	[ERR,2]=[5]	[DQ,2]=[6]
2	C, D	[SCI,1]=[1]	[ERR,1]=[2]	[DQ,1]=[3]

5.3.2 Subarrays

The default CCD readout mode is to read all pixels of both chips, including all available overscan regions. It is also possible to restrict the readout to rectangular subarray regions. Only data from the area within the subarray are stored in buffer memory, and the rest of the image is discarded. The subarray can be chosen from several pre-defined configurations.

UVIS subarray images contain no virtual overscan data and serial physical overscan is present only if the defined subarray boundaries overlap the physical overscan columns on either end of the chips. Thus all corner subarrays contain physical overscan data, while centered subarrays do not. ([Table 6.1](#)).

Subarrays are discussed in detail in [Section 6.4.4](#).

5.3.3 On-Chip Binning

The UVIS CCDs also provide an on-chip binning capability, in which several adjacent pixels may be read out as a single pixel. The available choices are 2×2 and 3×3 on-chip binning. On-chip binning and subarrays can not be used simultaneously. See [Section 6.4.4](#) for details on the use of on-chip binning in WFC3/UVIS observations. If on-chip binning is used, the overscan geometry is complicated by the need to truncate “odd” pixels, and each half of a row must be considered separately. As a result, depending on the binning mode, some science pixels adjacent to the overscan region may be binned together with overscan data. Details are given at the end of [Section 6.7.2](#).

5.4 WFC3 CCD Characteristics and Performance

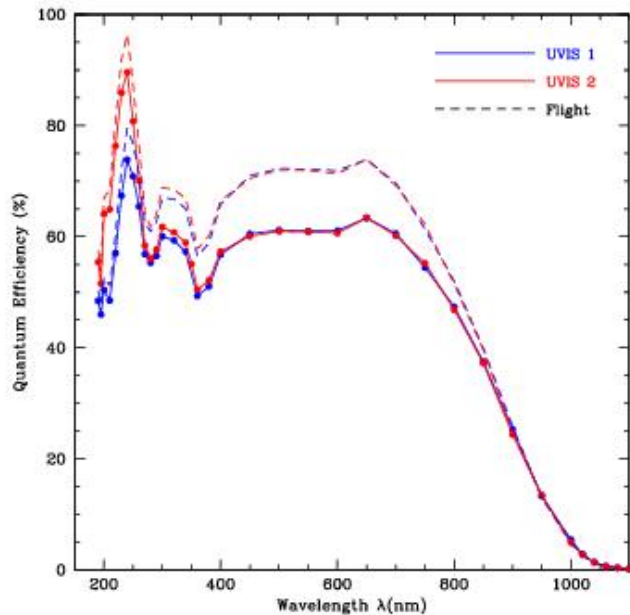
- 5.4.1 Quantum Efficiency
- 5.4.2 Multiple-Electron Events at Short Wavelengths
- 5.4.3 Flat Fields
- 5.4.4 Long-Wavelength Fringing
- 5.4.5 Linearity and Saturation
- 5.4.6 Gain
- 5.4.7 Read Noise
- 5.4.8 Dark Current
- 5.4.9 Bad Pixels
- 5.4.10 Cosmic Rays
- 5.4.11 Charge Transfer Efficiency

5.4.1 Quantum Efficiency

The quantum efficiencies (QEs) of the two WFC3 CCDs are plotted against wavelength in Figure 5.2. Here the QE is defined as electrons yielded per incident photon. The solid curves illustrate the QEs as measured at the Detector Characterization Laboratory (DCL) at Goddard Space Flight Center, slightly corrected downward by the TV3 ground tests. The plots demonstrate the high sensitivity of the CCDs in the UV down to 200 nm. On the other hand, the peak QE at ~600 nm is less than that of the ACS/WFC detectors which reach ~85% at their peaks. The QE measurements were made with the detectors perpendicular to the incident light. As installed in WFC3, the CCDs are tilted by 21 degrees with respect to the normal. The nominal change in optical thickness is ~6%, but the QE variations, as measured at the DCL on similar devices, turn out to be negligible.

The integrated system throughput of WFC3 depends on many factors including the *HST* OTA, pickoff mirror, filter transmission functions, QE, etc. Based on ground measurements of these components, the integrated system throughput was calculated and compared to the first on-orbit measurements during SMOV4. A 5 to 20% increase in the integrated system throughput was discovered, likely attributable to multiple components. The dashed curves represent the QE under the assumption that the entire flight correction is in the detector QE. For UV observations, UVIS2 achieves a higher sensitivity than UVIS1.

Figure 5.2: Quantum efficiency curves of the WFC3 UVIS1 and UVIS2 CCDs based on Goddard DCL measurements corrected (downward) by TV3 measurements (solid). The integrated system throughput of the UVIS detector was measured on-orbit to be higher than ground tests by 5–20%, and the dashed curves shows the QE under the assumption that this entire gain is due to the QE. In reality, some fraction of this gain is likely attributable to other *HST* and/or instrument components.



5.4.2 Multiple-Electron Events at Short Wavelengths

Like the ACS HRC and STIS CCDs (and unlike WFPC2), the WFC3 UVIS CCDs are directly sensitive to UV photons. In silicon, photons of energy higher than 3.65 eV (i.e., wavelength shorter than ~340 nm) can produce multiple electron-hole pairs when the energetic conduction-band electron collides with other valence-band electrons. At higher energies (energy above 3.65 eV, or wavelength below ~340 nm) the incident photons can directly extract more than one electron from the valence band. This effect (called “quantum yield”) of a single photon producing more than one electron must be taken into account properly when estimating the noise level for short-wavelength observations.

Because the generation of multiple electrons is a random phenomenon, an extra noise term must be added to account for an observed variance larger than that associated with the normal Poisson distribution of incoming photons. The correction is theoretically about $1.7 \text{ e}^-/\text{photon}$ at 200 nm, decreasing linearly to 1.0 at 340 nm. Measurements of ground-based data, however, have indicated that the effect in the WFC3 chips is much less, $1.07 \text{ e}^-/\text{photon}$ at 218 nm and $1.03 \text{ e}^-/\text{photon}$ at 275 nm in broadband data ([WFC3 ISR 2008-47](#)) as well as monochromatic narrowband data ([WFC3 ISR 2010-11](#)). The cause for this is unclear, but may be due to charge sharing (Janesick, J.R., 2007, “[Photon Transfer DM->λ](#)”, SPIE, Bellingham, Washington, p 45-48).

Given the low level of quantum yield measured in the WFC3 data, neither the QE curves presented in [Figure 5.2](#) nor the WFC3 [Exposure Time Calculator \(ETC\)](#) include the effects of quantum yield. The noise distortion from multiple electrons is not large compared to other contributions to the signal-to-noise ratio in the ultraviolet (see [Section 9.2](#)).

5.4.3 Flat Fields

Before launch, ground-based flats were obtained for all UVIS filters at a S/N of ~200 per pixel using an external optical stimulus ([WFC3 ISR 2008-12](#)). Because the overall illumination pattern of the ground-based flats did not precisely match the illumination attained on-orbit from the OTA, there are errors in these ground-based flats on large spatial scales. These errors were measured by performing stellar photometry on rich stellar fields that were observed using large-scale dither patterns during SMOV and cycles 17 and 18. In the SMOV exposures, calibrated with the ground-based flats, the rms difference between the average magnitude of a star and its magnitude in the first pointing varied from 1.5% to 4.5%, from the long to the short wavelengths ([WFC3 ISR 2009-19](#)). The needed corrections to the ground-based flats are now well understood, including the treatment of window ghosts (see [WFC3 ISR 2011-16](#), and [Section 6.5.3](#)). New reference files were delivered for all UVIS filters except the QUAD filters in December 2011 ([WFC3 ISR 2013-10](#)). They were expected to support photometry to ~1% accuracy over the full WFC3 UVIS field of view for most of the broadband filters (F336W, F390W, F438W, F555W, F606W, F775W, F814W), and to 2-3% accuracy for the remaining filters, for apertures of radius 0.4 arcsec. To verify the accuracy of these flat fields, a new calibration program observed bright *HST* standard stars on different portions of the detector in 8 filters to quantify any spatial variability in the photometry. (See [WFC3 ISR 2015-18](#).) For the UV filters, photometric residuals due to the crosshatch pattern in the flats (see [Figure 5.3](#)) were found to be 1.8% rms and 6.7% peak-to-peak. Color differences between the blue *HST* standards and the average color of Omega Cen, which was used to compute inflight corrections to the ground flats, were found to account for offsets in the UV photometry of up to 5% between the two UVIS chips. Based on this analysis, an improved set of flat fields was generated and delivered to the *HST* archive to support the new chip-dependent calibration implemented in *calwf3* version 3.3 in February 2016. (See [Appendix E](#))

A complete description of the new chip-dependent flat fields is given in [WFC3 ISR 2016-04](#). Flats were computed using the TV3 ground flats, corrected for a large internal reflection or flare ([WFC3 ISR 2011-06](#)). Low - frequency differences in the inflight response were derived from dithered observations of stars in the Omega Centauri cluster. The three key differences with respect to the prior (2011) set of flat field reference files are:

- 1) the star cluster observations were corrected for CTE (Charge Transfer Efficiency) effects before computing the L-flat,
- 2) the L-flat solutions were computed from photometry of stars dithered across a single chip only (i.e. they now exclude stars dithered between chips), and
- 3) the flats were independently normalized using the median value for each chip, rather than to a small region on amplifier A, which changed the normalization by less than 1% for filters with pivot wavelengths longer than 4000 Å.

The new UV flats are based on ground test data obtained in ambient conditions, and have been corrected for the ~3% sensitivity variations that correlate with a crosshatch pattern (on scales of 50 - 100 pixels) seen in the flats at short wavelengths.

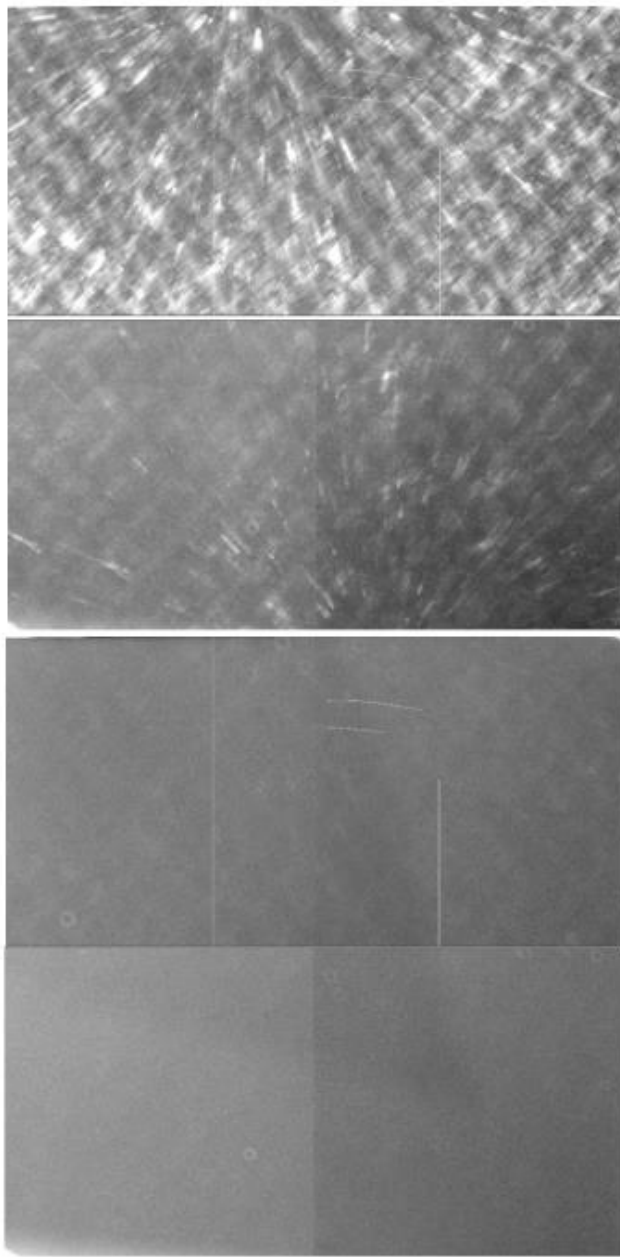
 *Information about the production of UVIS flats can be found on the WFC3 website: <http://www.stsci.edu/hst/instrumentation/wfc3/data-analysis/uvis-flats>*

During the time between anneals, reductions in sensitivity ~1% to several percent develop in some pixels, especially at the

bluer wavelengths ([WFC3 ISR 2014-18](#)). Reductions greater than 2-3% are rare in F438W and F814W (0.1% of the pixels), but occur in 3-10% of the pixels in F225W. About 90% of these pixels recover during an anneal, but the more strongly affected pixels can require more than one anneal to recover.

Figure 5.3 shows examples of bias-corrected ground-based flats for two wide-band filters. Both are displayed with an inverse greyscale stretch chosen to highlight features; the vignetting in the upper-right corner is not instrument-related but an artifact of the optical stimulus. The crosshatch features in the UV flat field (F336W) are normal, due to the detection-layer structure in the CCDs; the level is typically <5% peak-to-peak compared to the rest of the flat.

Figure 5.3: WFC3/UVIS ground-based flat fields at F336W (top) and F555W (bottom).



5.4.4 Long-Wavelength Fringing

Multiple reflections between the layers of a CCD detector can give rise to fringing, where the amplitude of the fringes is a strong function of the silicon detector layer thickness and the spectral energy distribution of the light source. Like most

back-thinned CCDs, the WFC3 CCDs exhibit fringing at wavelengths longward of ~700 nm (see [Figure 5.4](#)). The amplitude of the flat-field signal for monochromatic input increases gradually with wavelength and can reach levels of $\pm 50\%$ at the longest CCD wavelengths (fringe amplitude is the envelope of the curve shown in [Figure 5.5](#)).

An analysis of fringing effects in *broadband-illuminated* ground flats longward of 600nm ([WFC3 ISR 2010-04](#)) has shown that F953N has the greatest fringe amplitude (~16%), followed by the quad filters FQ889N, FQ906N, FQ942N, and FQ937N (~10%). Other narrowband and quad filters have fringe amplitudes in the range of 0.5-4.6% (F656N, F658N, FQ672N, F673N, FQ674N, FQ727N, and FQ750N). Although fringing is generally weak at wavelengths shorter than 700 nm, the very narrow H alpha filter (F656N) exhibits a fringe amplitude of up to several percent in flat fields acquired during ground testing ([WFC3 ISRs 2008-17, 2008-46](#) and [2010-04](#)).

Note, however, that the amplitudes of fringing listed here (and in [WFC3 ISR 2010-04](#)) should be used only as an estimate of the effect in science data. Fringing will be different for sources with spectral energy distributions (SEDs) which differ significantly from the calibration lamp used to generate the ground flat fields. For example, continuum sources in broad filters will effectively smooth out fringing effects but that same filter can show strong fringes when illuminated by sources with strong spectral lines or SEDs much narrower than the filter bandpass. Conversely, for sources with SEDs similar to the calibration lamp, the fringes can be corrected by the flat-fielding process.

The fringe pattern has been shown to be very stable, as long as the wavelength of light on a particular part of the CCD stays constant, so fringing can be corrected if an appropriate flat field is available. The fringe pattern can also be modeled, either by interpolating between or combining monochromatic patterns previously obtained in the laboratory, or from theoretical calculations. For a detailed explanation of efforts to model the WFC3 fringe pattern, see Malumuth et al. (2003, [Proceedings of SPIE 4854](#), Future EUV/UV and Visible Space Astrophysics Missions and Instrumentation, pp. 567-576) and "Fringing in the WFC3/UVIS Detector", presented by M. Wong at the [2010 STScI Calibration Workshop](#).

Figure 5.4: UVIS chip 1 (top) and chip 2 (bottom) fringe pattern for monochromatic illumination at 977 nm.

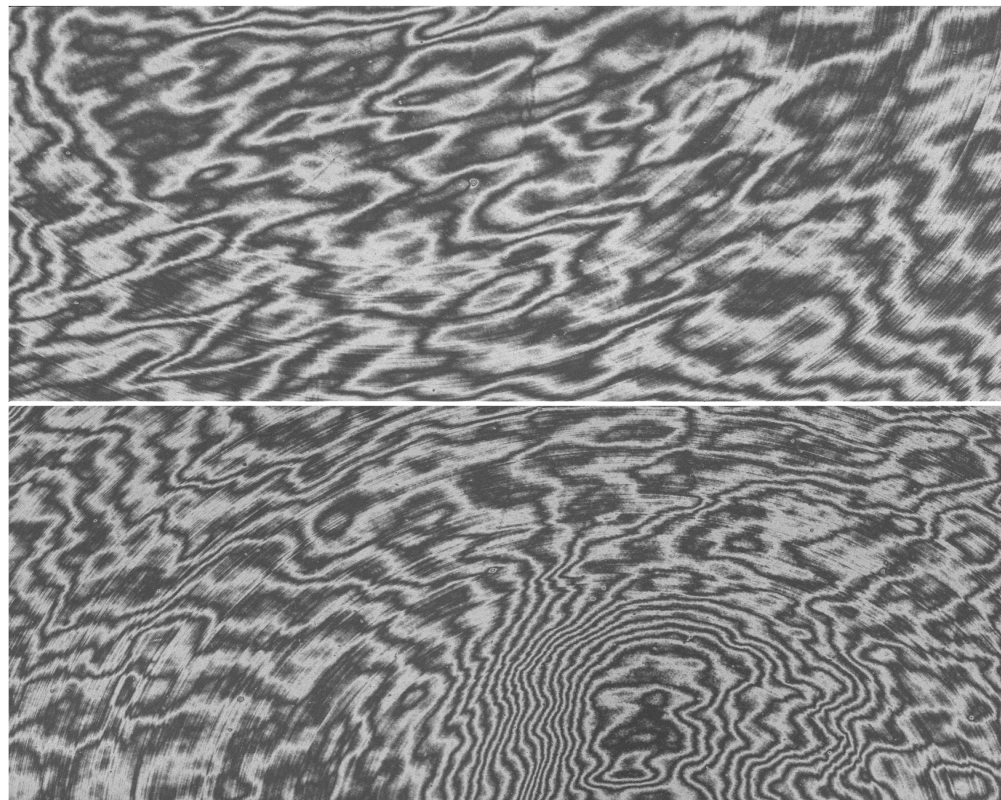
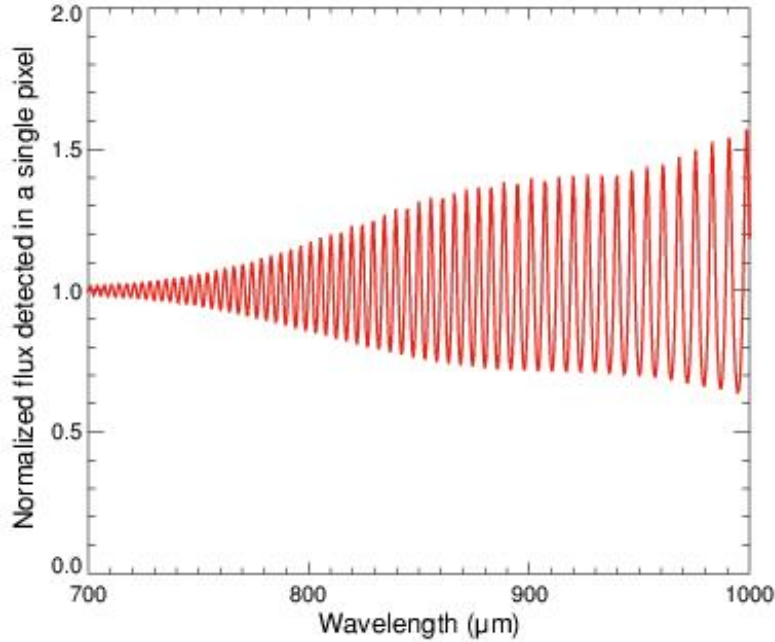


Figure 5.5: Flux (normalized to the mean of the image) as a function of wavelength for a single pixel, based on the Malumuth et al. (2003) model. Fringe phase (rapid oscillation) and fringe amplitude (curve envelope) vary as a function of wavelength. Due to wavelength averaging (even within narrow band filter bandpasses), actual WFC3 data exhibit peak to trough fringe amplitudes of < 30%.



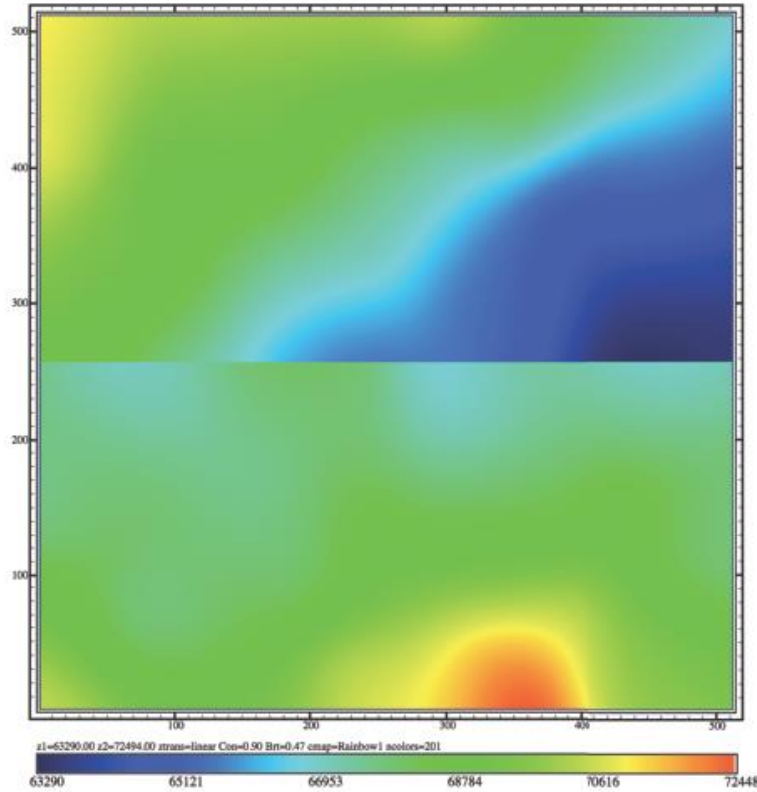
5.4.5 Linearity and Saturation

The dynamic range of a detector is limited either by the full-well capacity of the device or by the analog-to-digital converter (ADC) and gain setting that are used during readout to convert the accumulated charge into data numbers (DN). At the standard UVIS gain of $\sim 1.5 \text{ e}^-/\text{DN}$, saturation always occurs on chip unless binning is used, in which case saturation of the binned readout pixel can occur in the ADC. (See [Section 5.4.6](#) for the numerical limits on DN and electrons for unbinned and binned readouts.) If saturation occurs on chip, photometric information can be recovered with great accuracy, as described below. If the charge accumulated in a given (binned) readout pixel exceeds the ADC maximum, any additional charge does not result in any further increase in the DN and may, in cases of extreme saturation, result in values of zero.

On-orbit observations have shown that on UVIS2, the onset of saturation varies from about 67000 to 72000 electrons per pixel over the CCD, while UVIS1 has a somewhat larger range of 63000 to 71000 electrons per pixel ([WFC3 ISR 2010-10](#)). The distribution of full well depth on the detector is shown in [Figure 5.6](#). Once the charge exceeds the pixel full-well level, it can escape that pixel and spread into adjacent vertical pixels; as the signal continues to accumulate, these adjacent pixels themselves can accumulate charge up to full-well and leak into further adjacent vertical pixels, resulting in the “blooming,” or charge overflow, effect. The MPP (multi-phased pinned) operation of the detectors, used to minimize surface dark current, constrains the blooming along the detector columns, so the blooming is only vertical and not horizontal. Photometric information well beyond saturation can be recovered for relatively isolated sources in unbinned

images by defining a special aperture that encompasses all of the pixels that have been bled into. [WFC3 ISR 2010-10](#) presents an algorithm that can be invoked for UVIS1 to regain full linearity to ~1% up to nearly 7 magnitudes past saturation. UVIS2 is linear with simple summation over the saturated pixels. Some small non-linearities (a few percent) have been detected at the lowest signal levels at greater distances from the amplifiers, but the behavior is consistent with CTE loss ([Section 5.4.11](#)) rather than a true non-linearity in the chips.

Figure 5.6: UVIS1 and UVIS 2 Full-Well Levels



*The distribution of full well depth (electrons) for UVIS1 (top) and UVIS2 (bottom), taken to be the number of electrons at which charge spilling just starts to set in for point sources. FITS files for the 2 chips are available at:
<http://www.stsci.edu/hst/instrumentation/wfc3/data-analysis/full-well-depth>.*

Even extreme over-exposure is not believed to cause any long-term damage to the CCDs, so there are no bright-object limits for the WFC3 CCDs.

5.4.6 Gain

Electrons that accumulate in the CCD wells are read out and converted to data numbers (DNs), often called Analog-to-Digital Units (ADUs), by the analog-to-digital converter (ADC). The ADC output is a 16-bit number, so that the maximum DN that can be read out is 2¹⁶ - 1 or 65,535 for each readout pixel (single or binned detector pixel). A straightforward scheme in which one DN corresponded to one electron would make it impossible to measure signals larger than 65,535 electrons. Hence the conversion gain parameter provides a way of adjusting the scale so that multiple counts correspond to a single DN, allowing larger numbers of electrons to be measured. The conversion gain is defined as the number of electrons per DN.

The maximum full well depth of the pixels on the WFC3/UVIS chips is ~72500 e⁻ (see Figure 5.6). For the default gain ~1.5 e⁻/DN, this corresponds to ~48000 DN, well below the ADC limit of 65,535 DN. If the pixels are binned 2 × 2 or 3 × 3, the

binned pixels could reach flux levels of 4 or 9 times 48,000 DN, respectively, which would be truncated to 65,535 DN (~98,300 e⁻) during readout.

Although it is possible to operate the WFC3 CCD detector at gains of ~ 1, 1.5, 2, and 4 e⁻/DN, only a gain of ~1.5 e⁻/DN is supported. For unbinned readouts, this gain permits sampling of the entire dynamic range of the detectors, with negligible impact on the readout noise.

The gains for the WFC3 CCDs measured during Cycle 20 are summarized in Table 5.3 below. Uncertainties in the measurements are less than +/-0.01 e⁻/DN. Gain measurements made from ground-based data and from data taken in SMOV and cycles 17 to 22 have remained constant to within 1-2%. (See [WFC3 ISR 2014-05](#), [WFC3 ISR 2015-05](#), [WFC3 ISR 2016-09](#), [WFC3 ISR 2016-13](#))

Table 5.3: WFC3/UVIS Gains.

CCD Chip	Amp	Gain (e ⁻ /DN)
1	A	1.56
	B	1.55
2	C	1.58
	D	1.57

5.4.7 Read Noise

The read noise level in the science area pixels of bias frames for all of the amplifiers at the default gain setting was measured during SMOV ([WFC3 ISR 2009-26](#)). Table 5.4 shows the results obtained at the default gain setting of 1.5 e⁻/DN. The read noise was found to be stable to 1%, 0.4%, 0.7%, and 0.8%, for amps A,B,C, & D, respectively, based on measurements through the end of August 2009. A more recent study ([WFC3 ISR 2015-13](#)) has shown that the read noise has increased by 0.04 to 0.05 e⁻ in unbinned readouts from May 2009 to May 2015. This is attributable to radiation damage, increasing numbers of hot pixels, increasing CTE losses, and aging of the instrument.

Table 5.4: WFC3/UVIS readout noise (e⁻) and uncertainty for normal and binned modes.

	Amplifier A			Amplifier B			Amplifier C			Amplifier D		
Binning	1 × 1	2 × 2	3 × 3	1 × 1	2 × 2	3 × 3	1 × 1	2 × 2	3 × 3	1 × 1	2 × 2	3 × 3
Mean	2.91	3.11	3.22	2.99	3.15	3.26	2.90	2.99	3.09	3.01	3.29	3.38

Uncertainty	0.03	0.02	0.04	0.01	0.01	<0.01	0.02	<0.01	0.01	0.02	0.02	<0.01
-------------	------	------	------	------	------	-------	------	-------	------	------	------	-------

A preliminary analysis of the statistical behavior of the WFC3 ADCs shows some tendency for the least significant bit to be slightly biased at the readout speed adopted by the WFC3 electronics (see [WFC3 ISR 2005-27](#)). This minor effect should not degrade the photometric and noise characteristics of the WFC3/UVIS images.

5.4.8 Dark Current

The WFC3 CCDs, like most large-area scientific CCDs, operate with buried channels. Earlier generations of CCDs worked with surface channels, i.e., storing and transferring charges only along the surface of the semiconductor. In these earlier devices, the Si-SiO₂ interface between the detector material Si (p-doped conductor) and the surface layer of SiO₂ (isolator) created significant charge traps, which limited both the charge transfer efficiency and the dark current. In buried-channel devices, a shallow (~0.5 micron thick) n-type Si layer is implanted just below the surface between the p-doped Si and the SiO₂ surface, to store and transfer the collected signal charge away from the traps at the interface.

Dark current in WFC3 detectors is further reduced using MPP technology. The dark current generated at the Si-SiO₂ interface ultimately depends on two factors: the density of interface states and the density of free carriers (holes and electrons) that populate the interface. Electrons can thermally “hop” from the valence band to an interface state (sometimes referred to as a “mid-band state”) and from there to the conduction band, producing a dark electron-hole pair. Free carriers also fill interface states and, if these states were completely populated, can suppress hopping and conduction, reducing the surface dark current at levels comparable to the bulk dark. Unfortunately, normal CCD operations deplete the interface of free carriers, maximizing dark current generation.

In MPP technology, the Si-SiO₂ interface is populated with holes that suppress the hopping conduction process. MPP mode is applied to the CCD by significantly biasing the array clocks negatively to invert (push electrons away from) the n-buried channel and “pin” the surface potential beneath each phase to substrate potential (hence the name multi-pinned phase). Biasing the array clocks in this manner causes holes from the p+ channel stops to migrate and populate the Si-SiO₂ interface, eliminating surface dark-current generation. Note that it is not possible to invert conventional CCDs in this way, as the sensor’s full-well capacity would be annihilated since the potential wells within a pixel all assume the same level. To circumvent this difficulty in MPP CCD technology, an additional implant is included below one of the phases, allowing charge to accumulate in collecting sites when biased into inversion.

Besides eliminating surface dark current, MPP CCD technology offers additional advantages. For example, the charge transfer efficiency of a CCD generally degrades with decreasing operating temperature. MPP technology assists in the charge transfer process because it permits the use of higher operating temperatures.

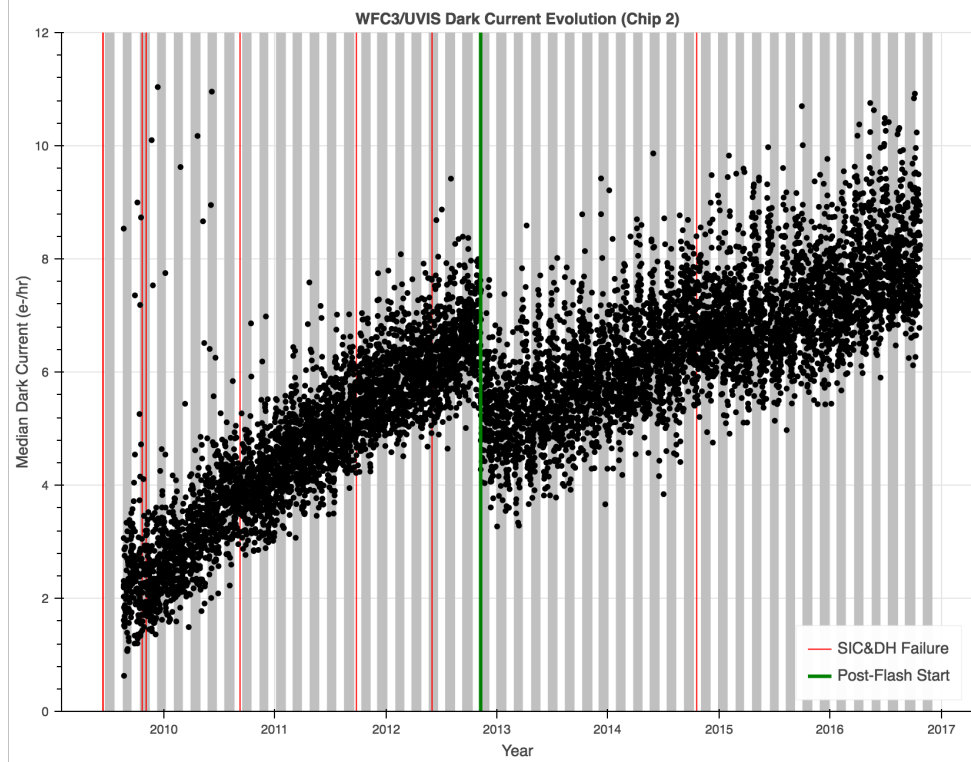
The MPP CCD also eliminates residual image, a serious problem that has plagued low-signal-level CCD users for many years. Residual image, also known as quantum-efficiency hysteresis, results when the sensor is either overexposed or first powered up. Under these circumstances, electrons are found trapped at the Si-SiO₂ interface that slowly release into the pixel’s potential well. Residual charge may take hours or even days before its level falls below the read-noise floor. Inverting the CCD causes holes to recombine immediately with the trapped residual electrons, eliminating remnant image effects during integration as well as readout.

During pre-flight tests, the CCD dark current was measured both in the cryogenic environment at the DCL, and in the instrument during thermal vacuum testing. The dark currents measured during the 2004 thermal vacuum testing are presented in [WFC3 ISR 2005-13](#). Early on-orbit dark currents were derived from SMOV and Cycle 17 calibration ([WFC3 ISR 2009-16](#)).

Like all CCDs operated in a low-earth-orbit radiation environment, the WFC3 CCDs are subject to radiation damage by energetic particles trapped in the radiation belts. Ionization damage and displacement damage are two types of damage caused by protons in silicon. The MPP mode is very effective in mitigating the damage due to ionization, such as the generation of surface dark current due to the creation of new trapping states in the Si-SiO₂ interface. Although protons lose only a minor fraction of their total energy via non-ionizing energy loss, lattice displacement damage can cause significant performance degradation in CCDs by decreasing the charge transfer efficiency (CTE), increasing the average dark current, and introducing pixels with very high dark current (hot pixels). Displacement damage to the silicon lattice occurs mostly due to the interaction between low-energy protons and silicon atoms. The generation of phosphorous-vacancy centers introduces an extra level of energy between the conduction band and the valence band of the silicon. As described above, new energy levels in the silicon bandgap increase the dark current as they allow thermally generated charges to reach the conduction band. As a consequence, the dark current of CCDs operated in a radiative environment is predicted to increase with time.

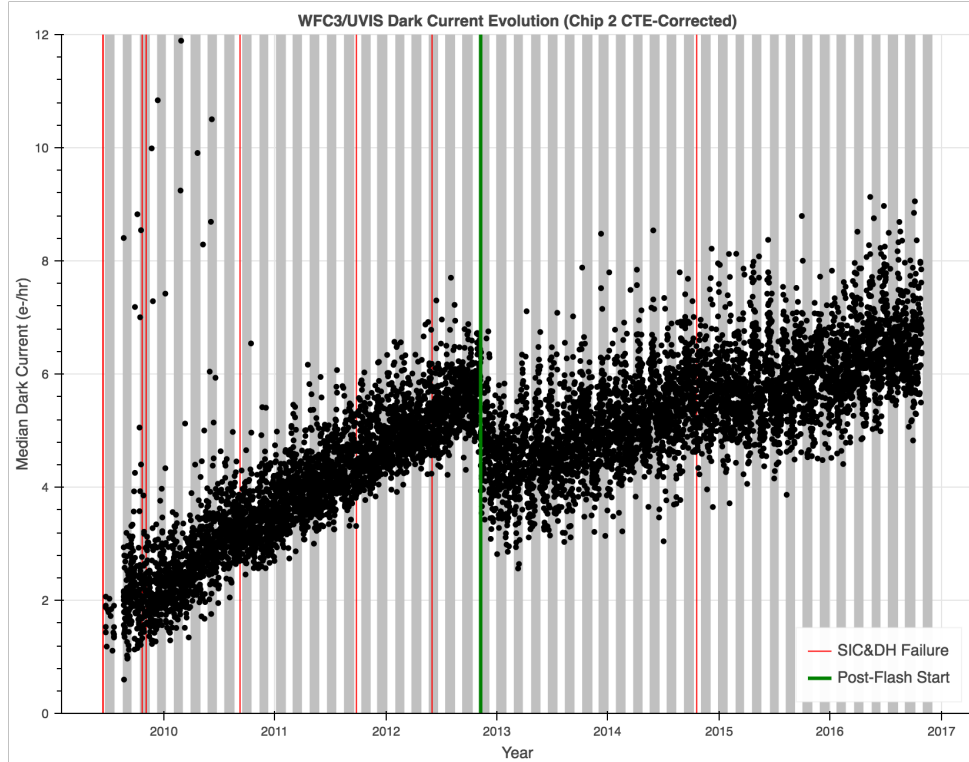
Indeed, the WFC3 dark current has been slowly increasing over time. The median dark level of pixels below the hot pixel threshold (<54 e⁻/hr) has been increasing by ~0.5 e⁻/hr/pix/year, and was ~8 e⁻/hr/pix as of Oct. 2016 as measured using the non-CTE corrected darks. This can be seen in [Figure 5.7](#). The rate of change has decreased recently, corresponding to an increase in solar activity. Such a correlation has been documented for the other CCD detectors on *HST*; e.g., see the discussion of dark current evolution in [WFPC2](#). The measured dark current changed significantly (on the date shown by the green line in Nov. 2012) when we began measuring darks made with post-flash ([WFC3 ISR 2014-04](#)), which is used to reduce CTE losses by increasing the background (see [Section 5.4.11](#)). Less flux appears to trail out of hot pixels and cosmic ray hits due to delayed release of electrons, thus decreasing the dark current. (There is a corresponding change in the measured number of hot pixels at that time; see [Section 5.4.9](#)).

Figure 5.7: Median dark current of the WFC3/UVIS detector measured on orbit from June 2009 to Oct 2016. The use of post-flash accounts for the discontinuity in Nov 2012. These measurements were made with non-CTE corrected darks.



As of February 2016, with the introduction of calwf3 version 3.3 into the calibration pipeline, we now offer users the chance to use CTE corrected images and calibration files. The production of CTE-corrected dark files on a daily basis is described in [WFC3 ISR 2016-08](#). The CTE correction helps return electrons that have trailed out of their original pixel back to the pixel they came from which allows a more accurate measurement of the dark current for each individual pixel. This correction has lead to an overall decrease in the median dark current of the detector over time as seen in Figure 5.8. We, of course, still see the increase in the median dark levels of pixels over time, and we see the same patterns of change in slope as described above (i.e., a recent decrease due to solar activity). However, we do see that the rate of those changes is slightly smaller than when measured with the non-CTE corrected darks. The median dark levels of pixels below the hot pixel threshold (still <54 e $^-$ /hr) can be seen in Figure 5.8 to be increasing at a level of >0.5 e $^-$ /hr/pix/year now, and was ~ 7 e $^-$ /hr/pix as of Nov. 2016 as measured using the CTE corrected darks.

Figure 5.8: Median dark current of the WFC3/UVIS detector measured on orbit from June 2009 to Oct 2016. The use of post-flash accounts for the discontinuity in Nov 2012. These measurements were made with CTE-corrected darks.



The on-going monitoring of the dark current is described at: <http://www.stsci.edu/hst/instrumentation/wfc3/performance/monitoring>.

5.4.9 Bad Pixels

Three types of bad pixels are routinely monitored using on-orbit WFC3 data: hot pixels (with higher than normal dark current), bad detector pixels (unstable, often with extremely low quantum efficiency), and, most recently, sink (charge trap) pixels. These pixels are flagged in the DQI array of the calibrated data with values 16, 4, and (since Feb 2016 with the installation of calwf3 version 3.3) 1024, respectively. (See Appendix E.) The CTE trails of sink pixels are also flagged with DQI value 1024. (See [WFC3 ISR 2014-19](#).)

On orbit, the number of hot pixels increases with time due to radiation damage, but is periodically reduced by annealing, when the UVIS detector is warmed to $\sim 20^{\circ}\text{C}$. The number of sink pixels also grows over time, presumably because they are radiation-induced. The extent of the sink pixel CTE trail to be flagged is based on the science image background: the lower the background is, the longer the sink pixel trail will be. (See [WFC3 ISR 2014-19](#).)

The bad detector pixel population, generally located along columns, is relatively constant. Bad detector pixels are shown for the upper chip (chip 1) and lower chip (chip 2) in Figure 5.9 and [Figure 5.10](#), respectively. Note that a pair of bad columns passes near the center (reference pixel) of the subarray aperture UVIS2-C512C-SUB, which is at [257,257] in the lower left corner of chip 2.

Figure 5.9: Bad detector pixels (DQI = 4) on the upper chip (chip 1) are in columns 1104, 2512, 2542, 2543, 2869, 3646, and 3667 in the fit image.

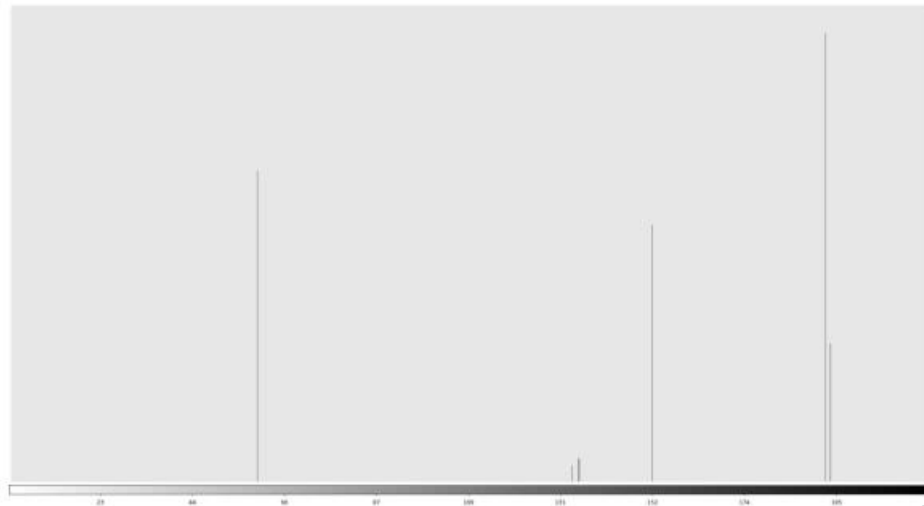


Figure 5.10: Bad detector pixels (DQI = 4) on the lower chip (chip 2) are in columns 223, 242, 243, 751, 1417, 1469, 2655, 2696, 2707, and 3915 in the fit image.



For WFC3, we have chosen a limit of $54 \text{ e-}/\text{hr}$ ($0.015 \text{ e-}/\text{s/pix}$) as a threshold above which we consider a pixel to be “hot,” based on the tail of the dark current distribution as well as a visual examination of 900 sec dark frames taken during Cycle 17. Figure 5.11 shows a histogram of CR-free pixels from 900 sec darks taken at three different times after the April 2010 anneal procedure: about 1 day (red line), 11 days (green line) and 29 days (blue line) later. The increase in hot pixels due to on-orbit radiation damage is apparent. The anneal procedure initially repaired 90% of the hot pixels which accumulate over time; in 2015, the repair rate is 20-30%. The hot pixel cutoff is shown with a vertical line at $54 \text{ e-}/\text{hr}$; at this threshold, the growth rate for WFC3 hot pixels is $\sim 1000 \text{ pix/day}$ per chip. (Radiation damage produces an overall higher dark current as well as an increase in the number of individual hot pixels. See [Section 5.4.8](#).)

Figure 5.11: Dark histograms illustrate the increase in the number of hot pixels ($>54 \text{ e}^-/\text{hr}$) between anneal procedures. The April 1, April 11, and April 29 curves (red, green, and blue, respectively) are from one day after an anneal procedure, about mid-way between anneals, and about one day prior to an anneal procedure.

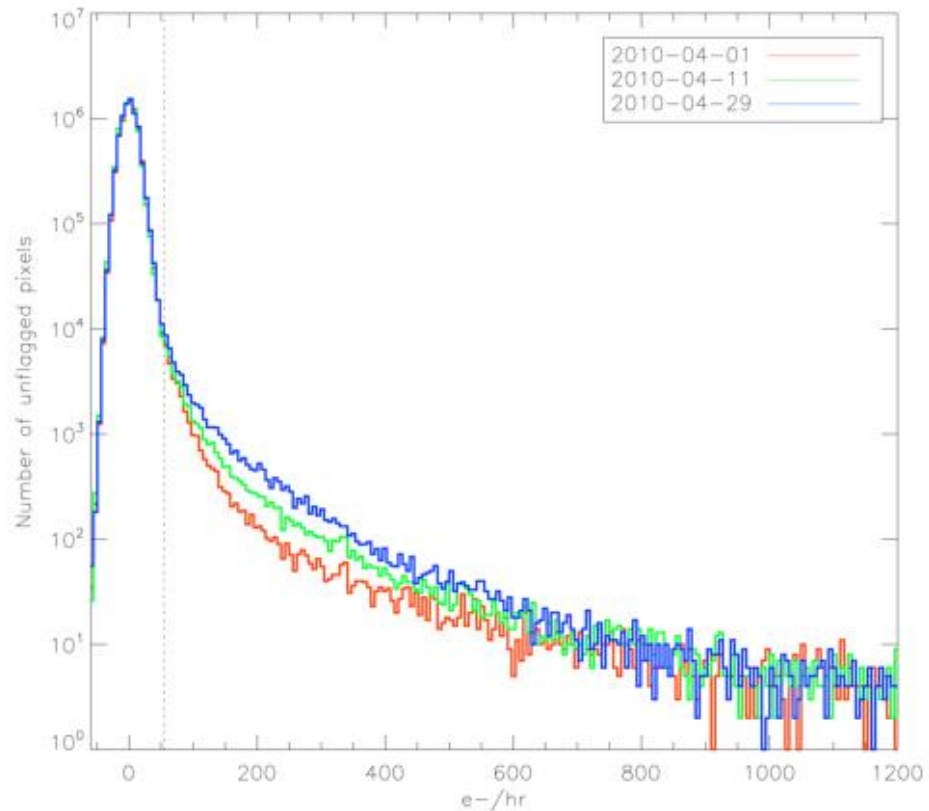


Figure 5.12 shows the number of hot pixels as a function of time since the installation of WFC3 on *HST* as measured using the non-CTE-corrected darks, while Figure 5.13 shows the same measurement made with the CTE-corrected darks which became available in February 2016. (See [WFC3 ISR 2016-08](#) and [Section 5.4.8](#).) In both figures, the alternating gray and white regions represent anneal cycles. The red vertical lines indicate the dates of the SIC&DH failures, when WFC3 was safed (prior to Oct. 2009, WFC3 safings warmed the chips to 20°C, the temperature attained in the annealing procedure). The green vertical line indicates when we began to measure darks made with post-flash in Nov. 2012 (see [WFC3 ISR 2014-04](#)) to reduce CTE losses (see [Section 5.4.11](#)). The increased background level introduced by the flash reduces the trailing of electrons from hot pixels along columns during the readout, so more hot pixels are detected above the threshold, accounting for the discontinuity in the number of hot pixels at that time. (There is a corresponding drop in the measured dark rate at that time; see [Section 5.4.8](#).) The number of permanent hot pixels, i.e., pixels that the anneals are unable to fix, is growing by 0.03-0.1% per month whether using non-CTE-corrected darks or CTE-corrected darks.

Figure 5.12: Hot pixel growth for chip 2 between anneals from June 2009 to Oct 2016 as measured with the non-CTE-corrected darks. Hot pixel anneal rate is ~20-30%. The use of post-flash accounts for the discontinuity in Nov 2012.

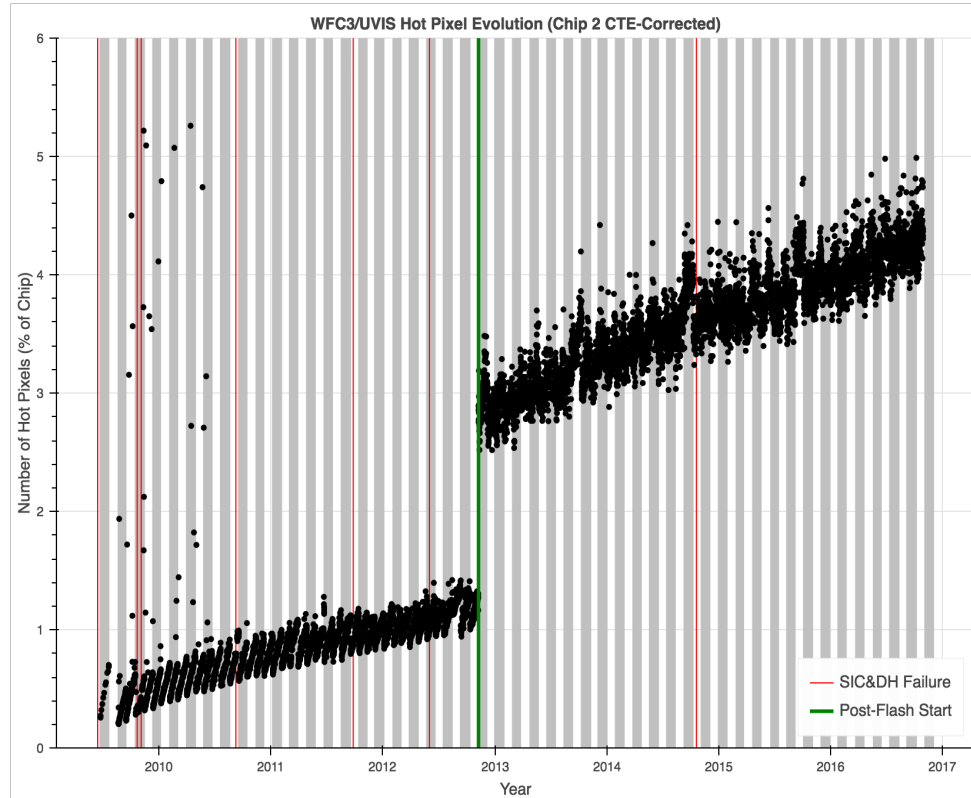
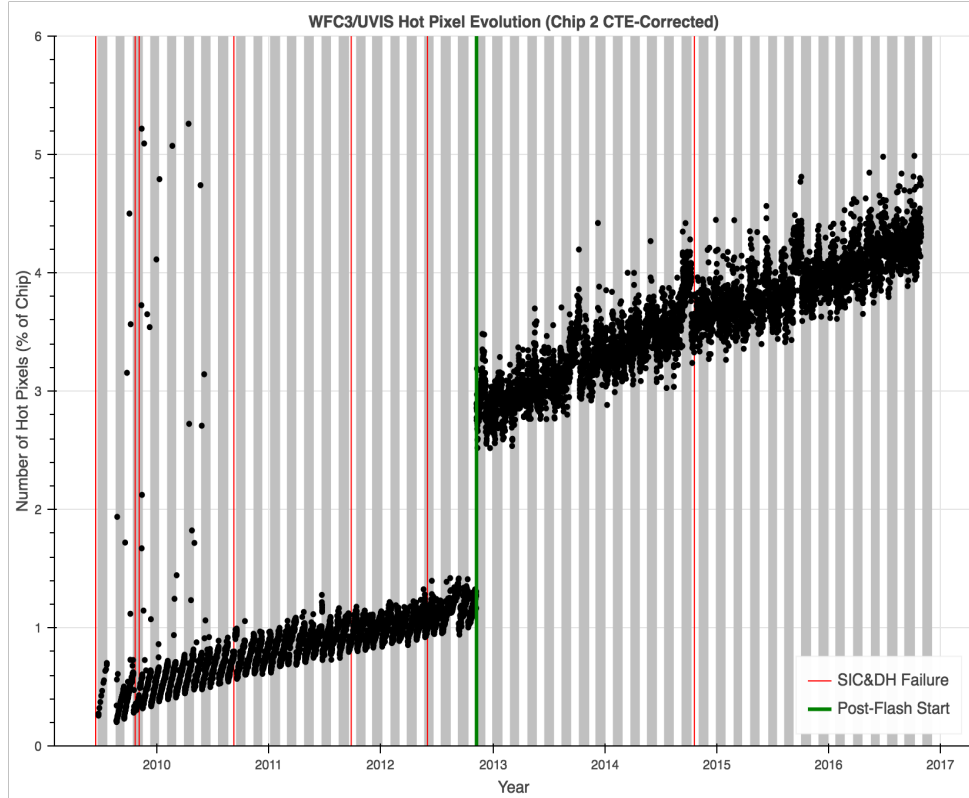


Figure 5.13: Hot pixel growth for chip 2 between anneals from June 2009 to Oct 2016 as measured with the CTE-corrected darks. Hot pixel anneal rate is ~20-30%. The use of post-flash accounts for the discontinuity in Nov 2012.



The main difference that we see between the measurement of hot pixels using the non-CTE-corrected darks (Figure 5.12) vs. the CTE-corrected darks (Figure 5.13) is a tightening of the spread of the measurements of the percentage of hot pixels over time, especially after the start of post-flashing in 2012. This difference occurs as the CTE correction algorithm helps return electrons that have trailed out of their original pixel back to the pixel they came from, which leads to there being fewer hot pixel false positives. Since we pick out hot pixels as any pixel with a value above a specific cut-off, when electrons trail into pixels they don't belong in we see a slight increase in the overall number of hot pixels. This leads to a larger spread in the measurements towards higher rates at a given date, as seen in the non-CTE-corrected measurements in Figure 5.12.

The on-going monitoring of hot pixels is described at: <http://www.stsci.edu/hst/instrumentation/wfc3/performance/monitoring>

Table 5.5 summarizes the number of hot pixels in each chip over several ranges of dates and the number of bad detector pixels, which is stable. The hot pixel range is the number of hot pixels observed between the sample anneal procedures noted.

Table 5.5: Summary of hot pixels and bad detector pixels for Chip 1 and 2.

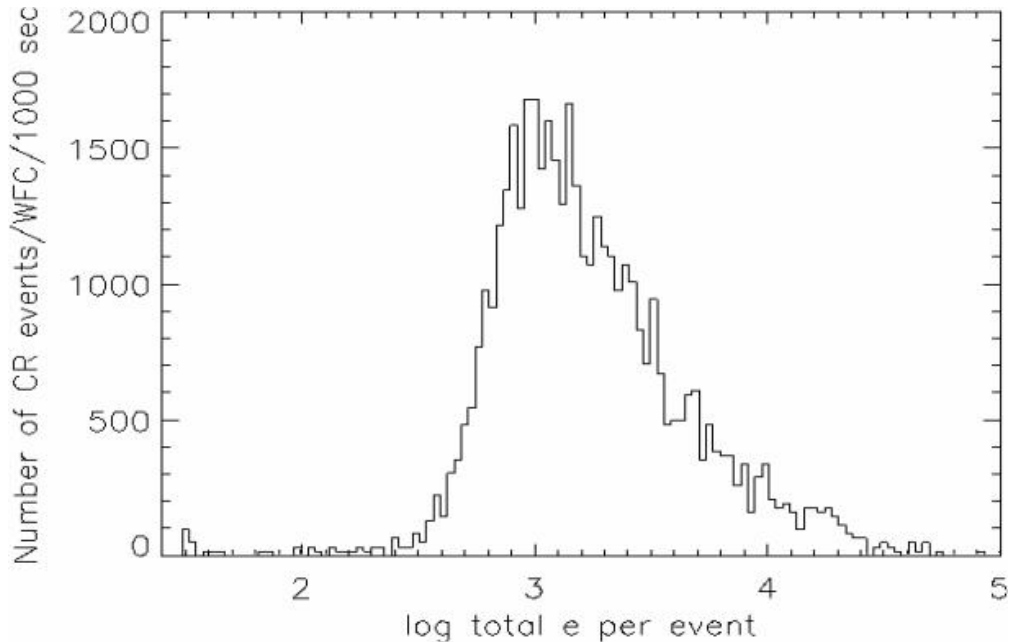
	Chip 1 (Amp A & B)		Chip 2 (Amp C & D)	
Bad Pixel Type (Date)	# of Pixels	% of Chip	# of Pixels	% of Chip
Hot Pixels				
• Aug 21 - Sep 14, 2009	15626 - 39568	0.186 - 0.471	16382 - 40492	0.195 - 0.482
• Nov 14 - Dec 11, 2009	22682 - 48641	0.270 - 0.579	25202 - 52337	0.300 - 0.623
• Feb 05 - Mar 02, 2010	28899 - 54857	0.344 - 0.653	30999 - 57294	0.369 - 0.682
Bad Detector Pixels	~6000	0.07	~16000	0.19

5.4.10 Cosmic Rays

The fraction of WFC3 pixels impacted by cosmic rays varies from 5% to 9% per chip during 1800 sec exposures in SAA-free orbits, providing a basis for assessing the risk that the target(s) in any set of exposures will be compromised. Observers seeking rare or serendipitous objects, as well as transients, may have stringent requirements on how many cosmic rays can be tolerated in an image combination. Assuming cosmic-rays affect 5-9% of a chip in 1800 sec, at least 4-5 images will be needed to ensure that fewer than 100 pixels will be hit in all images of the combination.

The flux deposited on a CCD from an individual cosmic ray depends less on the energy of the cosmic ray than on the distance it travels in the silicon substrate, and thus on its direction of incidence. The electron deposition due to individual cosmic rays measured with ACS/WFC has a well-defined cutoff, with negligible events of less than 500 e⁻ and a median of ~1000 e⁻ (see Figure 5.14). The overall characteristics of the cosmic ray population appear nominal in WFC3.

Figure 5.14: Electron deposition by cosmic rays on ACS/WFC.



5.4.11 Charge Transfer Efficiency

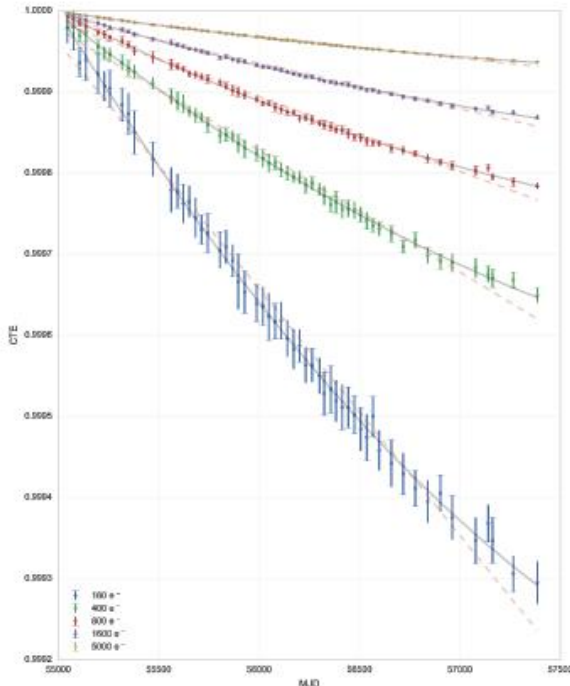
Uniform response within each pixel and excellent charge transfer efficiency (CTE) are key to achieving accurate photometric performance. CTE is a measure of how effective the CCD is at moving charge from one pixel location to the next when reading out the chip. A perfect CCD would be able to transfer 100% of the charge as it is shunted across the chip and then out through the serial register. In practice, small traps in the silicon lattice compromise this process by retaining electrons, and then releasing them at a later time. (Depending on the trap type, the release time ranges from a few microseconds to several seconds.) For large charge packets (many thousand electrons), losing a few electrons along the way is not a serious problem, but for smaller signals, it can represent a substantial fraction. The UVIS CCDs are large-format devices, similar in size to those in the ACS WFC, and thus require significantly more charge-shifting steps during readout, with more losses, than smaller devices like the STIS and WFPC2 CCDs. CTE inevitably declines over time as on-orbit radiation damage creates charge traps in the detector. WFC3 was installed during solar minimum, when the cosmic flux is greatest and radiation damage most rapid, so the UVIS detector has experienced a steeper decline in CTE in its early years than the ACS WFC, which was deployed at a more favorable time.

Several steps were taken in the design of WFC3 to reduce CTE losses on the UVIS detector. First, shielding (similar to ACS /WFC) has been used to protect the CCDs from the high-radiation space environment, thereby slowing the production of charge traps. Second, the WFC3 CCDs have been designed with a mini-channel (improved over ACS/WFC), which reduces the number of traps seen by small charge packets during read-out transfers. Third, the detector has a charge-injection capability (not generally available for science observations - see [Section 6.9.2](#)), which inserts charge electronically in equally spaced rows of pixels to fill the charge traps ([WFC3 ISR 2011-02](#)). Fourth, an operational mode has been developed to provide a flash of light from an LED at the end of an exposure to increase the background level in the exposure. Use of this post-flash mode is now strongly recommended for observations of faint objects when the

background level is expected to be less than 12 electrons. The rationale for using this mode was presented in [MacKenty and Smith \(2012\)](#). The state of the UVIS detector's CTE at that time is also discussed in [Baggett et al. \(2012\)](#).

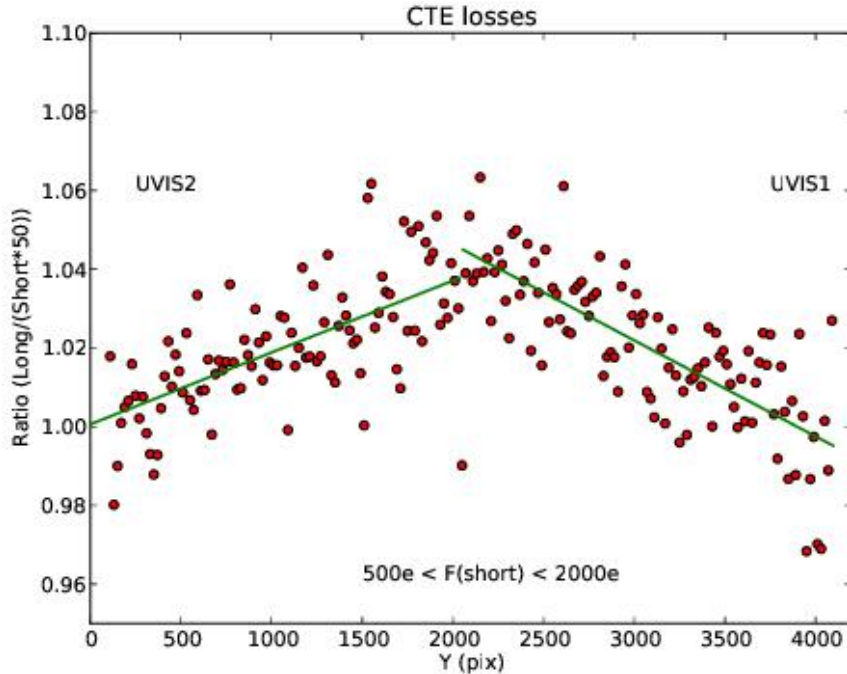
CTE is typically measured as a pixel-transfer efficiency, and would be unity for a perfect CCD. One indicator of CTE is the Extended Pixel Edge Response (EPER). Inefficient transfer of electrons in a flat-field exposure produces an exponential tail of charge in the overscan region. Analysis of EPER monitoring observations through January 2013 showed a linear decline of CTE over time ([WFC3 ISR 2013-03](#)). Analysis of continuing monitoring observations has shown that the rate of decline is no longer well-matched by a linear fit but, instead, is well fit by a quadratic function [WFC3 ISR 2016-10](#). This may indicate that the CTE decline is leveling off or reducing with time. See Figure 5.15, which shows CTE as a function of signal level in the flat field from September 2009 to January 2016.

Figure 5.15: CTE measured by the EPER method for indicated flat-field signal levels as a function of date (MJD).



The CTE changes tracked with EPER testing provide a guide to likely evolution in time, but cannot be directly interpreted to predict CTE loss as a function of target and background signal level. Observations of stellar clusters are being used to determine this. Preliminary work in this area is shown in Figure 5.16, presented by Rajan at the [2010 STScI Calibration Workshop](#). This figure illustrates how CTE affects stellar photometry for a stellar cluster as a function of the number of transfers along columns. The normalized ratio of stellar fluxes measured in a long exposure to fluxes measured in a short exposure is shown as a function of Y position on the detector for stars within a limited flux range. The ratio increasingly deviates from 1 at greater distances from the readout amplifiers because CTE losses are relatively greater for the short exposure, where the signal is smaller. Subsequent observations of stellar clusters have shown strong evolution of CTE on the UVIS CCDs, as expected from the commencement of on-orbit operations during the minimum of the solar cycle. See [Section 6.9](#) for further monitoring of CTE using exposures of stellar clusters and advice to observers, and <http://www.stsci.edu/hst/instrumentation/wfc3/performance/cte> for updated information on CTE and links to relevant documents.

Figure 5.16: Normalized ratio of stellar fluxes measured in a long exposure of NGC 1850 to fluxes measured in a short exposure, shown as a function of Y position on the detector. The ratio deviates from 1 because of the relatively greater CTE losses in the shorter (fainter) exposure.



5.4.12 Crosstalk

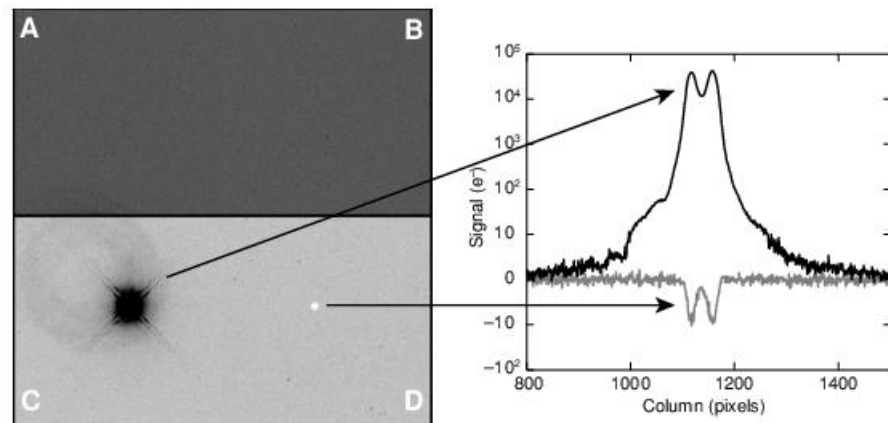
Crosstalk, a type of electronic ghosting, is common in devices where two or more quadrants are read out simultaneously and WFC3 is no exception. Both the UVIS and IR channel exhibit low levels of crosstalk (CT).

In the UVIS channel, point sources and extended targets generate a low-level, negative mirror images in the quadrant adjoining the target quadrant, on the same chip (i.e., CT does not cross between the chips). The crosstalk effect is linear with flux and is stronger for targets in quadrant A or C. In a full-frame, unbinned, four-amp readout with a target in quadrant A or C, the CT level is $\sim -2 \times 10^{-4}$ that of the source; for a target in quadrant B or D, the CT level is $\sim -7 \times 10^{-5}$ that of the source ([WFC3 ISR 2012-02](#)). To within the errors, the CT due to hot pixels and cosmic rays is the same as that due to point or extended sources. Figure 5.17, from [WFC3 ISR 2009-03](#), illustrates the crosstalk effect as observed in an image taken during instrument ground tests.

The low-level effects of CT can be mitigated by dithering: the mirror image nature of the CT moves the features in a direction opposite to the target motion, i.e., they will appear to be transients and thus be removed during the drizzling

procedure. Alternatively, CT can be removed from single images by scaling the target image quadrant by the amp-dependent factor noted above, flipping the image about the y-axis, and subtracting it from the CT image quadrant. An *IDL routine that performs this procedure, described in WFC3 ISR 2012-02, can be obtained from the WFC3 ISR webpage at WFC3 ISR 2012-02 Crosstalk Correction (zip file including example dataset and ISR).*

Figure 5.17: Crosstalk test frame (left), and 20-line average cuts through the target and crosstalk images (right). The image is displayed with a hard inverted greyscale stretch. The target was placed in quadrant C, and the crosstalk appears in quadrant D. The faint large ring in C offset from the primary target is an optical window ghost.



5.5 The WFC3 IR Channel Detector

[5.5.1 Overview](#)

[5.5.2 IR Detector Basics](#)

5.5.1 Overview

The infrared channel of WFC3 employs a low-noise, high-QE, 1024×1024 pixel HgCdTe array manufactured by Teledyne Imaging Sensors (formerly Rockwell Science Center). The detector area sensitive to light is 1014×1014 pixels. Active cooling by a six-stage thermoelectric cooler (TEC) keeps the detector at a nominal operating temperature of 145 K. Although the IR detector is sensitive between 400 and 1700 nm, the detector coating is optimized for wavelengths longward of ~ 1000 nm, where the QE reaches its peak ([Figure 5.23](#)). The IR channel filter set is also limited to wavelengths above 900 nm, making the IR channel complementary to the UVIS channel.

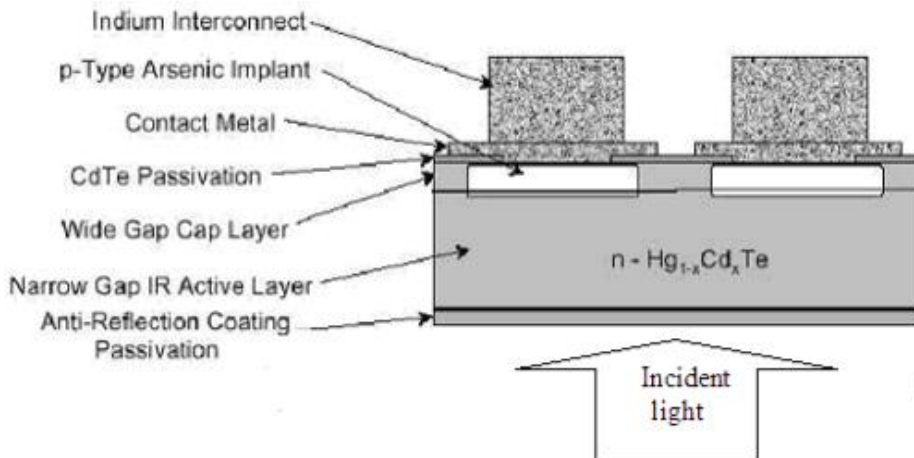
Compared to CCD detectors, IR detectors like the one used in the WFC3 IR channel have higher read noise and dark current. Unlike CCDs, however, IR detectors allow the accumulated signal in each pixel to be measured non-destructively multiple times. The capability to sample the signal multiple times during the integration can be exploited to reduce the effective read-out noise significantly. IR exposures are called “ramps” due to this capability to sequentially read the detector as signal accumulates. IR detectors are also immune to the charge bleeding exhibited by CCDs at high signal levels. Saturation is still a concern, however, because pixels subject to the highest signal levels show higher dark-current rates (“image persistence” or afterglow) in subsequent exposures ([WFC3 ISR 2010-17](#)). (See [Section 7.9.4](#) for the on-orbit characterization of persistence on the WFC3/IR detector and [Appendix D](#) for discussion of planning observations to minimize the impact of persistence.)

The capability of multiple readouts and the absence of bleeding makes IR detectors capable of very high dynamic-range observations. Non-destructive readouts also allow for the recovery of pixels affected by cosmic rays (CRs), because CR hits can be recognized and removed between adjacent reads. Unlike CCDs, IR detectors also show minimal long-term on-orbit CTE degradation, because they do not employ the charge transfer mechanism used in CCDs. IR detectors, however, are intrinsically non-linear. Nevertheless, at low and intermediate signal levels, the departure from linearity is quite modest and can be well calibrated by a low-order polynomial fit, whose parameters can in principle be determined for each pixel.

5.5.2 IR Detector Basics

In this section, we briefly describe the operational principles of the WFC3/IR detector. Figure 5.18 (adapted from McLean 1997, *Electronic Imaging in Astronomy: Detectors and Instrumentation*) shows the basic physical structure of the photovoltaic HgCdTe detector used in WFC3.

Figure 5.18: Cross-section of a WFC3-IR detector (not to scale).



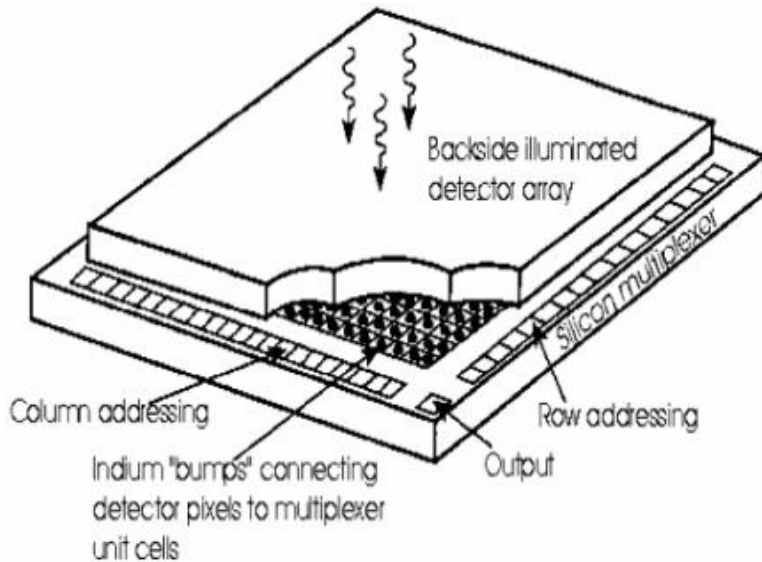
Infrared detectors used in astronomy today are basically two-dimensional arrays of p-n junctions working as photodetectors (photodiodes). In a p-n junction, negative charges migrate from the n-type doped material to saturate the unmatched covalent bonds of the adjacent p-type material. The displaced carriers establish an electric field across the junction, setting up an intermediate region depleted of free carriers. The depletion region is therefore both charged and highly resistive. The strength of the electric field and the size of the depletion region may be increased by applying an external electric field ("negative bias"). This biasing corresponds to the initial RESET applied at the beginning of the integration. When an incident IR photon is absorbed by the photosensitive material, it creates a free electron-hole pair. The two photo-generated charges drift in the material and would eventually recombine. However, if the mobility of the charge carrier (a hole in an n-type material) is high enough, it will reach the depletion region before recombining and be swept to the other side of the junction by the electric field. There, in the p-type region, it will recombine with one of the electrons of the ionized holes, causing a reduction of the voltage across the junction. This change of voltage can be measured and, being proportional to the number of photo-generated charges, provides a direct measure of the photons captured on each pixel.

In the case of the WFC3 IR detector, the photosensitive material is made of HgCdTe grown with a molecular beam epitaxial (MBE) process on a ZnCdTe substrate. The fraction (stoichiometric ratio) of Hg vs. Cd controls the long-wavelength cutoff of the material, whereas the doping material (As for the p-type, In for the n-type) creates the p-n junction. The MBE growth process is different from that used in the NICMOS detectors on *HST*, in which the HgCdTe was grown on sapphire in a liquid phase (PACE process). MBE growth on a ZnCdTe substrate is expected to provide a better lattice match to HgCdTe than sapphire, creating fewer defects and charge traps at the interface between the two materials. The MBE growth process is followed by the processing phase, in which the implants and contacts of each pixel are manufactured.

As usual with IR arrays, the readout circuitry is made on a separate CMOS chip (multiplexer or MUX), which is eventually hybridized to the detector with an indium contact for each pixel (see Figure 5.19). After the two chips have been hybridized, the ZnCdTe substrate is removed to reduce the susceptibility of the device to cosmic-ray events and to

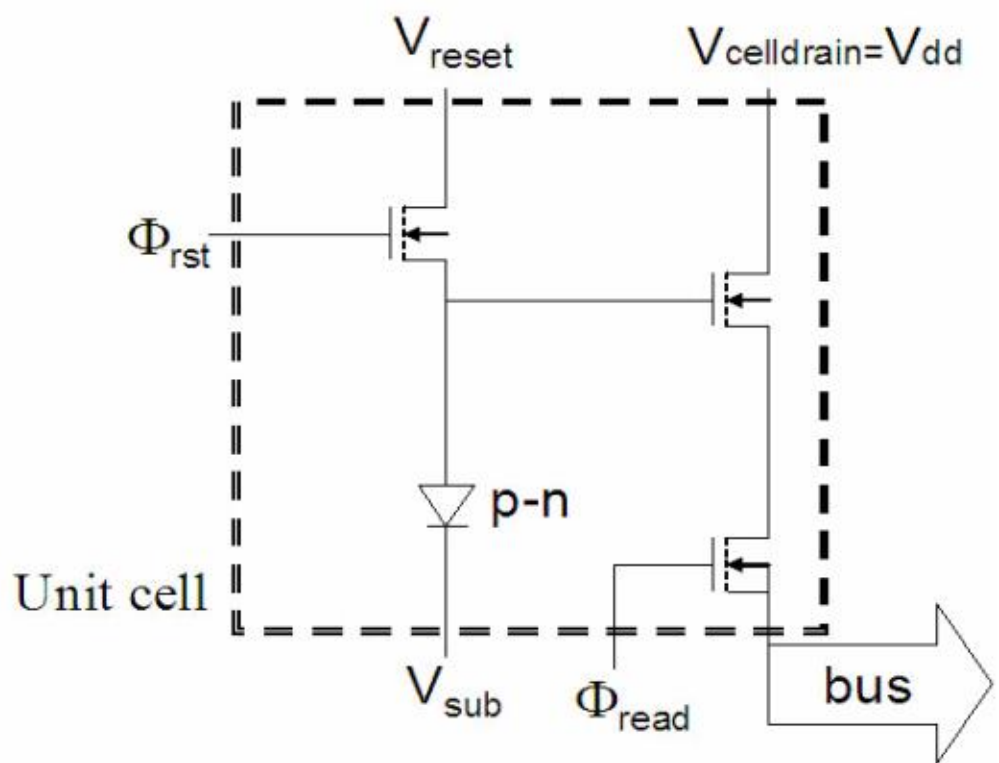
increase the sensitivity at short wavelengths. The final chip therefore is a CMOS device connected through indium columns to a thin layer of HgCdTe photosensitive material.

Figure 5.19: Basic “hybrid” structure of infrared array detectors (not to scale).



In the MUX, each pixel has its own dedicated readout circuitry (unit cell). In particular, the voltage change across the p-n junction is monitored by a field-effect transistor (FET) configured as a source-follower amplifier, which has gain of 1 and effectively decouples the detection process from the noisy readout circuitry. Two other FETs connect the pixel to the reset voltage and the output line. Figure 5.20 shows the equivalent circuit diagram for the WFC3 detector unit cell. Each WFC3 IR unit cell contains three transistors. For comparison, the NICMOS detectors have four transistors, whereas the latest generation of Hawaii-2RG detectors for JWST has seven transistors per unit cell. A higher number of transistors increases the versatility of the device. For example, on the NICMOS detectors it is possible to reset each individual cell, whereas on WFC3 detectors the reset is sent simultaneously to all cells on the same row. Note that since there are no potential barriers between pixels, pixels do not spill charges into nearby pixels when they reach a certain level (“blooming full well”) of accumulated charges, as in typical multiphase CCDs. Therefore, IR detectors do not show “bleeding” along columns. Moreover, due to individual readout, bad pixels do not block the rest of the column as they do in a CCD.

Figure 5.20: Equivalent circuit diagram of the WFC3/IR unit cell.



5.6 WFC3 IR Readout Formats

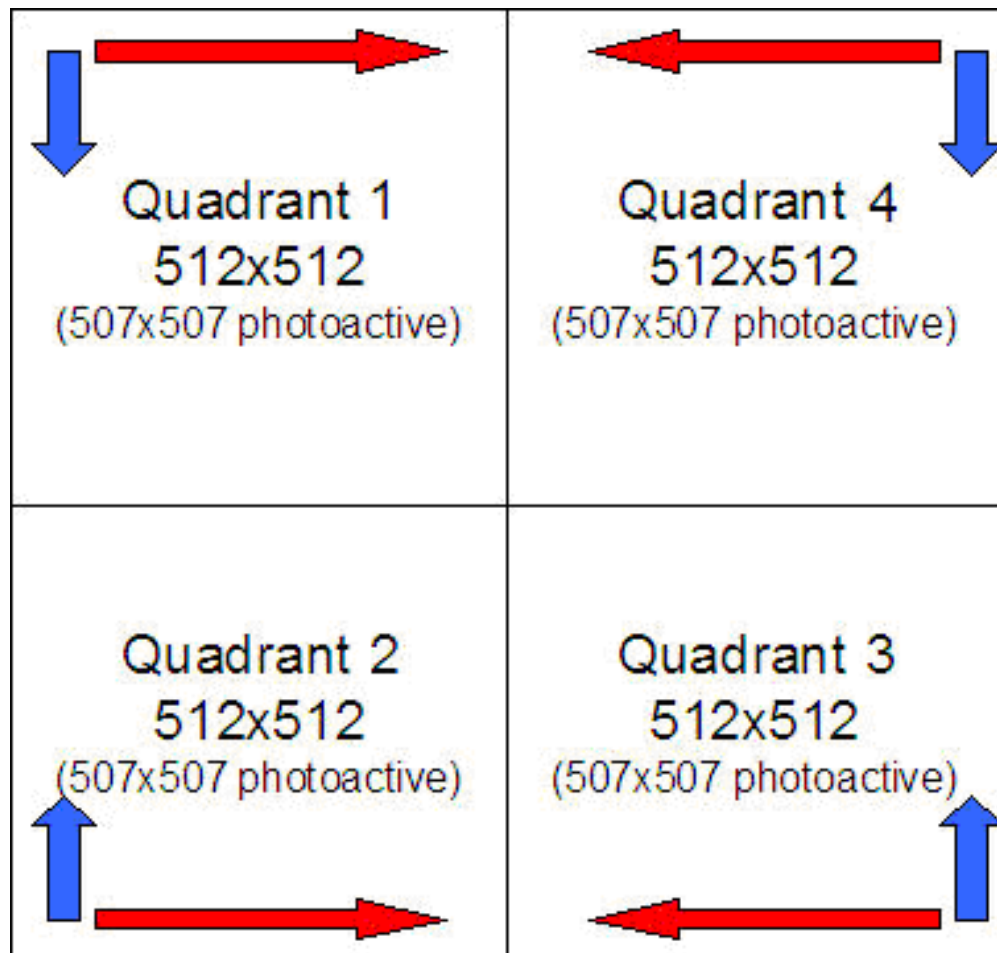
[5.6.1 Full-Frame Readouts and Reference Pixels](#)

[5.6.2 Subarrays](#)

5.6.1 Full-Frame Readouts and Reference Pixels

The WFC3 IR detector contains 1024×1024 square pixels of 18×18 micron physical size. The detector is divided into four quadrants of 512×512 pixels, each of which is read out independently from its outer corner, as illustrated in [Figure 5.21](#). The outermost rows are read first, proceeding along each row from the outermost column to the horizontal mid-point of the detector, and then continuing inwards on subsequent rows to the vertical mid-point.

Figure 5.21: Schematic layout of the WFC3 IR detector. The long (red) and short (blue) arrows indicate the direction of the fast and slow multiplexer clocking, respectively. In contrast to CCD “bucket-brigade” image-shifting to the output amplifier, the IR detector pixels are selected for readout in a raster pattern by multiplexer circuits.



A major effort has been made to eliminate both the amplifier glow and bias drifts that have affected the NICMOS detectors.

To eliminate the amplifier glow entirely, WFC3 uses external amplifiers located in the immediate vicinity of the detector, rather than those directly on the multiplexer (which are also present, but are not activated in the WFC3 implementation).

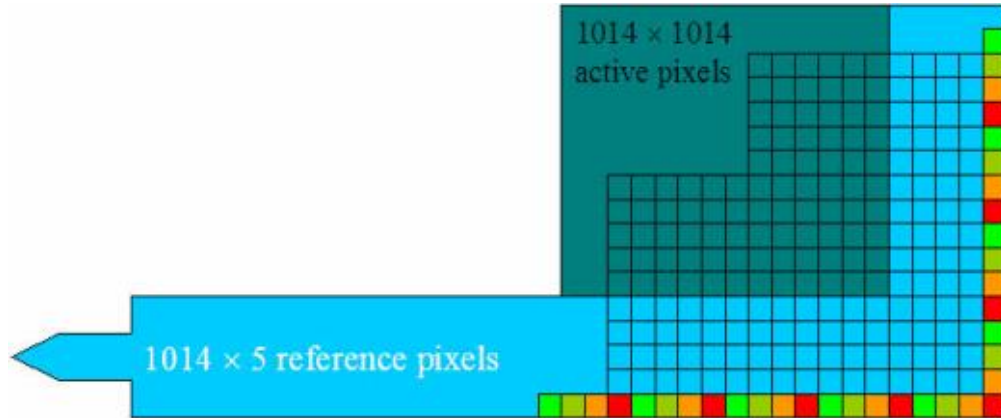
In regard to bias drifts, the WFC3 IR class of detectors is the first to use reference pixels, configured as follows (see [Figure 5.22](#)). Of the 1024×1024 pixels, only the inner 1014×1014 pixels are light-sensitive. The five outer rows and columns of pixels all around the array use fixed capacitances to provide constant-voltage reference values. There are actually two types of reference pixels: (1) the pixels on the outermost columns/rows are connected to capacitors located outside of the unit cells. Their values follow a 4 \times periodic pattern, providing 4 sequentially increasing voltage levels all within the range of the detector output signal; (2) the 4 inner rows/columns are instead connected to capacitors created within their

unit cells. These on-board capacitors are identical by design and all provide nearly the same reference signal. The current version of the WFC3/IR data reduction pipeline uses only the inner reference pixels, as they provide a more robust statistical estimate of the variable detector bias.

The reference pixels track the low-frequency drift of the readout electronics and efficiently remove the “pedestal” variations that affected, for example, NICMOS. Analysis of ground test data has shown that the reference pixel signal is also sensitive to the detector temperature and may therefore be used to assess the expected level of dark current during an exposure, independently from a reading of the detector temperature itself. Actual on-orbit experience indicates that detector temperature is very stable.

Full-frame exposures result in one raw 1024×1024 pixel image for each readout, which includes the 5 rows and columns of reference pixels on the periphery. After calibration, the reference pixels are trimmed off, leaving only the 1014×1014 arrays of light-gathering pixels.

Figure 5.22: Schematic layout of the active pixels (dark shading) and of the reference pixels at a corner of the WFC3/IR detector. The color coding represents different values of the reference pixel capacitance.



5.6.2 Subarrays

The default IR exposure mode is to read out the entire detector. It is also possible, however, to read out only a portion of the detector. WFC3 IR subarrays are implemented in four user-selectable sizes: 64×64 , 128×128 , 256×256 , and 512×512 pixels. All subarrays are centered on the detector with an equal number of pixels in each quadrant, using each of the 4 detector amplifiers to read the subarray pixels contained in its quadrant (as with full-frame readouts).

The 5-pixel wide bands of reference pixels that share rows or columns with the subarray are also included in subarray readouts. The reference pixels therefore come from the same detector rows and columns as the “live” portion of the subarray, with the 5×5 pixels at the subarray corners filled by the reference pixels at the corresponding corner of the detector.

Certain combinations of IR subarrays and sample sequences give rise to images containing a sudden low-level jump in the overall background level of the image. The cause of the artifact is under investigation. The use of IR subarrays is discussed in more detail in [Section 7.4.4](#).

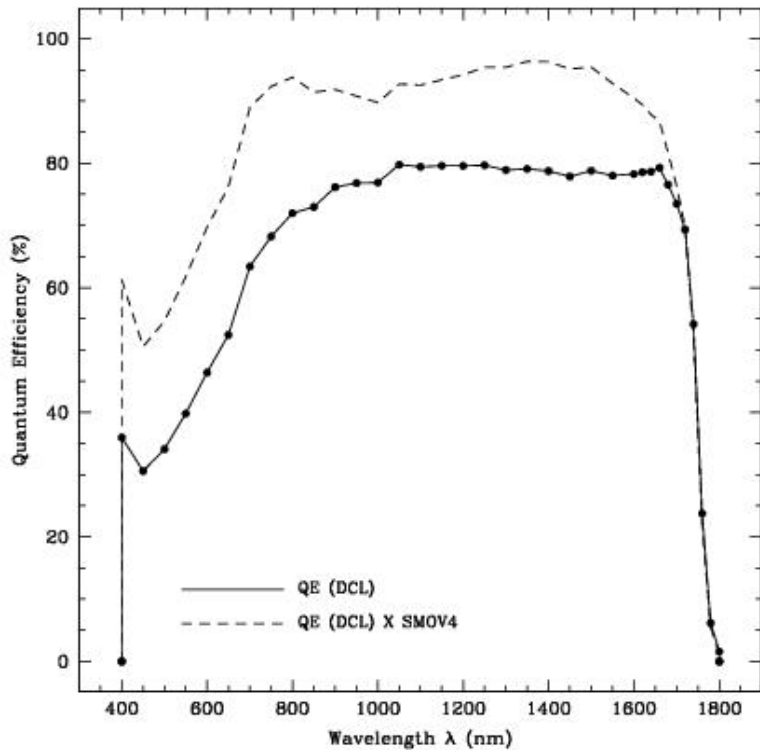
5.7 IR Detector Characteristics and Performance

- [5.7.1 Quantum Efficiency](#)
- [5.7.2 Dark Current](#)
- [5.7.3 Read Noise](#)
- [5.7.4 Flat Fields](#)
- [5.7.5 Linearity and Saturation](#)
- [5.7.6 Count Rate Non-Linearity](#)
- [5.7.7 Detector Cosmetics](#)
- [5.7.8 Crosstalk](#)
- [5.7.9 Image Persistence](#)

5.7.1 Quantum Efficiency

The QE of the flight IR detector, as measured at the Goddard Detector Characterization Lab (DCL), is shown as a solid curve in [Figure 5.23](#). The QE curve demonstrates very high sensitivity of the IR detector for wavelengths longer than 1000 nm. The actual total system throughput of WFC3 depends on many factors including the *HST* OTA, pick off mirror, filter transmission functions, QE, etc. Based on ground measurements of these quantities, the total system throughput was calculated and compared to the first on-orbit measurements. A 5–20% increase in the total system throughput was discovered, which we attribute to multiple factors. The dashed curve represents the QE under the assumption that the entire flight correction is in the QE. Note, however, that this assumption is unphysical given the realities of anti-reflection coatings and interpixel capacitance.

Figure 5.23: QE curve of the WFC3/IR detector based on Goddard DCL measurements (solid). The total system throughput of the IR detector was measured on-orbit to be higher than ground tests by up to 20%, and the dashed curve shows the QE under the assumption that this entire gain is due to the QE. In reality, some fraction of this gain must be attributable to other *HST* and/or instrument components.



5.7.2 Dark Current

To avoid the complexity and limited lifetime of a stored-cryogen system, while at the same time providing the low operating temperatures required for dark-current and thermal-background reduction, the WFC3 IR detector is refrigerated with a six-stage TEC to a nominal operating temperature of 145 K. This is an unusually high operating temperature for near-IR detectors, and required tailoring the composition of the HgCdTe material for a long-wavelength cutoff at \sim 1700 nm. The higher band-gap associated with the short cutoff wavelength effectively limits both the intrinsic detector dark current and its sensitivity to the internal thermal background.

Direct thermal control of the detector (via a sensor integrated in the MUX that controls the 6-stage TEC current) provides typical thermal stability of < 50 mK. Tests made on similar detectors indicate that the residual dark-current variations can be largely calibrated and subtracted out using reference pixels.

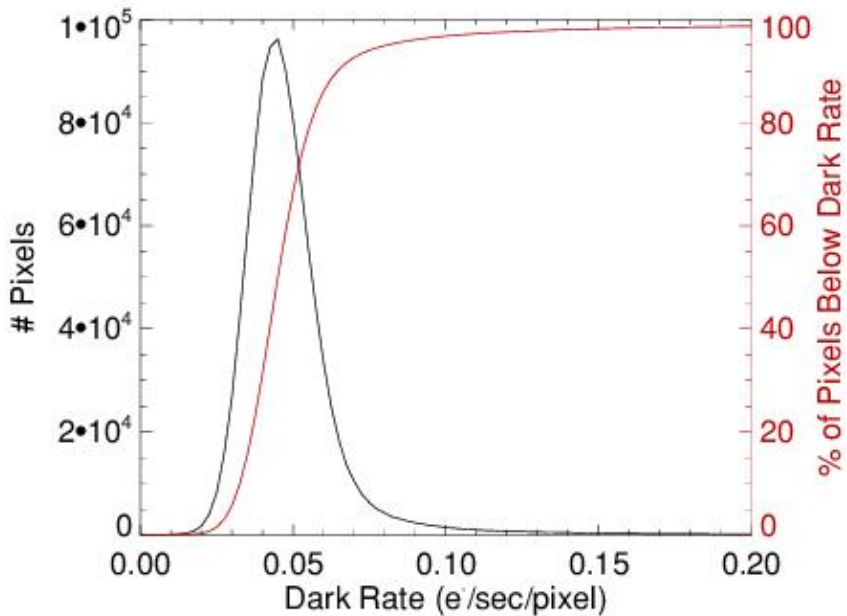
WFC3 IR exposures taken with an aluminum blank in place, rather than a filter, provide a measure of the detector dark current. The dark current of the flight array has a skewed distribution, with a mode, median, and mean of 0.045, 0.048, and $0.048 \text{ e}^-/\text{s}/\text{pixel}$ respectively. The shifted mode is due to the asymmetry of the dark-current distribution among the

pixels, characterized by a long tail of “hot pixels” randomly located across the detector. The mean dark current remained unchanged in the first three years of in-flight operations ([WFC3 ISR 2012-11](#)).

The histogram of dark current values, along with the cumulative dark-current distribution, i.e., the fraction of pixels with a dark current lower than a certain level, is shown in Figure 5.24. (see [WFC3 ISR 2009-21](#) for further details on dark current calculations). Improved superdark reference files have been created for all allowed full-frame and subarray modes using data collected during cycles 17, 18, 19, and 20 ([WFC3-ISR 2014-06](#)). The signal-to-noise has improved by a factor of 3-11 due to the use of a great deal more data, the use of a non-linearity correction, and the use of persistence masks.

Note that in broad filters, the zodiacal light background is $0.3\text{-}1.0 \text{ e}^-/\text{s/pixel}$, a factor of 10-20 times larger than the dark current. The WFC3 ETC can be used to compute the zodiacal light contribution for a given pointing, in addition to providing thermal and dark current estimates. See Sections [7.9.5](#) and [9.7](#).

Figure 5.24: Histogram of the WFC3/IR detector dark current.

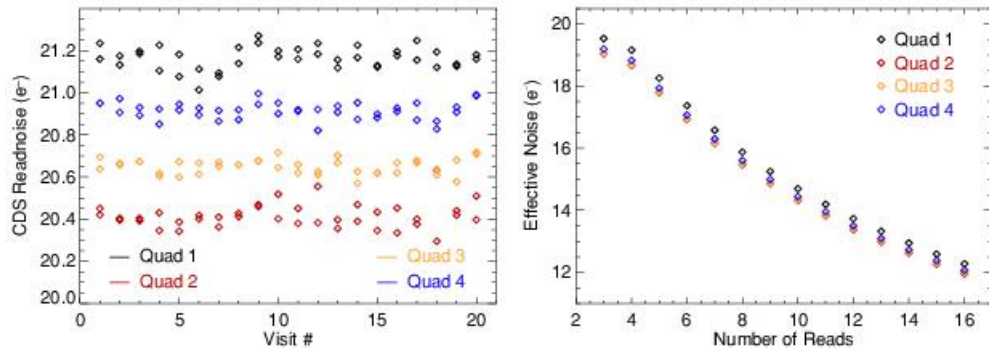


5.7.3 Read Noise

The IR detector has four independent readout amplifiers, each of which reads a 512×512 pixel quadrant. The four amplifiers generate very similar amounts of read noise. This is illustrated in Figure 5.25, which compares the correlated double sampling (CDS) read noise levels for the four quadrants of the detector. CDS read noise refers to the noise associated with subtracting a single pair of reads. These read noise values were derived from a series of RAPID ramps taken during SMOV testing, providing a measure of the total noise in a difference image. For short ramps, such as these RAPID ramps, the contribution of shot noise due to dark current accumulation is less than 0.01 e^- . Figure 5.25 therefore shows that the CDS read noise of the detector is between $20.2\text{--}21.4 \text{ e}^-$.

By averaging over multiple reads, the effective noise of an IR ramp can be reduced. As shown in Figure 5.25 (below, right plot), the effective noise in a SPARS200 ramp can be reduced from $\sim 20.0 \text{ e}^-$ down to $\sim 12.0 \text{ e}^-$ (2 reads plus zeroth read and 15 reads plus zeroth read, respectively). Similar reductions in noise can be achieved with other sample sequences ([WFC3 ISR 2009-23](#)).

Figure 5.25: CDS read noise values measured for each quadrant in 40 RAPID ramps during SMOV testing (left plot). Effective noise in a SPARS200 ramp versus the number of reads +1 (i.e., including the zeroth read) (right plot).



For some programs, read noise will not be an issue while for others, such as ultra-low-background observations, the read noise can be a non-negligible component of the noise floor. The relative contribution of read noise to the total noise will depend, of course, on infrared background levels as well (see [Section 7.9.5](#)). The contribution to the read noise in WFC3 IR data due to digitization errors associated with the conversion from electrons to data numbers (DN) is negligible.

5.7.4 Flat Fields

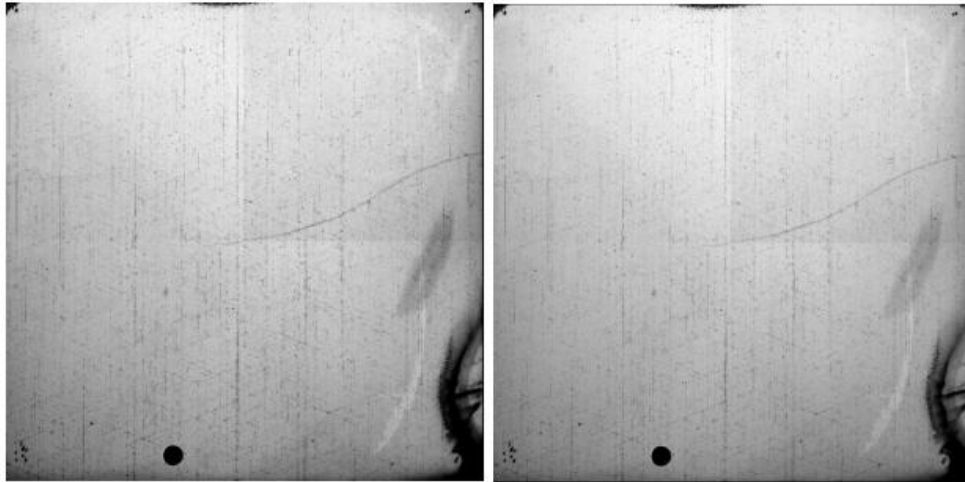
Before launch, ground-based flats were obtained for the 15 imaging IR filters at a mean S/N of ~500 per pixel using an external optical stimulus ([WFC3 ISR 2008-28](#)). On-orbit monitoring using flat fields made with a tungsten lamp shows no evidence of pixel-to-pixel variations in any of the filters ([WFC3 ISR 2015-11](#)). The lamp appears to be slowly degrading, with a slight decrease in count rate (~0.3% per year from Oct. 2010 to Dec. 2014).

Because the overall illumination pattern of the ground-based flats did not precisely match the illumination attained on-orbit from the OTA, there are errors in these ground-based flats on large spatial scales. These errors were initially measured by performing stellar photometry on rich stellar fields that were observed using large-scale dither patterns during SMOV and cycle 17. In the SMOV exposures for 4 of the wide (W) filters, the rms difference between the sigma-clipped average magnitude of a star and its magnitude in the first pointing was 1.5%, independent of wavelength ([WFC3 ISR 2009-39](#)). The errors have since been determined more accurately by creating sky flats from thousands of on-orbit exposures, masking out astronomical sources. Flat field reference files corrected using these sky flats were delivered in December 2011. These reference files are expected to support photometry to better than 1% rms accuracy over the full WFC3 IR field of view. A detailed description of their production and accuracy is given in [WFC3 ISR 2011-11](#). Analysis of a grid of observations of a standard star in 3 filters has shown that these flats produce consistent photometry over most of the detector, contributing rms uncertainty ~0.007 mag to photometric measurements ([WFC3 ISR 2013-01](#)). See [Section 7.9.6](#) for a discussion of “blob flat fields” that can be used to correct the photometry of blob-impacted stars in crowded stellar fields in WFC3/IR images.

- ✓ The latest information about IR flats can be found on the WFC3 website: <http://www.stsci.edu/hst/instrumentation/wfc3/data-analysis/ir-flats>

Figure 5.26 shows examples of bias-corrected ground-based flats taken with wide-band filters (left: F110W, right: F160W). Both flats are displayed with an inverse greyscale stretch chosen to highlight features.

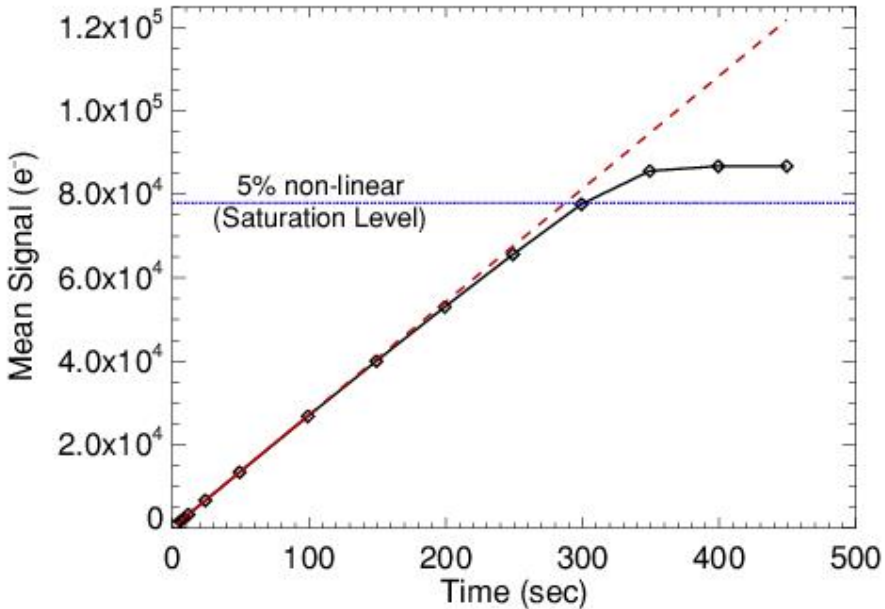
Figure 5.26: WFC3/IR ground-based flat fields at F110W (left) and F160W (right).



5.7.5 Linearity and Saturation

The WFC3 IR calibration program shows that the detector response is in fact (slightly) non-linear over the full dynamic range. This behavior is illustrated in Figure 5.27, which presents a plot of average counts as a function of time. The black diamonds are the measured average signal; a linear fit has been made to the signals up to $\sim 25,000$ electrons (solid red line). The dashed red line shows this best-fit line extended out to the total exposure time of the ramp. The blue horizontal line marks the level at which the counts deviate by more than 5% from linearity (about 78,000 electrons). For the purposes of non-linearity correction, the 5% nonlinearity level has been defined as “saturation.”

Figure 5.27: Non-linear response of mean signal (electrons) as a function of time (sec), measured in Thermal Vacuum 3 testing for the WFC3/IR detector.



The linearity correction implemented in the WFC3/IR calibration pipeline corrects pixels over the entire dynamic range between zero and saturation. Once the pixel value exceeds the saturation threshold, the pixel is flagged as saturated in the data-quality array within the FITS file and no linearity correction is applied. Pixels driven heavily into saturation can begin to show decreasing readout values, such that their DN values fall back below the defined saturation threshold. To prevent a situation where a pixel is flagged as saturated in one or more readouts, but then not flagged in later readouts, the calibration processing system flags saturated pixels in all subsequent readouts for pixels that are found to be above the saturation threshold in any given readout.

Trials of non-linearity corrections have shown that a third-order fit to the measured linearity versus signal for each pixel provides a better correction than the one currently implemented in the pipeline ([WFC3 ISR 2014-17](#)). Photometric results between short and long exposures are more consistent by up to 0.5% when this method is used. We expect to implement it in the pipeline sometime in 2015.

5.7.6 Count Rate Non-Linearity

Previous HgCdTe detectors on *HST* have suffered from a count-rate dependent non-linearity. We have been investigating this effect on the WFC3-IR detector. An initial measurement of this effect was made by comparing the photometry of star clusters observed over a wide dynamic range and at overlapping wavelengths in the WFC3/IR and NICMOS and/or ACS /WFC detectors. We found a non-linearity of ~1% per dex over a range of 10 magnitudes (4 dex) which was independent of wavelength. (See [WFC3 ISR 2010-07](#).) This measurement was confirmed using exposures that boosted count rates with

Earth limb light ([WFC3 ISR 2010-15](#)) and observations of groups of stars observed with 2MASS ([WFC3 ISR 2011-15](#)). The impact of this non-linearity is that photometry of faint (i.e., sky dominated) sources calibrated with WFC3/IR zeropoints will appear 0.04 ± 0.01 mag too faint. This effect is an order of magnitude smaller than the effect found for NICMOS, but large enough to potentially limit the accuracy of photometry.

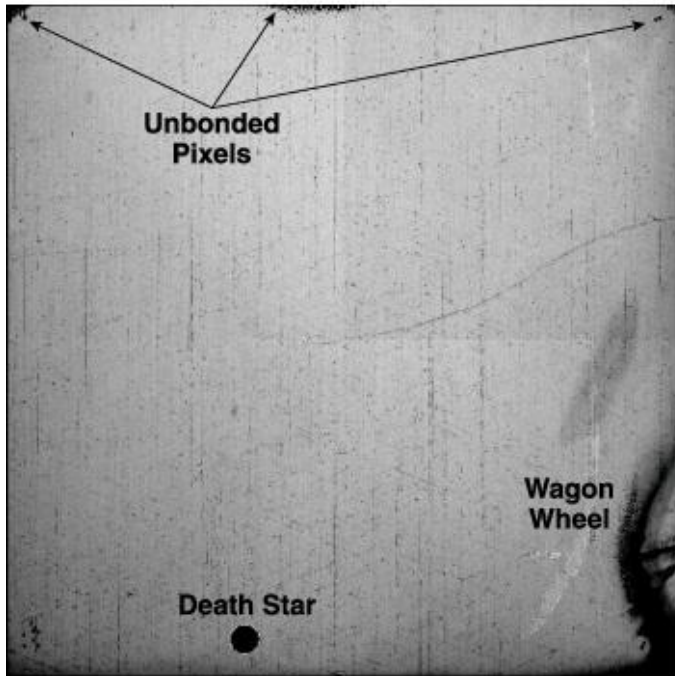
In 2019, more precise measurements of count-rate non-linearity (CRNL) were made by using a combination of comparisons of cluster star photometry between WFC3/IR and WFC3/UVIS and by using observed and synthetic magnitudes of white dwarfs ([WFC3 ISR 2019-01](#)). In this study, the measured range of CRNL was extended to higher count rates by comparing magnitudes between the ground and WFC3/IR for LMC and Milky Way Cepheids. Combining these results with all previous measurements and those from the WFC3 grism provides a consistent and improved characterization of the CRNL of WF3/IR, of $0.75\% \pm 0.06\%$ per dex, with no apparent wavelength dependence, measured across 16 astronomical magnitudes. This result may be used to correct IR photometry by using the difference in apparent flux (in dex) between where the WFC3-IR zeropoint is set (~12th mag) and the target source. Fainter sources appear even fainter and thus must be corrected to be brighter.

5.7.7 Detector Cosmetics

The make-up of the WFC3/IR detector's pixel population includes several flavors of anomalously responsive pixels: hot, cold, unstable, dead, and deviant in the zeroth read. Hot pixels, those showing excess charge, are defined as pixels with more than 100 times the average dark current. Cold pixels are inversely sensitive to incident photons and exhibit a negative slope when measured up the ramp (i.e., pixel value is lower in last frame up the ramp compared to first frame). The anomalous response of a cold pixel could be due to lower intrinsic QE in that pixel or to surface defects. Unstable pixels, as the name implies, are those that behave in an unpredictable fashion; that is, the signal up the ramp does not repeat reliably from ramp to ramp (see Appendix 2, [WFC3 ISR 2010-13](#) for examples). There are dead, or unbonded, pixels which do not respond to light ([Figure 5.28](#)). Overlapping the dead pixel population is the population of pixels which have bad zeroth read values, generally due to being short-circuit or unbonded ([WFC3 ISR 2003-06](#)).

In addition to randomly-distributed bad pixels, coherent regions of bad pixels exist in the IR detector ([Figure 5.28](#)).

Figure 5.28: IR Detector Cosmetic Defects



Pixels in the lower-right region (dubbed “wagon wheel”) have lower than normal quantum efficiency. There are dead pixels near the detector edge and in the circular “death star” feature near the bottom. Pixels with deviant zeroth read are concentrated in the areas of the death star, the upper corners of the detector, and the quadrant boundaries. (The death star region is marked in the WFC3 FOV in APT to aid in observation planning.) [WFC3 ISR 2008-28](#) describes the characterization of these defects based on ground-testing data; [WFC3 ISR 2010-13](#) describes the various types of populations of bad pixels as observed on-orbit.

The anomalously responsive pixels comprise a small percentage of the science pixel population. The current values of the percentages by type are: 0.4% hot, 1% unstable, 0.4% dead or cold, and 0.5% deviant in the zeroth read. (Some pixels are counted twice, as dead and as deviant in the zeroth read.)

5.7.8 Crosstalk

As is common in devices with multiple amplifiers being read out simultaneously, the IR channel exhibits crosstalk: a bright source in one quadrant causing electronic ghosting in another quadrant. In the IR, the crosstalk manifests itself as a very low-level negative mirror image; amplifiers 1 and 2 are coupled (upper left and lower left quadrants; see [Figure 5.21](#)) and amplifiers 3 and 4 are coupled (lower right and upper right quadrants). That is, sources in quadrant 1 generate crosstalk in quadrant 2, sources in quadrant 2 generate crosstalk in quadrant 1, and so on.

The level of the IR crosstalk is only $\sim 1e^{-6}$ that of the target flux ([WFC3 ISR 2010-02](#)); for unsaturated sources, the crosstalk is below the background noise. Once a source saturates, the crosstalk becomes visible at about the level of the background and remains constant as the voltage of the device is pinned.

5.7.9 Image Persistence

Image persistence is a common problem in HgCdTe and other types of IR arrays. Persistence manifests itself as ghost images or afterglows from earlier exposures. It was seen in NICMOS, and is also seen in a small but non-negligible fraction of the exposures taken obtained with the Hawaii 1R detector that is the heart of the WFC3 IR channel.

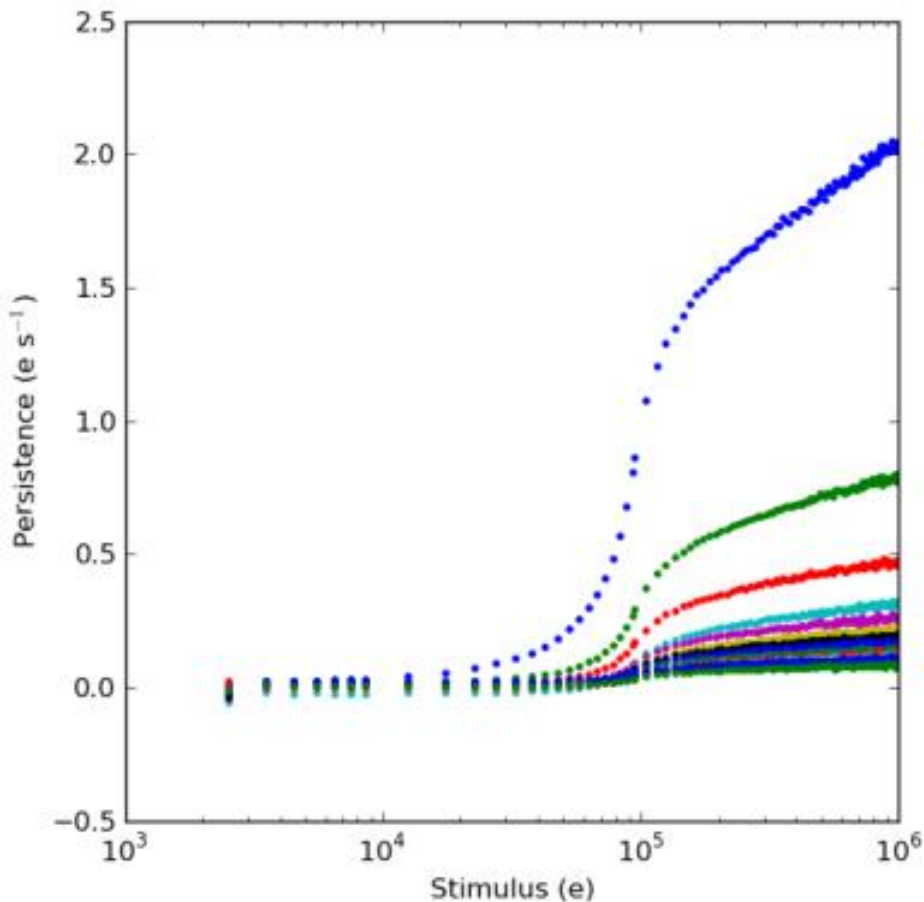
Persistence is caused by traps that exist in the active regions of the reverse-biased diodes that make up the pixels of the detector. Resets, which occur at the end of multi-accum exposures (and during the process of flushing the detector when not observing with the IR channel), maximize the reverse bias of the diodes. Light impinging on the diode creates photo-electrons which cause the reverse bias to decrease. Changing voltages within the diode expose portions of the depletion region to free charge. Dislocations in these newly exposed regions trap charge. More traps are exposed for bright sources than for faint ones. This trapped charge is released in later exposures, resulting in after-images. The greater the saturation of the detector, the greater the number of traps and the greater the afterglow. Smith, et al., 2008 ([Proc. SPIE, 7021](#)) has provided a very clear description of the physics of persistence and the effects in IR arrays.

The characteristics of persistence vary for different devices and device technologies, reflecting in part how traps are distributed within the diodes. Persistence in the WFC3 channel is primarily a function of the fluence (the total number of photo-electrons released) in an exposure, and secondarily a function of the amount of time the pixel is held at a high fluence level. As discussed by Long et al 2012 ([Proc. SPIE, 8442](#)), the amount of persistence in the IR detector on WFC3 is a non-linear function of the fluence. Persistence is observed mainly in situations where fluence levels approach or exceed saturation of the detector.

Several examples of persistence in WFC3 observations and strategies for avoiding persistence are described in [Section 7.9.4](#). A description of a phenomenological model of persistence used to aid in removing the effects of persistence is given in the [WFC3 Data Handbook](#).

[Figure 5.29](#) shows the characteristic shape of persistence versus fluence as observed in a series of darks following an image of Omega Cen which had been deliberately exposed to a level where many stars in the image were saturated. The first dark exposure took place a few minutes after the end of the Omega Cen exposure and the last dark exposure took place about one orbit later. (See [WFC3 ISR 2013-07](#).) The amount of persistence is fairly small until the exposure level reaches about half of full well and saturates near full well exposure. The persistence gradually decays with time from the first dark exposure (highest curve in figure) to the last dark exposure (lowest curve in figure).

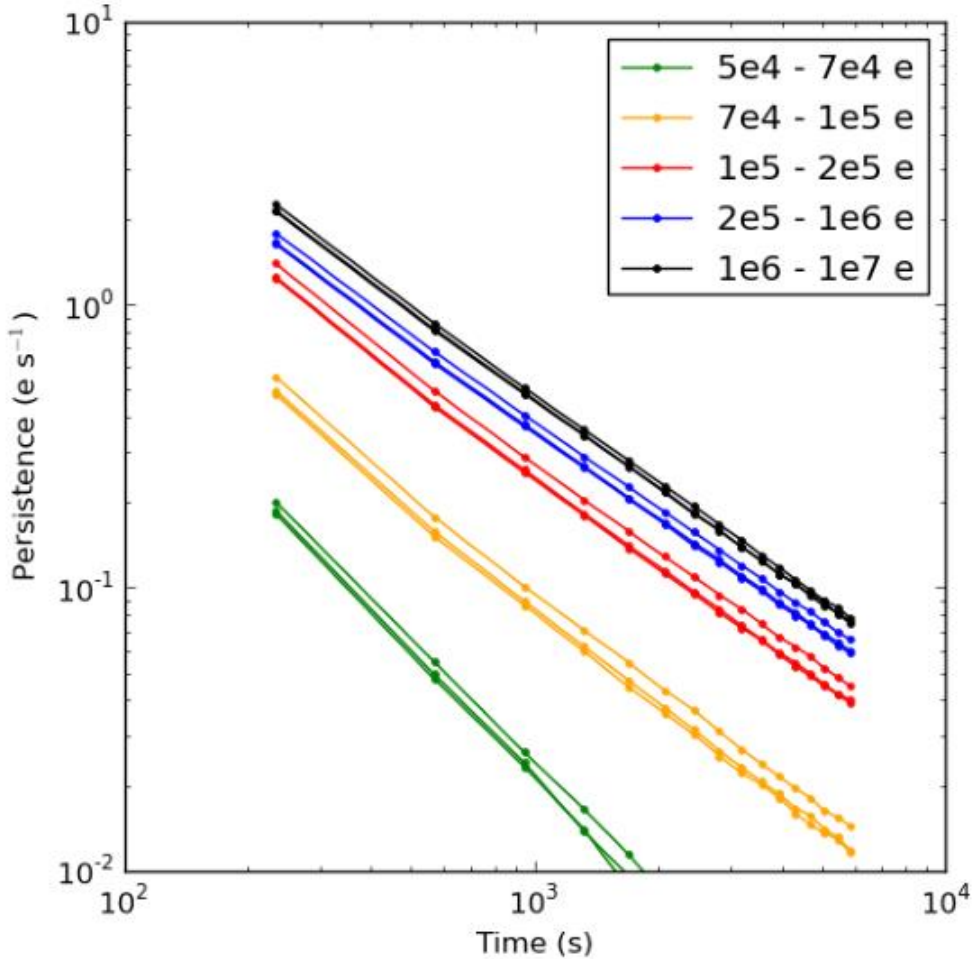
Figure 5.29: Persistence as a function of fluence (“stimulus” provided by exposure to Omega Cen) observed over the detector in a subsequent series of darks (color coded)



Persistence decays roughly as a power law with time, as illustrated in Figure 5.30, which is based on the data displayed in Figure 5.29. The different curves here show the decay for different levels of saturation, as measured in electrons.

Persistence at low fluence levels decays more rapidly than persistence at high fluence levels. There are 3 curves for each level corresponding to the 3 times this experiment was repeated. The differences are partially due to the fact that different pixels were illuminated to different levels each time, but may also indicate some intrinsic variability that is not understood. For comparison, the dark current is about 0.015 electrons/sec. If one assumes that a power law describes persistence from 100 to 10,000 seconds after an exposure, then one concludes that about 3% of charge is trapped in an exposure that has a nominal fluence level of 100,000 electrons.

Figure 5.30: Persistence as a function of time for pixels with selected (color coded) levels of fluence provided by exposure to Omega Cen



While fluence is the primary factor in determining how much persistence there will be after an observation, the amount of persistence actually depends on the time history of each pixel. Tests show that there is more persistence from a pixel exposed multiple times to the same brightness source ([WFC3 ISR 2013-07](#)) and the longer a pixel is held at a fixed flux level ([WFC3 ISR 2013-06](#)). This can be understood qualitatively as being due to the fact that traps have finite trapping times. More accurate prediction of persistence has been achieved using an exposure-time dependent power law decay model ([WFC3 ISR 2015-15](#)) along with a “correction flat” that takes into account large-scale variations over the detector ([WFC3 ISR 2015-16](#)). Observers are cautioned that variability in persistence has been found in dark exposures taken within 1000 sec of a brief (274 sec) stimulus ([WFC3 ISR 2018-03](#)).

[MAST](#) includes a search form that provides a persistence image for a specified exposure, which has been produced by applying this model to the preceding WFC3/IR exposures. (See the [WFC3 Data Handbook](#).) Since the model is imperfect, the persistence image is intended as a guide to which pixels to flag in an exposure rather than as a reliable indicator of flux corrections.

Chapter 6: UVIS Imaging with WFC3

Chapter Contents

- [6.1 WFC3 UVIS Imaging](#)
- [6.2 Specifying a UVIS Observation](#)
- [6.3 UVIS Channel Characteristics](#)
- [6.4 UVIS Field Geometry](#)
- [6.5 UVIS Spectral Elements](#)
- [6.6 UVIS Optical Performance](#)
- [6.7 UVIS Exposure and Readout](#)
- [6.8 UVIS Sensitivity](#)
- [6.9 Charge Transfer Efficiency](#)
- [6.10 Photometric Calibration](#)
- [6.11 Other Considerations for UVIS Imaging](#)
- [6.12 UVIS Observing Strategies](#)

6.1 WFC3 UVIS Imaging

As described in [Chapter 2](#), the optical design of WFC3 features two independent channels, each with its own separate optics, filters and grisms, and detectors. The **UVIS channel** is sensitive to UV and optical wavelengths (200-1000 nm), and the **IR channel** is sensitive to near-infrared wavelengths (800-1700 nm).

Only a single channel, either UVIS or IR, can be used at any one time. Thus they cannot be used in parallel, but they can be used sequentially within the same orbit.

A schematic diagram showing the locations of the fields of view of the UVIS and IR detectors in the *HST* focal plane is shown in [Figure 2.2](#).

This chapter describes the capabilities of the UVIS channel. The following chapter, [Chapter 7](#), describes the IR channel. Detailed performance characteristics of the detectors used in both channels are given in [Chapter 5](#) and summarized in [Table 5.1](#).

6.2 Specifying a UVIS Observation

Using the Astronomer's Proposal Tool ([APT](#)), it is relatively simple to specify the parameters for a UVIS observation. Detailed documentation of the specifications can be found in the [Phase II Proposal Instructions](#). The parameters available to General Observers for the UVIS channel are the following:

1. **Configuration:** always **WFC3/UVIS**
2. **Mode:** always **ACCUM**
3. **Aperture:** must be specified; see [Section 6.4.4](#) and [Section 6.4.5](#) for the dimensions, location, and reference point (target placement) of the full array and subarray apertures.
4. **Spectral Element:** must be specified for each exposure; see [Section 6.5](#)
5. **Optional Parameters:** the options include **FLASH** (to post-flash a specified number of electrons to reduce CTE losses; [Section 6.9.2](#)), **CR-SPLIT** (to split an exposure into a specified number of subexposures for cosmic ray rejection - but note that CR rejection can also be accomplished by combining dithered exposures; [Section 6.11.2](#)), **BIN** (to perform on-chip binning by a specified number - but beware that this increases the area affected by bad pixels and cosmic rays; [Section 6.4.4](#)), **BLADE** (to make short exposures with less vibration by selecting shutter blade A; requires approval - see [Section 6.11.4](#)), and **INJECT** (to implement charge injection to reduce CTE losses - but the use of this option is not generally permitted for science observations; see [Section 6.9.2](#)).
6. **Special Requirements:** see the [Phase II Proposal Instructions](#) for details of Special Requirements related to the timing of visits and for dithering and mosaicking. Also available is the exposure-level Special Requirement **POS TARG** for offsetting the target from the default reference point of the aperture (see [Section 6.4.3](#) for a discussion of the UVIS channel coordinate systems, [Section 6.4.5](#) for reference points, and [Appendix C](#) for the POS TARGs associated with the WFC3 patterns).
7. **Number of Iterations and Time per Exposure:** the exposure time for the UVIS channel must be an integer multiple of 0.1 s, ranging from 0.5 to 3600 s, except that 0.6 s is not allowed; see [Section 6.7.1](#) for details).

6.3 UVIS Channel Characteristics

In concept and functionality, as well as in many design details, the WFC3 UVIS channel is patterned after the ACS/WFC channel. The UVIS channel contains an optical train providing focus and alignment adjustments as well as a correction for the OTA spherical aberration, a filter-selection mechanism, a shutter mechanism, and a CCD detector assembly (which uses the same camera-head design as ACS/WFC). These are supported by a thermal-control subsystem and also by control and data-handling electronics subsystems.

As described in [Section 5.2.2](#), the detectors in the WFC3 UVIS channel are two 4096×2051 pixel CCDs, butted together to yield a 4096×4102 light-sensitive array with a ~ 31 pixel (1.2 arcsec) gap. The gap can, of course, be filled in by using appropriate telescope dithering strategies (see [Section 6.12.1](#) and [Appendix C](#)). The plate scale is approximately 0.04 arcsec per pixel, providing a good compromise between adequate sampling of the PSF and a wide field of view. Geometric distortions introduced by the WFC3 optics cause the nominally square detector to map onto the sky as a rhombus, about 162 arcsec on each side.

Upon the start of on-orbit operation, the UVIS CCDs had excellent CTE. As discussed in [Section 5.4.11](#), the CTE has degraded significantly over the first few years of operation due to the phase of the solar cycle. Observers of faint targets in exposures with low sky backgrounds should use the post-flash mode implemented for Cycle 20 to avoid large CTE losses. See [Section 6.9.2](#).

6.4 UVIS Field Geometry

- [6.4.1 Field of View and Pixel Size](#)
- [6.4.2 Geometric Distortion](#)
- [6.4.3 Coordinate Systems](#)
- [6.4.4 Subarrays and On-Chip Binning](#)
- [6.4.5 Apertures](#)

6.4.1 Field of View and Pixel Size

As described above, the UVIS channel uses two 4096×2051 CCDs, butted together to yield a 4096×4102 array with a ~31 pixel (1.2 arcsec) gap. Because the detector is tilted along its diagonal axis 21° with respect to the incident beam, the field of view projected onto the sky is rhombus-shaped, 162 arcsec on a side, with an angle of 86.1° between the sides at amplifiers B and C ([Figure 6.1](#)). The pixels projected onto the sky are also rhomboidal, ~0.04 arcsec on a side.

6.4.2 Geometric Distortion

Distortions due to the WFC3 optics cause the nominally square field of view of the UVIS detector to map onto the sky as a rhombus with small higher order distortion. Geometric distortions in both channels are discussed in more detail in [Appendix B](#).

Distortion must be taken into account when exposures are flat-fielded, photometrically calibrated, used for astrometric measurements, or combined with other dithered exposures. The *AstroDrizzle* software appropriately carries out those operations; a combination of software packages in *DrizzlePac* can be used to optimize the combination of dithered exposures. (See the [DrizzlePac](#) documentation.)

6.4.3 Coordinate Systems

There are three different coordinate systems defined for use with the CCDs in the UVIS channel, each tailored to specific purposes. They are shown in [Figure 6.1](#) and are as follows:

- **Data image-based system** (Axis1, Axis2; units of pixels)
- **Proposal POS TARG system** (Xpos, Ypos; units of arcsec)
- **HST-based system** (V2, V3 or U2, U3; units of arcsec)

Figure 6.1: UVIS Aperture Diagram

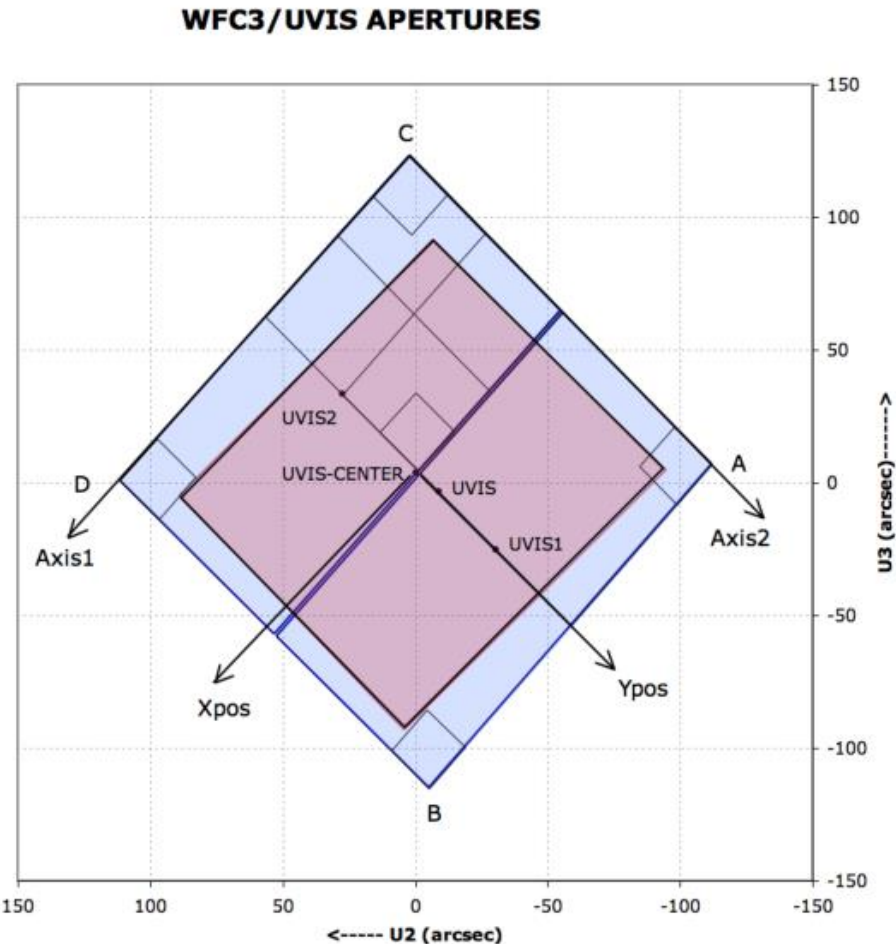


Figure 6.1 illustrates the fiducial points of the full-detector apertures (UVIS, UVIS1, UVIS2, and UVIS-CENTER), and the outlines of the $2K \times 2K$, $1K \times 1K$, and 512×512 subarray apertures. Also indicated are the positions of the four readout amplifiers (A, B, C, and D). The regions imaged by the UVIS detector (represented by blue fill) and by the IR detector (represented by red fill) are also indicated. The POSITION TARGET coordinate system for the UVIS-CENTER aperture, with its origin at that aperture's fiducial point, is illustrated. Although the POSITION TARGET coordinate systems for the other apertures are not illustrated, they are oriented the same, but have origins at each aperture's fiducial point (Section 6.4.5). ($U_2 = -V_2$ and $U_3 = -V_3$).

The **image-based coordinate system** (Axis1, Axis2, as shown in Figure 6.1) is an orthogonal system of detector pixel readouts. Axis1 is aligned with the detector data rows and Axis2 with the columns. It is used by the calibration pipeline and other data-analysis software and is sometimes also referred to as the user frame. When a detector image is displayed on a computer screen, this system has the X-axis (Axis1) increasing to the right and the Y-axis (Axis2) increasing

to the top of the screen, with 1 being the conventional index of the first pixel in both axes. For WFC3/UVIS, each chip has its own origin and Axis1, Axis2 system. The image-based coordinate system is used in most figures in this handbook, as well as in the aperture definitions available in the Science Instrument Aperture File.

The origin of this coordinate system is context specific. Logical or image coordinates have the origin at the lower left corner of the image, even for subarray images or images containing overscan data. These coordinates are shown as the “Image X,Y” coordinates in DS9. Physical or CCD coordinates have their origin at the lower left corner of the chip’s light sensitive area. Thus, pixels to the left of the science area within the physical overscan area (see [Figure 6.16](#)) actually have negative coordinates in the physical image-based system. These physical coordinates are displayed as “Physical X,Y” coordinates in DS9, which determines the coordinates using the LTV1 and LTV2 FITS header keywords. The lengths of the axes, in pixels, are stored in the FITS header keywords NAXIS1 and NAXIS2.

The **POS TARG reference frame**, sometimes referred to as the spacecraft system, is used for specifying the placement of an astronomical target relative to the aperture reference point (sometimes called the fiducial point) in the instrument field of view. Its units are arcseconds. For the UVIS channel, the POS TARG system is defined such that the POS TARG Y axis is parallel to Axis2 at the reference point of the aperture in use. The POS TARG X axis is orthogonal to the POS TARG Y axis; it is not parallel to Axis1 due to geometric distortion.

As is the case for other *HST* instruments, the POS TARG origin is defined to be at the reference point (fiducial point) of the user-selected UVIS aperture (such as the geometric center of a particular chip, or the optimum center of a quadrant, etc.; see [Table 6.1](#) below for the names of the various UVIS channel apertures). [Figure 6.1](#) illustrates the POS TARG reference frame for the “UVIS” aperture, whose center is near the middle of the WFC3 UVIS field of view; the POS TARG directions are indicated by arrows labeled Xpos and Ypos.

The **HST-based**, or vehicle (V2, V3), system is an orthogonal reference frame tied to the telescope and is used operationally for alignment, pointing, and slewing purposes. The V1 axis lies along the optical axis while V2,V3 run parallel and perpendicular, respectively, to the solar-array rotation axis (see [Figure 2.2](#)). Note that the (undistorted) diagonals of the WFC3 CCD detector run along the V2,V3 directions. Because WFC3 is on-axis, the origin of the V2,V3 system lies near the center of the WFC3 field of view. However, the V2,V3 (and U2, U3) coordinate axes have been shifted for clarity in [Figure 6.1](#). *HST* observers may be more familiar with the U2,U3 coordinate system than V2,V3; for example, the specification of the ORIENT angle Special Requirement in [APT](#) uses the position angle of the U3 axis. The U2,U3 coordinates are defined as $U2 = -V2$ and $U3 = -V3$, and are marked in [Figure 6.1](#). Observations of an astrometric field are made to locate the detector in the (V2, V3) system ([WFC3 ISR 2009-35](#)).

A fourth coordinate system (the **detector-based reference frame** in pixel units) is described here for completeness, but observers are unlikely to encounter this system other than in technical documents created during the development and ground-testing of WFC3. The detector-based system (Xdet, Ydet) is used by the flight software for commanding the detectors. It is a right-handed system based upon the orientation of the CCD serial registers, with its origin at Amplifier A (the four amplifiers are in the outer corners of the detectors, as shown in [Figure 6.1](#)). The +Xdet and +Ydet axes map to the -Axis2 and +Axis1 axes, respectively. Unlike the image-based Axis1, Axis2 system, the detector system is 0-indexed. Parallel shifting is performed along constant Xdet, and serial shifting is done along the constant Ydet direction ([Section 6.7.2](#)).

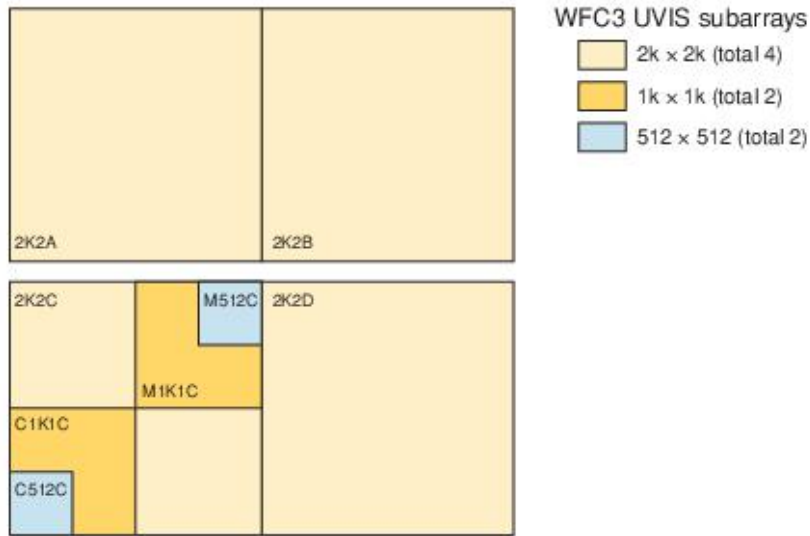
6.4.4 Subarrays and On-Chip Binning

While the default WFC3 UVIS readout mode is full-frame (i.e., both CCD chips), subarrays may be employed to read out and store only a portion of the full field of view. Subarrays may be used, for example, in cases where the full-field data-volume and/or instrument-overhead requirements would constrain the observations unacceptably. There are also circumstances in which on-chip binning may be desirable. Both modes have implications for the inclusion of physical overscan information in the readout, as listed in [Table 6.1](#) and discussed in [Section 6.7.2](#).

Subarrays

Beginning in Cycle 18, a wider range of subarray sizes was provided: 512×512 , $1k \times 1k$, and $2k \times 2k$. User-defined subarrays, and subarrays that span quadrant boundaries, are no longer supported. Subarrays are invoked via the appropriate Aperture parameter in the Phase II observing proposal; these apertures contain the string “SUB” in their names. Figure 6.2 shows the supported subarrays. See [Section 6.4.5](#) and [Table 6.1](#) for the reference points (default target positions) of these apertures.

Figure 6.2: WFC3 UVIS subarrays. See [Section 6.4.4](#) for reasons to prefer quadrant C. Full names of the subarrays are given in [Table 6.1](#).



The lower left quadrant (amp C, CCD chip 2) was chosen as the preferred site for most of the subarrays for a number of reasons. The CCD focal plane is tilted along the diagonal from amp C to amp B ([Figure 6.16](#)), so non-linear geometric distortion is greatest ([Figure B.1](#)) and PSFs are less well focused ([WFC3 ISR 2013-11](#)) near the A and D amplifiers. Bright stars imaged in the D quadrant form figure-eight ghosts that appear mostly in the D and A quadrants (see Figure 4 in [WFC3 ISR 2011-16](#)). The quantum efficiency is markedly higher below 3000 Å on chip 2 than it is on chip 1 ([Figure 5.2](#)). Note that full-quadrant subarrays have been defined for all four quadrants so that observers can use them to automatically align exposures made with continuum filters to exposures made with the quad filter apertures (discussed below; see [Table 6.1](#)). If not also using quad filters, observers who want to make observations with a single-quadrant aperture (e.g., to reduce the time used for buffer dumps of short exposures) should consider choosing the UVIS2-2K2C-SUB aperture rather than the subarray apertures in the other quadrants for the reasons outlined here.

For the special case of quad filters (which are optical elements that include four different bandpasses simultaneously, one bandpass per WFC3 UVIS quadrant), the observer must select one of the “QUAD” Aperture values in the Phase II proposal, in conjunction with the desired quad filter via the filter parameter. This combination of quad aperture and quad filter ensures that the target is automatically placed in the correct quadrant for imaging with the requested quad bandpass. Furthermore, specification of the subarray quad aperture (UVIS-QUAD-SUB) instructs the ground system to read out only the 2k × 2k quadrant of interest. If “-SUB” is omitted from the quad aperture name (i.e., UVIS-QUAD, UVIS-QUAD-FIX), the target is positioned in the proper quadrant for the bandpass requested in the filter parameter, but the entire frame, both CCDs, is still read out. [Table 6.1](#) indicates which apertures place the target at the geometric center of the subarray, and which apertures place it at a substantial offset from the center. See the [Phase II Proposal Instructions](#) for updates in aperture definitions at the beginning of a new cycle.

Use of any quad filter aperture, full-frame or subarray, is fully supported. However, if data volume and overhead time are not an issue, the observer is encouraged to allow full-frame readouts of quad-filter exposures, enabling serendipitous discoveries in the other quadrants of the image as well as enrichment of the *HST* data archive.

On-Chip Binning

The BIN optional parameter may be used in the observing proposal (see [Section 6.2](#)) to specify that the CCDs be read out in binned mode. Legal values for the parameter are NONE (the default), or 2 or 3, for 2×2 and 3×3 on-chip binning, respectively. On-chip binning is only allowed with full-frame readouts; it may not be used in conjunction with any subarray mode. To perform on-chip binning, multiple rows are parallel-shifted into the serial register, which is shifted multiple pixels at a time into a single output pixel, which is then read once. For the reasons discussed below, on-chip binning has not been useful for most programs, especially since the introduction of post-flash.

One supposed advantage of on-chip binning is that it reduces the readout noise: a 2×2 or 3×3 binned pixel contains approximately the same amount of read noise as a single pixel in an unbinned readout (see [Section 5.4.7](#)), but 4 times or 9 times the signal. However, binning increases the fraction of the image affected by cosmic rays and by the ever-increasing number of hot pixels (see [Section 5.4.9](#)). Moreover, if the background in an exposure is so low that read noise is a significant concern, then CTE losses, which are also ever-increasing over time, will make faint sources difficult or impossible to detect. CTE losses can be reduced by using post-flash to increase the background by a selected number of electrons per unbinned pixel (see [Section 6.2](#)), ideally bringing the total background up to a level of ~12 electrons/pixel (see [Section 6.9](#)). Note that the post-flash is applied before the readout, so if binning and post-flash were to be used together, a post-flash of 12 electrons per pixel would put 48 electrons into a 2×2 binned pixel, and 108 electrons into a 3×3 binned pixel, with a consequent increase in noise. The reduction in read noise due to binning would then have a minor effect on the overall signal-to-noise ([Section 9.6](#)), not worth the disadvantages of binning.

On-chip binning reduces the data volume, which affects the management of buffer dumps. Buffer dumps of unbinned full frame exposures can be done in parallel to the exposures only for exposure times at least as long as 348 sec. Shorter unbinned exposures require serial buffer dumps, using up valuable time during an orbit. Use of the binned modes can reduce or eliminate the time devoted to serial buffer dumps during an orbit, and thus increase the number of exposures that can be fit into an orbit. For example, the number of 100 sec exposures that can be executed in a typical orbit is 6 for unbinned data, 12 for 2×2 binned data, and 19 for 3×3 binned data. This gain is, of course, achieved at the expense of spatial resolution of the already under-sampled PSF (see [Section 6.6.2](#)) and at the cost of increasing the area affected by bad pixels and cosmic rays. A better way to reduce data dumping time is to make unbinned exposures in a subarray large enough to contain the target.

Binning affects the overscan data associated with an exposure. At the frame edges, some science and overscan pixels are binned together. [Section 6.7.2](#) gives details concerning the rows and columns affected by binning mixed science and overscan data.

6.4.5 Apertures

The **APERTURE** parameter in the Phase II observing proposal defines two quantities: the active **region** of the detector to be read out (full frame or subarray), as well as the positioning of the target within the region (**reference point**). The default is to place the target at the reference point (also called the fiducial point) of the chosen aperture, but a **POS TARG** Special Requirement may be added to offset the target from this position.

With regard to pointing *HST*, there are two types of apertures: “**fixed**” and “**optimum**.” The fixed positions have reference points near the geometric center of the aperture in question, and, as the name implies, their locations will remain fixed in image-based coordinates for the life of the instrument. The “optimum” apertures have reference points that are offset from the geometric center (if the need arises) so as to avoid any known CCD features (e.g., bad column, quad filter edge effects) that might compromise the observation of a target at that position. The locations of the “optimum” aperture reference points—in both the image-based coordinate system and the spacecraft V2,V3 coordinate system—may change over time as the characteristics and the characterization of the CCD evolve.

 **For updates on subarray and aperture definitions, check the Science Instrument Aperture File (SIAF) page:**
<http://www.stsci.edu/hst/instrumentation/focus-and-pointing/apertures>.

The choice of optimum or fixed aperture depends on the program’s objectives and target. For a very small target, or one which easily fits into the aperture’s field of view, the optimum aperture’s reference point is defined to ensure that the target center does not fall on known problematic areas of the detector. The WFC3 website and STAN will announce changes in optimum aperture definitions. On the other hand, when the observer needs precise control of the position of the target on the detector, fixed apertures should be used. Fixed apertures are therefore appropriate when target position relative to detector edges is important, or when mosaics are being designed with edges requiring positional accuracies of better than 10 arcsec or so. The available WFC3 UVIS apertures (Table 6.1) include both fixed and optimum versions for the primary locations: the center of the full two-chip detector (UVIS and UVIS-FIX), and the center of each chip (UVIS1 and UVIS2, and UVIS1-FIX and UVIS2-FIX).

Two new apertures with full detector readouts, UVIS2-C512C-CTE and UVIS2-C1K1C-CTE, were introduced for Cycle 23. They place the target near the C amplifier at the same reference positions as the optimum aperture subarrays UVIS2-C512C-SUB and UVIS2-C1K1C-SUB, respectively, for reduced CTE losses from the target.

There are fixed and optimum apertures for use with the quad filters. Because the filter wheel assembly is necessarily offset from the focal plane, the edges between quad filters are blurred at the focal plane, producing regions with contributions from multiple quad filter passbands (Figure 6.8). The UVIS-QUAD-SUB apertures (redefined for cycle 20) and UVIS-QUAD apertures have reference points centered within the useful single-passband regions, while the UVIS-QUAD-FIX apertures have reference points at the geometric centers of the quadrants (closer to the filter edge effects). In programs where targets are placed in different quadrants, the choice of quad aperture will affect the size of offsets and may require new guide star acquisition, as described in Section 10.2.

Subarray apertures pictured in Figure 6.2 are all “optimum”; no “fixed” apertures are available for these subapertures. The reference points for these apertures have initially been defined near the geometric center of the subarray, except for the 2K2 apertures, where the reference points match those of the UVIS-QUAD apertures.

Table 6.1: Predefined apertures for WFC3/UVIS (details can be found in the [Phase II Proposal Instructions](#)).

Aperture	Region	Reference (fiducial) point
----------	--------	----------------------------

	Over-scan ¹		
UVIS	P, V	Full detector	Optimum point near center (displaced from interchip gap) of full two-CCD field of view
UVIS-CENTER	P, V	Full detector	Geometric center of full two-CCD field of view
UVIS-FIX	P, V	Full detector	Near geometric center (displaced from interchip gap) of full two-CCD field of view
UVIS1	P, V	Full detector	Optimum point near center of CCD Chip 1
UVIS1-FIX	P, V	Full detector	Geometric center of CCD Chip 1
UVIS2	P, V	Full detector	Optimum point near center of CCD Chip 2
UVIS2-FIX	P, V	Full detector	Geometric center of CCD Chip 2
UVIS-IR-FIX	P, V	Full detector	Pointing matched to IR-FIX aperture in Table 7.1
G280-REF ²	P, V	Full detector	Reference point for undispersed exposures (coincides with reference point of exposures made with the G280 grism)
UVIS-QUAD	P, V	Full detector	Optimum point in the quadrant corresponding to the selected quadrant filter (offset from the center of the quadrant toward the nearest corner of the detector by about 8 to 10 arcsec in X and in Y; see Figure 6.8)
UVIS-QUAD-FIX	P, V	Full detector	Geometric center of quadrant corresponding to selected quadrant filter
UVIS2-C1K1C-CTE	P, V	Full detector	Same as UVIS2-C1K1C-SUB (see below), for better CTE performance
UVIS2-C512C-CTE	P, V	Full detector	Same as UVIS2-C512C-SUB (see below), for better CTE performance
UVIS-QUAD-SUB	P	2047 × 2050 on the quadrant corresponding to selected quadrant filter	Same as UVIS-QUAD (optimum point in the relevant quadrant) starting in Cycle 20. (Previously geometric center of the quadrant.)
	P	2047 × 2050	

UVIS1- 2K2A- SUB UVIS1- 2K2B- SUB UVIS2- 2K2C- SUB UVIS2- 2K2D- SUB			Optimum point for the corresponding quadrant filter FQ* (for matching N, M,W filter exposures to UVIS-QUAD or UVIS-QUAD-SUB aperture exposures), about 14 arcsec from the center of the 2k × 2k subarray. If not pairing with FQ* quadrant filter exposures, UVIS2-2K2C-SUB is preferred (Section 6.4.4).
UVIS2- M1K1C- SUB		1024 × 1024, quadrant C near detector center	Optimum point near center of 1k × 1k subarray
UVIS2- C1K1C- SUB	P	1025 × 1024, near Amplifier C	Optimum point near center of 1k × 1k subarray
UVIS2- M512C- SUB		512 × 512, quadrant C near detector center	Optimum point near center of 512 × 512 subarray
UVIS2- C512C- SUB	P	513 × 512, near amplifier C	Optimum point near center of 512 × 512 subarray;

¹ P indicates aperture includes physical overscan, V indicates aperture includes virtual overscan. Apertures with no symbol do not include any overscan data for bias level correction.

²See [Section 8.2](#) for information on the use of the G280-REF aperture.

6.5 UVIS Spectral Elements

- [6.5.1 Filter and Grism Summary](#)
- [6.5.2 Filter Red Leaks](#)
- [6.5.3 Ghosts](#)

6.5.1 Filter and Grism Summary

An overview of the UVIS spectral elements was given in [Section 2.3](#). This section gives further details of the UVIS filters and grism. [Table 6.2](#) contains a complete listing of the available spectral elements in the UVIS channel. Figures [6.3](#) through [6.6](#) show the effective throughput curves, including the filter transmission convolved with the OTA, WFC3 optics, and detector response. All of the UVIS filters are contained in a multi-wheel mechanism—identical to the mechanism on WFPC2—called the Selectable Optical Filter Assembly (SOFA). Values in [Table 6.2](#) have been calculated for UVIS chip 2, which has a higher UV sensitivity, except in the cases of quad filters which are restricted to the A and B quadrants.

More detailed information on the throughput curves of all of the filters is given in [Appendix A](#); in particular, [Section A.2.1](#) describes how to generate tabular versions of the throughput curves using *synphot*. All measurements of the UVIS filters which involve wavelengths, as tabulated in [Table 6.2](#) and plotted in Figures [6.3](#) through [6.6](#) and in [Appendix A](#), were done in air. The data have been converted to vacuum wavelengths using the formula given by D. C. Morton (1991, *ApJS* **77**, 119). It should also be noted that the laboratory measurements were done at a temperature of 20°C, whereas the UVIS filters are operated on orbit at 0°C. The temperature difference may lead to wavelength shifts that are no more than 0.14 nm in the worst cases, according to the filter manufacturing specifications.

The UVIS filters have been chosen to cover a wide variety of scientific applications, ranging from color selection of distant galaxies to accurate photometry of stellar sources and narrow-band imaging of nebular gas. The set includes several very wide-band filters for extremely deep imaging, filters that match the most commonly used filters on WFPC2 and ACS (to provide continuity with previous observations), the SDSS filters, and filters that are optimized to provide maximum sensitivity to various stellar parameters (e.g., the Strömgren and Washington systems, and the F300X filter for high sensitivity to the stellar Balmer jump). There is a variety of narrow-band filters, which allow investigations of a range of physical conditions in the interstellar medium, nebulae, and solar system. A few of the narrow-band filters are also provided with slightly redshifted wavelengths, for use in extragalactic applications. Finally, there is a UV grism that provides slitless spectra with useful dispersion covering 200–400 nm (although the grism transmission spans the full wavelength range of the CCD).

Table 6.2: WFC3/UVIS Filters and Grism

Name ¹	Description ²	Pivot ³ λ_p (nm)	Width ⁴ (nm)	Peak System Throughput
UVIS Long-Pass (LP) and Extremely Wide (X) Filters				
F200LP	Clear	488.3	502.2	0.33

F300X	Extremely wide UV; grism reference	280.7	66.3	0.17
F350LP	Long pass	584.6	475.8	0.29
F475X	Extremely wide blue	493.9	205.6	0.28
F600LP	Long pass	744.4	229.2	0.29
F850LP	SDSS z'	916.6	118.2	0.09

UVIS Wide-Band (W) Filters

F218W	ISM feature	222.4	32.2	0.05
F225W	UV wide	235.9	46.7	0.10
F275W	UV wide	270.4	39.8	0.13
F336W	U, Strömgren <i>u</i>	335.5	51.1	0.20
F390W	Washington <i>C</i>	392.1	89.6	0.25
F438W	WFPC2 <i>B</i>	432.5	61.8	0.24
F475W	SDSS <i>g'</i>	477.3	134.4	0.27
F555W	WFPC2 <i>V</i>	530.8	156.2	0.28
F606W	WFPC2 Wide <i>V</i>	588.7	218.2	0.29
F625W	SDSS <i>r'</i>	624.2	146.3	0.28
F775W	SDSS <i>i'</i>	764.7	117.1	0.23
F814W	WFPC2 Wide <i>I</i>	802.4	153.6	0.23

UVIS Medium-Band (M) Filters

F390M	Ca II continuum	389.7	20.4	0.22
F410M	Strömgren <i>v</i>	410.9	17.2	0.27
FQ422M	Blue continuum	421.9	11.2	0.19
F467M	Strömgren <i>b</i>	468.3	20.1	0.28
F547M	Strömgren <i>y</i>	544.7	65.0	0.26
F621M	11% passband	621.9	60.9	0.28
F689M	11% passband	687.6	68.3	0.25
F763M	11% passband	761.2	70.4	0.21
F845M	11% passband	843.6	78.7	0.14

UVIS Narrow-Band (N) Filters				
FQ232N	C II] 2326	241.3	3.4	0.04
FQ243N	[Ne IV] 2425	246.8	3.6	0.05
F280N	Mg II 2795/2802	283.1	4.3	0.06
F343N	[Ne V] 3426	343.5	25.0	0.21
F373N	[O II] 3726/3728	373.0	5.0	0.18
FQ378N	z ([O II] 3726)	379.2	9.9	0.20
FQ387N	[Ne III] 3868	387.4	3.4	0.18
F395N	Ca II 3933/3968	395.5	8.5	0.22
FQ436N	H γ 4340 + [O III] 4363	436.7	4.3	0.19
FQ437N	[O III] 4363	437.1	3.0	0.20
F469N	He II 4686	468.8	5.0	0.20
F487N	H β 4861	487.1	6.0	0.25
FQ492N	z (H β)	493.3	11.4	0.25
F502N	[O III] 5007	501.0	6.5	0.26
FQ508N	z ([O III] 5007)	509.1	13.1	0.26
FQ575N	[N II] 5754	575.8	1.8	0.23
FQ619N	CH ₄ 6194	619.9	6.1	0.26
F631N	[O I] 6300	630.4	5.8	0.25
FQ634N	6194 continuum	634.9	6.4	0.26
F645N	Continuum	645.4	8.4	0.25
F656N	H α 6562	656.1	1.8	0.24
F657N	Wide H α + [N II]	656.7	12.1	0.26
F658N	[N II] 6583	658.4	2.8	0.26
F665N	z (H α + [N II])	665.6	13.1	0.26
FQ672N	[S II] 6717	671.6	1.9	0.25
F673N	[S II] 6717/6731	676.6	11.8	0.25
FQ674N	[S II] 6731	673.1	1.8	0.19

F680N	$z(\text{H}\alpha + [\text{N II}])$	687.7	37.1	0.25
FQ727N	CH_4 7270	727.5	6.4	0.21
FQ750N	7270 continuum	750.3	7.0	0.18
FQ889N	CH_4 25 km-agt ⁵	889.2	9.8	0.10
FQ906N	CH_4 2.5 km-agt	905.8	9.9	0.08
FQ924N	CH_4 0.25 km-agt	924.8	9.2	0.08
FQ937N	CH_4 0.025 km-agt	937.2	9.3	0.07
F953N	[S III] 9532	953.0	9.7	0.05
UVIS Grism (G)				
G280 ⁶	UV grism	Useful range: 200–400 nm		0.17

1. The spectral-element naming convention is as follows for both the UVIS and IR channels. All filter names begin with F, and grisms with G; if the filter is part of a four-element quad mosaic, a Q follows F. Then there is a three-digit number giving the nominal effective wavelength of the bandpass, in nm (UVIS channel) or nm/10 (IR channel). (For long-pass filters, the number is instead the nominal blue cut-off wavelength in nm.) Finally, for the filters, one or two letters indicate the bandpass width: X (extremely wide), LP (long pass), W (wide), M (medium), or N (narrow).
2. Filters intended for imaging in a red-shifted bandpass are given descriptions similar to the following: “ $z(\text{H}\alpha + [\text{N II}])$ ”.
3. “Pivot wavelength” is a measure of the effective wavelength of a filter (see [Section 9.3](#) and Tokunaga & Vacca 2005, PASP, 117, 421). It is calculated here based on the integrated system throughput. Filter transmissions were measured in air, but the equivalent vacuum wavelengths are reported in this table.
4. Widths listed are passband rectangular width, defined as the equivalent width divided by the maximum throughput within the filter bandpass. Equivalent width is the integral with respect to wavelength of the throughput across the filter passband.
5. km-agt (km-amagat) is a unit of vertical column density, equal to 2.69×10^{24} molecules/cm².
6. See [Chapter 8](#) for UVIS Grism details.

Most of the UVIS filters, as well as the UVIS grism, are full-sized elements that cover the entire UVIS field of view. However, in order to provide a larger number of bandpasses, there are five sets of “quad” filters, identified with “FQ” in the filter name, where each bandpass covers ~1/6 of the WFC3 UVIS field of view (i.e., each bandpass covers less than half of a single CCD chip). The quad filters are discussed in more detail below.

The UVIS channel is designed to be used with a single filter or grism in the light path. Although possible in principle, unfiltered imaging, or imaging through a combination of two filters (from two different SOFA wheels), would lead to significantly degraded image quality and has not been tested; thus these options are not permitted. The F200LP filter provides a clear fused silica element that approximates unfiltered imaging.

While the red blocking in the WFC3 UV filters is generally very good, resulting in negligible red leaks for hot objects (typically $\ll 1\%$ for targets with effective temperature $T_{\text{eff}} > 10,000$ K), the red leak can become significant in some filters for cooler targets (e.g., $\sim 10\%$ in F225W for a star with $T_{\text{eff}} = 5000$ K). More details are available in [Section 6.5.2](#); [Table 6.5](#) in that section tabulates red-leak values as a function of stellar effective temperature.

Figure 6.3: Integrated system throughput of the WFC3 UVIS long-pass and extremely wide filters (top panel) and of the wide-band filters covering 2000-6000 Å (bottom panel). The throughput calculations include the *HST* OTA, WFC3 UVIS-channel internal throughput, filter transmittance, and the QE of the UVIS flight detector, and a correction factor to account for the gain sensitivity seen in SMOV4 on-orbit observations vs. TV3 ground tests. Throughputs in all plots below ~3200 Å contain contributions at the measured rate from all detected electrons, including UV multiple electrons.

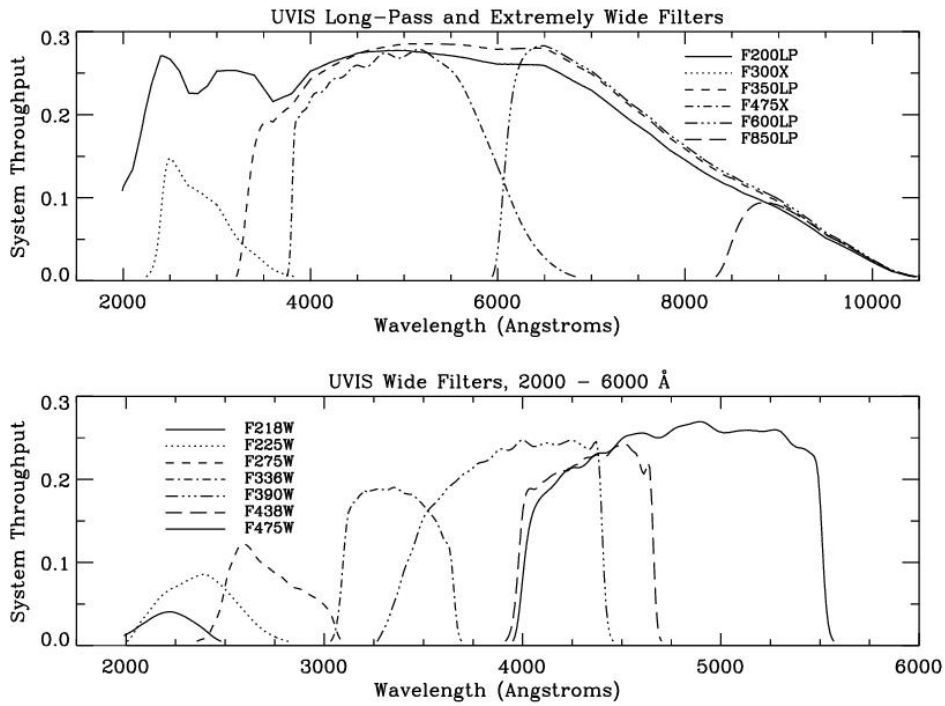


Figure 6.4: Integrated system throughput of the WFC3 UVIS wide-band filters covering 4000-10,000 Å (top panel) and the medium-band filters (bottom panel). The throughput calculations include the *HST* OTA, WFC3 UVIS-channel internal throughput, filter transmittance, and the QE of the UVIS flight detector, and a correction factor to account for the gain sensitivity seen in SMOV4 on-orbit observations vs. TV3 ground tests.

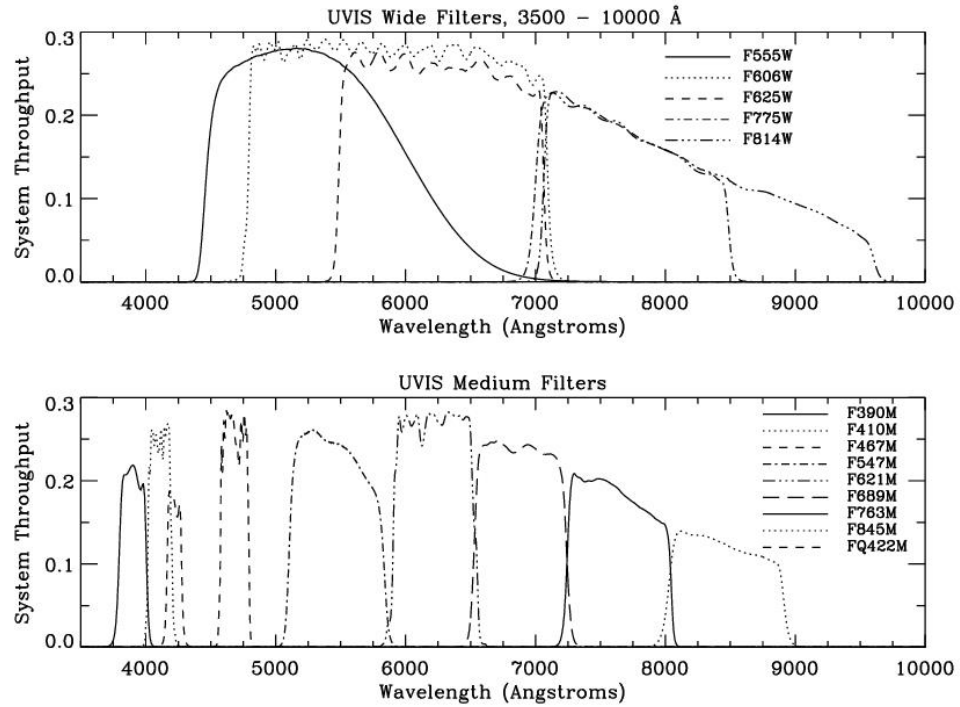


Figure 6.5: Integrated system throughput of the WFC3 UVIS narrow-band filters covering 2000-4500 Å (top panel) and the narrow-band filters covering 4500-6000 Å (bottom panel). The throughput calculations include the *HST* OTA, WFC3 UVIS-channel internal throughput, filter transmittance, and the QE of the UVIS flight detector, and a correction factor to account for the gain sensitivity seen in SMOV4 on-orbit observations vs. TV3 ground tests.

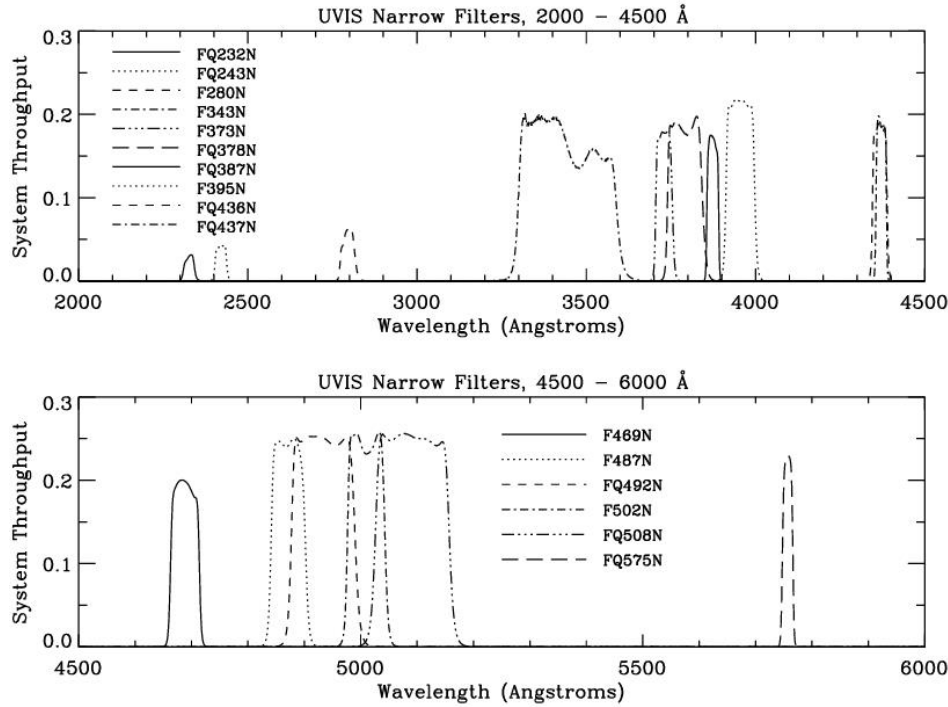
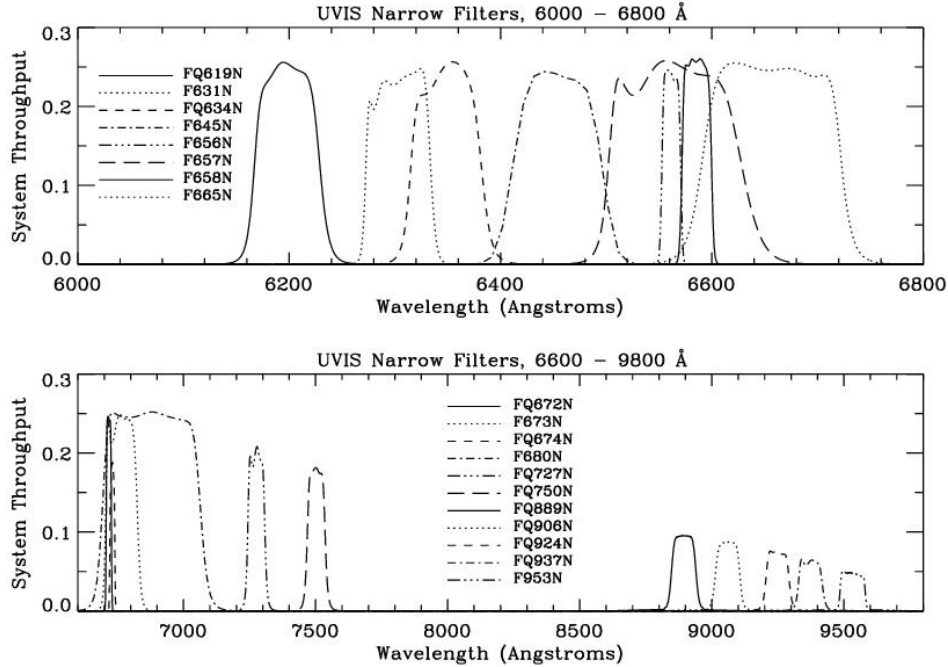


Figure 6.6: Integrated system throughput of the WFC3 UVIS narrow-band filters covering 6000–6800 Å (top panel) and the narrow-band filters covering 6600–9600 Å (bottom panel). The throughput calculations include the *HST* OTA, WFC3 UVIS-channel internal throughput, filter transmittance, and the QE of the UVIS flight detector, and a correction factor to account for the gain sensitivity seen in SMOV4 on-orbit observations vs. TV3 ground tests.



UV Filters

As mentioned earlier, the WFC3 UVIS optics and CCDs have been optimized for UV imaging. As such, the UV filters play a key role and considerable effort has been made to procure filters with the best possible characteristics, including maximum throughput, maximum out-of-band blocking, and minimal ghosts.

The UV filters include the shortest-wavelength F218W, intended for studies of the ISM absorption feature; the wide F225W and F275W for broad-band UV imaging; the Strömgren u (F336W) and Washington C (F390W) for stellar astrophysics; the extremely wide F300X for very deep imaging; and narrow bands such as F280N (Mg II) and the quad filters FQ232N and FQ243N (C II) and [Ne IV]).

Ultra-Wide Filters

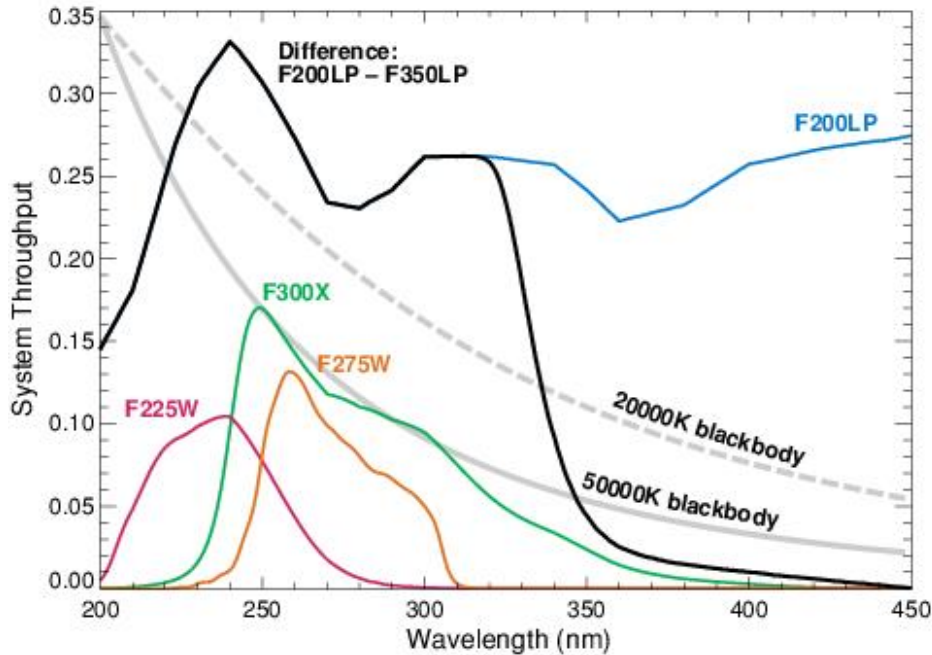
The selection of extremely wide (X) and long-pass (LP) filters is suited for deep imaging of faint sources. The ultra-wide F200LP filter is simply a fused-silica element with a UV-optimized anti-reflection coating which covers the UVIS channel's entire spectral range (200–1000 nm). The F200LP filter is analogous to the clear filter on STIS.

WFC3's maximum sensitivity to hot sources can be obtained by subtracting an F350LP image from an F200LP, thereby creating a very broad ultraviolet bandpass. In Figure 6.7, the blue curve shows the filter transmission for the F200LP filter,

and the black curve shows the effective transmission for a F200LP minus F350LP difference image. For redder targets, some additional calibration may be necessary to account for differences in the transmission of the two filters longward of ~450 nm.

The F850LP filter is part of the [Sloan Digital Sky Survey](#) (SDSS) *griz* filter set, and is the reddest of the ultra-wide filters.

Figure 6.7: Sensitivity of F200LP-F350LP compared to other UV filters (F225W, F275W and F300X). Light grey curves show blackbody functions for 20,000 and 50,000 K.



Wide-Band Filters

The most commonly used WFPC2 and ACS wide filters are also included in the WFC3 filter set. In addition to a wide V-band filter (F606W), there is the Johnson-Cousins BVI set (F438W, F555W, F814W).

The [Sloan Digital Sky Survey \(SDSS\) griz](#) filter set (F475W, F625W, F775W, F850LP) is designed to provide high throughput for the wavelengths of interest and excellent rejection of out-of-band wavelengths. These filters provide wide, non-overlapping filter bands that cover the entire range of CCD sensitivity from blue to near-IR wavelengths.

Medium-Band Filters

The medium-band filters include the Strömgren set (*u*, *v*, *b*, and *y*), as well as some continuum bands needed for use with narrow-band imaging (F390M, FQ422M). The four 11% passband filters were added to the WFC3 UVIS set in order to cover the ~600-900 nm wavelength region with equal-energy filters. The “11%” refers to the filter bandwidths, which are ~11% of the central wavelength.

Narrow-Band Filters

The WFC3 UVIS channel contains 36 different narrow-band filters, covering a variety of species and most of the astrophysically interesting transitions, including H α , H β , H γ , He II, C II], [N II], [O I], [O II], [O III], [Ne IV], [Ne V], [S II], and Ca II. The methane absorption bands seen in planets, cool stars, and brown dwarfs are also covered.

Cosmological emission lines can be detected across a range of redshifts within the bandpasses of the narrow-band filters. Table 6.3 lists the redshifts that can be probed using the specified narrow emission lines (hence, no entries for broad absorption bands or continuum or “off” bands). These redshift ranges are offered as a guide; exact values depend on the wavelengths of the filter cutoffs. Filter cutoffs used in Table 6.3 were defined using the passband rectangular widths (defined in Footnote ⁴ of Table 6.2). However, passband cutoffs were not centered on the filter pivot wavelengths λ_p (defined in Section 9.3), because red leaks shift the pivot wavelengths to longer wavelengths by 1-9% in some of the ultraviolet filters. Instead, the central wavelength for each filter was determined by maximizing the wavelength-integrated product of a rectangular passband of the specified width with the actual system throughput for the filter. In the most extreme case (FQ232N), the pivot wavelength of 241.3 nm is more than two bandpass widths to the red of the rectangular passband equivalent central wavelength (232.6 nm).

Table 6.3: Nominal redshift ranges for WFC3/UVIS narrow-band filters.

Filter	Description	Filter λ_p (nm)	Filter Width (nm)	Line Rest Wavelength (nm)	Minimum cz(km /sec)	Maximum cz(km /sec)
FQ232N	C II] 2326	241.3	3.4	232.6	-2191	2191
FQ243N	[Ne IV] 2425	246.8	3.6	242.5	-2843	1607
F280N	MgII 2795/2802	283.1	4.3			
F343N	[Ne V] 3426	343.5	25.0	342.6	-10763	11113
F373N	[O II] 3726+29	373.0	5.0	372.7	-1689	2333
FQ378N	z ([O II]) or continuum	379.2	9.9	372.7	1247	9210
FQ387N	[Ne III] 3869	387.4	3.4	386.9	-907	1728
F395N	Ca II 3933+68	395.5	8.5			
FQ436N	Hy 4340 + [OIII] 4363	436.7	4.3	434.0	414	3384
FQ437N	[O III] 4363	437.1	3.0	436.3	-412	1649
F469N	He II 4686	468.8	5.0	468.6	-1388	1811
F487N	H β 4861	487.1	6.0	486.1	-1252	2448
FQ492N	z (H β) or continuum	493.3	11.4	486.1	968	7998

F502N	[O III] 5007	501.0	6.5	500.7	-1754	2138
FQ508N	$z([O\ III])$ or continuum	509.1	13.1	500.7	1120	8964
FQ575N	[N II] 5755	575.8	1.8	575.5	-344	594
FQ619N	CH ₄ 6194 on	619.9	6.1			
F631N	[O I] 6300	630.4	5.8	630.0	-1156	1604
FQ634N	CH ₄ 6194 off	634.9	6.4			
F645N	continuum	645.4	8.4			
F656N	Hα 6562	656.1	1.8	656.3	-448	375
F657N	wide Hα + [NII]	656.7	12.1	656.3	-2709	2818
F658N	[NII] 6583	658.4	2.8	658.3	-519	756
F665N	$z(H\alpha + [NII])$ or continuum	665.6	13.1	656.3	1311	7295
FQ672N	[S II] 6717	671.6	1.9	671.7	-402	446
F673N	[S II] 6717+31	676.6	11.8	672.5	-847	4413
FQ674N	[S II] 6731	673.1	1.8	673.1	-437	365
F680N	$z(H\alpha + [NII])$ or continuum	687.7	37.1	656.3	5833	22781
FQ727N	CH ₄ 7270 on	727.5	6.4			
FQ750N	CH ₄ 7270 off	750.3	7.0			
FQ889N	CH ₄ 25 km-agt	889.2	9.8			
FQ906N	CH ₄ 2.5 km-agt	905.8	9.9			
FQ924N	CH ₄ 0.25 km-agt	924.8	9.2			
FQ937N	CH ₄ 0.025 km-agt	937.2	9.3			

F953N	[S III] 9532	953.0	9.7	953.1	-1494	1557
-------	--------------	-------	-----	-------	-------	------

Quad Filters

The WFC3 UVIS channel contains five quad filters: each is a 2×2 mosaic of filter elements occupying a single filter slot, with each quadrant providing a different bandpass (typically narrow-band, although there are also several bandpasses intended for continuum measurements). The five quad filter sets on WFC3 significantly increase the number of available narrow-band filters. The WFC3 quad filters are listed in [Table 6.4](#) with their readout amplifiers.

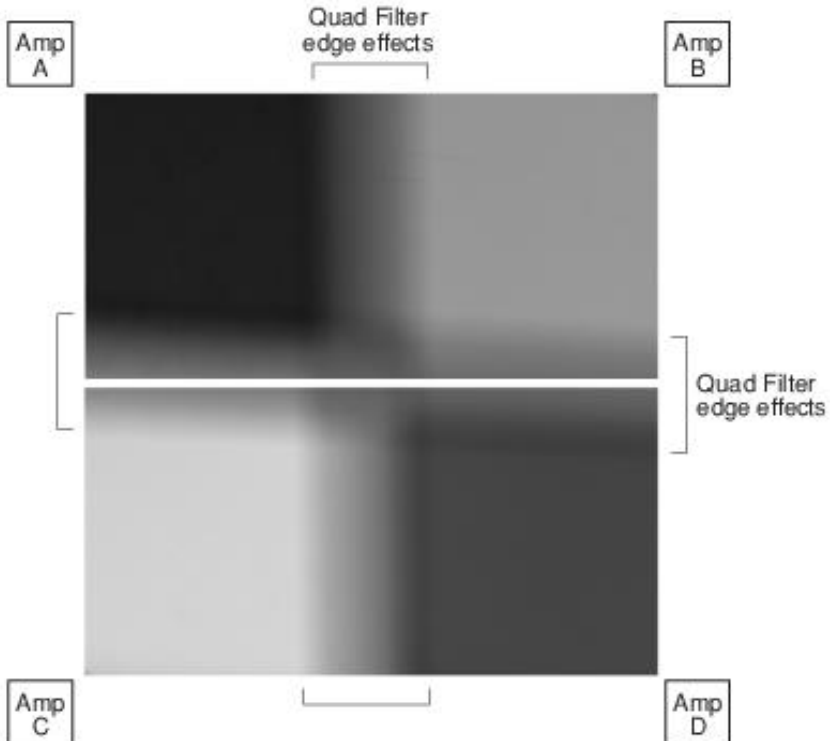
A quadrant nominally covers only 1/4 of the WFC3 total field of view or about $80'' \times 80''$, although edge effects ([Figure 6.8](#)) result in a useable field of about 1/6 of the field of view. The filter edges are out of focus on the focal plane, so light from multiple passbands reaches the detector in those areas.

In programs where targets are placed in different quadrants during a single orbit, spacecraft maneuvers may be large enough to force a new guide star acquisition. Guide star acquisition overheads are described in [Section 10.2](#).

Table 6.4: Quad filter names and positions (identified by readout amplifier).

Filter	Readout Amplifier						
FQ232N	C	FQ436N	D	FQ619N	A	FQ750N	B
FQ243N	D	FQ437N	A	FQ634N	C	FQ889N	A
FQ378N	B	FQ492N	B	FQ672N	D	FQ906N	C
FQ387N	A	FQ508N	A	FQ674N	B	FQ924N	D
FQ422M	C	FQ575N	C	FQ727N	D	FQ937N	B

Figure 6.8: Quad filter edge effects (indicated by brackets). QUAD-FIX apertures have reference points in the center of each quadrant. Starting in Cycle 18, QUAD and 2K2-SUB apertures have had reference points in the center of the areas unaffected by filter edge effects. QUAD-SUB apertures initially had quadrant-centered reference points, but will match the reference points in the QUAD apertures starting in cycle 20.



Grism

The UVIS channel has a UV grism (G280), the spare element from WF/PC-1. It provides slitless spectra with a dispersion of about 1.4 nm/pix and a spectral resolution of about 70, over the 200-400 nm wavelength range, but with transmission in the zeroth order over the entire response of the CCD (see [Figure 8.3](#)). Typically, a grism observation is accompanied by a direct image, for source identification and wavelength zero-point calibration; an ideal filter for the identification image is the F300X discussed above. [Chapter 8](#) discusses WFC3 slitless spectroscopy in detail.

6.5.2 Filter Red Leaks

The design and manufacture of the UV filters was based on a careful balance of the in- and out-of-band transmissions: in general, higher in-band transmission results in poorer suppression of out-of-band transmission, and vice versa. The WFC3 filters represent an attempt to achieve an optimum result, maximizing the in-band transmission while keeping the out-of-band transmission as low as possible in order to minimize red leaks.

Table 6.5 below summarizes the red-leak levels for the WFC3 UV filters. The table lists the fraction of the total signal that is due to flux longward of 400 nm, as a function of effective temperature. This was calculated by convolving a blackbody of the given T_{eff} with the system throughput in the listed filter. As can be seen from the table, red leaks should not be an issue for observations of any objects taken with F275W or F336W. The other UV filters have some red leaks, whose importance depends on stellar temperature. The red leaks in F218W and F300X, for example, exceed ~1% for objects cooler than ~6000 K, while in F225W the red leak reaches ~1% for objects with even cooler temperatures. The most extreme red leaks arise from F218W and F225W observations of objects with T_{eff} of ~4000 K or cooler, necessitating appropriate corrections.

Table 6.5: Fraction of flux longward of 400 nm as a function of effective temperature.

T_{eff} (K)	F218W	F225W	F275W	F300X	F336W
1000	1	1	1	1	1
2000	9.9E-01	9.9E-01	8.4E-01	5.5E-01	3.0E-02
3000	6.0E-01	2.7E-01	3.0E-02	8.9E-02	8.4E-04
4000	1.1E-01	1.8E-02	3.1E-03	3.3E-02	1.4E-04
5000	2.7E-02	3.2E-03	8.6E-04	1.7E-02	4.5E-05
6000	9.9E-03	1.0E-03	3.8E-04	1.0E-02	2.2E-05
7000	4.9E-03	4.6E-04	2.2E-04	7.3E-03	1.3E-05
8000	2.8E-03	2.5E-04	1.5E-04	5.5E-03	9.0E-06
9000	1.9E-03	1.6E-04	1.1E-04	4.4E-03	6.8E-06
10000	1.3E-03	1.1E-04	8.6E-05	3.7E-03	5.4E-06
11000	1.0E-03	8.6E-05	7.1E-05	3.2E-03	4.5E-06
12000	8.3E-04	6.9E-05	6.0E-05	2.8E-03	3.9E-06
13000	6.9E-04	5.7E-05	5.3E-05	2.6E-03	3.5E-06
14000	5.9E-04	4.8E-05	4.8E-05	2.3E-03	3.1E-06
15000	5.1E-04	4.2E-05	4.3E-05	2.2E-03	2.9E-06
20000	3.3E-04	2.6E-05	3.2E-05	1.7E-03	2.2E-06
30000	2.1E-04	1.7E-05	2.4E-05	1.3E-03	1.7E-06
40000	1.8E-04	1.4E-05	2.1E-05	1.2E-03	1.5E-06
50000	1.6E-04	1.3E-05	2.0E-05	1.1E-03	1.4E-06

6.5.3 Ghosts

The WFC3 UVIS channel exhibits three different types of optical ghosts: a) those due to reflections between the CCD front surface and the two detector package windows; b) those due to reflections between the window surfaces; and c) those due to reflections within the particular filter in use.

Window Ghosts

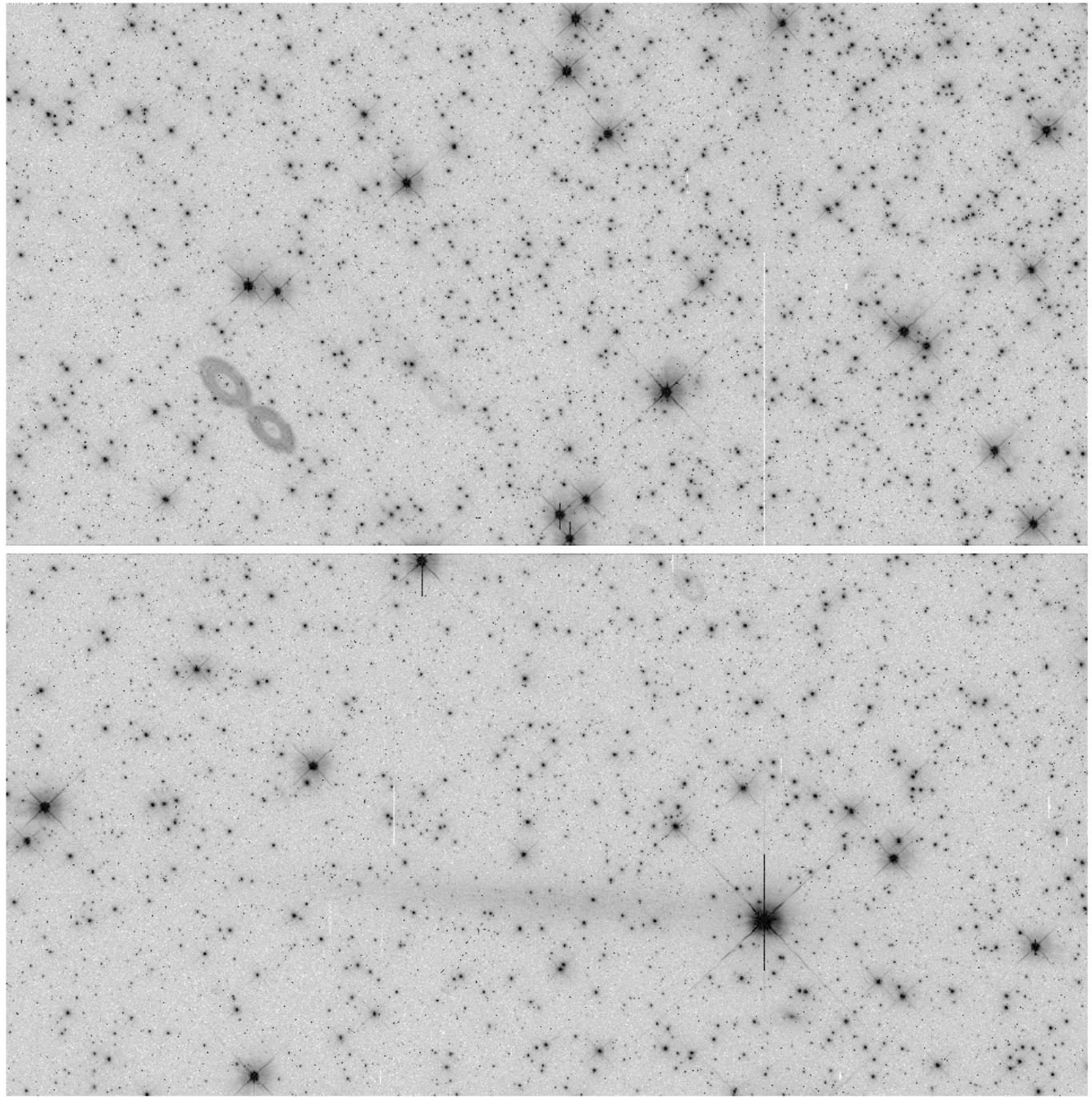
Window ghosts were predicted from early models of the UVIS detector ([WFC3 ISR 2001-17](#)) and were produced with an optical stimulus during ground testing ([WFC3 ISR 2004-04](#)).

When a point source is positioned in the lower right quadrant of the UVIS detector, out-of-focus reflections between the CCD and windows appear along a diagonal from the source towards the upper left, well removed from the source. These figure-eight shaped ghosts gradually move outside the field of view as the target moves out of the lower right corner. They contain a few percent of the flux of the target. The ghosts of several bright stars are visible in the exposure of 47 Tuc shown in Figure 6.9.

Smaller window ghosts appear closer to the target. They are due to reflections between the window surfaces. (See [Figure 6.13](#) for an image showing these ghosts.)

To prevent the worst effects of window ghosts, avoid placing very bright targets on the D quadrant. Also, pay attention to the location of key science targets if bright sources are in the lower right area of the field of view. The production of window ghosts has been modeled and an aid to observers has been produced to enable them to estimate the position of ghosts for a given field of view and ORIENT ([WFC3 ISR 2011-16](#)). If necessary, ORIENT special requirements can be imposed within APT at the Phase II proposal preparation stage to control the positioning of bright sources on the detector. See Section 7.2.2 of the [Phase II Proposal Instructions](#), which gives detailed information on the relationship between detector coordinates, spacecraft coordinates, and ORIENT.

Figure 6.9: UVIS figure-eight window ghosts. An F606W exposure of 47 Tuc (iabj01z7q_flt, display log stretched and saturated) shows figure-8 ghosts well removed along a diagonal from the bright stars in the lower right quadrant that produce them.



Filter Ghosts

Filter ghosts for the WFC3 filters were specified to be less than 0.2%, and in most cases were measured during ground testing to be less than 0.1%. A few filters however, were found during ground testing to have ghosts that exceeded the specification. Some of these, the ones deemed highest priority, were remanufactured and installed in the SOFA. Consequently, there are a relatively small number of filters that may be of concern for ghosts. These are listed in Table 6.6. They have been retained in the flight instrument either because they were of lower scientific priority, or because the ghost level was deemed acceptable in light of the otherwise excellent performance characteristics of the filters (e.g., in- and out-of-band transmission, sharpness of bandpass edges). While some scientific programs (e.g., stellar photometry) may be unaffected by filter ghosts, others (e.g., observations of extended targets or faint objects adjacent to bright ones) could be adversely affected. In such cases, extra planning and/or data-analysis efforts may be needed, e.g., combining images taken at different dither positions and/or roll angles, or applying a deconvolution algorithm.

Table 6.6: Filters exceeding the filter ghost requirement, measured during ground testing of the integrated instrument (see [WFC3 ISR 2007-09](#)).

Filter	Description	Ghost Level (% of total PSF flux)
F200LP	Clear	0.35 ¹
F218W	ISM feature	1.3
F225W	UV wide	0.4
FQ232N	CII] 2326	7.0
FQ243N	[Ne IV] 2425	5.0
F280N	Mg II 2795/2802	0.6
F300X	Extremely wide UV; grism reference	0.3
F656N	H α 6562	0.4
F658N	[N II] 6583	0.4
F673N	[S II] 6717/6731	0.3
F680N	z (H α + [NII])	0.3

¹ Laboratory measurement of stand-alone filter.

6.6 UVIS Optical Performance

- 6.6.1 PSF Width and Sharpness
- 6.6.2 Encircled and Ensquared Energy
- 6.6.3 Other PSF Behavior and Characteristics
- 6.6.4 Supersampled PSF Models

Following the alignment of WFC3 to the OTA ([WFC3 ISR 2009-45](#)), a series of observations through a variety of filters were obtained to demonstrate the WFC3 optical performance ([WFC3 ISR 2009-38](#)). The WFC3 UVIS channel is meeting or exceeding all image quality specifications. Analysis of repeat observations in March 2010 and November 2011 has shown that the PSF has remained stable over time within a radius of 6 arcsec ([WFC3 ISR 2013-13](#)).

The following subsections summarize the measured flight optical performance for the UVIS channel, as described by its point-spread function (PSF), i.e., the spatial distribution of the flux in an image of a point source. The results shown are produced using an optical model which has been adjusted and correlated to the PSFs measured on-orbit and represent mean values averaged over the field. (See [WFC3 ISR 2009-38](#).) This PSF model includes the pupil geometry, residual aberration, the mid-frequency wavefront error of the OTA, the effect of the detector charge diffusion, and first-order geometric distortion.

6.6.1 PSF Width and Sharpness

The PSFs over most of the UVIS wavelength range are well described by gaussian profiles (before pixelation). Two simple metrics of the size of the PSFs are the full width half maximum (FWHM) and the sharpness, defined as

$$S = \sum_{i,j}^2 f_{i,j}$$

where f_{ij} is the fraction of the flux from a point source in pixel i, j . Sharpness measures the reciprocal of the number of pixels that the PSF “occupies,” and can be used to determine the number of pixels for optimal photometric extraction.

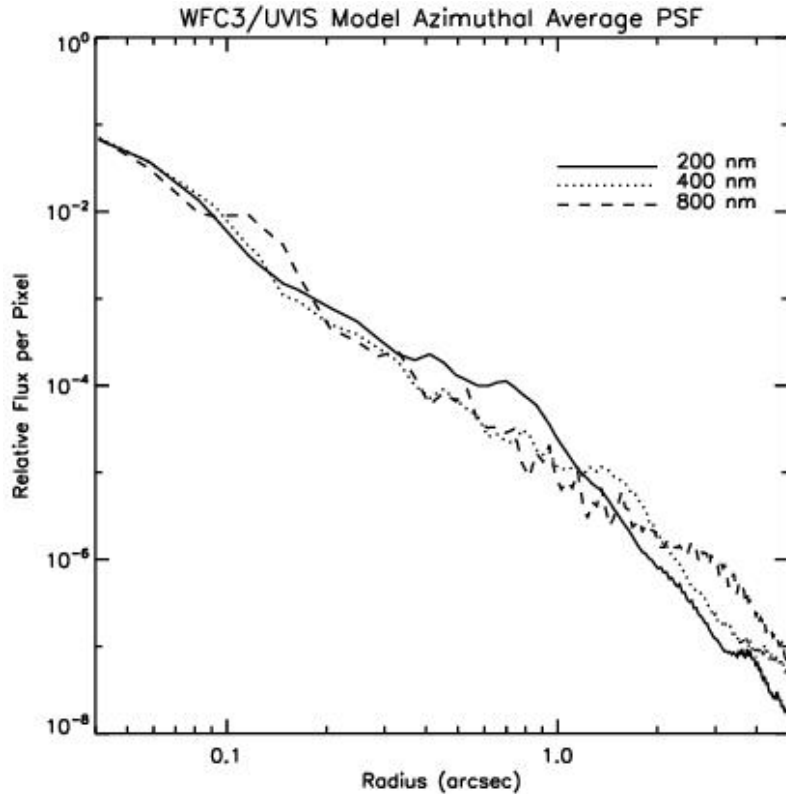
[Table 6.7](#) lists the FWHM of the model PSF core (i.e., before pixelation) in units of pixel and arcsec and the sharpness parameter for 10 wavelengths. The sharpness range shown for each wavelength indicates the values for the PSF centered on the pixel corners and center. The degradation in image width and other performance measures in the near UV is due predominantly to the OTA mid-frequency, zonal polishing errors, which effectively move power from image core into progressively wider and stronger non-gaussian wings as wavelength decreases.

[Figure 6.10](#) plots the azimuthally-averaged model OTA+WFC3 PSF at three different UVIS wavelengths, indicating the fractional PSF flux per pixel at radii from 1 pixel to 5 arcsec.

Table 6.7: WFC3/UVIS PSF FWHM (pre-pixelation, in units of pixels and arcseconds), and sharpness, vs. wavelength. (Note that attempts to measure the FWHM by fitting functions to the pixelated PSF will generally give larger values.)

Wavelength (nm)	FWHM (pix)	FWHM (arcsec)	Sharpness
200	2.069	0.083	0.040–0.041
300	1.870	0.075	0.051–0.056
400	1.738	0.070	0.055–0.061
500	1.675	0.067	0.055–0.061
600	1.681	0.067	0.053–0.058
700	1.746	0.070	0.050–0.053
800	1.844	0.074	0.047–0.048
900	1.960	0.078	0.042–0.043
1000	2.091	0.084	0.038–0.039
1100	2.236	0.089	0.034–0.035

Figure 6.10: Azimuthally averaged mean WFC3/UVIS PSF.



6.6.2 Encircled and Ensquared Energy

The **encircled energy** is the fraction of the total light from a point source that is contained within a circular aperture of a given radius. Since detectors have nominally square pixels, it is often more convenient to evaluate the energy falling within a certain number of pixels ("**ensquared energy**") instead of the encircled energy, which requires interpolation to account for the fractional pixels intercepted by a circular aperture. Correlated model encircled and ensquared energy values are presented below in Tables 6.8 and 6.9 respectively. Encircled energies are plotted in Figure 6.11 for 200, 400, and 800 nm.

Figure 6.11: Encircled Energy for the WFC3/UVIS channel.

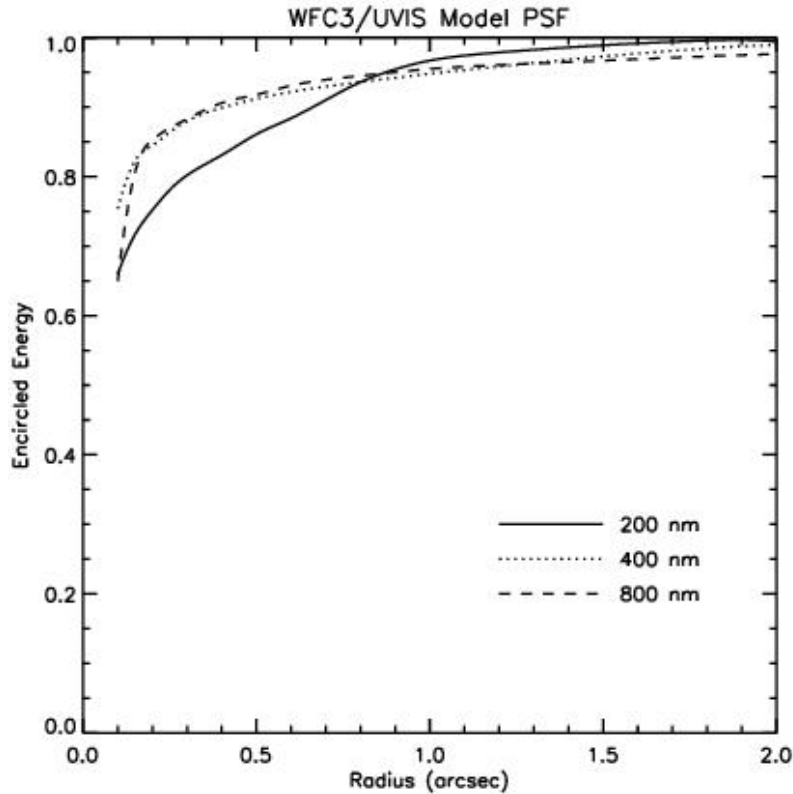


Table 6.8: WFC3/UVIS PSF Encircled Energy Fraction vs. Aperture radius (arcsec).

Aperture radius (arcsec)	Wavelength (nm)									
	200	300	400	500	600	700	800	900	1000	1100
0.10	0.660	0.739	0.754	0.745	0.720	0.687	0.650	0.623	0.612	0.605
0.15	0.717	0.793	0.823	0.834	0.832	0.823	0.807	0.778	0.742	0.699
0.20	0.752	0.822	0.845	0.859	0.859	0.857	0.853	0.847	0.844	0.829
0.25	0.781	0.844	0.864	0.875	0.877	0.874	0.870	0.867	0.868	0.864
0.30	0.802	0.858	0.880	0.888	0.890	0.889	0.883	0.879	0.879	0.876
0.40	0.831	0.880	0.899	0.911	0.910	0.907	0.906	0.904	0.900	0.894
0.50	0.861	0.894	0.912	0.923	0.925	0.923	0.918	0.915	0.918	0.917
0.60	0.884	0.906	0.922	0.932	0.934	0.933	0.931	0.927	0.927	0.923

0.80	0.936	0.928	0.936	0.944	0.947	0.946	0.945	0.942	0.944	0.942
1.00	0.967	0.946	0.948	0.954	0.955	0.955	0.955	0.952	0.955	0.952
1.50	0.989	0.984	0.973	0.970	0.970	0.969	0.967	0.966	0.970	0.968
2.00	0.994	0.992	0.989	0.985	0.980	0.977	0.976	0.975	0.978	0.976

Table 6.9: WFC3/UVIS PSF Ensquared Energy Fraction vs. Aperture size (pixels), where the target is centered on the aperture. Row 1 indicates the maximal (PSF centered on the pixel) peak pixel fraction, useful for determining the exposure time at which saturation may occur.

Aperture size (pixels)	Wavelength (nm)									
	200	300	400	500	600	700	800	900	1000	1100
1×1	0.126	0.165	0.184	0.188	0.180	0.166	0.149	0.132	0.117	0.103
2×2 ¹	0.354	0.412	0.431	0.437	0.434	0.423	0.405	0.380	0.352	0.322
3×3	0.546	0.610	0.613	0.600	0.578	0.563	0.553	0.543	0.531	0.510
5×5	0.681	0.760	0.784	0.783	0.767	0.738	0.699	0.662	0.638	0.624
7×7	0.725	0.800	0.827	0.839	0.839	0.832	0.821	0.802	0.775	0.737
9×9	0.757	0.826	0.849	0.861	0.861	0.860	0.856	0.851	0.849	0.838
11×11	0.782	0.845	0.866	0.876	0.878	0.874	0.870	0.869	0.869	0.864
13×13	0.801	0.858	0.880	0.889	0.890	0.888	0.883	0.878	0.880	0.877
15×15	0.816	0.868	0.891	0.900	0.900	0.899	0.895	0.889	0.888	0.884
17×17	0.830	0.879	0.898	0.909	0.909	0.907	0.905	0.900	0.898	0.892
19×19	0.843	0.887	0.905	0.916	0.916	0.914	0.911	0.909	0.909	0.902
21×21	0.857	0.893	0.910	0.922	0.923	0.920	0.917	0.914	0.917	0.911
23×23	0.868	0.899	0.916	0.926	0.928	0.926	0.923	0.919	0.921	0.919
25×25	0.879	0.905	0.920	0.930	0.932	0.931	0.928	0.924	0.926	0.923
51×51	0.978	0.964	0.957	0.962	0.962	0.961	0.961	0.959	0.962	0.960
101×101	0.996	0.994	0.992	0.992	0.987	0.984	0.982	0.980	0.983	0.981

¹ For the 2 × 2 aperture, the target is located at the center of the array.

6.6.3 Other PSF Behavior and Characteristics

Temporal Dependence of the PSF: *HST* Breathing

Short term variations in the focus of *HST* occur and affect all of the data obtained from all of the instruments on *HST*. A variety of terms, "OTA breathing," "HST breathing," "focus breathing," or simply "breathing" all refer to the same physical behavior. The focus changes are attributed to the contraction/expansion of the OTA due to thermal variations during an orbital period. Thermally induced *HST* focus variations also depend on the thermal history of the telescope. For example, after a telescope slew, the telescope temperature variation exhibits the regular orbital component plus a component associated with the change in telescope attitude. The focus changes due to telescope attitude are complicated functions of Sun angle and telescope roll. More information and models can be found on the "*HST* Thermal Focus Modeling" website at: <http://www.stsci.edu/hst/instrumentation/focus-and-pointing>.

For WFC3, breathing induces small temporal variations in the UVIS PSF ([WFC3 ISR 2012-14](#)). The variations of the UVIS PSF FWHM are expected to be as large as 8% at 200 nm, 3% at 400 nm and 0.3% at 800 nm, on typical time scales of one orbit. Some variation over the field of the PSF response to breathing is also expected, since the detector surface is not perfectly matched to the focal surface, and the optical design includes some field-dependent aberration. This field dependence has been analyzed using observations of a globular cluster with filter F606W ([WFC3 ISR 2013-11](#)) and deep observations of an isolated star with filter F275W ([WFC3 ISR 2013-13](#)). PSFs near the A amplifier on UVIS1 are noticeably elongated by astigmatism. The variation in the asymmetry of PSFs as a function of focus near this amplifier is being explored as a means of measuring breathing and long term focus changes on the UVIS detector ([WFC3 ISR 2015-08](#)).

Pixel Response Function

The point-spread function (PSF) is the distribution of light from a point source as spread over a number of pixels. Even with a very compact optical PSF, however, charge diffusion, or migration of charge from one pixel into adjacent neighbor pixels, can degrade the sharpness of a CCD PSF. The effect is usually described in terms of the pixel response function (PRF), which maps the response of the detector to light from a hypothetical very sharp PSF whose light all falls within an individual pixel. Observations using the integrated WFC3 instrument along with optical stimulus point-sources provided empirical PSFs for comparison with, and to provide constraints for, the models. Those models, which included an independent assessment of the low-order wavefront error, the pupil mask, and a reasonable estimate of the detector PRF, yield good agreement with the observed instrumental encircled-energy curves. The resulting best empirical fit to the pixel response convolution kernel is shown in [Figure 6.12](#).

Figure 6.12: CCD Pixel Response functions at 250 nm (top) and 800 nm (bottom).

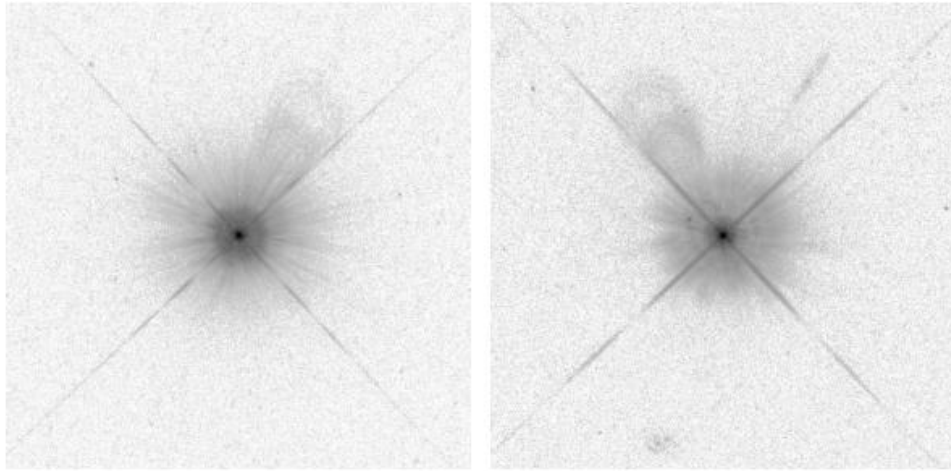
$$\begin{bmatrix} 0.023 & 0.105 & 0.023 \\ 0.105 & 0.488 & 0.105 \\ 0.023 & 0.105 & 0.023 \end{bmatrix}$$

$$\begin{bmatrix} 0.007 & 0.071 & 0.007 \\ 0.071 & 0.688 & 0.071 \\ 0.007 & 0.071 & 0.007 \end{bmatrix}$$

PSF Characteristics

The PSF of the UVIS channel was assessed during SMOV. As part of this assessment exposures of a field containing unsaturated data (highlighting the bright PSF core) were combined with highly saturated data (emphasizing the faint PSF wings). The results are illustrated in [Figure 6.13](#), which shows the select portions of the composite image with a logarithmic stretch. No geometric distortion correction has been applied, so the images appear elongated along the diagonal, due to the 21 degree tilt of the detector to the chief ray. Although the target was chosen to be isolated, a number of field galaxies appear in the F625W image (right) but are absent in the F275W image; these galaxies are also seen in the IR channel images of the same target ([Figure 7.6](#)). Some detector artifacts, including warm pixels and imperfectly removed cosmic ray hits are evident.

Figure 6.13: High dynamic range composite UVIS star images through F275W (left) and F625W (right) subtending ~20 arcsec on each side at different locations in the field.



No distortion correction has been applied. Stretch is logarithmic from 1 to 10^6 e⁻/pixel. (See text below for description of "ghost" artifacts.)

Two different types of "ghost" artifacts are visible in the images. As expected from the UVIS channel design, there are low-level ghosts due to reflections between the four surfaces of the two anti-reflection-coated detector windows: these are the sets of relatively large diameter, ring-shaped ghosts seen extending out at PA $\sim 330^\circ$ (left panel) and PA $\sim 30^\circ$ (right panel) for N up and E to the right. Ghosts due to reflections from the CCD to the windows, as discussed above in [Section 6.5.3](#), fall further from the PSF, along the diagonal from lower right to upper left of the field of view, and are not visible in these frames which image only subsections of the WFC3 field of view.

Also evident is a filter ghost, due to reflections between the surfaces of the F625W filter (right). In multi-substrate filters (a stack of two or more substrates bonded or laminated together with a layer of optical adhesive) filter ghosts appear as faint, point-like features, such as the ghost at PA ~ 65 degrees, radius 1.6 arcsec, in the F625W image, which contains much less than 0.1% of the stellar flux. In single-substrate or air-gap filters (the latter consisting of two substrates joined via thin spacers), filter ghosts appear as small extended shapes (typically rings), closer to the PSF centers than the window ghosts. For the F275W image in Figure 6.13 above the filter ghost level is <0.1% and is not obvious. A small number of filters exhibit brighter ghosts and are discussed in detail in [Section 6.5.3](#) and are tabulated in [Table 6.6](#).

6.6.4 Supersampled PSF Models

The PSF that we see exhibited in the image pixels is the combination of many factors: the telescope optics, the filter throughput, integration over the pixel-response function, etc. It is extremely hard to model all of these individual effects accurately, but fortunately that is not necessary. [Anderson & King \(2000 PASP 112 1360\)](#) showed that it is sufficient to model the net PSF, which they call the "effective" PSF. Their initial model was constructed for WFPC2, but since then accurate models have been constructed for a variety of *HST* instruments and filters. (See [ACS ISR 2006-01](#) and [ACS ISR 2004-15](#)).

Their model for the PSF is purely empirical. It is based on the most basic question that we want the PSF to answer: if a star is centered at location (x,y) on a detector, what fraction of its light will be recorded by pixel [i,j]? The "effective" PSF

thus tells us what fraction of a star's light will land in a pixel that is offset by (Δx , Δy) from the center of the star. As such, the effective PSF is simply a two-dimensional function $\Psi(\Delta x, \Delta y)$ that returns a number between 0.0 and 1.0.

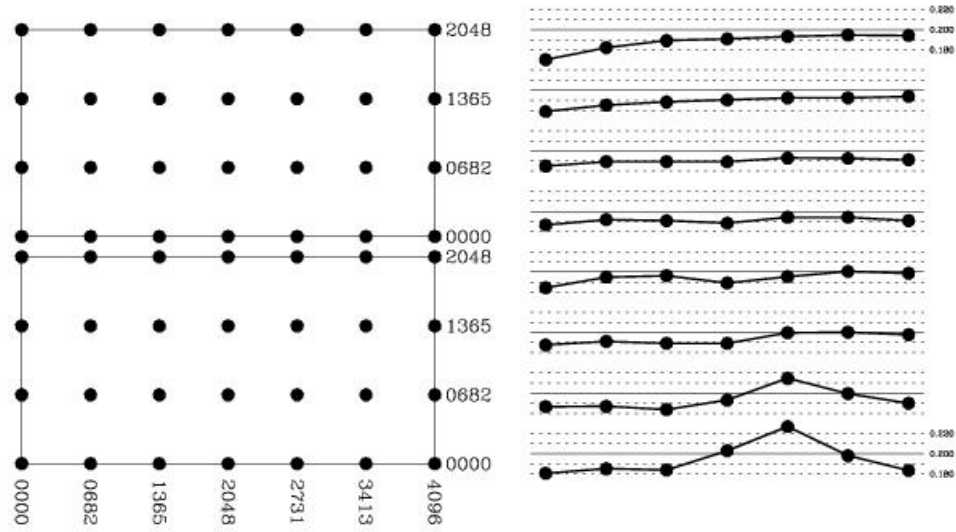
It makes sense that this "effective" PSF function must be smooth and continuous, since moving a star around the detector would result in a continuous variation of recorded flux in each pixel. That said, the if the detector is undersampled, then the "effective" PSF can have sharp variations.

The basis for the PSF model is a simple tabulation of the value of the effective PSF at an array of (Δx , Δy) offsets. This array is spaced by 0.25 flt image pixels, so that it can represent all the structure in WFC3's undersampled pixels. The PSF model thus consists of an array of 101×101 grid points that describe the behavior of the PSF out to a radius of 12.5 pixels. Beyond this distance, unsaturated stars have no measurable flux. The PSFs are normalized to have a total flux of 1.0 within 10.0 pixels for WFC3/UVIS and within 5.5 pixels for WFC3/IR. Bi-cubic spline interpolation is adequate to interpolate the table to locations between the grid points.

The PSF also changes with location on the detector, so the models provide the PSF at an array of fiducial locations across the detectors. Simple bi-linear interpolation is adequate to provide a complete 101×101 PSF model at any given location on the detector. The PSF is thus a four-dimensional function: $\Psi(\Delta x, \Delta y; x, y)$.

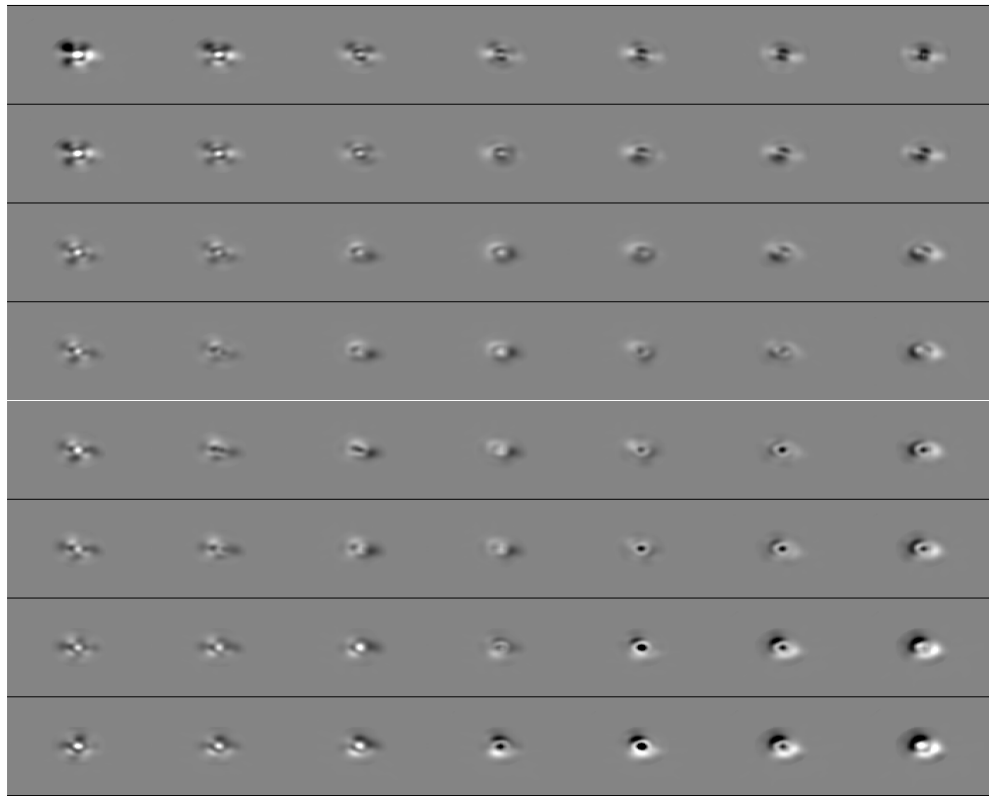
[Figure 6.14](#) shows the array of fiducial points where the WFC3/UVIS PSF is provided. On the left is a schematic of the detector and on the right the central value of the PSF, which represents the fraction of light from a point source that would land in a pixel if the star is exactly centered on that pixel. This goes from about 16 percent in the upper left corner to over 22 percent in the region of strong fringing in red narrow-band filters ([WFC3 ISR 2010-04](#)) in the lower right-middle of the bottom chip.

Figure 6.14: Locations of PSF models on the detector (left) and percentage of flux in the peak pixel for a pixel-centered PSF at each location.



[Figure 6.15](#) shows the full 2-dimensional spatial variation of the PSF. For each of the 7×8 fiducial PSFs, we show the difference between that supersampled PSF and the average PSF, where black indicates more flux. It is clear that PSF varies across the detector in complicated ways.

Figure 6.15: Difference between the supersampled PSF at the locations shown in Figure 6.14 and the average of these PSFs. Black indicates greater than average flux.



As discussed in the previous section (6.6.3), *HST*'s PSF is known to change with time due to "breathing", changes in the focal length due to changes in the telescope's thermal environment (going into and out of the Earth's shadow, changes in orientation relative to the Sun, etc). The many observations in the archive provide samples of the PSF through various filters at a variety of focus levels. In [WFC3 ISR 2018-14](#), Anderson cross-examined star images from the archival to trace out the focus locus for the PSF for the five of the most used filters, F275W, F336W, F438W, F606W, and F814W, and came up with a set of "focus-diverse" PSF models. These models can be used to determine the focus of an image empirically, by determining which focus-level best matches the image of a star, and once the focus of an exposure is determined, the models can provide an accurate model of the PSF for that exposure.

Note that the above PSF discussion applies only for unresampled "flt"-type images, since these are the images where each pixel can be a direct physical constraint on the scene. The "drz"-type images have been resampled, such that each pixel represents some combination of input pixels from one or multiple exposures. Such images are not well suited to high-precision PSF analysis. There are several challenges, however, in working in the "flt" frame. The first is that the images are generally undersampled, such that each exposure is not a full representation of the astronomical scene. One generally must combine several dithered "flt"-type images to fully constrain the scene delivered to the telescope. The second challenge is that the "flt" images are severely distorted, and it is non-trivial to collect these constraints on the scene and analyze them together. For these reasons, even if a user does have access to a perfectly accurate PSF for a given exposure, it still requires considerable expertise to use it for analysis. The instrument team is aware of these challenges and is working to provide tools that make the effort easier. One such early effort is [WFC3 ISR-2014-24](#), but now

that the focus-dependent PSFs have been developed, the next step is to provide tools for users to make proper use of them to make the most of their data.

6.7 UVIS Exposure and Readout

- [6.7.1 Exposure Time](#)
- [6.7.2 ACCUM Mode](#)

6.7.1 Exposure Time

Exposure times in the UVIS channel are controlled by a rotating mechanical shutter blade (see [Section 2.3.3](#)). The time per UVIS exposure must be between 0.5 s and 3600 s, excluding 0.6 s, in steps of 0.1 s.¹ Pre-flight testing has verified that shutter exposure times deviate by less than 1% for exposure times of 0.5 s, as well as those greater than or equal to 1 s. For example, typical variations of 4 ms were measured in a set of 1 s exposures. For exposure times between 0.7 s and 0.9 s (inclusive), exposure-time deviations were measured to be 2.6% (see [WFC3 ISR 2004-14](#)). On-orbit observations have shown that the shutter fails to meet the repeatability requirement of 0.01 sec ([WFC3 ISR 2009-25](#)).

The shutter uniformity requirement specifies that any differences in exposure time across the field of view must be <0.01 s. Comparisons of long (30 s) and short (0.5 s) exposures taken during instrument-level ground tests have shown that the shutter provides a uniform exposure time across the field of view to ~0.004 s, easily meeting the requirement. In on-orbit internal tungsten lamp exposures, the exposure time across the field was found to vary by less than 0.0009 sec ([WFC3 ISR 2009-25](#)). In tungsten lamp exposures and observations of a standard star made from Oct. 2014 to Aug. 2015, no noticeable difference was seen in the performance of the shutter ([WFC3 ISR 2015-12](#)). (Note that the point spread function will be affected by shutter-induced vibration in short exposures; see [Section 6.11.4](#).)

To allow for cosmic-ray removal during post-observation data processing, UVIS exposures can be split into multiple exposures. The Optional Parameter CR-SPLIT in the Phase II observing proposal can be used to equally divide the original exposure time into the specified number of subexposures (the default is NO, with option to select 2 to 8 subexposures). Note that the default value of CR-SPLIT was changed from 2 to NO in Cycle 18, because combining dithered exposures with [DrizzlePac](#) is generally the preferred method of removing cosmic rays. (See [Section 6.12.1](#).)

If CR-SPLIT is requested, the exposure time is first divided by the requested number of subexposures and the subexposure times are rounded down to the nearest multiple of 0.1 s. At the end of this process, if the resulting subexposure times are not legal values, the proposal software adjusts them so that they are allowed and reports those changes to the observer.

6.7.2 ACCUM Mode

“ACCUM” is the only observing mode for the UVIS channel. In ACCUM mode, the shutter is opened and photons strike the CCDs and generate charge, which is accumulated until the shutter is closed at the end of the requested exposure time and the charge is read out. During the readout, the analog-to-digital (A-to-D) converter translates the charge into data

numbers (DN) via the gain setting. There are four gain settings (1.0, 1.5, 2.0, and 4.0 e⁻/DN) that are possible in principle. However, the only gain setting offered to observers is the default value of 1.5 e⁻/DN, which provides gain 1.55 e⁻/DN ([Table 5.1](#)).

A full detector readout of both UVIS chips takes 96 s. The image contains all the exposed pixels from each CCD (2 times 2051 × 4096), as well as a variety of overscan pixels, described in more detail later in this section. Shorter readout times are possible by using smaller subarray readout sizes, as discussed in more detail in [Section 6.4.4](#).

Each of the two CCD chips contains two on-chip amplifiers used for reading out. The fastest—and default—way to read out the entire detector, at full spatial resolution, is to use all four amplifiers simultaneously. Other full-detector readout modes are possible but take more time and involve more charge transfer shifts. For example, two amplifier full frame readout takes more than twice as long as a four-amplifier readout (~193 s vs. 96 s). Non-default readout modes are not offered to General Observers.

Subarray frames, unlike full detector frames, are read out by a single amplifier (the closest amplifier to the subarray center).

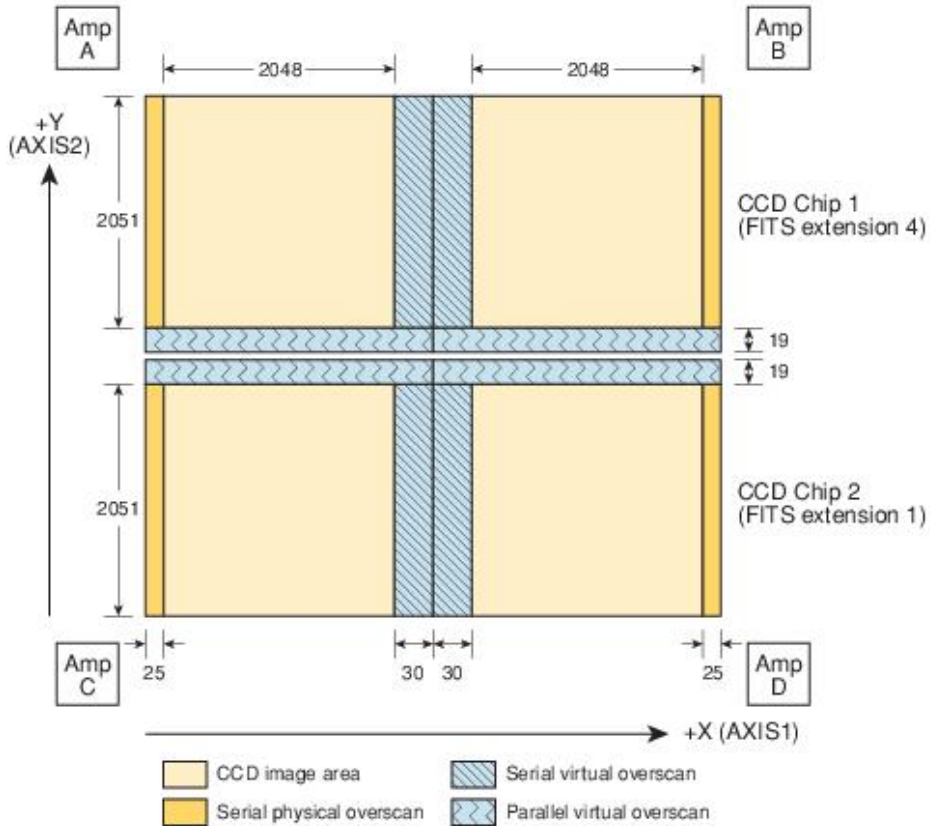
Overscan Regions

The UVIS CCD detectors each have 4096 × 2051 pixels that are exposed to light. In addition, both chips have 25 extra columns at both ends that are not exposed to light; these 25 columns are *physical* overscan pixels. Moreover, during readout of the chips, extra pixels can be clocked in order to create *virtual* overscan pixels.

The location of the overscan regions in a raw image varies, depending upon the type of readout that is performed. The overscan regions are used to monitor the instrument, and are needed to measure the bias level. The bias level is subtracted from the raw image, normally through the BLEVCORR step in the WFC3 calibration pipeline (see the [WFC3 Data Handbook](#)).

Figure 6.16 shows the format of a raw image obtained with full-chip unbinned four-amplifier readout. The raw image has 25 columns of physical overscan pixels and two areas of virtual overscan: 60 columns of serial overscan in the center of each row and 38 rows (19 per chip) of parallel overscan next to the inter-chip gap. The serial physical overscan pixels are also known as the serial prescan, or leading-edge, overscan; the serial virtual overscan pixels are also called the trailing-edge pixels.

Figure 6.16: Format of a Raw Full-Chip WFC3 UVIS Image.



As Figure 6.16 illustrates, a raw image resulting from a default full-frame, four-amplifier readout of the UVIS channel contains 110 columns of serial overscan (25×2 physical and 30×2 virtual) plus 38 rows of parallel virtual overscan, which combined with the 4096×2051 science pixels, result in a raw image size of 4206×4140 pixels. Other types of readouts have differing amounts and/or locations of overscan. Subarrays contain no virtual overscan of either type (serial or parallel), although they can contain physical overscan if a subarray is chosen that overlaps the physical overscan region. Subarrays containing physical overscan data are listed in Table 6.1. In general, it is desirable to include some physical overscan in observations using subarrays for accurate bias level subtraction.

Exposures taken with on-chip binning are complicated by the need to truncate “odd” pixels and to treat each half of the chip’s row separately. Also, due to the odd number of some overscan pixels, the boundary between the data and overscan pixels of a binned exposure can contain binned pixels resulting from a combination of both data and overscan pixels. A 2×2 binned frame readout, for example, contains $2070 \text{ rows} \times 2102 \text{ columns}$. That is, each binned chip readout has 1035 rows (9 binned virtual overscan + 1 combined data/virtual parallel overscan + 1025 data) and each binned chip readout contains 2102 columns (12 physical overscan + 1 combined data/overscan + 1023 columns of data + 1 combined data/virtual overscan column + 14 virtual overscan pixels for each of the two amps in a chip). A 3×3 binned image contains 1402×1380 pixels (8 overscan + 1 combined overscan/data + 682 data + 10 overscan columns in each amplifier of each chip and 6 overscan + 1 combined overscan/data + 688 data rows in each chip).

For completeness, we mention here that WFC3 can also be commanded to take EPER (extended pixel edge response) readouts. This capability is intended for calibration/engineering purposes only. The EPER images are a way to measure and monitor charge transfer inefficiency (CTI) effects using internal images, rather than external, pointed observations that would take *HST* observing time away from science observations. The EPER frame starts with an internal tungsten lamp flat field; any CTI present causes a fraction of charge from that flat field to be captured temporarily in traps. As the frame is read out, the trapped charge escapes and can appear in the overscan regions as an exponential tail of deferred charge. The EPER readout includes significantly larger areas of overscan so that the full extent of the exponential tail can be measured, ideally down to where it becomes indistinguishable from the nominal noise level of the detector. That is, the EPER image allows direct measurement of the charge losses during the readout since nearly all the lost electrons are expected to appear in the exponential tail.

¹ Under normal shutter operations, the 0.5 s exposure would not provide a sufficiently uniform exposure level. However, it has been implemented through a special “continuous sweep” operation, where the shutter disk moves smoothly through 180°, from one closed position to the next, thus meeting the uniformity requirement. All exposures longer than 0.5 s are obtained via pairs of closed-to-open and open-to-closed commands.

6.8 UVIS Sensitivity

6.8.1 Limiting Magnitudes

Table 6.10 presents the predicted limiting-magnitude performance of WFC3. The calculations are based on optimal extraction of a point source. The limiting ABMAG at a S/N of 10 was calculated for a 1-hour and a 10-hour exposure.

Table 6.10: Limiting-magnitude performance of WFC3 based on on-orbit sensitivity from SMOV4.
The table provides limiting ABMAGs at a S/N of 10 for the indicated WFC3 filters.

Band	Filter	Limiting magnitude in 1 hr	Limiting magnitude in 10 hrs
		WFC3	WFC3
NUV	F225W	26.7	28.1
<i>U</i>	F336W	27.3	28.7
<i>B</i>	F438W	27.3	28.7
<i>V</i>	F606W	27.9	29.2
<i>I</i>	F814W	27.1	28.4

Chapter 9 gives further details on estimation of exposure times. Current estimates require use of the WFC3 [Exposure Time Calculator \(ETC\)](#), available online.

6.9 Charge Transfer Efficiency

6.9.1 Overview

6.9.2 CTE-Loss Mitigation Before Data Acquisition: Observation Planning

6.9.3 CTE-Loss Mitigation After Data Acquisition: Post-Observation Image Corrections

The charge transfer efficiency (CTE) of the UVIS detector has inevitably been declining over time as on-orbit radiation damage creates charge traps in the CCDs. Faint sources in particular can suffer large flux losses or even be lost entirely if observations are not planned and analyzed carefully. In this section, we describe the effect of CTE losses on data, observational strategies for minimizing losses, and data analysis techniques which can to some extent correct for CTE losses.



For the latest information about CTE on the UVIS detector, see the WFC3 CTE webpage:
<http://www.stsci.edu/hst/instrumentation/wfc3/performance/cte>

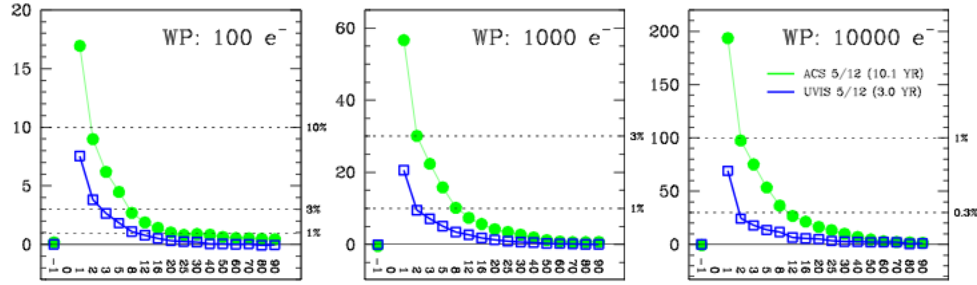
6.9.1 Overview

The flux of energetic particles in low-Earth orbit, mostly relativistic protons and electrons encountered during *HST*'s frequent passages through the South Atlantic Anomaly, continually damages the silicon lattice of the CCD detectors. This damage manifests itself as an increase in the number of hot pixels, an increase in the dark current, and an increase in the charge trap population.

The effect of hot pixels, about 1000 new/day/chip using a threshold of $54\text{e}^-/\text{hr}/\text{pix}$, is addressed with anneal procedures, dark calibration files, and dithering. The anneal procedures, performed monthly, warm the detectors to $+20^\circ\text{C}$ and restore 20-30% of the hot pixels to their original levels. Dark calibration files (running averages of daily dark images) can provide reasonable identification of hot pixels as well as a calibration for overall dark current (see [Section 5.4.8](#) for the median level and growth rate). The calibration darks allow hot pixels and dark current to be subtracted from science images in the calibration pipeline. Due to the time-variable behavior, the corrections are imperfect, but the dark current levels are low and dithering can help reduce any residual impact of hot pixels in final image stacks.

The effect of charge traps is more difficult to address, as the traps do not respond to the anneals and the damage appears to be cumulative and irreversible based upon both flight and ground test experience. The traps cause a loss in source flux as well as a systematic shift in the object centroid as the charge is trapped and slowly released during readout. The majority of the trapped charge is released during the readout within $\sim 1/2$ dozen pixel shifts, as evidenced by the charge trails which follow hot pixels, cosmic rays, and bright stars. A low percentage of the initial signal can be seen extending out to ~ 50 pixels in length (see [Figure 6.17](#)).

Figure 6.17: Residual Charge in Pixels Trailing Hot Pixels



Observed charge trailing 100, 1000, and 10000 e⁻ hot pixels in WFC3 (blue) and ACS (green) images from May 2012.
CTE flux losses at any given time depend on a variety of factors, including:

- The number of rows (and columns) between source and amplifier: sources further from the amplifiers require more transfers to read out and thus encounter more traps.
- The intrinsic brightness of the source: fainter sources lose proportionally more charge than brighter sources. Very bright sources ($>10^4$ e⁻) suffer relatively small amounts of CTE loss (a few percent). (see Figure 6.20.)
- The image background: a higher background fills some of the charge traps, thereby minimizing flux losses during readout of the source signal. WFC3/UVIS images can have very low intrinsic backgrounds due to the low detector readnoise and dark current as well as the small pixels of the CCDs. Furthermore, the WFC3 UV and narrowband filters have exceptionally low sky backgrounds.

Thus, the CTE loss will depend on the morphology of the source, the distribution of electrons in the field of view (from sources, background, cosmic rays, and hot pixels) and the population of charge traps in the detector column between the source and the transfer register. And, of course, the magnitude of the CTE loss increases continuously with time as new charge traps form. Further details of the current understanding of the state of the WFC3/UVIS charge transfer efficiency (CTE) are presented in Section 5.4.11 and can be found at: <http://www.stsci.edu/hst/instrumentation/wfc3/performance/cte>

The remainder of this section will discuss the available options for mitigating the impact of CTE losses and their associated costs. Broadly, the options fall into two categories: those applied before data acquisition, i.e., optimizing the observing strategy during the proposal planning stage, possibly including the use of post-flash, and those applied during image analysis after the images have been taken, i.e., formula-based corrections or image reconstruction.

6.9.2 CTE-Loss Mitigation Before Data Acquisition: Observation Planning

- 1) Consider the placement of the target within the field of view. For example, when possible, place a target close to a readout amplifier - a viable option when the target is small. This reduces the number of transfers during readout, thereby minimizing CTE losses. Naturally, this will only be appropriate for a small subset of programs but should also be considered e.g. for observations of compact targets where the scientific interest in the surrounding field is limited or where inferior CTE for those surrounding observations is acceptable. If the region of interest is sufficiently small, a

subarray aperture can be used. (See [Figure 6.2](#).) Subarray apertures UVIS2-C1K1C-SUB and UVIS2-C512C-SUB (see [Table 6.1](#)) place the target 512 and 256 pixels, respectively, from the edges of the UVIS detector near amplifier C. However, where possible, observers should use full frame exposures for the value they can add to the observing program and the archive. Note that the observing efficiency of full frame exposures greatly increases for exposure times longer than 347 sec, since data dumping can then be done in parallel to taking exposures (see [Section 10.3.1](#)). Starting in cycle 23, observers can use the apertures UVIS2-C1K1C-CTE and UVIS2-C512C-CTE to place the target at the same reference positions as UVIS2-C1K1C-SUB and UVIS2-C512C-SUB, respectively, and read out the full detector. POS TARGs can also be used to move the target to the lower part of the C quadrant (e.g., negative POS TARG X and negative POS TARG Y in aperture UVIS-CENTER) to reduce CTE losses. (See [Section 6.4.4](#) for reasons to prefer quadrant C over the other quadrants.)

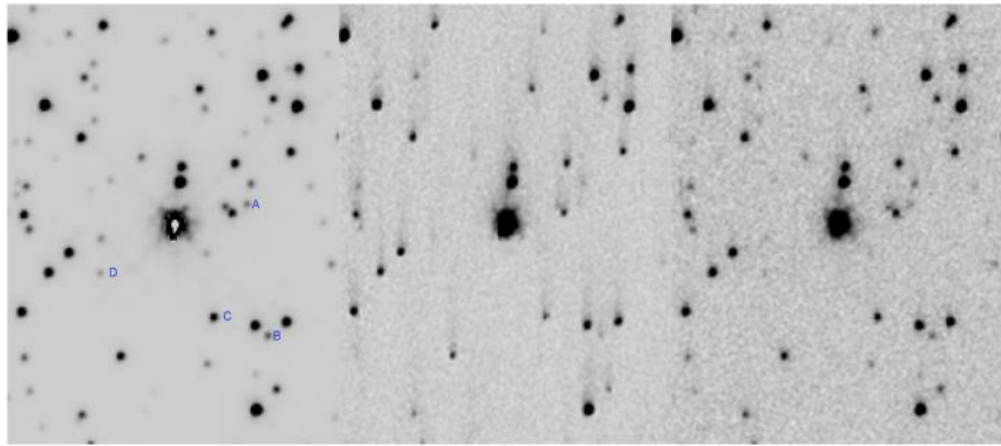
Another approach, suitable for sparsely populated fields in which the sources of scientific interest are relatively bright, involves obtaining observations at multiple spacecraft roll angles. In this case, the different roll angles (ideally at or near 90 degrees) will result in sources having large variations in the number of pixels over which they must be transferred during readout. This permits a direct assessment of the reliability of the available formulaic photometric CTE calibrations which can be applied during post-processing (discussed in more detail below in [Section 6.9.3](#)).

If observations are being taken on a field larger than the instantaneous field of view of the cameras, then stepping in the Y direction (i.e., along the CCD columns) with a small degree of overlap will place some sources at both small and large distances from the transfer register again permitting a direct assessment of the photometric reliability of the CTE corrections applied during data processing (see section on formula-based corrections below in [Section 6.9.3](#)).

2) Increase the image background by lengthening exposure times, using a broader filter, and/or applying an internal background (post-flash). *Ensuring that images with faint sources contain a minimum of $12\text{ e}^-/\text{pix}$ background is expected to be a key CTE mitigation strategy for many WFC3/UVIS science proposals in 2012 and beyond. Starting in Cycle 23, APT has provided a quantitative warning message in the Diagnostic Report if more or less FLASH appears to be needed on an exposure.*

On-orbit testing has shown that CTE losses are a non-linear function of both the source and image background signals: a faint source in a low-background ($<12\text{ e}^-$) image will lose a significantly larger proportion of signal than a similar source in a high-background image. In some cases, faint sources can even disappear completely during the readout transfers, as illustrated in Figure 6.18 ([Anderson et al. 2012](#)). The left panel is the result of a stack of long exposures minimally impacted by CTE losses, i.e., effectively ‘truth’ image. The middle panel presents the result of a stack of short, very low background exposures; the CTE trails are clearly visible above each source and the charge traps have completely smeared out the signal from the faintest sources (e.g., A and D). The right panel is a stack of short exposures where each image had $\sim 16\text{ e}^-$ total background. The CTE trails have been reduced considerably and stars lost in the stack of very low background images are recovered in the stack of higher-background images, a clear qualitative demonstration of how a small amount of background can preserve even small charge packets of signal.

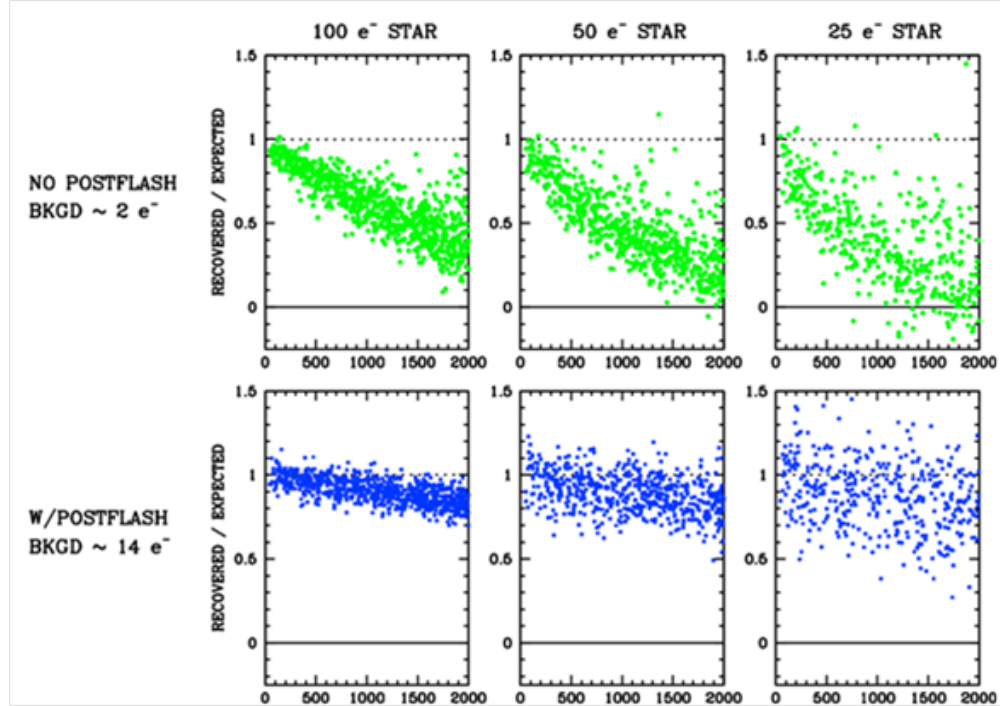
Figure 6.18: Mitigation of CTE Losses Using a Modest Increase in Image Background



A portion of the Omega Cen central field far from the readout amplifier. The left panel shows the result of a stack of eight 700s images, with minimal CTE losses. The middle panel shows a stack of nine 10s exposures with only $\sim 2e^-$ natural background each; note the charge trails due to CTE loss extending upwards from each source in the field. The right panel is a stack of nine 10s exposures with $\sim 16e^-$ background total (sky + post-flash) in each image.

A more qualitative measure of how relatively low levels of background can significantly improve the CTE and increase the S/N of very faint sources is presented in Figure 6.19. Shown are aperture photometry results for faint stars in very low background (top row) and higher-background data (bottom row), as a function of the number of transfers, i.e., distance from the amplifier. The target sources are faint: 100, 50, and 10e- total in a 3×3 pixel aperture from left to right. Sources far from the amplifiers (~2000 on the x-axis) in images with little background (top row) effectively disappear. The same faint sources embedded in images with slightly higher background are detectable at the 50-75% level ([Anderson et al. 2012](#)).

Figure 6.19: Efficacy of Post-Flash



Recovered versus expected photometry for faint stars ($100e^-$, $50e^-$, $25e^-$ from left to right) embedded in low ($\sim 2e^-$) and higher ($\sim 14e^-$) background images (top and bottom panels, respectively), as a function of pixel transfers.

The required increase in background necessary to provide effective CTE-loss mitigation can sometimes be obtained simply by lengthening exposure times or by using as broad a filter as possible. Sky levels in the UVIS filters are such that with exposure times of 2000 sec or longer, about half the filters will have natural background levels $>10e^-$ (WFC3 ISR 2012-12). The remaining filters, mostly UV and narrowbands plus some medium band filters, will have relatively low backgrounds and a post-flash is recommended as a means of boosting the total background. While using a post-flash to increase the underlying background in images may seem counter-productive from a S/N perspective, it will significantly increase the CTE for low-level sources and as a result, source signal will accumulate much faster than the noise will increase. Observers with faint sources in e.g. narrowband or UV filters or with science programs requiring the coaddition of multiple images to reach very faint limits should plan to achieve a totalbackground level of $\sim 12 e^-$ per exposure. This recommendation represents the optimum value as of late 2012: a balance between the level of CTE mitigation achieved and the additional noise penalty incurred from adding extra background. Note that once backgrounds exceed $\sim 12 e^-/\text{pix}$, there is minimal improvement in retaining charge from faint sources (Anderson et al., 2012).

In order to determine the necessary post-flash level to use for mitigating CTE losses, observers will first need to estimate the expected natural backgrounds. The [Exposure Time Calculator](#) provides such estimates, including contributions from sky, dark, zodiacal light, earthshine, airglow, and a selected level of post-flash. In addition, empirical backgrounds as measured on all WFC3/UVIS frames in the archive are summarized in the Appendix of [WFC3 ISR 2012-12](#). If the natural background of the exposure will be higher than $12 e^-/\text{pix}$ then there is no need to add post-flash. For images with very low background levels, enough post-flash should be applied to achieve $\sim 12 e^-/\text{pix}$ total background (natural+post-flash).

Observers invoke post-flash in APT by choosing the exposure optional parameter ‘FLASH’ and specifying the desired number of electrons per pixel to be added to the image using the LED post-flash lamp. (See Section 13.2.4 in the [Phase II Proposal Instructions](#).) The additional overhead times required for post-flash are generally very small (typically ~ 6 sec). The flash is performed on WFC3 after the shutter has closed at the end of the exposure: an LED is activated to illuminate the side of the shutter blade facing the CCD detector. The experience so far with these lamps (corroborated by the design analysis) indicates that the illumination pattern is very repeatable (to <<1%); it is similar for the two sides of the shutter blade. The intensity is likewise very repeatable, as expected. The brightness of the flash has shown fluctuations of rms~1.2%; the long-term stability is ~0.1%. Calibration reference files have been delivered to CDBS for the calibration of exposures using post-flash. (See [WFC3 ISR 2013-12](#).)

The main disadvantage of post-flash is, of course, the increase in the background noise. In the worst case, a short exposure with low background and dark current would require the addition of about 12 e⁻/pix of post-flash. Thus the original readout noise of ~3.1 electrons is effectively increased to 4.6 e⁻ in un-binned exposures. (See [Section 9.6](#) for S/N equations.) For a noise-limited observation, the exposure time would need to be increased by more than a factor of 2 to retain the same noise floor. In most cases, however, the impact will be significantly less severe as exposures will generally contain some natural background already and will not require a full 12e⁻/pix post-flash.

Finally, please note that even with a moderate background, larger charge packets from brighter stars, hotter pixels, or cosmic rays will still experience some loss and trailing of their initial number of electrons. Thus, even with 12 e⁻ background, all sources will still suffer some CTE losses (see Figure 6.20) and it will be necessary to apply an additional correction during data processing.

3) Use charge injection. For completeness, this mode is included as an observing strategy option for CTE-loss mitigation but, in practice, it is not considered as useful as e.g., increasing image backgrounds or applying corrections during image processing. Its use will be permitted only in exceptional cases where the science requires it. Observers who wish to use this mode are advised to consult their Contact Scientist or contact the help desk at <http://hsthelp.stsci.edu>.

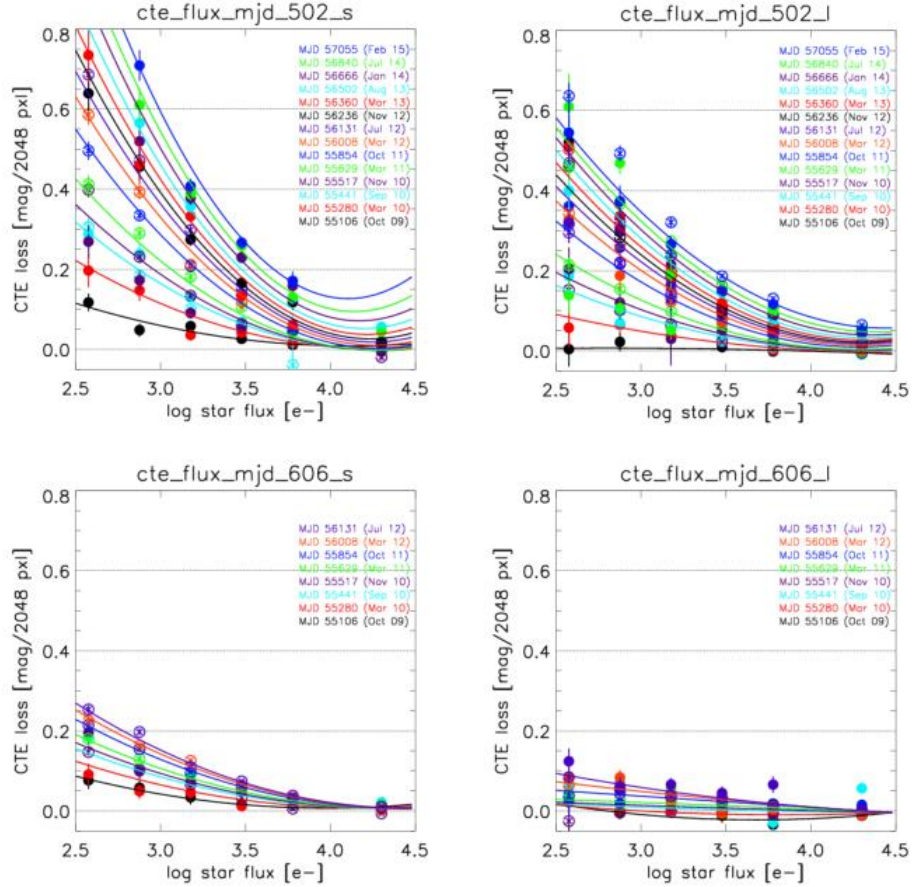
Charge injection is performed by electronically inserting charge as the chip is initialized for the exposure, into either all rows or spaced every 10, 17, or 25 rows. Only the 17 row spacing is supported as of mid-2012. The injected signal is ~15000 electrons (not adjustable) and results in about 18 electrons of additional noise in the injected rows ([Baggett et al., 2011](#)). The rows adjacent to the charge-injected rows have between 3 and 7 electrons of effective noise due to CTE effects. The charge injection capability was supported in Cycle 19, but experience has demonstrated that it is useful for very few types of observations. Its primary drawbacks are the uneven degree of protection from charge trapping in the rows between the injected charge rows, an increase in noise in the rows closest to the injected charge, and a very difficult calibration problem posed by the combination of sources in the field and the injected rows, which give rise to different levels of CTE at different places within the image. Furthermore, the strong dependence of CTE losses on image backgrounds makes it challenging to produce a suitable calibration, as typically there will be a mismatch in image backgrounds between the charge injected calibration and science frames (i.e., differing levels of CTE losses).

6.9.3 CTE-Loss Mitigation After Data Acquisition: Post-Observation Image Corrections

1) **Apply formula-based corrections for aperture photometry.** One way to correct CTE losses after the images have been acquired is to apply an empirical photometric calibration. The current model, based on stellar aperture photometry results, provides corrections for CTE losses as a function of observation date, image background, source flux, and source

distance from the amplifiers. Figure 6.20 illustrates the necessary corrections for low, intermediate, and high background images. As expected, larger corrections are required for fainter sources and/or lower image backgrounds. The top left panel represents the worst-case scenario: in short exposures in the narrowband F502N filter, with effectively zero background, losses exceeded 1 mag for the faintest sources farthest from the readout amplifiers by July 2014. The top right panel shows that even a background \sim 1-2 electron per pixel produces a noticeable improvement. Observations were made with the F606W filter until July 2012. A modest increase in the background level (to $2\text{-}3e^-$, bottom left panel) produced a significant improvement in CTE, with corrections of \sim 25% required for the faintest sources, vs \sim 55% for a background level of $1 e^-$ on the same date. The losses for high background data ($20\text{-}30 e^-$) slowly rose to \sim 10% for the faintest sources by July 2012 (lower right panel). Losses for the brightest sources were $<6\%$ regardless of background level. More details on how the analysis was performed can be found in [WFC3 ISR 2015-03](#). Note that these results are for small apertures; corrections for larger apertures will be smaller as more of the trailed charge is included in the aperture.

Figure 6.20: CTE Losses as a Function of Star Flux, Observation Date, and Image Background.



CTE losses in magnitudes per 2048 detector rows as a function of star flux (within 3-pixel radius), observation date, and image background. Top row panels show results based on narrowband images with short and long exposure times (left and right, $\sim 0 e^-/\text{pix}$ and $\sim 1-2 e^-/\text{pix}$ background, respectively) while bottom row panels are for broadband images with short and long exposure times (left and right, $2-3 e^-/\text{pix}$ and $20-30 e^-/\text{pix}$, respectively). Open and filled symbols are based on NGC104 (47Tuc) and the sparse cluster NGC6791; lines denote the best fits.

An updated analysis, based on data taken from Oct 2009 to Aug 2016, is presented in [WFC3 ISR 2017-09](#). As previously, flux loss due to CTE degradation was measured as a function of source brightness, observation date, background level, and vertical distance from the readout amplifier and fit with a 2nd degree polynomial, whose coefficients are provided to allow observers to estimate flux corrections for their point-source photometry. As of Aug 2016, flux losses for images with the recommended minimum $12 e^-/\text{pix}$ background were 5 - 15 percent, depending on source brightness. These losses can be further reduced by using the CTE-corrected images now available from the [MAST](#) (see below). There appears to be a flattening in the CTE degradation rate that may be correlated with the Solar cycle maximum.

The formula-based correction method can be quite effective for isolated point sources on flat backgrounds, but it is less suitable for extended sources or sources in crowded regions. One benefit of this formula-based recalibration is that it is

not impacted by the possibility of readnoise amplification, which can be a concern for the pixel-based reconstruction discussed in the next section. Photometric corrections are also useful for planning observations: they allow an estimate of the CTE losses for point-like sources that can be expected in a near-future observation for a given background and source flux. The expected losses should be taken into consideration during observation planning and if necessary, total integration times increased to achieve signal to noise requirements.

2) Apply the empirical pixel-based correction algorithm. The ACS team developed and implemented a post-observation correction algorithm employing the Anderson and Bedin methodology (2010; PASP 122 1035). A similar capability was made available for WFC3 from the [WFC3 CTE webpage](#) in mid-2013, and was implemented in the [MAST](#) pipeline in Feb 2016. (See the article on [calwf3](#) version 3.3 in [WFC3 STAN issue 22](#) and the discussion of the calibration pipeline in [Section E.1](#).) See [WFC3 ISR 2017-09](#) for quantification of the reduction in CTE losses that can be achieved by using the corrected _FLC images.

The correction algorithm is calibrated using the behavior of hot pixels and their charge trails. In the absence of CTE losses, the full charge of a hot pixel is entirely contained within a single pixel and its noise is the combination of its shot noise and the noise due to readout and background in that one pixel. If some of the hot pixel charge is lost due to imperfect CTE, there will be fewer electrons in the hot pixel itself, and more in the trailing pixels. (see [Figure 6.17](#).) To obtain the original value of the hot pixel, the correction algorithm must determine how many electrons the original hot pixel would have to have in order to be read out as the observed number, given the number of traps left full and empty by the preceding pixels. The resulting correction essentially redistributes the counts in the image, “putting the electrons back where they belong”, i.e., undoing the effects of degraded CTE ([Anderson et al., 2012](#)).

While the pixel-based algorithm has been successful at removing trails behind stars, cosmic rays, and hot pixels, it has one serious and fundamental limitation: it cannot restore any lost S/N in the image. Faint sources, and faint features of extended sources, may be so strongly affected by CTE losses that they become undetectable and cannot be recovered (e.g., see [Figure 6.18](#) and [Figure 6.19](#)). In addition, this pixel-based method is effectively a deconvolution algorithm, and it can amplify noise or sometimes generate artifacts. Even so, despite the limitations, the reconstruction algorithm provides the best estimate of the original image before it was read out and also aids in understanding how the value of each pixel may have been modified by the transfer process.

The pixel-based correction algorithm does not correct for sink pixels, which contain a number of charge traps ([WFC3 ISR 2014-19](#)). They comprise about 0.05% of the UVIS pixels, but can affect up to 1% of the pixels when the background is low. A calibration program to identify sink pixels and pixels impacted by them has been carried out. The strategy for flagging these pixels is presented in [WFC3 ISR 2014-22](#). Since February 23, 2016, when [calwf3](#) version 3.3 was implemented in the pipeline, sink pixels and their trails have been identified in the DQI array with value 1024 (see [Table E.2](#)).

Serial CTE losses (along the X direction on the detector) can easily be seen in deep exposures of the point spread function (see Figure 1 in [WFC3 ISR 2013-13](#)). The pixel-based correction algorithm currently corrects only for parallel CTE losses (along the Y direction on the detector). Serial CTE losses affect the X coordinate of bright stars and faint stars at the level of 0.0015 pixels and 0.004 pixels, respectively ([WFC3 ISR 2014-02](#)).

We end this Mitigation section by noting that, depending on the science goals, a single mitigation method may not be sufficient for some programs. Observers, particularly those with faint sources, may need to consider applying both pre- and post-observation CTE-loss mitigation strategies, e.g., increasing the image background to $\sim 12\text{e}^-/\text{pix}$ to reduce CTE effects followed by an application of either the formulaic photometric or pixel-based corrections. We note that the pixel-based correction algorithms are not able to operate on binned data, but binning is not an effective way of increasing the detectability of faint sources (See [Section 6.4.4](#)).

For the most current information on the WFC3 CTE and mitigation options, as well as updates on the availability of a pixel-based correction algorithm for WFC3, please refer to the page CTE webpage at:

<http://www.stsci.edu/hst/instrumentation/wfc3/performance/cte>

6.10 Photometric Calibration

The two WFC3/UVIS CCDs have very different quantum efficiencies, particularly in the UV where UVIS2 is nearly 30% more sensitive at $\sim 2200 \text{ \AA}$. At wavelengths longer than $\sim 4500 \text{ \AA}$, the sensitivity of the two chips is within about $\sim 1\%$, as shown in [Figure 5.2](#). Starting on 23 February 2016, an independent photometric calibration is applied for the two UVIS CCDs in calibrated FLT/FLC data products. In addition to populating new chip dependent photometry header keywords in the image header, the enhanced version of calwf3 (v3.3 and higher) included other improvements for UVIS data such as a pixel-based correction for charge transfer losses (CTE) and data quality flags to allow for rejection of sink pixels ([WFC3 ISR 2016-01](#)).

Three new keywords were added to the image headers to support the chip-dependent calibration:

- PHTFLAM1= inverse sensitivity for UVIS1 + filter
- PHTFLAM2= inverse sensitivity for UVIS2 + filter
- PHTRATIO = PHTFLAM2/PHTFLAM1

The inverse sensitivity keyword used prior to 2016, PHOTFLAM, was retained and set to the same value as the new PHTFLAM1 keyword for backward compatibility with any existing user software. When performing the PHOTCORR step, calwf3 now populates the chip-dependent inverse sensitivity keywords, PHTFLAM1 and PHTFLAM2 and computes PHTRATIO, the UVIS2 to UVIS1 inverse sensitivity ratio.

FLUXCORR, a new calwf3 keyword switch, scales the flux of UVIS2 (the bottom chip) to match UVIS1 such that the UVIS science array is multiplied by PHTRATIO. As a result, users working with calibrated FLT/FLC files will only need to keep track of a single zeropoint value for each UVIS filter. If desired, users can reprocess the RAW files with FLUXCORR set to OMIT to maintain calibration independence between the two chips, as described in Sections [3.2.13](#) and [9.1.4](#) of the [WFC3 Data Handbook](#). Treating the two chips separately may be important for UV filter observations (eg. F218W, F225W, F275W, and F200LP) which have significant color terms across the two CCDs (see WFC3 ISRs [2017-07](#) and [2018-08](#)).

To support the chip-dependent approach, the image photometry reference table, or IMPHTTAB, was modified to have five extensions. The first three extensions contain the same data values as in the pre-2016 reference table, namely, PHOTFLAM, PHOTPLAM and PHOTBW for each observing mode. The new fourth and fifth extensions contain the chip-dependent PHTFLAM1 and PHTFLAM2 values. Changes to the structure of this reference file structure are described in [WFC3 ISR 2016-01](#).

For the 2016 delivery, the inverse sensitivity values populated in the image header were reported for a circular aperture with radius $r = 10$ pixels, corresponding to $r = 0.3962$ arcsec in the ‘native’ resolution of the UVIS channel ([WFC3 ISR 2016-03](#)). This was a departure from the approach implemented at the time WFC3 was installed in 2009. Based on feedback from the WFC3 user community and for consistency with other HST instruments, the photometric keyword values reverted to the infinite aperture convention, starting on 15 Jun 2017. A summary of changes to the values populated in the IMPHTTAB reference file over the WFC3 lifetime may be found in [WFC3 ISR 2017-11](#). A comparison of the 2016 and 2017 inverse sensitivity values for all 42 full frame UVIS filters may be found in [WFC3 ISR 2017-14](#). A comparison of the improved calibration for ACS/WFC and WFC3/UVIS wide filters with similar passbands is discussed in [WFC3 ISR 2018-02](#).

For the latest information about the photometric calibration and the inverse sensitivity tables, users may visit the WFC3 Photometry [webpage](#). The accuracy of the inverse sensitivity values is $\sim 2\%$ on average, with $\sim 5\text{-}10\%$ errors for narrowband filters.

6.11 Other Considerations for UVIS Imaging

- [6.11.1 Gain and Full-Well Saturation](#)
- [6.11.2 Cosmic Rays and Hot Pixels](#)
- [6.11.3 Image Persistence](#)
- [6.11.4 Shutter-Induced Vibration](#)
- [6.11.5 Droplets](#)
- [6.11.6 Optical Anomalies](#)

6.11.1 Gain and Full-Well Saturation

When the default gain for the UVIS detector is used, photometric information well beyond saturation can be recovered for relatively isolated sources in unbinned exposures (where the CCD full well is the limiting factor), but not in binned exposures (where the ADC is the limiting factor). This is discussed in detail in [Section 5.4.5](#) and [Section 5.4.6](#).

6.11.2 Cosmic Rays and Hot Pixels

The cosmic-ray fluxes for WFC3 UVIS are comparable to the levels seen in ACS, STIS CCD, and WFPC2. As with these previous HST instruments, typical WFC3 imaging observations need to be dithered (in preference to CR-SPLIT) to obtain adequate cosmic-ray removal (see [Section 5.4.10](#)). Dithering can also mitigate bad pixel effects, and can be used to sample the point spread function; it is recommended for the vast majority of observations.

6.11.3 Image Persistence

No significant image-persistence effects following over-exposure were observed in instrument-level ground test or on-orbit data using the UVIS CCDs, as expected for back-illuminated devices.

6.11.4 Shutter-Induced Vibration

Shutter-induced vibration, or shutter jitter, affects only very short exposures. Shutter jitter causes slight blurring in image data and is not to be confused with exposure time deviation. Exposure time deviation is discussed in [Section 6.7.1](#), and the UVIS shutter mechanism is described in [Section 2.3.3](#).

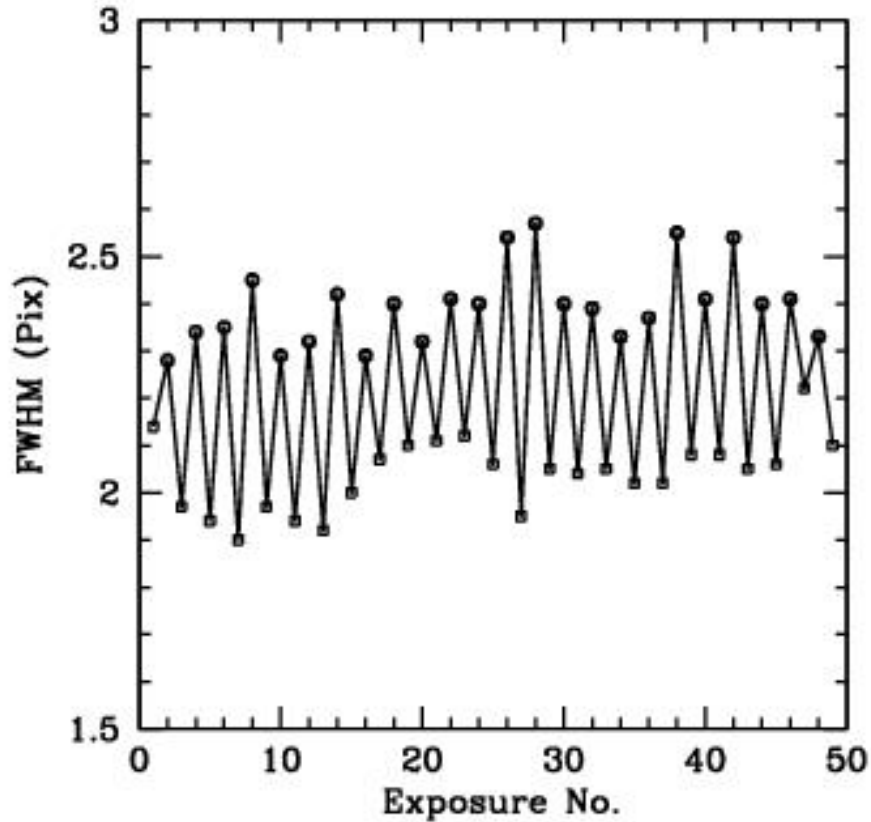
The image quality analysis carried out during the third thermal-vacuum campaign revealed that vibration associated with the operation of the UVIS shutter caused systematic changes in the width and in the central pixel flux of point sources in

a series of short exposures ([WFC3 ISR 2008-44](#)). The shutter mechanism employs a rotary disc blade with 180 degree symmetry, including two cut-outs for the open (expose) positions.

The blade is rotated 90 degrees from closed to open, for exposure, then another 90 degrees in the same direction from open to closed, etc., such that consecutive exposures use alternating cut-outs (sides) of the blade, designated A and B. Vibration is apparent when the servo-control electronics are enabled to rotate the blade to side B. The observed PSF is thus alternately broader and narrower as sides B and A are used. The vibration lasts 0.7 sec, and thus has diminishing effects on the PSF as longer time exposure times are executed and more time is spent in the quiescent state.

To test on-orbit performance of the shutter, observations of the calibration standard star GD153 were made during SMOV ([WFC3 ISR 2009-20](#)). Series of exposures were made for a given exposure time, from 0.5 sec to 20 sec. The widths of the PSFs in the consecutive 0.5 sec exposures are shown in Figure 6.21.

Figure 6.21: FWHM of a star in a consecutive series of 0.5 sec exposures; alternate exposures were made with different shutter blades.



The shutter-dependent fluctuations in FWHM are superimposed on the gradual change in FWHM that is generally observed over the course of an HST orbit due to “breathing”, a gradual periodic change in focus. In these SMOV observations, breathing had become the primary determinant of FWHM for exposures of 3 sec (see Figure 2 in [WFC3 ISR 2009-20](#)).

Photometric consistency can be achieved in short exposures made with side A and side B by using a sufficiently large aperture (see [WFC3 ISR 2009-20](#)). Fluctuating PSF sizes pose a greater problem for science programs with very bright targets when the results depend on PSF stability or on the highest possible spatial resolution. Such programs may now be able to make short exposures with less vibration using the exposure-level option BLADE=A in APT (introduced in version 21.2.2). Testing of this mode is described in [WFC3 ISR 2014-09](#). Since this option causes additional movement of the shutter mechanism, using only the SHUTRPOS=A reported in the science header and bypassing B, its use will be allowed only as an available mode when sufficiently justified. The interested PI should send a scientific justification for using this mode for exposures with less than a specified exposure time to the Contact Scientist or the Program Coordinator, who will forward it to the appropriate instrument scientist for consideration.

6.11.5 Droplets

The outer window is contaminated, seemingly by a mineral residue introduced during acceptance testing of WFC3. These contamination features have been dubbed "droplets" due to their appearance at the time of discovery. In external flat-field images, these features have a strength of approximately $\pm 0.5\%$. The droplets cause changes in PSF profile, such that flux in the core is redistributed to the near wings. In large-aperture (10 pixel radius) photometry of point sources stepped across a strong window feature, the feature does not significantly increase the photometric scatter. For small-aperture (3 pixel radius) photometry of point sources stepped across a strong window feature, the photometric scatter increases from $\sim 0.5\%$ to $\sim 1\%$. Quadrant A has the lowest density of features. There are approximately 50, 129, 108, and 179 droplets in quadrants A, B, C, and D, respectively.

The best strategy for mitigating the flat-field features is an appropriate dither pattern. Although there are positions within a flat-field feature that cause systematic errors at the level of a few percent in point source photometry, other positions separated by 20 to 40 pixels show much smaller errors, suggesting that dithers on this scale would be sufficient for most photometric programs. To ensure a point source does not hit a particular feature twice requires larger dithers of approximately 100 pixels, which is the typical diameter of these features.

[WFC3 ISR 2008-10](#) describes the characterization of the droplets and their photometric effects based on ground testing, and [WFC3 ISR 2009-27](#) reports that about 30% of droplet positions have shifted by about 1 pixel after launch, but have been stable since then.

6.11.6 Optical Anomalies

In rare cases, the optical system causes stray light from sources outside the CCD FOV to be scattered into images. Analysis of this stray light, known as "dragon's breath", is given in [WFC3 ISR 2017-02](#). This and other anomalies, found by daily monitoring of incoming WFC3 data, are illustrated in [WFC3 ISR 2017-22](#).



Examples of stray light and other optical anomalies may be found on the WFC3 website:
<http://www.stsci.edu/hst/instrumentation/wfc3/performance/anomalies>

6.12 UVIS Observing Strategies

- [6.12.1 Dithering Strategies](#)
- [6.12.2 Parallel Observations](#)
- [6.12.3 Spatial Scans](#)
- [6.12.4 PSF Subtraction](#)
- [6.12.5 The Drift and Shift \(DASH\) Observing Strategy](#)

6.12.1 Dithering Strategies

For imaging programs, STScI generally recommends that observers employ dithering patterns. Dithering refers to the procedure of moving the telescope by pre-determined amounts between individual exposures on a target. The resulting images are subsequently combined via post-observation processing techniques using software such as [Drizzlepac](#).

Use of dithering can provide improved sampling of the point spread function (PSF) and better correction of undesirable artifacts in the images (e.g., hot pixels, cosmic rays, the UVIS channel’s inter-chip gap, and the UVIS “droplets”). Cosmic ray removal is more effective if more than 2 images are obtained, using CR-SPLIT exposures and/or dithers, especially for exposure times greater than 1000s. A sequence of offsets of a few pixels plus a fractional pixel in each coordinate is generally used to simultaneously remove hot pixels and cosmic rays and to sample the PSF. A larger offset along the image Y axis is needed to fill in the interchip gap in full-frame images (the WFC3-UVIS-MOS-DITH-LINE pattern uses a conservative step size of 2.4 arcsec). To ensure the best accuracy consider dithering to compensate for droplets ([Section 6.11.5](#)).

Larger offsets, up to sizes approaching the detector’s field of view, can also be used to create mosaics. However, as a result of geometric distortion ([Appendix B](#)), some objects shift by an integer number of rows (or columns), while others shift by an integer plus some fraction of a pixel. The PSF is not resampled in that dimension in the former case, but is resampled in the latter case. Where the exposures overlap, the PSF is thus better sampled for some objects than for others. If PSF sampling is important, a combination of mosaic steps and small dither steps should therefore be used. Note that, in practice, mosaic steps must be contained within a diameter ~130 arcsec or less (depending on the availability of guide stars in the region) to use the same guide stars for all exposures. The rms pointing repeatability is significantly less accurate if different guide stars are used for some exposures. (see Appendix B of the [DrizzlePac Handbook](#).)

The set of Pattern Parameters in the observing proposal provides a convenient means for specifying the desired dither pattern of offsets. The pre-defined mosaic and dither patterns that have been implemented in APT to meet many of the needs outlined above are described in detail in the [Phase II Proposal Instructions](#). The WFC3 patterns in effect in APT at the time of publication of this Handbook are summarized in [Appendix C](#). Observers can define their own patterns to tailor them to the amount of allocated observing time and the desired science goals of the program. Alternatively, they can use POS TARGs to implement dither steps ([Section 6.4.3](#)). Observers should note that thermally driven drift of the image on the detector, typically 0.1 to 0.2 pixels per coordinate within one orbit ([WFC3 ISR 2012-14](#)), will limit the accuracy of execution of dither patterns.

Dither strategies for WFC3 are further discussed in [WFC3 ISR 2010-09](#), which provides a decision tree for selecting patterns and combining them with subpatterns.

6.12.2 Parallel Observations

While the design of WFC3 precludes the simultaneous use of both the UVIS and IR channel, it is possible to use one or more of the other *HST* instruments in parallel with WFC3. Since each instrument covers a different location in the *HST* focal plane (see [Figure 2.2](#)), parallel observations typically sample an area of sky several arc minutes away from the WFC3 target. For extended targets such as nearby galaxies, parallel observations may be able to sample adjacent regions of the primary target. In other cases, the parallel observations may look at essentially random areas of sky.

For processing and scheduling purposes, *HST* parallel observations are divided into two groups: coordinated and pure.

A **coordinated parallel** is an observation directly related to (i.e., coordinated with) a specific primary observation, such as in the extended galaxy example above. A **pure parallel** is an observation typically unrelated to the primary observation, for example, parallel imaging scheduled during long spectroscopic observations. The primary restriction on parallel observations, both coordinated and pure, is that they must not interfere with the primary observations: they may not cause the primary observations to be shortened; and they must not cause the stored-command capacity and data-volume limits to be exceeded. The proposal software (APT) enforces these rules and notifies the observer when a specified parallel is not permitted.

In order to prolong the life of the *HST* transmitters, the number of parallels acquired during each proposal cycle is limited. Proposers must provide clear and strong justification in order to be granted parallel observing time. Please refer to the [HST Call for Proposals](#) for current policies and procedures concerning parallels.

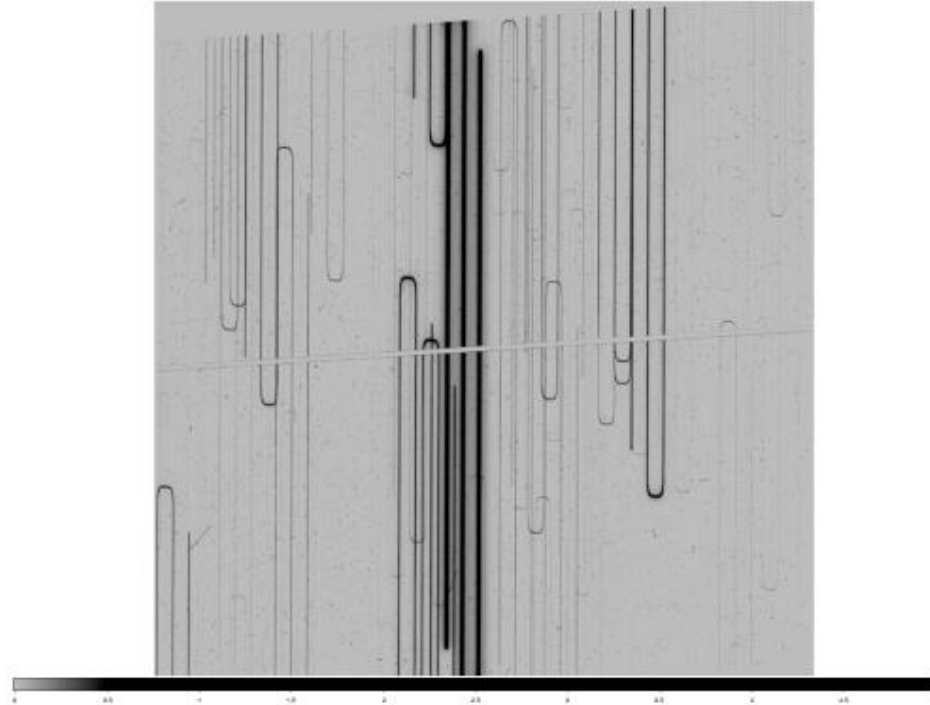
6.12.3 Spatial Scans

Spatial scanning of stellar images upon the UVIS detector creates the potential for astrometry of unprecedented precision. Two representative scientific examples are parallax measurement of Cepheid variable stars (program 12679, Riess P.I.) and the astrometric wobble of a stellar binary (program 12909, Debes P.I.). Results from non-proprietary data of program 12679 (Riess, priv. comm.) indicate that differential astrometry a few times less precise than that set by diffraction and Poisson statistics are attainable. For *HST*, a 2.4-m telescope, operating at 600 nm, the diffraction limit is $\Theta \sim \lambda/D = 51$ mas. In the theoretical limit, astrometry in one dimension is approximately equal to the FWHM Θ divided by the signal to noise ratio, \sqrt{N} , where N is the number of photo-electrons recorded. If we adopt N equal to the full well of the UVIS CCD, $\sim 64,000$ e⁻, times a trail of length 4000 pixels, i.e., $N = 128$ million e⁻, then the theoretical astrometric limit is ~ 3 microarcsec per exposure. A more conservative estimate of ~ 13 microarcsec can be derived as follows: the nominal, state-of-the-art astrometric precision of a staring-mode exposure is ~ 0.01 pixel, so the astrometric precision of a 1000-pixel-long scan could be $\sim \sqrt{1000}$ or ~ 30 times smaller, which, for the 40 mas WFC3 UVIS pixels, is 13 microarcsec. In 2012 the TAC recommended programs 13101 and 12909, which anticipated a per-exposure precision of 30 to 40 microarcsec. Some data analysis tools for spatial scans are currently being developed by the WFC3 team to aid users in reducing spatial scan data, but for the most part users should expect to develop their own analysis software to reduce images and obtain useful astrometric results. (See [Riess et al. 2014](#).) Please contact the WFC3 help desk for more information on the analysis tools being developed.

Scans can be made at any angle, although users typically orient the scans approximately but not exactly parallel to rows or to columns of the detector. For example, in order to sample pixel phase, program 12679 prescribed an angle of 90.05 degrees; the extra 0.05 degrees corresponds to a shift of ~1 pixel every 1000 pixels along the trail. In the interest of observing efficiency, this program performed forward and reverse scans alternately. Observers are cautioned that there will be a spatial offset between forward and reverse scans in the scan direction. Forward scans are centered in the frame as predicted in the APT display; reverse scans are offset by an amount that is greater for greater scan rates.

Boustrophedonic (from the Greek, literally, “as an ox turns in plowing”) scans, are possible too. In boustrophedonic scans, a.k.a. serpentine scans, the user specifies a set of constant-speed scan lines separated by a specified angular distance, like rows in a farmer’s field. An example is illustrated in [Figure 6.22](#). The advantage is that more scan lines are possible per exposure, which may be more efficient. The trajectory of such scans has been modeled ([WFC3 ISR 2017-06](#)).

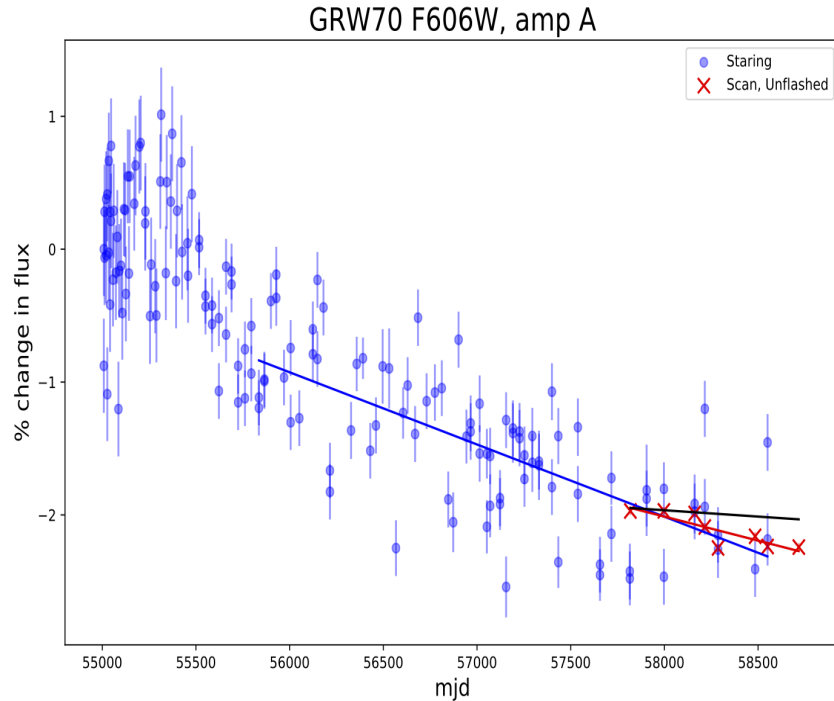
Figure 6.22: A boustrophedonic scan (vertically) of a star field on the UVIS focal plane (from program 12679).



The three thickest black lines in the center are the target star scanned upward, downward, and upward again in the same exposure. The U-shaped trails are from the turning points of nearby fainter stars.

Spatial scanning could in principle permit more precise photometry than staring mode, by collecting more photons and averaging over more detector pixels. However, actual photometric precision may not approach the theoretical limits due to at least two factors: 1) flat field errors (typically ~0.5%) and 2) shutter-timing non-repeatability (~0.004 s r.m.s. for the UVIS shutter). [WFC3 ISR 2017-21](#) shows that the photometric repeatability of spatial scans is much better than staring mode – typically around 0.1-0.5% between visits. More preliminary results that will be published in a future ISR confirm this result. See [Figure 6.23](#) for a comparison between photometry of staring mode observations of GRW70 versus spatial scans. These data are obtained for calibration programs that monitor the temporal stability of UVIS photometry.

Figure 6.23: Monitoring results for UVIS throughput using staring mode and scan mode

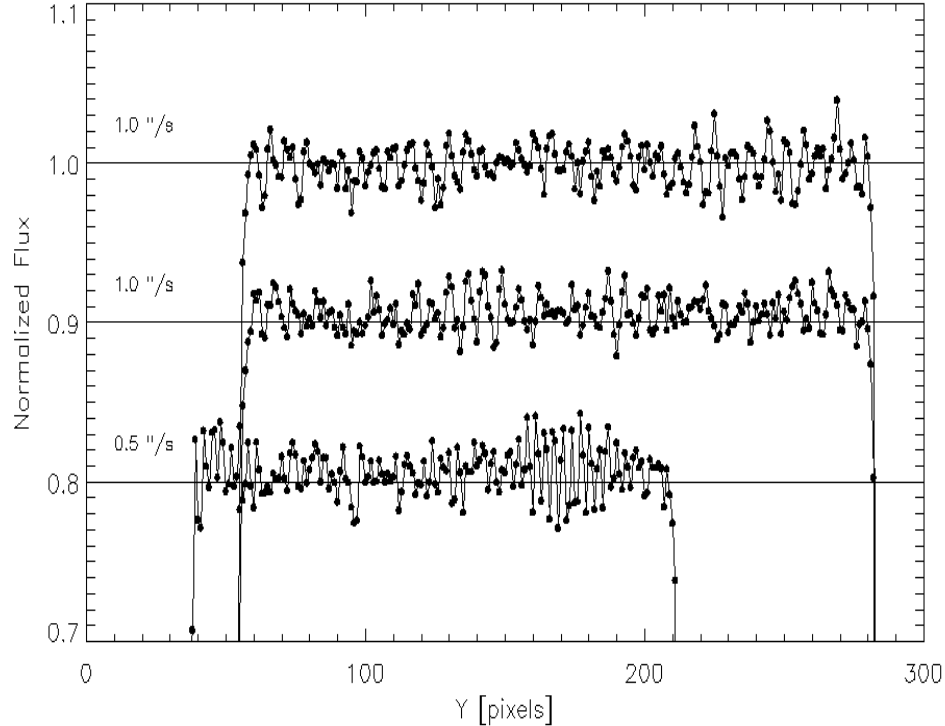


For routine monitoring of UVIS photometry, the changes over time in countrate of standard white dwarf stars are tracked. Historically, this has been done with staring mode observations (blue points) obtained frequently each cycle. Beginning in cycle 24, spatial scans (red points) were obtained for the same purpose. The scatter in the spatial scan data is much less than in the staring mode data, and time dependent changes in throughput can be assessed on a shorter timescale.

Two examples of utilizing spatial scans for precision time-series photometry are program 14621 (P.I. Wang) and program 15129 (P.I. Burke). These programs take advantage of the orbit-to-orbit and visit-to-visit stability of the UVIS detector.

Attempts to obtain precise photometric time-series within a single exposure, by using the trailed image of a star to record its flux versus time, have not been successful, because the positional feedback loop of the FGS control introduces lateral and longitudinal displacements from an idealized, constant-velocity scan, which results in photometric “flicker” of a few per cent (Figure 6.24). Although differential photometry of two or more stars would mitigate the FGS-induced “flicker”, the two flat-field and shutter factors would remain.

Figure 6.24: Photometric “flicker” appears in scans under FGS control.



The same star was trailed across the WFC3 IR detector repeatedly, with rates of 1, 1, and 0.5 arcsec s⁻¹ respectively. Photometry integrated transverse to each of the three trails, show intermittent oscillations with ~3% amplitude at ~1.3 Hz, due to image motion or “jitter” during the scans. The 2nd and 3rd trails have been offset vertically by 0.1 and 0.2 for clarity.

For those preparing a phase II program description, we recommend [WFC3 ISR 2012-08](#) and [WFC3 ISR 2017-21](#). Also, IR imaging with spatial scanning is discussed in [Section 7.10.4](#), and slitless spectroscopy with spatial scanning is discussed in [Section 8.6](#). See [Figure 8.9](#) for a diagram provided in APT to assist observers planning spatial scan observations.

Note: starting in Cycle 24, the Exposure Time Calculator ([ETC](#)) supports spatial scanning for UVIS and IR imaging and IR spectroscopy. (See [WFC3 STAN issue 22](#).)

6.12.4 PSF Subtraction

UVIS imaging has been shown to be highly effective in detecting faint point sources near bright point sources ([WFC3 ISR 2011-03](#)). For a variety of narrow, medium, and wide filters, when a high signal-to-noise drizzled image of a star was scaled down by 10 magnitudes and shifted and added to the original image, the simulated faint companion could usually be seen for separations greater than 1.0 arcsec. Based on the annular signal-to-noise of the deep stellar image, 5 sigma

detections of companions fainter by two magnitudes could be made at a separation of 0.1 arcsec. Theoretically, companions several magnitudes fainter could be detected at that separation in deeper images, but, in practice, variations in the PSF (point spread function) due to telescope breathing limit the detectability within about 0.3 arcsec of a bright star. If observers want to use stellar images to subtract the PSF from a target comprised of a point source and an extended source to detect or measure the extended source, they should keep several points in mind:

- UVIS pixels undersample the PSF ([Section 6.6](#)), so the stellar and target exposures should be dithered to produce good sampling of the PSF.
- Position drift and reacquisition errors can broaden the PSF ([WFC3 ISR 2009-32](#), [WFC3 ISR 2012-14](#)).
- If a single guide star is used for a visit, roll angle drift causes a rotation of the target around that star, which in turn introduces a small translational drift of the target on the detector. In recent years, as gyroscopes have failed and been replaced, the typical roll angle drift rate has increased from 1.5 mas/sec to ~17 mas/sec, producing a translation of up to 60 mas (1.5 UVIS pixel) in 1000 sec.
- The characteristics of the PSF depend on the focus, which generally changes measurably during an orbit; its range in a particular orbit will not be known in advance ([WFC3 ISR 2012-14](#), [WFC3 ISR 2013-11](#)).
- The characteristics of the PSF vary with location on the detector (e.g., see [ACS ISR 2003-06](#), [WFC3 ISR 2013-11](#)); PSFs near the A amplifier on UVIS1 are noticeably elongated by astigmatism ([WFC3 ISR 2013-11](#), [WFC3 ISR 2013-13](#)).
- More than one exposure time may be needed to produce an image that is unsaturated in the core and has good signal-to-noise to the desired radius.
- For exposures shorter than about 10 seconds, the UVIS PSF will be affected by vibration of the shutter ([WFC3 ISR 2009-20](#)). In some cases, use of the APT exposure-level option BLADE=A may be justified ([Section 6.11.4](#)).

While [Tiny Tim](#) modeling is available for the WFC3 UVIS detector, it has not been optimized to reproduce observed PSFs. See [Section 6.6.4](#) for a discussion of on-going work to provide PSF models to observers.

6.12.5 The Drift and Shift (DASH) Observing Strategy

The term DASH (for “drift-and-shift”, [Momcheva et al., 2016](#)) has been adopted to describe the observing strategy of taking a series of WFC3/IR exposures of many targets within one orbit while the telescope is being guided under gyroscope control, thus avoiding the overhead cost of acquiring a new pair of guide stars for every slew between targets of greater than about 2 arcmin. A WFC3/IR sample sequence comprised of short exposure times is selected to avoid image smearing within each time step, and the differential samples in one exposure are later aligned and combined to compensate for the greater drift due to gyroscope control. The technique was designed to allow users to carry out shallow large-scale mosaic observations with the WFC3/IR camera, but has since been adapted to efficiently observe a collection of bright targets within a field ~1 deg across with WFC3/IR subarray apertures (which have shorter time steps for a given sample sequence) and WFC3/UVIS subarray apertures. More detailed discussions of *HST* guiding and considerations for program design are given in [Section 7.10.6](#). A brief discussion of WFC3/UVIS observations is given here.

Given that WFC3/UVIS is read-out as a traditional CCD, it is necessary to specify short exposure times in place of the non-destructive reads made in an IR sample sequence in a DASH program. Subarray apertures are used to increase the number of exposures that can be fit into the on-board buffer before a time-consuming serial buffer dump must be made. Note, however, that specifying small subarray apertures is risky, especially towards the end of an orbit, when the high drift rates could cause a target to fall outside the aperture. A mitigating strategy is to specify increasing subarray sizes as

the orbit progresses, to allow for the uncertainty in predicting the drift. As discussed in [Section 7.10.6](#), DASH visits should be limited to one orbit, and the exposures in an orbit should be grouped into a non-interruptible sequence container in APT. The first exposure should be taken using guide stars to start the observations with accurate positioning.

Examples of programs that use WFC3/UVIS (and WFC3/IR) subarrays to observe many targets in one orbit are GO programs 14648 and 15146 (P.I. Riess).

Chapter 7: IR Imaging with WFC3

Chapter Contents

- [7.1 WFC3 IR Imaging](#)
- [7.2 Specifying an IR Observation](#)
- [7.3 IR Channel Characteristics](#)
- [7.4 IR Field Geometry](#)
- [7.5 IR Spectral Elements](#)
- [7.6 IR Optical Performance](#)
- [7.7 IR Exposure and Readout](#)
- [7.8 IR Sensitivity](#)
- [7.9 Other Considerations for IR Imaging](#)
- [7.10 IR Observing Strategies](#)

7.1 WFC3 IR Imaging

As described in [Chapter 2](#), the optical design of WFC3 features two independent channels, each with its own separate optics, filters and grisms, and detectors. The **UVIS channel** is sensitive to UV and optical wavelengths (200-1000 nm), and the **IR channel** is sensitive to near-infrared wavelengths (800-1700 nm).

Only a single channel, either UVIS or IR, can be used at any one time. Thus they cannot be used in parallel, but they can be used sequentially.

A schematic diagram showing the locations of the fields of view of the UVIS and IR detectors in the HST focal plane is given in [Figure 2.2](#).

This chapter describes the capabilities of the IR channel. The previous chapter, [Chapter 6](#), describes the UVIS channel. Detailed characteristics of the detectors used in both channels are given in [Chapter 5](#) and summarized in [Table 5.1](#).

7.2 Specifying an IR Observation

In the *HST* proposal system, the parameters for an IR observation available to General Observers are:

1. **Configuration:** always **WFC3/IR**.
2. **Mode:** always **MULTIACCUM**.
3. **Aperture:** must be specified; see Sections 7.4.4 and 7.4.5 for the dimensions, location, and reference point (target placement) of the full array and subarray apertures.
4. **Spectral Element:** must be specified for each exposure; see [Section 7.5](#).
5. **Optional Parameters:** in the IR channel **SAMPSEQ** specifies a predefined sequence of times at which the detector is read out, and **NSAMP** specifies the total number of readouts (and thus the total exposure time); see [Section 7.7](#). **SAMPSEQ** and **NSAMP** are required for IR observations.
6. **Special Requirements:** see the [*Phase II Proposal Instructions*](#) for details of Special Requirements related to the timing of visits and for dithering and mosaicking. Also available is the exposure-level Special Requirement **POS TARG** for offsetting the target from the default reference point of the aperture (see [Section 7.4.3](#) for a discussion of the IR channel coordinate system).
7. **Number of Iterations and Time per Exposure:** in cases where two or more identical exposures are desired, the Number of Iterations may be set to 2 or more. In the IR channel, the Time per Exposure is fixed by the combination of **SAMPSEQ** and **NSAMP** (see item 5 above) and thus is not specified separately. Through various combinations it is possible to select times per exposure ranging from 2.93 to 2756 s (for readouts of the full detector array; considerably shorter exposures are possible using subarrays).

7.3 IR Channel Characteristics

The WFC3 IR channel has been optimized for observing over the wavelength range 800-1700 nm. All the IR reflective optics (except for the WFC3 pick-off mirror) are coated with a silver layer for maximum IR throughput.

A schematic mechanical diagram showing both channels of WFC3 is given in [Figure 2.1](#). Components of the IR channel include: the Channel Select Mechanism (CSM), which directs on-axis light from the *HST* OTA to the IR channel; a flat folding mirror; a two-mirror mechanism for providing focus and alignment adjustments; the Refractive Corrector Plate (RCP), which applies the spherical-aberration correction; the IR filter wheel (FSM or Filter Selection Mechanism); and finally the HgCdTe IR detector package.

The WFC3 IR detector is a HgCdTe 1024×1024 array, with 18 micron pixels, bonded to a silicon multiplexer, with 1014×1014 pixels sensitive to incoming light. It is a direct descendant of the NICMOS 256×256 and Hawaii-1 1024×1024 arrays (more details on the detector are given in [Chapter 5](#)).

7.4 IR Field Geometry

- [7.4.1 Field of View and Pixel Size](#)
- [7.4.2 Geometric Distortion](#)
- [7.4.3 Coordinate Systems](#)
- [7.4.4 Subarrays](#)
- [7.4.5 Apertures](#)

7.4.1 Field of View and Pixel Size

The inner 1014×1014 pixels of the IR detector are exposed to incoming light. There are no gaps in the field (such as the gap between the two CCDs in the UVIS channel), or mechanical occultations (such as the coronagraphic spots in NICMOS camera 2).

The IR focal plane is tilted by $\sim 22^\circ$ with respect to the incoming beam. Thus the field of view as projected onto the sky is rectangular, with an aspect ratio of ~ 0.90 . The pixels projected onto the sky are also rectangular, covering approximately 0.135×0.121 arcsec, with the shape varying slightly across the field. The field of view on the sky is 136×123 arcsec, or 4.65 arcmin^2 .

7.4.2 Geometric Distortion

In addition to the rectangular field shape described above, the optical design of the IR channel also produces appreciable geometric distortion. Geometric distortions in both channels are discussed in more detail in [Appendix B](#).

Distortion must be taken into account when exposures are flat-fielded, photometrically calibrated, used for astrometric measurements, or combined with other dithered exposures. The AstroDrizzle software appropriately carries out those operations; a combination of software packages in DrizzlePac can be used to optimize the combination of dithered exposures. (See the [DrizzlePac](#) documentation.)

7.4.3 Coordinate Systems

Like the CCD, the IR channel requires multiple coordinate reference frames, each relevant for a specific goal. Readers may also wish to refer to [Section 6.4.3](#), which describes the coordinate systems for the UVIS channel. The coordinate systems used for the IR channel are illustrated in Figure 7.1 and are the following:

- **Data image-based system** (Axis1, Axis2; units of pixels)
- **Proposal POS TARG system** (X pos, Ypos; units of arcsec)
- **HST-based system** (V2, V3 or U2, U3; units of arcsec)

Figure 7.1: IR Aperture Diagram

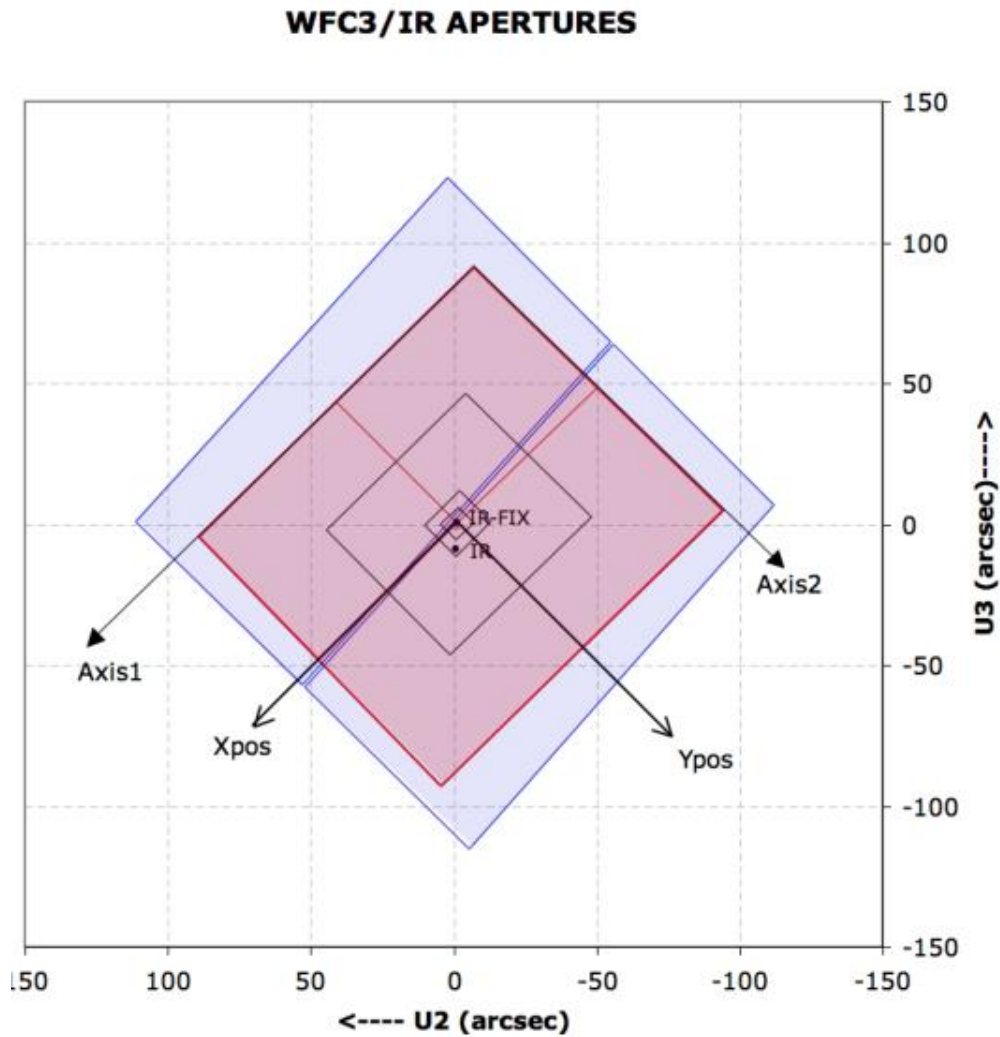


Figure 7.1 illustrates the fiducial points of the full-detector apertures (IR and IR-FIX), and the outlines of the concentric subarray apertures (512×512 , 256×256 , 128×128 , and 64×64). The regions imaged by the UVIS detector (represented by blue fill) and by the IR detector (represented by red fill) are also indicated. The POSition TARGet coordinate system for the IR-FIX aperture, with its origin at that aperture's fiducial point, is illustrated. Although the POSition TARGet coordinate systems for the other apertures are not illustrated, they are oriented the same, but have origins at each aperture's fiducial point (Section 7.4.5). ($U2 = -V2$ and $U3 = -V3$).

The **image-based coordinate system**, (Axis1, Axis2) in Figure 7.1, is a generic system used when an image is displayed on a computer screen. Coordinates are expressed in pixel units. This system is used primarily by the generic conversion pipeline software, which creates science FITS files from the data telemetry coming from the telescope.

The **POS TARG reference frame**, (Xpos, Ypos), is orthogonal on the sky, in units of arcseconds. It can be used to specify target placement at an offset location within the field of view, or for dithering or mosaicking purposes. In the IR channel, the POS TARG reference frame is designed to be virtually co-linear with the Axis reference frame, and it has its center located at the reference point (sometimes called the fiducial point) of the chosen IR aperture. The transformation between the undistorted POS TARG (arcsec) frame and Axis frame (pixels) contains non-linear distortion coefficients. For the IR detector, the POS TARG axes are almost exactly parallel to the detector edges. Note, however, that the IR POS TARG X,Y axes are not parallel to the UVIS POS TARG X,Y axes; the former are rotated a few degrees counterclockwise with respect to the latter.

The **HST-based**, or vehicle (V2, V3), system is an orthogonal reference frame tied to the telescope and is used operationally for alignment, pointing, and slewing purposes. The V1 axis lies along the optical axis while V2,V3 run parallel and perpendicular, respectively, to the solar-array rotation axis (see [Figure 2.2](#)). Note that the edges of the IR detector are rotated by approximately 45° with respect to the V2, V3 axes. Because WFC3 is on-axis, the origin of the V2,V3 system lies near the center of the WFC3 field of view. However, the V2,V3 (and U2, U3) coordinate axes have been shifted for clarity in [Figure 7.1](#). HSTobservers may be more familiar with the U2,U3 coordinate system than V2,V3; for example, the specification of the ORIENT angle Special Requirement in APT uses the position angle of the U3 axis. The U2,U3 coordinates are defined as $U2 = -V2$ and $U3 = -V3$, and are marked in [Figure 7.1](#). Observations of an astrometric field are made to locate the detector in the (V2, V3) system ([WFC3 ISR 2009-36](#)). See Section 7.2.2 of the [Phase II Proposal Instructions](#), which gives detailed information on the relationship between detector coordinates, spacecraft coordinates, and ORIENT.

7.4.4 Subarrays

In addition to obtaining standard full-field images, users can choose to read out smaller portions of the detector, called subarrays. Subarrays are useful to achieve reduced data volume, and/or to allow shorter exposure times. Shorter exposure times are especially important for the IR channel, because there is no physical shutter and the minimum integration time is limited by the time to read out the detector (2.9 s for full-frame readout). Very bright sources—including some of the primary “faint” IR photometric standards—may easily exceed the detector full-well of ~80,000 electrons in only a fraction of a second. Because the readout time is nearly proportional to the number of pixels read, subarrays can be used to reduce the effective integration time and make such observations feasible. Shorter integration times per readout have been implemented in the IR channel for several readout modes ([Section 7.7.4](#)).

All of the IR subarrays are centered on the detector field of view. Target placement on the subarray depends on the aperture selected ([Section 7.4.5](#)). Four subarray sizes are supported, with pixel dimensions of 512×512 , 256×256 , 128×128 , and 64×64 . Note that the sizes of the subarrays refer to the actual active pixels, i.e., they do not include the reference pixels. (Of the 1024×1024 pixels of the WFC3 IR detector, only the inner 1014×1014 pixels are light-sensitive. The 5 rows and columns of pixels around the edge of the array use fixed capacitances to provide constant-voltage reference values.) The reference pixels, however, are still included in the output images, resulting in final datasets of 522×522 , 266×266 , 138×138 , and 74×74 pixels. For subarray images, the reference pixels come from the same rows and columns of the subarray, with the 5×5 pixels at the subarray corners filled with the reference pixels at the corresponding corner of the detector (see [Section 5.5](#) for details on reference pixels).

Beginning in Cycle 18, subarrays were provided for grism spectroscopy, in addition to imaging. The actual selection of a subarray is accomplished by requesting one of the IR channel’s subarray apertures, as described in [Section 7.4.5](#).

A small fraction of WFC3/IR subarray and full-frame exposures exhibit an anomaly known as banding. It is characterized by a rectangular region in which background pixel values are a few DN above or below the level in the rest of the image. This region is centered vertically, and extends horizontally across the entire image and into the reference pixels. The height of the band is always either 64, 128, 256, or 512 pixels. The structure of the vertical profile is more variable and irregular in full frame images than in subarray images. A systematic study of banded data (see [WFC3 ISR 2011-04](#)) has revealed that the size of the band is always directly related to the size of prior subarray image(s). This coincidence accounts for the height of the bands, but the nature of the memory of prior subarray readout modes is not yet understood. As an operational solution, we recommend that observers avoid mixing different IR aperture sizes in a single visit whenever possible. If mixed aperture sizes are unavoidable, observations should be sequenced by aperture size from largest to smallest.

7.4.5 Apertures

The **APERTURE** parameter in the Phase II observing proposal defines two quantities: the active **region** of the detector to be read out (full frame or subarray), as well as the positioning of the target within the region (**reference point**). The default is to center the target at the reference point (also called the fiducial point), but a **POS TARG** Special Requirement may be added to offset the target from this position.

The available IR apertures are listed in [Table 7.1](#). As with other HST instruments, there are two kinds of apertures with regard to their target reference point: “**fixed**” and “**optimum**.” Apertures with their reference point at the geometric center of the array (or subarray) have “-FIX” appended of their name. These reference positions will never be adjusted during the HST mission. Apertures with their reference point at an “optimum” location (determined on the basis of best image quality, or detector cosmetics) have unadorned names. The reference point of these aperture may be optimized from time to time by STScI as circumstances warrant. At present, those reference points are offset from the boundaries of the amplifier quadrants.

 For updates on subarray and aperture definitions, check the Science Instrument Aperture File (SIAF) page:
<http://www.stsci.edu/hst/instrumentation/focus-and-pointing/apertures>

Table 7.1: WFC3 IR Apertures

Aperture Name	Reference (fiducial) point
IR	Optimum point near center of IR detector
IR-FIX	Geometric center of IR detector
IRSUB64	Optimum point near center of 64×64 subarray
IRSUB64-FIX	Geometric center of 64×64 subarray

IRSUB128	Optimum point near center of 128×128 subarray
IRSUB128-FIX	Geometric center of 128×128 subarray
IRSUB256	Optimum point near center of 256×256 subarray
IRSUB256-FIX	Geometric center of 256×256 subarray
IRSUB512	Optimum point near center of 512×512 subarray
IRSUB512-FIX	Geometric center of 512×512 subarray
IR-UVIS	Pointing matched to UVIS aperture in Table 6.1
IR-UVIS-CENTER	Pointing matched to UVIS-CENTER aperture in Table 6.1
IR-UVIS-FIX	Pointing matched to UVIS-FIX aperture in Table 6.1
GRISM64	Optimum point in 64×64 subarray for grism spectrum or reference image
GRISM128	Optimum point in 128×128 subarray for grism spectrum or reference image
GRISM256	Optimum point in 256×256 subarray for grism spectrum or reference image
GRISM512	Optimum point in 512×512 subarray for grism spectrum or reference image
GRISM1024	Optimum point in full frame for grism spectrum or reference image
G102-REF	Unsupported after cycle 18. (Optimum point for reference image intended to accompany G102 grism image. Use GRISM apertures above instead.)
G141-REF	Unsupported after cycle 18. (Optimum point for reference image intended to accompany G141 grism image. Use GRISM apertures above instead.)

7.5 IR Spectral Elements

- [7.5.1 Filter and Grism Summary](#)
- [7.5.2 Filter Blue Leaks](#)
- [7.5.3 Ghosts](#)

7.5.1 Filter and Grism Summary

An overview of the IR spectral elements and of the process by which they were selected was given in [Section 2.3](#). This section gives details of the IR filters and grisms. [Table 7.2](#) lists the IR channel's filters, with a general description and fundamental parameters of each. Figures [7.2](#) and [7.3](#) show the effective throughput curves, including the filter transmission multiplied by the throughput of the OTA, WFC3 optics, and detector response.

More detailed information on the throughput curves of all of the filters is given in [Appendix A](#); in particular, [Section A.2.1](#) describes how to generate tabular versions of the throughput curves using *synphot*. All measurements of the IR filters which involve wavelengths, as tabulated in Table 7.2 and plotted in Figures [7.2](#) and [7.3](#) and in [Appendix A](#), were done in helium rather than vacuum. It should be noted that the laboratory measurements were done at a temperature of -30°C , whereas the filters are operated on orbit at -35°C ; this may lead to wavelength shifts which are expected to be very small.

The IR channel is equipped with a single filter wheel with 18 slots, containing 15 passband filters, two grisms, and an opaque element (also referred to as the BLANK) for dark current measurements. The filter complement samples the spectral region between 800 and 1700 nm. All of the IR filter elements are full-sized, covering the entire field of view of the IR detector. Since all of the elements are mounted in a single wheel, only one element can be used at a given time.

The 900–1700 nm wavelength range is covered by a series of wide- and medium-band filters, with little wavelength overlap. Additional medium-band filters are centered on molecular bands and nearby continua, and several narrow-band filters are available for probing interstellar and nebular recombination lines.

The filter set is designed to include the most popular passbands used in extragalactic, stellar, and solar-system astronomy, as well as passbands similar to those already used in previous *HST* instruments.

Table 7.2: WFC3 IR Channel Filters and Grisms.

Name ¹	Description	Pivot ² λ_p (nm)	Width ³ (nm)	Peak System Throughput
IR Wide-Band (W) Filters				
F105W	Wide Y	1055.2	265.0	0.52
F110W	Wide YJ	1153.4	443.0	0.56

F125W	Wide <i>J</i>	1248.6	284.5	0.56
F140W	Wide <i>JH</i> gap; red grism reference	1392.3	384.0	0.56
F160W	WFC3 <i>H</i>	1536.9	268.3	0.56
IR Medium-Band (M) Filters				
F098M	Blue grism reference	986.4	157.0	0.47
F127M	H ₂ O/CH ₄ continuum	1274.0	68.8	0.54
F139M	H ₂ O/CH ₄ line	1383.8	64.3	0.54
F153M	H ₂ O and NH ₃	1532.2	68.5	0.55
IR Narrow-Band (N) Filters				
F126N	[Fe II]	1258.5	15.2	0.50
F128N	Paschen β	1283.2	15.9	0.52
F130N	Paschen β continuum	1300.6	15.6	0.54
F132N	Paschen β (redshifted)	1318.8	16.1	0.52
F164N	[Fe II]	1640.4	20.9	0.47
F167N	[Fe II] continuum	1664.2	21.0	0.46
IR Grisms (G)				
G102	"Blue" high-resolution grism	Useful range: 800–1150 nm ⁴		0.41
G141	"Red" low-resolution grism	Useful range: 1075–1700 nm ⁴		0.48

1 See Footnote 1 of [Table 6.2](#) for naming conventions.

2 "Pivot wavelength" is defined as in [Table 6.2](#) and [Section 9.3](#). Filter transmissions were measured in helium but have been converted to vacuum wavelengths for this table.

3 Passband rectangular width, defined as in [Table 6.2](#).

4 See [Chapter 8](#) for IR Grism details.

Figure 7.2: Integrated system throughput of the WFC3 IR wide-band filters, presented in two panels for clarity. The throughput calculations include the *HST* OTA, WFC3 IR-channel internal throughput, filter transmittance, and the QE of the IR detector.

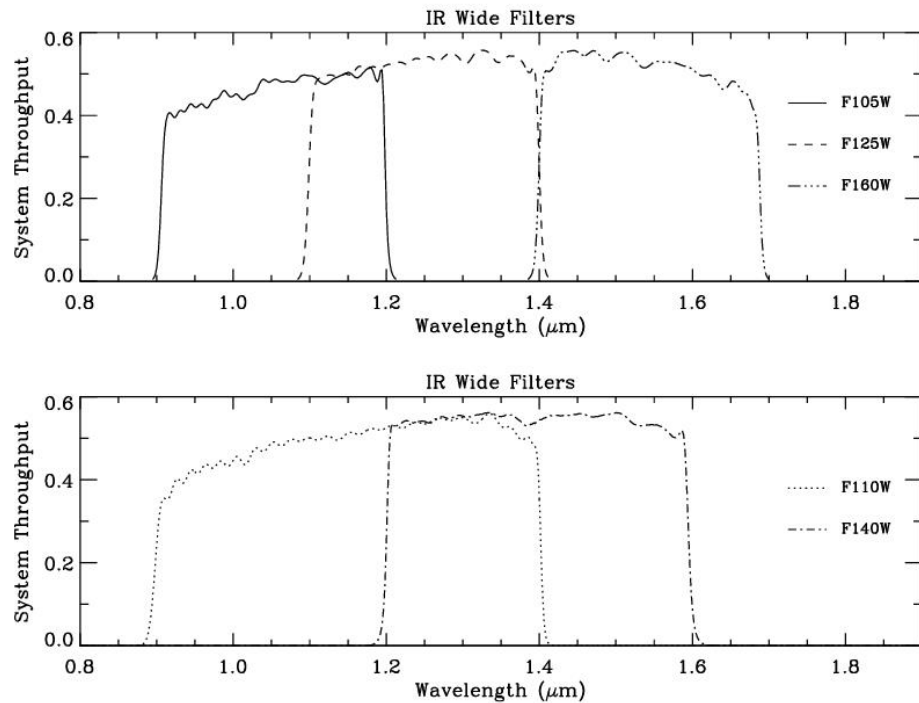
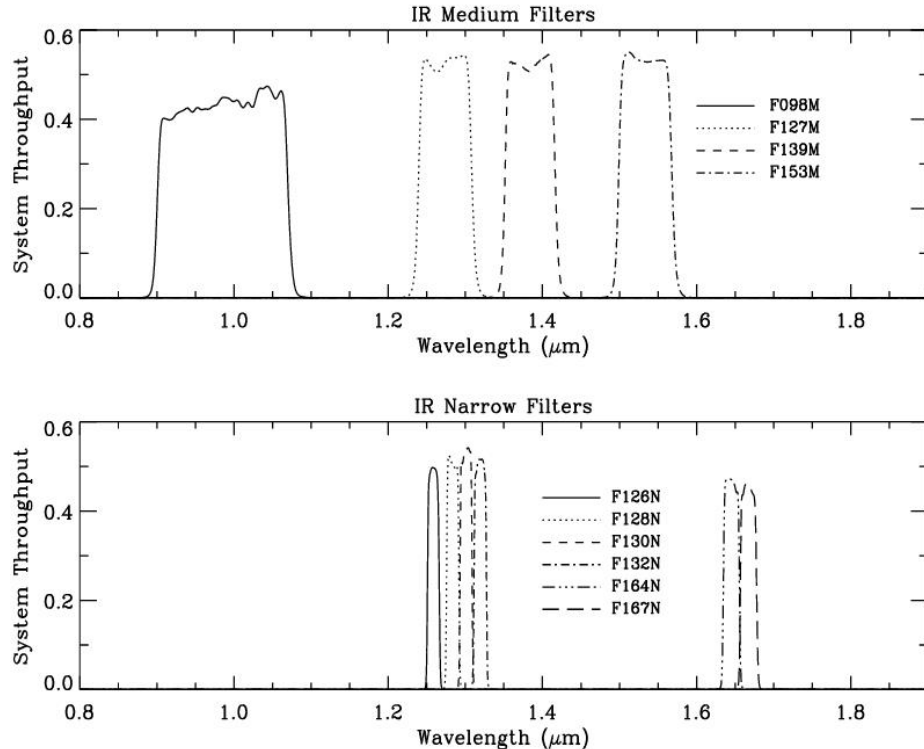


Figure 7.3: Integrated system throughput of the WFC3 IR medium-band filters (top panel) and narrow-band filters (bottom panel). The throughput calculations include the *HST* OTA, WFC3 IR-channel internal throughput, filter transmittance, and the QE of the IR detector.



Wide-Band Filters

The IR channel's versions of the ground-based *J* and *H* filters are F125W and F160W, respectively. The F125W filter has a width somewhat wider than that of a typical *J* passband used in ground-based cameras. The F160W filter's bandpass has been modified relative to ground-based *H* in order to give a better fit to the QE curve of the IR detector. Specifically, the WFC3 *H* filter's bandpass has been narrowed to approximately 1400-1700 nm, in order to limit thermal background and to have the filter define the bandpass on the red side rather than the detector sensitivity cutoff. By contrast, NICMOS *H* filter (NICMOS F160W) covers about 1400-1800 nm. This narrowing for WFC3 reduces photometric errors due to spatial variations in the detector's QE cutoff.

The wide F140W filter covers the gap between the *J* and *H* bands that is inaccessible from the ground. F105W has a central wavelength similar to ground-based *Y*, but is considerably wider. The IR channel also includes a very wide filter, F110W, spanning the ground-based *Y* and *J* bands. This filter can be used for deep imaging, with a bandpass fairly similar to that of the corresponding wide-band filter in NICMOS (also called F110W).

Medium-Band filters

The F098M filter is useful as the G102 grism reference, allowing source selection and wavelength zero-point determination. It also complements the UVIS F845M filter, whose red 50% critical wavelength is ~900 nm. The overlap allows coverage over a continuous wavelength range across both WFC3 detectors.

The other medium filters span absorption bands of water and methane (F139M) and water and ammonia (F153M), with an adjacent continuum filter (F127M). These filters were intended for compositional studies of planets searching for water vapor ([WFC3 ISR 2000-09](#)). Solar system objects with visible inventories of these gas species are too bright to observe with the medium-band filters, and WFC3 lacks occulting hardware to access the high contrast ratios and small angular separations that would enable direct imaging of exoplanets. However, the high sensitivity of WFC3 enables compositional studies of the atmospheres of cool stars, brown dwarfs, and transiting exoplanets with the medium-band filters.

Narrow-Band Filters

The IR channel includes six narrow-band filters which sample some of the most astrophysically important planetary, stellar, and nebular spectral features in the near-IR (e.g., [Fe II] and Paschen- β).

Cosmological emission lines can be detected across a range of redshifts within the bandpasses of the narrow-band filters. [Table 7.3](#) lists the redshifts that can be probed using the specified emission lines. These redshift ranges are offered as a guide; exact values depend on the wavelengths of the filter cutoffs. Filter cutoffs used in [Table 7.3](#) were defined using the passband rectangular widths (defined in footnote 4 of [Table 6.2](#)). For consistency with [Table 6.2](#), passband cutoffs were not centered on the filter pivot wavelengths λ_p (defined in [Section 9.3](#)). Instead, a central wavelength for each filter was determined by maximizing the wavelength-integrated product of a rectangular passband of the specified width with the actual system throughput for the filter. For the IR narrow-band filters, these rectangular passband equivalent central wavelengths are within 0.3% of the pivot wavelengths.

Table 7.3: Nominal redshift ranges for WFC3/IR narrow-band filters.

Filter	Description	Filter λ_p (nm)	Filter Width (nm)	Line Rest Wavelength (nm)	Minimum cz(km/sec)	Maximum cz(km/sec)
F126N	[Fe II] on	1258.5	15.2	1256.7	-1312	2314
F128N	Pa β on or [Fe II] off	1283.2	15.9	1281.8	-1415	2304
F130N	z (Pa β) or Pa β off	1300.6	15.6	1281.8	2690	6338
F132N	[Fe II] off or Pa β off	1318.8	16.1			
F164N	[Fe II] on	1640.4	20.9	1643.6	-1632	2180

F167N	[Fe II] off	1664.2	21.0	1643.6	2371	6202
-------	-------------	--------	------	--------	------	------

Grisms

The IR channel has two grisms that provide slitless spectra (see [Chapter 8](#) for more details). The “blue” G102 grism provides a dispersion of 2.5 nm/pix (or a resolution of ~210) over the 800-1150 nm wavelength range. The “red” G141 grism has a dispersion of 4.7 nm/pix (resolution of ~130) over the 1100-1700 nm range. In most cases, a grism observation will be accompanied by a direct image, for source identification and wavelength calibration (see [Section 8.3](#)).

7.5.2 Filter Blue Leaks

All of the IR filters have been constructed using IR-transmitting colored glass with thin-film coatings to achieve the desired bandpasses. As with the UVIS filter designs, better in-band transmission generally means somewhat less suppression of out-of-band transmission. While the final IR filters have excellent in-band transmission (>90%), a few also have a small, narrow peak of transmission between 750-800 nm. After the filters were manufactured, a new IR detector was chosen which has appreciable sensitivity well down into the optical wavelength range (see [Figure 5.23](#)). Some of the IR filters thus have a small amount of blue leak (i.e., a small amount of short-wavelength out-of-band light is detected). None of the IR filters have significant red leaks.

Table 7.4 presents estimates of the blue-leak effect, listing the fraction of detected count rate expected from 710 to 830 nm for each filter. The throughput calculation includes transmission of the filter, the throughputs of the *HST* OTA and the IR optics, and the QE of the IR detector.

As can be seen from the table, blue leaks in all the wide-band and some of the narrow- and medium-band filters are minimal; however, several filters, notably F126N, F128N, and F153M, have some blue leak (e.g., ~1% for objects with effective temperatures of 5000 K.) In programs that may suffer adverse effects due to the blue leaks, it may be useful to obtain UVIS images in the F763M filter, which covers the problematic wavelength region (750-800 nm).

Table 7.4: Fraction of detected count rate arising between wavelengths 710 to 830 nm as a function of effective temperature.

Filter	T_{eff} (K)										
	3500	5000	10000	15000	20000	25000	30000	35000	40000	45000	50000
F098M	3.8E-05	6.1E-05	8.4E-05	9.3E-05	9.8E-05	1.0E-04	1.0E-04	1.1E-04	1.1E-04	1.1E-04	1.1E-04
F105W	1.5E-05	2.2E-05	3.2E-05	3.5E-05	3.7E-05	3.9E-05	4.0E-05	4.1E-05	4.1E-05	4.1E-05	4.1E-05
F110W	8.8E-08	1.4E-07	2.4E-07	2.7E-07	2.9E-07	3.0E-07	3.1E-07	3.2E-07	3.2E-07	3.2E-07	3.2E-07
F125W	1.5E-07	2.4E-07	4.6E-07	5.3E-07	5.7E-07	6.1E-07	6.3E-07	6.5E-07	6.5E-07	6.5E-07	6.5E-07
F126N	6.4E-03	1.3E-02	2.6E-02	3.0E-02	3.3E-02	3.5E-02	3.6E-02	3.7E-02	3.8E-02	3.8E-02	3.8E-02
F127M	1.6E-03	3.2E-03	6.9E-03	8.0E-03	8.7E-03	9.2E-03	9.6E-03	9.8E-03	9.9E-03	1.0E-02	1.0E-02

F128N	5.7E-03	1.2E-02	2.7E-02	3.1E-02	3.3E-02	3.5E-02	3.6E-02	3.7E-02	3.7E-02	3.7E-02	3.7E-02
F130N	3.8E-04	6.7E-04	1.4E-03	1.6E-03	1.8E-03	1.9E-03	2.0E-03	2.0E-03	2.1E-03	2.1E-03	2.1E-03
F132N	3.7E-04	6.6E-04	1.4E-03	1.7E-03	1.8E-03	1.9E-03	2.0E-03	2.1E-03	2.1E-03	2.1E-03	2.1E-03
F139M	2.2E-03	3.9E-03	9.0E-03	1.1E-02	1.2E-02	1.3E-02	1.3E-02	1.4E-02	1.4E-02	1.4E-02	1.4E-02
F140W	6.3E-05	1.0E-04	2.4E-04	2.9E-04	3.2E-04	3.4E-04	3.5E-04	3.7E-04	3.7E-04	3.7E-04	3.7E-04
F153M	5.6E-03	9.9E-03	2.8E-02	3.3E-02	3.6E-02	3.9E-02	4.1E-02	4.2E-02	4.3E-02	4.3E-02	4.3E-02
F160W	9.4E-05	1.7E-04	4.8E-04	5.7E-04	6.3E-04	6.8E-04	7.1E-04	7.4E-04	7.4E-04	7.5E-04	7.5E-04
F164N	3.8E-03	8.0E-03	2.6E-02	3.1E-02	3.4E-02	3.7E-02	3.9E-02	4.0E-02	4.0E-02	4.1E-02	4.1E-02
F167N	3.3E-03	7.0E-03	2.2E-02	2.7E-02	3.0E-02	3.2E-02	3.4E-02	3.6E-02	3.6E-02	3.6E-02	3.6E-02

7.5.3 Ghosts

No significant optical ghosts are present in the IR channel.

7.6 IR Optical Performance

- [7.6.1 PSF Width and Sharpness](#)
- [7.6.2 Encircled and Ensquared Energy](#)
- [7.6.3 Other PSF Behavior and Characteristics](#)
- [7.6.4 Supersampled PSF Models](#)

Following its alignment to the OTA ([WFC3 ISR 2009-46](#)), a series of observations through a variety of filters were obtained to demonstrate the WFC3 optical performance. The WFC3 IR channel meets or exceeds all image quality expectations. The following subsections summarize the measured flight optical performance for the IR channel, as described by its point-spread function (PSF), i.e., the spatial distribution of the flux in an image of a point source. The results shown are produced using an optical model which has been adjusted and correlated to the PSFs measured on-orbit and represent mean values averaged over the field. (See [WFC3 ISR 2009-37](#).) This PSF model includes the pupil geometry, including the cold stop, residual aberration, the mid-frequency wavefront error of the OTA, the effect of the detector inter-pixel capacitive cross-talk, and first-order geometric distortion.

7.6.1 PSF Width and Sharpness

The IR channel PSFs are well approximated by Gaussian profiles (before pixelation). As was discussed in more detail for the UVIS channel in [Section 6.6.1](#), the PSFs can usefully be characterized by their FWHM or their sharpness (effectively the reciprocal of the number of pixels occupied by a point source, as defined in [Section 6.6.1](#)). [Table 7.5](#) lists the FWHM of the model PSF core (i.e., before pixelation) in units of pixel and arcsec and the sharpness parameter for 10 wavelengths. The sharpness range shown for each wavelength indicates the values for the PSF centered on the pixel corners and center. The monotonic increase in FWHM and decrease in sharpness with wavelength is due to diffraction.

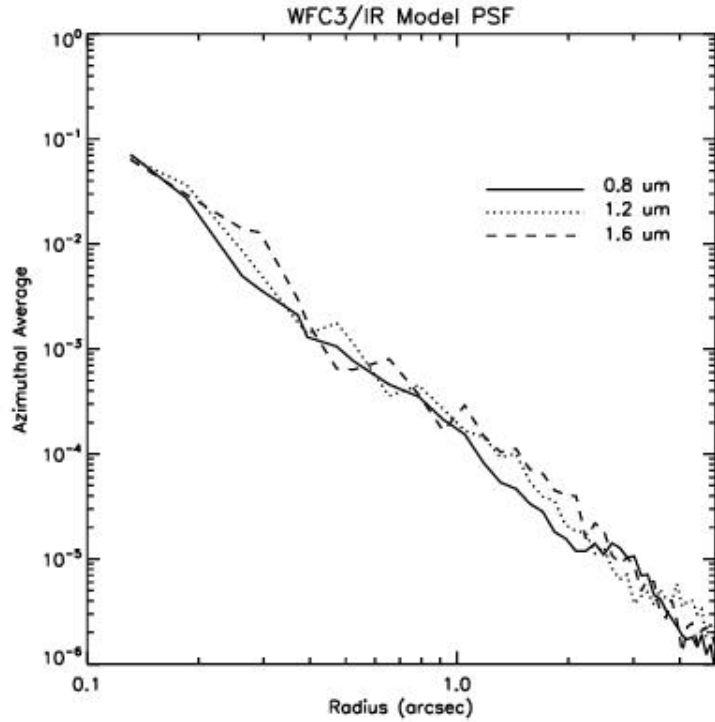
Table 7.5: WFC3/IR PSF FWHM (pre-pixelation, in units of pixels and arcseconds), and sharpness, vs. wavelength. (Note that attempts to measure the FWHM by fitting functions to the pixelated PSF will generally give larger values.)

Wavelength (nm)	FWHM (pix)	FWHM (arcsec)	Sharpness
800	0.971	0.124	0.127–0.197
900	0.986	0.126	0.118–0.182
1000	1.001	0.128	0.109–0.169
1100	1.019	0.130	0.100–0.156
1200	1.040	0.133	0.093–0.144
1300	1.067	0.137	0.087–0.132
1400	1.100	0.141	0.083–0.121

1500	1.136	0.145	0.080–0.112
1600	1.176	0.151	0.077–0.102
1700	1.219	0.156	0.074–0.093

Figure 7.4 plots the azimuthally-averaged model OTA+WFC3 PSF at three different IR wavelengths., indicating the fractional PSF flux per pixel at radii from 1 pixel to 5 arcsec.

Figure 7.4: Azimuthally averaged WFC3/IR PSF.



7.6.2 Encircled and Ensquared Energy

As described in more detail in [Section 6.6.2](#) for the UVIS channel, encircled energy, the fraction of light contained in a circular aperture, and ensquared energy, the fraction of energy falling within a certain number of pixels, are two other useful ways of characterizing well-behaved profiles.

Encircled-energy profiles for the IR channel at three representative wavelengths are plotted in Figure 7.5. The corresponding numerical values are presented in [Table 7.6](#). The ensquared energy, which provides the flux per pixel, is presented in [Table 7.7](#).

Figure 7.5: Encircled Energy for the WFC3/IR channel.

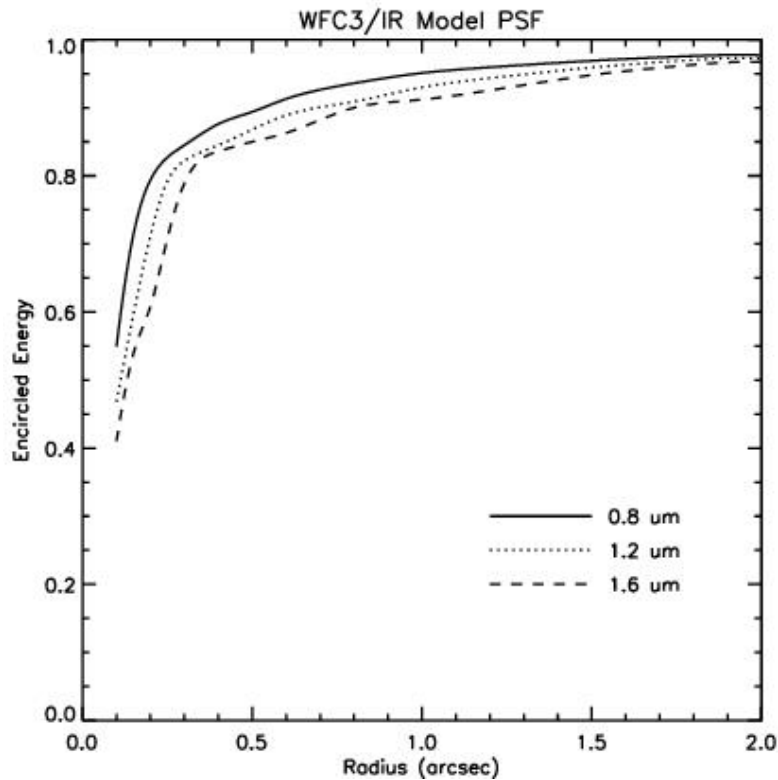


Table 7.6: WFC3/IR PSF Encircled Energy Fraction vs. Aperture Radius (arcsec).

Aperture radius (arcsec)	Wavelength (nm)										
	700	800	900	1000	1100	1200	1300	1400	1500	1600	1700
0.10	0.575	0.549	0.524	0.502	0.484	0.468	0.453	0.438	0.426	0.410	0.394
0.15	0.736	0.714	0.685	0.653	0.623	0.596	0.575	0.558	0.550	0.539	0.531
0.20	0.802	0.794	0.780	0.762	0.739	0.712	0.683	0.653	0.631	0.608	0.590
0.25	0.831	0.827	0.821	0.813	0.804	0.792	0.776	0.756	0.735	0.708	0.679
0.30	0.850	0.845	0.838	0.833	0.828	0.822	0.816	0.808	0.803	0.789	0.770
0.40	0.878	0.876	0.869	0.859	0.850	0.845	0.841	0.838	0.840	0.836	0.832
0.50	0.899	0.894	0.889	0.884	0.878	0.868	0.858	0.852	0.854	0.850	0.848
0.60	0.916	0.913	0.904	0.897	0.893	0.889	0.883	0.875	0.870	0.863	0.859
0.80	0.937	0.936	0.929	0.924	0.918	0.909	0.903	0.900	0.903	0.900	0.895
1.00	0.951	0.951	0.946	0.941	0.935	0.930	0.925	0.920	0.917	0.912	0.909

1.50	0.967	0.969	0.967	0.965	0.963	0.959	0.954	0.951	0.952	0.948	0.943
2.00	0.974	0.977	0.976	0.975	0.973	0.972	0.969	0.967	0.970	0.967	0.963

Table 7.7: WFC3/IR PSF Ensquared Energy Fraction vs. Aperture size (pixels), where the target is centered on the aperture. Row 1 indicates the maximal (PSF centered on the pixel) peak pixel fraction, useful for determining the exposure time at which saturation may occur.

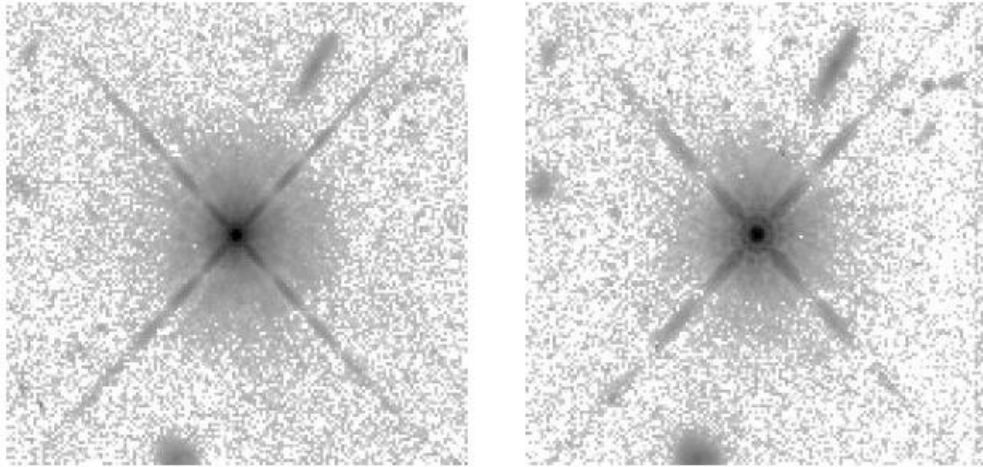
Aperture size (pixels)	Wavelength (nm)										
	700	800	900	1000	1100	1200	1300	1400	1500	1600	1700
1 × 1	0.435	0.417	0.398	0.381	0.365	0.348	0.331	0.314	0.299	0.283	0.267
2 × 2 ¹	0.728	0.707	0.679	0.648	0.618	0.592	0.571	0.554	0.545	0.534	0.524
3 × 3	0.815	0.811	0.802	0.790	0.776	0.757	0.733	0.706	0.682	0.655	0.631
5 × 5	0.872	0.868	0.858	0.849	0.844	0.840	0.836	0.830	0.830	0.826	0.821
7 × 7	0.905	0.900	0.894	0.888	0.882	0.872	0.862	0.855	0.856	0.854	0.852
9 × 9	0.927	0.924	0.917	0.909	0.904	0.898	0.893	0.888	0.886	0.876	0.868
11 × 11	0.941	0.939	0.934	0.928	0.921	0.914	0.910	0.905	0.905	0.901	0.897
13 × 13	0.951	0.951	0.946	0.941	0.936	0.930	0.924	0.917	0.919	0.915	0.911
15 × 15	0.957	0.958	0.955	0.951	0.946	0.942	0.936	0.931	0.931	0.925	0.921
17 × 17	0.961	0.963	0.962	0.958	0.955	0.950	0.945	0.942	0.942	0.938	0.933
19 × 19	0.964	0.967	0.966	0.964	0.961	0.958	0.954	0.949	0.951	0.947	0.942
21 × 21	0.967	0.969	0.969	0.967	0.965	0.963	0.960	0.956	0.957	0.953	0.950
23 × 23	0.970	0.972	0.971	0.970	0.969	0.967	0.964	0.961	0.964	0.960	0.956
25 × 25	0.972	0.974	0.973	0.972	0.971	0.970	0.968	0.965	0.968	0.965	0.962
51 × 51	0.993	0.993	0.991	0.990	0.988	0.987	0.986	0.985	0.988	0.987	0.986
101 × 101	0.998	0.999	0.998	0.998	0.997	0.997	0.996	0.996	0.998	0.997	0.997

¹ For the 2 × 2 aperture, the target is located at the center of the array.

During SMOV, high-dynamic-range isolated star images were obtained through several filters ([WFC3 ISR 2009-37](#)). These are shown with a logarithmic stretch in Figure 7.6. The images appear slightly elongated vertically, due to the 24 degree tilt of the detector to the chief ray and the fact that a distortion correction has not been applied. Although the target was chosen to be isolated, a number of field galaxies appear in both the F098M and the F160W filter images; these are also seen in long wavelength UVIS channel images of the same target ([Figure 6.13](#)). Some detector artifacts, including cold

and warm pixels and imperfectly removed cosmic ray hits are evident.

Figure 7.6: High dynamic range WFC3/IR star images through F098M (left) and F160W (right) subtending ~20 arcsec on each side near field center. No distortion correction has been applied. Stretch is logarithmic from 10^{-3} to $10^3 \text{ e}^- \text{ sec}^{-1} \text{ pixel}^{-1}$. Faint galaxies appear in the background.



7.6.3 Other PSF Behavior and Characteristics

Temporal Dependence of the PSF: *HST* Breathing

All *HST* observations are affected to some extent by short-term focus variations (“breathing”), which arise from the changing thermal environment of *HST* (See [Section 6.6.3](#)). For the IR channel, breathing is expected to produce variations of ~0.3% and less than 0.1% in the FWHM of the PSF of WFC3/IR at 700 nm and at wavelengths longer than 1100 nm, respectively, on typical time scales of one orbit.

Intra-Pixel Response

The response of a pixel of an IR detector to light from an unresolved source varies with the positioning of the source within the pixel due to low sensitivity at the pixel’s edges and dead zones between pixels. For NICMOS, the intra-pixel sensitivity was found to be an important effect: it varies by as much as 40% (peak to valley). This effect has an impact on point sources which depends on the sampling, and therefore, for a given pixel scale, on the wavelength of the diffraction-limited images. Well-dithered exposures average out this effect, but photometric accuracy for stellar sources with few dither positions can be limited by uncertainties related to intra-pixel response.

For the WFC3/IR flight detector, no measurable intra-pixel sensitivity variation was found during ground testing ([WFC3 ISR 2008-19](#)) or in-flight testing ([WFC3 ISR 2011-19](#)). The smaller pixel size (18 μm vs. 40 μm) and the much higher WFC3/IR detector temperature (compared to NICMOS) are probably responsible for this improvement.

Inter-Pixel Capacitance

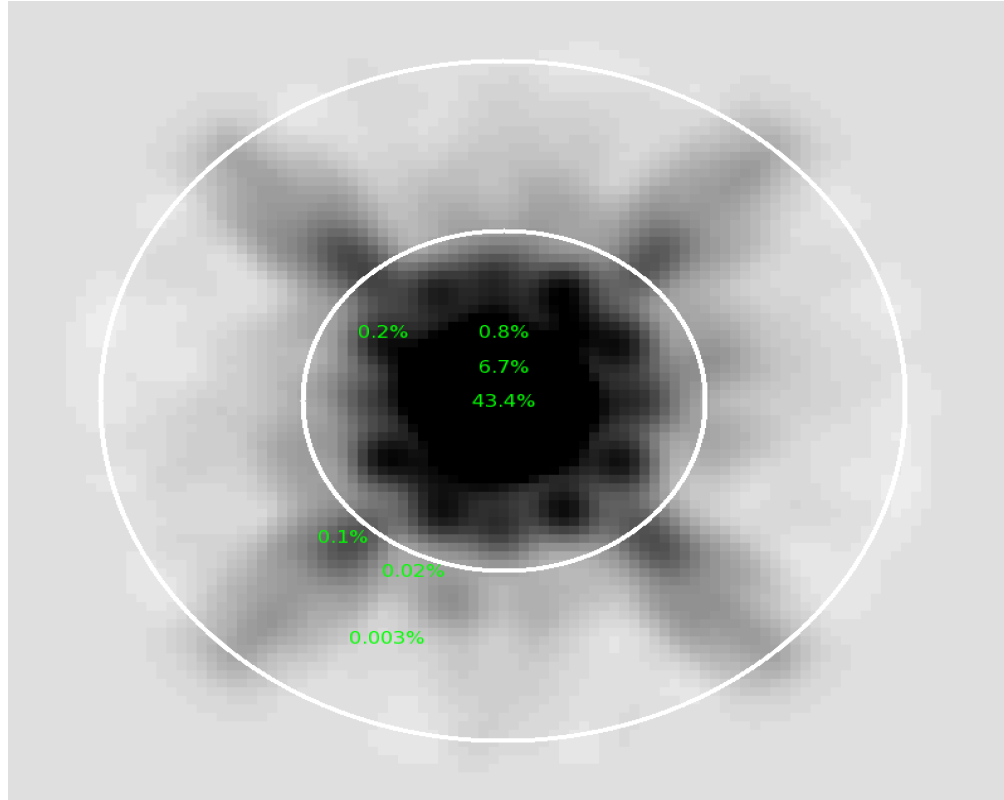
The small pixel size, relative to that in NICMOS, increases the relevance of capacitive coupling between nearby pixels (see Brown et. al., 2006, *PASP*, **118**, 1443; Moore et. al., 2006, *Opt. Eng.*, 076402). It affects the gain measurements and the PSF. The easiest method of estimating the inter-pixel capacitance is to measure the ratio of DNs in pixels adjacent to a “hot” (high-dark-current) pixel to the DNs in the hot pixel. In the WFC3 IR channel, on the order of 5% of electrons may leak to the adjacent pixels. [WFC3 ISR 2008-26](#) describes a method for correcting inter-pixel capacitance using Fourier deconvolution, and demonstrates its effectiveness on WFC3/IR ground-testing data. [WFC3 ISR 2011-10](#) provides an improved deconvolution kernel with distinct values for each of the 8 pixels surrounding the central pixel.

7.6.4 Supersampled PSF Models

The concept of empirical net (“effective”) models of PSFs is introduced in [Section 6.6.4](#). The WFC3/IR PSF has recently been modeled in [WFC3 ISR 2016-12](#) for five commonly used filters (F105W, F110W, F125W, F140W, and F160W).

Figure 7.7 shows a log image of the F105W PSF in supersampled (4x) pixels. The WFC3/IR PSF is extremely undersampled by the detector pixels: over 40 percent of a star's flux will land in its central pixel if the star is centered on that pixel. Only 4 percent will fall in the directly adjacent pixels. Even with this extreme undersampling, the 4x supersampled grid-base model is easily able to represent the PSF.

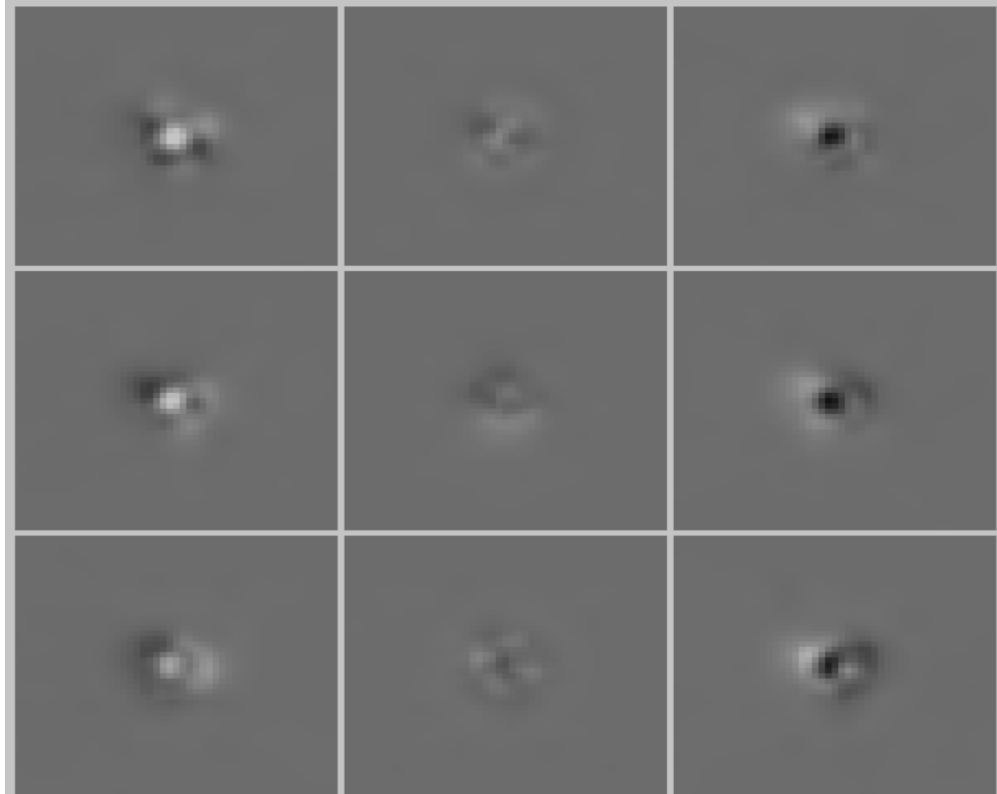
Figure 7.7: This is an image of the central WFC3/IR PSF for F105W. The PSF is supersampled by a factor of 4 relative to the WFC3/IR image pixels.



The white circles are drawn at $r=5$ and $r=10$ image pixels. The central label (43.4%) shows how much of the star's flux should be received by a pixel if the star happens to be centered on exactly that pixel. The label above it (6.7%) tells us what fraction of a star's flux would land in a pixel that is exactly one image-pixel above the center of the star. The 0.8% label tells us how much light would land in a pixel two up from the center of a star. The other labels show the fraction of light that lands in pixels at various other locations in the PSF: on inner-halo bumps (0.2%), on diffraction spikes at a distance of ~ 5 image pixels (0.1%), in the outer PSF halo at ~ 5 image pixels (0.02%) and in the outer halo at ~ 7.5 image pixels (0.003%).

Figure 7.8 shows how the WFC3/IR PSF varies across the face of the 1014×1014 pixel detector. A 3×3 array of models is adequate to represent the PSF across the detector.

Figure 7.8: For 9 locations on the detector in a 3×3 grid, a greyscale image shows the difference between each supersampled PSF and the average of the PSFs. Dark represents more flux, and light less flux. The largest variation is about 0.04, which is about 10% of the central value of the PSF.



As mentioned in [Section 6.6.4](#), the `flt`-frames provide the only clean constraints on the scene. Our high-precision PSF models are designed to be used in this frame, even though dithering and distortion make such analysis complicated. The WFC3 instrument team is working to produce some tools that can help users make use of these PSFs. [WFC3 ISR 2016-12](#) contains some FORTRAN routines that show how to use the PSFs, but higher-level tools are also under development.

7.7 IR Exposure and Readout

- [7.7.1 Exposure Time](#)
- [7.7.2 MULTIACCUM Mode](#)
- [7.7.3 MULTIACCUM Timing Sequences: Full Array Apertures](#)
- [7.7.4 MULTIACCUM Timing Sequences: Subarray Apertures](#)

The general operating modes of IR detectors have been described in [Chapter 5](#). In this section we will detail the readout modes implemented in WFC3.

7.7.1 Exposure Time

Unlike the UVIS channel, the IR channel does not have a mechanical shutter. Integration times are thus determined purely electronically, by resetting the charge on the detector, and then accumulating signal until the exposure is completed. A second major difference from the UVIS channel is that the IR detector can be read out non-destructively as the exposure accumulates, as opposed to the single destructive readout at the end of a CCD exposure.

There is a set of pre-defined accumulation and readout sequences available to IR observers, which are used to set the total exposure time as described in the next subsection.

7.7.2 MULTIACCUM Mode

In IR observing it is possible, and desirable, to sample the signal multiple times as an exposure accumulates, and the MULTIACCUM mode accomplishes this. MULTIACCUM is the only observing mode available for the IR channel.

Multiple readouts offer three major advantages. First, the multiple reads provide a way to record a signal in a pixel before it saturates, thus effectively increasing the dynamic range of the final image. Second, the multiple reads can be analyzed to isolate and remove cosmic-ray events. Third, fitting to multiple reads provides a means for reducing the net effective read noise, which is relatively high for the IR detector.

The disadvantage of multiple readouts is that they are data-intensive. The HgCdTe detector array is 1024×1024 pixels, which is only about 1/16 by pixel number of the 4096×4102 UVIS array. However, since up to 16 IR readouts are used, the total data volume of a single IR exposure approaches that of a single UVIS frame. A maximum of 32 IR full array readouts can be stored in the instrument buffer, after which the content of the buffer must be dumped to the *HST* Solid State Recorder (SSR). A buffer dump of 16 full array reads takes about 5.8 minutes.

MULTIACCUM readout consists of the following sequence of events:

1. **Array reset:** After a fast calibration of the Analog to Digital Converters, all pixels are set to the detector bias level, with two rapid reset cycles of the entire chip.

2. **Array read:** The charge in each pixel is measured and stored in the on-board computer's memory. This is done as soon as practical after the second array reset in step 1. In effect, given the short delay and the time needed to read the array, a very short-exposure image is stored in memory. This is known as the zero read.
3. **Multiple integration-read cycles:** The detector integrates for a certain amount of time and then the charge in each pixel is read out. This step can be repeated up to a total of 15 times following the zero read during the exposure. All frames are individually stored in the on-board computer memory. Note that it takes a finite time (2.93 sec) to read the full array, so there is a time delay between reading the first and last pixel. Because this delay is constant for each read, it cancels out in difference images.
4. **Return to idle mode:** The detector returns to idle mode, where it is continuously flushed in order to prevent charge build-up and to limit the formation of residual images.

All sequences start with the same “reset, reset, read, read” sequence, where the two reads are done as quickly as possible. This “double reset read” was originally implemented because the very first read after the reset may show an offset that does not reproduce in the following reads.

7.7.3 MULTIACCUM Timing Sequences: Full Array Apertures

There are 12 pre-defined sample sequences, optimized to cover a wide range of observing situations, available for the full-frame IR apertures. (See [Section 7.7.4](#) for a discussion of the sample sequences available for the IR subarray apertures. *The same names are used for the sample sequences, but the times are different.*) The maximum number of reads (following the zero read) during an exposure is 15, which are collected as the signal ramps up. It is possible to select less than 15 reads, thus cutting short the ramp and reducing the total exposure time. However, the timing of the individual reads within any of the 12 sequences cannot be adjusted by the user. This approach has been adopted because optimal calibration of IR detectors requires a dedicated set of reference files (e.g., dark frames) for each timing pattern.

In summary, a WFC3/IR exposure is fully specified by choosing:

- one of the 12 available pre-defined timing sequences, and
- the total number of samples (NSAMP, which must be no more than 15), which effectively determines the total exposure time

The 11 timing sequences for the IR channel are:

- One **RAPID** sequence: the detector is sampled with the shortest possible time interval between reads.
- Six linear (**SPARS**) sequences: the detector is sampled with uniform time intervals between reads, a so-called “linear sample up the ramp.” (“SPARS” is a contraction of the word “sparse.”)
- Five rapid-log-linear (**STEP**) sequences: the detector is initially sampled with the shortest possible time interval between reads, then uses logarithmically spaced reads to transition to a sequence of uniform samples.

All 12 of the sequences above refer to readouts of the full 1024×1024 detector array. See [Section 7.7.4](#) below for the timing sequences available for subarrays. Details of the sequences are in the following paragraphs. The timings of the individual reads are given in [Table 7.8](#).

RAPID Sequence

The RAPID sequence provides linear sampling at the fastest possible speed. For the full array, this means one frame every 2.9 s, and the entire set of 16 reads completed in less than 44 s. The RAPID mode is mainly intended for the brightest targets. Due to the overheads imposed by buffer dumps (see [Chapter 10](#)), observations in this mode done continuously would have low observing efficiency.

SPARS Sequences

The SPARS sequences use evenly spaced time intervals between reads. The six available SPARS sequences are designated SPARS5, SPARS10, SPARS25, SPARS50, SPARS100 and SPARS200, corresponding to sampling intervals of approximately 5, 10, 25, 50, 100, and 200 s, respectively.

The SPARS modes can be regarded as the most basic readout modes, and they are applicable to a wide range of target fluxes. They provide flexibility in integration time and are well suited to fill an orbital visibility period with several exposures.

SPARS5, introduced during cycle 23, has time steps intermediate between those of RAPID and SPARS10. It is expected to be especially useful for spatially scanned grism observations of bright stars (see [Section 8.6](#)) with subarray apertures (see [Section 7.7.4](#)).

STEP Sequences

The five available rapid-logarithmic-linear sequences are STEP25, STEP50, STEP100, STEP200, and STEP400. They begin with linear spacing (the same as the RAPID sequence), continue with logarithmic spacing up to the given number of seconds (e.g., 50 s for STEP50), and then conclude with linear spacing in increments of the given number of seconds for the remainder of the sequence.

The STEP mode is intended to provide a more uniform sampling across a wide range of stellar magnitudes, which is especially important for imaging fields containing both faint and bright targets. The faint targets require a long, linearly sampled integration, while the bright targets need to be sampled several times early in the exposure, before they saturate. Thus, the dynamic range of the final image is increased.

Figure 7.9: Example of STEP sequence with NSAMP=4. NSAMP+1 images are stored in the observer's FITS image

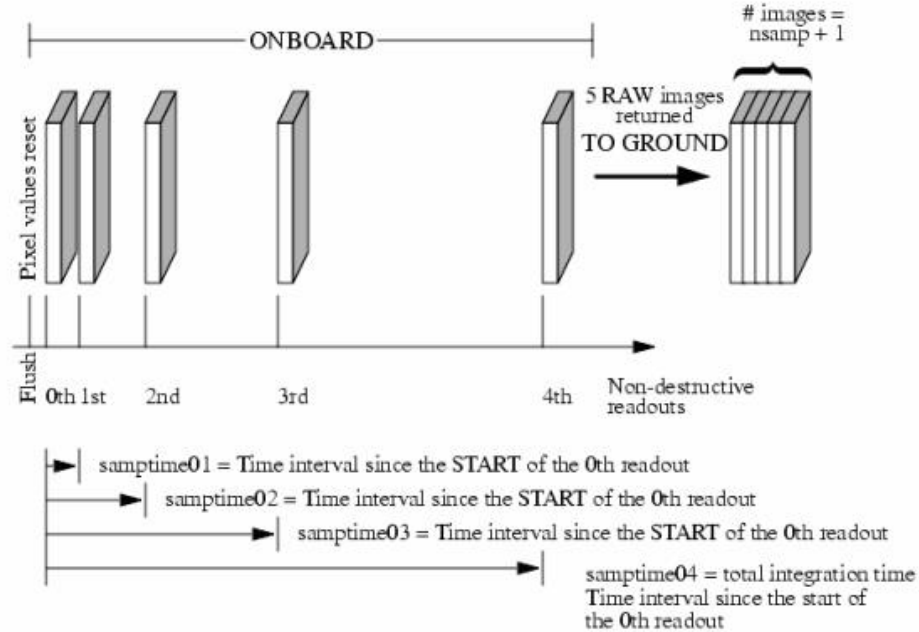


Table 7.8: Sample times of 1024×1024 MULTIACCUM readouts in seconds. The information in this table can also be found in Table 13.4 of the *Phase II Proposal Instructions*.

NSAMP	RAPID (sec)	SPARS (sec)						STEP (sec)			
		SPARS5	SPARS10	SPARS25	SPARS50	SPARS100	SPARS200	STEP25	STEP50	STEP100	STEP2
1	2.932	2.932	2.932	2.932	2.932	2.932	2.932	2.932	2.932	2.932	2.932
2	5.865	7.933	12.933	27.933	52.933	102.933	202.932	5.865	5.865	5.865	5.865
3	8.797	12.934	22.934	52.933	102.933	202.933	402.932	8.797	8.797	8.797	8.797
4	11.729	17.935	32.935	77.934	152.934	302.933	602.932	11.729	11.729	11.729	11.729
5	14.661	22.935	42.936	102.934	202.934	402.934	802.933	24.230	24.230	24.230	24.230
6	17.594	27.936	52.937	127.935	252.935	502.934	1002.933	49.230	49.230	49.230	49.230

7	20.526	32.937	62.938	152.935	302.935	602.934	1202.933	74.231	99.231	99.231	99.231	99.231
8	23.458	37.938	72.939	177.936	352.935	702.935	1402.933	99.231	149.231	199.231	199.231	199.231
9	26.391	42.938	82.940	202.936	402.936	802.935	1602.933	124.232	199.232	299.231	399.231	399.231
10	29.323	47.939	92.941	227.937	452.936	902.935	1802.933	149.232	249.232	399.232	599.232	599.232
11	32.255	52.940	102.942	252.937	502.937	1002.936	2002.933	174.233	299.232	499.232	799.232	799.232
12	35.187	57.941	112.943	277.938	552.937	1102.936	2202.933	199.233	349.233	599.232	999.232	999.232
13	38.120	62.942	122.944	302.938	602.938	1202.936	2402.933	224.234	399.233	699.233	1199.233	1199.233
14	41.052	67.942	132.945	327.939	652.938	1302.936	2602.933	249.234	449.234	799.233	1399.233	1399.233
15	43.984	72.943	142.946	352.940	702.939	1402.937	2802.933	274.235	499.234	899.233	1599.233	1599.233

7.7.4 MULTIACCUM Timing Sequences: Subarray Apertures

As described in [Section 7.4.4](#), subarrays are available in order to reduce data volume and enable short exposure times, defined in sample sequences. *For a given sample sequence name, the sample times are shorter for smaller subarrays.* However, only certain combinations of subarrays and sample sequences are supported by STScI. Other MULTIACCUM sequences can be used in principle but are not supported, and additional calibration observations would have to be made by the observer. The supported combinations are presented in [Table 7.9](#). The exposure times may be found in the [Phase II Proposal Instructions](#), Chapter 13 (Wide Field Camera 3).

 See Section 13.3.6 of the GO [Phase II Proposal Instructions](#), Table 13.4, for the sample times associated with each combination of sample sequence and subarray size. Note that the sample times for a given sample sequence name are shorter for smaller subarrays.

SPARS5, introduced during cycle 23, is expected to be especially useful for spatially scanned grism observations of bright stars (see [Section 8.6](#)).

Certain combinations of IR subarrays and sample sequences give rise to images containing a sudden low-level jump in the overall background level of the image. The cause of the artifact is under investigation (see [Section 7.4.4](#)).

Table 7.9: Supported subarray sample sequences.

Aperture	Sample Sequence				
	RAPID	SPARS5	SPARS10	SPARS25	STEP25
IRSUB64	yes	no	no	no	no
IRSUB64-FIX	yes	no	no	no	no
IRSUB128	yes	no	yes	no	no
IRSUB128-FIX	yes	no	yes	no	no
IRSUB256	yes	yes	yes	yes	no
IRSUB256-FIX	yes	yes	yes	yes	no
IRSUB512	yes	yes	no	yes	yes
IRSUB512-FIX	yes	yes	no	yes	yes

7.8 IR Sensitivity

7.8.1 Limiting Magnitudes

Table 7.10 presents the predicted limiting-magnitude performance of the WFC3 IR channel and compares it with that of the NIC3 camera. The calculations are based on an optimal extraction of a point source. The limiting ABMAG at a S/N of 10 was calculated for a 1-hour and a 10-hour exposure. The throughput curves for the WFC3 filters listed in column 2 were used; for NIC3, the most similar wide-band filter was used, and its name is given in column 3.

An [Exposure Time Calculator \(ETC\)](#) is available online. See [Section 9.2](#).

Table 7.10: Limiting-magnitude performance of WFC3 compared with that of NIC3 based on on-orbit sensitivity from SMOV4.

Band	Filter		Limiting magnitude in 1 hr		Limiting magnitude in 10 hrs	
	WFC3	NIC3	WFC3	NIC3	WFC3	NIC3
J	F110W	F110W	27.3	26.1	28.6	27.4
H	F160W	F160W	26.6	25.9	27.9	27.1

The table provides limiting ABMAGs at a S/N of 10 for the indicated WFC3 filters and for NIC3 with its most similar filters.

7.9 Other Considerations for IR Imaging

[7.9.1 Gain and Full-Well Saturation](#)

[7.9.2 Cosmic Rays and Snowballs](#)

[7.9.3 On-Orbit Degradation](#)

[7.9.4 Image Persistence](#)

[7.9.5 The IR Background](#)

[7.9.6 Blobs](#)

[7.9.7 Optical Anomalies](#)

7.9.1 Gain and Full-Well Saturation

Like the UVIS channel, the IR channel uses 16-bit Analog to Digital Converters (ADCs), providing a digital output signal in the range between 0 and 65,535 data numbers (DNs). The default gain setting for the IR channel is 2.5 electrons/DN and is the only one offered to observers. In ground-based testing, the measured gain for this setting was 2.3 to 2.4 e⁻/DN, depending on quadrant ([WFC3 ISR 2008-50](#)). Values of 2.2 to 2.3 e⁻/DN were measured using internal flat field exposures taken from Oct 2010 to June 2015 ([WFC3 ISR 2015-14](#)).

The default gain is compatible with the full-well saturation level of the IR channel, which is about 78,000 electrons (~34,000 DN at the default gain), and with the detector readout noise, of order 20-22 electrons per correlated double sampling.

7.9.2 Cosmic Rays and Snowballs

Cosmic rays affect the image quality. On-orbit measurements indicate that cosmic ray events occur at a rate of 11 ± 1.5 CR/s for WFC3/IR. The use of MULTIACCUM mode makes it possible to filter out cosmic rays because it provides a series of intermediate non-destructive reads. The intermediate reads are used by the WFC3 data pipeline to identify cosmic ray hits, similar to the use of CR-SPLITs in CCD observations. AstroDrizzle also checks for and attempts to remove cosmic rays from the “drizzled” images when there are multiple (usually dithered) exposures of the same field. (See the [DrizzlePac](#) documentation.)

Passages through the South Atlantic Anomaly (SAA) cause the highest number of cosmic ray hits. When the HST is within the predefined SAA exclusion zone, IR observations are not normally taken and the detector is set to auto-flush mode to minimize the effects of SAA passage on instrument performance. Unlike NICMOS, where the detector electronics had to be switched off during SAA passage, it is possible to perform time-critical observations in the SAA with WFC3/IR.

Snowballs (named for their fuzzy appearance) are transient extended sources that appear in IR exposures at the rate of about one per hour. They were characterized during ground-based testing ([WFC3 ISR 2009-43](#)) and were hypothesized to be caused by the emission of alpha particles by radioactive isotopes in the detector ([WFC3 ISR 2009-44](#)). The rate of appearance of snowballs has remained constant over 5 years of on-orbit observations, consistent with the hypothesis that the uranium-238 decay chain is the source ([WFC3 ISR 2015-01](#)). Typical snowballs affect about 8 to 25 pixels, saturate

2-5 of those, and deposit about 200,000 to 500,000 electrons on the detector. The energy is deposited in the pixels instantaneously, so snowballs can be removed via up-the-ramp fitting, like cosmic rays.

7.9.3 On-Orbit Degradation

Unlike the CCDs, minimal cosmic-ray damage to the IR detectors was anticipated, and essentially none has been observed. During ground testing using a particle accelerator, the WFC3/IR arrays were subjected to radiation doses much higher than expected in their entire orbital lifetime, without sustaining significant long-term damage or measurable degradation in QE. Searches for the development of new bad pixels are conducted as part of the regular calibration program; the number is growing slowly if at all ([WFC3 ISR 2010-13](#), [WFC3 ISR 2012-10](#)). The mean dark current remained unchanged in the first three years of in-flight operations ([WFC3 ISR 2012-11](#)). (See [Section 5.7.2](#))

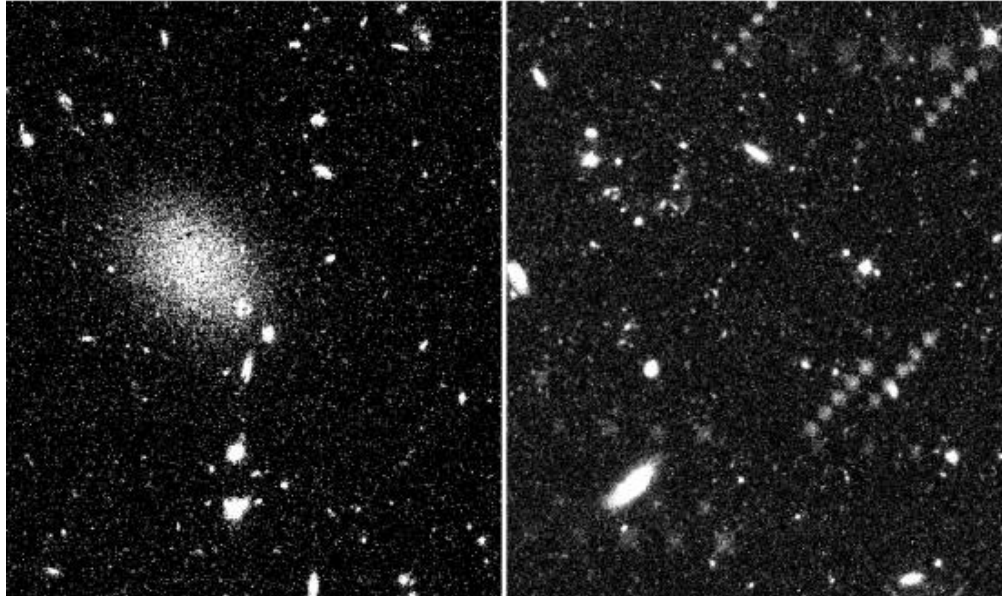
In-flight dark reference files made from SMOV and cycle 17 data were delivered in March 2010 (full array) and October 2010 (subarrays) to replace the ground-based reference files. Subarray darks made from non-banded data taken in cycle 18 (see [WFC3 ISR 2010-16](#) and [Section 7.4.4](#)) were delivered in February 2011. Full array darks with better signal-to-noise, made using data from cycles 17 through 20, were delivered in October 2013. Summaries of WFC3 reference files are displayed at: <http://newcdbs.stsci.edu/doc/ICD47/Section11.html>.

7.9.4 Image Persistence

As discussed in [Section 5.7.9](#), the WFC3/IR detector exhibits image persistence, particularly during and following observations of targets that saturate the detector by more than the pixel full well depth. The amount of image persistence depends primarily on the brightness of the amount of charge accumulated by a pixel in an exposure, and secondarily on the length of time in an exposure. (There is also some dependence on the location on the detector.) The basic reason for this behavior is that the traps involved in persistence have finite trapping times, as well as finite release times.

Image persistence has been observed both within exposures in a single orbit and in observations where the target observed in a previous orbit was particularly bright. Two examples of persistence are shown in Figure 7.10. The left panel shows an image obtained with WFC3/IR in parallel to a COS exposure from program 11519, Visit 0V. The bright diffuse object in the center of the field is the persistence after-image of the nearby Sb galaxy NGC 2841 observed two hours earlier in program 11360 visit R1. The right panel shows an image obtained of the gamma ray burst GRB090423 as part of program 11189 visit H2, which followed observations of globular cluster 47 Tuc (program 11677 visit 19) and a stellar field in Orion (program 11548 visit AJ). The patterns seen going diagonally across the image are the result of the dither pattern used in the previous observations (as persistence is manifested in the same pixels where the causing source previously landed). Persistence may also be caused by sources observed previously in the same visit. This is known as self persistence, and often contributes the strongest persistence signals due to temporal proximity.

Figure 7.10: Persistence seen in WFC3/IR exposures following exposures of a bright nearby galaxy (left) and following dithered exposures of two fields of bright stars (right).



Such obvious examples of persistence from previous visits are fairly rare in the *HST* data. Using information in the [Phase II Proposal Instructions](#), STScI scientists attempt to identify visits that are likely to cause this much persistence. STScI planners inhibit WFC3/IR observations for several orbits after observations from these “bad actors”, long enough for the afterglow images to fade. *Observers can help in preventing persistence from affecting future observations with appropriate observing strategies, and, in cases where persistence cannot be avoided, by flagging the problem with written comments in the phase II proposal and notifying the Contact Scientist or Program Coordinator.*

While the screening process generally eliminates the worst cases of persistence, such as those in Figure 7.10 (above), the process is not perfect and so observers need to be aware of the possibility of persistence in their images. Indeed, in light of the fact that WFC3/IR exposures constitute a significant fraction of the overall *HST* observing program and in order to maintain *HST* scheduling efficiency, only a small fraction of the visits can be declared to be “bad actors”. This means that many IR images have some pixels that are affected by persistence. In the vast majority of cases, the number of pixels that are affected by persistence due to exposures from earlier visits is small compared to the number of pixels that should be flagged for other reasons. The tools and procedures needed to identify pixels affected by persistence and to mitigate its affect are described in the [WFC3 Data Handbook](#). Observers are advised to take advantages of these tools to check whether the ability to extract science from their data has been adversely affected by persistence. *It is the responsibility of observers to check their data and request a repeat of a visit that has been compromised by persistence by filing a HOPR within the prescribed period.*

While avoiding persistence created by other programs is largely outside of the control of an individual investigator, evaluating whether persistence within a visit will affect the quality of their data is the responsibility of the observer. Specifically, observers need to consider whether persistence within a single visit will affect their ability to extract science from their data.

In carrying out this evaluation, it is important to remember that fairly short exposures (100 sec) of relatively bright (18th mag) stars observed through the broad-band filters saturate pixels in the IR array and so there will often be self persistence within visits. Furthermore, the amount of persistence decays inversely with time. So, as shown in Figure 5.30 in [Section 5.7.9](#), a pixel that has been saturated to an effective fluence of ~100,000 electrons will show an afterglow of about 0.3 electrons per sec at 1000 seconds, but ~2 electrons per sec at 200 seconds. Persistence at short time scales is not as well characterized, though the behavior is seen to change at short time scales, that is persistence decays more slowly at first ([WFC3 ISR 2019-02](#)).

In most cases, persistence will not turn out to be a serious problem, particularly if the objects that have the potential to cause persistence are spatially separated from the area of the image from which science is obtained, and/or if the number of affected pixels is small, and/or if dither patterns are small. In these cases, the procedures described in the [WFC3 Data Handbook](#) should be sufficient to address any issues associated with internal persistence in the images that will be obtained.

However, in some cases, persistence will be an issue, especially if the science target is faint, but the field is filled with considerably brighter objects. In these cases, one should avoid the tendency to set the exposure time for the fainter science target, ignoring the problem that will be caused by the rest of the field. Observers should take care that bright or saturated sources within a field are not dithered across the same parts of the detector that record the highest science priority areas of the field.

Planning observations of dense fields, globular clusters, or very bright star formation regions may be complicated in instances where precise photometry or very large dynamic range are required.

Measured flux rises with the number of exposures in a series of undithered exposures ([WFC3 ISR 2016-11](#)). This can affect photometry at the level of 0.02-0.04 magnitudes. This phenomenon, likely associated with persistence, is related to the slow rise in measured flux seen in grism observations of planetary transits. Even in the cases where data is dithered, persistence may affect the photometric results at the level of 0.02-0.04 magnitudes ([WFC3 ISR 2019-07](#)), often because the dithers are too small to avoid pixels previously illuminated.

There are a variety of strategies one can adopt to minimize the effects of persistence. In many cases, the best approach is to take more shorter exposures to limit the numbers of pixels affected. In addition, executing dithers greater than 10 pixels, always to unique positions, substantially aids in persistence mitigation ([WFC3 ISR 2019-07](#)). However, this incurs a greater cost in overheads, and becomes less effective as crowding increases. Taking shorter exposures or narrow band exposures before long or wide band exposures yields less fluence in previous exposures, thus leading to less persistence.

Various tools to estimate which regions of an image are likely to cause persistence and additional strategies to mitigate its effects are described in [Appendix D](#).



Updates on persistence characterization and tools for persistence artifact removal will be posted on the WFC3 persistence page.

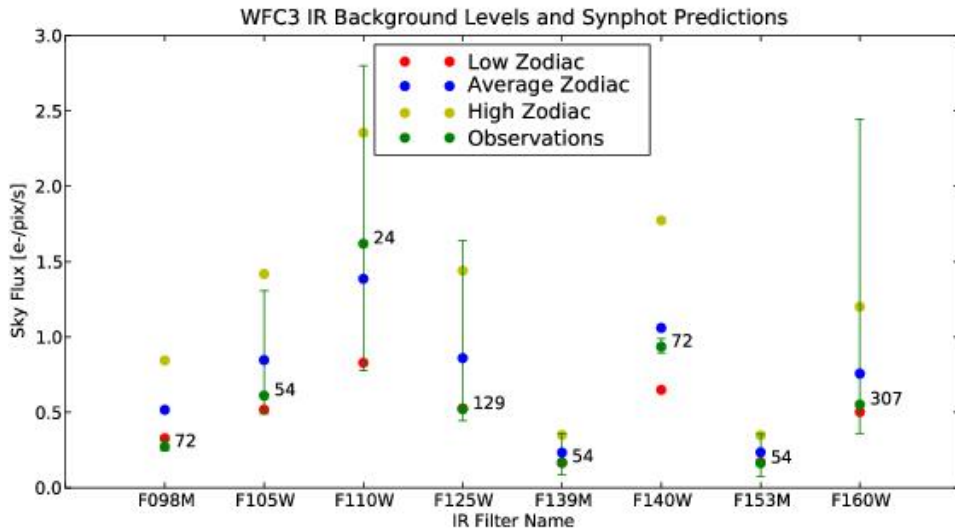
See: <http://www.stsci.edu/hst/instrumentation/wfc3/data-analysis/ir-persistence>

7.9.5 The IR Background

In space, the dominant sources of background radiation are zodiacal light and earthshine at shorter IR wavelengths, and the telescope thermal emission at longer wavelengths. For *HST*, the sum of these two background components has a minimum at about 1600 nm (e.g., see section [4.7 in the NICMOS Instrument Handbook](#)). This wavelength lies near the red end of the reddest WFC3/IR filter, F160W (WFC3 H). A variable airglow line of He I at 10830 Å can be a significant, even dominant, component of the sky background in the F105W and F110W filters and the G102 and G141 grisms. (See [WFC3 ISR 2014-03](#).)

Figure 7.11 shows the observed background levels in the first few months of WFC3’s operation (green points and error bars), compared with values predicted from known instrument sensitivities and three levels of zodiacal light selectable in the [Exposure Time Calculator](#) (ETC). Even allowing for small sample sizes and possible systematics in the observations, it is apparent that a rough estimate of the zodiacal light level may not adequately predict the observed background level of an exposure. The WFC3 team has performed extensive studies of zodiacal light and earth-shine in WFC3/IR exposures (thereby discovering the impact of the He I airglow line) to improve our understanding of the sky background and to enable us to provide practical advice to observers.

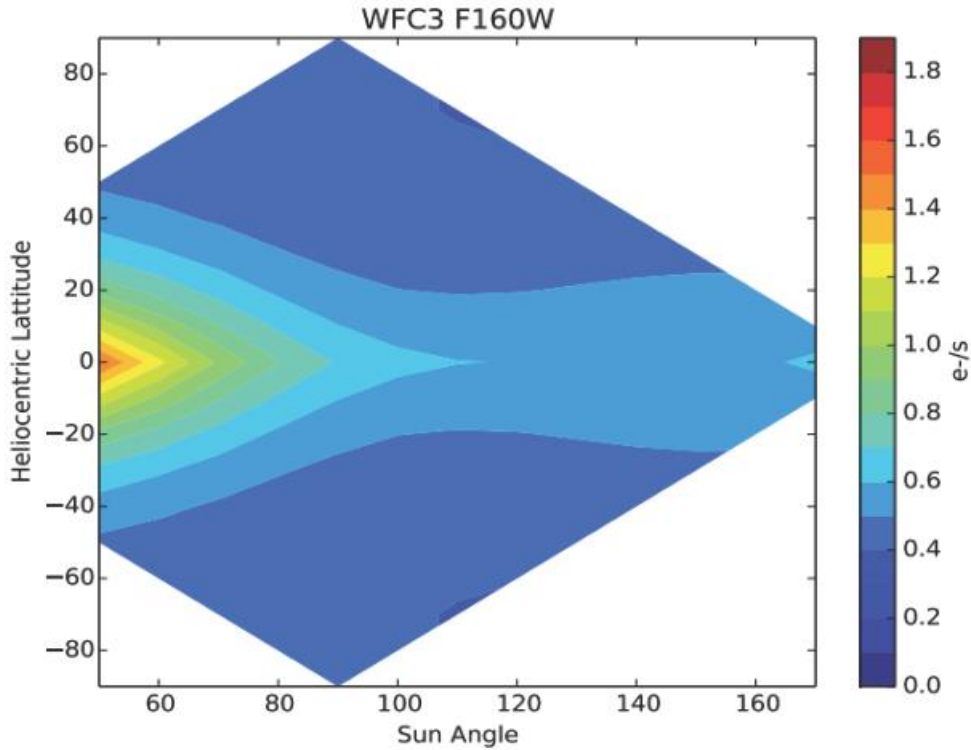
Figure 7.11: Infrared background levels for WFC3.



The average, low and high zodiac points show the synphot predictions for three levels of zodiacal light and no earth-shine. The observations selected include calibration and GO images of empty or sparsely populated fields, giving an accurate representation of early WFC3 observations but not covering all background conditions. Observational means (green points), ranges (error bars), and exposure counts are plotted.

The zodiacal background level observed in WFC3/IR exposures has been modeled as a function of ecliptic latitude and angular distance of the target from the sun ([WFC3 ISR 2014-11](#)). (The dependence can be formulated as a function of ecliptic latitude and angular separation of the target from the sun in ecliptic longitude, or ecliptic latitude and the angle between the target and the sun as viewed by *HST*. The latter coordinate system has been adopted because it has practical advantages for planning and analyzing *HST* observations.) The model derived for filter F160W is shown in Figure 7.12. The Sun Angle in the figure corresponds to the keyword SUNANGLE in the *HST* science header. [WFC3 ISR 2014-11](#) gives scaling factors to apply this model to other IR filters and the G141 grism, and shows that the model provides significantly better estimates of the zodiacal light than the model used by the ETC.

Figure 7.12: Zodiacal background level for filter F160W as a function of the target's ecliptic latitude and angular distance from the sun.



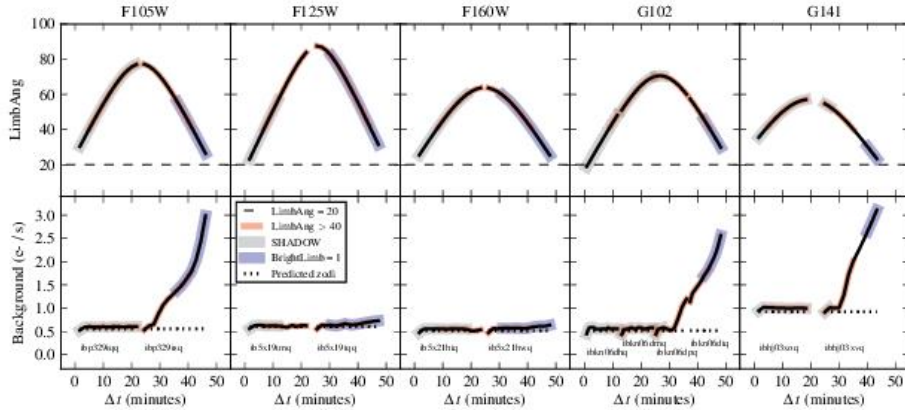
The highest levels of zodiacal light are avoided automatically by the *HST* observatory requirement that the Sun Angle be greater than 55°. For programs where a low background level is critical to the science goals, observers with a target at low ecliptic latitude may want to increase the solar avoidance angle from the default minimum of 55° to 60° or greater by excluding the range of dates when the target would be at the undesired angles, using Figure 7.12 as a guide. This can be implemented by applying BETWEEN statements to visits in the phase II proposal. The range of dates corresponding to the 55° exclusion rule can be displayed in the Visit Planner window in [APT](#) by clicking on the arrowhead that expands the schedulability plot for a visit into its components; Sun is the Sun Angle component. (Hold the cursor on a date range band to read the dates.) At low ecliptic latitudes, the Sun Angle of a target changes about 1° per day, so trimming 5 days from each end of the Sun schedulability date range increases the minimum Sun Angle to 60°. This approach provides much greater opportunities for scheduling than the use of the LOW-SKY option ([Section 9.7.1](#)).

For pointings very close to the bright Earth limb, the zodiacal background may be exceeded by earth-shine. The brightness of the earth-shine falls very rapidly with increasing angle from the Earth's limb (due to the effectiveness of the *HST* baffles), and for most observations only a few minutes at the beginning and end of the target visibility period are significantly affected. Selective data reduction, excluding some frames of the timing sequence in the affected exposures, can be a better option than accepting the shorter visibility period required by LOW-SKY. (See [WFC3 ISR 2014-03](#) and [Section 9.7.1](#)). Targets observed in the continuous viewing zone (CVZ) will always be rather close to the Earth's limb, and so can sometimes see an elevated background for a larger part of the orbit, even at shorter wavelengths where zodiacal

emission ordinarily dominates. Observers have the possibility of specifying a non-standard Bright Earth Avoidance (BEA) angle, which increases the angle from the Earth's limb from 20° to 25°, but this comes at the cost of observing time and would not significantly improve most programs. Note that this is an available mode and must be specially requested through a Contact Scientist.

Investigation of unexpectedly high background levels in some WFC3/IR imaging and spectroscopic exposures led to the identification of a He I airglow line at 10,830 Angstroms as the source ([WFC3 ISR 2014-03](#)). This line is included in the passbands of the F105W and F110W filters and both IR grisms. It is negligible in the Earth's shadow, generally strongest at low Earth limb angles outside the shadow, but sometimes strong even 40° above the Earth limb. In the worst cases, the airglow line strongly dominates the background emission. Examples of strongly affected exposures (with F105W, G102, G141) and unaffected exposures (with F125W, F160W) are illustrated in Figure 7.13.

Figure 7.13: Earth limb angle and background count rate for some of the spectral elements affected by He I airglow (F105W, G102, G141) and unaffected (F125W, F160W).



Top panels: Variation of Earth limb angle through an orbit. The curves are colored following the labels in the legend.

Bottom panels: Variation of the background count rate throughout an orbit for specific filters and grisms.

The predicted background level from the Synphot/ETC zodiacal model is shown in the dotted line.

Where possible, observers should consider selecting alternative filters to F105W and F110W to avoid elevated background due to the He I airglow line. If other filters are used in the proposal, the observer should consider placing exposures unaffected by the airglow line at the beginning and end of an orbit. The exposures in that orbit should be placed in a non-interruptible exposure sequence, as described in the [APT Training Materials](#). Use of the APT special requirement SHADOW to exclude the airglow line is not generally recommended because of the severe restrictions that it places on observing opportunities and orbit length (see [Section 9.7.2](#)). The APT special requirement LOW-SKY may be helpful, but it also limits scheduling opportunities and orbit length ([Section 9.7.1](#)) and will not always exclude the airglow line, which can be bright at the permitted limb angles ($>40^\circ$).

Strategies for processing exposures with frames affected by strongly variable airglow are described in [WFC3 ISR 2014-03](#) and [WFC3 ISR 2016-16](#). If an `flt` image has an unexpectedly high background or excessive cosmic ray flagging, the observer should check the `ima` files for evidence of a variable background. The standard up-the-ramp fitting of the non-destructive reads in a WFC3/IR exposure does not work properly on images with a variable background since the variations are treated as cosmic rays. An improved `flt` image (at least for unsaturated sources) can be obtained by rerunning `calwf3` with `CRCORR=OMIT` to turn off the ramp fitting and cosmic ray rejection. Cosmic rays can then be removed by using AstroDrizzle to combine sets of exposures. Alternatively, after running `calwf3` without cosmic ray rejection, one can “flatten” the nonlinear ramps by subtracting the variable background of each read averaged over many pixels and adding back a constant for the overall average background count rate, then feed the flattened `ima` files back to `calwf3` for the final step of identifying the cosmic rays. Scripts and examples are provided in [WFC3 ISR 2016-16](#).

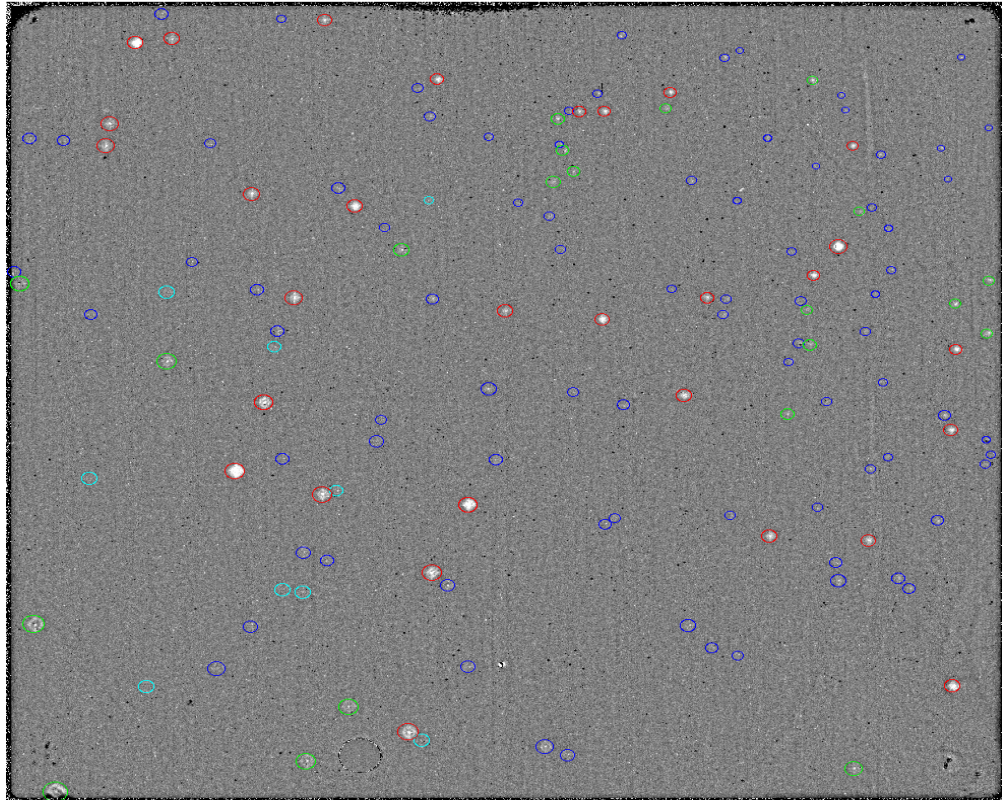
There is noticeable diversity in the background of G102 and G141 exposures due to the varying contributions of zodiacal light and the He I airglow line. Because these contributions are spectrally distinct, the background can best be modeled using a combination of these components ([WFC3 ISR 2015-17](#)). See [Section 8.5](#) for a discussion of this technique in the processing of WFC3/IR grism spectra.

7.9.6 Blobs

Image blemishes peculiar to the WFC3-IR detector have been described in [Section 5.7.7](#). Other spots of reduced sensitivity in IR images, dubbed “blobs”, are caused by reduced reflectivity of the Channel Select Mechanism mirror. They typically have a measured half-light radius of 10-15 pixels and absorb up to 15% of the incoming light at their centers.

Blobs were first noticed in IR images shortly after WFC3 was installed on *HST*. Their characteristics and the history of their occurrence are described in detail in [WFC3 ISR 2010-06](#), [WFC3 ISR 2012-15](#), [WFC3 ISR 2014-21](#), and [WFC3 ISR 2018-06](#). Pixels affected by blobs were initially identified in a single bad pixel table (BPIXTAB) that was designed to be applied to data taken after June 13, 2010 ([WFC3 ISR 2012-10](#)). This table has been superseded by a series of date-dependent bad pixel tables that track the appearance of “strong” and “medium” blobs ([WFC3 ISR 2014-21](#)). [Figure 7.14](#) shows the location of blobs on the detector as of January 2018.

Figure 7.14: Blobs on the WFC3/IR detector, identified by circles color-coded for strength. Red and green circles identify blobs that are flagged in the BPIXTAB.



A “blob flat field” can be used to improve stellar photometry in crowded fields. Blob flats made as described in [WFC3 ISR 2014-21](#) are available at the [WFC3 IR flats webpage](#). Corrections as large as 0.1 mag have been found for blob-impacted stars in Omega Centauri, and the accuracy of the corrected photometry is comparable to the photometric accuracy for stars in blob-free regions ([WFC3 ISR 2015-06](#)). Most observations will not be significantly affected by blobs, since blobs occupy only 2.25% of the detector area and their effects can be mitigated by dithering and drizzling. Appropriate dither strategies to mitigate the effects of blobs and other artifacts in IR images are described in [WFC3 ISR 2010-09](#). See [Section C.2](#) for the specifications of the WFC3-IR-DITHER-BLOB pattern implemented in APT.

7.9.7 Optical Anomalies

Anomalous features are found in some IR detector images. For example, the optical system may cause stray light from sources outside the detector FOV to be scattered into images. Scattered earthlight can greatly increase the background on part of the detector when *HST* is pointing near the bright earth limb. (See the [WFC3 Data Handbook](#).) Optical anomalies and image artifacts found by daily monitoring of incoming WFC3 data are illustrated in [WFC3 ISR 2017-22](#).



Examples of optical anomalies may be found on the WFC3 website.
See: <http://www.stsci.edu/hst/instrumentation/wfc3/performance/anomalies>

7.10 IR Observing Strategies

- [7.10.1 Dithering Strategies](#)
- [7.10.2 Parallel Observations](#)
- [7.10.3 Exposure Strategies](#)
- [7.10.4 Spatial Scans](#)
- [7.10.5 PSF Subtraction](#)
- [7.10.6 The Drift and Shift \(DASH\) Observing Strategy](#)

7.10.1 Dithering Strategies

For imaging programs, STScI generally recommends that observers employ dithering patterns. Dithering refers to the procedure of moving the telescope by small angle offsets between individual exposures on a target. The resulting images are subsequently combined in the pipeline or by the observer using software such as AstroDrizzle. (See the *DrizzlePac* documentation.)

Dithering is used to improve image quality and resolution. By combining multiple images of a target at slightly different positions on the detector, one can compensate for detector artifacts (blemishes, dead pixels, hot pixels, transient bad pixels, and plate-scale irregularities) that may not be completely corrected by application of the calibration reference files. Combining images, whether dithered or not, can also remove any residual cosmic ray flux that has not been well removed by the up-the-ramp fitting procedure used to produce flt images (see [Section 7.7.2](#) and [Appendix E](#)). Effective resolution can be improved by combining images made with sub-pixel offsets designed to better sample the PSF. This is especially important for WFC3/IR, because the PSF is undersampled by about a factor of 2 (see [Table 7.5](#)).

Larger offsets are used to mosaic a region of sky larger than the detector field of view. (Large offsets can also be used for “chopping” to sample the thermal background. This has been recommended for NICMOS exposures at wavelengths longer than 1.7 microns, where the telescope thermal background becomes increasingly dominant, but the thermal background is not a problem for WFC3/IR). In WFC3, all offsets must be accomplished by moving the telescope (whereas in NICMOS it was also possible to move the Field Offset Mirror).

Dithers must be contained within a diameter ~130 arcsec or less (depending on the availability of guide stars in the region) to use the same guide stars for all exposures. The rms pointing repeatability is significantly less accurate if different guide stars are used for some exposures. (See Appendix B of the *DrizzlePac Handbook*). Mosaic steps and small dither steps are often combined to increase the sky coverage while also increasing resolution and removing artifacts. (See [Section 6.12.1](#) for a discussion of the effect of geometric distortion on PSF sampling for mosaic steps).

The set of Pattern Parameters in the observing proposal provides a convenient means for specifying the desired pattern of offsets. The pre-defined mosaic and dither patterns that have been implemented in APT to meet many of the needs outlined above are described in detail in the [Phase II Proposal Instructions](#). The WFC3 patterns in effect in APT at the time of publication of this Handbook are summarized in [Appendix C](#). Observers can define their own patters to tailor them to the amount of allocated observing time and the desired science goals of the program. Alternatively, they can use POS TARGs to implement dither steps ([Section 7.4.3](#)). Observers should note that thermally driven drift of the image on the

detector, occasionally larger than 0.15 pixels in two orbits, will limit the accuracy of execution of dither patterns. ([WFC3 ISR 2009-32](#)) Additional information on dither strategies can be found in [WFC3 ISR 2010-09](#), which provides a decision tree for selecting patterns and combining them with subpatterns. [WFC3 ISR 2016-14](#) provides compact patterns with up to 9 steps with the intent of preserving subpixel sampling as much as possible over the face of the detector, given the scale changes introduced by geometric distortion.

7.10.2 Parallel Observations

Parallel observations, i.e., the simultaneous use of WFC3 with one or more other *HST* instruments, are the same for the IR channel as for the UVIS channel, previously described in [Section 6.12.2](#).

7.10.3 Exposure Strategies

Given the variety of requirements of the scientific programs that are being executed with WFC3/IR, it is impossible to establish a single optimum observing strategy. In this section we therefore provide a few examples after guiding the reader through the main constraints that should be taken into account when designing an observation:

- Integrate long enough to be limited by background emission and not read noise. Dark current is rarely the limiting factor.
- Dither enough so that resolution can be restored to the diffraction limit and bad pixels and cosmic-ray impacts can be removed, while maintaining a homogeneous S/N ratio across the field.
- Split the MULTIACCUM ramps into as many reads as possible for readout noise suppression.

In this regard, it is useful to consider [Table 7.11](#), which summarizes the total background seen by a pixel, including sky, telescope, and nominal dark current, and the time needed to reach 400 e⁻/pixel of accumulated signal, corresponding to 20 e⁻/pixel of Poisson-distributed background noise. This last value, higher than the expected readout noise of ~12 electrons after 16 reads, is used here to set the threshold for background-limited performance. The passage from readout-limited performance to background-limited performance can be regarded as the optimal exposure time for that given filter, in the sense that it allows for the largest number of dithered images without significant loss of S/N ratio (for a given total exposure time, i.e., neglecting overheads). For faint sources, the optimal integration time strongly depends on the background (zodiacal, Earth-shine thermal, and dark current) in each filter, ranging from just 220 s for the F110W filter to 2700 s for some of the narrow-band filters.

These constraints put contradictory requirements on the ideal observing strategy. It is clear that, given a certain amount of total observing time, the requirement of long integrations for background limited performance is incompatible with a large number of dithering positions. Also, to split ramps for readout noise suppression decreases the observing efficiency, with a negative impact on the signal to noise ratio. Because the background seen by each pixel depends on the filter ([Section 7.9.5](#)), the optimal compromise must be determined on a case-by-case basis.

The optimal integration time needed to reach background-limited performance (see [Table 7.11](#)) can be compared with the integration times of the sampling sequences from [Table 7.8](#). [Table 7.12](#) synthesizes the results, showing for each filter which ramp (SPARS, STEP) most closely matches the optimal integration times for NSAMP=15.

Table 7.11: Background (e-/pix/s) levels at the WFC3/IR detector.

Filter	Background (e-/pix/s)	Optimal Integration Time (s)
F110W	~0.001	~220
F125W	~0.001	~220
F140W	~0.001	~220
F160W	~0.001	~220
F222W	~0.001	~220
F240M	~0.001	~220
F280M	~0.001	~220
F330M	~0.001	~220
F360M	~0.001	~220
F390M	~0.001	~220
F430M	~0.001	~220
F450M	~0.001	~220
F480M	~0.001	~220
F500M	~0.001	~220
F545M	~0.001	~220
F550M	~0.001	~220
F560M	~0.001	~220
F580M	~0.001	~220
F600M	~0.001	~220
F625M	~0.001	~220
F650M	~0.001	~220
F670N	~0.001	~220
F680N	~0.001	~220
F700N	~0.001	~220
F720N	~0.001	~220
F750N	~0.001	~220
F770N	~0.001	~220
F790N	~0.001	~220
F810N	~0.001	~220
F830N	~0.001	~220
F850LP	~0.001	~220
F900LP	~0.001	~220
F920LP	~0.001	~220
F940LP	~0.001	~220
F950LP	~0.001	~220
F960LP	~0.001	~220
F970LP	~0.001	~220
F980LP	~0.001	~220
F990LP	~0.001	~220
F1000LP	~0.001	~220
F1010LP	~0.001	~220
F1020LP	~0.001	~220
F1030LP	~0.001	~220
F1040LP	~0.001	~220
F1050LP	~0.001	~220
F1060LP	~0.001	~220
F1070LP	~0.001	~220
F1080LP	~0.001	~220
F1090LP	~0.001	~220
F1100LP	~0.001	~220
F1110LP	~0.001	~220
F1120LP	~0.001	~220
F1130LP	~0.001	~220
F1140LP	~0.001	~220
F1150LP	~0.001	~220
F1160LP	~0.001	~220
F1170LP	~0.001	~220
F1180LP	~0.001	~220
F1190LP	~0.001	~220
F1200LP	~0.001	~220
F1210LP	~0.001	~220
F1220LP	~0.001	~220
F1230LP	~0.001	~220
F1240LP	~0.001	~220
F1250LP	~0.001	~220
F1260LP	~0.001	~220
F1270LP	~0.001	~220
F1280LP	~0.001	~220
F1290LP	~0.001	~220
F1300LP	~0.001	~220
F1310LP	~0.001	~220
F1320LP	~0.001	~220
F1330LP	~0.001	~220
F1340LP	~0.001	~220
F1350LP	~0.001	~220
F1360LP	~0.001	~220
F1370LP	~0.001	~220
F1380LP	~0.001	~220
F1390LP	~0.001	~220
F1400LP	~0.001	~220
F1410LP	~0.001	~220
F1420LP	~0.001	~220
F1430LP	~0.001	~220
F1440LP	~0.001	~220
F1450LP	~0.001	~220
F1460LP	~0.001	~220
F1470LP	~0.001	~220
F1480LP	~0.001	~220
F1490LP	~0.001	~220
F1500LP	~0.001	~220
F1510LP	~0.001	~220
F1520LP	~0.001	~220
F1530LP	~0.001	~220
F1540LP	~0.001	~220
F1550LP	~0.001	~220
F1560LP	~0.001	~220
F1570LP	~0.001	~220
F1580LP	~0.001	~220
F1590LP	~0.001	~220
F1600LP	~0.001	~220
F1610LP	~0.001	~220
F1620LP	~0.001	~220
F1630LP	~0.001	~220
F1640LP	~0.001	~220
F1650LP	~0.001	~220
F1660LP	~0.001	~220
F1670LP	~0.001	~220
F1680LP	~0.001	~220
F1690LP	~0.001	~220
F1700LP	~0.001	~220
F1710LP	~0.001	~220
F1720LP	~0.001	~220
F1730LP	~0.001	~220
F1740LP	~0.001	~220
F1750LP	~0.001	~220
F1760LP	~0.001	~220
F1770LP	~0.001	~220
F1780LP	~0.001	~220
F1790LP	~0.001	~220
F1800LP	~0.001	~220
F1810LP	~0.001	~220
F1820LP	~0.001	~220
F1830LP	~0.001	~220
F1840LP	~0.001	~220
F1850LP	~0.001	~220
F1860LP	~0.001	~220
F1870LP	~0.001	~220
F1880LP	~0.001	~220
F1890LP	~0.001	~220
F1900LP	~0.001	~220
F1910LP	~0.001	~220
F1920LP	~0.001	~220
F1930LP	~0.001	~220
F1940LP	~0.001	~220
F1950LP	~0.001	~220
F1960LP	~0.001	~220
F1970LP	~0.001	~220
F1980LP	~0.001	~220
F1990LP	~0.001	~220
F2000LP	~0.001	~220
F2010LP	~0.001	~220
F2020LP	~0.001	~220
F2030LP	~0.001	~220
F2040LP	~0.001	~220
F2050LP	~0.001	~220
F2060LP	~0.001	~220
F2070LP	~0.001	~220
F2080LP	~0.001	~220
F2090LP	~0.001	~220
F2100LP	~0.001	~220
F2110LP	~0.001	~220
F2120LP	~0.001	~220
F2130LP	~0.001	~220
F2140LP	~0.001	~220
F2150LP	~0.001	~220
F2160LP	~0.001	~220
F2170LP	~0.001	~220
F2180LP	~0.001	~220
F2190LP	~0.001	~220
F2200LP	~0.001	~220
F2210LP	~0.001	~220
F2220LP	~0.001	~220
F2230LP	~0.001	~220
F2240LP	~0.001	~220
F2250LP	~0.001	~220
F2260LP	~0.001	~220
F2270LP	~0.001	~220
F2280LP	~0.001	~220
F2290LP	~0.001	~220
F2300LP	~0.001	~220
F2310LP	~0.001	~220
F2320LP	~0.001	~220
F2330LP	~0.001	~220
F2340LP	~0.001	~220
F2350LP	~0.001	~220
F2360LP	~0.001	~220
F2370LP	~0.001	~220
F2380LP	~0.001	~220
F2390LP	~0.001	~220
F2400LP	~0.001	~220
F2410LP	~0.001	~220
F2420LP	~0.001	~220
F2430LP	~0.001	~220
F2440LP	~0.001	~220
F2450LP	~0.001	~220
F2460LP	~0.001	~220
F2470LP	~0.001	~220
F2480LP	~0.001	~220
F2490LP	~0.001	~220
F2500LP	~0.001	~220
F2510LP	~0.001	~220
F2520LP	~0.001	~220
F2530LP	~0.001	~220
F2540LP	~0.001	~220
F2550LP	~0.001	~220
F2560LP	~0.001	~220
F2570LP	~0.001	~220
F2580LP	~0.001	~220
F2590LP	~0.001	~220
F2600LP	~0.001	~220
F2610LP	~0.001	~220
F2620LP	~0.001	~220
F2630LP	~0.001	~220
F2640LP	~0.001	~220
F2650LP	~0.001	~220
F2660LP	~0.001	~220
F2670LP	~0.001	~220
F2680LP	~0.001	~220
F2690LP	~0.001	~220
F2700LP	~0.001	~220
F2710LP	~0.001	~220
F2720LP	~0.001	~220
F2730LP	~0.001	~220
F2740LP	~0.001	~220
F2750LP	~0.001	~220
F2760LP	~0.001	~220
F2770LP	~0.001	~220
F2780LP	~0.001	~220
F2790LP	~0.001	~220
F2800LP	~0.001	~220
F2810LP	~0.001	~220
F2820LP	~0.001	~220
F2830LP	~0.001	~220
F2840LP	~0.001	~220
F2850LP	~0.001	~220
F2860LP	~0.001	~220
F2870LP	~0.001	~220
F2880LP	~0.001	~220
F2890LP	~0.001	~220
F2900LP	~0.001	~220
F2910LP	~0.001	~220
F2920LP	~0.001	~220
F2930LP	~0.001	~220
F2940LP	~0.001	~220
F2950LP	~0.001	~220
F2960LP	~0.001	~220
F2970LP	~0.001	~220
F2980LP	~0.001	~220
F2990LP	~0.001	~220
F3000LP	~0.001	~220
F3010LP	~0.001	~220
F3020LP	~0.001	~220
F3030LP	~0.001	~220
F3040LP	~0.001	~220
F3050LP	~0.001	~220
F3060LP	~0.001	~220
F3070LP	~0.001	~220
F3080LP	~0.001	~220
F3090LP	~0.001	~220
F3100LP	~0.001	~220
F3110LP	~0.001	~220
F3120LP	~0.001	~220
F3130LP	~0.001	~220
F3140LP	~0.001	~220
F3150LP	~0.001	~220
F3160LP	~0.001	~220
F3170LP	~0.001	~220
F3180LP	~0.001	~220
F3190LP	~0.001	~220
F3200LP	~0.001	~220
F3210LP	~0.001	~220
F3220LP	~0.001	~220
F3230LP	~0.001	~220
F3240LP	~0.001	~220
F3250LP	~0.001	~220
F3260LP	~0.001	~220
F3270LP	~0.001	~220
F3280LP	~0.001	~220
F3290LP	~0.001	~220
F3300LP	~0.001	~220
F3310LP	~0.001	~220
F3320LP	~0.001	~220
F3330LP	~0.001	~220
F3340LP	~0.001	~220
F3350LP	~0.001	~220
F3360LP	~0.001	~220
F3370LP	~0.001	~220
F3380LP	~0.001	~220
F3390LP	~0.001	~220
F3400LP	~0.001	~220
F3410LP	~0.001	~220
F3420LP	~0.001	~220
F3430LP	~0.001	~220
F3440LP	~0.001	~220
F3450LP	~0.001	~220
F3460LP	~0.001	~220
F3470LP	~0.001	~220
F3480LP	~0.001	~220
F3490LP	~0.001	~220
F3500LP	~0.001	~220
F3510LP	~0.001	~220
F3520LP	~0.001	~220
F3530LP	~0.001	~220
F3540LP	~0	

Filter	Thermal	Zodiacal	Earth-shine	Dark Current	Total	Optimal Integration Time (sec)
F105W	0.051	0.774	0.238	0.048	1.111	360
F110W	0.052	1.313	0.391	0.048	1.804	222
F125W	0.052	0.786	0.226	0.048	1.112	360
F140W	0.070	0.968	0.267	0.048	1.353	296
F160W	0.134	0.601	0.159	0.048	0.942	425
F098M	0.051	0.444	0.140	0.048	0.683	586
F127M	0.051	0.183	0.052	0.048	0.334	1198
F139M	0.052	0.159	0.044	0.048	0.303	1320
F153M	0.060	0.153	0.041	0.048	0.302	1325
F126N	0.051	0.037	0.011	0.048	0.147	2721
F128N	0.051	0.040	0.011	0.048	0.150	2667
F130N	0.051	0.041	0.011	0.048	0.151	2649
F132N	0.051	0.039	0.011	0.048	0.149	2685
F164N	0.065	0.036	0.009	0.048	0.158	2532
F167N	0.071	0.035	0.009	0.048	0.163	2454

The columns show, from left to right: a) filter name; b) thermal background from the telescope and instrument; c) zodiacal background; d) earth-shine background; e) dark current; f) total background; g) integration time needed to reach background-limited performance, set at an equivalent readout noise of 20 electrons.

The selection of which sample sequence type (RAPID, SPARS, STEP; [Section 7.7.3](#)) must take into account the science goals and the restrictions placed on their use. Most observers have found that the SPARS ramps best meet the needs of their programs. Here are some factors to consider when selecting a sample sequence:

- The RAPID ramp is a uniform sequence of short exposures. With its relatively short maximum exposure time, is suitable for a target consisting of bright objects that would saturate after a few reads in the other sequences. It is not appropriate for background-limited performance.
- SPARS ramps, with their uniform sampling, provide the most robust rejection of cosmic-ray events, and can be trimmed by removing a few of the final reads to fine-tune the integration time with little degradation of the achieved readout noise. Thus they are considered the standard sampling mode.
- STEP ramps are preferable where large dynamic range is needed; e.g., for photometry of stellar clusters. These ramps begin with a sequence of four uniform (RAPID) reads and end with a sequence of much longer uniform

reads. The transition between the two uniform read rates is provided by a short sequence of logarithmically increasing read times. This design provides for correction of any non-linearities early in the exposure and allows for increased dynamic range for both bright and faint targets.

Finally, the selection of a given sample sequence type should also be made in conjunction with the number of samples (nsamp) that will be used to achieve the desired total exposure time for the observation. Long exposures should in general use a minimum of 5-6 samples in order to allow for reliable CR rejection and to allow for at least a few unsaturated samples of bright targets in the field. For very faint targets in read-noise limited exposures, a larger number of samples will result in greater reduction of the net read noise and a more reliable fit to sources with low signal. Short exposures of bright targets, on the other hand, can get by with fewer samples. This is especially true, for example, for the direct images that accompany grism observations. Because the purpose of the direct image is to simply measure the location of sources - as opposed to accurate photometry - they can reliably use an nsamp of only 2 or 3.

Table 7.12: Optimal exposure time needed to reach background-limited performance (see [Table 7.11](#)) for each WFC3/IR filter, along with the NSAMP=15 sequences that provide the closest match.

Filter	Optimal exposure time (sec)	SPARS	STEP
F105W	360	SPARS25	STEP50
F110W	222	SPARS25	STEP25
F125W	360	SPARS25	STEP50
F140W	296	SPARS25	STEP25
F160W	425	SPARS25	STEP50
F098M	586	SPARS50	STEP50
F127M	1198	SPARS100	STEP200
F139M	1320	SPARS100	STEP200
F153M	1325	SPARS100	STEP200
F126N	2721	SPARS200	STEP400
F128N	2667	SPARS200	STEP400
F130N	2649	SPARS200	STEP400
F132N	2685	SPARS200	STEP400
F164N	2532	SPARS200	STEP400
F167N	2454	SPARS200	STEP400

The benefits and disadvantages of each sequence type are discussed in the accompanying text.

7.10.4 Spatial Scans

Spatial scanning is available with either WFC3 detector, UVIS or IR. Conceptually producing star trails on the IR detector is the same as producing star trails on the UVIS detector, with a few differences discussed in [WFC3 ISR 2012-08](#). This document is recommended to anyone preparing a phase II proposal that uses spatial scans for any purpose. Spatial scans are discussed more extensively in [Section 6.12.5](#)(UVIS imaging) and [Section 8.6](#) (IR slitless spectroscopy). The former section describes star trails and the latter section describes spectra trailed perpendicular to the dispersion direction.

7.10.5 PSF Subtraction

IR imaging has been shown to be highly effective in detecting faint point sources near bright point sources ([WFC3 ISR 2011-07](#)). In this study, deep dithered exposures of a star were made at a variety of roll angles. Unsaturated exposures of a star, scaled down in flux to simulate faint companions of various magnitudes, were added to the deep exposures. The faintness of the companion that can be detected at a certain separation from the bright star depends on the degree of sophistication used to generate a reference image of the PSF to subtract from each set of dithered exposures. For a separation of 1.0 arcsec, five sigma detections could be made fairly easily for companions 8 or 9 magnitudes fainter than the bright star, and companions more than 12 magnitudes fainter than the bright star could be detected at separations of a few arcsec. Substantial improvements in detectability at separations less than about 2 arcsec could be made using the methodology described in the ISR to generate the reference PSF.

If observers want to use stellar images to subtract the PSF from a target comprised of a point source and an extended source to detect or measure the extended source, they should keep several points in mind:

- IR pixels undersample the PSF ([Section 7.6](#)), so the stellar and target exposures should be dithered to produce good sampling of the PSF.
- Position drift and reacquisition errors can broaden the PSF ([WFC3 ISR 2009-32](#), [WFC3 ISR 2012-14](#)).
- If a single guide star is used for a visit, roll angle drift causes a rotation of the target around that star, which in turn introduces a small translational drift of the target on the detector. In recent years, as gyroscopes have failed and been replaced, the typical roll angle drift rate has increased from 1.5 mas/sec to ~17 mas/sec, producing a translation of up to 60 mas (0.45 IR pixel) in 1000 sec.
- The characteristics of the PSF depend on the focus, which generally changes measurably during an orbit; its range in a particular orbit will not be known in advance ([WFC3 ISR 2012-14](#)).
- The characteristics of the PSF vary with location on the detector (e.g., see [ACS ISR 2003-06](#)).
- If exposures long enough to have good signal-to-noise to the desired radius will saturate the central pixels, one should consider making shorter exposures to avoid the effects of persistence. ([Section 7.9.4](#), [Appendix D](#).)

While [Tiny Tim](#) modeling is available for the WFC3 IR detector, it has not been optimized to reproduce observed PSFs. Progress has been made in understanding the short-comings in the model implemented in version 7.4 ([WFC3 ISR 2012-13](#), [WFC3 ISR 2014-10](#)). See [Section 7.6.4](#) for a discussion of on-going work to provide PSF models to observers.

7.10.6 The Drift and Shift (DASH) Observing Strategy

The term DASH (for “drift-and-shift”, [Momcheva et al., 2016](#)) has been adopted to describe the observing strategy of taking a series of WFC3/IR exposures of many targets within one orbit while the telescope is being guided under gyroscope control, thus avoiding the overhead cost of acquiring a new pair of guide stars for every slew between targets of greater than about 2 arcmin. A WFC3/IR sample sequence comprised of short exposure times is selected to avoid image smearing within each time step, and the differential samples in one exposure are later aligned and combined to compensate for the greater drift due to gyroscope control. The technique was designed to allow users to carry out shallow large-scale mosaic observations with the WFC3/IR camera, but has since been adapted to efficiently observe a collection of bright targets within a field ~1 deg across with WFC3/IR subarray apertures (which have shorter time steps for a given sample sequence) and WFC3/UVIS subarray apertures. More detailed discussions of *HST* guiding and considerations for program design are given below. See [Section 6.12.5](#) for further discussion of the WFC3/UVIS observations.

Whenever a pointing offset larger than about 2 arcmin is executed by the spacecraft within a visit, the currently used guide stars will move outside the field of regard of the Fine Guiding Sensors (FGS). Therefore, in normal operating mode, a new guide star acquisition becomes necessary in order to guide the telescope using the FGS. A complete guide star acquisition requires about 6 minutes (see [Table 10.1](#)), thus increasing the observation overheads and limiting the total number of >2 arcmin offsets that can be performed within a single *HST* orbit.

While the current nominal mode of operation of *HST* uses the FGS for guiding the telescope during an exposure, *HST* can also be operated by guiding using the spacecraft gyroscopes (gyros). Turning off the FGS guiding merely stops the stream of corrections and redirects the pointing control system to use information from the gyros alone. The effect of this switch is that the guiding is less precise, and the telescope begins to drift by typically 0.001 to 0.002 arcseconds per second. This translates into ~2.25 WFC3/UVIS or ~0.7 WFC3/IR pixels per minute. Thus, the longer an exposure in gyro mode, the worse the degradation of the image quality along the drift axis; exposures longer than a minute are not recommended.

The WFC3/IR channel detector naturally achieves “short” equivalent exposures, even when the total exposure times are longer than a minute. This is due to the fact that the WFC3/IR detector is read out in MultiAccum mode, i.e. by sampling the accumulated charge at regular time intervals. If these intervals are shorter than about a minute, then the native image quality of *HST* can be almost fully recovered even when guiding in gyro mode, by using the difference images between consecutive reads. The difference images can then be registered with respect to each other, shifted and stacked. This technique was first illustrated by [Momcheva et al., 2016](#); see also Figure 7.15.

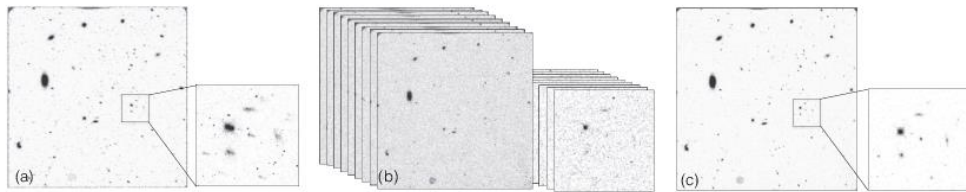
As an example, the majority of exposures in GO program 14114 (P.I. van Dokkum), described in [Momcheva et al., 2016](#), were taken with the full array using the SPARS25 SAMP-SEQ, with NSAMP=11, thus having a total exposure time of ~250 seconds and providing effectively 10 images of 25 seconds each. The drift in each 25 second interval was thus, on average, less than half of a WFC3/IR pixel. Using the DASH mode, a total of 8 such exposures could be packed within a single orbit, with offsets between exposures a bit less than the dimensions of the WFC3/IR detector in X and Y, 2.3 and 2.1 arcmin, respectively. Different combinations of SAMP-SEQ, NSAMP, and number of offsets can be used.

When planning DASH observations, observers should carefully consider the offset pattern that minimizes the length of moves. Offsets up to 1.0 degree are possible with a small angle maneuver (SAM); however, the repositioning overheads increase with the offset size. Overheads for small and large SAMs are shown in [Table 10.1](#) and in [WFC3 STAN Issue 23](#), respectively. Details on planning DASH observations are also presented in the STAN article.

DASH visits should be limited to one orbit. It has been observed that the drift rate becomes higher than one would assume by extrapolating the quoted 0.001 to 0.002 arcseconds per second, and becomes more unpredictable as well. The drift rate grows with time, so will often be quite large after an orbit occultation and ~90 minutes after the original guide star acquisition. To confine the exposures to one uninterrupted orbit, they should be grouped together into a non-interruptible sequence container in APT. The exposures placed in this container will be observed without gaps due to Earth occultation or SAA passages. As a further precaution, if subarrays are used, the minimum size should be carefully chosen, and a series of increasingly large subarrays should be used over the course of the orbit as needed to allow for the accumulating drift. The first exposure should be taken using guide stars to start the observations with accurate positioning.

A new set of tools will be released in a DASH pipeline following the conclusion of testing in early 2020. These tools, along with a Jupyter notebook providing a walk through, will be available through GitHub to assist users with calibrating DASH observations. Information regarding the pipeline and where to access it will be available through an ISR (C. Martlin et al., in prep.) and a future [STAN article](#), also available in early 2020. For users interested in receiving [STAN publication](#) announcements, please subscribe via the instructions at the bottom of our last issue.

Figure 7.15: Illustration of the “drift and shift” (DASH) method of restoring unguided WFC3/IR images.



(a) Shows the standard data product (the *FLT* file) of an unguided, gyro-controlled exposure. The objects are smeared due to the lack of fine guidance sensor corrections.

(b) Shows an example of the individual samples that comprise the final exposure. The smearing is small in each individual sample.

(c) Shows the reconstructed image after shifting the samples to a common frame and adding them.

Chapter 8: Slitless Spectroscopy with WFC3

Chapter Contents

- 8.1 Grism Overview
- 8.2 Slitless Spectroscopy with the UVIS G280 Grism
- 8.3 Slitless Spectroscopy with the IR G102 and G141 Grisms
- 8.4 Sensitivities and Exposure-Time Estimation
- 8.5 Extraction and Calibration of Spectra
- 8.6 Slitless Spectroscopy with Spatial Scanning

8.1 Grism Overview

WFC3 provides a slitless spectroscopy mode in both of its channels. The UVIS channel has a single grism and the IR channel two grisms, enabling low-resolution slitless spectroscopy over the entire field of view of both detectors.

In the UVIS channel, the G280 grism provides spectroscopy over a useful wavelength range of 190–450 nm, at an average dispersion of about 1.3 nm per pixel in the first order. Reduced sensitivity and second-order contamination interfere with grism observations at wavelengths longer than 400 nm.

The two grisms for the IR channel cover the wavelength ranges 800–1150 nm (G102), and 1075 nm to 1700 nm (G141). The dispersions are 2.45 and 4.65 nm per pixel, respectively.

The observing technique of spatial scanning can be used for WFC3 spectroscopic observations. See [Section 8.6](#).

Table 8.1 summarizes the capabilities of the three WFC3 grisms in first-order mode. The resolving power is listed for each grism at a wavelength near the center of its range of coverage. The dispersion differs slightly between the two chips of the UVIS channel, and the mean value is listed. The tilt of the dispersion direction relative to the detector x-axis is also listed.

 For the latest information on WFC3 spectroscopy, see the WFC3 Spectroscopy Resource page: <http://www.stsci.edu/hst/instrumentation/wfc3/documentation/grism-resources>

Table 8.1: WFC3 UVIS and IR Grisms.

Grism	Channel	Wavelength range (nm)	Resolving power ¹	Dispersion (nm/pixel)	Tilt (deg) ²
G280	UVIS	190–450	70 @ 300 nm	1.3	-3
G102	IR	800–1150	210 @ 1000 nm	2.45 ³	+0.7
G141	IR	1075–1700	130 @ 1400 nm	4.653	+0.5

¹ Resolving power is based on the FWHM of the Gaussian image core measured in direction perpendicular to the dispersion.

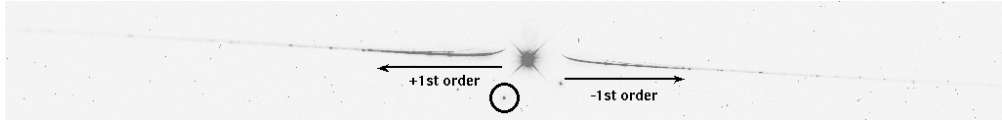
² Tilt of dispersion direction with respect to the positive x-axis of the image frame.

³ The dispersion varies over the field by $\pm 4\%$; the tabulated value refers to the field center.

8.2 Slitless Spectroscopy with the UVIS G280 Grism

The G280 grism is a WF/PC1 spare. [Figure 8.1](#) shows a spectrum of the wavelength calibration star WR14 observed as part of the Cycle 17 calibration program 11935. The circled spot shows the location of a direct image of the source obtained with a separate (undispersed) F300X filter exposure, but superposed on the grism image for illustrative purposes only. The prominent star-like feature near the center of the picture is the zeroth-order grism image, and the positive and negative higher orders extend towards the left and right of the zeroth order, respectively. The +1st order is defined to be the order with the higher throughput (due to the grating blaze), even though it falls at lower x-pixels than the position of the zeroth order. The +1st order extends to the left of the zeroth order a distance of about 1/4 of the image size. Further left there is heavy overlap with higher orders. Some prominent emission lines can be seen along the spectral trace.

Figure 8.1: Appearance of the G280 spectral orders on the detector.



The circled source is the position of the direct image formed by summing an F300X image with the grism image. The stronger 1st order is to the left and the 0th order is in the center. Above the 1st orders, much weaker 2nd and 3rd orders are barely visible. The image shows the full extent of the detector in the x-axis and about 500 pixels in the y-axis.

There are several features of this grism that differ, for example, from the G800L grism on ACS. There is an offset of about 175 pixels in the y-direction between the direct image and the spectra, the zeroth-order is relatively bright due to a lower grating efficiency and clear substrate, and there is curvature of the spectra at the blue ends of the first orders (nearest the zeroth order). The amplitude of the curvature is about 30 pixels in the detector y-direction. [Figure 8.2](#) shows a close up view of the first few positive orders of the WR14 spectrum, which illustrates the curvature at the short-wavelength end of each order.

Figure 8.2: Close up view of the first few positive orders of the WR14 spectrum

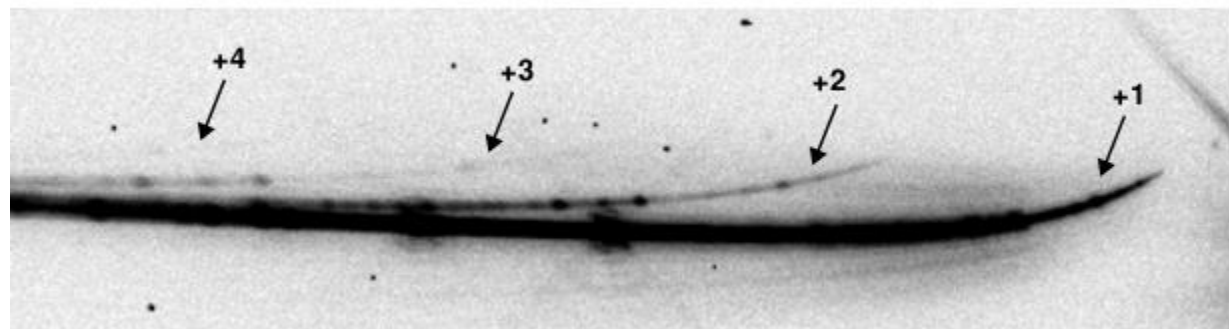
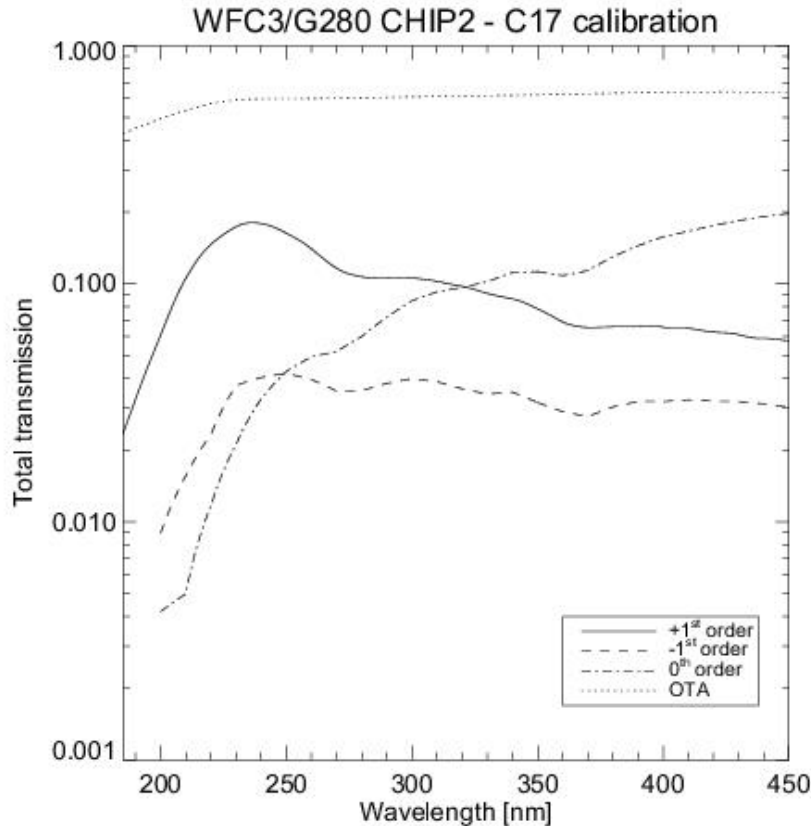


Figure 8.3: The absolute throughput of the G280 grism as a function of wavelength for the lowest orders.



The spectral trace and dispersion have been measured both during ground calibration and on-orbit using the wavelength calibration star WR14. The mean dispersion in the 1st order at 2200 Å is 12.2 Å/pixel, varying from 10.8 Å/pixel at 1850 Å to 14.4 Å/pixel at 4000 Å. The dispersion per pixel in the higher orders is higher by the approximate ratio of the orders; for example, in +3rd order it is 48 Å/pixel.

New field-dependent calibrations of the trace and dispersion for the -1 and +1 orders over the entire UVIS field of view are presented in [WFC3 ISR 2017-20](#). The best fit to the shape of the G280 curved spectra on multiple locations on the detector was achieved using a 6th order trace polynomial with a linear 2D field dependence. The model reproduces the location of the curved traces of the +1 and -1 order spectra to within a fraction of a pixel. It fits a longer portion of the red part of each spectrum than the earlier ground calibration, and overall is a significant improvement over that calibration. The accuracy of the wavelength calibration is estimated to be ± 7 Å, or about half of a UVIS resolution element. The new calibration files are available at:

<http://www.stsci.edu/hst/instrumentation/wfc3/calibration>

The flux calibration of G280 spectra is best at the center of chip 2, and next best at the center of chip 1. (There is no field dependent flux calibration.) Observers having a single target of interest are encouraged to place the target near the center of chip 2, due to the higher QE of chip 2 at very short wavelengths.

[Figure 8.3](#) shows the total 1st-order transmission for the WFC3 G280 mode (including the instrument and telescope) for observations on chip 2, as determined from observations of the *HST* standard star GD-71 during Cycle 17. The +1st order is more sensitive than the zeroth order at wavelengths less than 320 nm, but longward of this wavelength the zeroth order dominates. On deep exposures, orders out to at least -8 and +8 have been detected. The current absolute flux calibration of the G280 is estimated to be accurate to better than 10%. Due to the relatively high throughput of the 2nd order, 1st order spectra longward of 400 nm are likely to be overlapped by 2nd order light longward of 200 nm, at least for sufficiently hot sources.

Grism exposures of a given target field should always be accompanied by a direct image. The direct image provides source sizes and identifications, from which the corresponding locations of spectra in the grism images are determined. Knowledge of the direct-to-grism exposure source offsets is necessary to set the wavelength zero-point for each extracted spectrum and the source size measurements enable the software extraction slit to be tuned to each object (see [Section 8.5](#)). The 0th-order trace in G280 images is slightly dispersed (making it difficult to centroid) and often saturated (making it impossible to centroid), therefore it cannot be used in place of a direct image.

The natural choice of a direct-imaging filter to provide the reference image for G280 exposures is the F300X, because its response matches most closely the +1st-order grism response. The broader F200LP filter may be preferable for fainter objects. The shape of the spectra in G280 exposures varies significantly across the field of view but has been calibrated. The sensitivity of the +1 order also varies, but its field variation cannot be handled by the aXe package and is only calibrated at the center of chip 2. Small dithers of G280 exposures and accompanying direct image exposures is recommended to remove the effects of bad pixels. In addition, it is recommended that CR_SPLIT be used in both the direct and dispersed exposures to allow for cosmic-ray identification and removal.

G280 exposures can only be obtained using the “UVIS” aperture selection, which places the target at the reference point of the UVIS field of view, about 10" above the inter-chip gap. Accompanying direct images should use the G280-REF aperture selection, which places the target at the same location as in the dispersed exposures. If your observations are of a single primary target, it is best to specify a POS TARG Y of -50", for both the dispersed and direct exposures, to place the target at the center of chip 2, where the spectral calibrations are best determined and the near-UV sensitivity is somewhat higher than on chip 1.

For sufficiently bright objects, the multiple spectral orders may extend across the full field of view of the camera. This leads to overlapping of fainter spectra in the vicinity of the bright-object spectrum. Therefore, a careful determination of the optimum telescope roll angle is required to obtain non-overlapped spectra of faint objects in the vicinity of much brighter objects. i.e., the observer needs to set the orientation of the detector on the sky by using the Visit Orientation Requirements parameter “ORIENT” in the phase II proposal; e.g. ORIENT = 135.17 degrees aligns the Y axis of the UVIS detector with North for the G280 and G280-REF apertures. See [Section 6.2. of the Phase II Proposal Instructions](#), which gives detailed information on the relationship between detector coordinates, spacecraft coordinates, and ORIENT.

CTE losses can be large for faint spectra on faint backgrounds. They should be taken into account when planning UVIS exposures. See Sections [5.4.11](#) and [6.9](#) for information on CTE and observing strategies.

8.3 Slitless Spectroscopy with the IR G102 and G141 Grisms

8.3.1 IR G102

8.3.2 IR G141

IR grism observations can be obtained using either full-frame or subarray apertures. Subarrays are useful for reducing exposure times for bright objects and for reducing data volume to avoid time lost to serial buffer dumps. First-order spectra for both the G102 and G141 grisms comfortably fit within 512×512 and 256×256 pixel subarrays.

Grism observations of a given target field should always be accompanied by a direct image, which is used to locate sources and determine source sizes. The locations of sources in the direct image are then used to guide the placement of extraction apertures in dispersed images, and to tune the size of the extraction apertures to the source size. The location of sources in direct images is also used to establish the wavelength zero-point for extracted spectra by using offsets from the direct image. Appropriate filters to use for direct images are discussed in the following sections for each IR grism. As with normal imaging observations, grism observations should be dithered to aid in the removal of bad pixels. Accompanying direct images can be obtained at each of the same grism dither positions, but this is not strictly necessary. It is usually sufficient to obtain a direct image at just 1 or 2 of the dither positions. Direct imaging is best taken at the beginning and/or end of a visit so that the grism observations are less likely to be impacted by temporal variations in the background from the bright Earth limb and scattered light.

While a direct image is required for identifying the full complex of overlapping orders in spectral images, wavelength assignments for sources with known coordinates can be derived using the offsets from the zero order grism images (see [WFC3 ISR 2015-10](#)). The inaccuracy caused by any non-linearity in the dispersion is estimated at ~ 0.1 pixel or $\sim 2.5 \text{ \AA}$ for G102 and $\sim 5 \text{ \AA}$ for G141. The rms precision of the assigned wavelengths for individual spectra is better than 0.2 pixel. For the same or very similar POSTARGs, the separation from direct image to zero order varies by up to 0.5 pixels in both x and y directions, corresponding to an uncertainty of about $\sim 12 \text{ \AA}$ (G102) and $\sim 23 \text{ \AA}$ (G141).

The GRISM apertures ([Table 7.1](#)) are designed to be used for both the grism exposure and the associated direct image. At a given telescope pointing, the first order spectrum and the location of the target in the direct image are roughly aligned in the x direction. The G102 spectrum starts at about 55 pixels to the right of the target image location and extends about 155 pixels; the G141 spectrum starts at about 35 pixels to the right of the target image location and extends about 135 pixels. For either grism, the same pointing can thus be used to place the target image and the first order spectrum on an array with dimensions greater than about 210 pixels. The apertures GRISM1024, GRISM512, and GRISM256 have been designed to take advantage of this, with the placement of the target optimized for the dimensions of the array, which is indicated by the number in the aperture name. For the smaller apertures, GRISM128 and GRISM64, different pointings are automatically used for the direct image and the grism exposure so that the target is within the aperture in the direct image and the target's spectrum is also inside the aperture in the grism image. See <http://www.stsci.edu/hst/instrumentation/wfc3/documentation/grism-resources> for details on selecting GRISM apertures and using combinations of these apertures.

Objects that are off the edges of the detector will still produce dispersed spectra since the detector field of view is smaller than the rest of the WFC3 optics. Any object that is within -183 pixels (-22 arcsec) of the left edge, or +85 pixels (+10 arcsec) of the right edge of the detector will result in positive or negative orders spectra, respectively. This is described in ([WFC3 ISR 2016-15](#)).

The performance of the IR grisms was analyzed during SMOV ([WFC3 ISR 2009-17](#), [WFC3 ISR 2009-18](#)). The flux calibration was revised based on calibration observations made in cycle 17 ([WFC3 ISR 2011-05](#)). Analysis of monitoring observations made from SMOV through cycle 20 has shown that the flux calibrations of the +1st order spectra have excellent temporal stability, varying by less than 1%, and that the calibration of the large-scale throughput variations over the detector are good to 4% ([WFC3 ISR 2012-06](#) and [WFC3 ISR 2014-01](#)). Point source aperture corrections measured in cycle 20 ([WFC3 ISR 2014-01](#)) are generally consistent with those derived in cycle 17 ([WFC3 ISR 2011-05](#)) to 1%. Sky images for the IR grisms have been constructed using publicly available data; the average sky brightness measured in the G102 and G141 images is 0.8 e-/s and 1.3 e-/s, respectively ([WFC3 ISR 2011-01](#)). Multiple components of the sky backgrounds have been modeled and include three components: Zodiacal light, He I glow, and scattered light. These new background components and software to background-subtract G102 and G141 datasets are available on the [WFC3 Grism Resources web page](#).

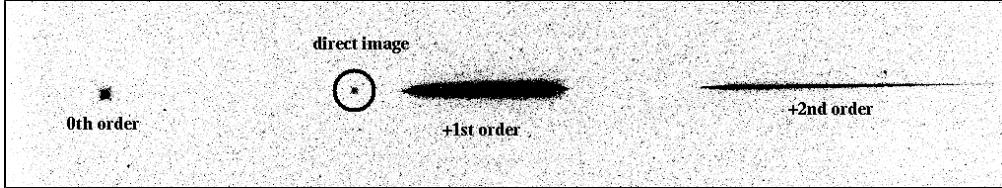
The wavelength calibration of the +1, -1, and +2 G102 and G141 orders were re-derived using all of the available multi-cycle calibration data ([WFC3 ISR 2016-15](#)). The accuracy of this new calibration is estimated to be better than 0.1 pixel for the trace description and better than 0.5 pixel (~10A and 20A for the G102 and G141 grisms, respectively) for the wavelength calibration. Previous calibration assumed that grism observations would be paired with F098M and F140W direct images for the G102 and G141 grisms, respectively. New calibration solutions that include the effect of the filter wedge offset ([WFC3 ISR 2010-12](#)) are now also available. See the calibration web pages for [G102](#) and [G141](#).

8.3.1 IR G102

The G102 grism provides first-order spectra over the wavelength range from the grism short-wavelength cutoff at about 800 nm up to 1150 nm. The dispersion is high enough that only the positive first and second-order spectra, as well as the zeroth-order image, are visible on the detector when the positive first-order spectrum is centered in the field of view.

[Figure 8.4](#) shows the disposition of the zeroth-order image and +1st-order spectrum (which has much higher sensitivity than the -1st order due to the grating blaze) for the G102 grism. The location of the direct image (superposed from an F098M undispersed exposure) is indicated in the figure.

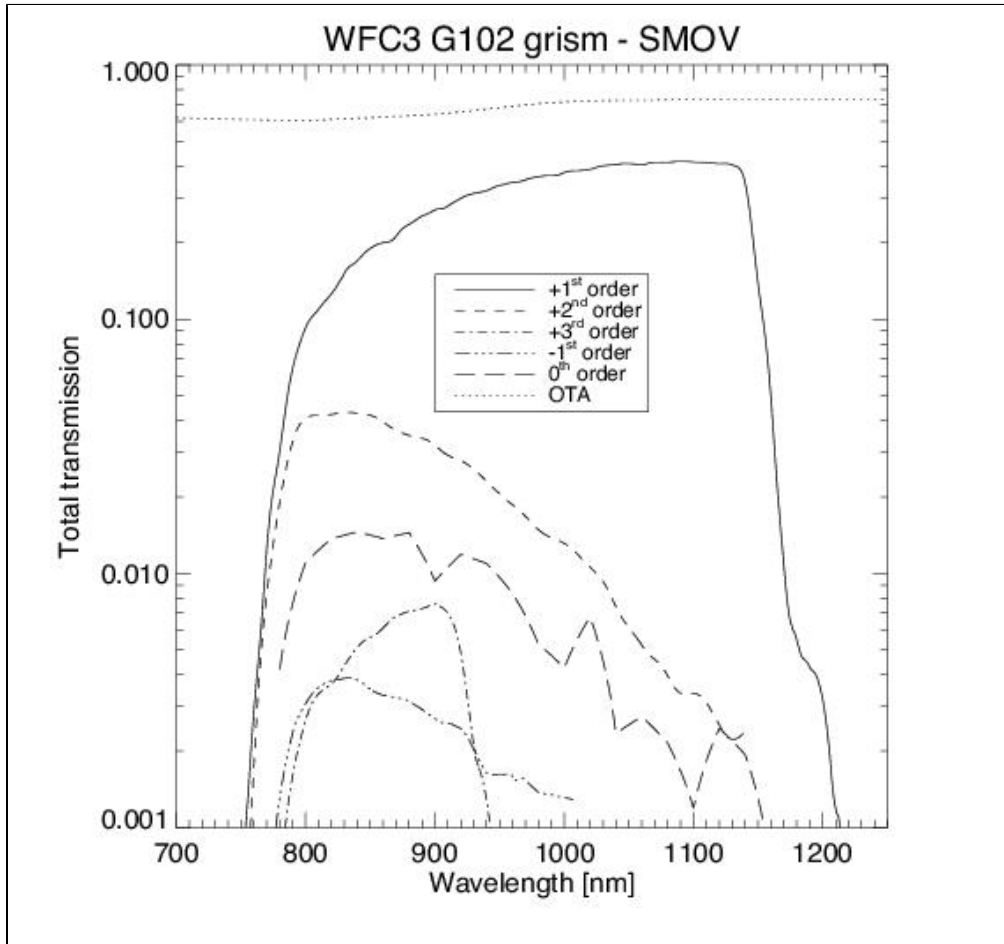
Figure 8.4: G102 grism observation of the flux standard star GD153 (program 11552) with a F098M direct image (circled) superimposed to illustrate the relative positions. Spectral orders 0, +1, and +2 can be seen on the image.



The image shows the full extent of the detector in the x-axis and about 200 pixels in the y-axis.

The trace of the first-order spectrum is well described by a first-order polynomial, however the offset and slope are a function of source position in the field. The tilt of the spectrum is 0.7° with respect to the detector x-axis. The total throughput (including *HST* optics) of the G102 grism has a maximum of 41% at 1100 nm in the positive first order and is above 10% between 805 and 1150 nm. The zeroth order and other negative and positive orders show much lower throughput (see [Figure 8.5](#)). The dispersion in the +1st order varies over the field from 2.36 to 2.51 nm/pixel; this variation was calibrated from both ground and on-orbit data to allow absolute wavelength calibration to better than one pixel. The absolute throughput of the G102 orders -1 to +3, including the instrument and the detector, is shown in [Figure 8.5](#). Suitable filters for the accompanying direct images for source selection and wavelength zero-point determination are F098M (preferred) or F105W (see [Section 7.9.5](#) for discussion of the IR background), but any of the narrower filters can also be used to prevent bright sources from saturating.

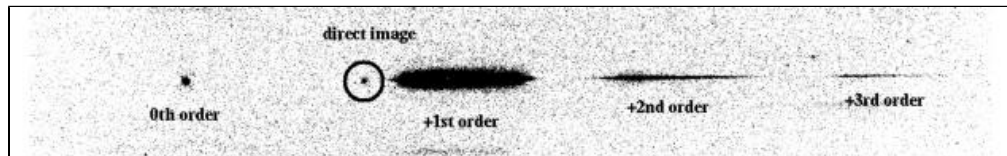
Figure 8.5: The absolute throughput of the G102 grism as a function of wavelength.



8.3.2 IR G141

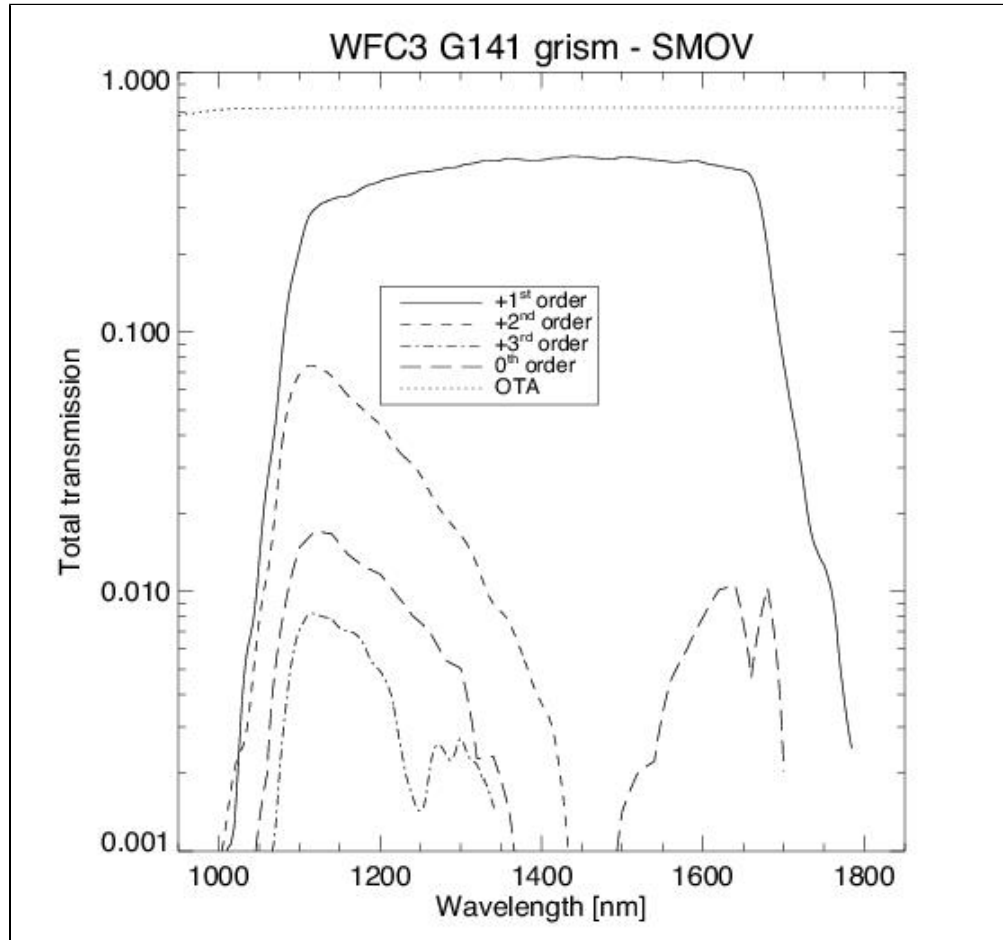
For the lower-dispersion G141 grism, the 0th-, 1st-, 2nd-, and 3rd-order spectra all lie within the field of view when the positive first-order is roughly centered. [Figure 8.6](#) shows the appearance of the spectra on the detector, with the superposed direct image, for the G141 grism. The useful spectral range is from 1075 nm to about 1700 nm, limited in the red by the grism bandpass. Over most of the spectral range, more than 80% of the throughput is in the +1st-order spectrum. The trace of the first-order spectrum is well described by a first-order polynomial. The average tilt of the spectrum is 0.5 degrees with respect to the detector x-axis. The dispersion in the +1st-order varies over the field from 4.47 to 4.78 nm/pixel; this variation has been measured from both ground and on-orbit data to allow absolute wavelength calibration to better than one pixel. The total throughput (including *HST* optics) of the G141 grism reaches a maximum of 48% at ~1450 nm in the positive first order and is above 10% between 1080 and 1690 nm (see [Figure 8.7](#)).

Figure 8.6: G141 grism observation of the flux standard star GD153 (program 11552) with a F140W direct image (circled) superimposed to illustrate the relative positions. Spectral orders 0, +1, +2, and +3 can be seen in the image.



The image shows the full extent of the detector in the x-axis and about 200 pixels in the y-axis.

Figure 8.7: The absolute throughput of the G141 grism as a function of wavelength.



Suitable filters for the accompanying direct images for source selection and wavelength zero-point determination are F140W (preferred) or F160W in the case of extremely red sources. Any of the narrower IR filters can also be used in order to avoid saturation of bright targets.

8.4 Sensitivities and Exposure-Time Estimation

Table 8.2 lists current estimates of the detection limits for slitless spectroscopy with the UVIS and IR modes. The numbers in the table are the V magnitudes of point sources for which a 1-hour exposure yields a spectrum with a S/N of 5 per resolution element, with extraction boxes of 1×5 and 1×3 pixels for the UVIS and IR, respectively. V magnitudes are given for three different assumed source spectral types.

Table 8.2: V -band detection limits for the WFC3 grism modes for 1-hour exposure and 5σ detection.

Mode	Spectral Type			Wavelength (nm)
	O3 V	A0 V (Vega)	G2 V	
UVIS2/G280	25.0	21.9	18.2	250
IR/G102	21.3	22.0	22.9	1050
IR/G141	20.5	21.3	22.8	1550

For more accurate estimations of exposure times, observers should use the WFC3 [Exposure Time Calculator \(ETC\)](#). The ETC supports all three spectroscopic modes.

For more detailed simulations of WFC3 slitless data, a simulator is available that can generate 2D images (dispersed as well as direct) of synthetic target fields. The simulator package, aXeSIM, is available via a Web interface (reduced functionality) and as a stand-alone IRAF package (full functionality). For further information, see: <http://www.stsci.edu/hst/instrumentation/wfc3/documentation/grism-resources>

8.5 Extraction and Calibration of Spectra

Because there is no slit in the WFC3 grism mode, the PSF of the target determines the spectral resolution. In the case of non-stellar sources, it is the extent of the target in the direction of dispersion that limits the spectral resolution. The height of the software extraction slit is based on the object extent in the cross-dispersion direction of the direct image.

The dispersion of the grisms is well characterized, but in order to set the wavelength zero-point, it is necessary to know the position of the target in the direct image. The zeroth-order is generally too weak and is also slightly extended in a dispersed image to allow the wavelength zero-point to be set reliably. Given the typical spacecraft jitter, wavelength zero-points to ± 0.5 pixels should be routinely achievable using a direct image taken just before or after the grism image.

A spectral extraction software package, called **aXe**, is available to extract, flat-field, wavelength- and flux-calibrate WFC3 grism spectra. Full details can be found at:

<http://www.stsci.edu/hst/instrumentation/wfc3/documentation/grism-resources>

An outline for reducing full array and subarray G280 grism observations is given in [WFC3 ISR 2011-18](#).

The spectral trace and dispersion solutions are a function of source position within the field of view. These 2-dimensional variations were determined during the ground calibration campaigns and from on-orbit data. The resulting reference and calibration files are used in the extraction software aXe and are also available from the WFC3 area of the aXe website. For bright sources, the multiple spectral orders of the G280, G102 and G141 grisms may extend across the full detector extent. Therefore, a careful selection of the optimum telescope roll angle is required to obtain non-overlapping spectra of faint sources in the vicinity of brighter objects. i.e., the observer needs to set the orientation of the detector on the sky by using the Visit Orientation Requirements parameter “ORIENT” in the phase II proposal; e.g. ORIENT ~ 135 degrees aligns the Y axis of the IR detector with North. See [Section 6.2.2 of the Phase II Proposal Instructions](#), which gives detailed information on the relationship between detector coordinates, spacecraft coordinates, and ORIENT, and works out this example for aperture GRISM1024 (ORIENT = 135.3). Using the information in that section, one finds ORIENT ranging from 135.12 to 135.32 for the IR GRISM apertures (used for the grism exposures and matching reference images) and ORIENT = 135.17 for the G280 and G280-REF apertures.

The quality of extracted spectra from single grism exposures can be degraded by bad pixels (e.g., dead, hot, strong cosmic ray hit). We recommend a dithering strategy for grism exposures. The aXe software automatically takes dither steps into account by using the information in the image headers to produce a combined spectrum with cosmic rays and bad pixels removed.

Extraction of WFC3/IR slitless spectra depends on an accurate determination of the diffuse background light that is observed in all grism exposures. The two-dimensional structure in the background of WFC3/IR grism exposures is caused primarily by overlapping grism spectral orders that are vignetted at different locations within the detector field of view and by the spectrum of the diffuse background. To remove this structure, the aXe analysis software (and related pipelines) fit and subtract “master sky” images, which have been generated for each grism from on-orbit science exposures. However, the single images used by aXe do not take into account the full complexity of the sky background of grism observations.

A more accurate background subtraction can be achieved by using separate images for each of these background components: zodiacal light, He I emission, and scattered light. These components are shown for G102 and G141 in Figure 8.8 and Figure 8.9, respectively. The He I component is due to a 1.083 μm emission line in the Earth’s upper atmosphere

and often appears in exposures obtained while the spacecraft is outside of the earth's shadow (see [Section 7.9.5](#)). The intensity of this airglow line varies on timescales of an orbit or even a single sample sequence. Scattered light produces a different structure, having bypassed the grism to reach the detector. [WFC3 ISR 2015-17](#) presented a file containing all three component images for G141 and two of the component images for G102 (zodiacal light and He I emission) and an algorithm for applying them to observed WFC3/IR grism data. Images of all three background components for both IR grisms and software to background-subtract grism datasets are now available on the [WFC3 Grism Resources web](#) page.

Figure 8.8: Background components for G102

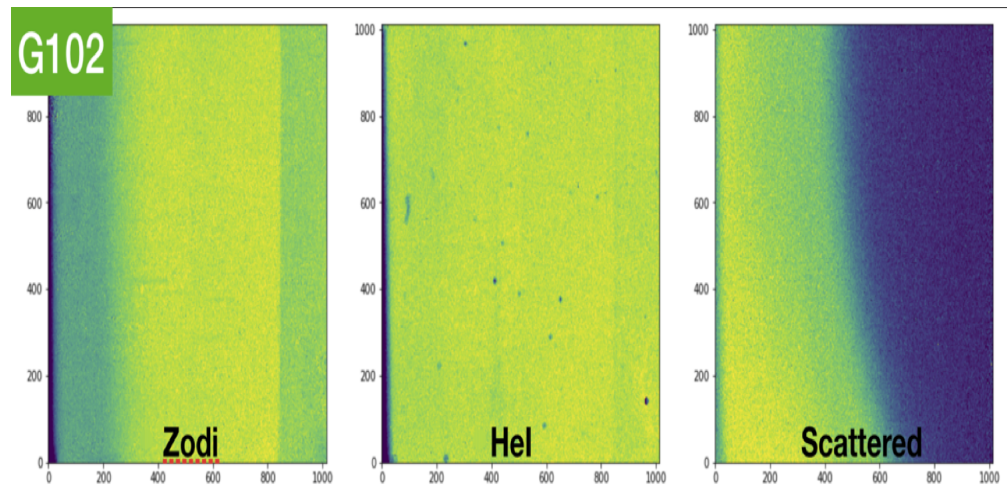
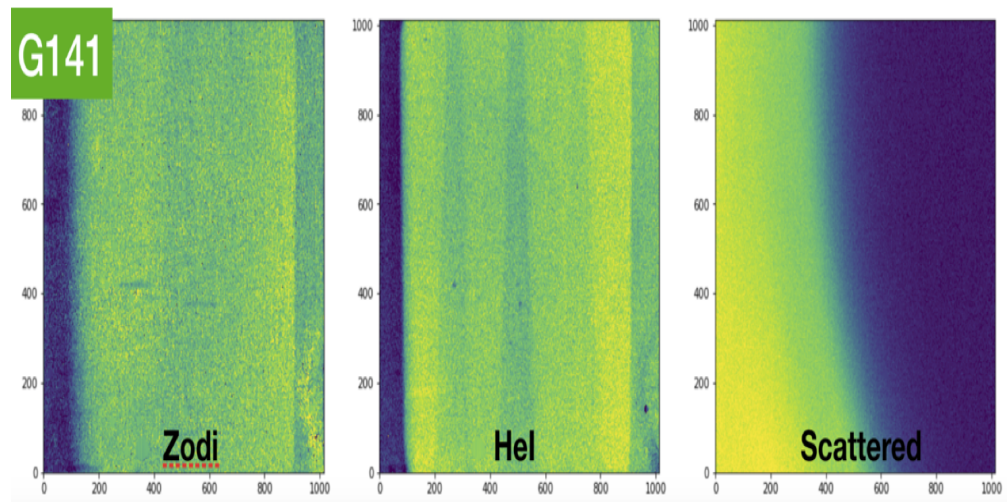


Figure 8.9: Background components for G141

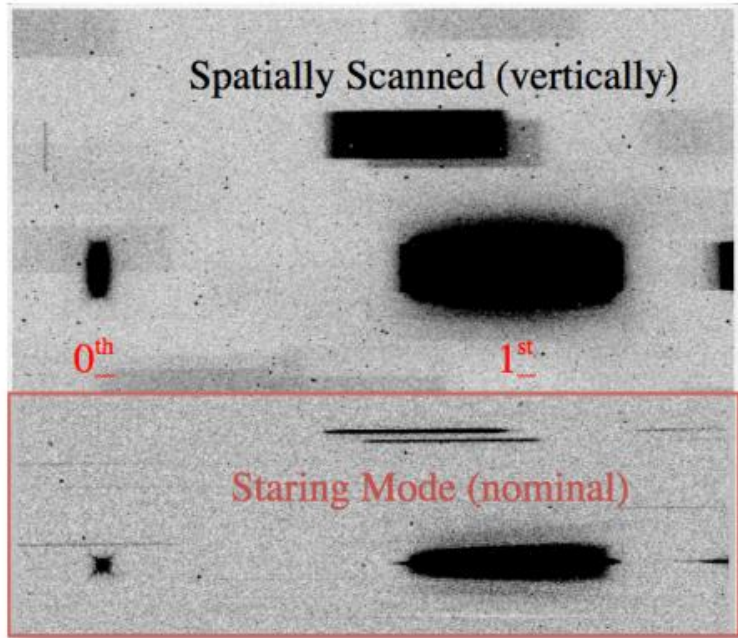


8.6 Slitless Spectroscopy with Spatial Scanning

Spatial scanning of stellar spectra upon the IR detector creates the potential for spectrophotometry of unprecedented precision. By spreading a stellar spectrum perpendicular to its dispersion (Figure 8.10), more photons can be collected per exposure, and the exposure times can be longer without saturating the detector. The most prevalent scientific application is transit spectroscopy, in which a time series of stellar spectra are obtained before, during, and after an exoplanet transit or eclipse; examples are programs 11622, 12181, 12325, 12449, 12473, 12495, 12881, 12956, and 13021. Results for exoplanet transit spectroscopy have been published by numerous investigators; examples include [Knutson et al. 2014](#), [Kreidberg et al. 2014](#) and [McCullough et al. 2014](#). [Knutson et al. 2014](#) report observations of this type with one-sigma precision of ~20 ppm in ~20 nm spectral bins from two transits.

In time series, the integrated flux of a spectrum exhibits a hook-shaped rise repeated with each *HST* orbit. Attempts to mitigate the “hook” have been attempted, in observational technique ([WFC3 ISR 2014-14](#)) and in post-observation modeling ([Zhou et al. 2017](#)).

Figure 8.10: A Spatially-Scanned IR Spectrum



A spatially-scanned IR spectrum, labeled with its 0th and +1st order light, and compared to a nominal staring-mode slitless spectrum of the same field (red outlined inset) ([WFC3 ISR 2012-08](#)). The images are 512 columns wide, of the detector's 1024. The scan was 40 pixels high (4.8 arcsec).

Spatial scanning is available with either WFC3 detector, UVIS or IR. However, overlap of spectral orders will compromise scanning's utility for the UVIS grism. In this section, we assume that for IR spectroscopy, the observer desires the +1st order spectrum. Spatial scans are discussed elsewhere in this Handbook (for UVIS imaging in [Section 6.12.3](#), for IR imaging in [Section 7.10.4](#)) and in [WFC3 ISR 2012-08](#). The latter is particularly relevant for anyone preparing a phase II proposal.

Potential benefits of spatial scanning are 1) reducing overhead for time-series of short exposures due to detector operations required before and after each exposure, 2) avoiding saturation for very bright stars, 3) improved spectrophotometry due to collecting more photons per *HST* orbit. We note that the main disadvantages are 1) STScI pipelines do not work on spatially-scanned IR data so the observer will need to reduce IR data themselves even to produce simple images, and 2) astronomical sources will overlap more often than with staring-mode observations, especially for spectra.

The scan rate can be any real number between 0.0 and 7.84 arcsec s⁻¹. Without FGS control, referred to as "gyro control"¹, rates as high as 7.5 arcsec s⁻¹ have been demonstrated. Under fine-guidance-sensor (FGS) control, rates between 0.0 and 4.8 arcsec s⁻¹ are supported for exposures with a single scan line. Due to a software limitation, boustrophedonic

(serpentine) scans at rates greater than 1 arcsec s^{-1} must be executed under gyro control. Observing under gyro control should be avoided if possible because the increased drift on the detector significantly degrades the measurement precision.

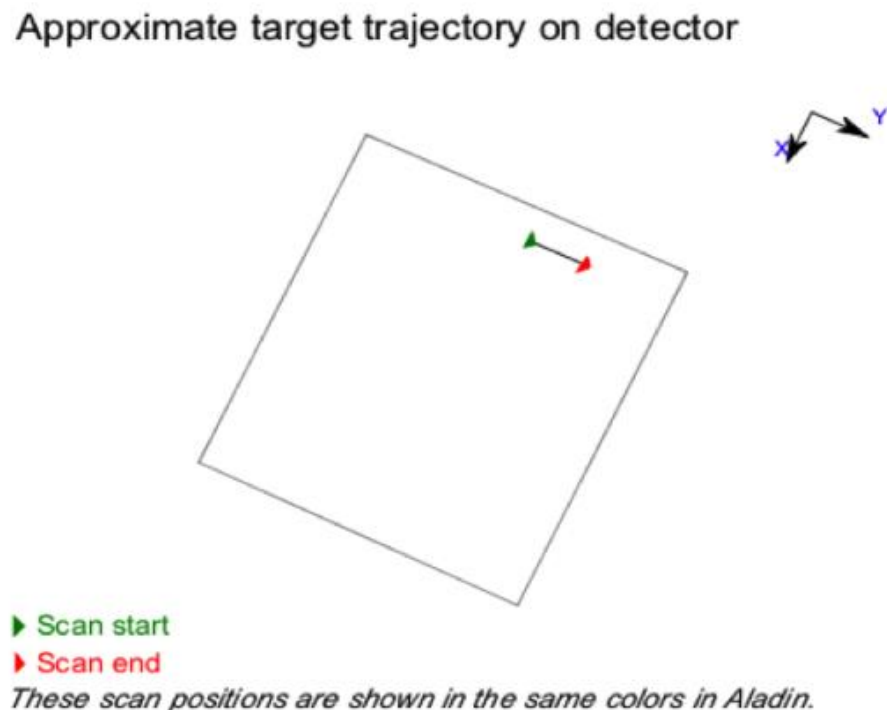
In [WFC3 ISR 2012-08](#), McCullough and MacKenty recommend scan rates for WFC3 IR spectroscopy of bright stars and include formulae to predict appropriate scan rates. For stars with H-band apparent brightnesses fainter than $H = 4.1$ mag, G141 spectra can be unsaturated with scan rates less than or equal to $4.8 \text{ arcsec s}^{-1}$, which is the maximum achievable under FGS control. FGS control is recommended for time-series applications such as exoplanet transit spectroscopy, in order to keep the spectrum from drifting on the detector from one scan to the next, during an *HST* orbit. For stars in the range $4.1 > H > 3.7$ mag, WFC3 G141 spectra can be obtained with less than 25,000 DN/pixel only under gyro control, i.e. with rates between 4.8 and $7.8 \text{ arcsec s}^{-1}$. For stars brighter than $H = 3.7$ mag, spectral orders other than the +1st must be used to avoid saturation of the IR detector; e.g., observations of Vega in Visit 1 of *HST* calibration program 12336 used the -1st order ([WFC3 ISR 2014-15](#)), thus demonstrating that stars as bright as $V \sim H \sim 0.0$ mag can be observed.

Python code and web tools are available to assist observers in designing spatial scanning observations. See [Batalha, N.E. et al. 2017](#) for descriptions of the PandExo code and of extensive testing that was performed using WFC3 observations. ExoCTK (Exoplanet Characterization Toolkit) can be used to make one-off calculations in a web form. [PandExo_HST](#) can be used to perform more detailed calculations on one's own computer.

The sample sequence SPARS5, introduced during cycle 23, has time steps intermediate between those of RAPID and SPARS10. As for all WFC3/IR sample sequences, the time intervals depend on the size of the aperture. (See Sections [7.7.3](#) and [7.7.4](#).) SPARS5 was designed to allow the efficiency and uninterrupted time series of SPARS10 and yet be short enough in cadence to better isolate a target exoplanet-host star from a nearby stellar companion in spatially-scanned observations using an IR grism. Better isolation may enable the observer to specify wider orient ranges, which may increase scheduling opportunities, which are often rare for these time-constrained observations. We expect that SPARS5 will be advantageous especially for G141 or G102 grism observations of stars brighter than approximately 7th magnitude in H band, scanned at approximately 1 arcsec per second or faster. The subarray apertures are especially useful for IR grism observations of bright stars with the sample sequences RAPID, SPARS5, and SPARS10 because of their short time steps and efficient orbit packing. The combination of SPARS10 with a 512×512 aperture is not currently supported (and therefore has a lower quality dark reference file), but spectroscopic spatial scan observers who need it for improved observing efficiency and consequent increases in S/N may send a justification for available mode use to the Contact Scientist or the Program Coordinator, who will forward it to the appropriate instrument scientist for consideration.

APT provides a diagram to assist observers planning spatial scan observations, shown in Figure 8.11. The line connecting the green and red arrows corresponds to where the target's direct image would appear. In grism observations, the first order spectrum appears at larger X coordinate values than the direct image (see Figures [8.4](#) and [8.6](#)). By design of the GRISM128, GRISM256 and GRISM512 subarrays, a POSTARGX = 0 centers the first order spectrum in each subarray in the X coordinate. Because the diagram is only approximate and because of on-going developments in APT and spacecraft operations, users of fast spatial scans ($\sim 1 \text{ arcsec/sec}$ or faster) should consult with their contact scientist to optimize the POSTARGY value.

Figure 8.11: Diagram provided in APT to assist planning of spatial scan observations.



¹ *HST* uses gyros at all times to maintain spacecraft pointing, regardless of whether the FGS are used also. Here, the phrase “gyro control” means “without FGS control”.

Chapter 9: WFC3 Exposure-Time Calculation

Chapter Contents

- [9.1 Overview](#)
- [9.2 The WFC3 Exposure Time Calculator - ETC](#)
- [9.3 Calculating Sensitivities from Tabulated Data](#)
- [9.4 Count Rates: Imaging](#)
- [9.5 Count Rates: Slitless Spectroscopy](#)
- [9.6 Estimating Exposure Times](#)
- [9.7 Sky Background](#)
- [9.8 Interstellar Extinction](#)
- [9.9 Exposure-Time Calculation Examples](#)

9.1 Overview

[Chapter 4](#) of this Handbook describes the procedures for designing a Phase I WFC3 observing proposal. Two of the steps involved in this process are estimating the exposure times needed to achieve your scientific goals, and then combining these individual exposures with their associated overheads to derive the number of spacecraft orbits that you will request in your Phase I proposal.

This chapter gives guidance on estimating exposure times. The following chapter, [Chapter 10](#), then describes how to include the various overheads so as to determine the total number of spacecraft orbits needed for your program.

You should also refer to the [*HST Call for Proposals*](#), which includes information on policies and practices with respect to orbit-time requests. The [*HST Primer*](#) provides specific advice on orbit determination. Below, we provide a summary of the WFC3 sensitivities and give several examples that illustrate how to calculate your exposure times for Phase I Proposals.

9.2 The WFC3 Exposure Time Calculator

- ETC

In most cases, you will find it convenient to use the online WFC3 [Exposure Time Calculator \(ETC\)](#) to make estimates of the required exposure times for your project. The ETC is available from the WFC3 website at:

<http://www.stsci.edu/hst/instrumentation/wfc3/software-tools/exposure-time-calculators>

The ETC calculates counts (e^-) and count rates (e^-/s) for given source and background parameters and assumed characteristics of the detectors. Once these are entered, the ETC then outputs signal-to-noise (S/N) ratios achieved for a given exposure time, or the exposure times required to achieve a given S/N ratio. The ETC supports both direct-imaging and spectroscopic (grism) observations. Starting in Cycle 24, it supports spatial scanning for UVIS and IR imaging and IR spectroscopy. (See [WFC3 STAN issue 22](#).) The aXeSIM tool is available for simulation of grism observations (see [Section 8.4](#)). A variety of circular and square extraction apertures are available in the ETC, allowing the user to select either a radius in arcseconds or a size in pixels. It is also possible to input a calibrated spectral-energy distribution (SED) of your source directly into the ETC. The ETC also outputs peak per-pixel count rates and total count rates, to aid in feasibility assessment. Warnings will appear if the source will saturate the detector, which would not only compromise CCD and IR observations, but might even affect subsequent exposures with the IR channel (see [Appendix D](#)). The ETC has online help for its execution and interpretation of results.

There are some items worth noting:

- For the UVIS channel, the ETC uses a CCD full-well value of 63,000 e^- , the minimum value for either CCD chip, to determine saturation; users wishing to strictly avoid this occurrence should allow a buffer of at least 10% below this. (See [Section 5.4.5](#) for a detailed discussion of saturation.)
- For the UVIS channel, to the extent possible, one should select Detector chip 2 for UV filter exposures and place the target on chip 2 (e.g., aperture UVIS2 in [Figure 6.1](#) or the subarray apertures in the lower left quadrant of [Figure 6.2](#)) since chip 2 has better quantum efficiency than chip 1. (See [Figure 5.2](#).) Note, however, that the quad filters have quadrant-dependent passbands as specified in Table 13.5 in Section 13.4.1 of the [Phase II Proposal Instructions](#). The user should be careful to select the Detector chip corresponding to the relevant quadrant for a given filter name, since the ETC will incorrectly allow either chip to be selected. (Quads A and B are on chip 1; quads C and D are on chip 2.)
- The user can add background to UVIS exposures by using the post-flash option ([Section 6.9.2](#)). See [Section 9.6](#) for equations that show how the post-flash background affects the calculation of S/N and exposure time.
- For the IR channel, when the # of Frames = 1, the ETC assumes a complete timing sequence (NSAMP = 15). For smaller NSAMP, the read noise is greater. (See [Section 5.7.3](#).) For most programs, NSAMP should be greater than 5 for individual exposures, and larger if possible, to provide the best readnoise and best protection against cosmic rays. (See [Section 7.10.3](#).)
- The He I airglow line at 10,830 Angstroms is being added as a component of the IR sky background for Cycle 24. (See [Section 7.9.5](#)) It only contributes to the background observed in the F105W and F110W filters and the G102 and G141 grisms. The default ETC value of "None" will provide ETC estimates unchanged from those of previous cycles. The other available options---Average, High, Very High---are the 50%, 75% and 95% percentile values of the excess background, per exposure, observed over the value estimated for the zodiacal light alone (e.g., [Figure 7.11](#))

). Determined from an analysis of archival exposures, these percentiles correspond to an additional 0.1, 0.5, and 1.5 e-/s, respectively, normalized in the F105W filter. Note that the “Average” value of 0.5 e-/s is comparable to the flux predicted for the zodiacal background ([Figure 7.11](#)). Furthermore, achieving the He I value of “None” is essentially only possible if the SHADOW special requirement is used, though this is not recommended as the available usable orbit duration is then dramatically reduced; it is almost always preferable to keep observing even in the presence of elevated backgrounds for part of the orbit ([WFC3 ISR 2014-03](#)).

It is also possible to use *synphot* in [STSDAS](#) to calculate count rates and the wavelength distribution of detected counts.

The remaining sections of this chapter give detailed information on the sensitivities of the UVIS and IR channels when combined with the various spectral elements, and the use of this information in the determination of count rates, for those who wish to understand the subject in depth.

9.3 Calculating Sensitivities from Tabulated Data

Most observers will use the ETC or synphot to determine count rates and sensitivities for WFC3 observations. However, it is also possible to calculate count rates and S/N ratios by hand, and this exercise will give the observer better insight into the sensitivity calculations. The formulae and tabular values required to calculate sensitivities for the WFC3 imaging and spectroscopic modes are provided in this section. Using them, one can calculate the expected count rates and the S/N ratio achieved in a given exposure time, based on the spectral energy distribution of a source. The formulae are given in terms of sensitivities, but we also provide transformation equations between throughput (Q) and sensitivity (S) for imaging and spectroscopic modes.

The tabular data presented here was derived using on-orbit data that was processed with ground-based flat field reference files. (See [WFC3 ISR 2009-30](#) and [WFC3 ISR 2009-31](#).) These flat fields are in error by up to several percent on large spatial scales. More accurate zeropoints (see Online arrow below) have been determined by using better flat fields (see Sections [5.4.3](#) and [5.7.4](#)) and by deriving filter-specific solutions instead of making a low-order fit across wavelengths. Monitoring of photometric performance over the first year of operations has shown the WFC3/UVIS detector to be stable to rms $\sim 0.5\%$ ([WFC3 ISR 2010-14](#)) and the WFC3/IR detector to be stable to rms $\sim 0.5\%$ to 1.0% , depending on filter ([WFC3 ISR 2011-08](#)).



For more accurate photometric zeropoints, see the [WFC3 Photometric Zeropoints website](#).

Throughputs are presented in graphical form as a function of wavelength for each of the imaging filters and grisms in [Appendix A](#). Given the source characteristics and the sensitivity of the WFC3 configuration, calculating the expected count rate over a given number of pixels is straightforward. The additional information required is the encircled energy fraction (ϵ_f) in the peak pixel, the plate scale, and (for the spectroscopic modes) the dispersions of the grisms.

The sensitivity information is summarized in Tables [9.1](#) and [9.2](#). In these two tables, and in the following discussion, the filter transmission functions are denoted $T(\lambda)$, and the overall system response function (apart from the filter transmission) is denoted $Q(\lambda)$. The terms “counts” and “count rates” always refer to the number of detected electrons, which is converted to data numbers, or DNs, upon readout according to the gain factors for the detectors. The measured gain is $1.55 \text{ e}^-/\text{DN}$ for the UVIS channel and $\sim 2.4 \text{ e}^-/\text{DN}$ for the IR channel (see [Table 5.1](#)).

In Tables [9.1](#) and [9.2](#), the following quantities are listed:

1. The filter or grism designation.
2. The “pivot wavelength” for that filter or grism, λ_p . Pivot wavelength is a source-independent measure of the characteristic wavelength of a bandpass, defined such that it is the same if the input spectrum is given in units of F_λ or F_ν (see A. TokunagW.Vacca 2005, *PASP*, **117**, 421):

$$\lambda_p = \sqrt{\frac{\int Q(\lambda)T(\lambda)\lambda d\lambda}{\int Q(\lambda)T(\lambda)d\lambda}}.$$

3. The integral $\int Q_\lambda T_\lambda d\lambda/\lambda$, used to determine the count rate when given the astronomical magnitude of the source.
4. The ABmag zero-point, defined as the AB magnitude of a source with a flat F_ν that yields $1 \text{ e}^- \text{ s}^{-1}$ with the specified configuration.
5. The sensitivity integral, $\int S_\lambda d\lambda$, defined (see [Section 9.4](#)) as the count rate that would be detected from a flat F_λ source with a flux of $1 \text{ erg cm}^{-2} \text{ s}^{-1} \text{ \AA}^{-1}$.
6. The ensquared energy, defined as the fraction of PSF flux enclosed in the default photometry aperture (5×5 pixels for the UVIS and 3×3 pixels for the IR).
7. The fraction of the total PSF flux in the central pixel for a centered stellar source, useful for determining the peak count rate to check for saturation (see also [Appendix D](#)).
8. The sky background count rate ($\text{e}^- \text{ s}^{-1}$), which is the count rate that would be measured with average zodiacal background and average earth-shine. For the IR channel, this quantity also includes the thermal background from HST and the instrument. It does not include the contribution from the detectors themselves (i.e., dark current and read noise).

The next two sections describe how to calculate two quantities:

- The count rate in $\text{e}^- \text{ s}^{-1}$, C , from your source over some selected area on the detector containing N_{pix} pixels.
- The peak count rate in $\text{e}^- \text{ s}^{-1} \text{ pixel}^{-1}$, P_{cr} , from your source, which is useful for avoiding saturated exposures.

We consider the cases of point sources and diffuse sources separately in each of the following imaging and spectroscopy sections.

Table 9.1: Sensitivity Data for WFC3/UVIS Channel.

Spectral Element	Pivot λ (Å)	$\int Q_\lambda T_\lambda d\lambda / \lambda$	ABMAG zero-point	$\int S_\lambda d\lambda$	Ensquared energy	Energy in central pixel	Background (sky) rate
F200LP	4970.9	0.3543	27.36	1.99 E+19	0.75	0.17	0.1277
F218W	2230.6	0.0060	22.93	6.77 E+16	0.70	0.13	0.0005
F225W	2373.6	0.0169	24.06	2.17 E+17	0.71	0.14	0.0066
F275W	2710.1	0.0183	24.14	3.06 E+17	0.74	0.15	0.0037
F280N	2833.5	0.0010	20.93	1.74 E+16	0.74	0.16	0.0000
F300X	2822.1	0.0378	24.93	6.86 E+17	0.74	0.16	0.0133
F336W	3354.8	0.0292	24.65	7.49 E+17	0.77	0.17	0.0018

F343N	3435.2	0.0146	23.90	3.93 E+17	0.77	0.17	0.0011
F350LP	5858.4	0.2425	26.95	1.90 E+19	0.76	0.17	0.1077
F373N	3730.2	0.0024	21.94	7.63 E+16	0.78	0.18	0.0003
F390M	3897.3	0.0115	23.63	3.97 E+17	0.78	0.18	0.0017
F390W	3924.5	0.0567	25.37	1.99 E+18	0.78	0.18	0.0098
F395N	3955.2	0.0047	22.67	1.68 E+17	0.78	0.18	0.0008
F410M	4109.0	0.0112	23.61	4.31 E+17	0.78	0.18	0.0028
F438W	4326.5	0.0345	24.83	1.47 E+18	0.78	0.19	0.0099
F467M	4682.6	0.0122	23.70	6.10 E+17	0.78	0.19	0.0046
F469N	4688.1	0.0021	21.81	1.07 E+17	0.78	0.19	0.0008
F475W	4773.6	0.0763	25.69	3.96 E+18	0.78	0.19	0.0278
F475X	4941.4	0.1173	26.16	6.52 E+18	0.78	0.18	0.0444
F487N	4871.4	0.0031	22.22	1.68 E+17	0.78	0.19	0.0012
F502N	5009.6	0.0034	22.31	1.93 E+17	0.78	0.19	0.0014
F547M	5447.4	0.0312	24.72	2.11 E+18	0.78	0.18	0.0148
F555W	5308.1	0.0835	25.79	5.36 E+18	0.78	0.18	0.0377
F600LP	7451.3	0.0892	25.86	1.13 E+19	0.72	0.16	0.0575
F606W	5887.5	0.1090	26.08	8.60 E+18	0.77	0.18	0.0569

F621M	6218.6	0.0280	24.60	2.47 E+18	0.76	0.18	0.0163
F625W	6241.4	0.0651	25.52	5.78 E+18	0.76	0.18	0.0374
F631N	6304.3	0.0023	21.90	2.09 E+17	0.76	0.18	0.0014
F645N	6453.6	0.0032	22.26	3.07 E+17	0.75	0.17	0.0019
F656N	6561.4	0.0007	20.54	6.48 E+16	0.75	0.17	0.0004
F657N	6566.6	0.0048	22.68	4.70 E+17	0.75	0.17	0.0029
F658N	6584.0	0.0011	21.09	1.08 E+17	0.75	0.17	0.0006
F665N	6655.9	0.0051	22.74	5.10 E+17	0.75	0.17	0.0031
F673N	6765.9	0.0044	22.58	4.54 E+17	0.74	0.17	0.0027
F680N	6877.4	0.0137	23.83	1.47 E+18	0.74	0.17	0.0086
F689M	6876.4	0.0249	24.48	2.68 E+18	0.74	0.17	0.0156
F763M	7613.6	0.0196	24.21	2.58 E+18	0.71	0.16	0.0130
F775W	7648.3	0.0354	24.86	4.72 E+18	0.71	0.16	0.0236
F814W	8029.9	0.0443	25.10	6.51 E+18	0.70	0.15	0.0299
F845M	8437.6	0.0133	23.79	2.15 E+18	0.68	0.14	0.0092
F850LP	9168.4	0.0123	23.71	2.35 E+18	0.66	0.13	0.0086
F953N	9530.6	0.0005	20.34	1.14 E+17	0.65	0.12	0.0004
FQ232N	2431.1	0.0005	20.13		0.71	0.14	0.0000

				6.12 E+15			
FQ243N	2476.4	0.0007	20.52	9.10 E+15	0.72	0.14	0.0000
FQ378N	3792.4	0.0052	22.78	1.70 E+17	0.78	0.18	0.0006
FQ387N	3873.7	0.0015	21.44	5.21 E+16	0.78	0.18	0.0002
FQ422M	4219.2	0.0050	22.73	2.02 E+17	0.78	0.18	0.0013
FQ436N	4367.2	0.0019	21.67	8.16 E+16	0.78	0.19	0.0005
FQ437N	4371.0	0.0014	21.32	5.92 E+16	0.78	0.19	0.0004
FQ492N	4933.4	0.0058	22.90	3.23 E+17	0.78	0.19	0.0023
FQ508N	5091.0	0.0066	23.03	3.89 E+17	0.78	0.19	0.0028
FQ575N	5757.7	0.0007	20.64	5.51 E+16	0.77	0.18	0.0004
FQ619N	6198.5	0.0025	21.99	2.20 E+17	0.76	0.18	0.0015
FQ634N	6349.2	0.0026	22.02	2.38 E+17	0.76	0.18	0.0015
FQ672N	6716.4	0.0007	20.61	7.30 E+16	0.75	0.17	0.0004
FQ674N	6730.7	0.0005	20.22	5.09 E+16	0.75	0.17	0.0003
FQ727N	7275.2	0.0018	21.65	2.21 E+17	0.73	0.16	0.0012
FQ750N	7502.5	0.0017	21.57	2.19 E+17	0.72	0.16	0.0011
FQ889N	8892.2	0.0011	21.05	1.91 E+17	0.67	0.13	0.0007
FQ906N	9057.8	0.0010	20.94	1.79 E+17	0.66	0.13	0.0007

FQ924N	9247.6	0.0008	20.70	1.50 E+17	0.66	0.13	0.0005
FQ937N	9372.3	0.0007	20.53	1.31 E+17	0.65	0.13	0.0005
G280	5047.0	0.3172	25.87	2.89 E+18	0.81	0.27	0.1136

Table 9.2: Sensitivity Data for WFC3/IR Channel.

Spectral Element	Pivot λ (Å)	$\int Q_\lambda T_\lambda d\lambda/\lambda$	ABMAG zero-point	$\int S_\lambda d_\lambda$	Ensquared energy	Energy in central pixel	Background (sky + thermal) rate
F098M	9864.7	0.0753	25.68	1.67 E+19	0.79	0.38	0.6106
F105W	10551.0	0.1297	26.27	3.29 E+19	0.78	0.37	1.0150
F110W	11534.4	0.2161	26.82	6.55 E+19	0.76	0.36	1.6611
F125W	12486.1	0.1269	26.24	4.51 E+19	0.74	0.34	0.9986
F126N	12584.6	0.0060	22.93	2.16 E+18	0.74	0.34	0.0957
F127M	12740.2	0.0293	24.65	1.08 E+19	0.74	0.34	0.2697
F128N	12831.5	0.0065	23.01	2.43 E+18	0.74	0.33	0.0984
F130N	13005.4	0.0065	23.02	2.50 E+18	0.73	0.33	0.0993
F132N	13187.5	0.0063	22.98	2.49 E+18	0.73	0.33	0.0976
F139M	13837.5	0.0252	24.49	1.10 E+19	0.71	0.32	0.2391
F140W	13922.8	0.1550	26.46	6.84 E+19	0.71	0.32	1.1694
F153M	15321.9	0.0245	24.46	1.31 E+19	0.67	0.29	0.2361

F160W	15369.1	0.0970	25.95	5.22 E+19	0.67	0.29	0.8002
F164N	16403.1	0.0060	22.93	3.67 E+18	0.65	0.28	0.1050
F167N	16641.1	0.0058	22.89	3.65 E+18	0.64	0.27	0.1092
G102	9970.4	0.1110	26.10	2.51 E+19	0.79	0.42	1.2040
G141	13860.0	0.1796	26.62	7.86 E+19	0.73	0.34	1.8619

9.4 Count Rates: Imaging

- 9.4.1 Point Source
- 9.4.2 Diffuse Sources
- 9.4.3 Emission-Line Sources

9.4.1 Point Source

For a point source, the count rate, $C(\text{e}^- \text{s}^{-1})$, can be expressed as the following integral over the bandpass of the filter:

$$C = A \int F_\lambda \frac{\lambda}{hc} Q_\lambda T_\lambda \epsilon_f d\lambda = \int F_\lambda S_\lambda \epsilon_f dh ,$$

where:

- A is the area of an unobstructed 2.4-m telescope (i.e., $45,239 \text{ cm}^2$)
- F_λ is the flux from the astronomical source in $\text{erg cm}^{-2} \text{s}^{-1} \text{\AA}^{-1}$.
- The factor λ/hc (where h is Planck's constant and c is the speed of light) converts ergs to photons.
- $Q_\lambda T_\lambda$ is the system fractional throughput, i.e., the probability of detecting an electron per incident photon, including losses due to obstructions of the full 2.4-m OTA aperture. It is specified this way to separate out the instrument sensitivity Q_λ and the filter transmission T_λ .
- ϵ_f is the fraction of the point-source energy encircled within N_{pix} pixels.
- S_λ is the total imaging point-source sensitivity in units of $\text{e}^- \text{s}^{-1} \text{\AA}^{-1}$
per incident $\text{erg cm}^{-2} \text{s}^{-1} \text{\AA}^{-1}$.

The peak $\text{e}^- \text{s}^{-1} \text{pixel}^{-1}$ from the point source, C_{peak} , is given by the following integral over the bandpass:

$$C_{peak} = \int F_\lambda S_\lambda \epsilon_f(1) d\lambda ,$$

where:

- F_λ and S_λ are as above.
- $\epsilon_f(1)$ is the fraction of energy contained within the peak pixel.

If the flux from the source can be approximated by a flat continuum ($F_\lambda = \text{constant}$) and ϵ_f is roughly constant over the bandpass, then:

$$C = F_\lambda \epsilon_f \int S_\lambda d\lambda .$$

We can now define an equivalent bandpass of the filter, B_λ , such that:

$$\int S_\lambda d\lambda = S_{peak} B_\lambda ,$$

where:

- S_{peak} is the peak sensitivity.
- B_λ is the effective bandpass of the filter.

The count rate from the source can now be written as:

$$C = F_\lambda \epsilon_f S_{peak} B_\lambda .$$

In Tables 9.1 and 9.2 above, we give the value of:

$$\int S_\lambda d\lambda ,$$

for each of the filters.

Alternatively, we can write the count-rate equation in terms of V magnitudes:

$$C = 2.5 \times 10^{11} \epsilon_f \left(\int Q T d\lambda / \lambda \right) \times 10^{-0.4(V+AB_\nu)} ,$$

where V is the visual magnitude of the source, the quantity under the integral is the mean sensitivity of the detector+filter combination (also tabulated in Tables 9.1 and 9.2), and AB_ν is the filter-dependent correction for the deviation of the source spectrum from a constant F_ν spectrum. This latter quantity is tabulated for some representative astronomical spectra in [Appendix A](#).

9.4.2 Diffuse Sources

For a diffuse source, the count rate, C ($e^- s^{-1} pixel^{-1}$), which is now per pixel, due to the astronomical source can be expressed as

$$C = \int I_\lambda S_\lambda m_x m_y d\lambda ,$$

where:

- I_λ is the surface brightness of the astronomical source, in $\text{erg cm}^{-2} \text{s}^{-1} \text{\AA}^{-1} \text{arcsec}^{-2}$.
- S_λ is as above.
- m_x and m_y are the plate scales in arcsec pixel^{-1} along orthogonal axes.

9.4.3 Emission-Line Sources

For a source where the flux is dominated by a single emission line, the count rate can be calculated from the equation

$$C = 2.28 \times 10^{12} \times (QT)_{\lambda} \times F(\lambda) \times \lambda ,$$

where C is the observed count rate in $e^- s^{-1}$, $(QT)_{\lambda}$ is the system throughput at the wavelength of the emission line, $F(\lambda)$ is the emission-line flux in units of $\text{erg cm}^{-2} s^{-1}$, and λ is the wavelength of the emission line in angstroms. $(QT)_{\lambda}$ can be determined by inspection of the plots in [Appendix A](#). See [Section 9.9.4](#) for an example of count-rate estimation for an emission-line source.

9.5 Count Rates: Slitless Spectroscopy

We now turn to estimation of count rates for slitless spectroscopy using the WFC3 grisms. In this case we are dealing with a dispersed image of the source.

For a point source with a continuous spectrum, the count rate, C , is calculated per pixel along the dispersed spectral trace, and is integrated over a fixed extraction height N_{spix} in the spatial direction perpendicular to the dispersion. The count rate is:

$$C = F_\lambda S'_\lambda \epsilon'_{N_{spix}} = F_\lambda A \frac{\lambda}{hc} Q_\lambda T_\lambda \epsilon'_{N_{spix}} d ,$$

where:

- S'_λ is the total point source sensitivity in units of $e^- s^{-1}$ per incident erg $cm^{-2} s^{-1} \text{\AA}^{-1}$; and $S'_\lambda = S_\lambda \times d$.
- d is the spectral dispersion in $\text{\AA} \text{ pixel}^{-1}$.
- $\epsilon'_{N_{spix}}$ is the fraction of the point-source energy within N_{spix} in the spatial direction.
- the other quantities are as defined in the previous section.

For a source with an unresolved emission line with a flux of F in units of $erg cm^{-2} s^{-1}$, the total count rate recorded over the N_{spix} extraction height is:

$$C = FS'_\lambda \epsilon'_{N_{spix}} .$$

These counts will be distributed over pixels in the dispersion direction according to the instrumental line-spread function.

In contrast to the case of imaging sensitivity S_λ , the spectroscopic point source sensitivity calibration ($S'_\lambda \times \epsilon'_{N_{spix}}$) for a default extraction height of N_{spix} was measured directly from observations of stellar flux standards during SMOV and Cycle 17 calibration programs 11934, 11936, and 11552. Therefore, the accuracy in laboratory determinations of T_λ for the WFC3 grisms are not crucial to the final accuracy of their sensitivity calibrations.

The peak $e^- s^{-1} \text{ pixel}^{-1}$ from the point source is given by:

$$P_{cr} = \epsilon'_f(1) F_\lambda S'_\lambda ,$$

where:

- $\epsilon'_f(1)$ is the fraction of energy contained within the peak pixel.
- the other quantities are as above.

9.6 Estimating Exposure Times

[9.6.1 S/N Reached in a Given Exposure Time](#)

[9.6.2 Exposure Time to Reach a Given S/N](#)

[9.6.3 Exposure Time Estimates for Red Targets in F850LP](#)

9.6.1 S/N Reached in a Given Exposure Time

To derive the exposure time to achieve a given S/N ratio, or to derive the S/N ratio achieved in a given exposure time, there are four principal ingredients:

- Expected count rate $C(\text{e}^- \text{s}^{-1})$ from your source over some area.
- The area (in pixels) over which those e^- are received (N_{pix}).
- Sky background (B_{sky}) in $\text{e}^- \text{s}^{-1} \text{pixel}^{-1}$.
- The detector background, or dark, (B_{det}) in $\text{e}^- \text{s}^{-1} \text{pixel}^{-1}$ and the read noise (R) in e^- . (Section 9.7 provides information for determining the sky-plus-detector background.)

The S/N ratio Σ achieved in exposure time t seconds, is given by

$$\Sigma = \frac{Ct}{\sqrt{Ct + N_{pix}(B_{sky} + B_{det})t + N_{pix}N_{read}P + \frac{N_{pix}}{N_{bin}}N_{read}R^2}} ,$$

where:

- C = the signal from the astronomical source in $\text{e}^- \text{s}^{-1}$. (Note that the raw output image uses DN, which will be equal to C/G , where G is the gain.)
- N_{pix} = the total number of detector pixels integrated over to achieve C .
- N_{bin} = the number of detector pixels binned to one read-out pixel when on-chip binning is used.
- B_{sky} = the sky background in $\text{e}^- \text{s}^{-1} \text{pixel}^{-1}$.
- B_{det} = the detector dark current in $\text{e}^- \text{s}^{-1} \text{pixel}^{-1}$.
- R = the read noise in electrons; 3.1 e^- for the UVIS channel and 12. e^- for the IR channel (this is the effective read noise achieved by fitting the ramp of IR readouts, if close to the full sequence of 16 readouts is used).
- N_{read} = the number of detector readouts.
- P = the background added using the post-flash option (Section 6.9.2) in $\text{e}^- \text{pixel}^{-1}$

The above equation assumes the optimistic (but often realistic) condition that the background zero-point level under the object that is subtracted could be well known (from integrating over many pixels) but is still noisy in N_{pix} and does not significantly contribute to the error budget; in crowded fields this may not be true. In general, C in the numerator should be the signal in N_{pix} from the component to be measured (e.g., the point source in an image or the line emission in a

spectrum), while C in the denominator is the total astronomical signal in N_{pix} (e.g., including light from the underlying galaxy in the image or from the continuum in the spectrum).

9.6.2 Exposure Time to Reach a Given S/N

Observers normally take sufficiently long integrations that the read noise is not important. This condition is met when:

$$Ct + N_{pix}(B_{sky} + B_{det})t + N_{pix}N_{read}P > 2\frac{N_{pix}}{N_{bin}}N_{read}R^2 .$$

In the regime where read noise is unimportant, and virtually all of the astronomical signal in N_{pix} comes from the component being measured, the integration time to reach a given signal-to-noise ratio Σ is:

$$t = \frac{\Sigma^2 [C + N_{pix}(B_{sky} + B_{det}) + N_{pix}N_{read}P]}{C^2} .$$

If the source count rate is much higher than that of the sky plus detector backgrounds, then this expression reduces further to:

$$t = \frac{\Sigma^2}{C} ,$$

i.e., the usual result for Poisson statistics of $\Sigma = \sqrt{\text{total counts}}$.

More generally, the required integration time to reach a given S/N ratio is:

$$t = \frac{\Sigma^2 [C + N_{pix}(B_{sky} + B_{det})] + \sqrt{\Sigma^4 [C + N_{pix}(B_{sky} + B_{det})]^2 + 4\Sigma^2 C^2 \left[N_{pix}N_{read}P + \frac{N_{pix}}{N_{bin}}N_{read}R^2 \right]}}{2C^2} .$$

9.6.3 Exposure Time Estimates for Red Targets in F850LP

At long wavelengths, ACS CCD observations are affected by a red halo due to light scattered off the CCD substrate. An increasing fraction of the light as a function of wavelength is scattered from the center of the PSF into the wings. This problem affects particularly the very broad z-band F850LP filter, for which the encircled energy depends on the underlying spectral energy distribution the most. At the current time, it is thought that this problem has been fixed for WFC3, and so this should not be a concern for those planning WFC3 observations.

9.7 Sky Background

[9.7.1 Zodiacal Light, Earth Shine, and LOW-SKY](#)

[9.7.2 Geocoronal Emission, Airglow, and SHADOW](#)

As noted in the previous section, the backgrounds from the sky and from the detector must be taken into account when calculating expected S/N ratios or exposure times.

Detector backgrounds (as well as read-out noise) for the CCDs and IR detector are discussed in [Chapter 5](#). Background added to CCD exposures using the post-flash option is discussed in [Section 6.9.2](#). This section deals with the sky backgrounds that can affect WFC3 observations.

The most important sources of sky background are:

- Earthshine (ES).
- Zodiacal light (ZL).
- Geocoronal emission (GC).

$$B_{\text{sky}} = \int I_\lambda S_\lambda m_x m_y d\lambda .$$

The background in counts $\text{e}^- \text{s}^{-1} \text{pixel}^{-1}$ for imaging observations can be computed as:

where:

- I_λ is the surface brightness of the sky background, in $\text{erg cm}^{-2} \text{s}^{-1} \text{\AA}^{-1} \text{arcsec}^{-2}$.
- S_λ is the point-source sensitivity for the imaging mode.
- m_x and m_y are the plate scales in arcsec pixel^{-1} along orthogonal axes.

In the case of slitless spectroscopy, the image of the sky through a disperser is not uniform, because some wavelengths fall off the detector for regions of sky near the edge of the field of view. The regions of lower sky background will be strips at the long- and short-wavelength edges of the field of view; a UVIS grism spectrum is roughly 270 pixels long, while an IR grism spectrum is roughly 170 pixels long. The maximum width of the strips from where the signal starts to decline to the edge, where the signal is down by roughly a factor of 2, will be about half the total length of a spectrum of a point source, i.e., roughly 135 pixels (UVIS) or 85 pixels (IR), in the case of a sky background with a continuum of wavelengths. These small strips of lower sky background are ignored in the following formulae. Furthermore, since the spectra do not lie along the direction of the anamorphic distortion, the plate scales of m_x and m_y above must be replaced by the plate scales m_s and m_d in the orthogonal spatial and dispersion directions, respectively. Interior to the strips, a point on the detector sees a region of sky over the full wavelength coverage of the disperser. Thus, for **spectroscopic observations**:

$$B_{sky}^{\lambda} = \int I_{\lambda} S'_{\lambda} m_s m_{\lambda} d\lambda .$$

For a **monochromatic** sky emission line at $\lambda = L$ like [O II] 2471, which will dominate the background through the UVIS /G280 grism:

$$B_{sky}^L = I_L S'_L m_s \frac{m_{\lambda}}{d} ,$$

where

- I_L is the monochromatic intensity of a line at wavelength L in $\text{erg cm}^{-2} \text{s}^{-1} \text{arcsec}^{-2}$.

The total sky background is:

$$B_{sky} = B_{sky}^{\lambda} + B_{sky}^L .$$

[Figure 9.1](#) and [Table 9.3](#) show "high" sky background intensity as a function of wavelength, identifying the separate components which contribute to the background. The "shadow" and "average" values of the earth-shine contribution in the WFC3 [Exposure Time Calculator \(ETC\)](#) correspond, respectively, to 0% and 50% of the "high" values in [Figure 9.1](#) and [Table 9.3](#). For the zodiacal sky background, the values in [Figure 9.1](#) and [Table 9.3](#) correspond to the high value of V -band surface brightness of 22.1 mag arcsec^{-2} from [Table 9.4](#), while the "low" and "average" zodiacal light is scaled to V surface brightnesses of 23.3 and 22.7 mag arcsec^{-2} , respectively.

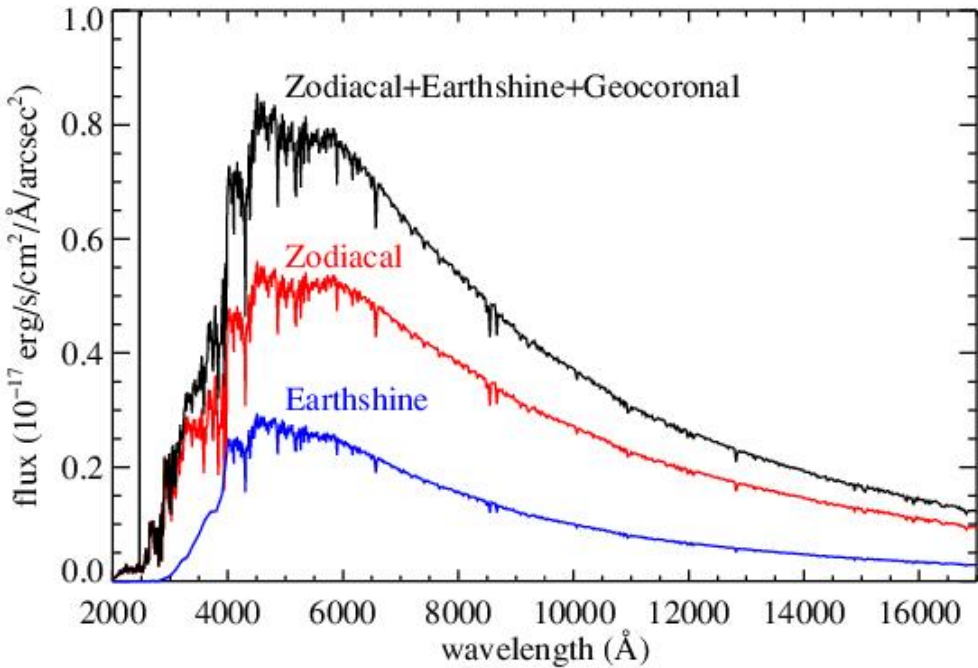
In Table 9.3 we present the "high" sky-background numbers, which are plotted in [Figure 9.1](#). See the text and the caption of [Figure 9.1](#) for more details. These high sky values are defined as the earth-shine at 38° from the limb and the high zodiacal light of $V = 22.1$ mag arcsec^{-2} .

Table 9.3: High Sky Backgrounds.

Wavelength (Å)	Earth-shine ($\text{erg cm}^2 \text{s}^{-1} \text{Å}^{-1} \text{arcsec}^{-2}$)	Zodiacal light ($\text{erg cm}^2 \text{s}^{-1} \text{Å}^{-1} \text{arcsec}^{-2}$)	Total sky background ($\text{erg cm}^2 \text{s}^{-1} \text{Å}^{-1} \text{arcsec}^{-2}$)
2000	7.69E-22	7.94E-20	8.02E-20
2500	1.53E-21	3.83E-19	3.84E-19
3000	1.43E-19	1.63E-18	1.77E-18
3500	8.33E-19	2.72E-18	3.55E-18
4000	1.66E-18	3.12E-18	4.78E-18
4500	2.59E-18	4.97E-18	7.57E-18
5000	2.63E-18	5.07E-18	7.70E-18
5500	2.55E-18	5.17E-18	7.72E-18

6000	2.42E-18	5.14E-18	7.56E-18
7000	1.95E-18	4.48E-18	6.42E-18
8000	1.56E-18	3.82E-18	5.38E-18
9000	1.23E-18	3.18E-18	4.40E-18
10000	9.97E-19	2.70E-18	3.70E-18
11000	8.02E-19	2.26E-18	3.06E-18
12000	6.65E-19	1.94E-18	2.61E-18
13000	5.58E-19	1.68E-18	2.24E-18
14000	4.70E-19	1.46E-18	1.93E-18
15000	3.97E-19	1.26E-18	1.66E-18
16000	3.35E-19	1.09E-18	1.43E-18
17000	2.79E-19	9.27E-19	1.21E-18

Figure 9.1: Sky background intensity as a function of wavelength.



The total sky spectrum (black) for the "high-background" case adopted in the WFC3 ETC, along with the individual contributions from zodiacal light and earth-shine. These data correspond to a V-band surface brightness of 22.1 mag arcsec⁻². The geocoronal emission line [O II] 2471 Å has a flux of 1.5×10^{-15} erg cm⁻² s⁻¹ arcsec⁻², extending beyond the upper limit of the plot. See [Section 7.9.5](#) for discussion of the He I emission line at 10830 Å, not plotted here.

9.7.1 Zodiacal Light, Earth Shine, and LOW-SKY

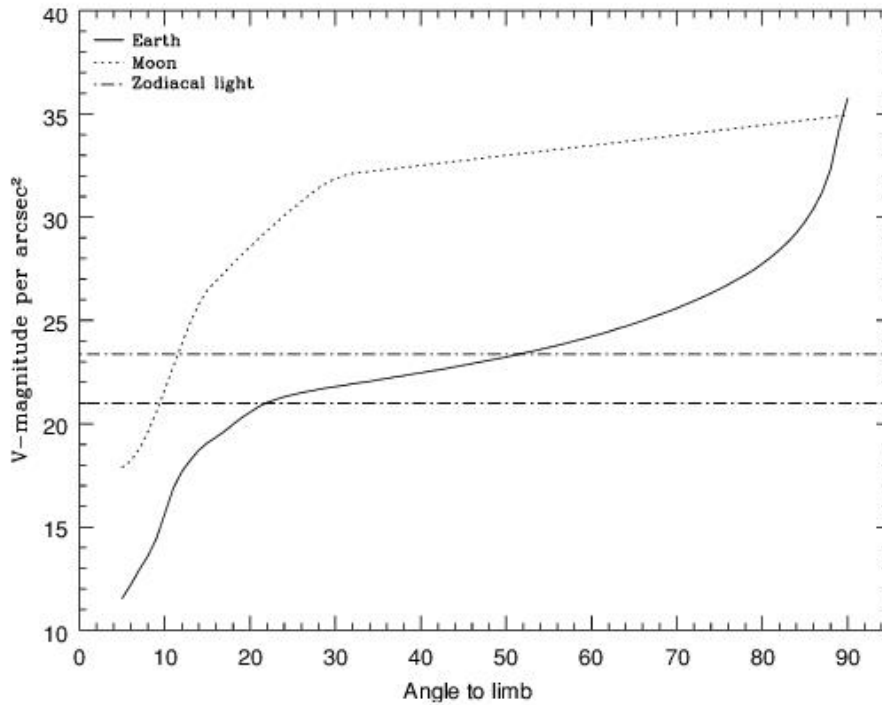
Zodiacal light varies as a function of angular distance of the target from the Sun and from the ecliptic. [Table 9.4](#) gives the variation of the zodiacal background as a function of heliocentric ecliptic longitude and ecliptic latitude in V-mag arcsec⁻². As shown by this table, over most of the sky the zodiacal background is within 1 magnitude of the minimum value of 23.4 V-mag arcsec⁻². It is greater than that at low ecliptic latitudes and at angles from the sun approaching the minimum permitted observing angle of 55°. At the lower ecliptic latitudes, it rises rapidly as this 55° limit is approached. For a target near heliocentric ecliptic coordinates (50,0) or (-50,0), not shown in the table, the zodiacal light level is 20.9 V-mag arcsec⁻², i.e., about 10 times the faintest value. For an empirical determination of the dependence of zodiacal light on the ecliptic latitude and the angle between the target and the sun for WFC3/IR observations, see [Section 7.9.5](#). [Figure 7.12](#) illustrates this dependence.

Table 9.4: Approximate zodiacal sky background as a function of heliocentric ecliptic longitude and ecliptic latitude (in V-mag per arcsec²). SA stands for Solar Avoidance zone (*HST* pointing within 55 deg of the sun), where observations may not be made.

Ecliptic longitude (degrees)	Ecliptic latitude (degrees)						
	0	15	30	45	60	75	90
0	SA	SA	SA	SA	22.6	23.0	23.3
15	SA	SA	SA	SA	22.6	23.1	23.3
30	SA	SA	SA	22.3	22.7	23.1	23.3
45	SA	SA	22.1	22.5	22.9	23.1	23.3
60	21.3	21.9	22.4	22.7	23.0	23.2	23.3
75	21.7	22.2	22.6	22.9	23.1	23.2	23.3
90	22.0	22.3	22.7	23.0	23.2	23.3	23.3
105	22.2	22.5	22.9	23.1	23.3	23.3	23.3
120	22.4	22.6	22.9	23.2	23.3	23.3	23.3
135	22.4	22.6	22.9	23.2	23.3	23.4	23.3
150	22.4	22.6	22.9	23.1	23.3	23.4	23.3
165	22.3	22.5	22.8	23.0	23.2	23.4	23.3
180	22.1	22.4	22.7	23.0	23.2	23.4	23.3

Earth-shine varies strongly depending on the angle between the target and the bright Earth limb. The variation of the earth-shine as a function of limb angle from the sunlit Earth is shown in [Figure 9.2](#). The figure also shows the contribution of the moon, which is typically much smaller than the zodiacal contribution, for which the upper and lower limits are shown. For reference, the limb angle is approximately 24° when the *HST* is aligned toward its orbit pole (i.e., the center of the CVZ). The earth-shine contribution shown in [Figure 9.1](#) and [Table 9.3](#) corresponds to this position.

Figure 9.2: Background contributions in V magnitude per arcsec² due to the zodiacal light, Moon, and sunlit Earth, as a function of angle between the target and the limb of the Earth or Moon. The two zodiacal light lines show the extremes of possible values.



For observations taken longward of 3500 Å, earth-shine dominates the background at small ($<22^\circ$) limb angles. In fact, the background increases exponentially for limb angles $<22^\circ$. The background near the bright limb can also vary by a factor of ~ 2 on timescales as short as two minutes, which suggests that the background from earth-shine also depends upon the reflectivity of the terrain and the amount of cloud cover over which *HST* passes during the course of an exposure.

Observations of the faintest objects may benefit from the use of the Phase II Special Requirement `LOW-SKY`, which should be requested and justified in the Phase I proposal. `LOW-SKY` observations are scheduled during the part of the year when the zodiacal background light is no more than 30% greater than the minimum possible zodiacal light for the given target position. `LOW-SKY` also invokes the restriction that exposures will be taken only at angles greater than 40° from the bright Earth limb to minimize earth-shine and the airglow lines (but also see [Section 9.7.2](#)). It is not always effective in suppressing the He I 10830 Å airglow line ([Section 7.9.5](#)).

One disadvantage of using the `LOW-SKY` requirement is that it greatly reduces scheduling opportunities due to the restriction on zodiacal light. That restriction may be stricter than scientifically necessary, especially for targets at high ecliptic latitudes where even the maximum attainable zodiacal background is quite low, and for filters where other background components dominate the noise.

For targets and filters where high zodiacal background could be a problem, observers may want to limit that background by placing their own less stringent restrictions on scheduling dates to avoid observing the target when it is too near the

sun. *HST* is already constrained to point at least 55° from the sun. For targets at low ecliptic latitude, that limit can be extended to ~60° by excluding 5 days from the ends of the default solar exclusion window, as described in [Section 7.9.5](#).

Another disadvantage of using the `LOW-SKY` requirement is that it limits visibility to about 48 minutes per orbit. Rather than accept an automatic reduction in observing time by using `LOW-SKY`, the observer may be able to structure an orbit so that the exposures that would be most significantly affected by earth-shine do not occur at the beginning or end of the orbit, where the earth-shine is likely to be highest. The exposures in that orbit should be placed in a non-interruptible exposure sequence, as described in the [APT Training Materials](#). For WFC3/IR exposures, frames in the non-destructive readouts that are badly affected by earth-shine can be excluded from the data reduction. (See [Section 7.9.5](#))

WFC3/UVIS observers should keep in mind that the total background should be at least 12 electrons/pix/s to minimize CTE losses during the readout of faint sources, so for some targets and filters it may be advisable to increase the background using post-flash rather than to attempt to minimize it. ([Section 6.9](#)).

The [ETC](#) provides the user with the flexibility to adjust separately both the zodiacal and earth-shine sky background components to help observers decide where special care is needed to avoid background levels that could be detrimental to their science. The RA, Dec and date option can be used to compute the zodiacal light for specific targets, which is especially useful for targets at low ecliptic latitudes where the zodiacal background increases rapidly as the angle between the target and the sun approaches the *HST* observable limit of 55°. Note that the standard normalizations for zodiacal light and earth-shine (from none to high or extremely high) provide approximations that may not accurately predict the levels in individual exposures. For WFC3/IR exposures, one can check the empirically determined zodiacal light model discussed in [Section 7.9.5](#).

9.7.2 Geocoronal Emission, Airglow, and SHADOW

Background due to geocoronal emission originates mainly from hydrogen and oxygen atoms in the exosphere of the Earth. In the far-UV spectral region, the strongest geocoronal emission lines are Lyman- α at 1216 Å, O I at 1304 Å, and O II] at 1356 Å, but WFC3 is of course not sensitive at these wavelengths. The only significant UV geocoronal emission line to which WFC3 is sensitive is [O II] 2471 Å, shown in [Figure 9.1](#). This line varies in intensity from day to night and as a function of *HST* orbital position. It can be the dominant sky contribution in the UV both for imaging and spectroscopic observations. In sunlight it can be as bright as $\sim 1.5 \times 10^{-15}$ erg cm $^{-2}$ s $^{-1}$ arcsec $^{-2}$, while in Earth shadow it is much fainter, typically $\sim 7.5 \times 10^{-18}$ erg cm $^{-2}$ s $^{-1}$ arcsec $^{-2}$.

To minimize geocoronal emission, the Special Requirement `SHADOW` can be requested. Exposures using this special requirement are limited to roughly 25 minutes per orbit, exclusive of the guide-star acquisition (or re-acquisition), and can be scheduled only during a small percentage of the year. `SHADOW` therefore restricts scheduling opportunities and orbit duration much more severely than `LOW-SKY` (see [Section 7.9.1](#)). `SHADOW` reduces the contribution from the geocoronal emission lines by roughly a factor of ten while the continuum earth-shine is set to zero. `SHADOW` requirements must be included and justified in your Phase I proposal (see the [Call for Proposals](#)). Observers should keep in mind that the total background should be at least 12 electrons/pix/s to minimize CTE losses during the readout of faint sources, so it may be advisable to increase the background using post-flash rather than to attempt to minimize it. (See [Section 6.9](#))

Analysis of archival WFC3/IR grism and broad-band filter observations has shown that a variable airglow line of He I at 10830 Å can be a significant component of the sky background for the F105W and F110W filters and the G102 and G141

grisms. See [Section 7.9.5](#) for discussion of the WFC3/IR sky background and observing strategies. The use of SHADOW is generally not recommended for WFC3/IR exposures.

9.8 Interstellar Extinction

Interstellar extinction can dramatically reduce the count rate detected from your source, particularly if you are working in the ultraviolet range but are inferring source brightnesses from optical data. Conversely, optically obscured objects may be much brighter in the IR than in the optical.

The [Exposure Time Calculator](#) includes the ability to correct exposure-time estimates for interstellar extinction based on the color excess $E(B-V)$. It may also be useful to refer to the standard references on interstellar extinction and its variations with location and metallicity, e.g., [Fitzpatrick \(1999, PASP, 111, 63\)](#) and references therein.

9.9 Exposure-Time Calculation Examples

- 9.9.1 Example 1: UVIS Imaging of a Faint Point Source
- 9.9.2 Example 2: UVIS Imaging of a Faint Source with a Faint Sky Background
- 9.9.3 Example 3: IR Imaging of a Faint Extended Source
- 9.9.4 Example 4: Imaging an H II region in M83 in H-alpha

In the following sections you will find a set of examples for the two different channels and for different types of sources. The examples were chosen in order to present typical objects for the two channels and also to present interesting cases as they may arise with the use of WFC3.

9.9.1 Example 1: UVIS Imaging of a Faint Point Source

What is the exposure time needed to obtain a signal-to-noise of 10 for a point source of spectral type F0 V (Castelli and Kurucz Model, T=7250 K), normalized to $V = 27.5$, when using the UVIS F555W filter? Assume a photometry box size of 5×5 pixels, detector chip 2 (generally the preferred chip; see [Section 6.4.4](#)), average standard zodiacal light and earth shine, and, to start with, 1 frame.

The WFC3 [Exposure Time Calculator \(ETC\)](#) gives an exposure time of 4579 sec = 76.3 min. A single long exposure ~48 min will fit the typical *HST* orbit, so this observation will require more than 1 orbit. One long exposure per orbit would be a poor choice because many pixels would have bad fluxes in both of the exposures due to cosmic rays ([Section 5.4.10](#)). For multi-orbit observations, taking two dithered exposures per orbit (to move bad pixels as well as to allow for cosmic ray removal) is generally sufficient. Recalculating the needed exposure time using 4 frames (more read noise, higher fluxes and flux-dependent noise components to preserve S/N=10) gives 5088 sec, or 1272 sec = 21.2 min per frame. In a typical *HST* orbit, there is time for two 23 min exposures, so a box pattern (for optimal sampling of the PSF; see [Appendix C](#)) will nicely fit two orbits. The background level per frame far exceeds the level where CTE losses become a concern (see [Section 6.9](#)), so post-flash is not needed and the ETC does not post an advisory.

Using the pencil-and-paper method, for filter F555W [Table 9.1](#) gives the integral $\int QTd\lambda/\lambda$ as 0.0835 and indicates that the fraction of the star's light included in the 5×5 pixel square aperture is 0.78. [Table A.1](#) shows an AB_V correction term of 0.03 for filter F555W for a star with an effective temperature of 7,500 K (the closest value to our star's effective temperature 7250 K). The count rate for our $V = 25$ mag star can then be calculated from the equation

$$C = 2.5 \times 10^{11} \epsilon_f \left(\int QT \frac{d\lambda}{\lambda} \right) \times 10^{-0.4(V+AB_V)},$$

or

$$C = 2.5 \times 10^{11} \times 0.0835 \times 0.78 \times 10^{-0.4(27.5+0.03)} = 0.1584 e^- s^{-1},$$

which agrees with the ETCReturned value of $0.158 e^- s^{-1}$. The exposure time can then be found by using the equation

$$t = \frac{\Sigma^2 [C + N_{pix}(B_{sky} + B_{det})] + \sqrt{\Sigma^4 [C + N_{pix}(B_{sky} + B_{det})]^2 + 4\Sigma^2 C^2 \left[\frac{N_{pix}}{N_{bin}} N_{read} R^2 \right]}}{2C^2},$$

to where we use

$\Sigma = 10$

$N_{pix} = 25$

$B_{sky} = 0.0377 \text{ e-}/\text{s}/\text{pix}$ from [Table 9.1](#)

$B_{det} = 0.0015 \text{ e-}/\text{s}/\text{pix}$ from [Table 5.1](#)

$R = \text{read noise} = 3.1 \text{ e-}$ from [Table 5.1](#)

$N_{read} = 4$

$N_{bin} = 1$

$P = 0$ (no post-flash, so the post-flash noise term is not included)

which gives $t = 5265 \text{ sec}$, compared to the ETC-derived value of 5088 sec.

9.9.2 Example 2: UVIS Imaging of a Faint Source with a Faint Sky Background

Calculate the signal to noise obtained in 1200 seconds for a point source of spectral type F0 V (Kurucz & Castelli Model, T=7250 K), normalized to Johnson V = 23.5 mag, using the UVIS F225W filter, a photometry box size of 5×5 pixels, 1 frame, detector chip 2, and with average standard zodiacal light, average standard earth shine and average Air Glow values.

The ETC returns SNR=5.1886, as well as a warning message indicating that the background electrons per pixel (3.22) is less than the recommended threshold of 12 electrons to avoid charge transfer efficiency effects. For a discussion on CTE effects please refer the [CTE webpage](#).

Recalculate the SNR as before, but this time adding 9 post-flash electrons. Now the ETC returns SNR=4.17, and no warning messages. This SNR value is lower than the case without postflash because the postflash electrons contribute to the noise.

To calculate the signal to noise by hand, the procedure is to calculate the count rate using the equation given in [Section 9.6.1](#)

$\Sigma = 10$ First calculate the count rate for the object using:

$$C = 2.5 \times 10^{11} \epsilon_f \left(\int Q T \frac{d\lambda}{\lambda} \right) \times 10^{-0.4(V+AB_V)},$$

and values of:

$AB_V = 2.84$

$V = 23.5 \text{ mag}$

$\int Q T d\lambda / \lambda = 0.0169$

$$\epsilon_f = 0.71$$

to obtain $C = 0.0789 \text{ e}^-/\text{second}$.

Now calculate the signal-to-noise ratio, using

$$N_{pix} = 25$$

$$B_{sky} = 0.0066 \text{ e}^-/\text{s/pix} \text{ from } \text{Table 9.1}$$

$$B_{det} = 0.0015 \text{ e}^-/\text{s/pix} \text{ from } \text{Table 5.1}$$

$$R = \text{read noise} = 3.1 \text{ e}^- \text{ per read from } \text{Table 5.1}$$

$$N_{read} = 1$$

$$N_{bin} = 1$$

$$P = 9 \text{ post flash electrons}$$

This gives a signal-to-noise ratio of 3.7. The SNR calculated this way is an estimate of the expected signal-to-noise, and results in a more pessimistic value than the ETC. Note that the count rate calculated by the ETC is ~12% greater than the result from the equation given here, which is an approximation. The ETC utilizes the model spectrum to determine the object count rate in a given filter. The equation given here calculates an estimated count rate based on approximations to the true color of a star.

9.9.3 Example 3: IR Imaging of a Faint Extended Source

What is the exposure time needed to obtain a signal-to-noise of 10 for an E0 elliptical galaxy that subtends an area of 1 arcsec² with an integrated V-magnitude of 26.7, when using the IR F140W filter? Assume a photometry box size of 9 × 9 pixels, and average sky values. The galaxy has a diameter of 1.13 arcsec, a surface brightness of 26.7 mag/arcsec², and fits within the 9 × 9 pixel box. For simplicity we will assume a redshift of 0.

The WFC3 [Exposure Time Calculator \(ETC\)](#) gives a total exposure time of 1206 sec to obtain this S/N in a single exposure. Although the non-destructive MULTIACCUM sequences on the IR channel can mitigate cosmic rays in a single read sequence, users are encouraged to dither their observations so that there are least 2 read sequences per field, to mitigate hot pixels and resample the point spread function. Re-running the calculation with 2 exposures gives an exposure time of 1320 sec. If we assume (as in Example 1) that we can fit two 1200-second exposures in an orbit, this program fits within a single orbit. Two SPARS50 sequences, with 15 samples (703 sec) per sequence should work well for this program.

Using the pencil-and-paper method, [Table 9.2](#) gives the integral $\int QTd\lambda/\lambda$ as 0.1550. We will assume that the elliptical galaxy resembles an old (10 Gyr) burst of star formation; looking in [Table A.2](#), the AB_V correction term is -1.41. We will assume that the 9 × 9 pixel box encloses all of the light for this object. The count rate can then be calculated from the equation

$$C = 2.5 \times 10^{11} \epsilon_f \left(\int QT \frac{d\lambda}{\lambda} \right) \times 10^{-0.4(V+AB_V)} ,$$

or $2.5 \times 10^{11} \times 0.1550 \times 1.0 \times 10^{-0.4(26.7-1.41)} = 2.97 \text{ e}^- \text{ s}^{-1}$, which is close to the ETCReturned value of 3.24. The exposure time can then be found by using the equation

$$t = \frac{\Sigma^2 [C + N_{pix}(B_{sky} + B_{det})] + \sqrt{\Sigma^4 [C + N_{pix}(B_{sky} + B_{det})]^2 + 4\Sigma^2 C^2 \left[\frac{N_{pix}}{N_{bin}} N_{read} R^2 \right]}}{2C^2},$$

to give $t = 1364$ s, which is close to the ETC-derived value of 1320 s. We have inserted the background rates of $B_{sky} = 1.1694$ (Table 9.2), $B_{det} = 0.05$ (Chapter 5), an effective read noise of 12.5 e⁻ per read (Chapter 5, assuming we are fitting the MULTIACCUM sequence), and 2 reads.

9.9.4 Example 4: Imaging an H II region in M83 in H-alpha

What is the exposure time needed to obtain a signal-to-noise of 10 for H α emission in an HII region which has a diameter of 2" and a flux F λ in H α of 5×10^{-16} ergs/cm²/s? Suppose that the H II region is in the outskirts of M83 (i.e., insignificant continuum radiation in a narrowband filter). It has a redshift of 0.0017, so H α appears at approximately 6574 Å. From an inspection of the throughput curves in Appendix A, we find the H α (F656N) filter cuts off at too short a wavelength, so we elect to use the Wide H α + [N II] (F657N) filter, which has a system throughput (QT_λ) of 25% at 6574 Å.

We use the equation in Section 9.4.3 to estimate the total count rate C for the emission line to be $2.28 \times 10^{12} * 0.25 * 5 \times 10^{-16} * 6574 = 1.87$ e⁻/s. The source covers approximately 2012 pixels, and the sky for this filter contributes 0.0029 e⁻/s/pixel (Table 9.1) while the dark rate is 0.0015 e⁻/s/pixel (Table 5.1). Thus the total background rate is 8.85 e⁻/s. Assuming 2 reads, no binning and a read noise of 3.1 e⁻ per read (Table 5.1), we find using the same formula as in Section 9.9.1 that the time to reach a S/N of 10 is 1217 sec.

For comparison, using the ETC, specify the source size as 2 arcsec in diameter, use a circular 1 arcsec radius extraction region, enter the emission line flux in ergs/cm²/s/arcsec² as 1.6×10^{-16} at 6574 Å. Assume a FWHM of 1 Å. The linewidth is not critical since the system throughput of this filter varies slowly with wavelength at 6574 Å, as can be seen in the throughput plot provided by the ETC. Assume average zodiacal light and average earthshine. The ecliptic latitude of the target is 18.4 deg; Figure 9.2 shows that this precludes very high levels of zodiacal light. To start with, assume that post-flash will not be used (0 electrons). The ETC computes that the exposure time for the two frames must sum to 1219 sec (20.3 minutes) to achieve S/N = 10. However, it gives a warning that the electrons per pixel due to background (2.6) is less than the recommended threshold of 12 e⁻/pix to avoid poor charge transfer efficiency (see Section 6.9). A post-flash level ~10 e⁻, to be added to each of the two frames, will be needed to bring the background up to the recommended level. Repeating the ETC calculation with Post Flash = 10 e⁻, you find that you need a total of 1691 sec (28.2 minutes) to make exposures with optimal CTE mitigation over the entire field of view.

Chapter 10: Overheads and Orbit Time Determinations

Chapter Contents

- [10.1 Overview](#)
- [10.2 Observatory Overheads](#)
- [10.3 Instrument Overheads](#)
- [10.4 Orbit Use Examples](#)

10.1 Overview

This chapter provides information for Phase I proposers who plan to use WFC3 for some or all of their planned *HST* observations. Because your Phase I proposal must state a specific integer number of *HST* orbits that are requested for your program, it is important that this number be as accurate as possible.

After you establish a set of scientific exposures, as well as any additional calibration exposures required for your program, you are ready to determine the total number of orbits to request in your Phase I proposal. The time requested should include not only the total exposure time, but also the additional time for the observatory and instrument operations needed to support those exposures. Those operations usually include acquiring (and possibly re-acquiring) guide stars, configuring WFC3 in preparation for an exposure, transferring data, and possibly repositioning the target in the focal plane between exposures.

It will often be necessary or desirable to achieve the total exposure time through a sequence of shorter exposures. For example, an exposure totaling several hours will be interrupted by target occultations. Moreover, UVIS exposures will almost always be obtained as a sequence of shorter exposures, in order to remove cosmic-ray hits. For your Phase I proposal, you should plan the sequences of exposures and overhead activities for each of the requested orbits. An overview of observation planning is given in [Chapter 4](#).

Generally, you will need to compile the overheads for your individual exposures, having packed an integer number of exposures and their supporting activities into individual orbits. Some activities may be executed while the target is occulted by the Earth, allowing more efficient utilization of an orbit. Finally, you will tally the exposure times and resulting overhead times required during visibility of the target in order to determine the total number of orbits needed. This may be an iterative process as you refine your exposures to better use the targets' orbit visibility (for non-CVZ targets).

The Phase I *Call for Proposals* includes instructions on observatory policies and practices regarding orbit time requests; see:

<https://hst-docs.stsci.edu/display/HSP/HST+Proposal+Opportunities+and+Science+Policies>

The *HST Primer* provides additional specific advice on how to determine the number of required orbits for your scientific program; see:

<https://hst-docs.stsci.edu/display/HSP/HST+Proposal+Opportunities+and+Science+Policies>

In the following sections, we provide a summary of the WFC3-specific overheads and give several examples that illustrate how to calculate your orbit request for a Phase I proposal.

The overheads presented below are approximate. These overhead times are to be used, in conjunction with the exposure times you determine and the instructions in the *HST Primer*, in order to estimate the total number of orbits for your Phase I proposal. If your *HST* proposal is accepted, you will then develop and submit a Phase II proposal to support the actual scheduling of your approved observations. At that time you will use the APT scheduling software (which employs more precise values for the various overheads) to craft exposure sequences that match orbital target visibility intervals and your allocation of orbits. Therefore, requesting sufficient time in your Phase I proposal for overhead operations is important; additional time to cover unplanned overhead will not be granted later.

10.2 Observatory Overheads

This section discusses the overheads involved in preparing the telescope for observations of a target. The next section describes the additional instrument-specific overheads involved in obtaining and storing the actual individual WFC3 exposures.

At the beginning of a sequence of WFC3 exposures, the telescope must acquire guide stars. The time required for this initial guide-star acquisition is 6 minutes. If the observations extend into the following orbit(s) following Earth occultation, you must also include the overhead for guide-star re-acquisition (another 5 minutes at the beginning of each new orbit). The only exception to this re-acquisition overhead occurs when you are observing a target in the Continuous Viewing Zone (CVZ; see the [HST Primer](#)), in which case guide-star re-acquisitions are unnecessary.

Following guide-star acquisition (or re-acquisition) and the first exposure during the orbit, it is likely that you will want to make a series of small telescope motions for the purpose of obtaining dithered observations. Each commanded movement of the telescope requires an amount of time ranging from 0.3 to 1.3 minutes, depending on the size of the motion. Furthermore, each time the telescope is moved more than 2 arcmin (e.g., for the purpose of constructing a mosaicked image), an additional guide-star acquisition will be necessary, requiring another 6 minutes.

When using WFC3's UVIS quad filters, it will often be necessary to repoint the telescope to place the target in the desired quadrant. This repositioning will require 1 minute. Due to the large field of view of WFC3/UVIS, offsets to different quadrants may require new guide stars to be acquired. Offsets between adjacent quadrants (e.g., A to B, or A to C) are small enough to maintain the same guide stars in many cases. However, offsets between diagonal quadrants (i.e., A to D, or B to C) are larger than 2 arcmin when using the "optimum" apertures, so the same guide stars cannot be used for diagonal quadrant offsets. For the "fixed" apertures, diagonal quadrant offsets are very close to 2 arcmin, so it is possible that the same guide stars may be used, depending on the placement of the particular guide stars. To determine whether quad filter observing sequences may require new guide star acquisitions, refer to [Table 6.4](#) for quad filter positions, to [Table 6.1](#) for aperture descriptions, and to the [SIAF](#) for aperture reference point definitions.

Table 10.1 summarizes the observatory-level overheads involved in WFC3 observing.

Table 10.1: Observatory Overhead Times.

Action	Overhead Time
Guide-star acquisition	6 minutes (first orbit)
Guide-star re-acquisitions	5 minutes at beginning of each new orbit for non-CVZ observing
	0 minutes for CVZ observing
New guide-star acquisition following dither of >2 arcmin	6 minutes
Spacecraft maneuvers	1 minute for offsets between 60 and 120 arcseconds
	0.8 minute for offsets between 28 and 60 arcseconds

	0.6 minute for offsets between 10 and 28 arcseconds
	0.5 minute for offsets between 1.25 and 10 arcseconds
	0.3 minute for offsets less than 1.25 arcsecond
	1 minute to offset to different UVIS quadrant (for quad filters)

10.3 Instrument Overheads

[10.3.1 Exposure Overheads](#)

[10.3.2 Reducing Overheads with Subarrays and Binning](#)

10.3.1 Exposure Overheads

The instrument-specific overhead times for WFC3 exposures are dominated by the time to move the filter wheels, to read out the detector, and especially to transfer and store the data. Although in a Phase II proposal the overheads computed with APT may prove to be smaller than the values given in this section, it is nevertheless important to plan your Phase I proposal using the conservative values given here in order to ensure the award of time adequate to attain your scientific goals.

Several kinds of overhead activities are associated with each exposure, and the specific activities depend on whether the exposure is a new one, or part of a series of associated ones. Associated exposures are defined as exposures of the same target, using the same filter and aperture, executed with or without dithering. Identical exposures are undithered associated exposures.

For UVIS ACCUM exposures (i.e., CCD exposures), identical exposures are generated if the observer specifies a CR-SPLIT number greater than 1 or specifies a Number of Iterations greater than 1. Dithered associated exposures are generated if the observer applies POS TARGs to the exposures or creates them in a Pattern container.

For IR MULTIACCUM exposures, CR-splitting is not used, but identical exposures can still be generated with Number of Iterations greater than 1, and dithered associated exposures can be generated as for UVIS. The full set of samples generated by a Sample Sequence is considered to be one exposure.

At the end of each UVIS or IR exposure, images are read into WFC3's internal buffer memory, where they are stored until they are transferred to *HST*'s solid-state data recorder. The time needed to read a UVIS CCD image is 98 seconds. The time needed for a single read of an IR image is 3 seconds, leading to a total of 48 seconds for a full 16-read exposure. These times are included in the overhead times for the first and subsequent exposures presented in [Table 10.2](#) below.

Dumping of the WFC3 Buffer

The WFC3 buffer provides temporary storage of images read from the WFC3 detectors before they are dumped through the *HST* science data formatter (SDF) to the solid state recorder (SSR). The buffer can be dumped either between exposures (a "serial" dump), or during an exposure (a "parallel" dump), but cannot overlap any commands executed in WFC3, including the commands at the beginning or at the end of an exposure. The buffer may be dumped during pointing maneuvers, but not during acquisition of guide stars. The buffer may be dumped during target occultation, which does not deduct from the target visibility time. Switching channels (IR and UVIS) does not require dumping the buffer. Observers will generally prefer to use parallel dumps, in order to more fully utilize the time when a target is visible for science exposures. Although buffer dumps are typically forced by science data volume, a buffer dump will also be

forced whenever the buffer holds 304 image headers, regardless of the size of the images themselves. The 304-file limit is unlikely to be reached under typical conditions.

The rules for dumping the buffer in parallel with UVIS exposures differ in some respects from those for dumping in parallel with IR exposures. The two channels are considered separately in the following paragraphs.

UVIS Parallel Buffer Dumps

The buffer can hold up to two full-frame UVIS images. A single full-frame image can be dumped in parallel with a UVIS exposure greater than 347 seconds, and two full-frame images can be dumped in parallel with a UVIS exposure greater than 663 seconds. When the buffer is dumped, all stored images must be dumped. Consequently, a sequence of 348-second (or longer) exposures will incur no overhead for dumping the buffer. Whether a sequence comprised of short exposures (less than 348 seconds) and long exposures (greater than 347 seconds) will require serial buffer dumps will depend upon the order of the long and short exposures and the duration of the long exposures. Dumping the buffer during a sequence of short and long exposures will be more efficient if the long exposures are 664 seconds (or longer). For example, an orbit with exposures with exposure times in the sequence 10-348-10-664-10-664-10 will incur no serial dump penalty. The observer will plan such sequences with APT in Phase II. Sequences of full-frame, un-binned exposures less than 348 seconds will require the overhead of serial buffer dumps. For short exposures, using subarrays or binning may be advantageous in order to reduce the overhead of serial buffer dumps. The time to dump a subarray or binned exposure scales approximately with the number of pixels stored in the buffer.

IR Parallel Buffer Dumps

The buffer can hold up to two full-frame, 15-sample IR images. To dump one such image in parallel with an IR exposure requires that exposure to be longer than 348 seconds. To dump two such images requires an exposure longer than 646 seconds. The rules for dumping IR exposures are somewhat more efficient than those for dumping UVIS exposures. For purposes of dumping IR exposures, each sample is treated individually; all samples in the buffer are not required to be dumped together; and samples can be dumped during the non-destructive read of the FPA. Sequences of full-frame, 15-sample exposures shorter than 349 seconds will require serial dumps after the second and subsequent exposures. Sequences of longer-exposure (i.e., greater than 348 seconds), full-frame, 15-sample exposures will incur no overhead for dumping the buffer. Sequences comprised of short (less than 349 seconds) full-frame, 15-sample exposures and long exposures (greater than 348 seconds) may incur overhead for serial dumps, depending upon the sequence of exposures and the duration of the long exposures. The observer will plan such sequences with APT in Phase II. The time to dump an n -sample, full-frame exposure is approximately $39 + 19 \times (n + 1)$ seconds. Subarrays may also be used to reduce the overhead of serial buffer dumps.

Filter and Channel Select Overheads

Both the UVIS and IR channels may be used during a single orbit, although not simultaneously. The time required to reconfigure between the two channels is 1 minute. If the buffer is full when switching channels, then time must also be taken to dump it before the exposure can begin with the other channel. Because the centers of the fields of view of the UVIS and IR channels are the same, acquisition of new guide stars is not required when changing channels to observe the same target.

The overhead for each exposure includes an allowance for the time required to position the filter or grism; however, selecting a UVIS quad filter requires an additional 1 minute of overhead to re-position the telescope, as indicated in [Table 10.1](#).

Table 10.2 summarizes all of the instrument overheads described in this subsection.

Table 10.2: WFC3 Instrument Overhead Times.

Action	Overhead Time (minutes)
Reconfiguration between UVIS & IR channels during a single orbit	1.0
UVIS ACCUM Mode	
Single exposure or first exposure in a set of associated exposures (e.g., the first sub-exposure of a Pattern or CR-SPLIT set)	2.6
Subsequent exposures in set of associated exposures (e.g., subsequent exposures in a Pattern or CR-SPLIT set), per exposure	2.1
Buffer dump if exposure is not last one in an orbit, or if next exposure is less than 348 seconds	5.8
Post-flash added to UVIS exposure	0.1
IR MULTIACCUM Mode	
Each exposure	1.0
Buffer dump if 16-read exposure is not last one in an orbit, or if next exposure is less than 346 seconds	5.8

10.3.2 Reducing Overheads with Subarrays and Binning

If your science program is such that a field of view smaller than the full detector size is adequate and you require many short exposures, then one way to reduce the frequency of buffer dumps, and hence their associated overheads, is to use a WFC3 subarray. Subarrays are described for the UVIS channel in [Section 6.4.4](#), and for the IR channel in [Section 7.4.4](#).

When subarrays are used, only a small region of the detector is read out and stored in WFC3's buffer. The reduced data volume permits a larger number of exposures to be stored in the buffer before the memory fills and it becomes necessary to transfer them to the telescope's solid-state recorder. Use of subarrays reduces the amount of time spent dumping the buffer, and also usually reduces detector readout time. (Note, however, that the full-quadrant UVIS 2K2 and UVIS-QUAD-SUB apertures have somewhat longer readout times than the full-detector apertures because of the way that the readout is performed.) A dump is still required if the 304-file limit is reached before buffer memory is filled.

Table 10.3 illustrates the advantage in orbit packing to be gained by using UVIS subarray apertures. We consider the case of a sequence of 5-second exposures without FLASH that fill a 3200 sec orbit as fully as possible. The table lists three subarray apertures of different sizes and a full detector aperture. The subarray apertures have been defined such that

they can be read out by one amplifier. The quadrants of the full detector aperture are read out by the four amplifiers simultaneously.

Table 10.3: Orbit structure for an orbit filled with 5-second exposures

Aperture	size (pixels)	#exp	Location of Buffer Dumps
UVIS2-C512C-SUB	513×512	44	In occultation
UVIS2-M1K1C-SUB	1024×1024	28	In occultation
UVIS2-2K2C-SUB	2047×2050	12	After 8 exposures & in occultation
UVIS-CENTER	$4 \times 2048 \times 2051$	7	After pairs of exposures & in occultation

The areas (A_{SA}) of the supported UVIS subarrays are 1/4, 1/16, or 1/64 of the area (A_{FF}) of a full-frame image. The areas of the IR subarrays are 1/4, 1/16, 1/64, or 1/256 of the area of a full-frame image. The number of subarray exposures that may be stored in the buffer, limited by image data volume, is $n = 2 (A_{FF}/A_{SA})$. For example, eight 1/4-area exposures may be stored in the buffer, which would allow eight 4-minute exposures to be taken and stored before having to dump the buffer. If the exposures were full-frame, the buffer would have to be dumped after each pair of observations, thus leading to very low observing efficiency.

The 304-file limit must also be considered in optimizing buffer dumps. For UVIS exposures, the limit will almost never be encountered. For IR exposures, each read (not each exposure) counts against the limit. The number of IR exposures that can be stored before a buffer dump is forced is therefore $n = 304/(NSAMP + 1)$, or 19 exposures for NSAMP = 15.

In the IR channel, certain combinations of subarrays and sample sequences give rise to images containing a sudden low-level jump in the overall background level of the image (see [Section 7.4.4](#)).

Data volume and overhead time can also be reduced for UVIS images by using on-chip binning of adjacent pixels, as described in [Section 6.4.4](#). By using 2×2 pixel binning, the data volume is reduced by a factor of 4, although the readout time is only reduced by about a factor of 2 to 50 sec. For 3×3 pixel binning it is reduced by a factor of 9, and the readout time by a factor of 4 to 23 s. IR readouts cannot be binned, but data volume may be reduced by taking less than the default 15 samples during an exposure.

10.4 Orbit Use Examples

- 10.4.1 Example 1: UVIS, 1 Orbit, 1 Filter
- 10.4.2 Example 2: UVIS, 1 Orbit, Short Exposures
- 10.4.3 Example 3: IR, 1 Orbit, 2 Filters
- 10.4.4 Example 4: UVIS, Dithering, 2 Orbits, 1 Filter
- 10.4.5 Example 5: IR, 1 Orbit, Grism

The easiest way to learn to estimate total orbit time requests is to work through a few examples. Below we provide five different examples:

1. A simple UVIS CR-SPLIT image using one filter.
2. A set of short UVIS exposures that require large overheads associated with buffer dumps.
3. A one-orbit IR observation using two different filters.
4. A two-orbit UVIS observation using dithering.
5. A one orbit IR grism spectroscopic observation.

10.4.1 Example 1: UVIS, 1 Orbit, 1 Filter

These examples represent fairly typical usage scenarios of WFC3. However, it should be noted that in several of the examples we have used un-dithered images. In most actual cases, observers are advised to use dithering. Furthermore, although observers can use the shadow or low-sky target visibility restrictions, the examples below are all for the standard (i.e., unrestricted) target visibility (see the [HST Primer](#), Section 6.3, for further discussion).

Consider a target to be imaged with UVIS in a given filter in one orbit. Let us suppose that, by using the [Exposure Time Calculator \(ETC\)](#) (see [Chapter 9](#)), we find that we need a total exposure time of 2400 s (40 minutes) to reach the desired S/N. Given that we desire the observation to be split into two exposures for cosmic-ray removal (using the default CR-SPLIT=2), we map the overheads and the science exposure times onto the orbit as follows:

Table 10.4: Orbit Calculation for Example 1

Action	Time (minutes)	Explanation
Guide-star acquisition	6.0	Needed at start of observation of new target
UVIS overhead for first sub-exposure	2.6	Includes filter change, camera set-up, and readout
First science sub-exposure	20.0	
UVIS overhead for second sub-exposure	2.1	Includes readout
Second science sub-exposure	<u>20.0</u>	Total exposure time is 40 min
Total time used	50.7	

Thus, with a total time of nearly 51 minutes, this set of observations would fit into all unrestricted *HST* orbits. The exposure time could, if needed, be adjusted so as to fill the actual target visibility interval (which depends on several factors, including the date and target location in the sky, as described in Chapter 6 of the *HST Primer*). The time needed to dump the buffer following the second sub-exposure incurs no overhead in this example, because it can be performed during target occultation.

It should be noted that this simple sequence of two fairly long, non-dithered exposures would produce an image with a gap between the two CCD chips (see [Section 6.3](#)), and that cosmic-ray removal might not be optimal (see [Section 5.4.10](#)).

10.4.2 Example 2: UVIS, 1 Orbit, Short Exposures

This example illustrates the impact of short exposures on the useful time in the orbit. Suppose we intend to use one orbit to observe a target with UVIS in two filters, F606W and F814W. The observation consists of two sequences, each one with two identical CR-SPLIT exposures, for a total of four individual sub-exposures. Suppose that the [ETC](#) shows that the exposure time must be 540 seconds for each of the filters, so each of the CR-SPLIT sub-exposures must be at least 270 seconds long. For the target declination, which in this example is -35° , we find that the unrestricted visibility time is 55 minutes. The time budget for the orbit is as follows:

Table 10.5: Orbit Calculation for Example 2

Action	Time (minutes)	Explanation
Guide-star acquisition	6.0	Needed at start of observation of new target
UVIS overheads for first sub-exposures in both series	$2 \times 2.6 = 5.2$	Includes filter change, camera set-up, and readouts
UVIS overheads for subsequent sub-exposures in both series	$2 \times 2.1 = 4.2$	Includes readouts
Buffer dump after 2nd sub-exposure	$2 \times 5.8 = 11.6$	Full buffer must be dumped in target visibility in order to obtain last two exposures, which are too short to accommodate dump ($270\text{ sec} < 339\text{ sec}$).
Science exposures	<u>$4 \times 4.5 = 18.0$</u>	
Total time used	45.0	

Compared with Example 1, we see that the efficiency is very low due to the large overheads associated with buffer dumps. We have achieved only 18 minutes of exposure time during 45 minutes of target visibility, whereas in Example 1

we obtained 40 minutes of exposure time during 51 minutes of visibility. Of course, this is caused by the short exposures of this example, versus the long exposures of Example 2, where “short” and “long” are relative to the time to dump the buffer, 339 seconds.

This time that is “lost” to dumping the buffer can be recovered by sufficiently increasing the exposure time. For example, if the 540-second exposure time is required to obtain a minimum S/N (and not to avoid saturation), then increasing the exposure times to 720 s will improve the S/N and require the same amount of target visibility time, 45 min.

Alternatively, if compatible with the scientific goals, a subarray could have been used to read out only a fraction of the detector area, allowing more frames to be stored in the buffer before requiring a dump. In this example, using UVIS 2k × 2k subarrays for 4 short (<339 seconds) exposures would save about 8 minutes of readout time and 12 minutes of dump time.

10.4.3 Example 3: IR, 1 Orbit, 2 Filters

The third example demonstrates the orbit calculation for a simple IR observation. We want to obtain full-frame images of a target in two filters, F110W and F160W. Suppose that the [ETC](#) has shown that the exposure times adequate for our scientific goals are 10 minutes in F110W and 20 minutes in F160W. These times can be achieved with the up-the-ramp MULTIACCUM sequences SPARS50 (11.7 min) and SPARS100 (23.4 min), respectively. From the orbit visibility table (see Chapter 6 of the [HST Primer](#)), suppose that we find that at the target declination (here assumed to be 0°) the unrestricted target visibility time is 54 minutes. The orbit calculation goes like this:

Table 10.6: Orbit Calculation for Example 3

Action	Time (minutes)	Explanation
Guide-star acquisition	6.0	Needed at start of observation of new target
IR overheads for 2 exposures	$2 \times 1.0 = 2.0$	Includes filter changes, camera set-ups, and readouts
Science exposure in F110W	11.7	
Science exposure in F160W	<u>23.4</u>	
Total time used	43.1	

The total time used in the orbit shows that our target can indeed be imaged in the selected filters within one orbit. Furthermore, the first exposure can be dumped from the buffer during the second exposure. The ~9 minutes of unused time could be used for an additional exposure, during which the second exposure would be dumped.

10.4.4 Example 4: UVIS, Dithering, 2 Orbits, 1 Filter

This example illustrates the orbit calculation for a UVIS observation with a WFC3 UVIS box dithering pattern, which implements imaging at four pointings. The goal of the observation is to obtain a dithered image of a field in such a way that would allow us to bridge the ~1.2 arcsec inter-chip gap between the UVIS CCDs in the combined image. As indicated

in Table 10.1, for a 2-arcsec offset maneuver, the three dithers will take 0.5 minutes each. Suppose we have determined that the exposure time necessary to reach the desired S/N ratio is 80 minutes, and that the visibility time at our target declination, assumed to be $+53^\circ$, is 58 minutes. Furthermore, we will use the cosmic-ray removal provided by the dither data-reduction package, and therefore set CR-SPLIT=NONE. As a result, the orbit calculation will involve a sequence of four exposures of 20-minutes duration (i.e., one exposure at each of the four dither pointings). These observations will be distributed across two *HST* orbits, as shown in the following Table 10.7.

Table 10.7: Orbit Calculation for Example 4.

Action	Time (minutes)	Explanation
Orbit 1		
Guide-star acquisition	6.0	Needed at start of observation of new target
UVIS overhead for first exposure	2.6	Includes filter change, camera set-up, and readout
UVIS overhead for second exposure	2.1	Includes readout
Spacecraft maneuver	0.5	To offset from first to second dither pointing
Two science exposures	<u>$2 \times 20 = 40.0$</u>	Exposures at the first two pointings in the dither pattern
Total time used in orbit 1	51.2	
Orbit 2		
Guide-star re-acquisition	5.0	Needed at start of new orbit to observe same target
UVIS overheads for 3rd and 4th exposures	$2 \times 2.1 = 4.2$	Includes readouts
Spacecraft maneuvers	$2 \times 0.5 = 1.0$	To offset to the 3rd and 4th dither pointings
Two science exposures	<u>$2 \times 20 = 40.0$</u>	Exposures at the final two pointings in the dither pattern
Total time used in orbit 2	50.2	

No overhead is incurred to dump the exposures, because they are all longer than 339 seconds. Thus the desired exposures can be accomplished within the two orbits, and in fact there are $\sim 7\text{--}8$ minutes of unused visibility time per orbit that could be used to increase the exposure times.

10.4.5 Example 5: IR, 1 Orbit, Grism

This example illustrates the orbit calculation for an IR G102 grism spectroscopic observation. We will use the full-frame, up-the-ramp MULTIACCUM sequence SPARS200 with NSAMP=13, requiring 40 minutes to expose. We will also obtain undispersed images to calibrate target positions and wavelengths, using a SPARS10 (2.4-minute) exposure before and after the grism exposure. The overhead calculations are presented in Table 10.8.

Table 10.8: Orbit Calculation for Example 5.

Action	Time (minutes)	Explanation
Guide-star acquisition	6.0	Needed at start of observation of new target
IR overheads for 3 exposures	$3 \times 1.0 = 3.0$	Includes filter changes, camera set-ups, and readouts
Science exposure (undispersed)	$2 \times 2.4 = 4.8$	SPARS10, NSAMP=15
Science exposure (grism)	<u>40.0</u>	SPARS200, NSAMP=13
Total time used	53.8	

The buffer dumps incur no overhead because the first undispersed exposure can be dumped during the long grism exposures, and the last two can be dumped during the subsequent target occultation. Thus, since at least 54 minutes of target visibility are available at any target's declination, this set of observations can be obtained in one orbit.

Appendix A: WFC3 Filter Throughputs

Appendix Contents

- [A.1 Introduction](#)
- [A.2 Throughputs and Signal-to-Noise Ratio Data](#)
 - [UVIS F200LP](#)
 - [UVIS F218W](#)
 - [UVIS F225W](#)
 - [UVIS F275W](#)
 - [UVIS F280N](#)
 - [UVIS F300X](#)
 - [UVIS F336W](#)
 - [UVIS F343N](#)
 - [UVIS F350LP](#)
 - [UVIS F373N](#)
 - [UVIS F390M](#)
 - [UVIS F390W](#)
 - [UVIS F395N](#)
 - [UVIS F410M](#)
 - [UVIS F438W](#)
 - [UVIS F467M](#)
 - [UVIS F469N](#)
 - [UVIS F475W](#)
 - [UVIS F475X](#)
 - [UVIS F487N](#)
 - [UVIS F502N](#)
 - [UVIS F547M](#)
 - [UVIS F555W](#)
 - [UVIS F600LP](#)
 - [UVIS F606W](#)
 - [UVIS F621M](#)
 - [UVIS F625W](#)
 - [UVIS F631N](#)
 - [UVIS F645N](#)
 - [UVIS F656N](#)
 - [UVIS F657N](#)
 - [UVIS F658N](#)
 - [UVIS F665N](#)
 - [UVIS F673N](#)
 - [UVIS F680N](#)
 - [UVIS F689M](#)
 - [UVIS F763M](#)

- [UVIS F775W](#)
- [UVIS F814W](#)
- [UVIS F845M](#)
- [UVIS F850LP](#)
- [UVIS F953N](#)
- [UVIS FQ232N](#)
- [UVIS FQ243N](#)
- [UVIS FQ378N](#)
- [UVIS FQ387N](#)
- [UVIS FQ422M](#)
- [UVIS FQ436N](#)
- [UVIS FQ437N](#)
- [UVIS FQ492N](#)
- [UVIS FQ508N](#)
- [UVIS FQ575N](#)
- [UVIS FQ619N](#)
- [UVIS FQ634N](#)
- [UVIS FQ672N](#)
- [UVIS FQ674N](#)
- [UVIS FQ727N](#)
- [UVIS FQ750N](#)
- [UVIS FQ889N](#)
- [UVIS FQ906N](#)
- [UVIS FQ924N](#)
- [UVIS FQ937N](#)
- [IR F098M](#)
- [IR F105W](#)
- [IR F110W](#)
- [IR F125W](#)
- [IR F126N](#)
- [IR F127M](#)
- [IR F128N](#)
- [IR F130N](#)
- [IR F132N](#)
- [IR F139M](#)
- [IR F140W](#)
- [IR F153M](#)
- [IR F160W](#)
- [IR F164N](#)
- [IR F167N](#)

A.1 Introduction

This appendix contains plots of throughputs and sensitivities for each WFC3 filter. It is organized by *detector* and *filter*. For each imaging mode the following are provided:

- Plots of integrated system throughput for each filter as a function of wavelength.
- Plots of the time needed to achieve a desired signal-to-noise ratio vs. magnitude for each filter for a point-source and for a 1"×1" extended source.
- Tables of color corrections AB_V to go from Johnson V magnitude to AB magnitude for stellar spectra (as a function of effective temperature) and composite populations (as a function of age). The stellar spectra come from the Lejeune et al. (1997, *A&AS*, **125**, 229) grid, and assume a surface gravity of $\log g = 5$ and solar metallicity. The composite populations come from the "instantaneous burst" and "continuous star formation" models of Bruzual & Charlot (1993, *ApJ*, **405**, 539), updated in 1995, assuming a Salpeter IMF spanning 0.1 to 125 solar masses.

The plots presented here were derived using on-orbit data that was processed with ground-based flat field reference files. (See [WFC3 ISR 2009-30](#) and [WFC3 ISR 2009-31](#)) These flat fields are in error by up to several percent on large spatial scales (see Sections 5.4.3 and 5.7.4.). Monitoring of photometric performance over the first year of operations showed the WFC3/UVIS detector to be stable to rms $\sim 0.5\%$ ([WFC3 ISR 2010-14](#)) and the WFC3/IR detector to be stable to rms $\sim 0.5\%$ to 1.0%, depending on filter ([WFC3 ISR 2011-08](#)). Small photometric drifts have been detected in the UVIS channel during continued monitoring from 2009 to mid-2014 ([WFC3 ISR 2014-20](#)). There has been a slight increase in throughput in the UV filters ($\sim 0.1\%/\text{year}$) and slight decreases in throughput in red and visible filters ($0.2\%/\text{year}$ and $0.4\%/\text{year}$, respectively). No contamination effects have been detected.

We provide photometric transformation coefficients for converting magnitudes from the native WFC3/UVIS passbands to Johnson/Cousins UBVRI passbands in the ABMAG, STMAG, and VEGAMAG systems in [WFC3 ISR 2014-16](#).



For more information on system throughputs and tabular files to download, see the [HST System Throughputs website](#).

A.2 Throughputs and Signal-to-Noise Ratio Data

A.2.1 Sensitivity Units and Conversions

A.2.2 Signal-to-Noise Ratio

A.2.1 Sensitivity Units and Conversions

This appendix contains plots of throughputs for each WFC3 filter. [Section 9.3](#) explains how to use these throughputs to calculate expected count rates from your source.

The first figure for each filter gives the integrated system throughput based on on-orbit observations of spectrophotometric standards. This is the combination of the efficiencies of the detector and of the optical elements in the light path. The throughput is defined as the number of detected counts/second/cm² of telescope area relative to the incident flux in photons/cm²/s. For both the UVIS and IR channels, "counts" is the number of electrons detected. In both channels the detected counts obey Poisson statistics, except that at short wavelengths in the UVIS channel, a single incoming photon has a finite chance of producing multiple electrons in the CCD. [Section 5.4.2](#) describes this phenomenon, which was measured to have a much smaller effect in the UVIS detectors compared to theoretical predictions. The plots in this appendix have been corrected to remove multiple electrons generated by UV photons, using a correction that is intermediate between the theoretical and measured UVIS "quantum yields." The throughput includes all obscuration effects in the optical train (e.g., due to the *HST* secondary).

All wavelength measurements for the UVIS and IR channel filters were done in a gaseous medium: air for UVIS measurements and helium for IR measurements. The results have been converted to vacuum wavelengths using the indices of refraction of the gaseous media. The UVIS laboratory measurements were done at a temperature of 20°C, whereas the filters are operated on orbit at 0°C; this may lead to wavelength shifts which are expected to be small. The IR laboratory measurements were done at a temperature of -30°C, whereas the filters are operated on orbit at -35°C; this may lead to wavelength shifts which are expected to be very small.

Note that the tables in the [synphot](#) package and the [WFC3 Exposure Time Calculator](#) all assume vacuum wavelengths for both the UVIS and IR filter transmission data.

Because we have applied a correction to the throughputs for quantum yield in order to derive appropriate counting statistics for the source, the sensitivity calculations shown here are conservative in background- or read-noise-dominated regimes; the additional signal electrons from the enhanced UV quantum yield will increase the detection of faint sources in the 200–300 nm range somewhat vs. these sample calculations.

To recalculate the throughput with the most recent detector QE tables in [synphot](#), you can create total-system-throughput tables (instrument plus OTA) using the [synphot calcband](#) task. **calcband** takes any valid **obsmode** command string as input and produces a table with two columns of data called "wavelength" and "throughput" as its output. For

example, to evaluate the throughput for the F475W filter and the UVIS detector, Chip 1, you would use the command `calcband wfc3, uvis1, f475w sdssg_thpt`. The resulting throughput table is stored in an IRAF table, `sdssg_thpt`. The table can be converted to standard text format with `tdump "sdssg_thpt" datafile="sdssg_thpt.txt" columns="wavelength, throughput"`.

A.2.2 Signal-to-Noise Ratio

For each imaging mode, plots are provided to estimate the signal-to-noise ratio (S/N) for a representative source. The first figure shows S/N for point sources. The second figure shows S/N for uniform extended sources of area 1 arcsec².

The different line styles in the S/N figures delineate regions where different sources of noise dominate. If the total noise from backgrounds (read noise, sky, thermal, dark) is larger than the noise from the source, the observation is considered to be background-dominated, and the line style reflects which background source is largest. Note that for the WFC3 detectors, the dark current can never be the largest source of noise when a source is background-dominated, because the read noise is always larger than the dark count noise when exposures are 1000 s or less. The point- and extended-source S/N figures assume average sky levels. These plots also indicate where an observation will saturate the full well of the detector.

For point sources, an aperture size of 5 × 5 pixels has been used for the UVIS channel, while an aperture size of 3b × b3 pixels has been used for the IR channel. For extended sources, a 1 arcsec² aperture was used. The read noise has been computed assuming a number of readouts `NREAD= integer` ($t/1000$ s), where t is the exposure time, with a minimum `NREAD=2`.

In situations requiring more detailed calculations (non-stellar spectra, extended sources, other sky background levels, unknown target V magnitude, etc.), the WFC3 [Exposure Time Calculator](#) should be used.

Follow these steps to use the signal-to-noise plots:

1. Determine the AB magnitude of your source at the wavelength of interest. There are several ways to do this.
 - Examine Tables A.1, A.2, or A.3 and find AB_{ν} for the desired spectral type and filter. Sum the V magnitude of the target and AB_{ν} derived from the table.
 - Alternatively, compute $ABMAG (=V+AB_{\nu})$ from the source flux, using the relation.

$$ABMAG = -2.5 \log f_{\nu} - 48.60 ,$$

or

$$ABMAG = -2.5 \log f_{\lambda} - 5 \log \lambda - 2.406 .$$

2. Find the appropriate plot for the filter in question, and locate $V+AB_{\nu}$ on the horizontal axis. Then read off the signal-to-noise ratio for the desired exposure time, or vice-versa.

Note that the plots show the S/N as a function of source magnitude for exposure times as short as 0.1 s, although the minimum exposure time for the UVIS channel is actually 0.5 s.

UVIS F200LP

Description

Clear.

Figure A.1: Integrated system throughput for F200LP.

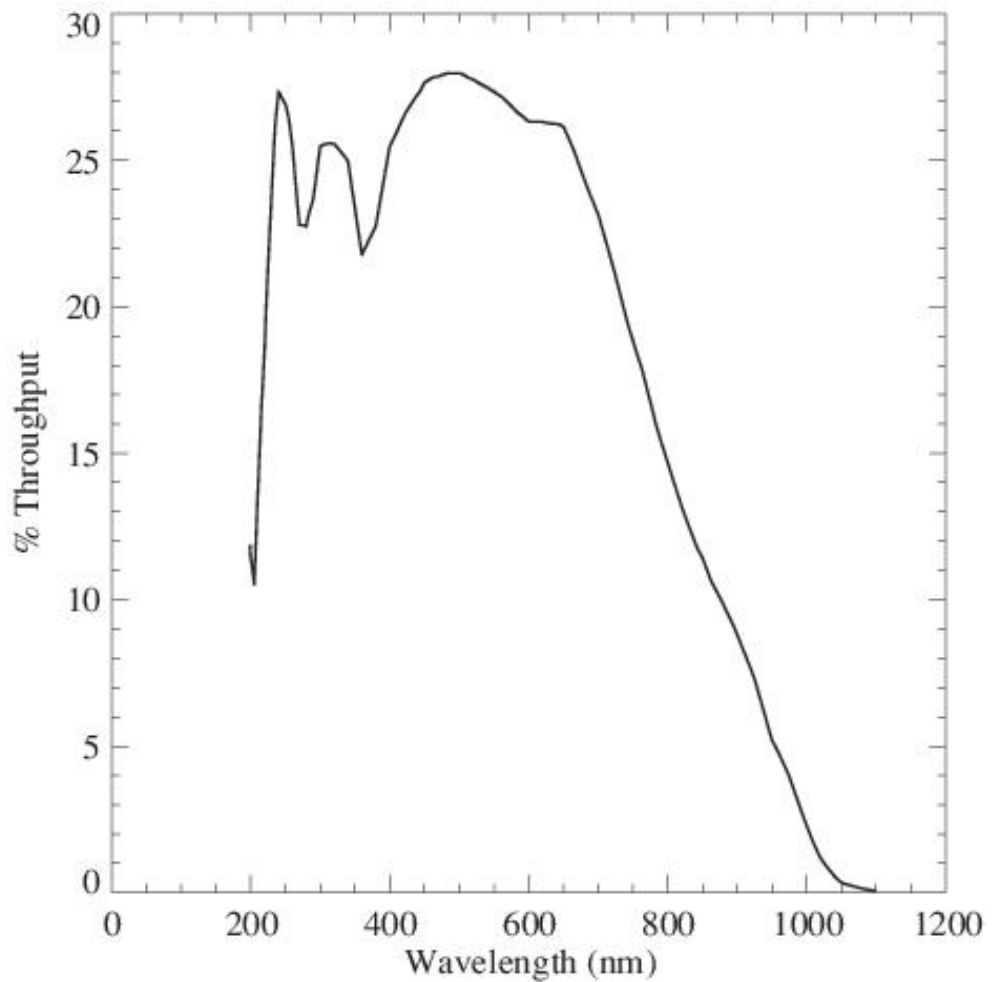


Figure A.2: Point source S/N vs. $V+AB_v$ for the F200LP filter, assuming high sky backgrounds and a 5×5 pixel aperture.

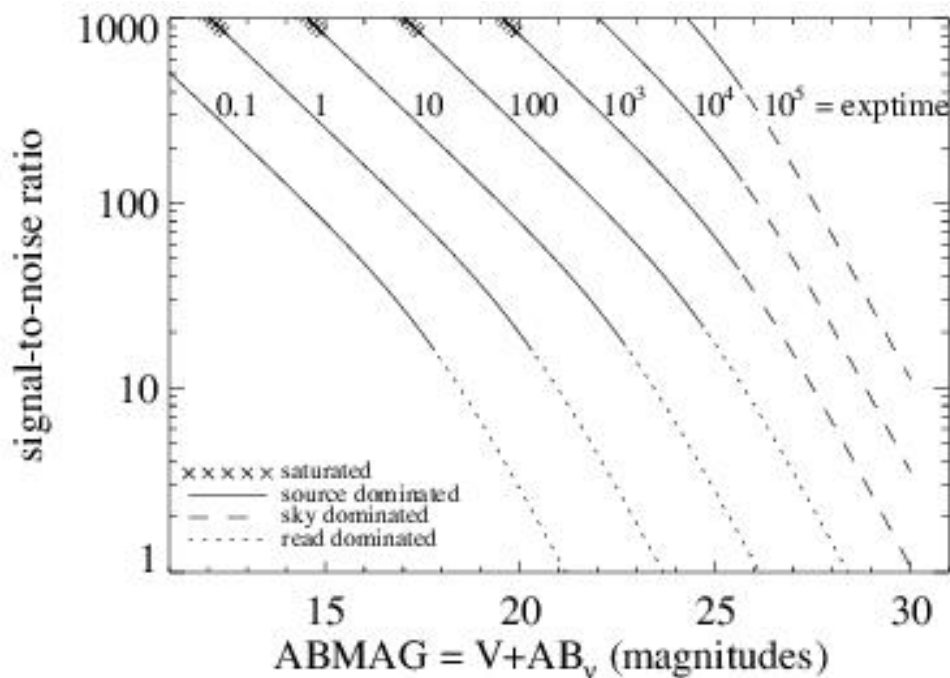
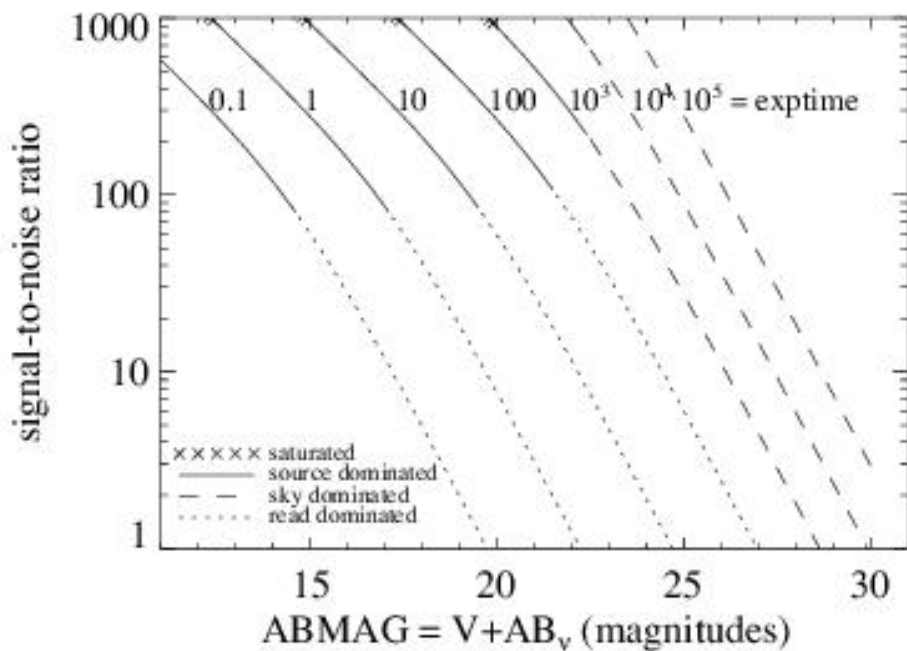


Figure A.3: Extended source S/N vs. $V+AB_V$ for the F200LP filter, assuming high sky backgrounds and a source uniformly filling a 1 arcsec^2 aperture.



UVIS F218W

Description

ISM feature filter.

Figure A.4: Integrated system throughput for F218W.

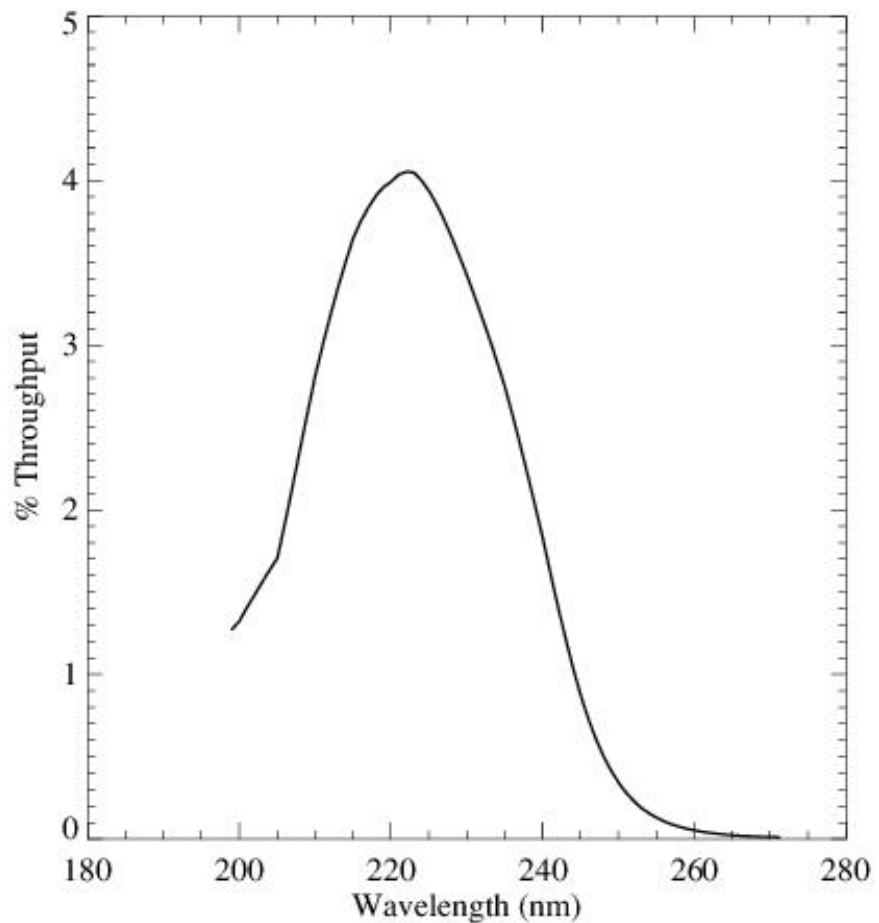


Figure A.5: Point source S/N vs. $V+AB_v$ for the F218W filter, assuming high sky backgrounds and a 5×5 pixel aperture.

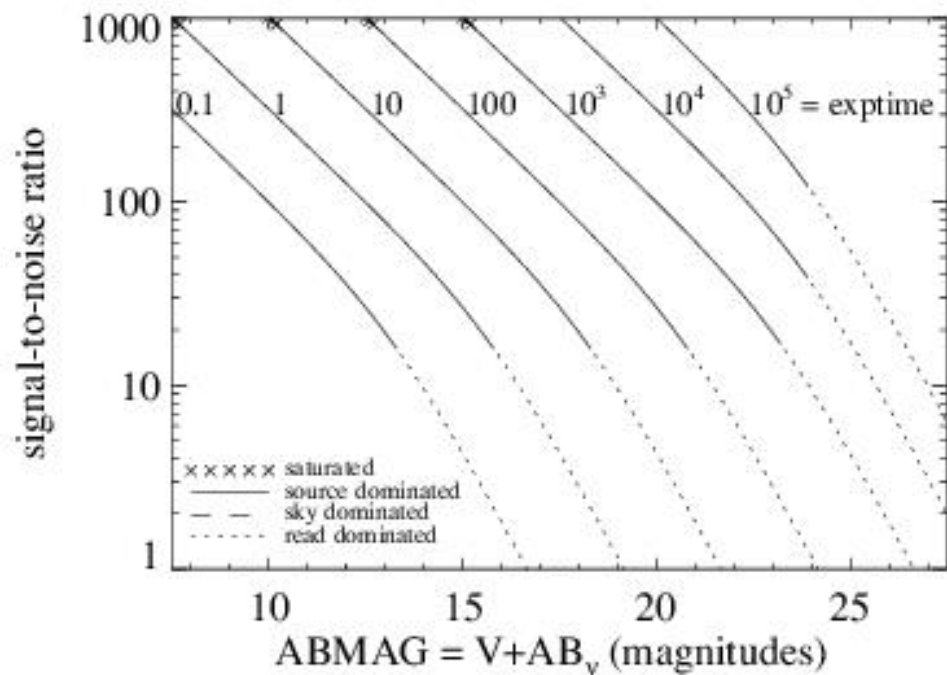
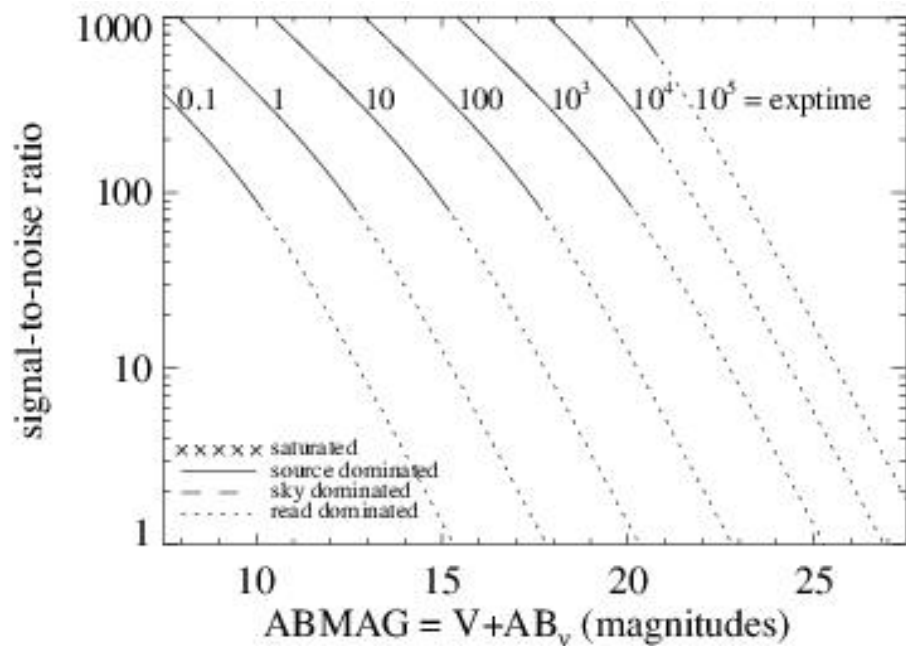


Figure A.6: Extended source S/N vs. $V+AB_v$ for the F218W filter, assuming high sky backgrounds and a source uniformly filling a 1 arcsec^2 aperture.



UVIS F225W

Description

UV wide filter.

Figure A.7: Integrated system throughput for F225W.

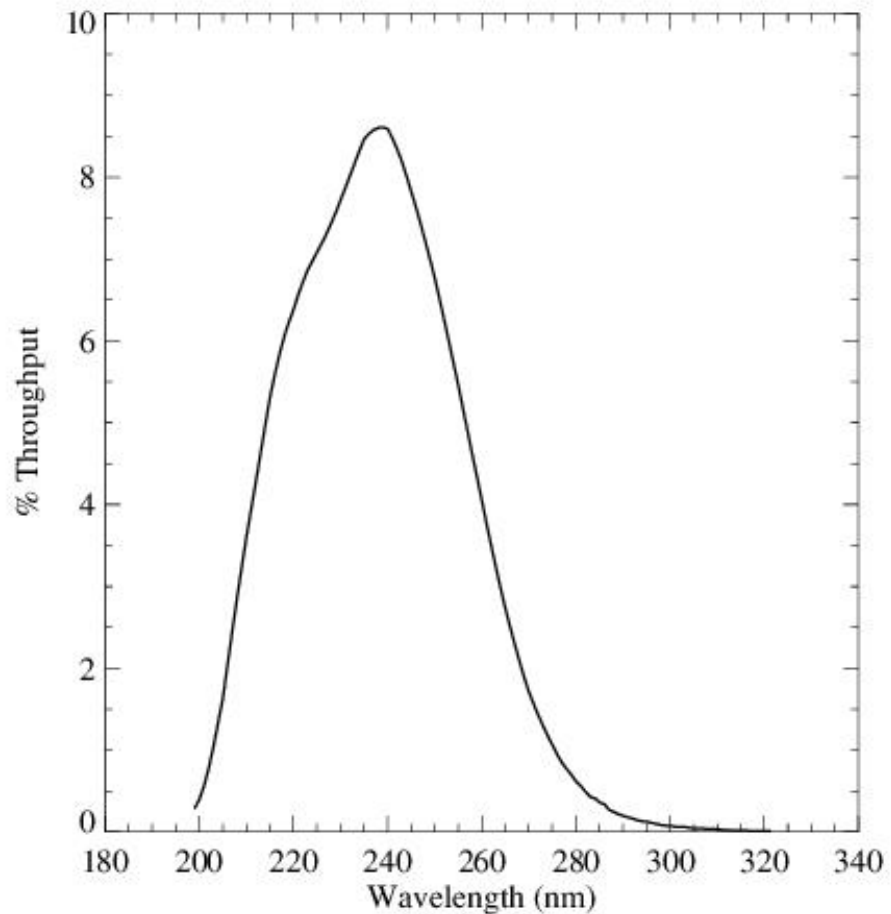


Figure A.8: Point source S/N vs. $V+AB_v$ for the F225W filter, assuming high sky backgrounds and a 5×5 pixel aperture.

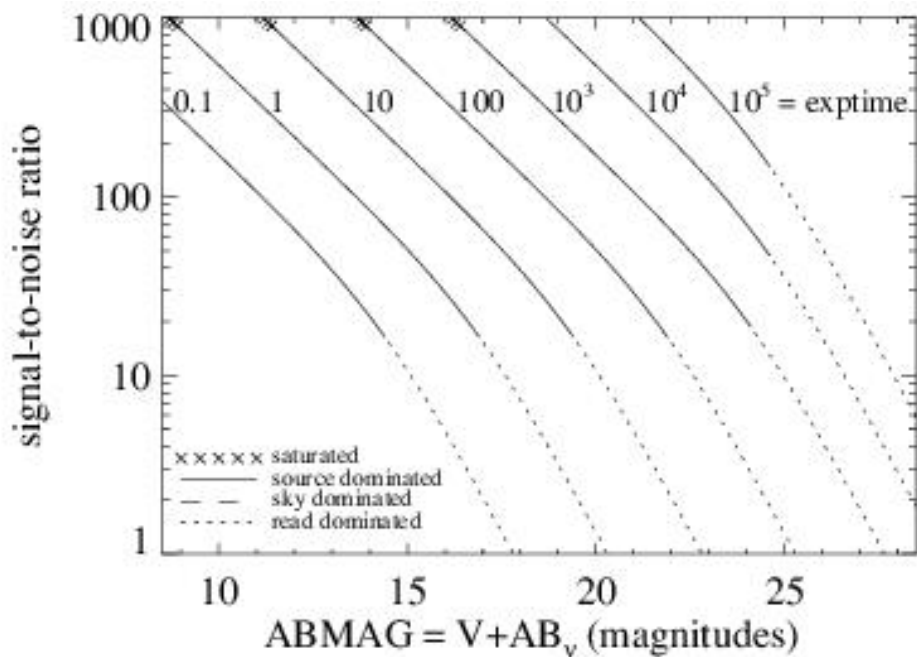
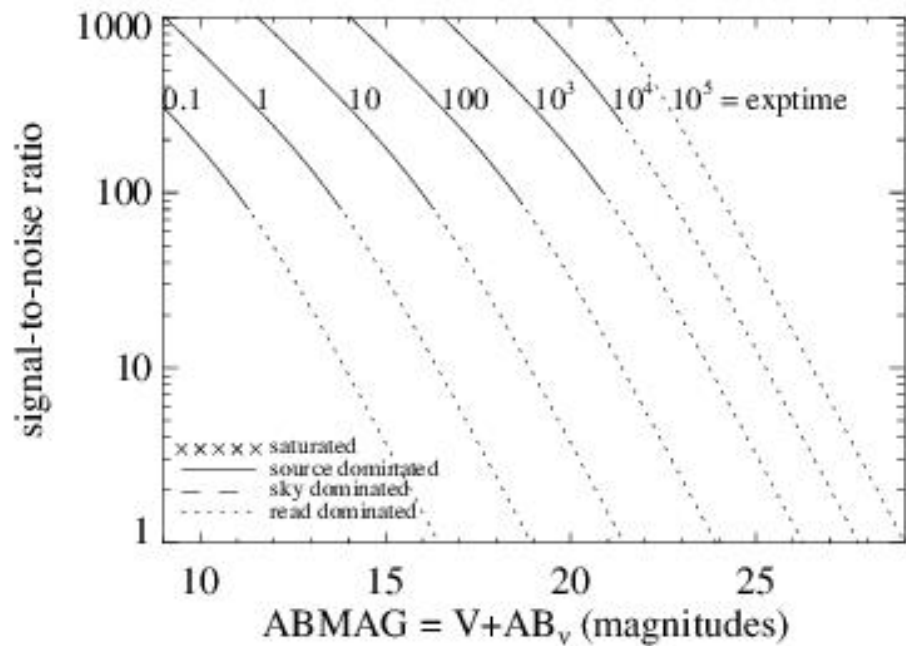


Figure A.9: Extended source S/N vs. $V+AB_V$ for the F225W filter assuming high sky backgrounds and a source uniformly filling a 1 arcsec^2 aperture.



UVIS F275W

Description

UV wide filter.

Figure A.10: Integrated system throughput for F275W.

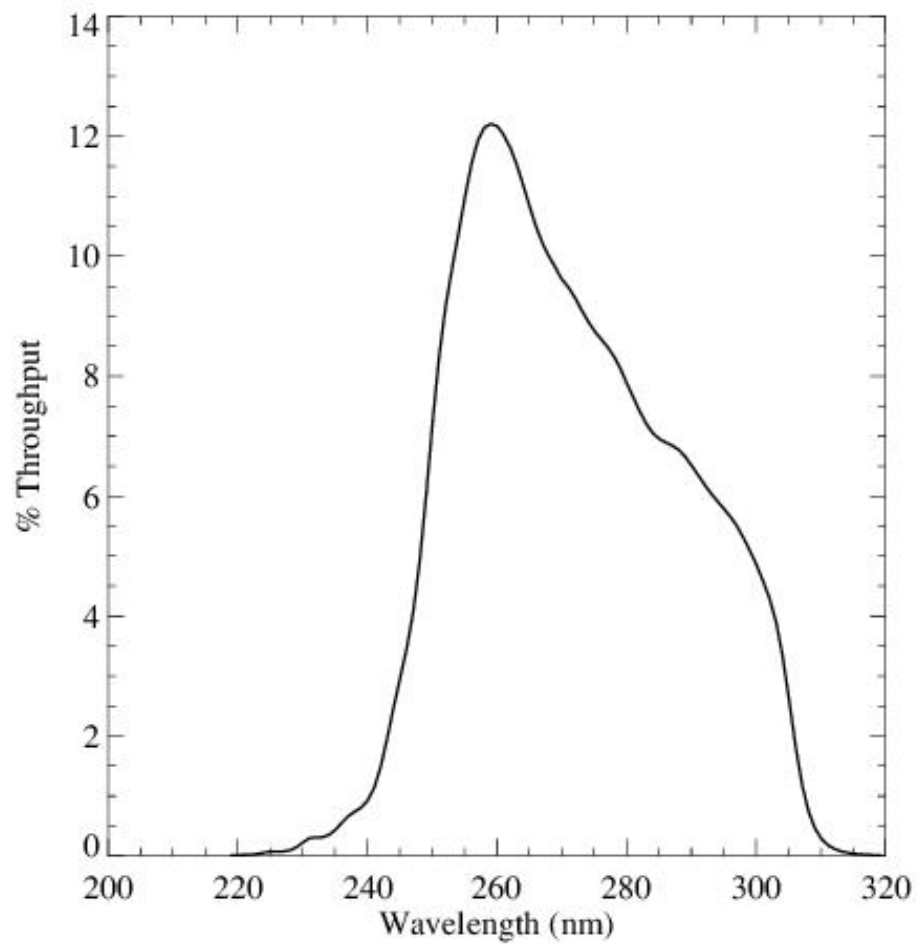


Figure A.11: Point source S/N vs. $V+AB_v$ for the F275W filter, assuming high sky backgrounds and a 5×5 pixel aperture.

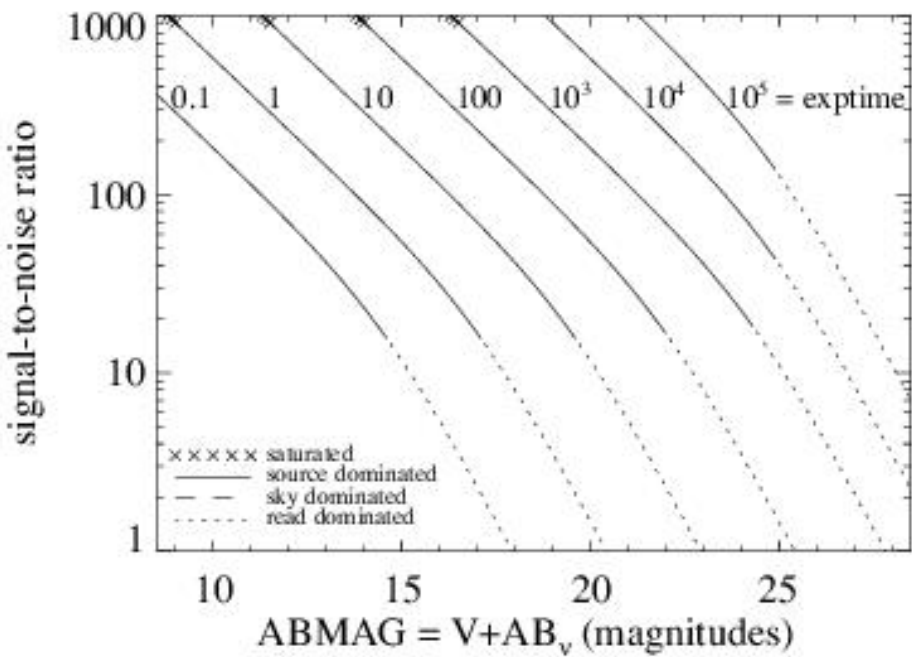
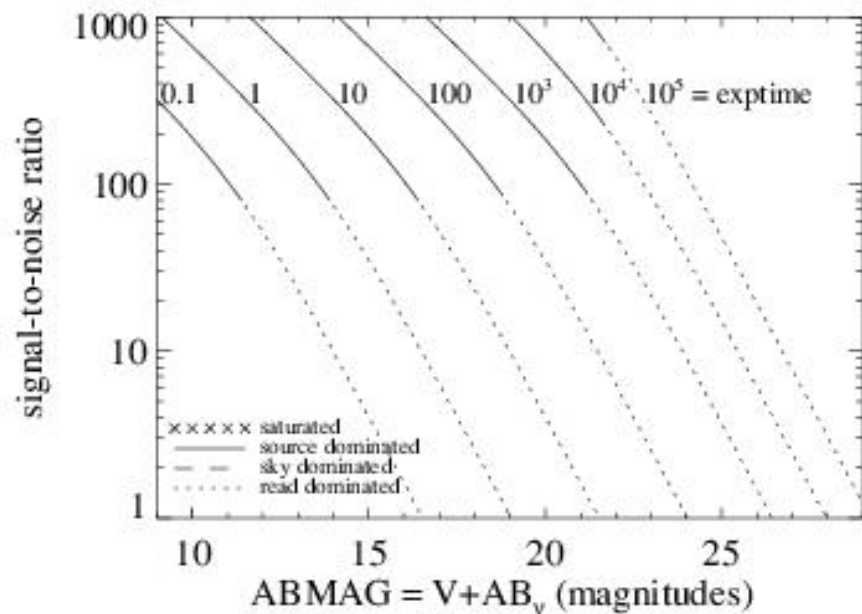


Figure A.12: Extended source S/N vs. $V+AB_V$ for the F275W filter, assuming high sky backgrounds and a source uniformly filling a 1 arcsec^2 aperture.



UVIS F280N

Description

Mg II 2795/2802 filter.

Figure A.13: Integrated system throughput for F280N.

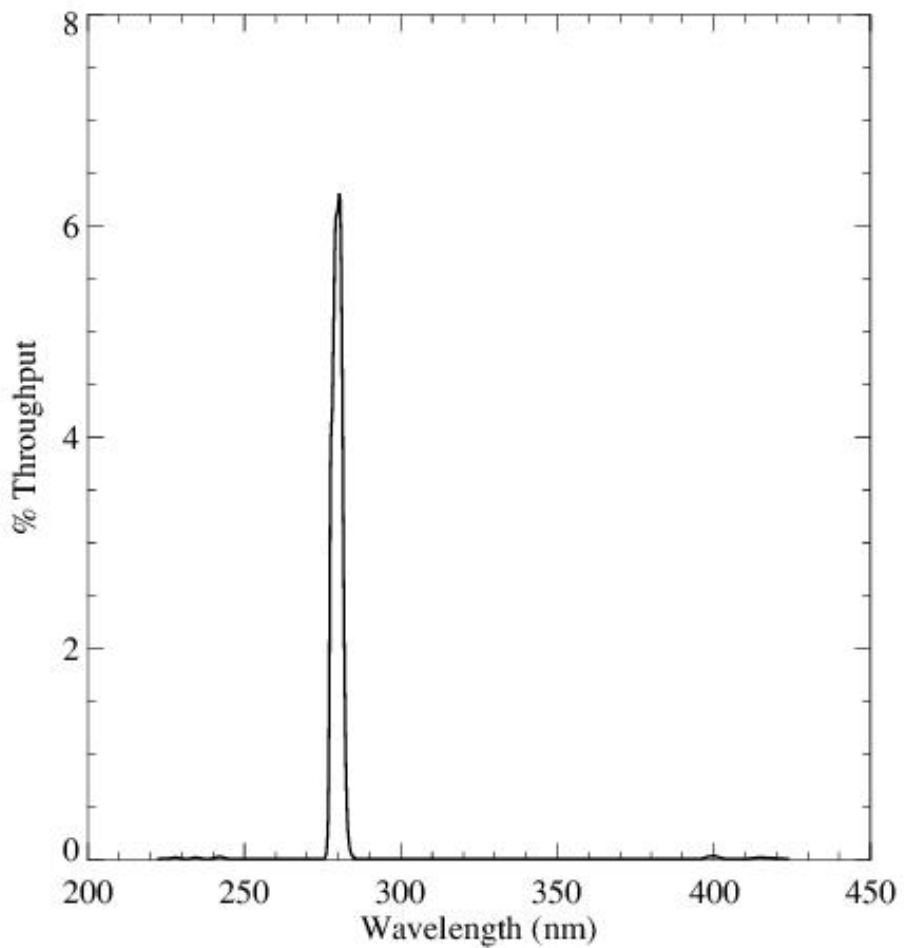


Figure A.14: Point source S/N vs. $V+AB_v$ for the F280N filter, assuming high sky backgrounds and a 5×5 pixel aperture.

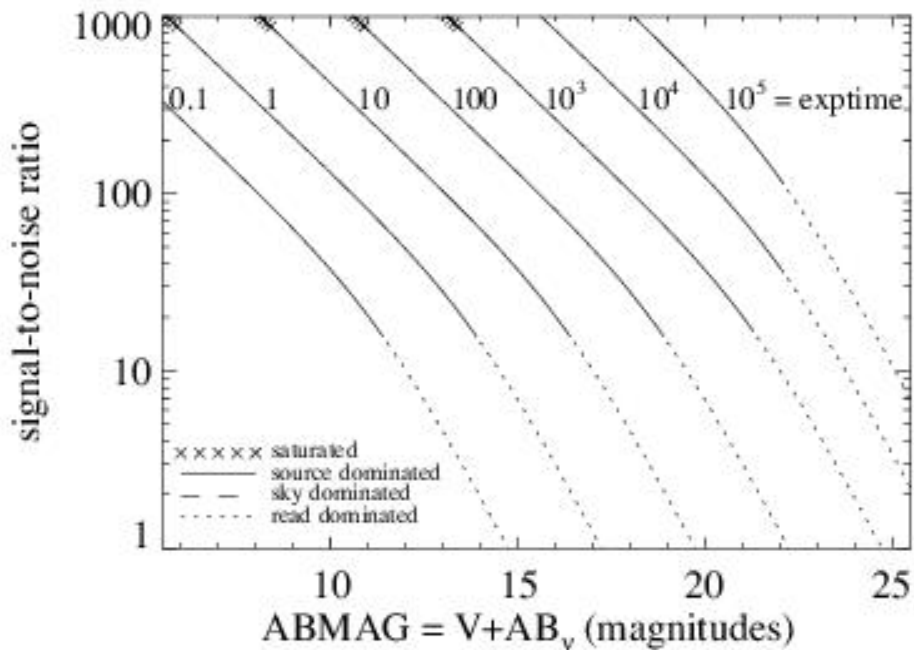
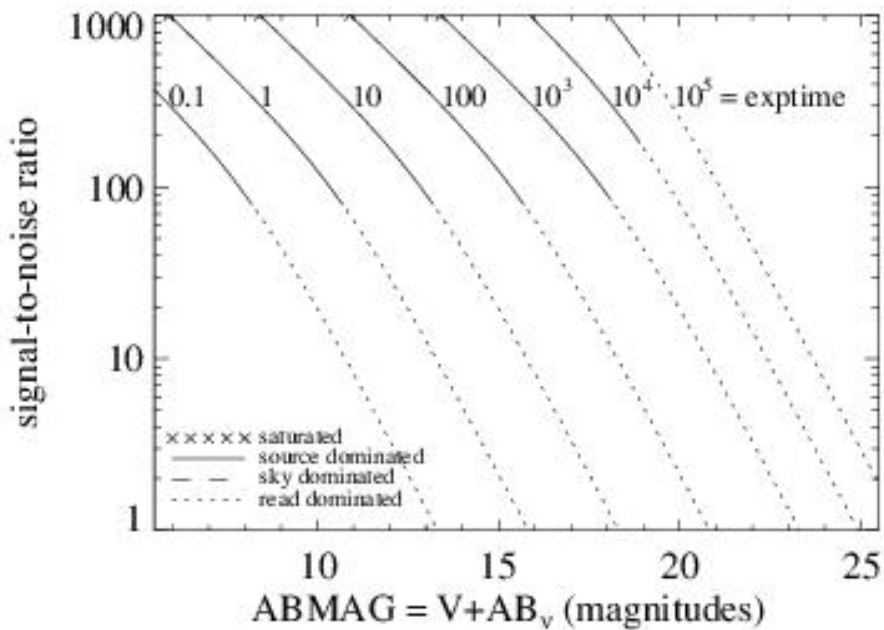


Figure A.15: Extended source S/N vs. $V+AB_V$ for the F280N filter, assuming high sky backgrounds and a source uniformly filling a 1 arcsec^2 aperture.



UVIS F300X

Description

Extremely wide UV filter; grism reference.

Figure A.16: Integrated system throughput for F300X.

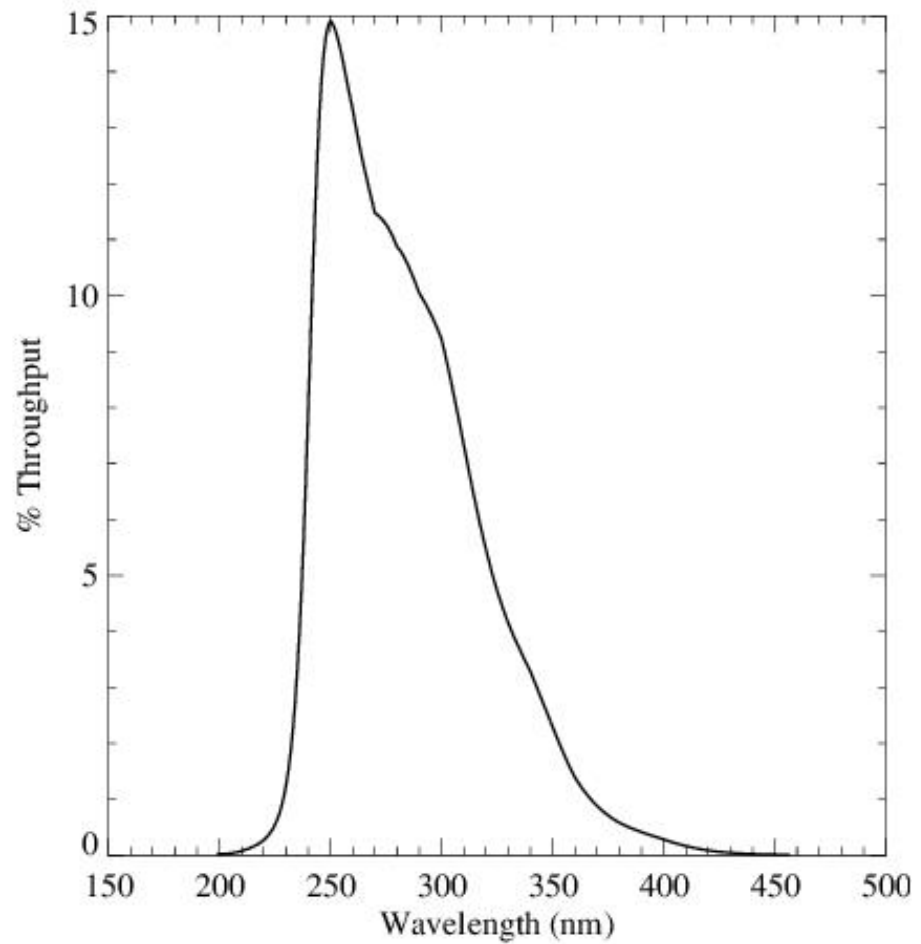


Figure A.17: Point source S/N vs. $V+AB_v$ for the F300X filter, assuming high sky backgrounds and a 5×5 pixel aperture.

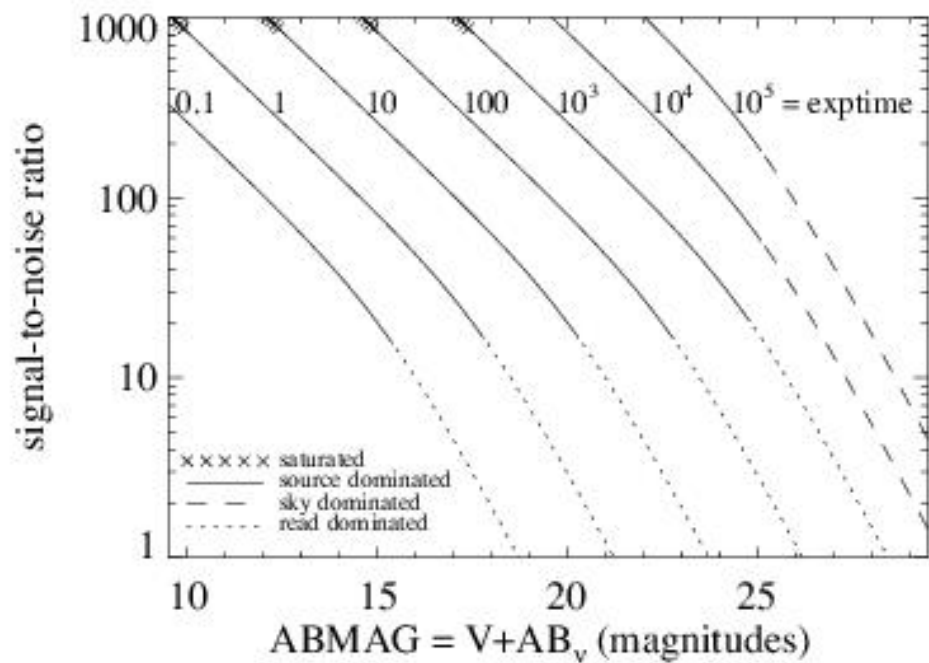
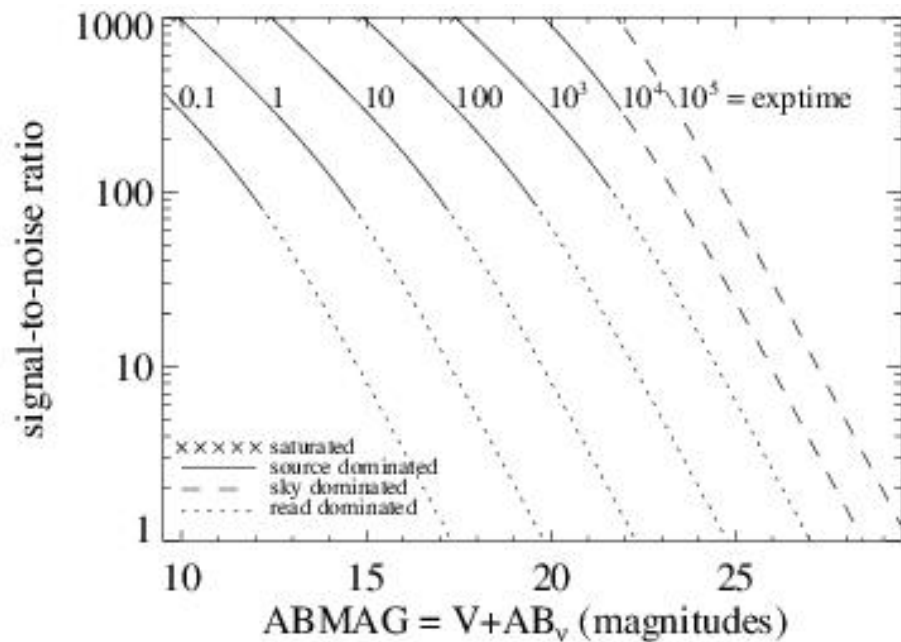


Figure A.18: Extended source S/N vs. $V+AB_V$ for the F300X, assuming high sky backgrounds and a source uniformly filling a 1 arcsec^2 aperture.



UVIS F336W

Description

U, Strömgren *u* filter.

Figure A.19: Integrated system throughput for F336W.

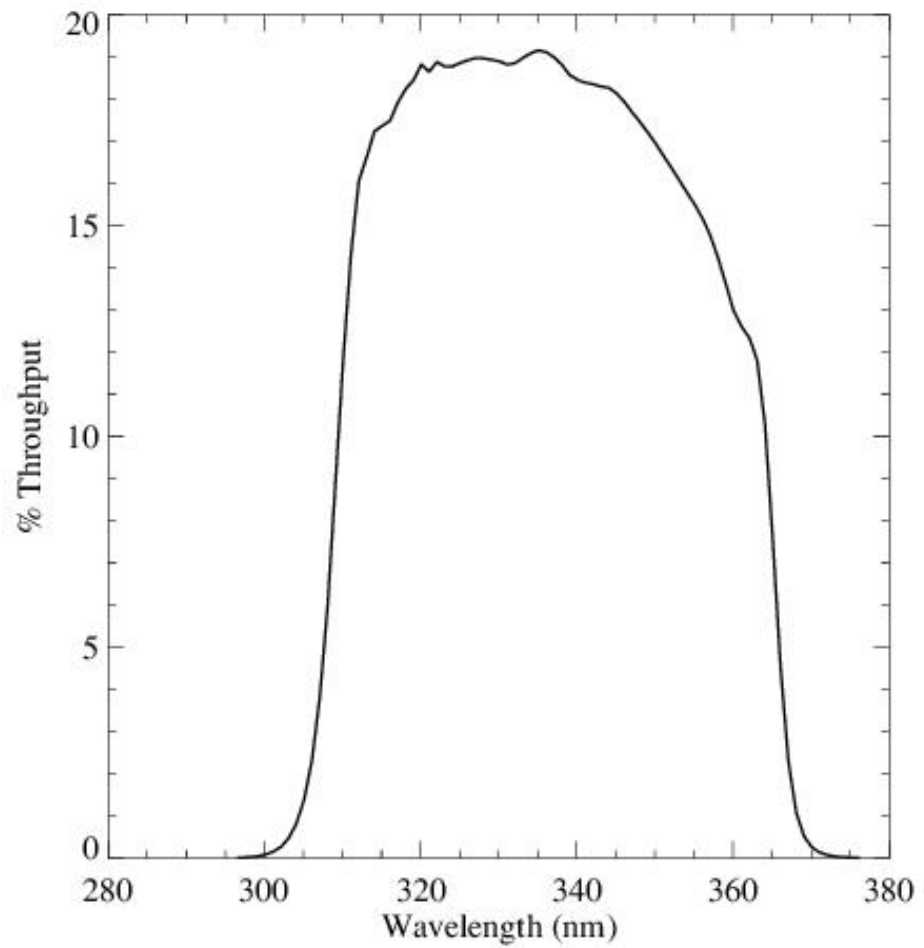


Figure A.20: Point source S/N vs. $V+AB_v$ for the F336W filter, assuming high sky backgrounds and a 5×5 pixel aperture.

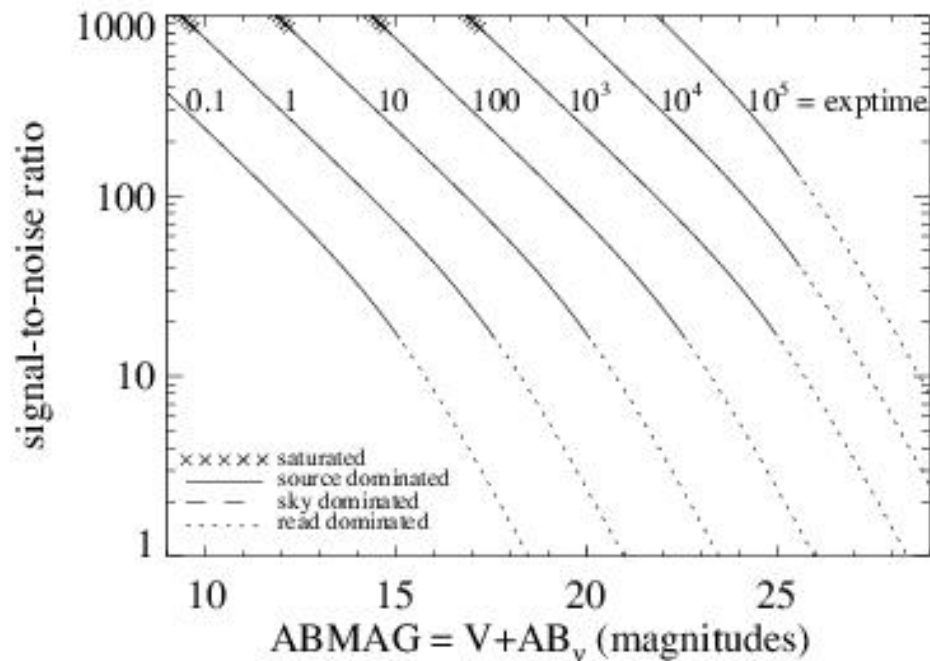
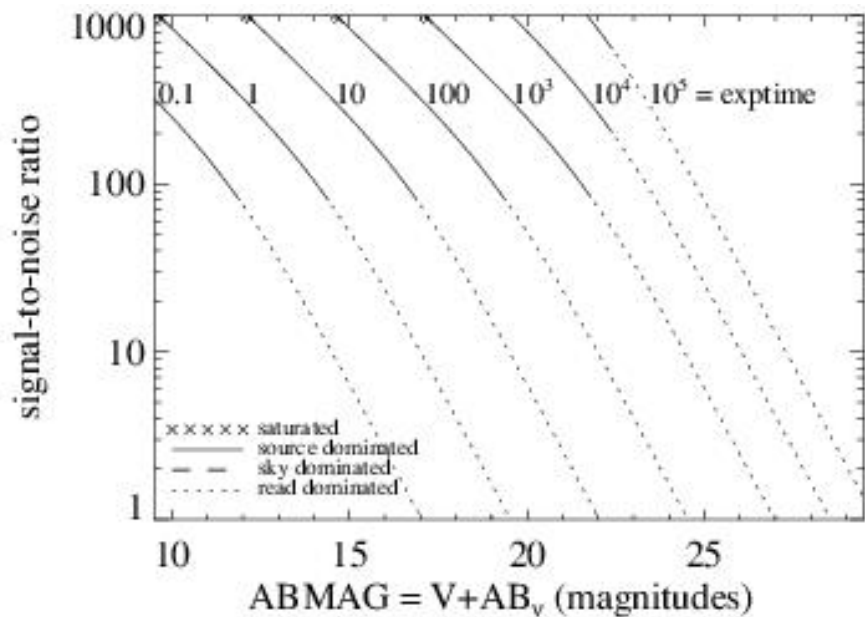


Figure A.21: Extended source S/N vs. $V+AB_v$ for the F336W filter, assuming high sky backgrounds and a source uniformly filling a 1 arcsec^2 aperture.



UVIS F343N

Description

[Ne v] 3426 filter.

Figure A.22: Integrated system throughput for F343N.

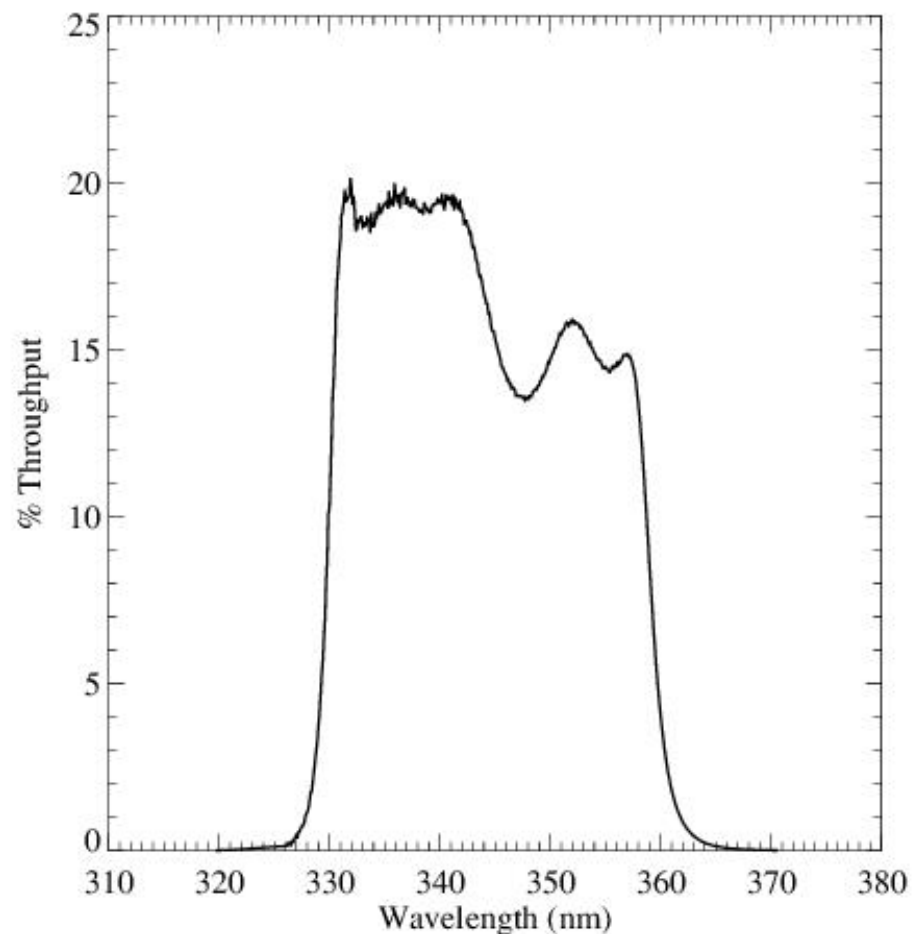


Figure A.23: Point source S/N vs. $V+AB_v$ for the F343N filter, assuming high sky backgrounds and a 5×5 pixel aperture.

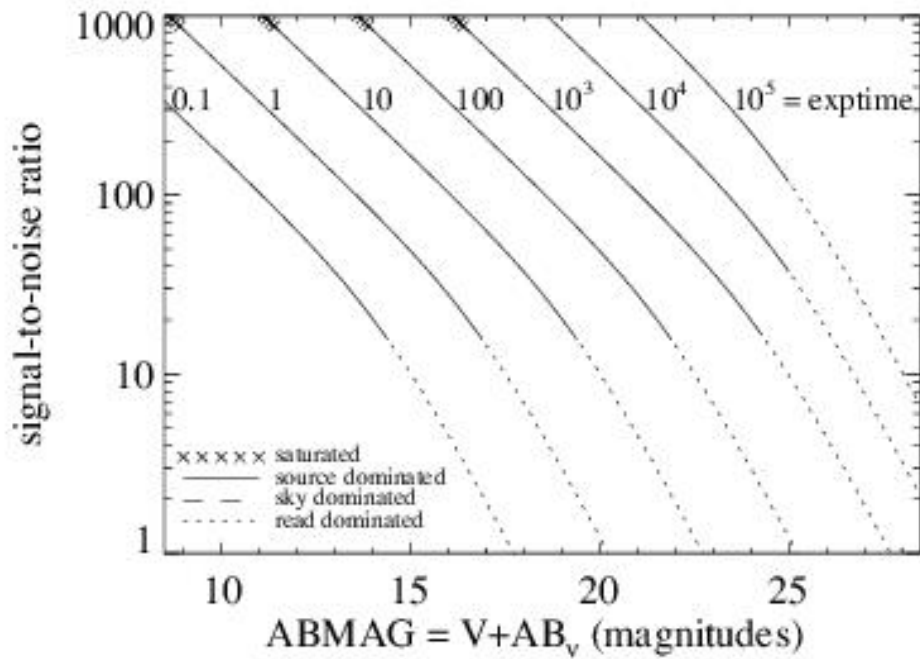
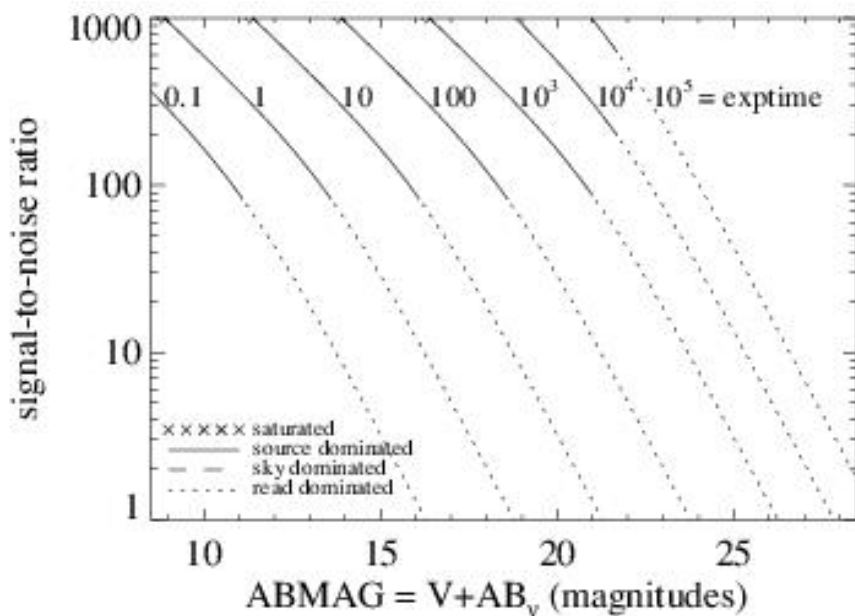


Figure A.24: Extended source S/N vs. $V+AB_v$ for the F343N filter, assuming high sky backgrounds and a source uniformly filling a 1 arcsec^2 aperture.



UVIS F350LP

Description

Long pass filter.

Figure A.25: Integrated system throughput for F350LP.

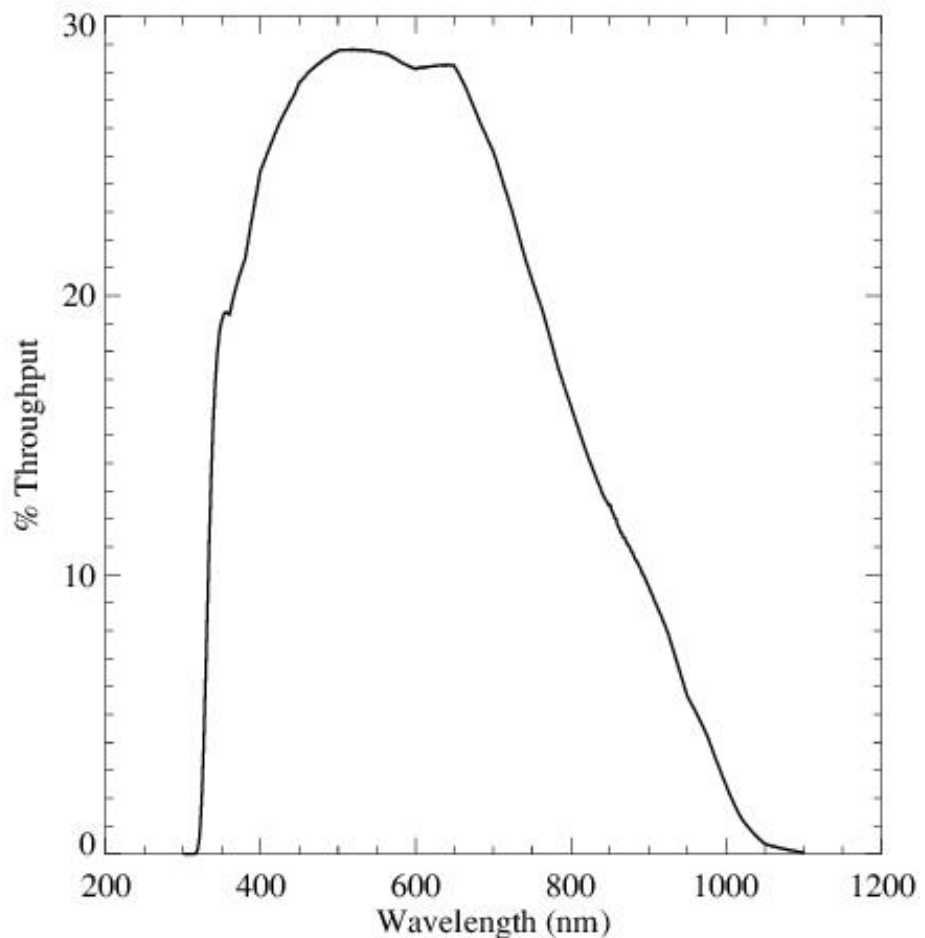


Figure A.26: Point source S/N vs. $V+AB_v$ for the F350LP filter, assuming high sky backgrounds and a 5×5 pixel aperture.

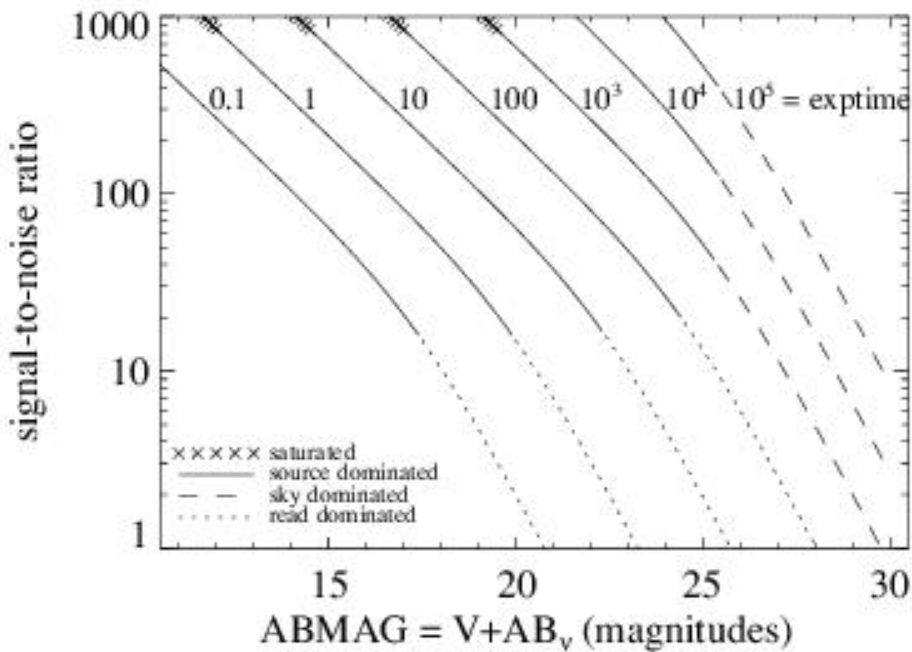
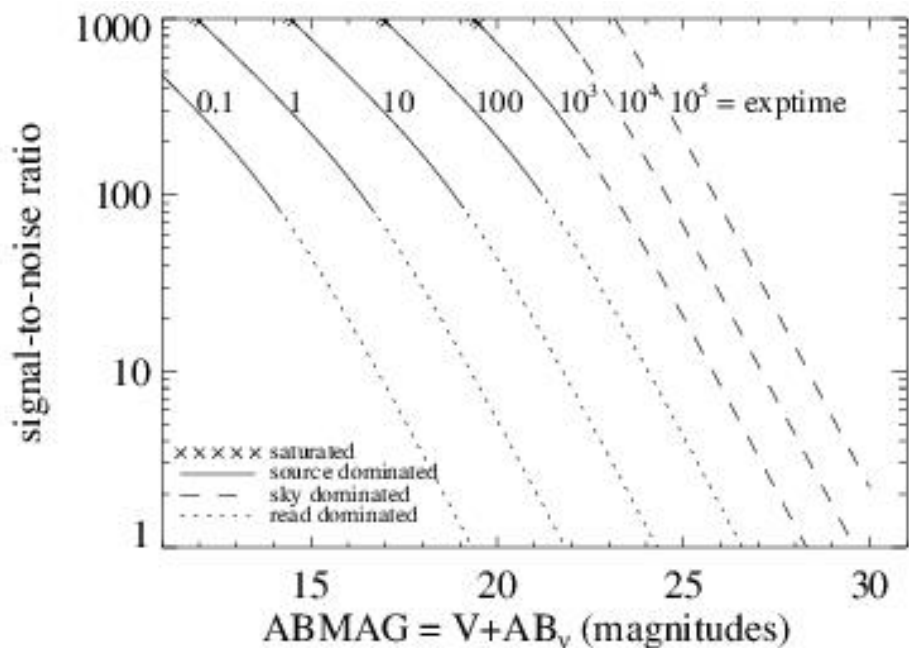


Figure A.27: Extended source S/N vs. $V+AB_V$ for the F350LP filter, assuming high sky backgrounds and a source uniformly filling a 1 arcsec^2 aperture.



UVIS F373N

Description

[O II] 3726/3728 filter.

Figure A.28: Integrated system throughput for F373N.

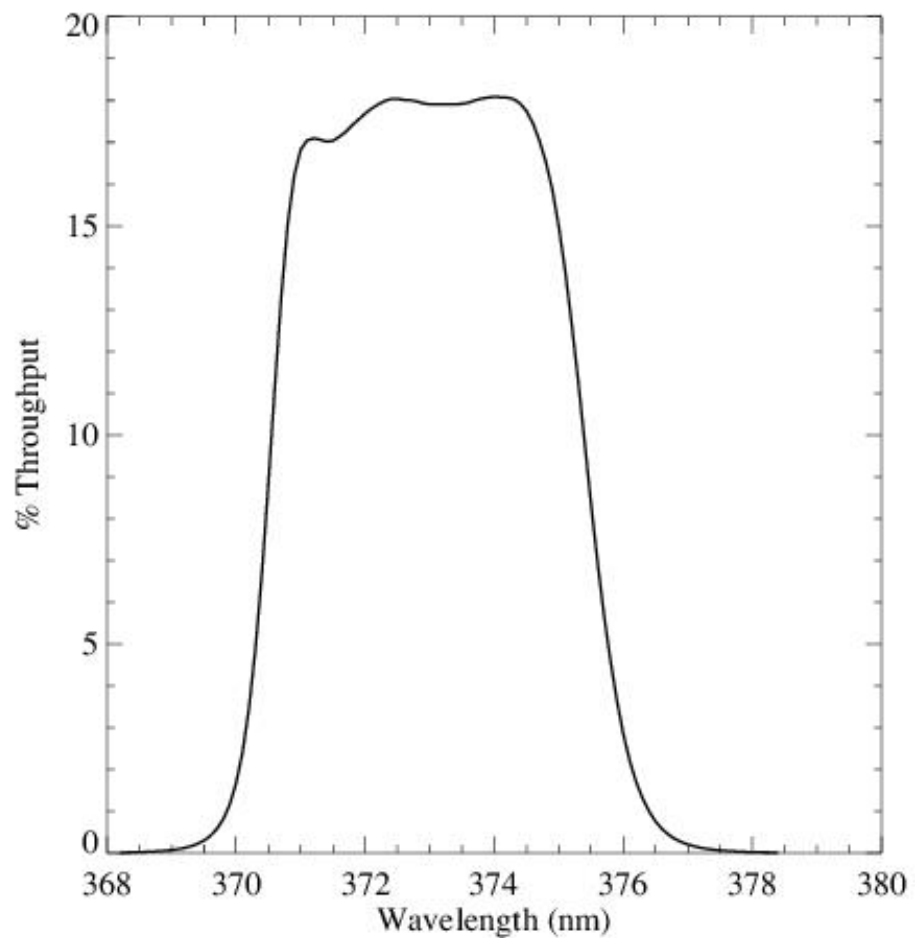


Figure A.29: Point source S/N vs. $V+AB_v$ for the F373N filter, assuming high sky backgrounds and a 5×5 pixel aperture.

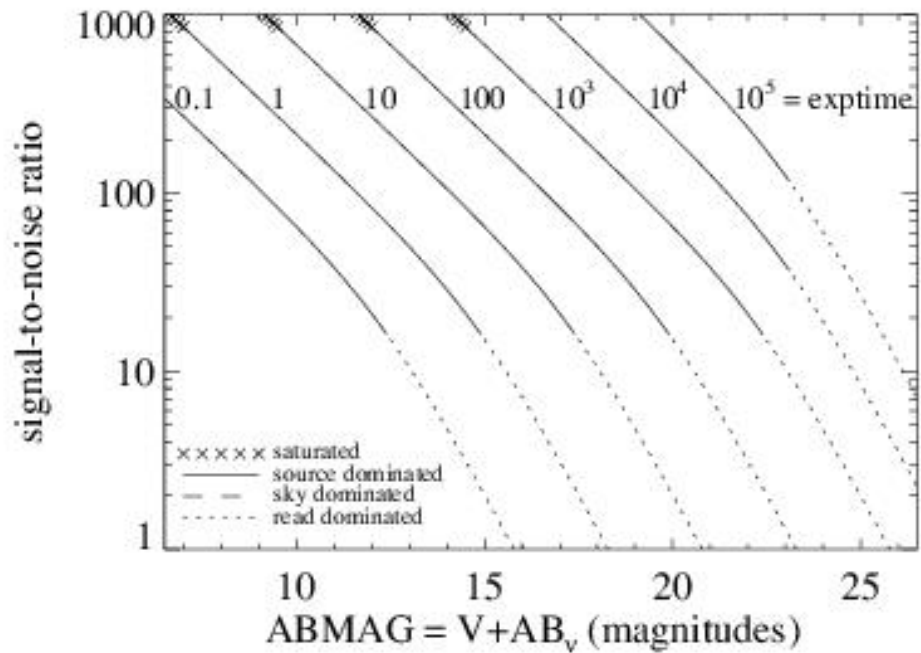
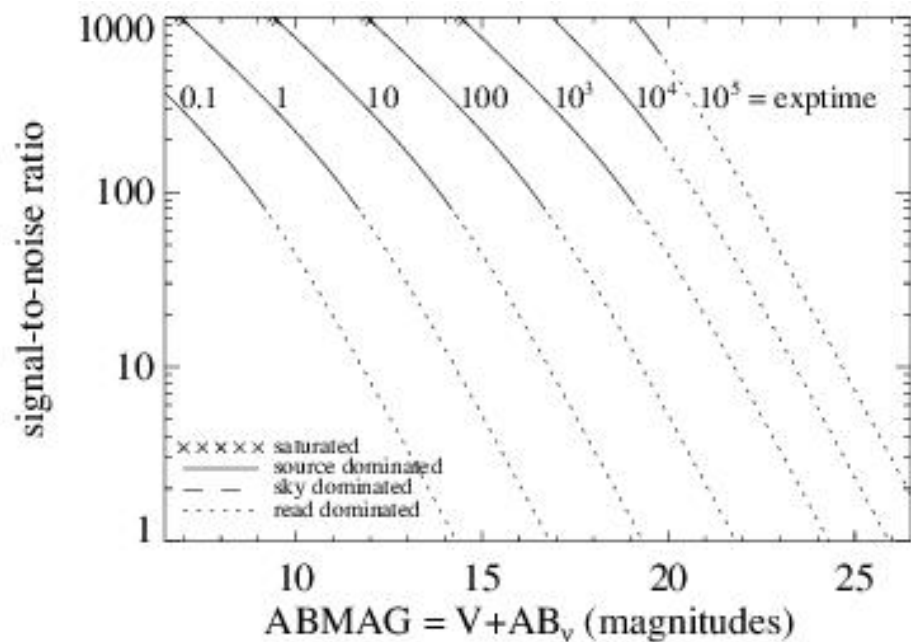


Figure A.30: Extended source S/N vs. $V+AB_V$ for the F373N filter, assuming high sky backgrounds and a source uniformly filling a 1 arcsec^2 aperture.



UVIS F390M

Description

Ca II continuum filter.

Figure A.31: Integrated system throughput for F390M.

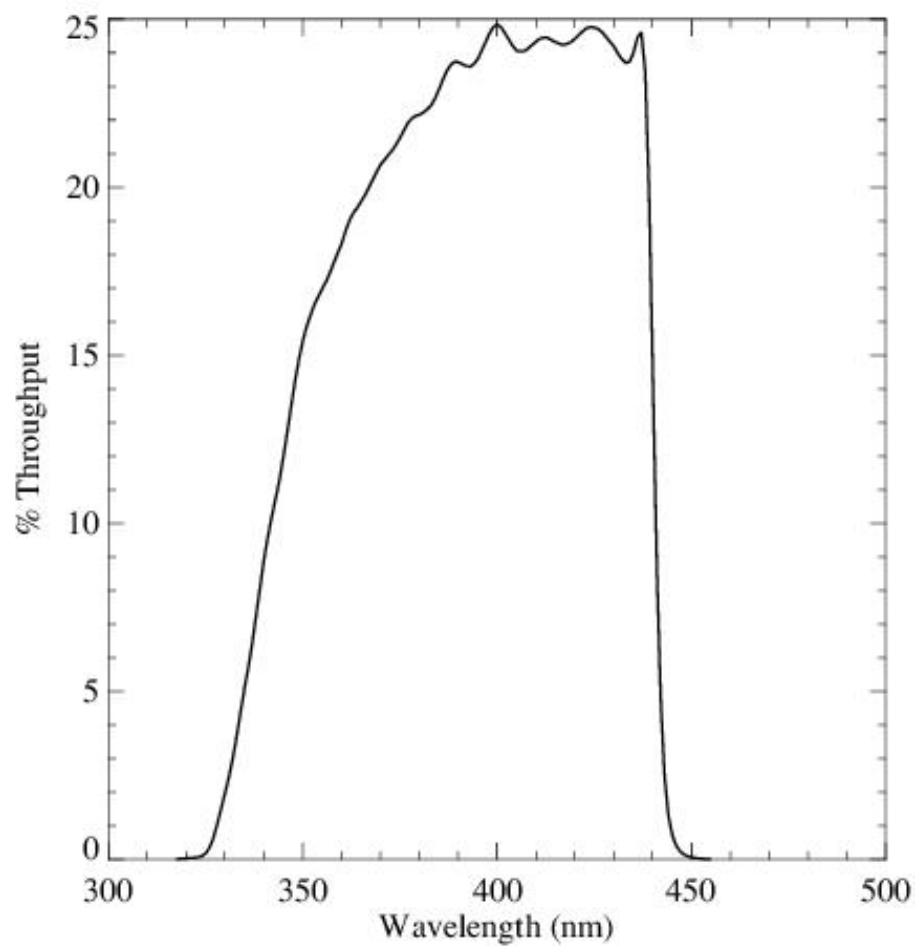


Figure A.32: Point source S/N vs. $V+AB_v$ for the F390M filter, assuming high sky backgrounds and a 5×5 pixel aperture.

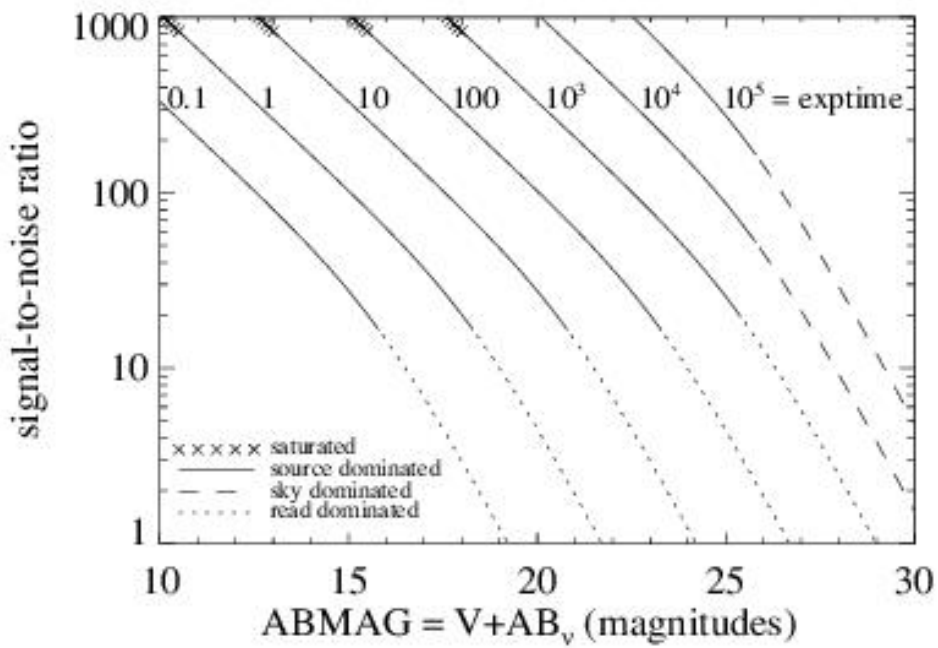
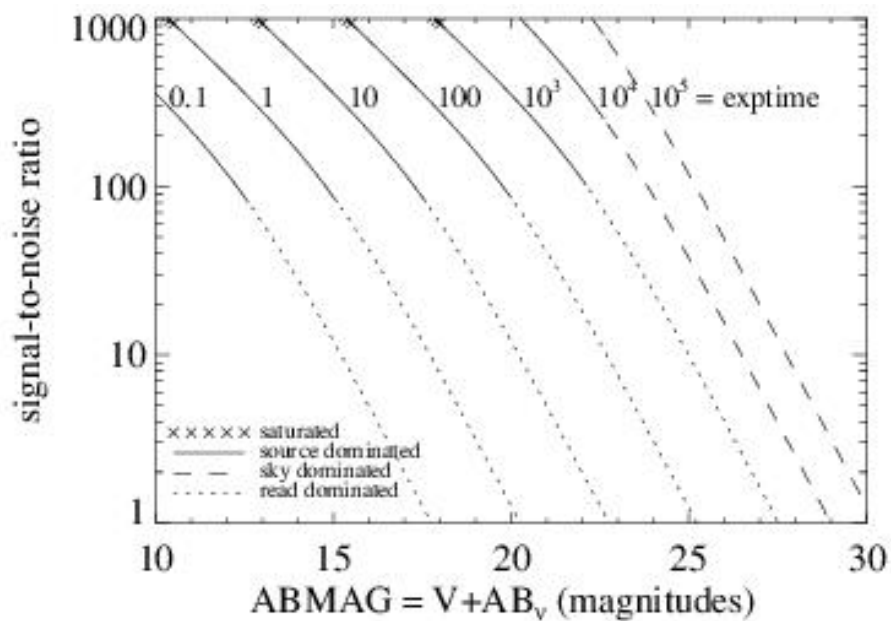


Figure A.33: Extended source S/N vs. $V+AB_V$ for the F390M filter, assuming high sky backgrounds and a source uniformly filling a 1 arcsec^2 aperture.



UVIS F390W

Description

Washington C filter.

Figure A.34: Integrated system throughput for F390W.

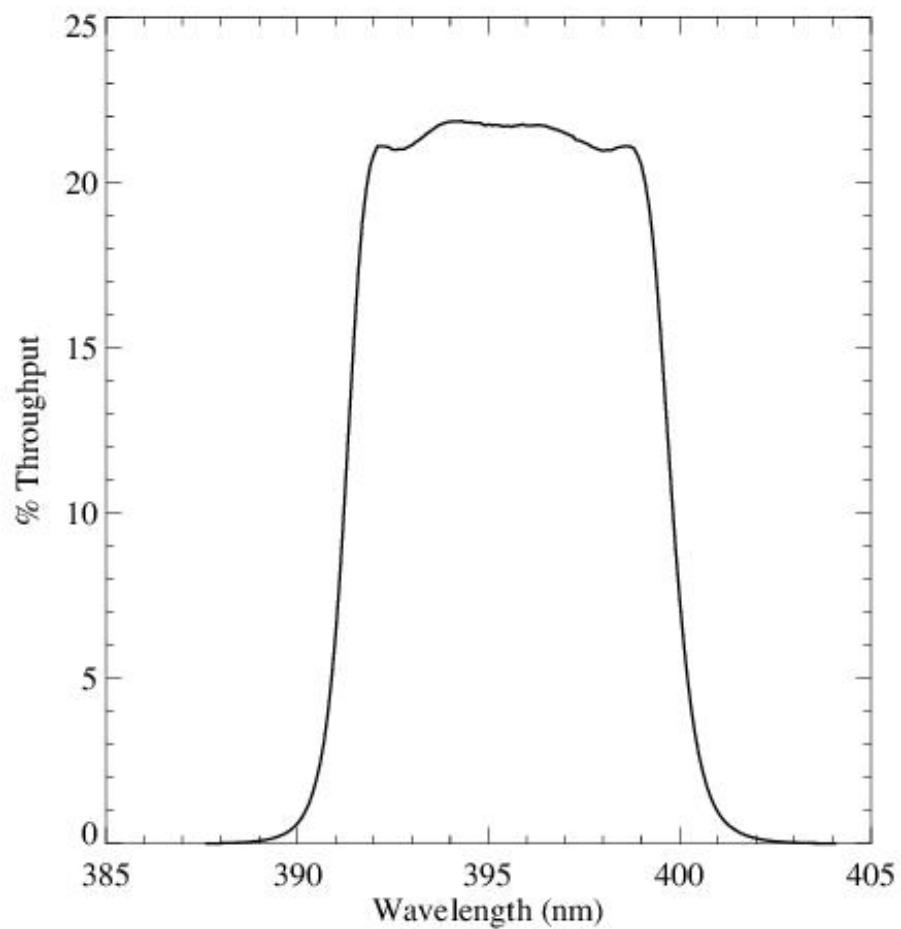


Figure A.35: Point source S/N vs. $V+AB_V$ for the F390W filter, assuming high sky backgrounds and a 5×5 pixel aperture.

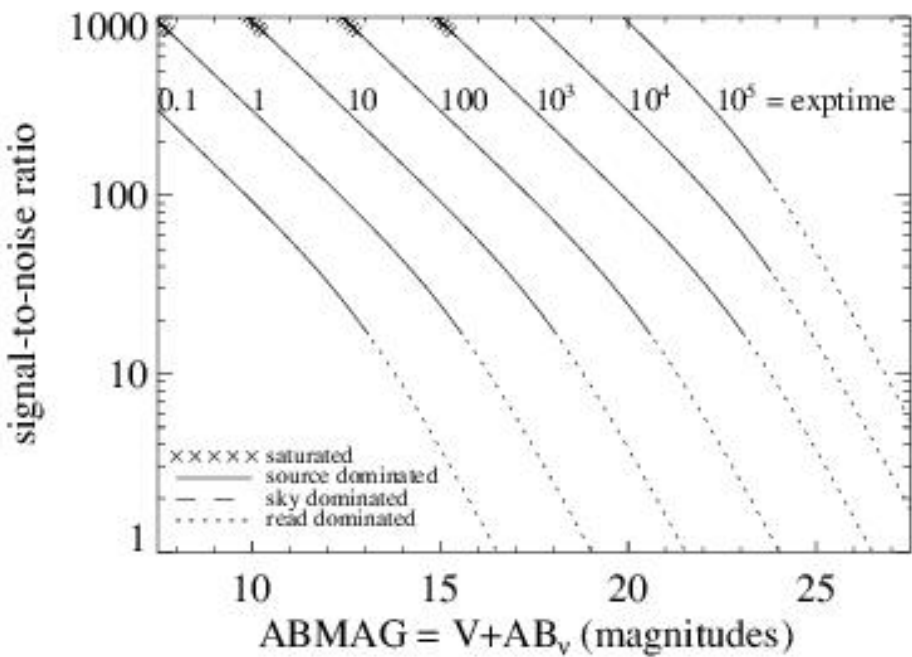
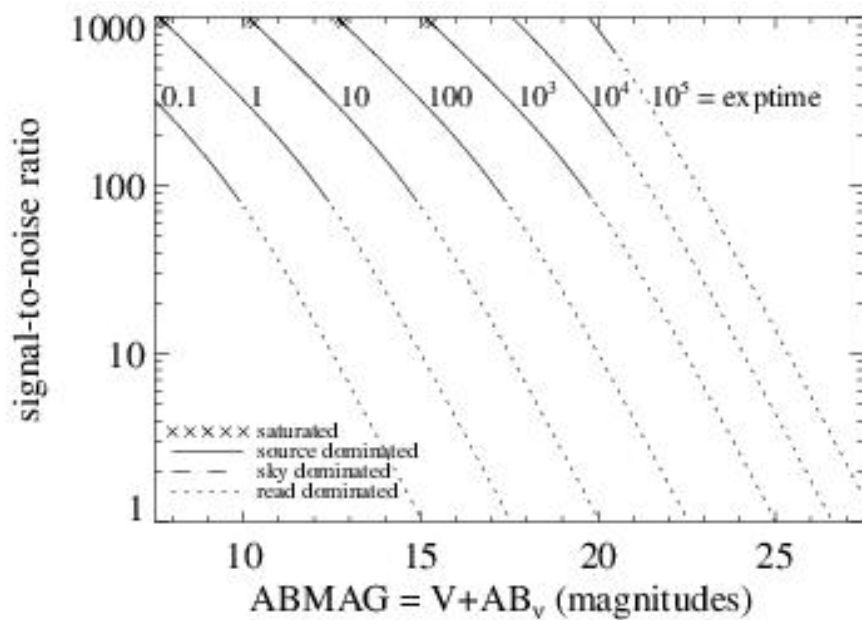


Figure A.36: Extended source S/N vs. $V+AB_v$ for the F390W filter, assuming high sky backgrounds and a source uniformly filling a 1 arcsec^2 aperture.



UVIS F395N

Description

Ca II 3933/3968 filter.

Figure A.37: Integrated system throughput for F395N.

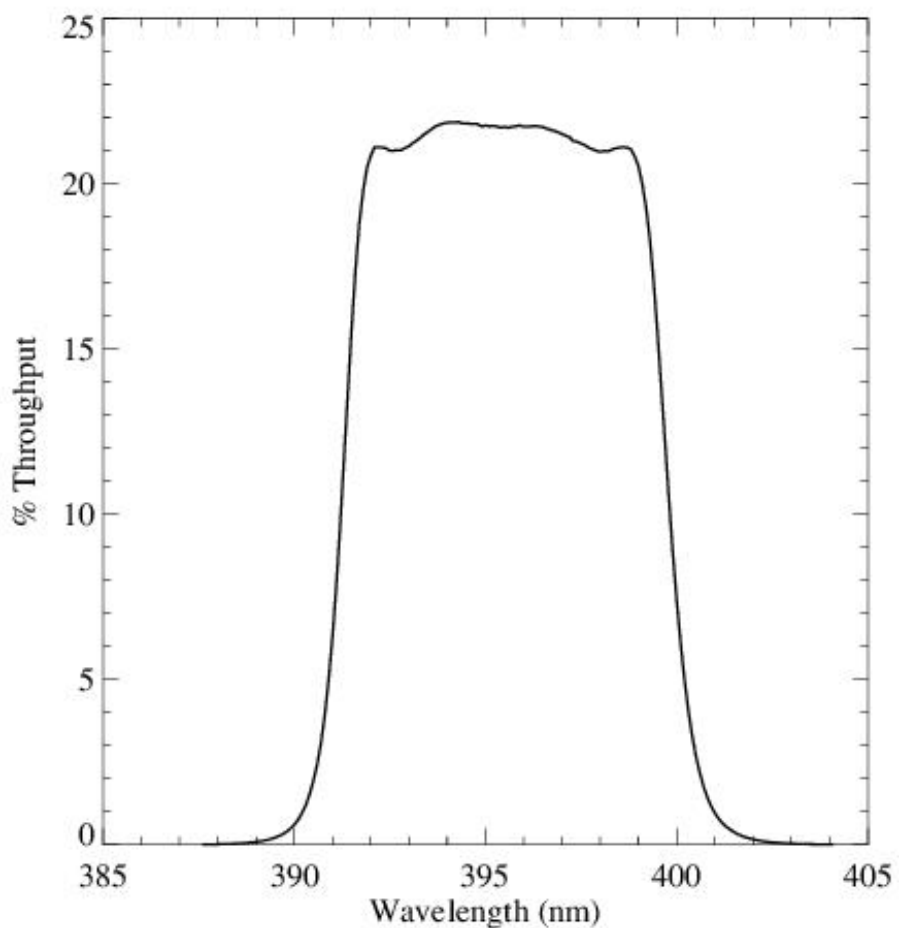


Figure A.38: Point source S/N vs. $V+AB_V$ for the F395N filter, assuming high sky backgrounds and a 5×5 pixel aperture.

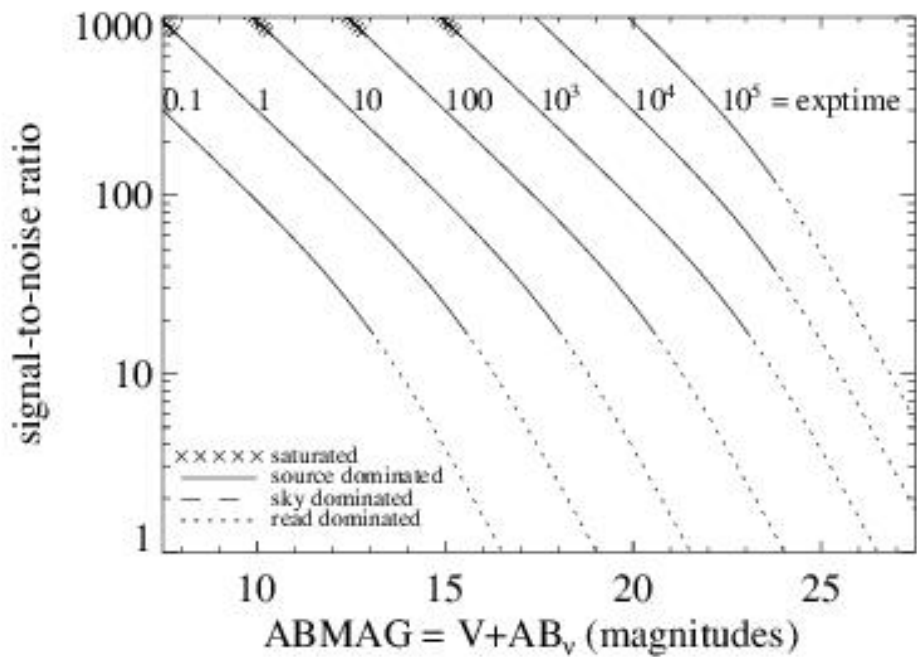
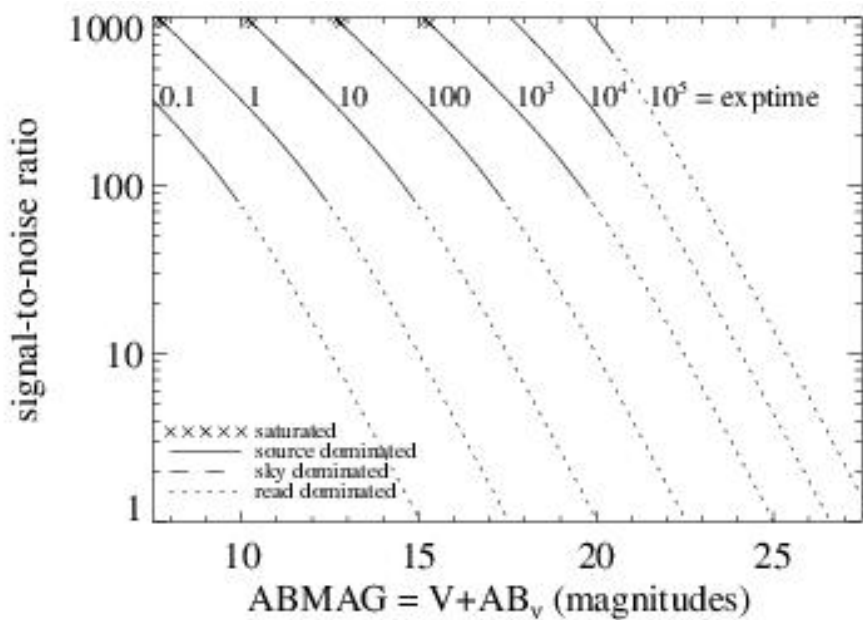


Figure A.39: Extended source S/N vs. $V+AB_v$ for the F395N filter, assuming high sky backgrounds and a source uniformly filling a 1 arcsec^2 aperture.



UVIS F410M

Description

Strömgren v filter.

Figure A.40: Integrated system throughput for F410M.

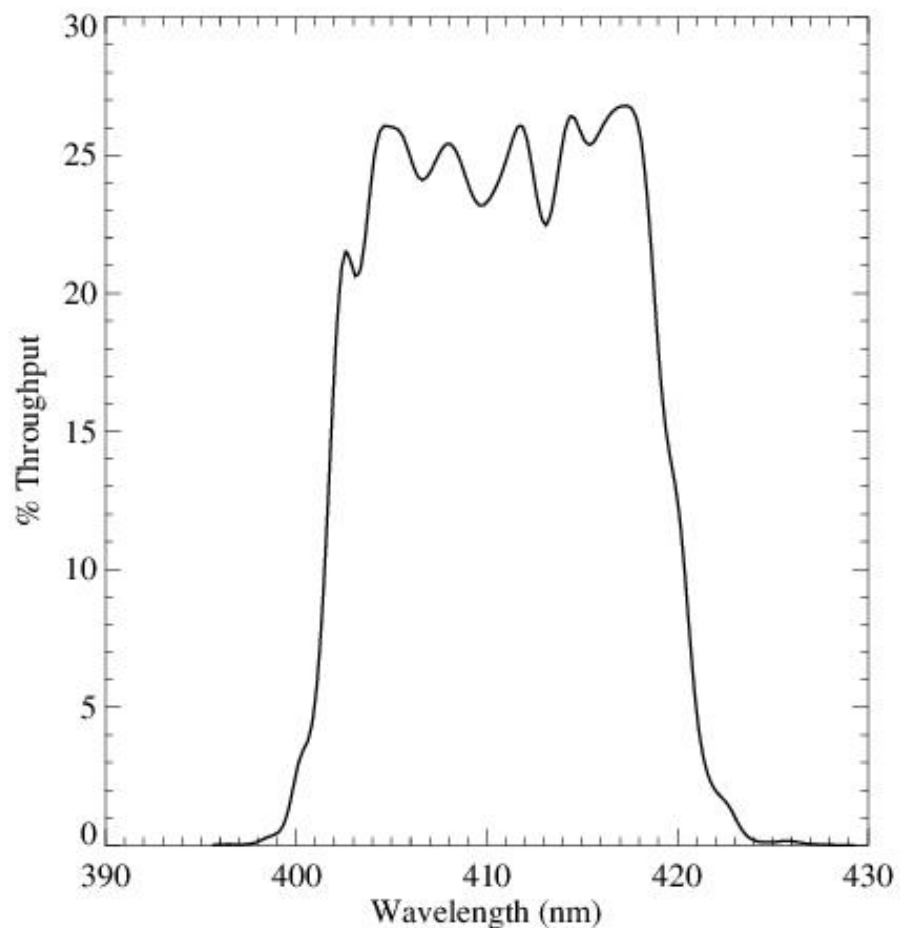


Figure A.41: Point source S/N vs. $V+AB_V$ for the F410M filter, assuming high sky backgrounds and a 5×5 pixel aperture.

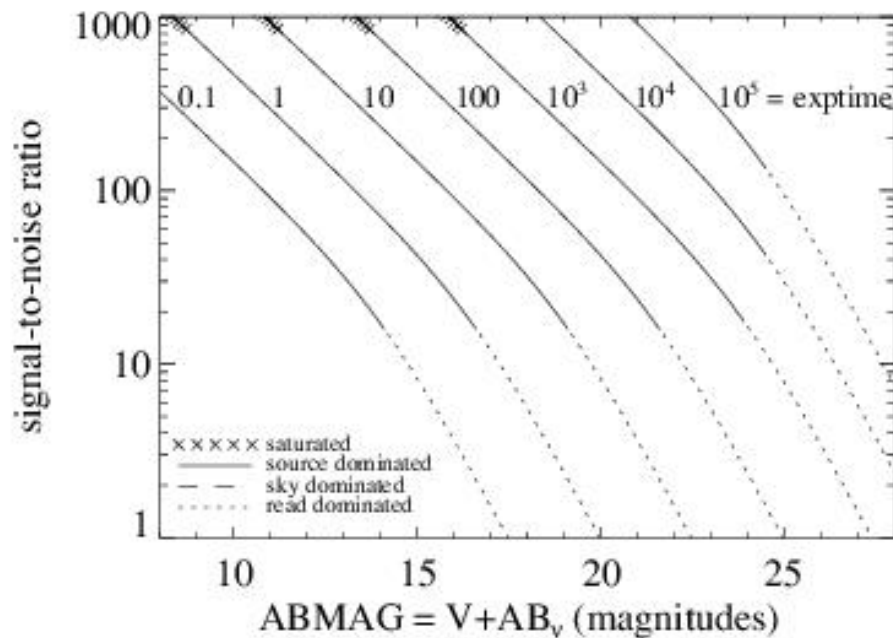
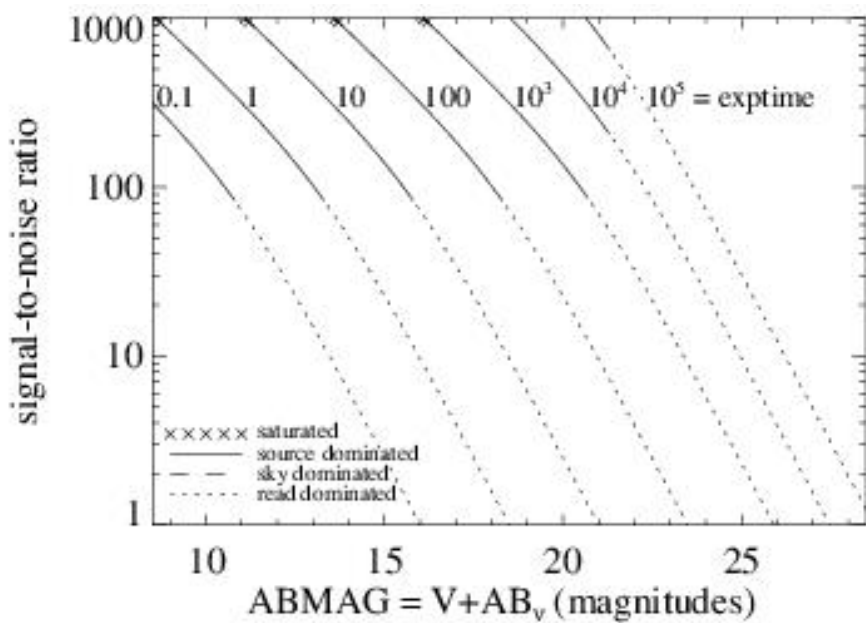


Figure A.42: Extended source S/N vs. $V+AB_v$ for the F410M filter, assuming high sky backgrounds and a source uniformly filling a 1 arcsec^2 aperture.



UVIS F438W

Description

WFPC2 *B* filter.

Figure A.43: Integrated system throughput for F438W.

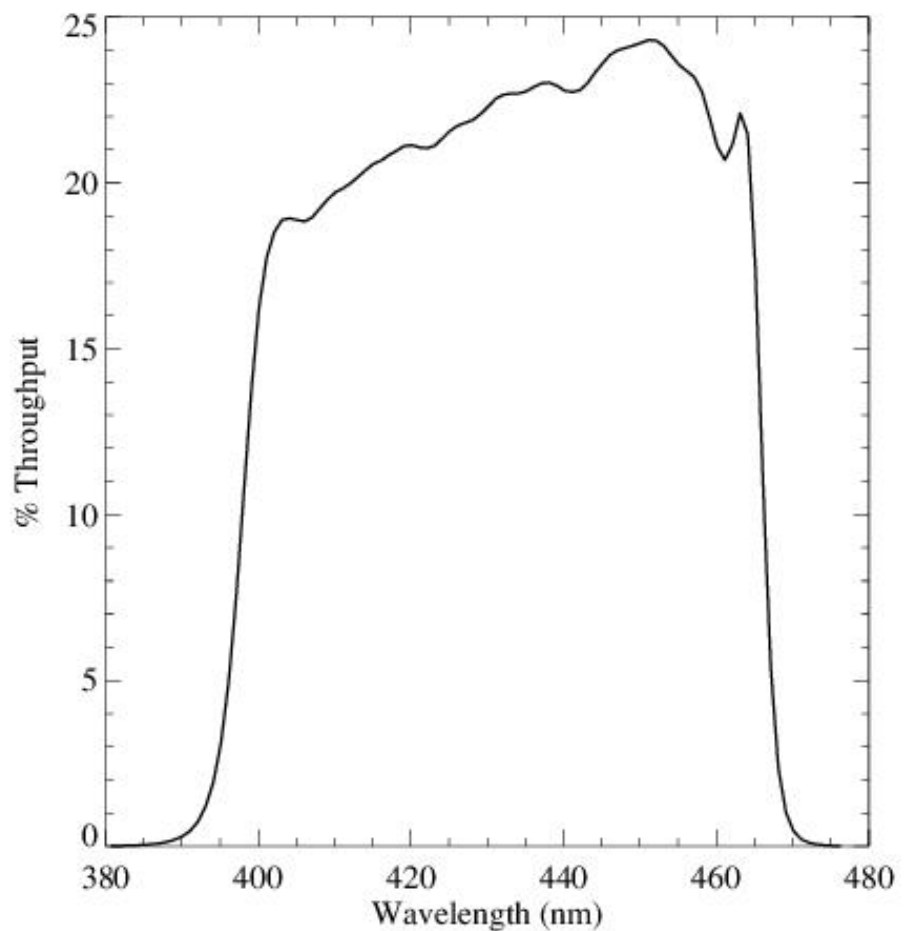


Figure A.44: Point source S/N vs. $V+AB_v$ for the F438W filter, assuming high sky backgrounds and a 5×5 pixel aperture.

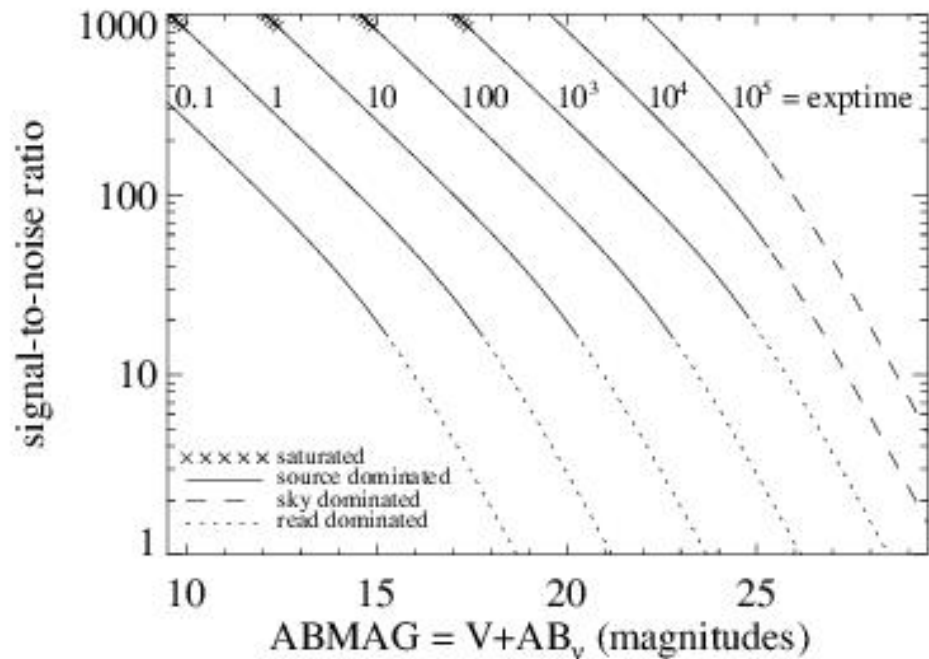
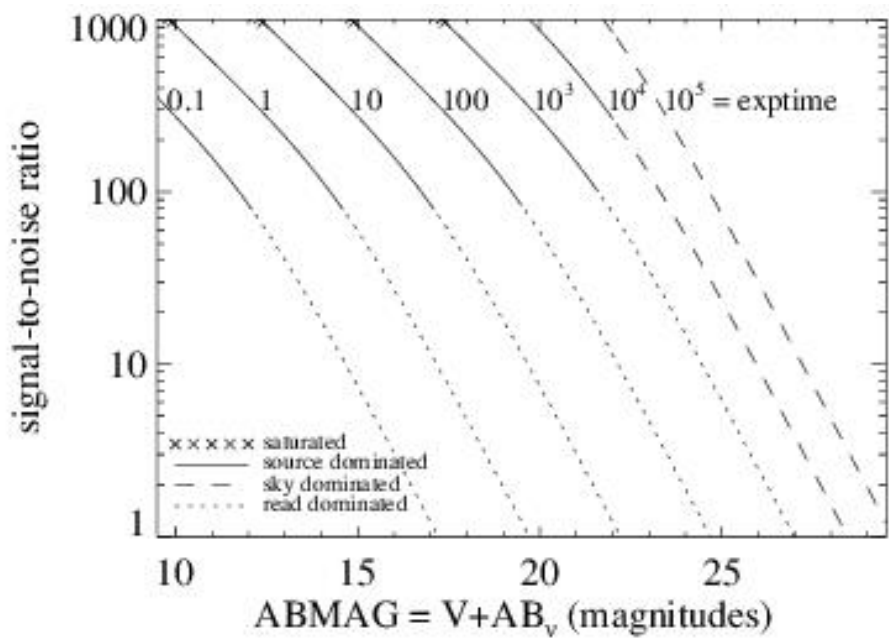


Figure A.45: Extended source S/N vs. $V+AB_V$ for the F438W filter, assuming high sky backgrounds and a source uniformly filling a 1 arcsec^2 aperture.



UVIS F467M

Description

Strömgren *b* filter.

Figure A.46: Integrated system throughput for F467M.

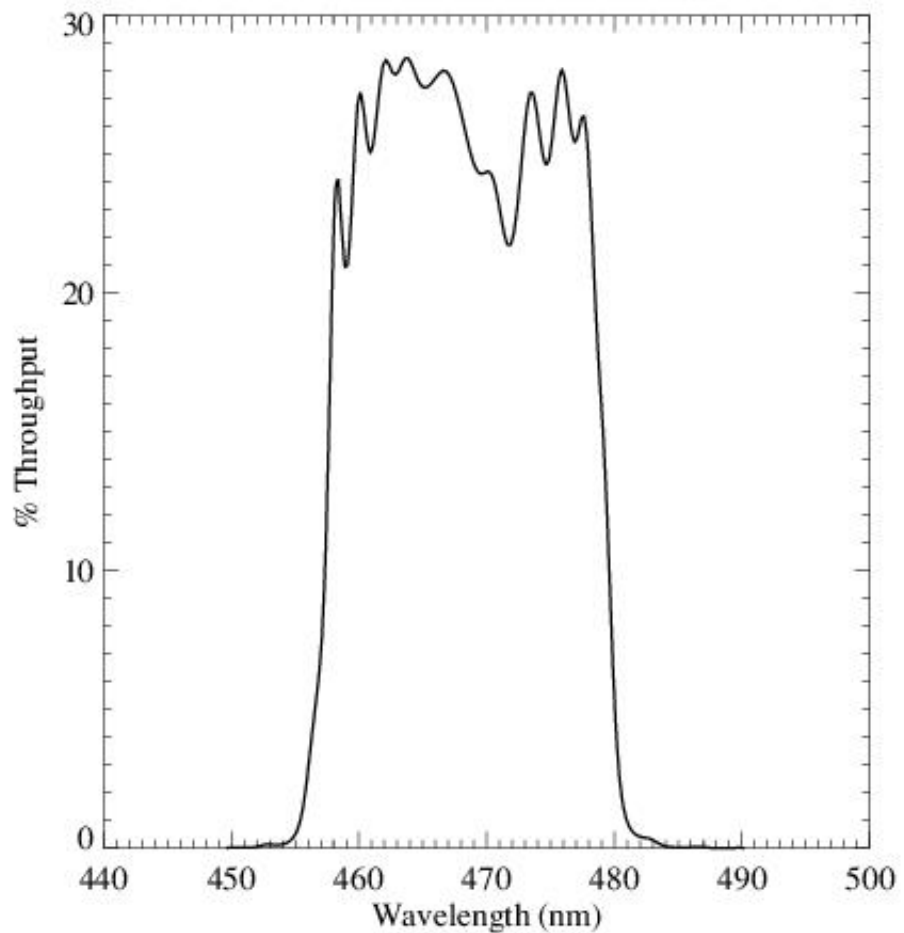


Figure A.47: Point Source S/N vs. $V+AB_V$ for the F467M filter, assuming high sky backgrounds and a 5×5 pixel aperture.

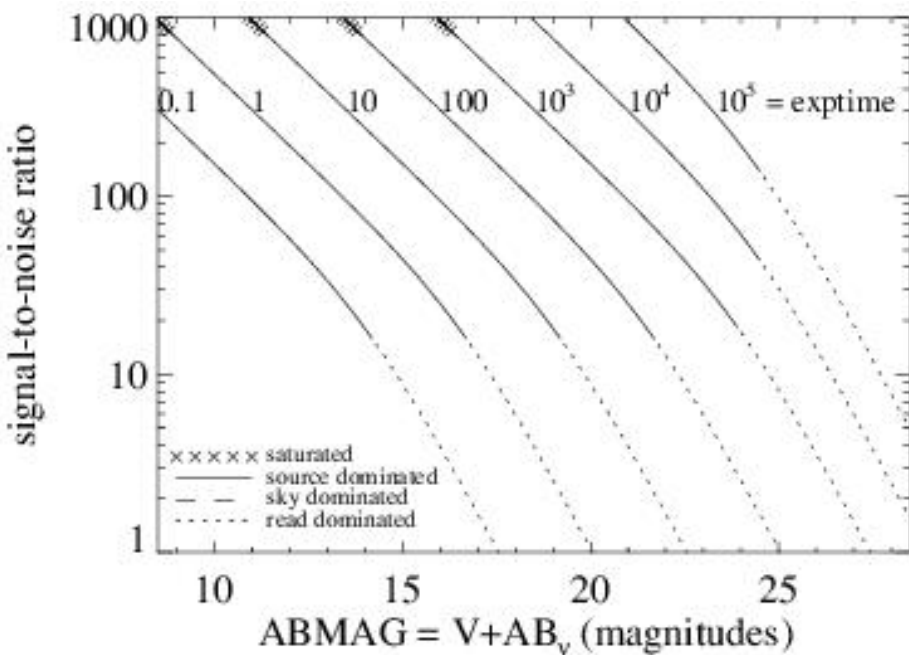
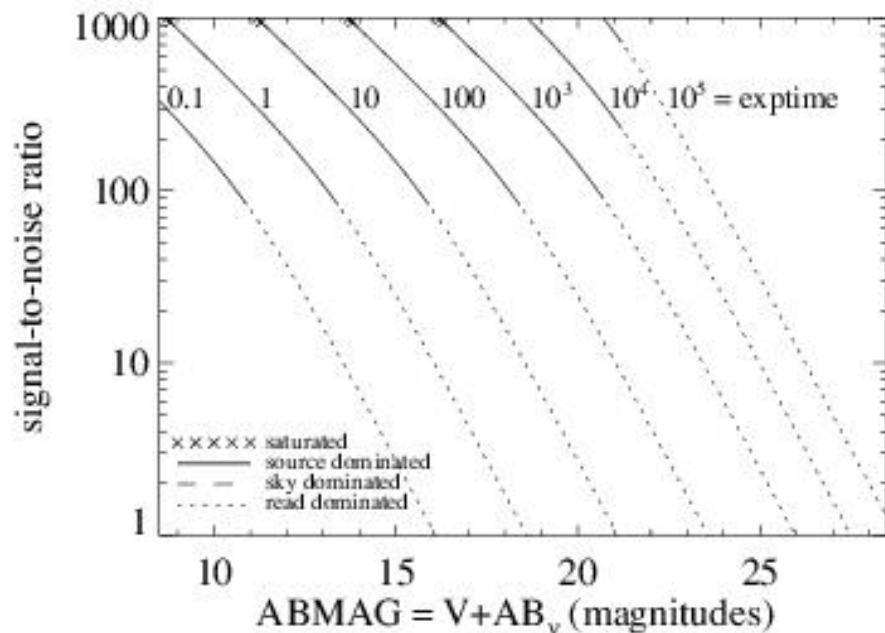


Figure A.48: Extended Source S/N vs. $V+AB_V$ for the F467M filter, assuming high sky backgrounds and a source uniformly filling a 1 arcsec^2 aperture.



UVIS F469N

Description

He II 4686 filter.

Figure A.49: Integrated system throughput for F469N.

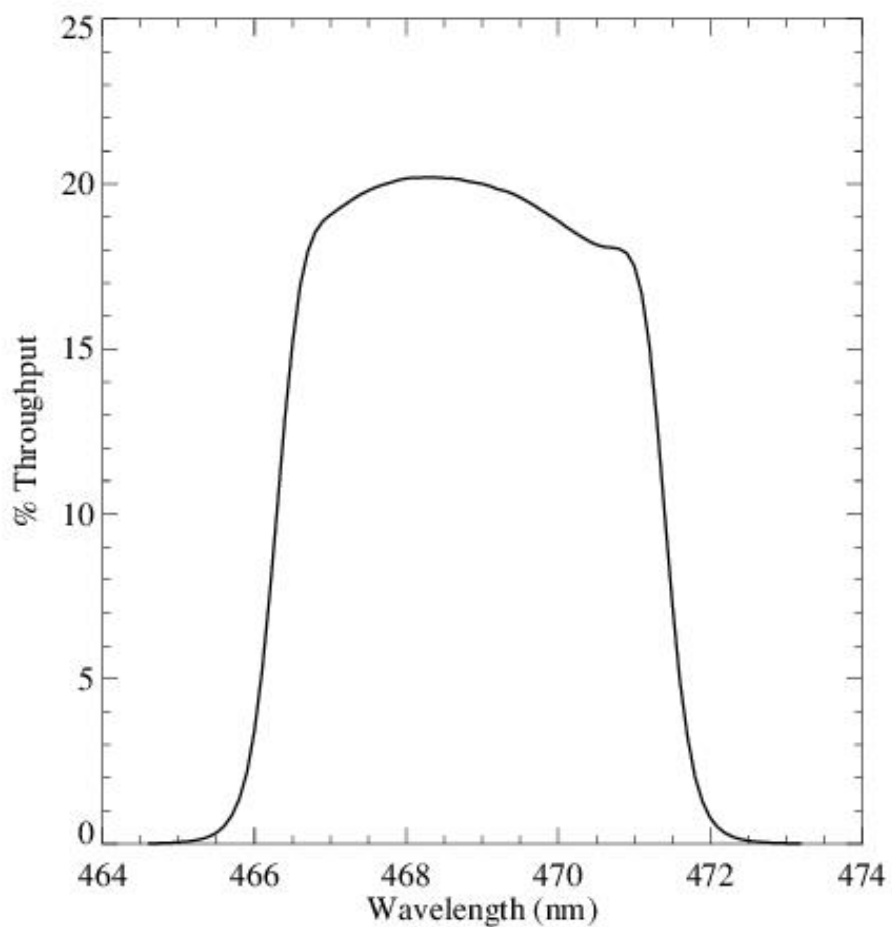


Figure A.50: Point source S/N vs. $V+AB_v$ for the F469N filter, assuming high sky backgrounds and a 5×5 pixel aperture.

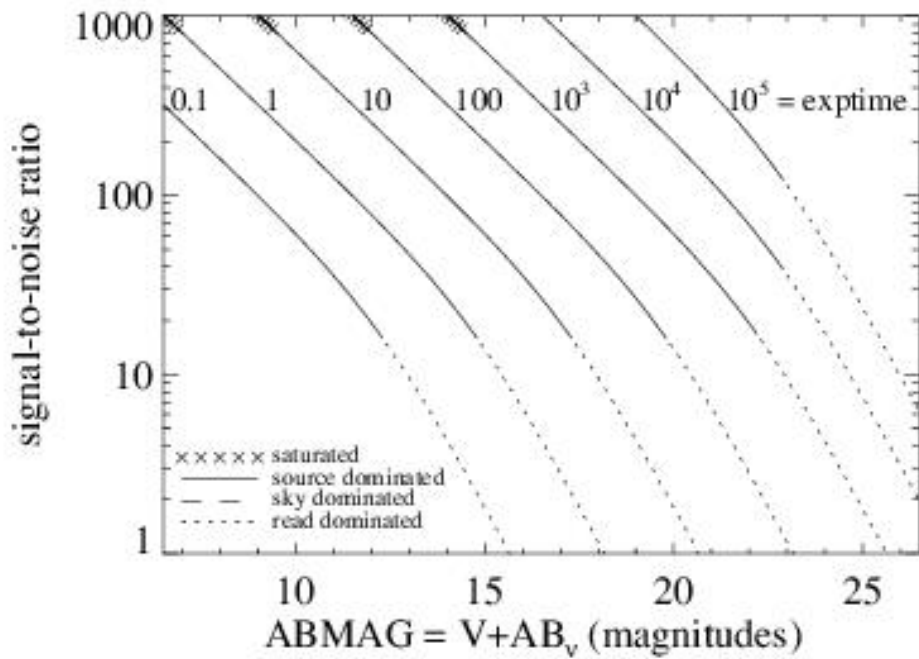
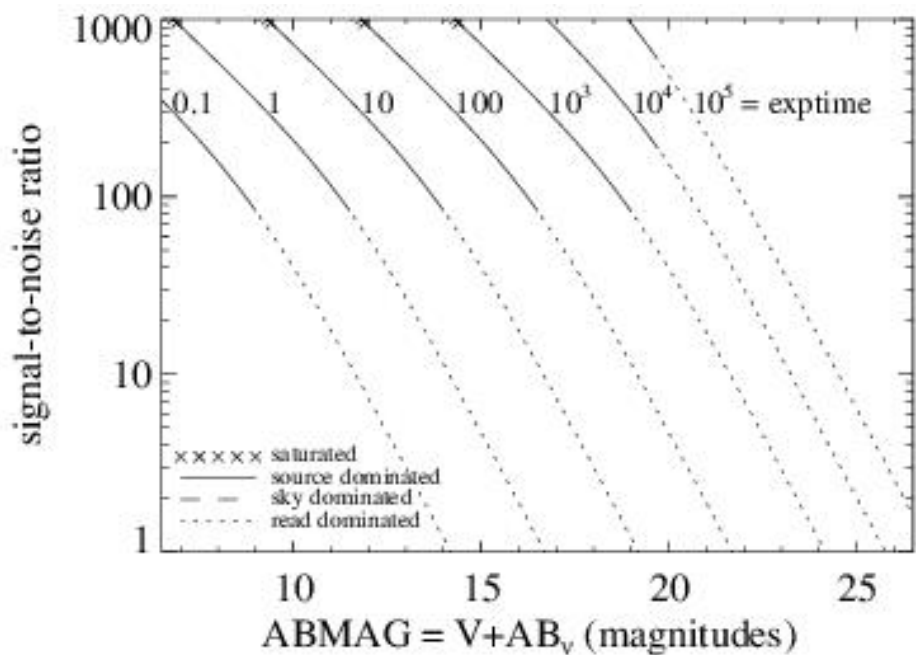


Figure A.51: Extended source S/N vs. $V+AB_V$ for the F469N filter, assuming high sky backgrounds and a source uniformly filling a 1 arcsec^2 aperture.



UVIS F475W

Description

Sloan Digital Sky Survey g' filter.

Figure A.52: Integrated system throughput for F475W.

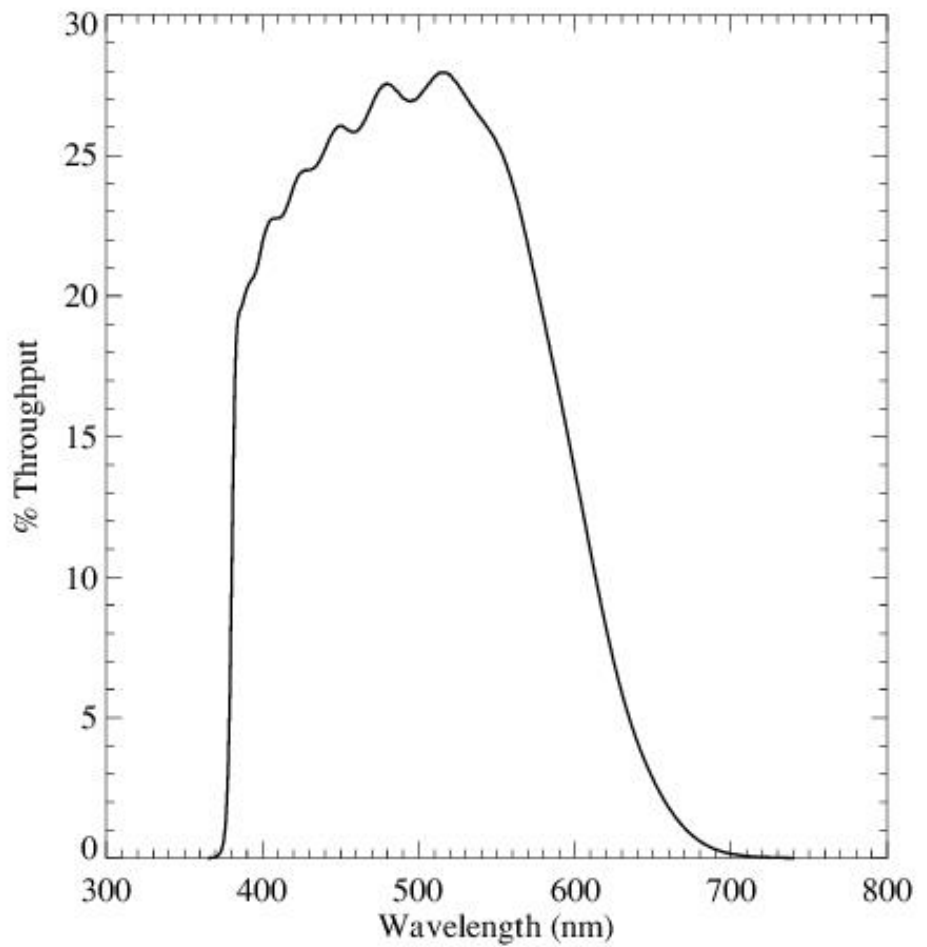


Figure A.53: Point source S/N vs. $V+AB_V$ for the F475W filter, assuming high sky backgrounds and a 5×5 pixel aperture.

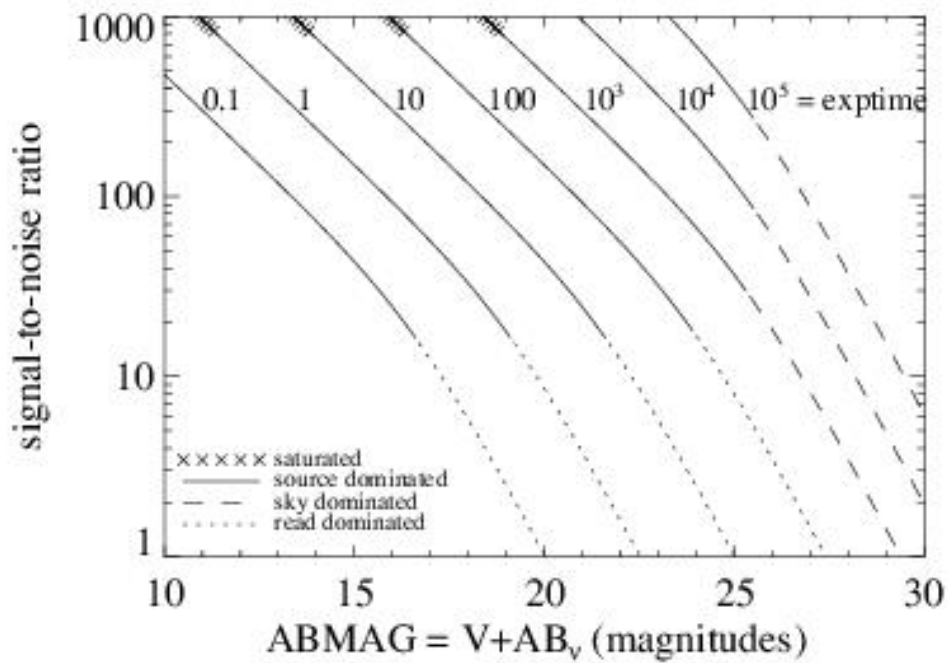
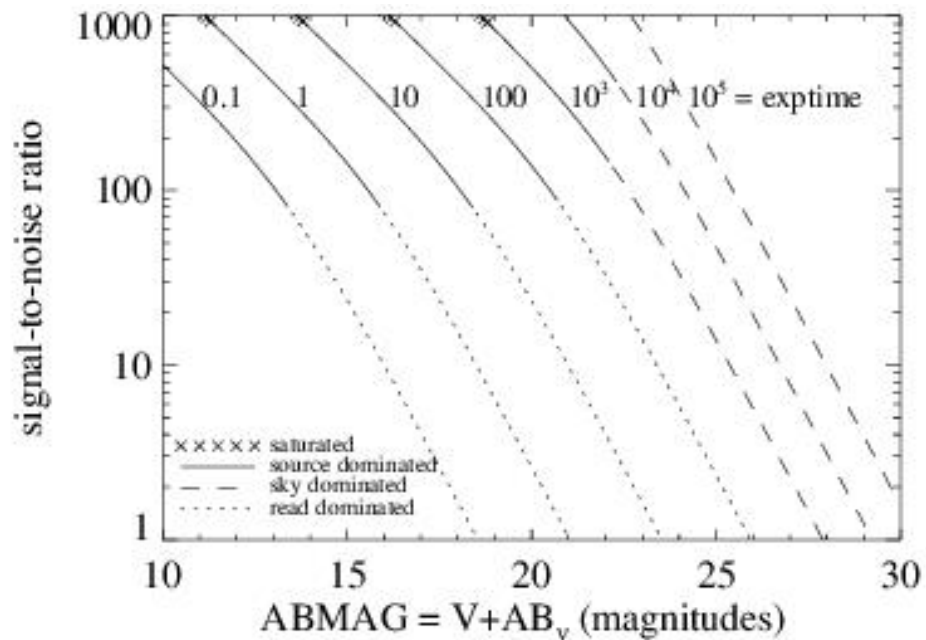


Figure A.54: Extended source S/N vs. $V+AB_v$ for the F475W filter, assuming high sky backgrounds and a source uniformly filling a 1 arcsec^2 aperture.



UVIS F475X

Description

Extremely wide blue filter.

Figure A.55: Integrated system throughput for F475X.

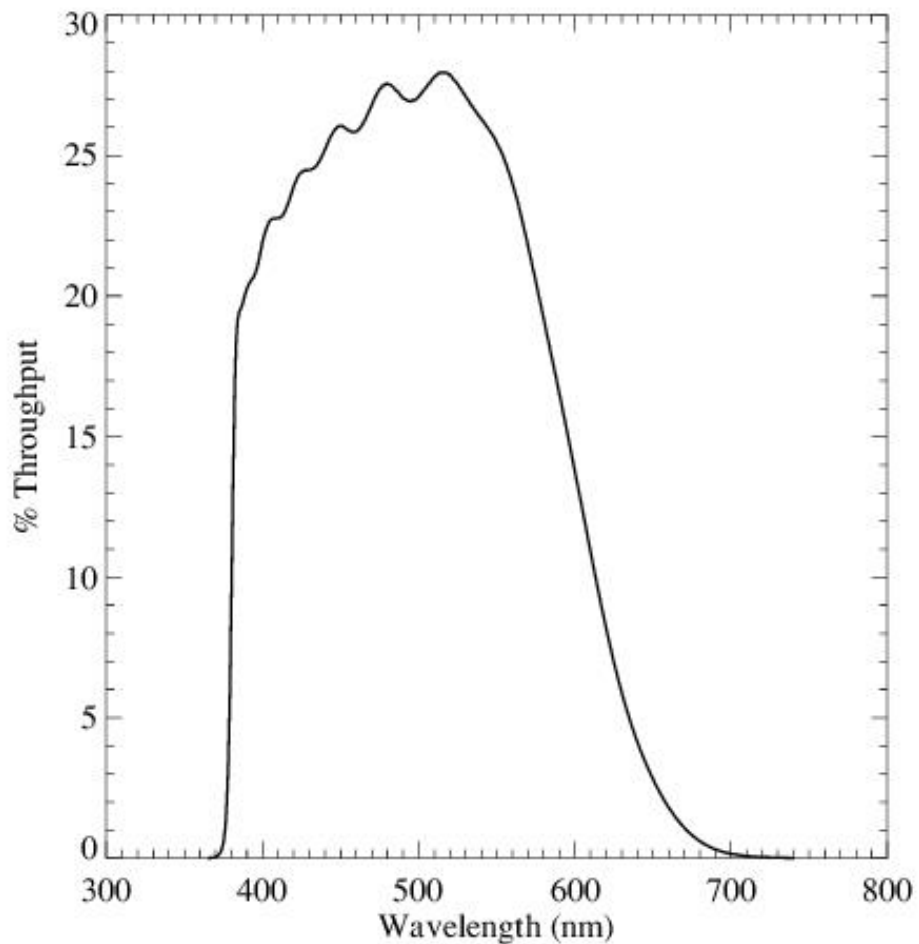


Figure A.56: Point source S/N vs. $V+AB_v$ for the F475X filter, assuming high sky backgrounds and a 5×5 pixel aperture.

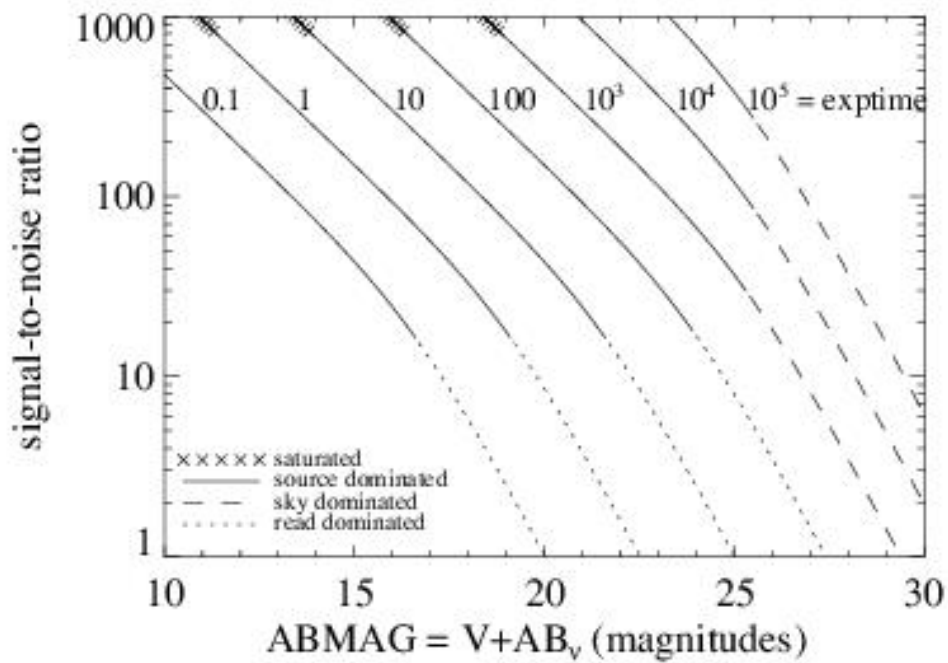
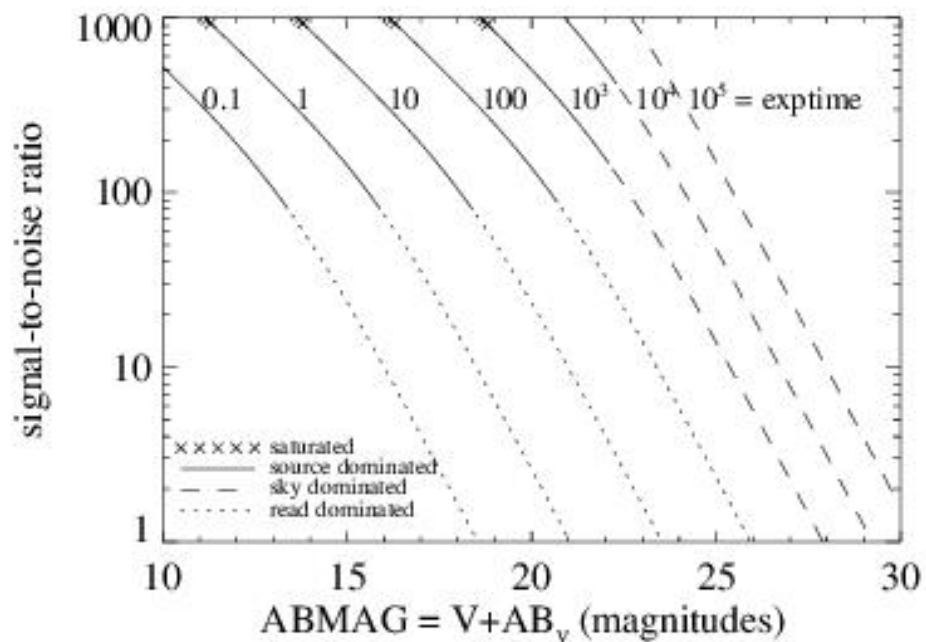


Figure A.57: Extended source S/N vs. $V+AB_v$ for the F475X filter, assuming high sky backgrounds and a source uniformly filling a 1 arcsec^2 aperture.



UVIS F487N

Description

H β 4861 filter.

Figure A.58: Integrated system throughput for F487N.

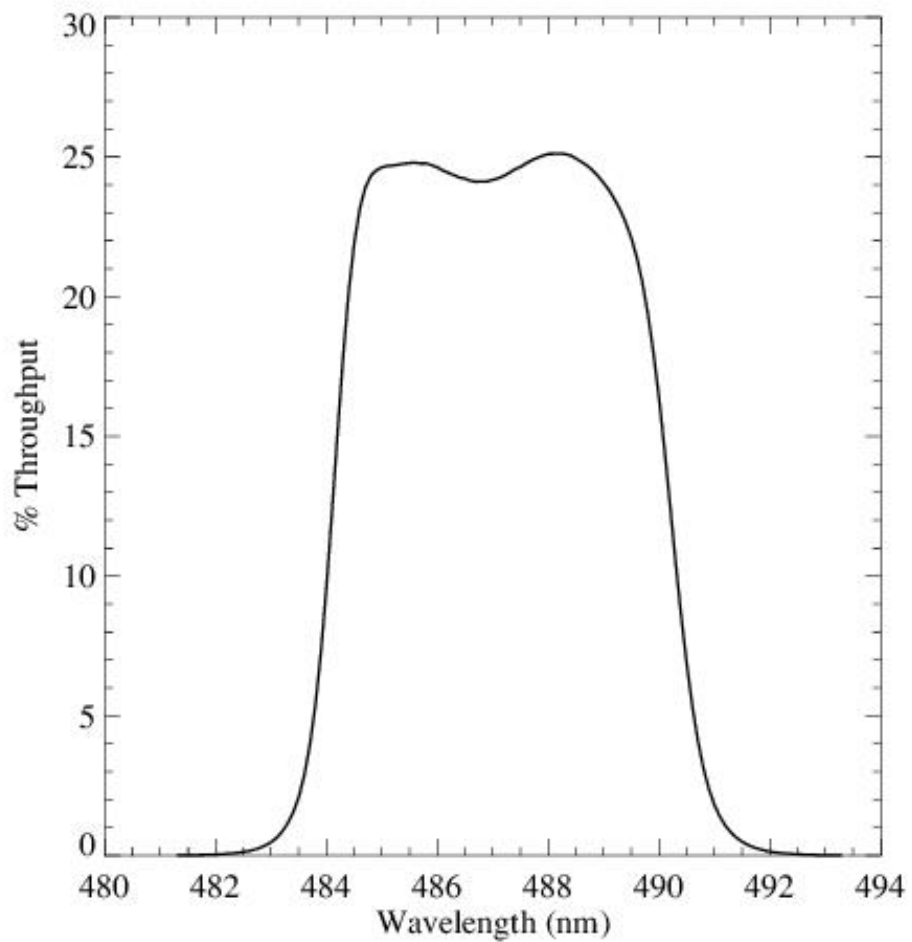


Figure A.59: Point source S/N vs. $V+AB_V$ for the F487N filter, assuming high sky backgrounds and a 5×5 pixel aperture.

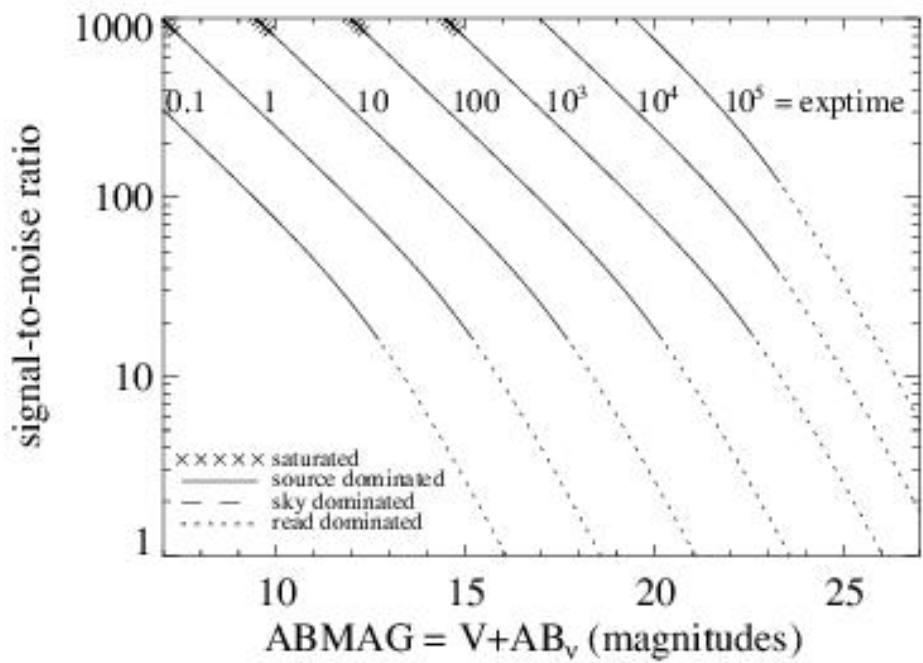
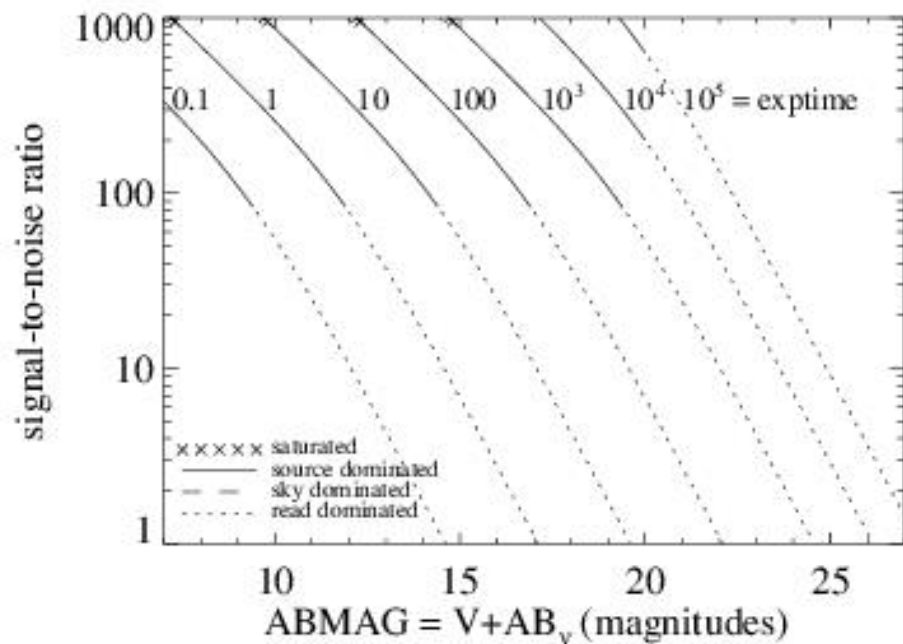


Figure A.60: Extended source S/N vs. $V+AB_V$ for the F487N filter, assuming high sky backgrounds and a source uniformly filling a 1 arcsec^2 aperture.



UVIS F502N

Description

[O III] 5007 filter.

Figure A.61: Integrated system throughput for F502N.

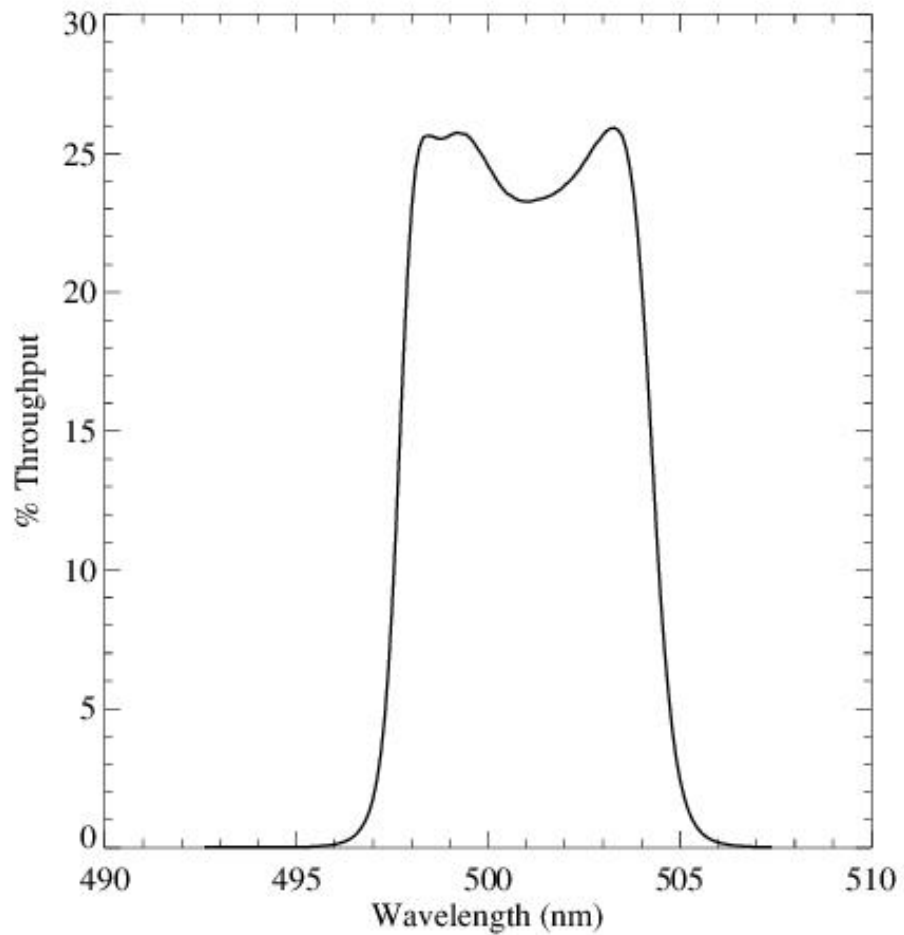


Figure A.62: Point source S/N vs. $V+AB_v$ for the F502N filter, assuming high sky backgrounds and a 5×5 pixel aperture.

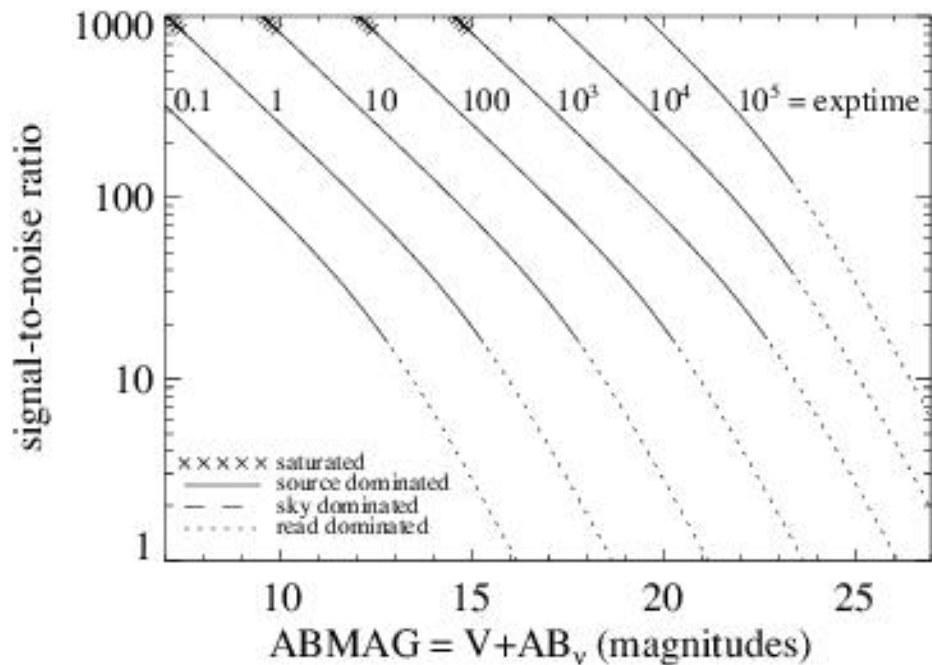
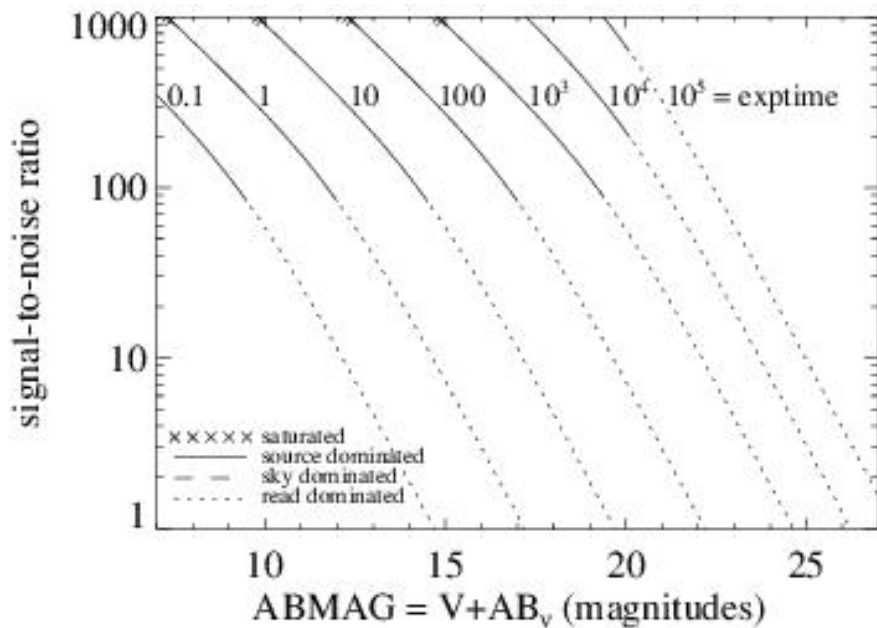


Figure A.63: Extended source S/N vs. $V+AB_V$ for the F502N filter, assuming high sky backgrounds and a source uniformly filling a 1 arcsec^2 aperture.



UVIS F547M

Description

Strömgren *y* filter.

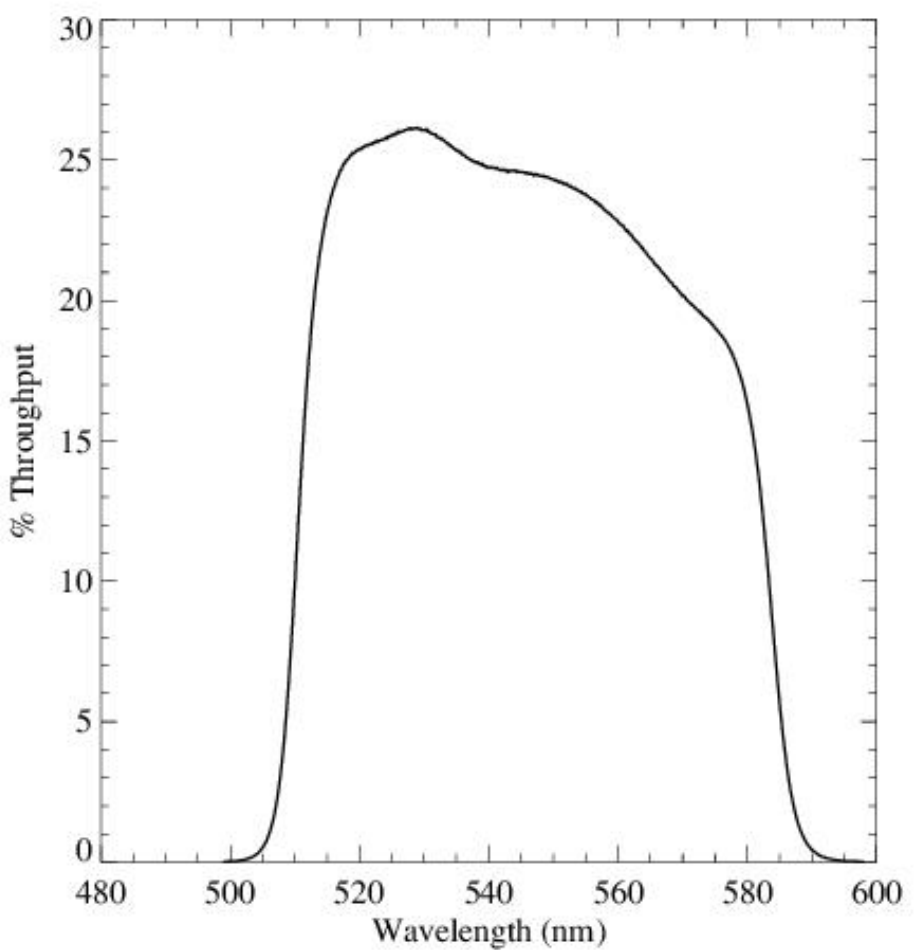


Figure A.65: Point source S/N vs. $V+AB_v$ for the F547M filter, assuming high sky backgrounds and a 5×5 pixel aperture.

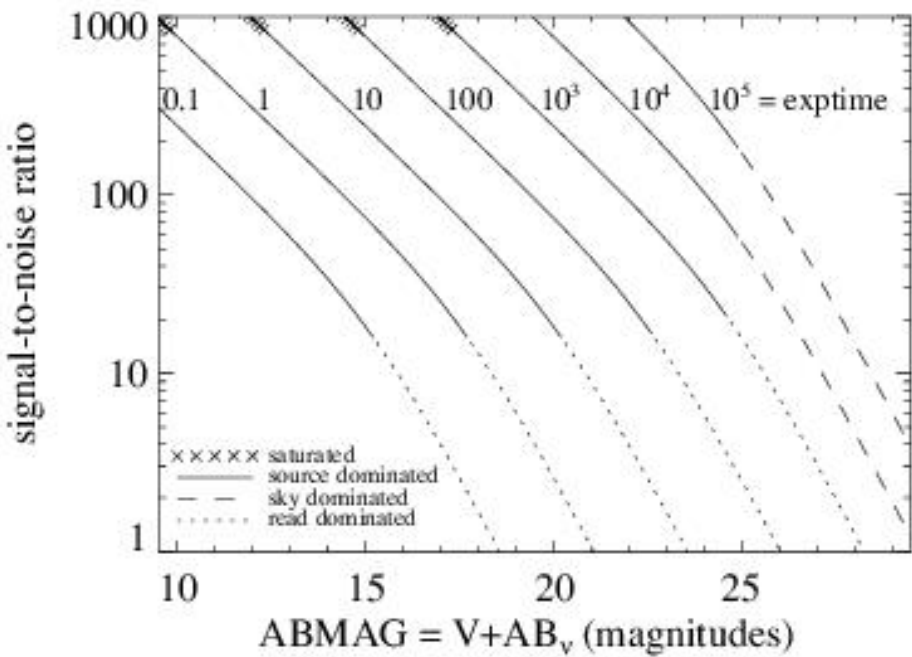
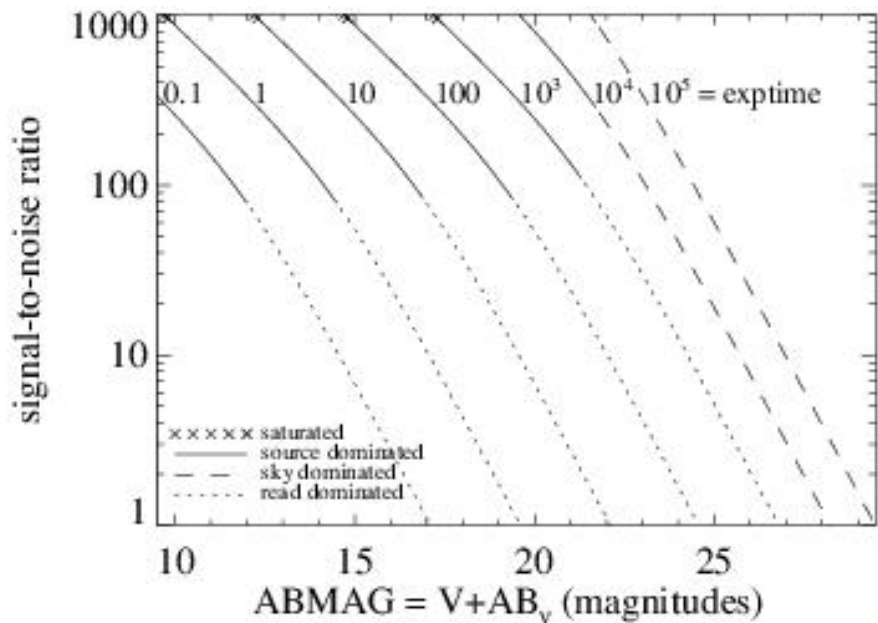


Figure A.66: Extended source S/N vs. $V+AB_v$ for the F547M filter, assuming high sky backgrounds and a source uniformly filling a 1 arcsec^2 aperture.



UVIS F555W

Description

WFPC2 *V*filter.

Figure A.67: Integrated system throughput for F555W.

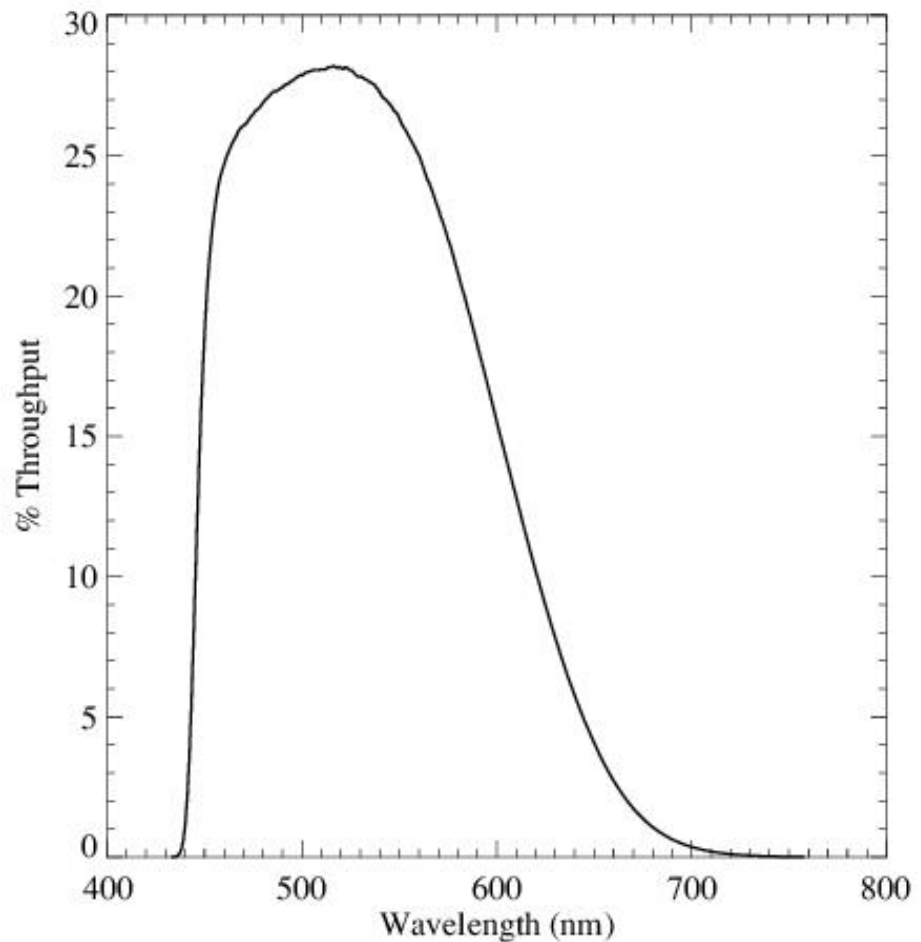


Figure A.68: Point source S/N vs. $V+AB_v$ for the F555W filter, assuming high sky backgrounds and a 5×5 pixel aperture.

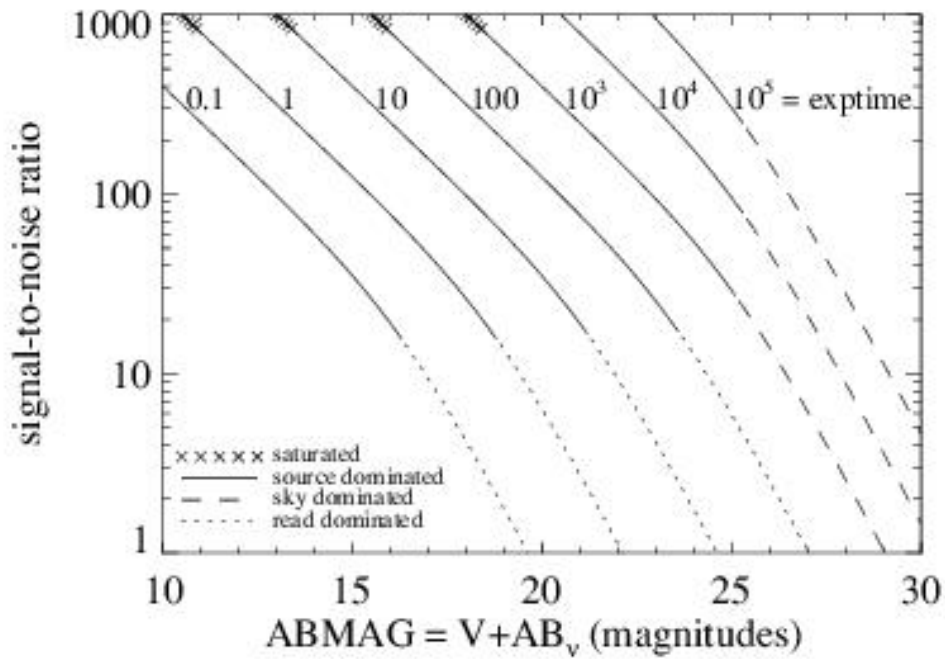
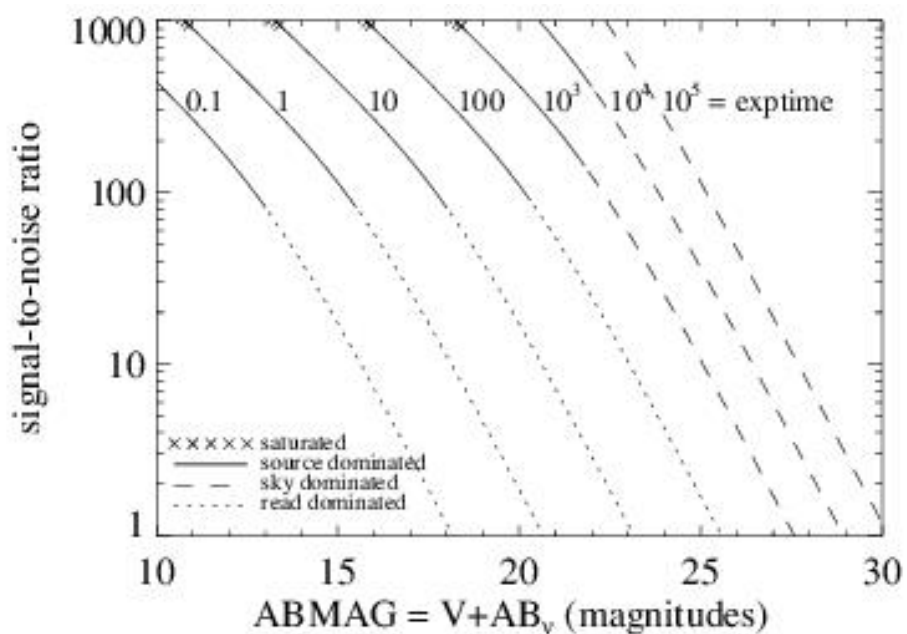


Figure A.69: Extended source S/N vs. $V+AB_V$ for the F555W filter, assuming high sky backgrounds and a source uniformly filling a 1 arcsec^2 aperture.



UVIS F600LP

Description

Long-pass filter.

Figure A.70: Integrated system throughput for F600LP.

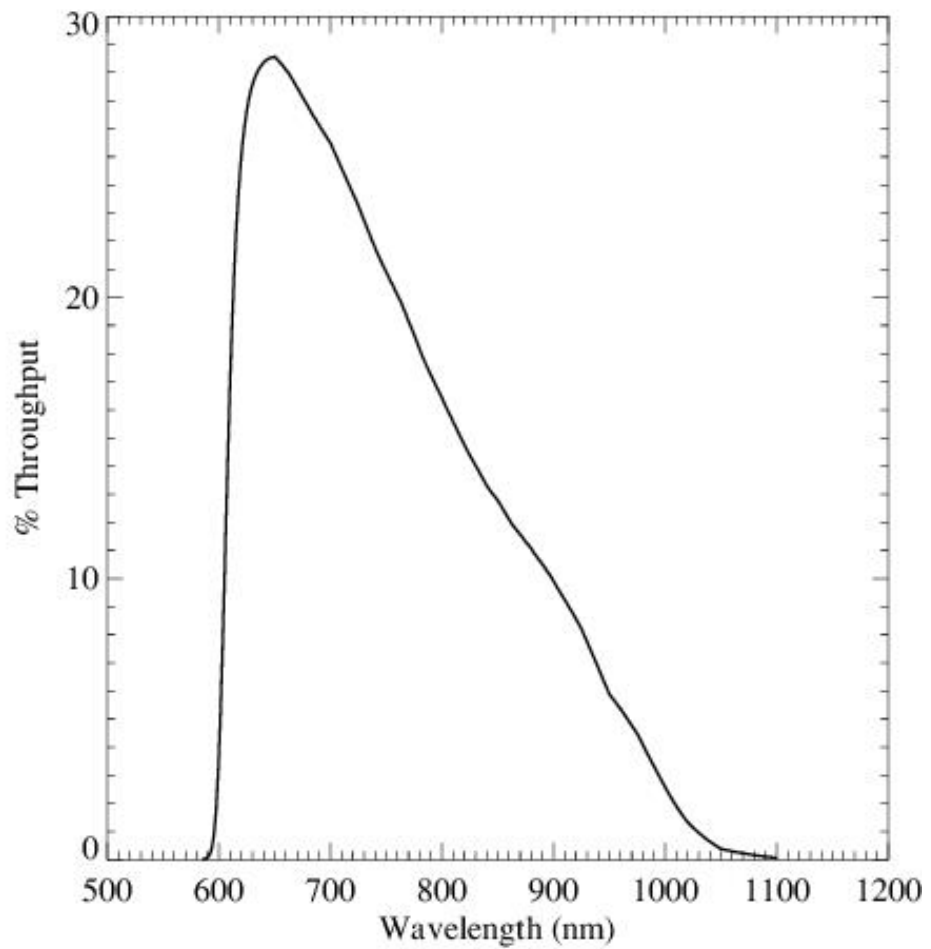


Figure A.71: Point source S/N vs. $V+AB_V$ for the F600LP filter, assuming high sky backgrounds and a 5×5 pixel aperture.

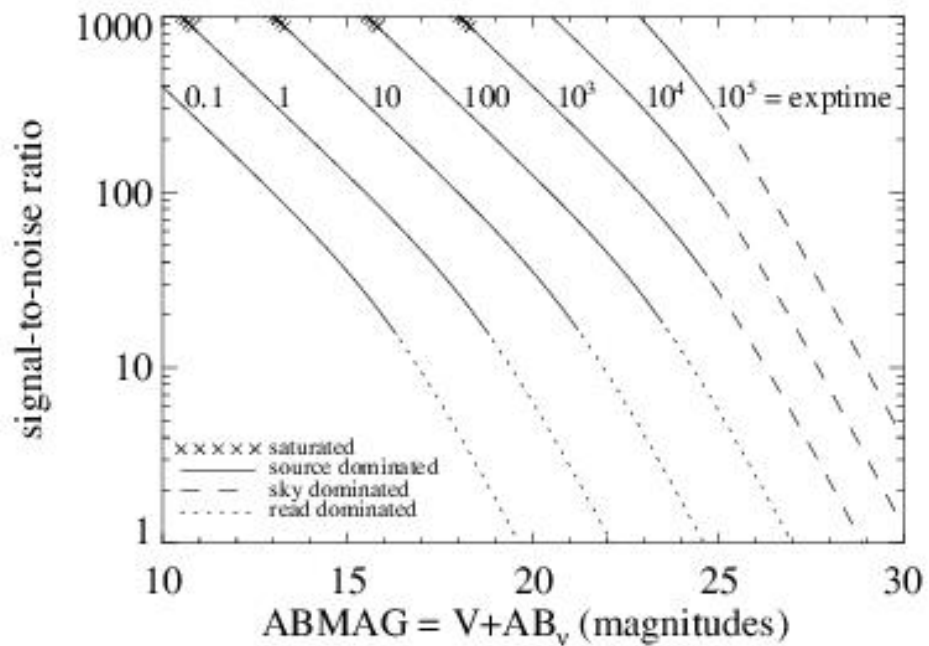
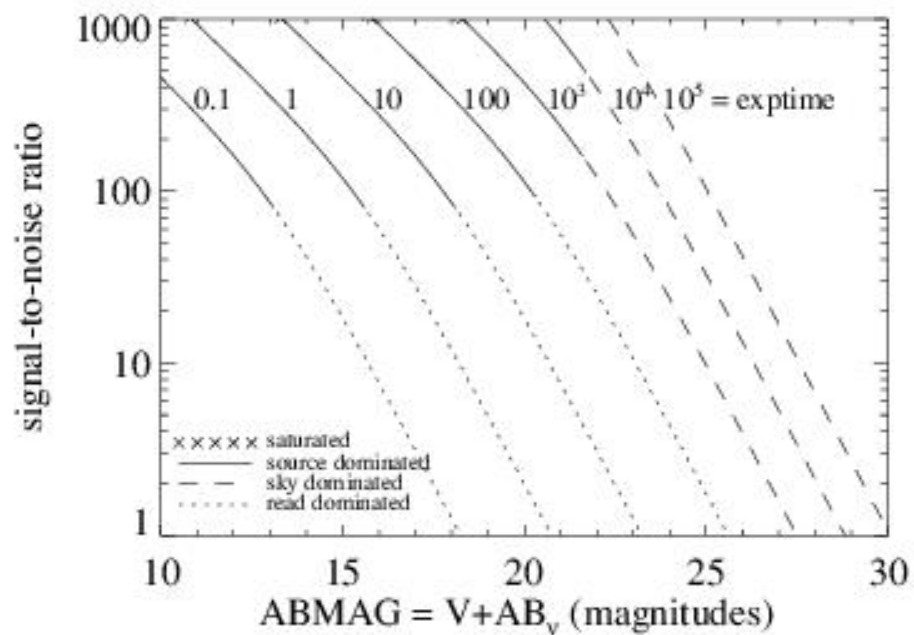


Figure A.72: Extended source S/N vs. $V+AB_v$ for the F600LP filter, assuming high sky backgrounds and a source uniformly filling a 1 arcsec^2 aperture.



UVIS F606W

Description

WFPC2 Wide *V*filter.

Figure A.73: Integrated system throughput for F606W.

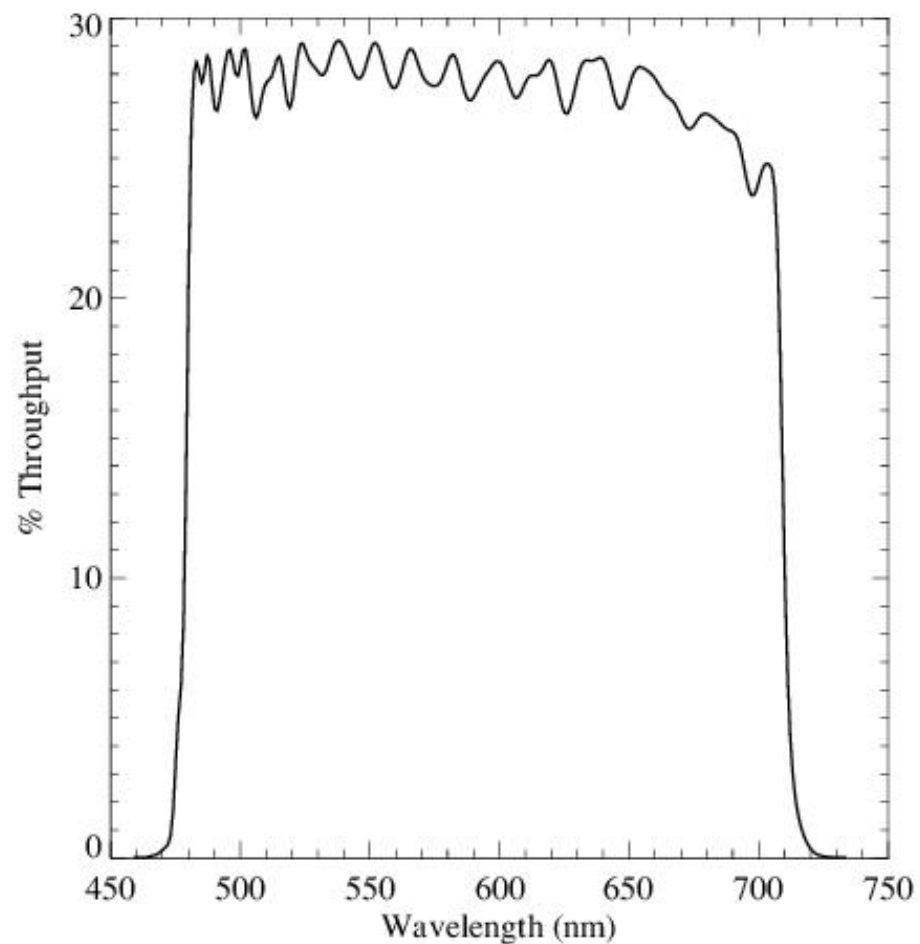


Figure A.74: Point source S/N vs. $V+AB_v$ for the F606W filter, assuming high sky backgrounds and a 5×5 pixel aperture.

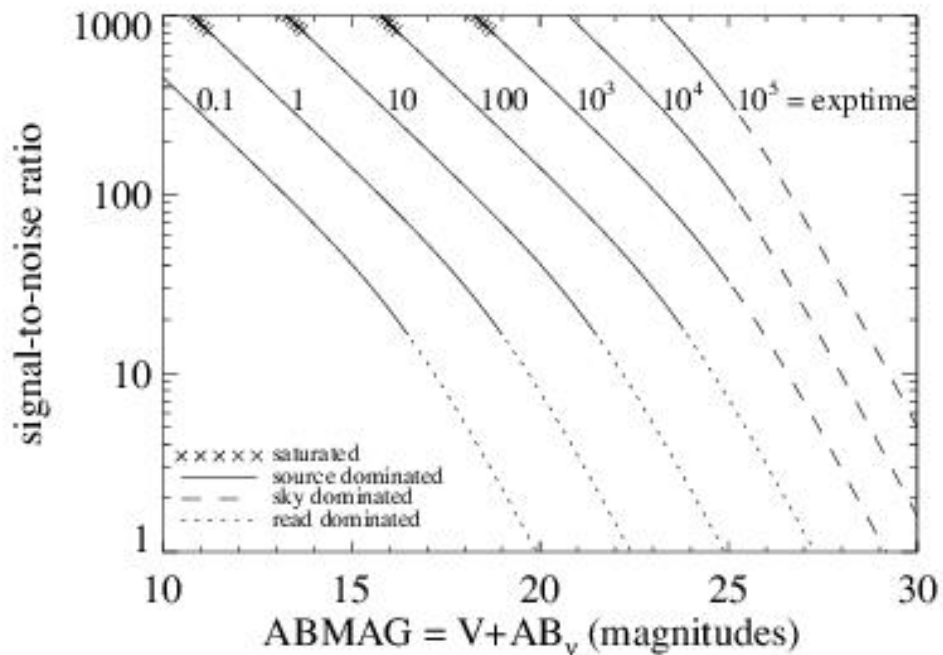
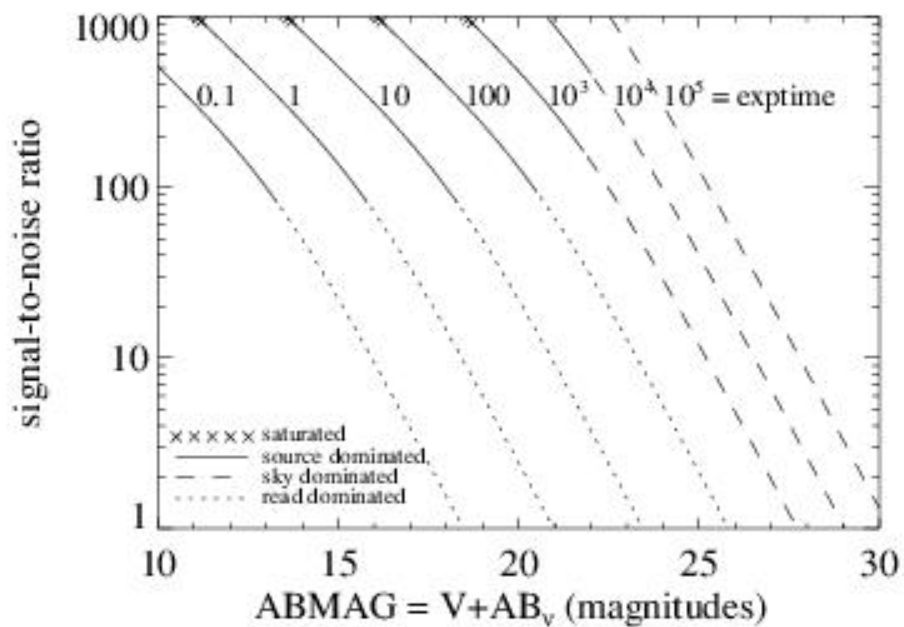


Figure A.75: Extended source S/N vs. $V+AB_V$ for the F606W filter, assuming high sky backgrounds and a source uniformly filling a 1 arcsec^2 aperture.



UVIS F621M

Description

11% passband filter.

Figure A.76: Integrated system throughput for F621M.

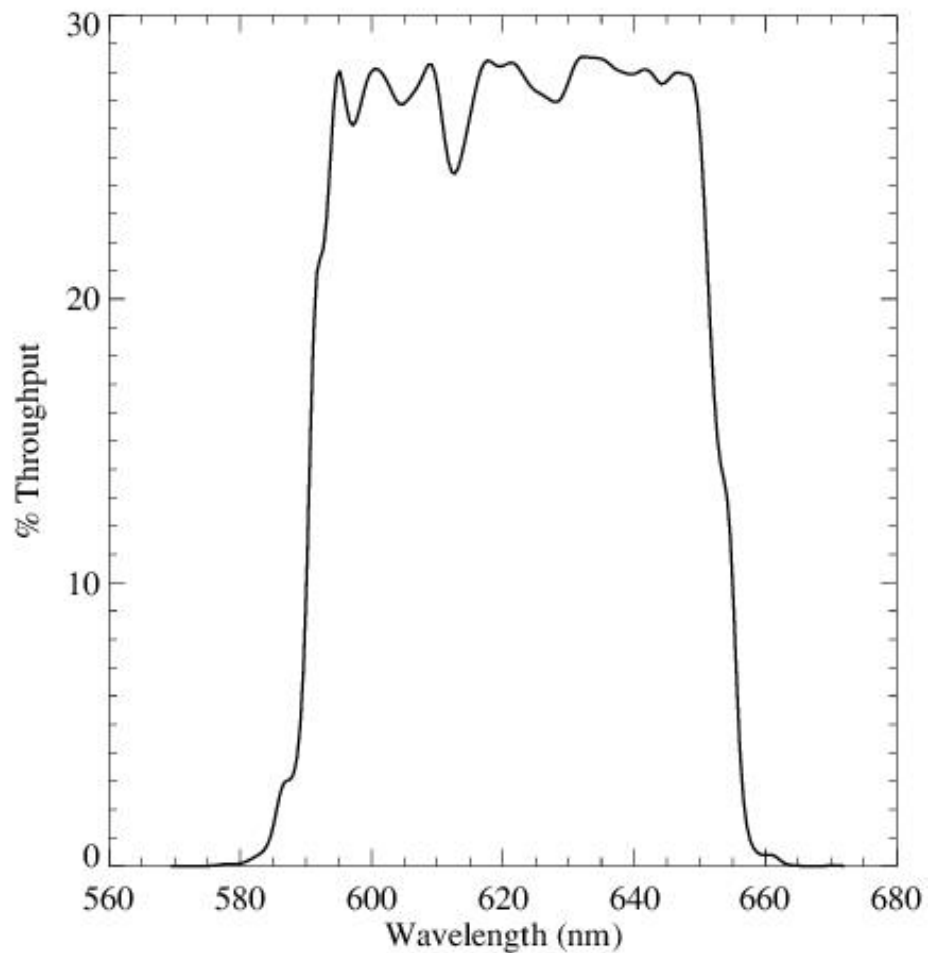


Figure A.77: Point source S/N vs. $V+AB_v$ for the F621M filter, assuming high sky backgrounds and a 5×5 pixel aperture.

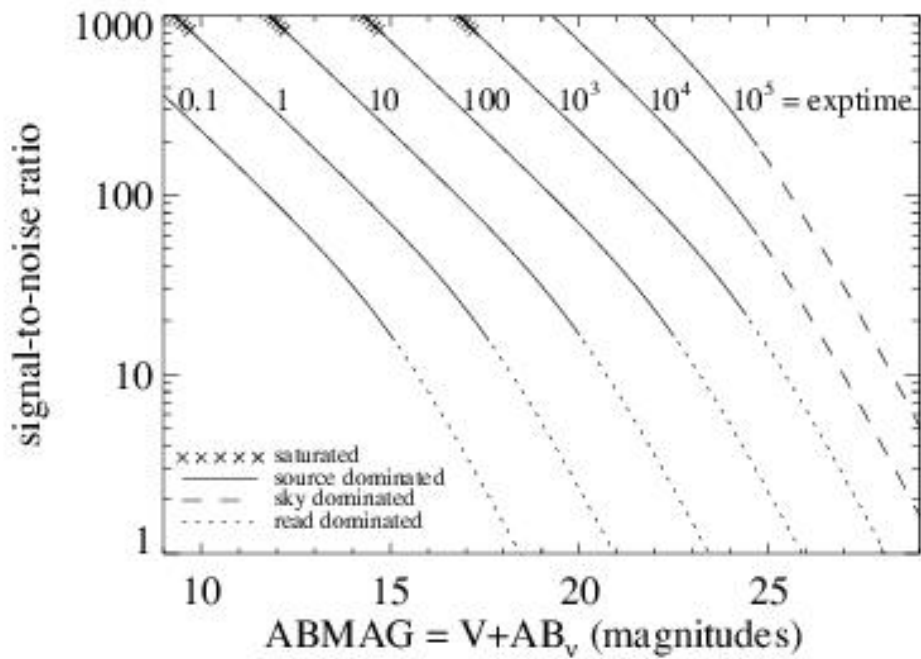
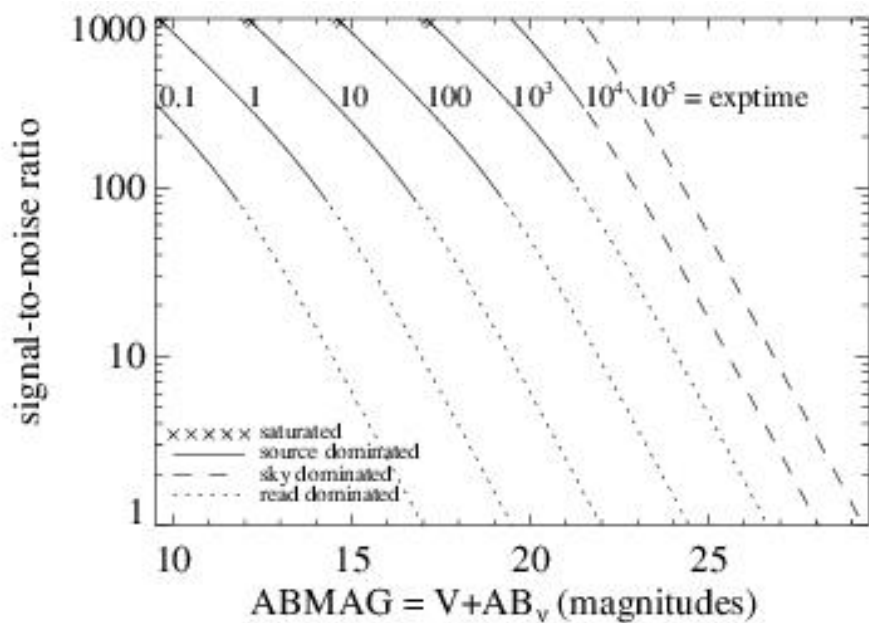


Figure A.78: Extended source S/N vs. $V+AB_V$ for the F621M filter, assuming high sky backgrounds and a source uniformly filling a 1 arcsec^2 aperture.



UVIS F625W

Description

Sloan Digital Sky Survey r' filter.

Figure A.79: Integrated system throughput for F625W.

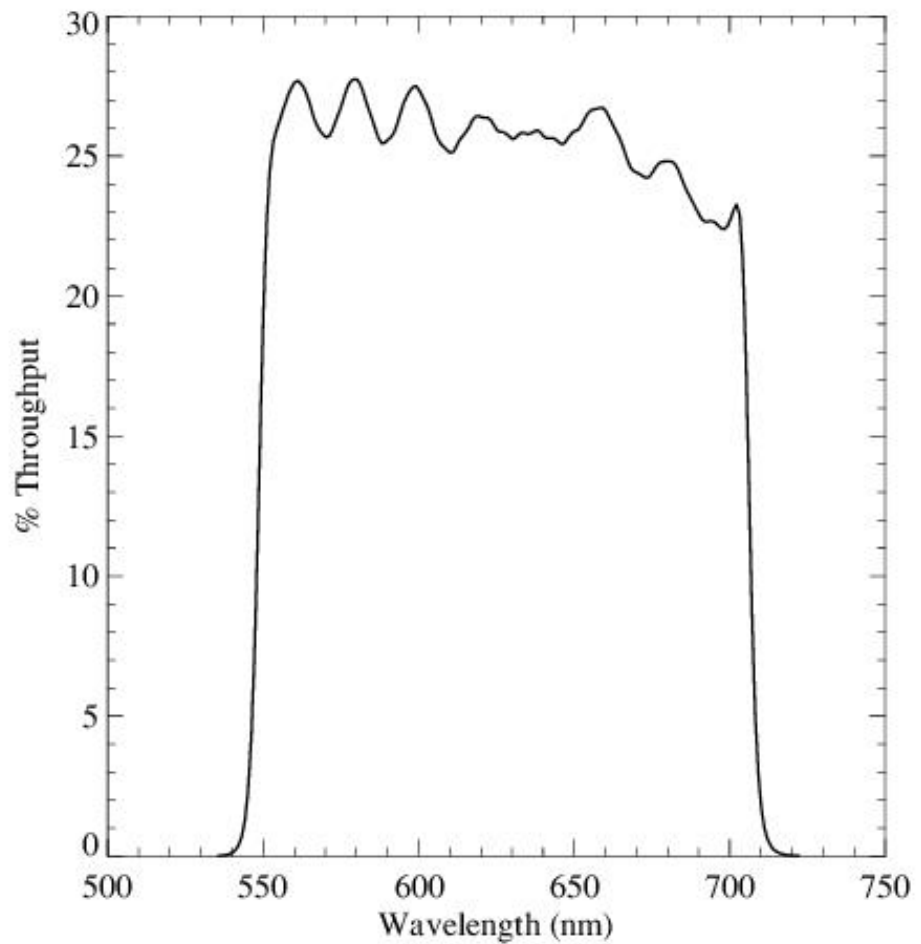


Figure A.80: Point source S/N vs. $V+AB_v$ for the F625W filter, assuming high sky backgrounds and a 5×5 pixel aperture.

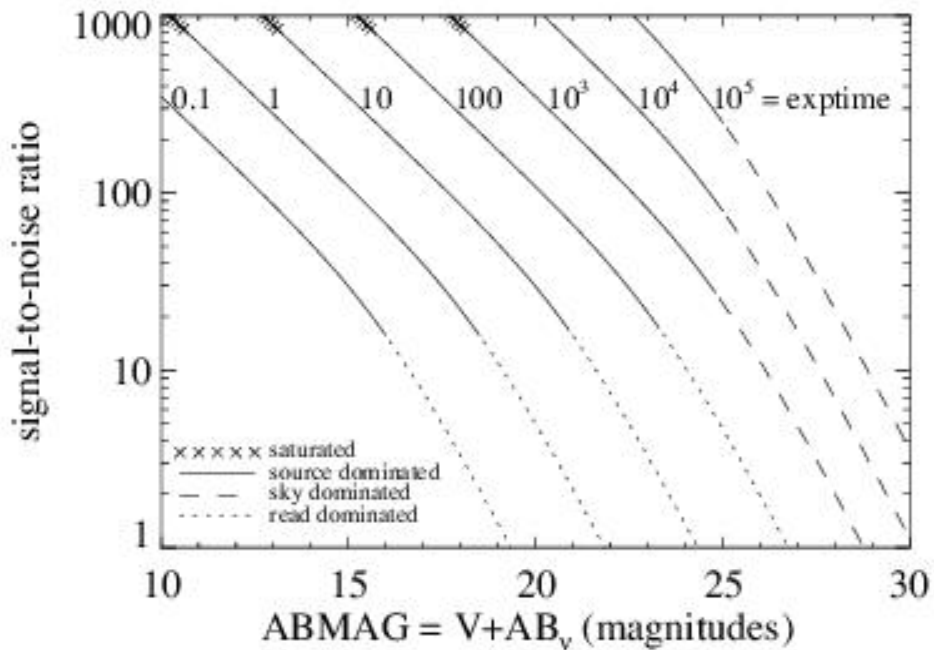
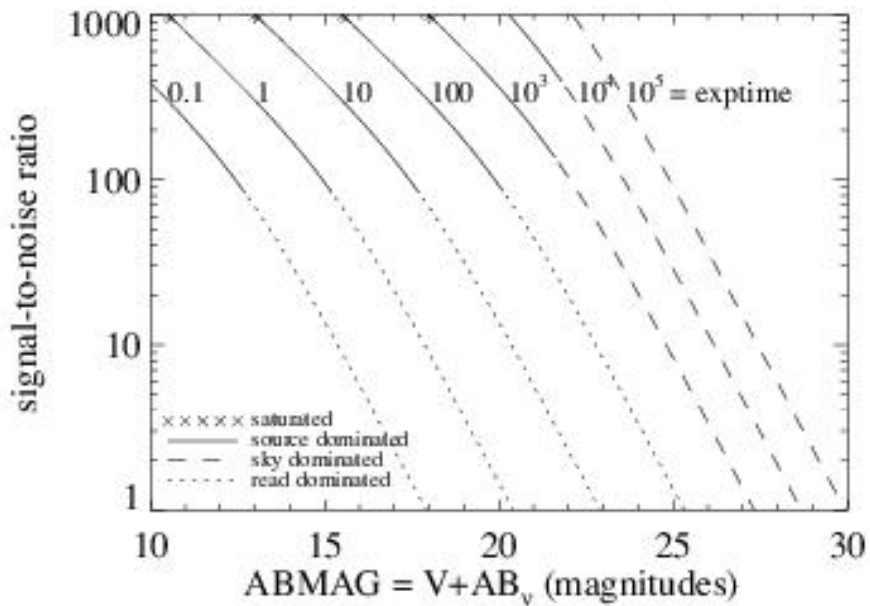


Figure A.81: Extended source S/N vs. $V+AB_v$ for the F625W filter, assuming high sky backgrounds and a source uniformly filling a 1 arcsec^2 aperture.



UVIS F631N

Description

[O I] 6300 filter.

Figure A.82: Integrated system throughput for F631N.

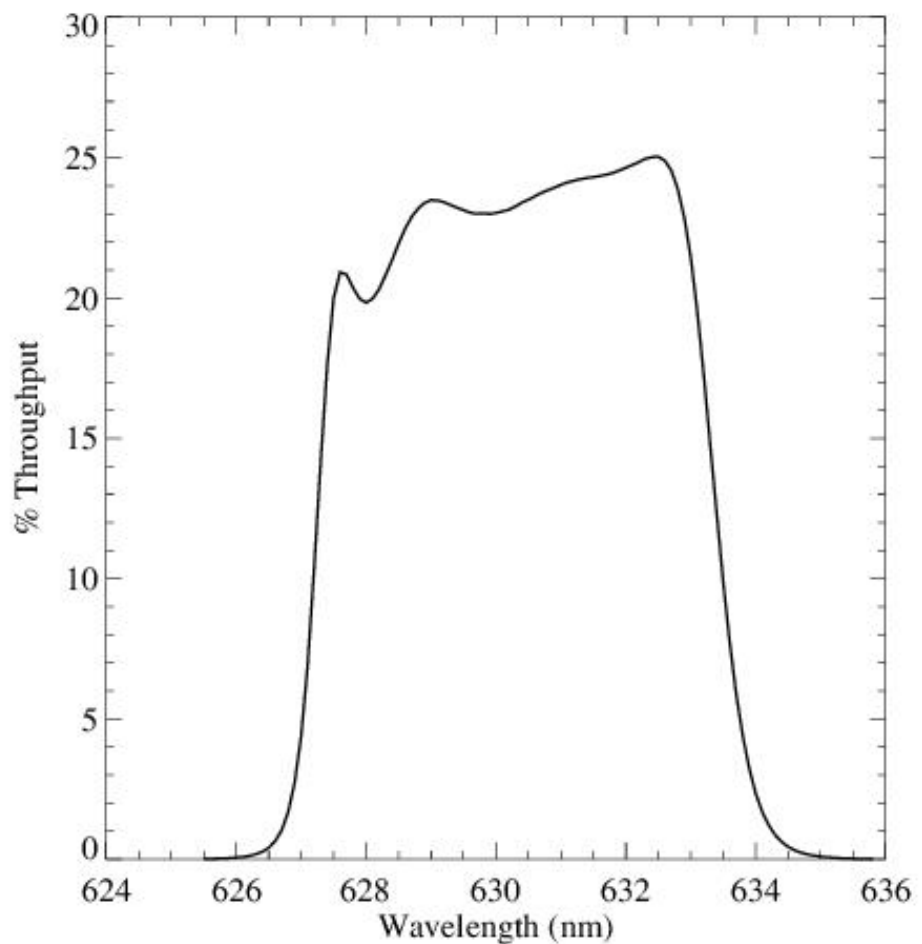


Figure A.83: Point source S/N vs. $V+AB_v$ for the F631N filter, assuming high sky backgrounds and a 5×5 pixel aperture.

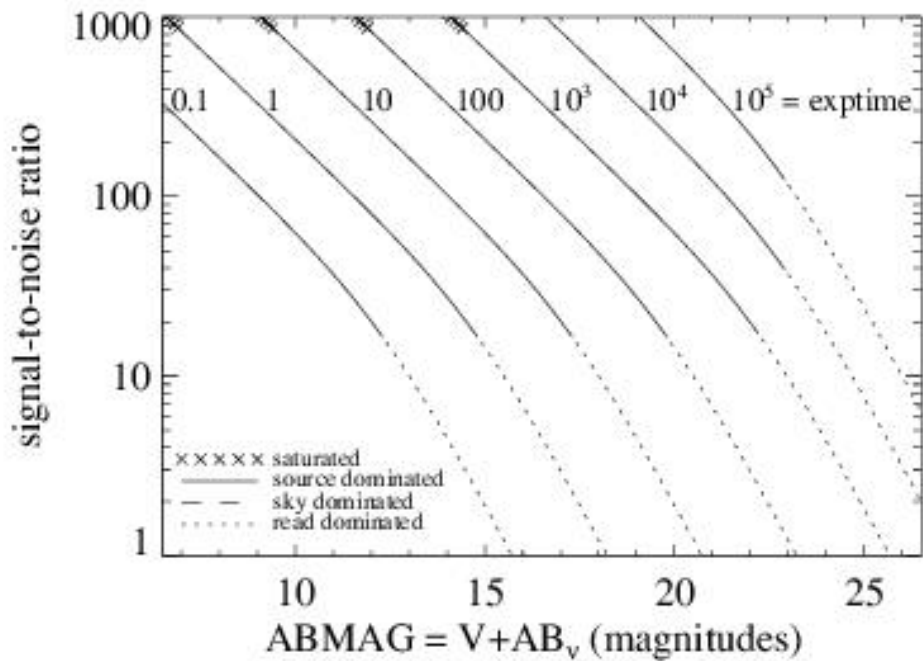
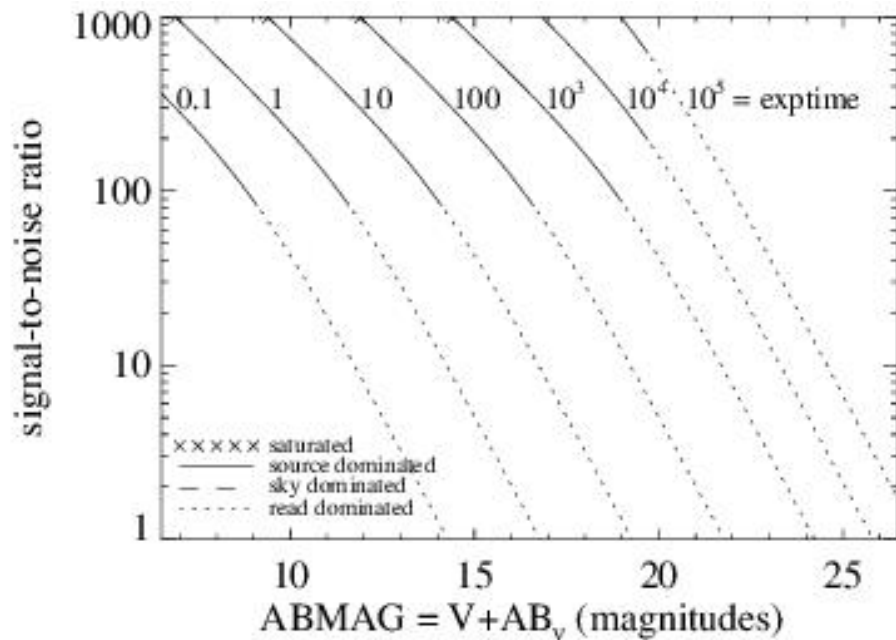


Figure A.84: Extended source S/N vs. $V+AB_v$ for the F631N filter, assuming high sky backgrounds and a source uniformly filling a 1 arcsec^2 aperture.



UVIS F645N

Description

Continuum filter.

Figure A.85: Integrated system throughput for F645N.

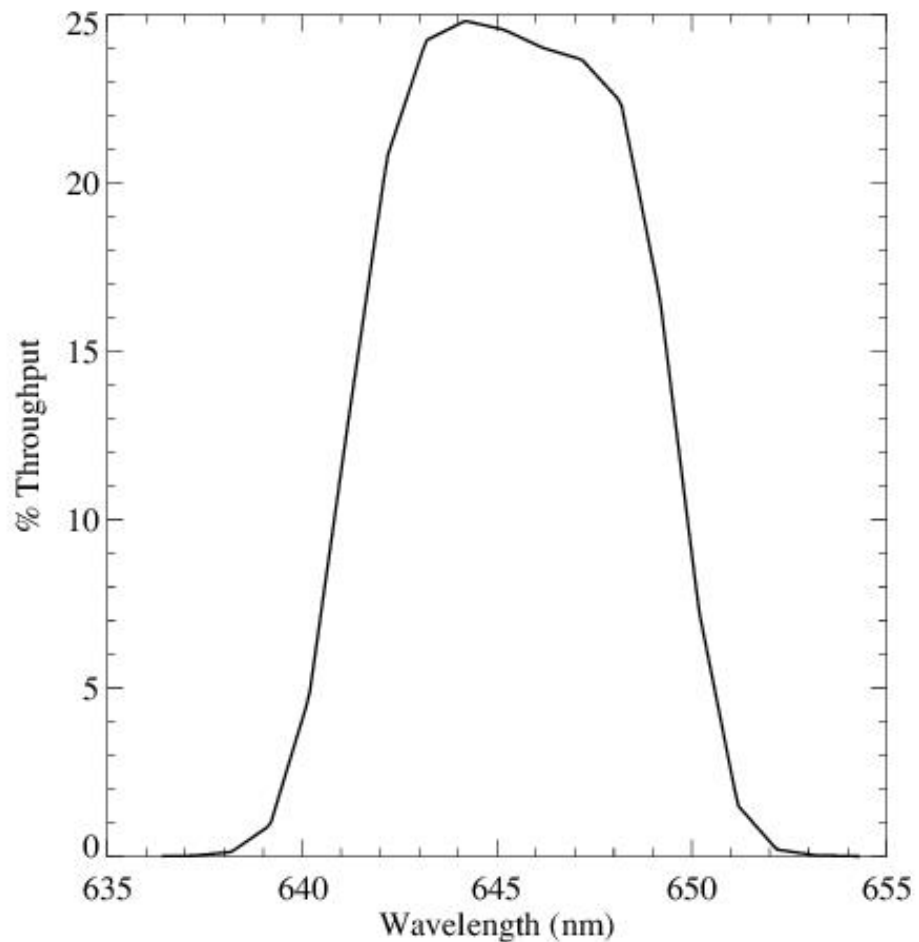


Figure A.86: Point source S/N vs. $V+AB_v$ for the F645N filter, assuming high sky backgrounds and a 5×5 pixel aperture.

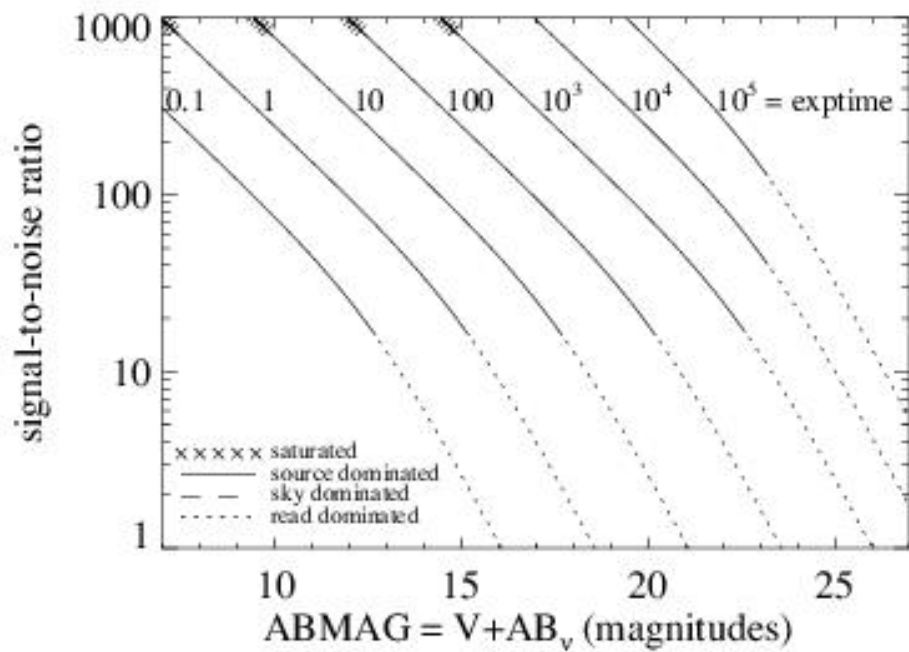
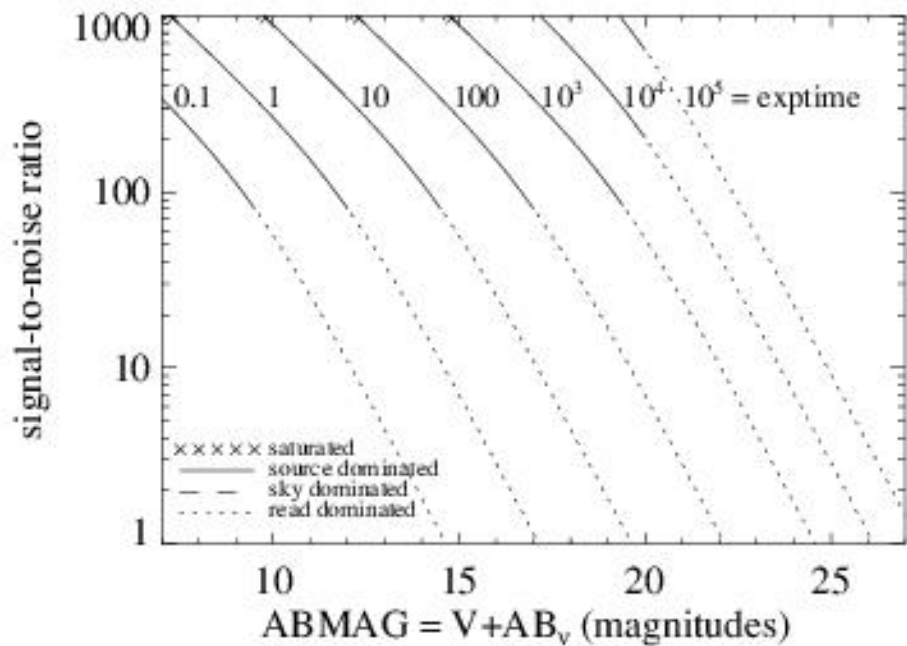


Figure A.87: Extended source S/N vs. $V+AB_V$ for the F645N filter, assuming high sky backgrounds and a source uniformly filling a 1 arcsec^2 aperture.



UVIS F656N

Description

H α 6562 filter.

Figure A.88: Integrated system throughput for F656N.

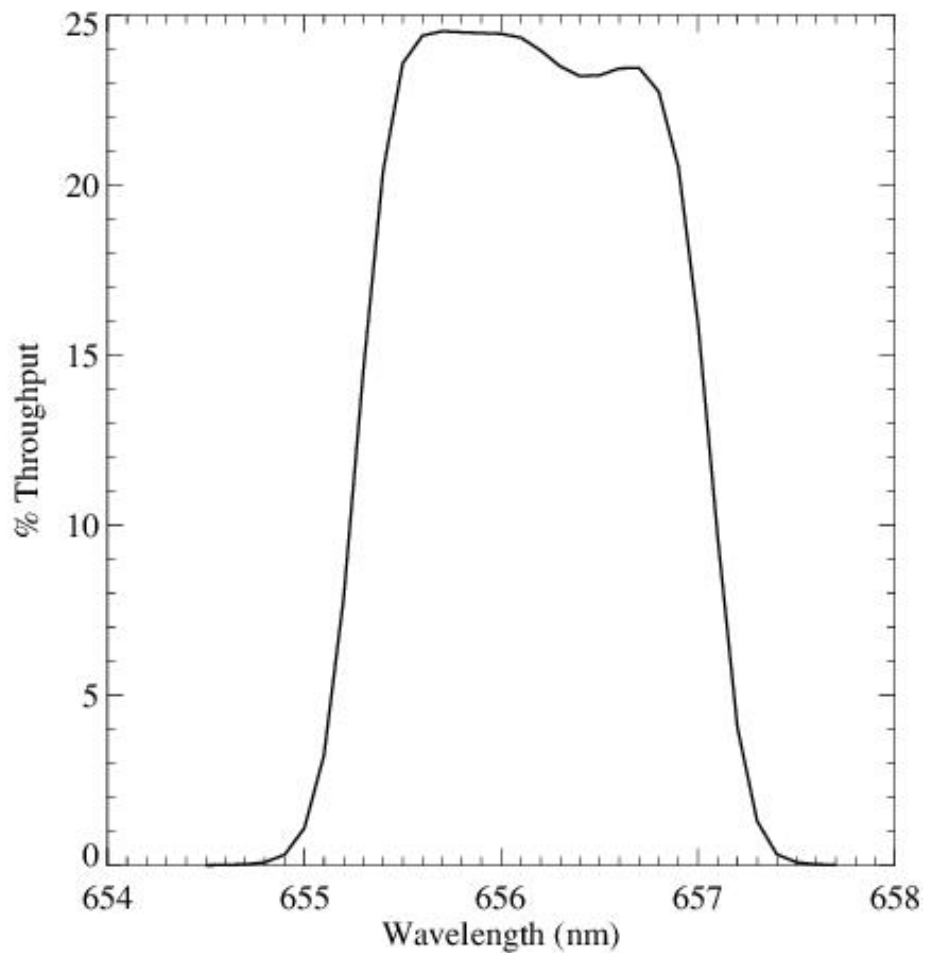


Figure A.89: Point source S/N vs. $V+AB_v$ for the F656N filter, assuming high sky backgrounds and a 5×5 pixel aperture.

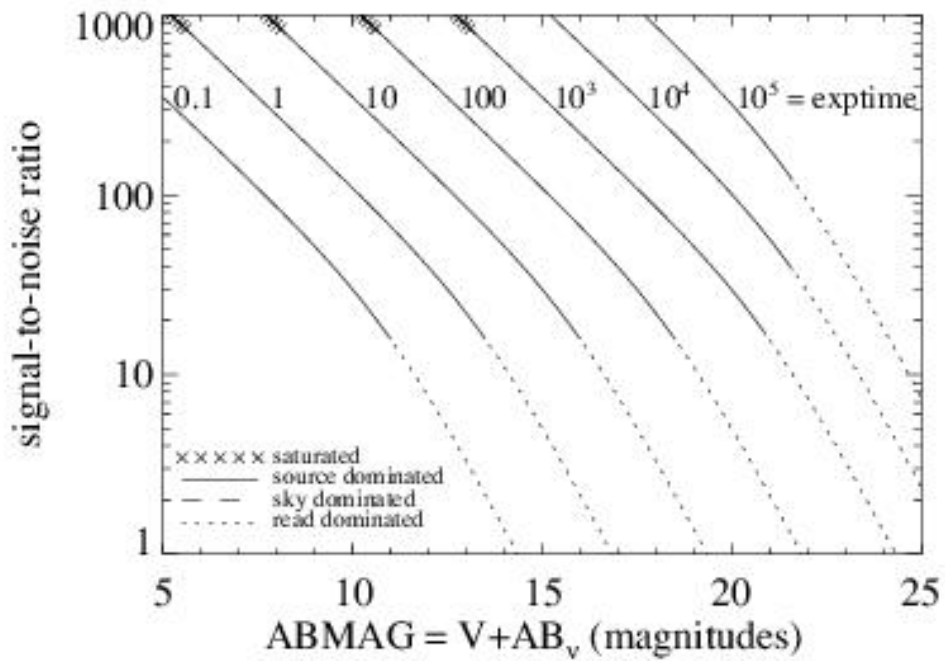
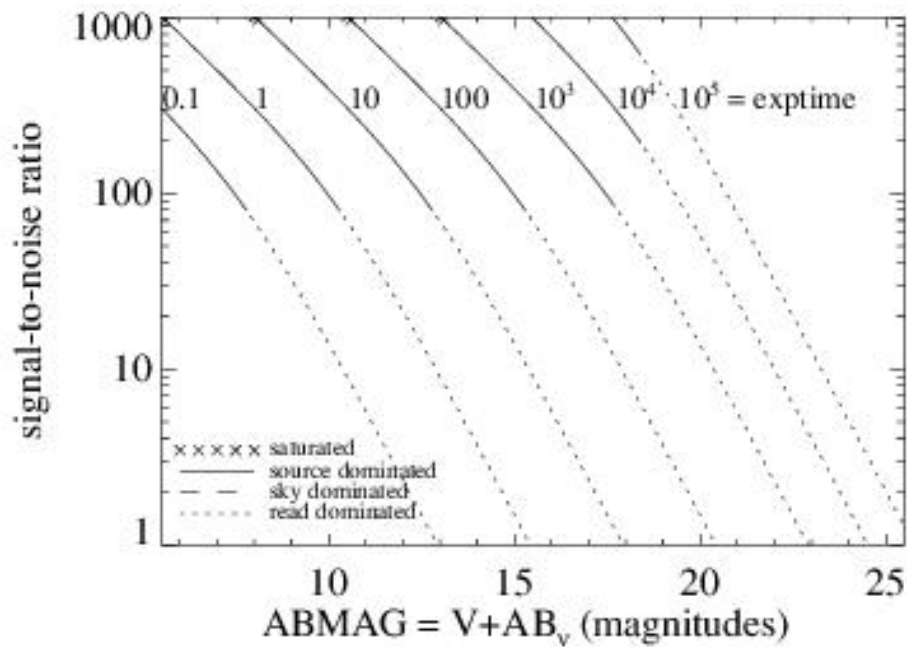


Figure A.90: Extended source S/N vs. $V+AB_V$ for the F656N filter, assuming high sky backgrounds and a source uniformly filling a 1 arcsec^2 aperture.



UVIS F657N

Description

Wide H α + [N II] filter.

Figure A.91: Integrated system throughput for F657N.

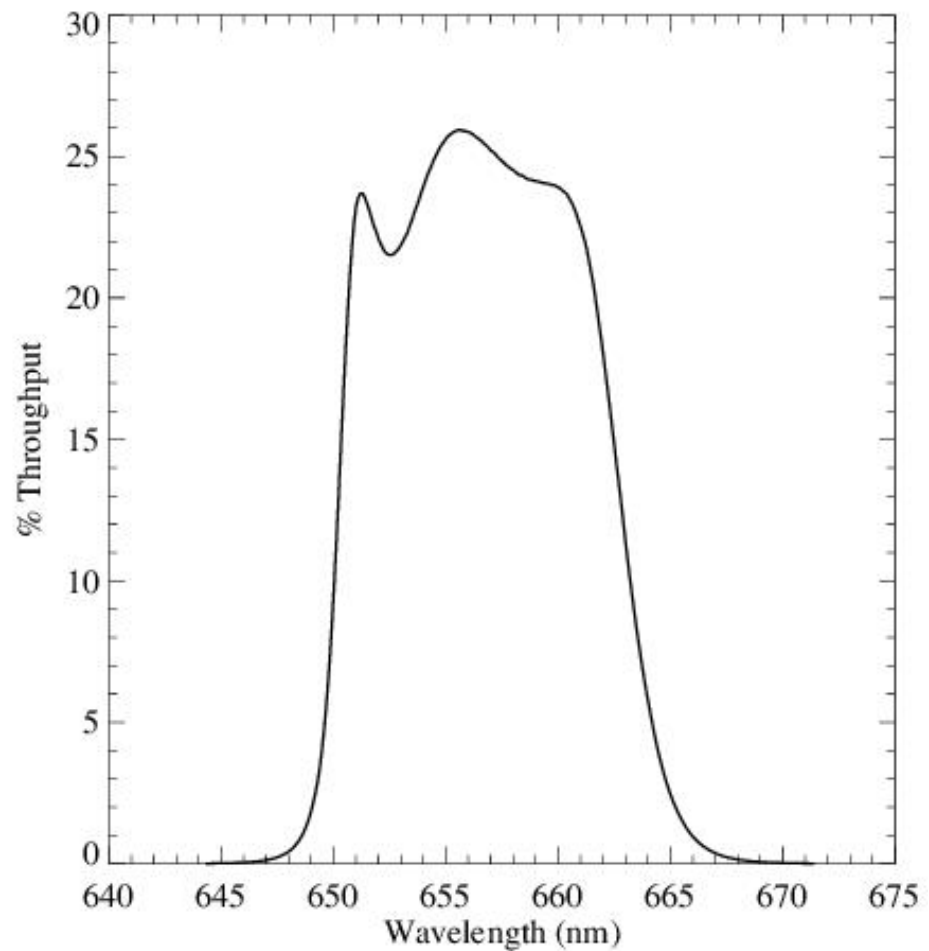


Figure A.92: Point source S/N vs. $V+AB_v$ for the F657N filter, assuming high sky backgrounds and a 5×5 pixel aperture.

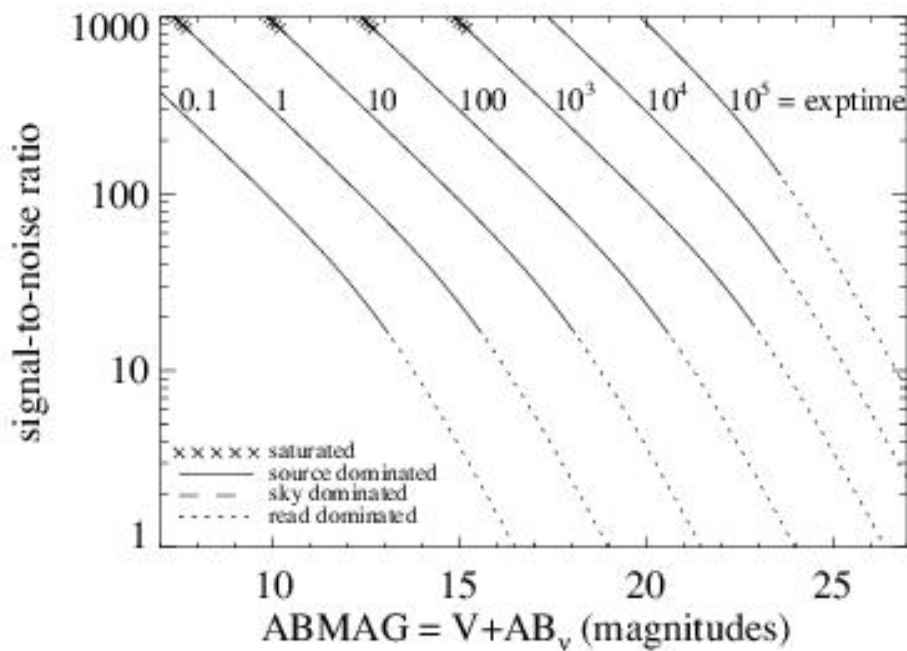
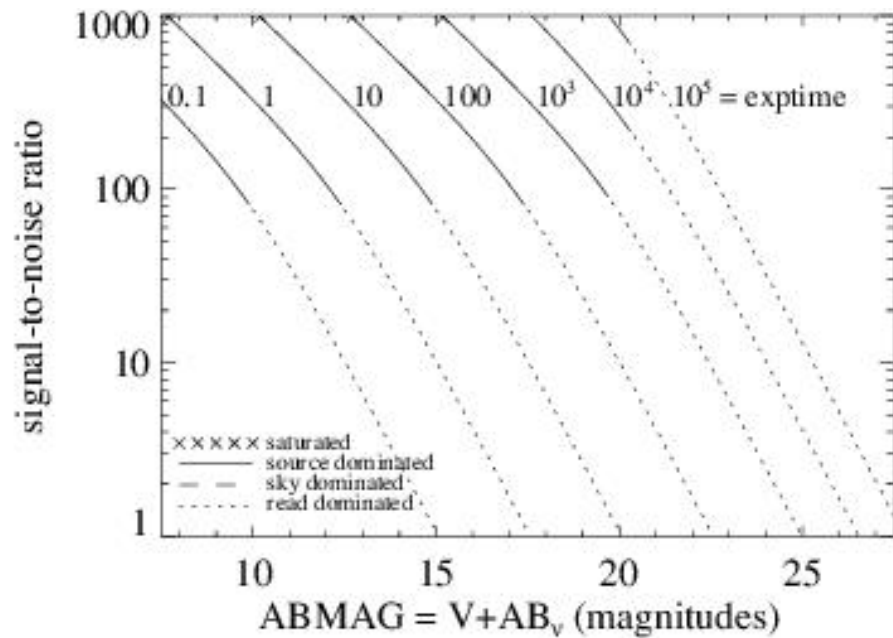


Figure A.93: Extended source S/N vs. $V+AB_V$ for the F657N filter, assuming high sky backgrounds and a source uniformly filling a 1 arcsec^2 aperture.



UVIS F658N

Description

[N II] 6583 filter.

Figure A.94: Integrated system throughput for F658N.

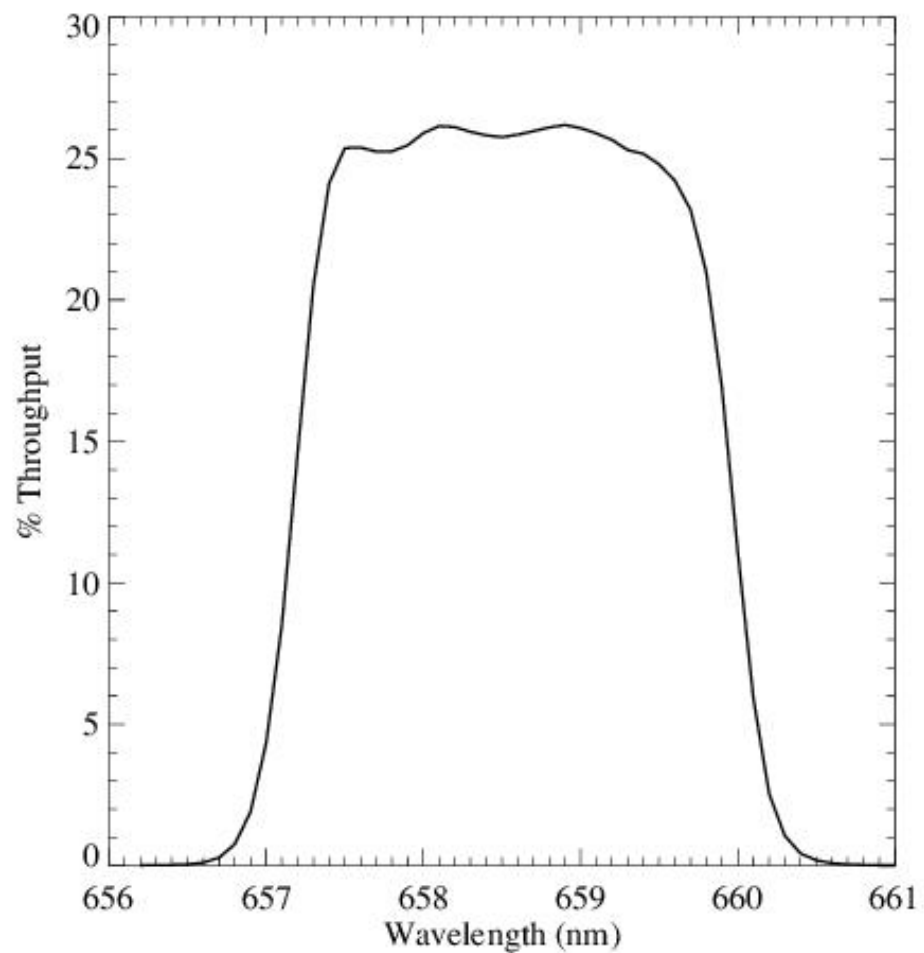


Figure A.95: Point source S/N vs. $V+AB_v$ for the F658N filter, assuming high sky backgrounds and a 5×5 pixel aperture.

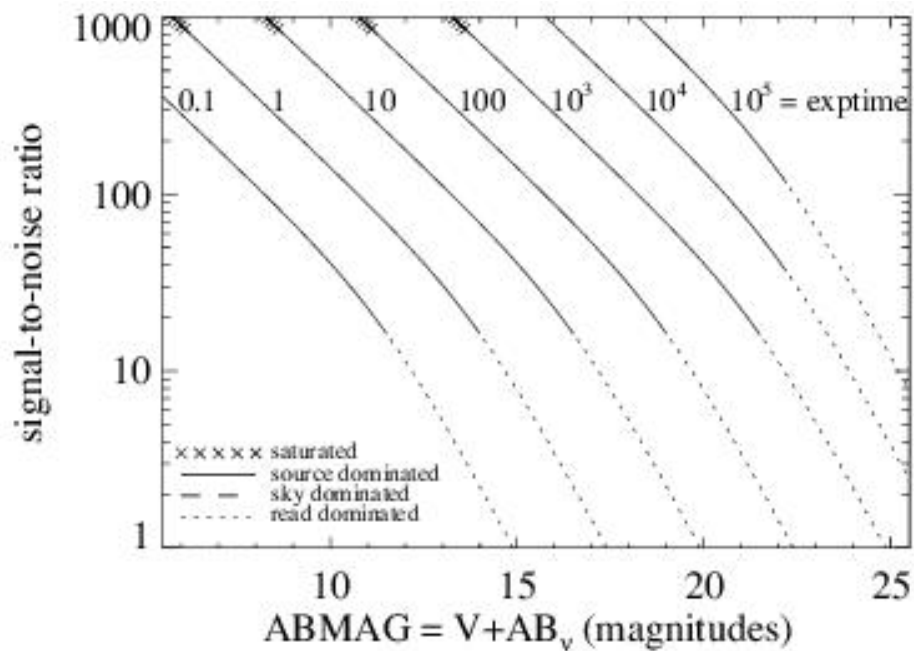
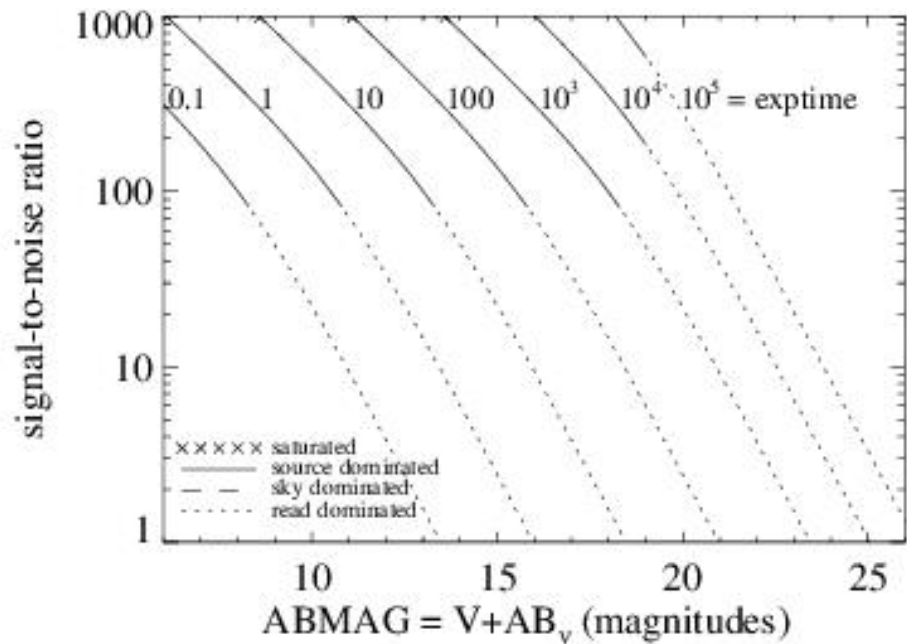


Figure A.96: Extended source S/N vs. $V+AB_V$ for the F658N filter, assuming high sky backgrounds and a source uniformly filling a 1 arcsec^2 aperture.



UVIS F665N

Description

$z(\text{H}\alpha + [\text{N II}])$ filter.

Figure A.97: Integrated system throughput for F665N.

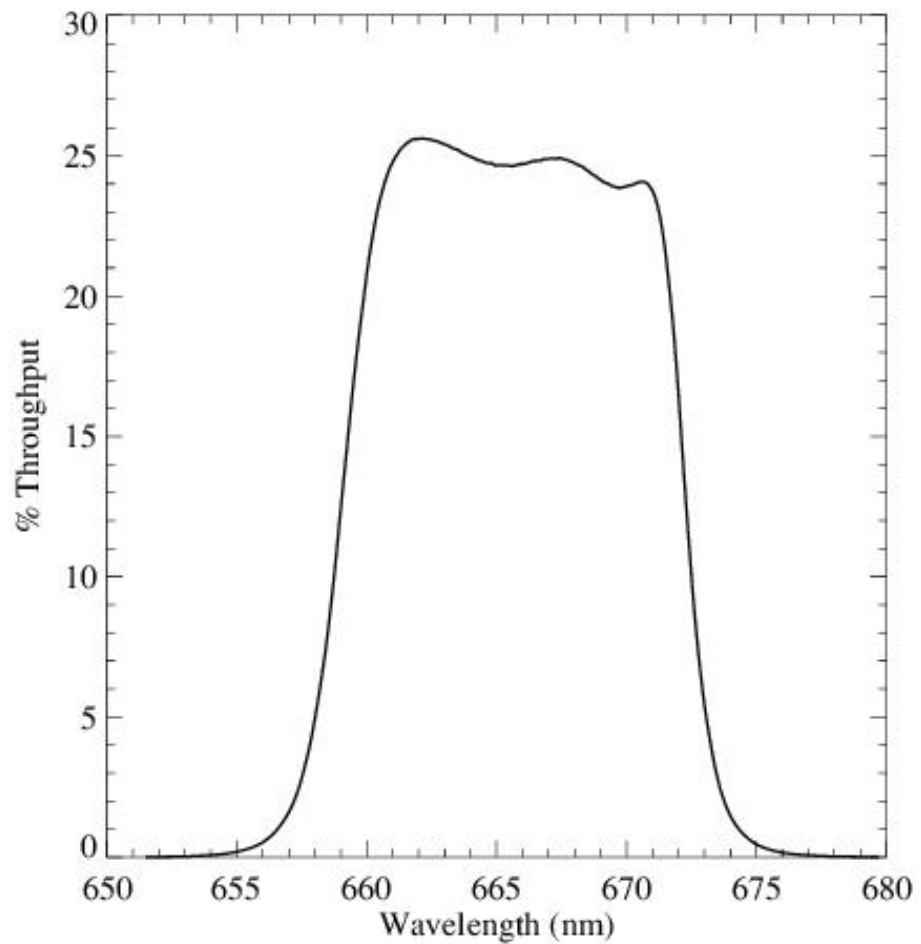


Figure A.98: Point source S/N vs. $V+AB_v$ for the F665N filter, assuming high sky backgrounds and a 5×5 pixel aperture.

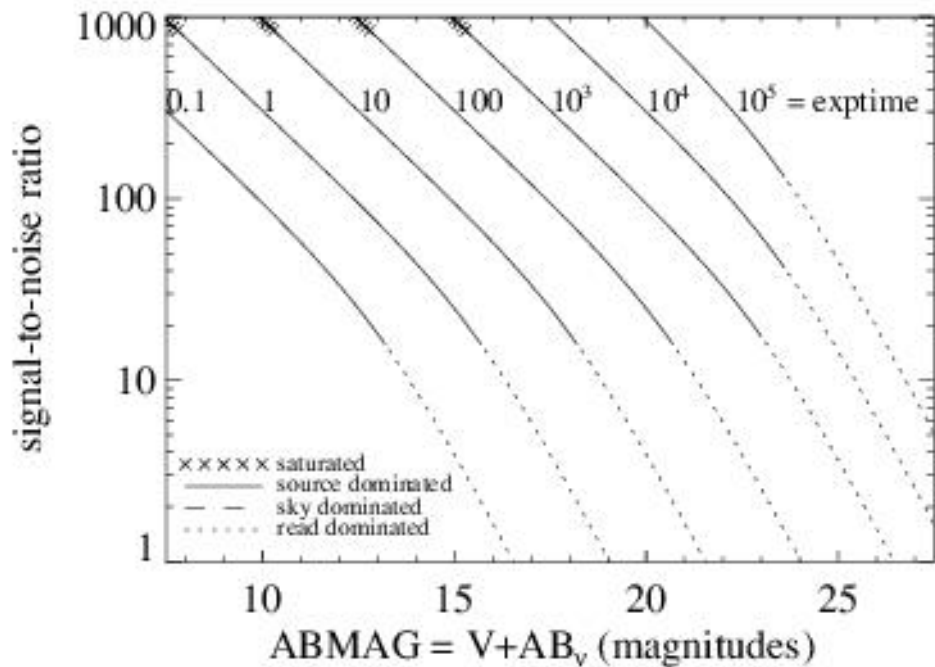
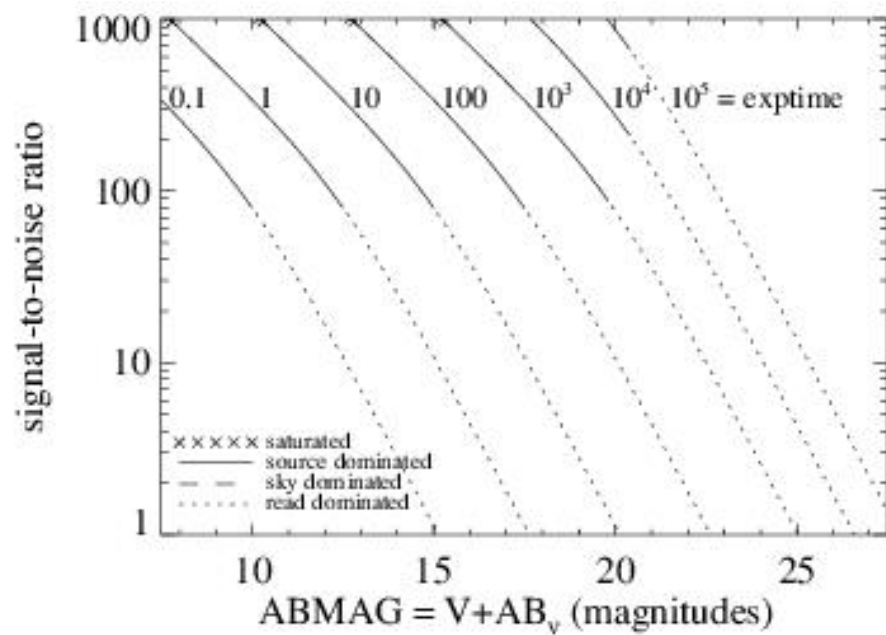


Figure A.99: Extended source S/N vs. $V+AB_V$ for the F665N filter, assuming high sky backgrounds and a source uniformly filling a 1 arcsec^2 aperture.



UVIS F673N

Description

[S II] 6717/6731 filter.

Figure A.100: Integrated system throughput for F673N.

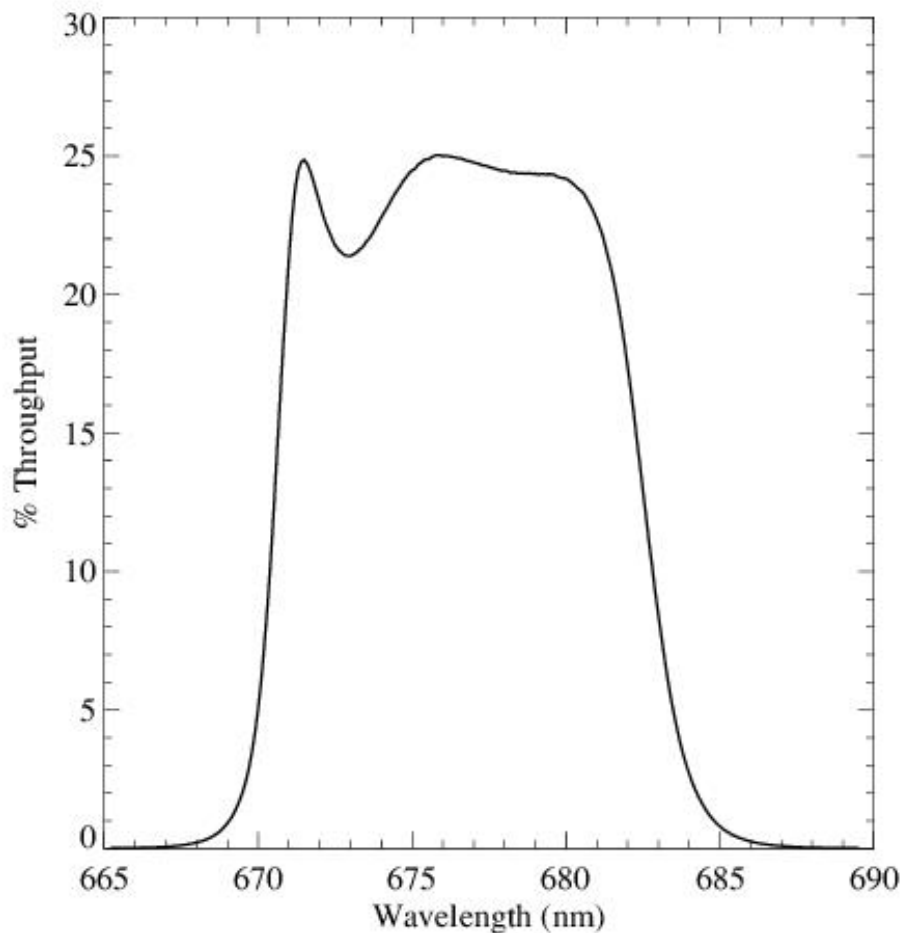


Figure A.101: Point source S/N vs. $V+AB_v$ for the F673N filter, assuming high sky backgrounds and a 5×5 pixel aperture.

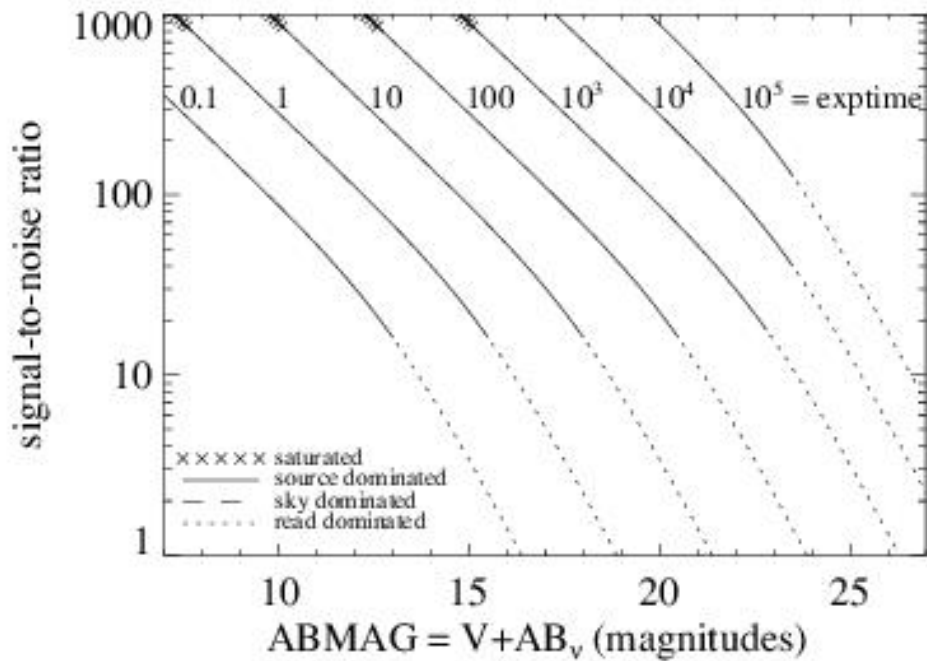
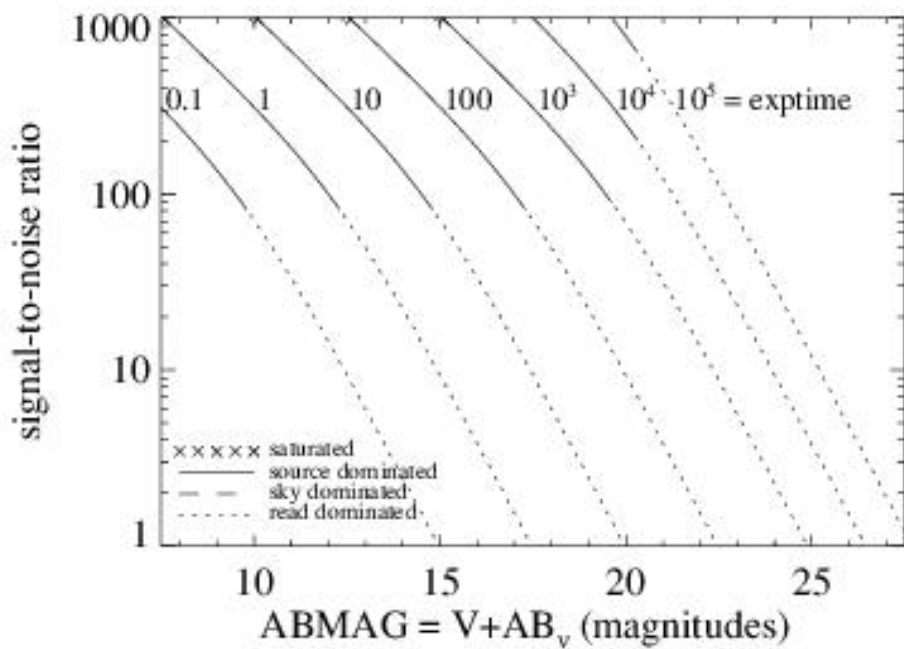


Figure A.102: Extended source S/N vs. $V+AB_V$ for the F673N filter, assuming high sky backgrounds and a source uniformly filling a 1 arcsec^2 aperture.



UVIS F680N

Description

$z(\text{H}\alpha + [\text{N II}])$ filter.

Figure A.103: Integrated system throughput for F680N.

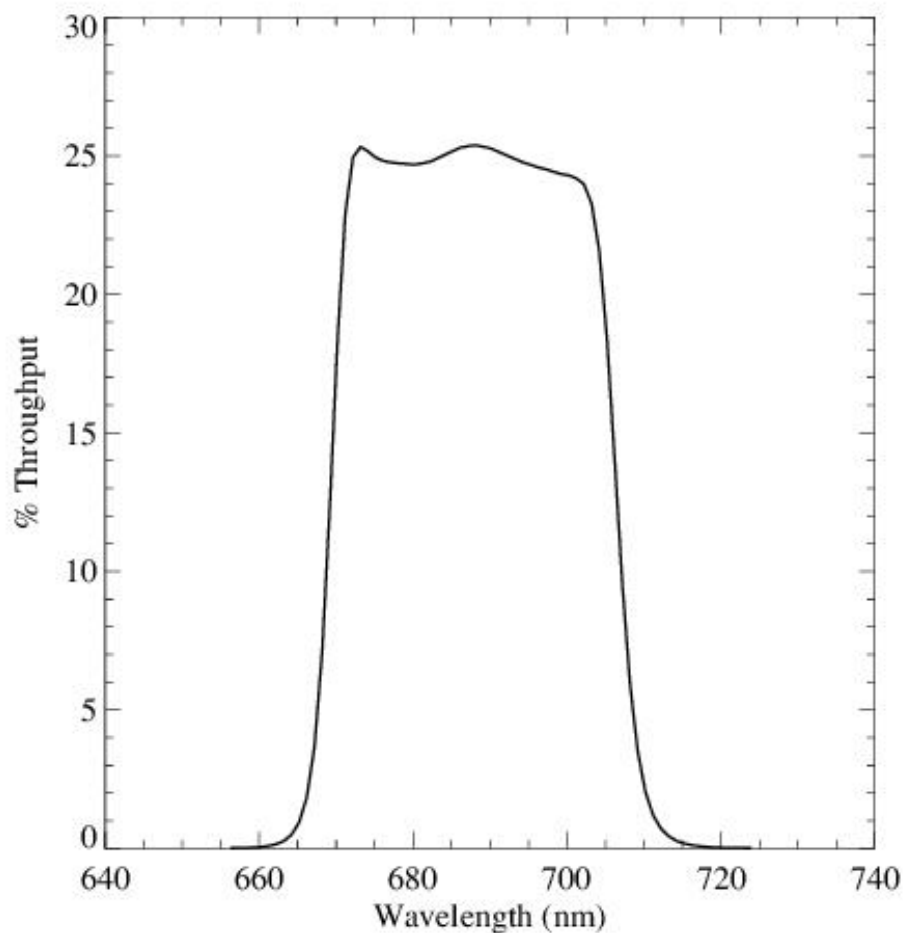


Figure A.104: Point source S/N vs. $V+AB_v$ for the F680N filter, assuming high sky backgrounds and a 5×5 pixel aperture.

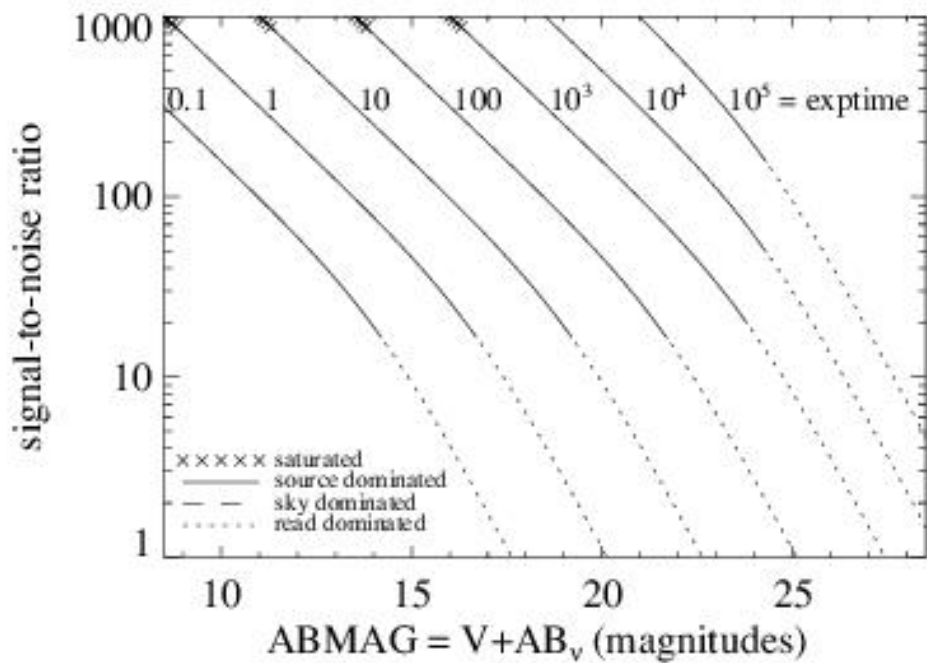
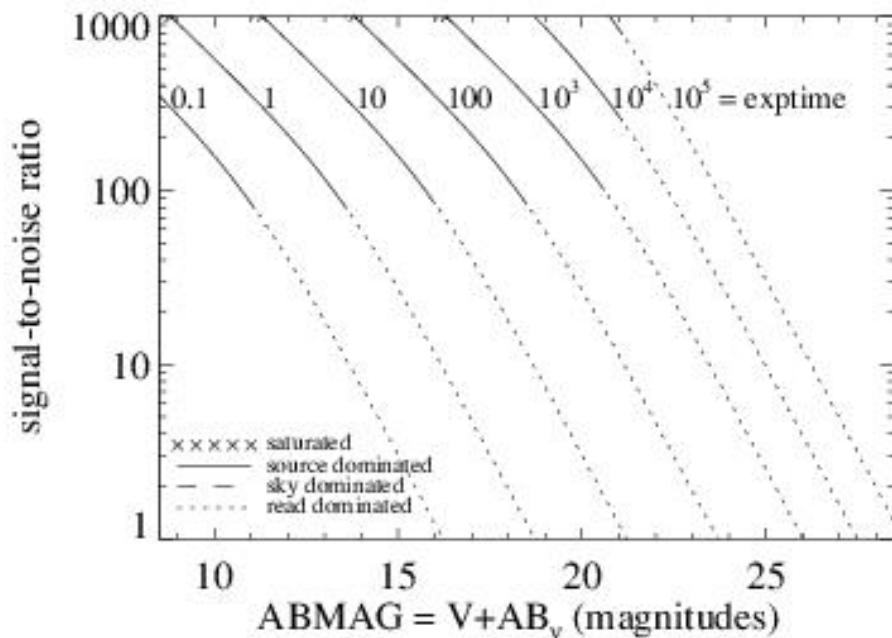


Figure A.105: Extended source S/N vs. $V+AB_V$ for the F680N filter, assuming high sky backgrounds and a source uniformly filling a 1 arcsec^2 aperture.



UVIS F689M

Description

11% passband filter.

Figure A.106: Integrated system throughput for F689M.

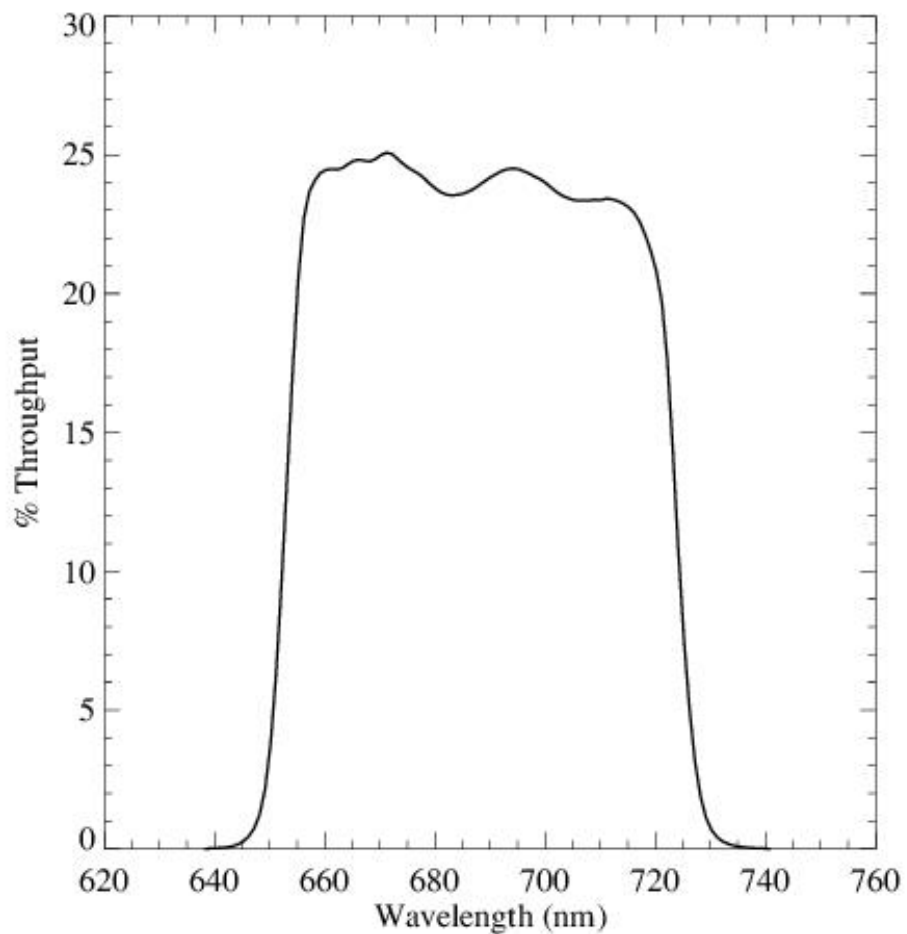


Figure A.107: Point source S/N vs. $V+AB_v$ for the F689M filter. Top curves are for low sky; bottom curves are for average sky.

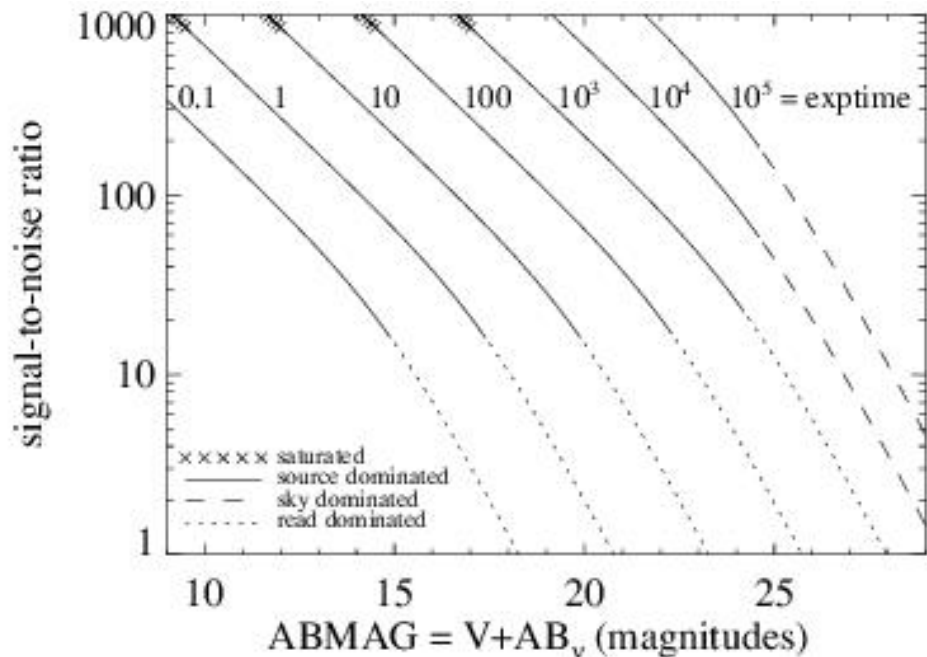
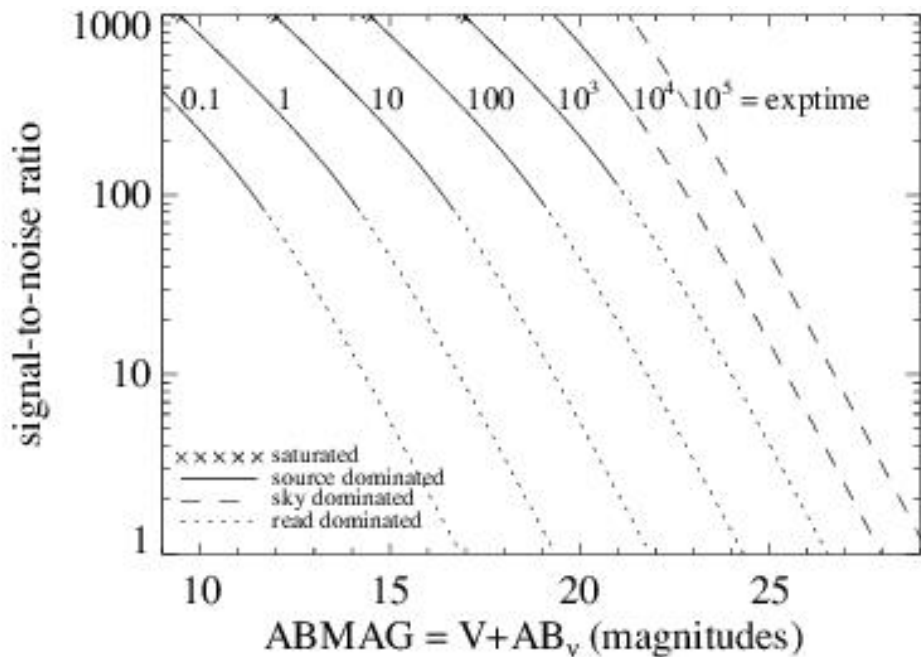


Figure A.108: Extended source S/N vs. $V+AB_v$ for the F689M filter, assuming high sky backgrounds and a source uniformly filling a 1 arcsec^2 aperture.



UVIS F763M

Description

11% passband filter.

Figure A.109: Integrated system throughput for F763M.

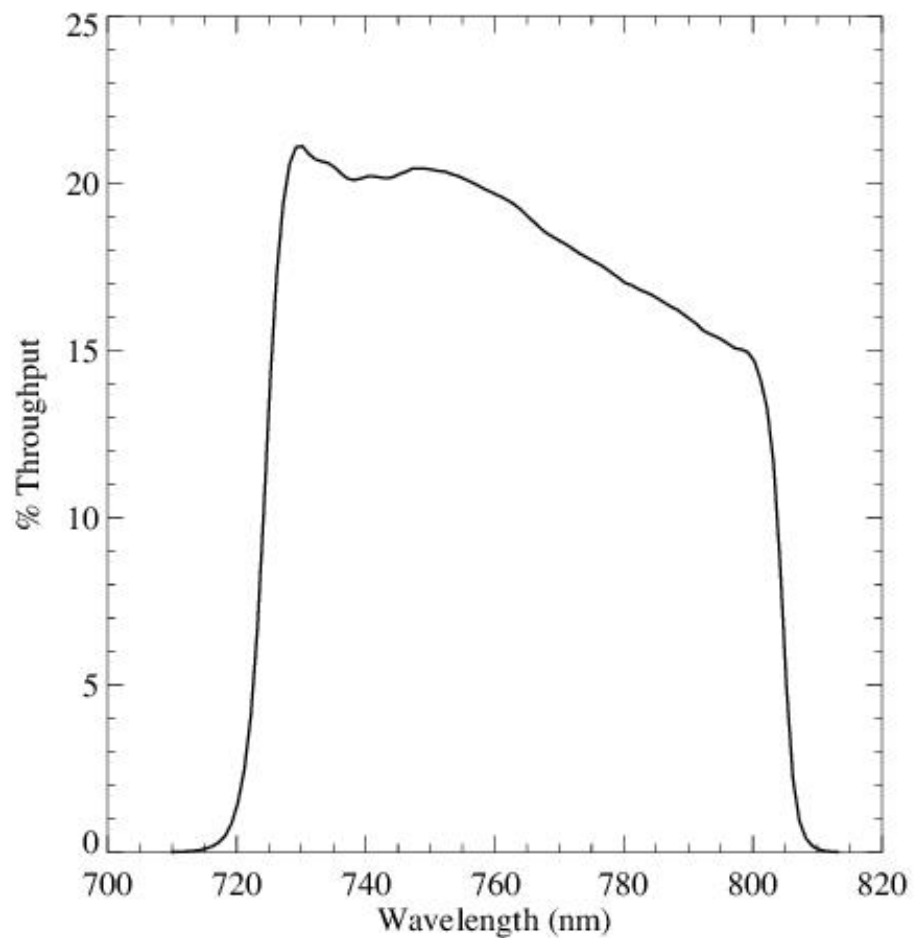


Figure A.110: Point source S/N vs. $V+AB_v$ for the F763M filter. Top curves are for low sky; bottom curves are for average sky.

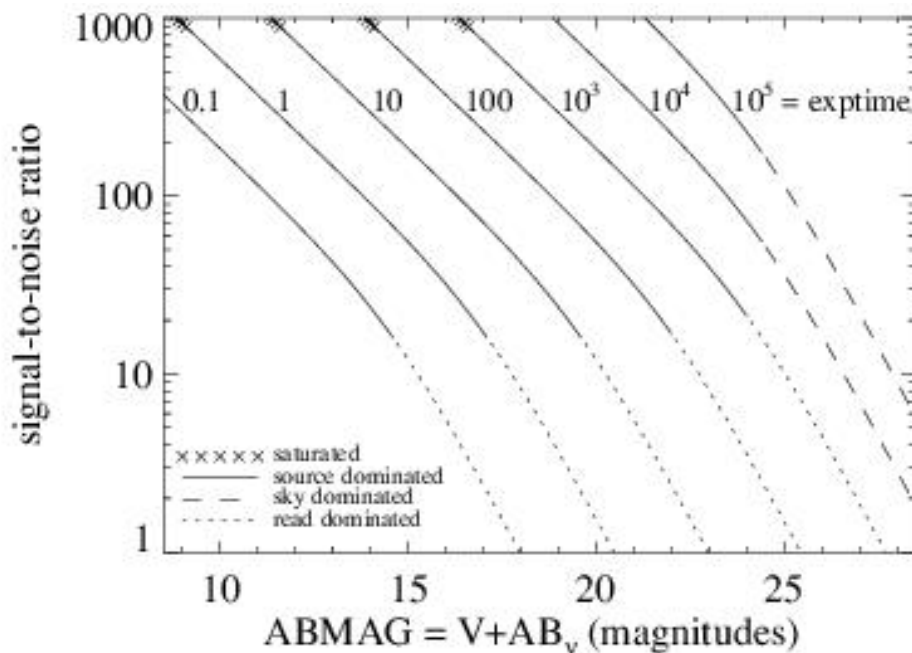
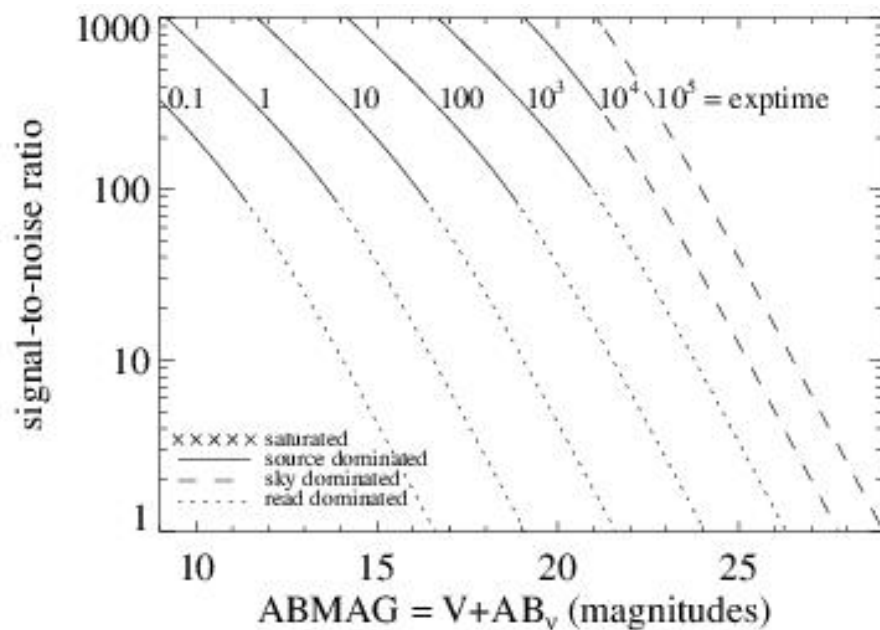


Figure A.111: Extended source S/N vs. $V+AB_V$ for the F763M filter, assuming high sky backgrounds and a source uniformly filling a 1 arcsec^2 aperture.



UVIS F775W

Description

Sloan Digital Sky Survey i' filter.

Figure A.112: Integrated system throughput for F775W.

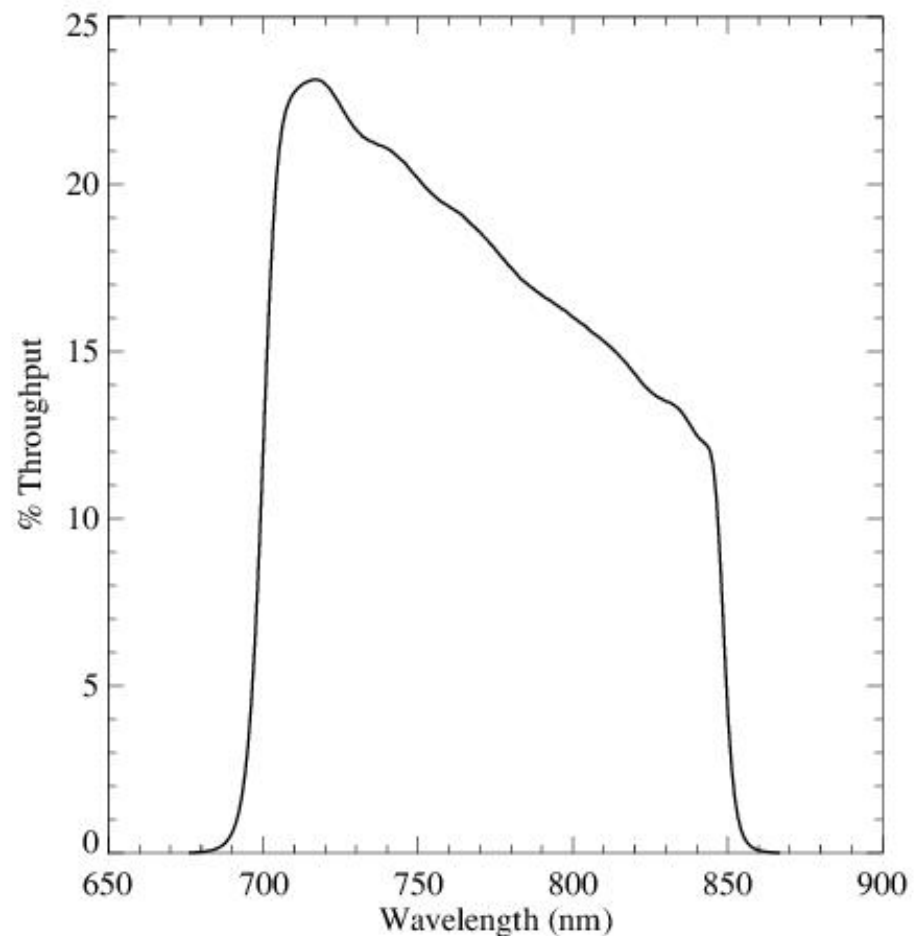


Figure A.113: Point source S/N vs. $V+AB_v$ for the F775W filter, assuming high sky backgrounds and a 5×5 pixel aperture.

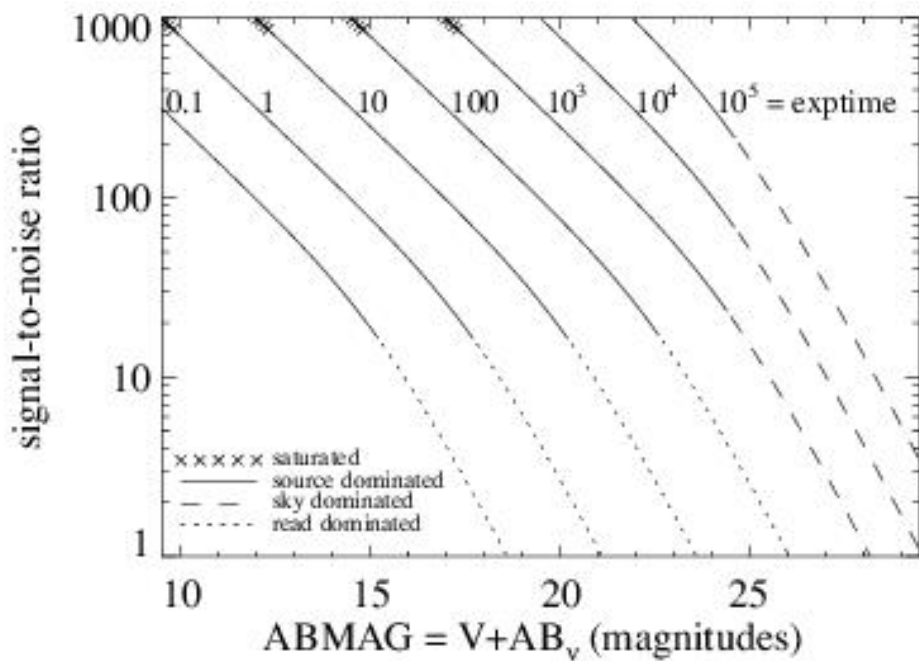
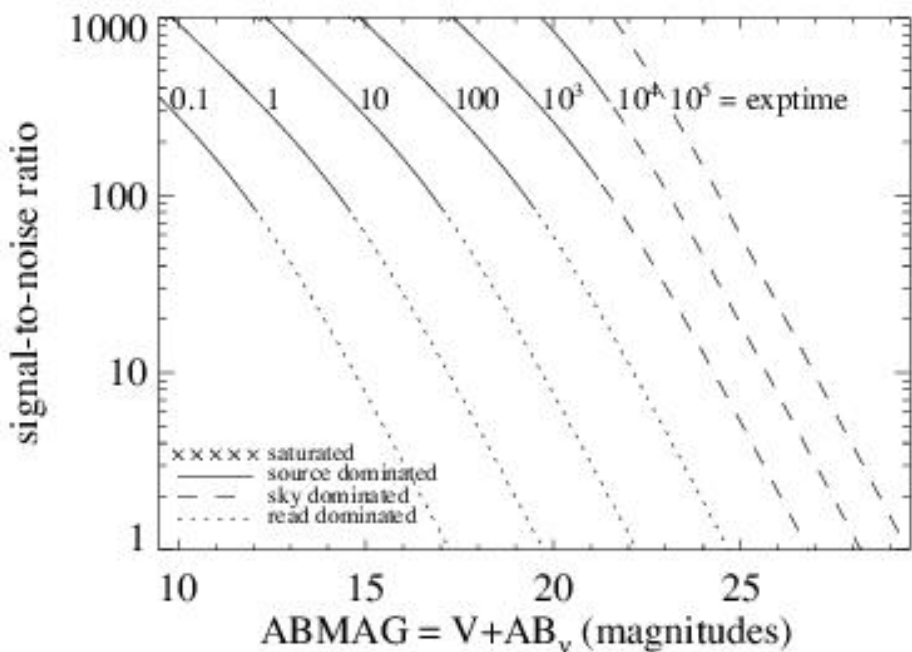


Figure A.114: Extended source S/N vs. $V+AB_v$ for the F775W filter, assuming high sky backgrounds and a source uniformly filling a 1 arcsec^2 aperture.



UVIS F814W

Description

WFPC2 Wide *I* filter.

Figure A.115: Integrated system throughput for F814W.

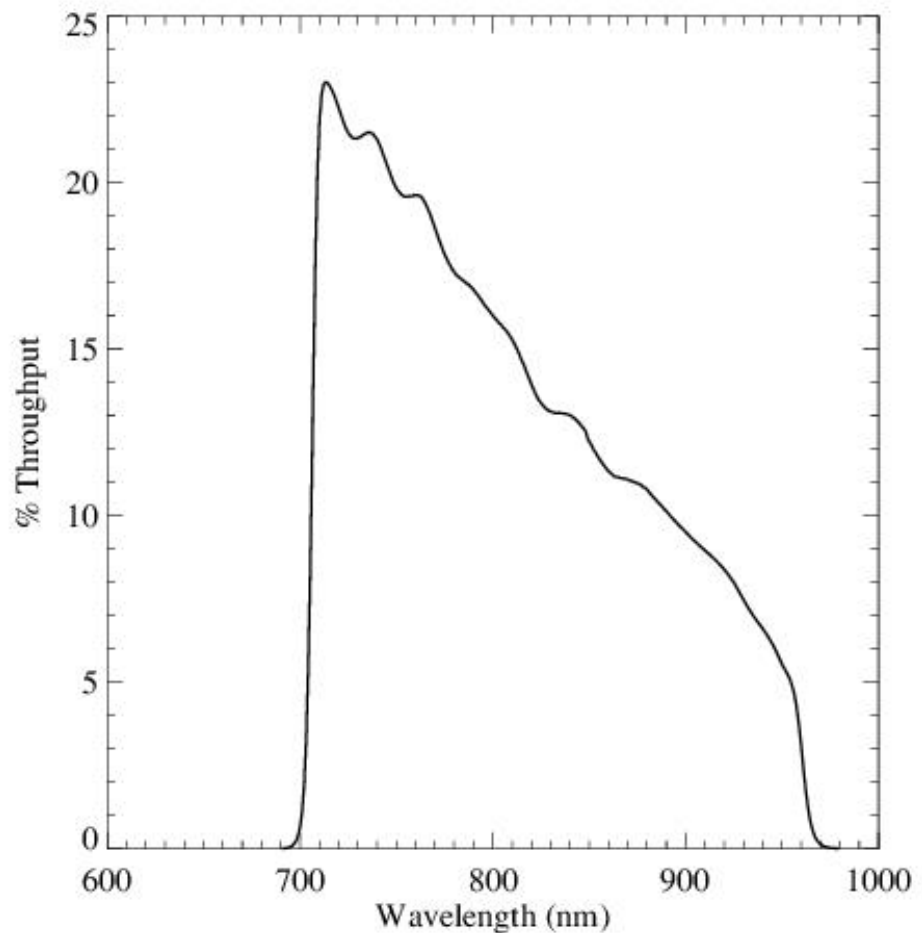


Figure A.116: Point source S/N vs. $V+AB_v$ for the F814W filter, assuming high sky backgrounds and a 5×5 pixel aperture.

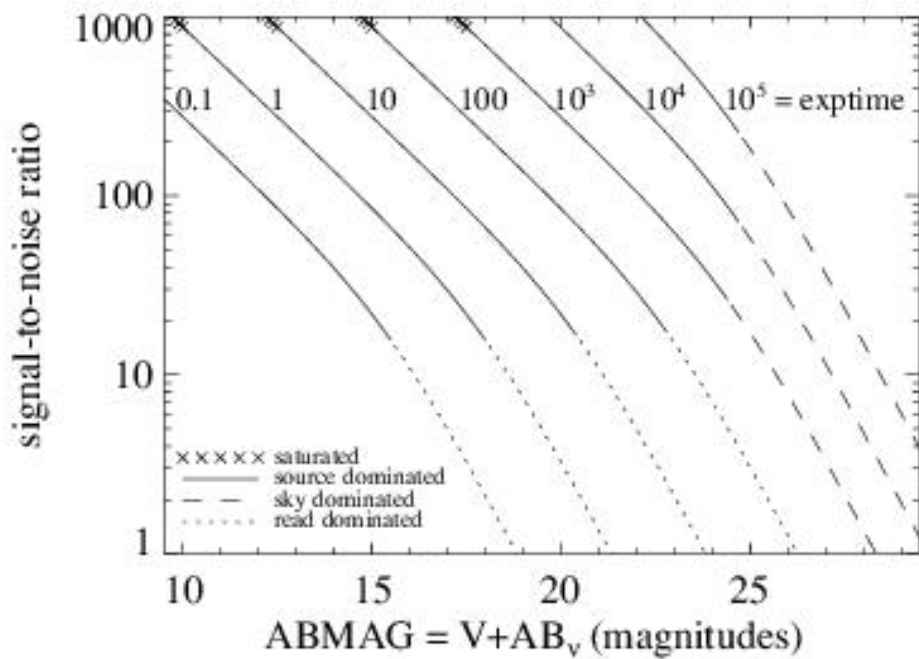
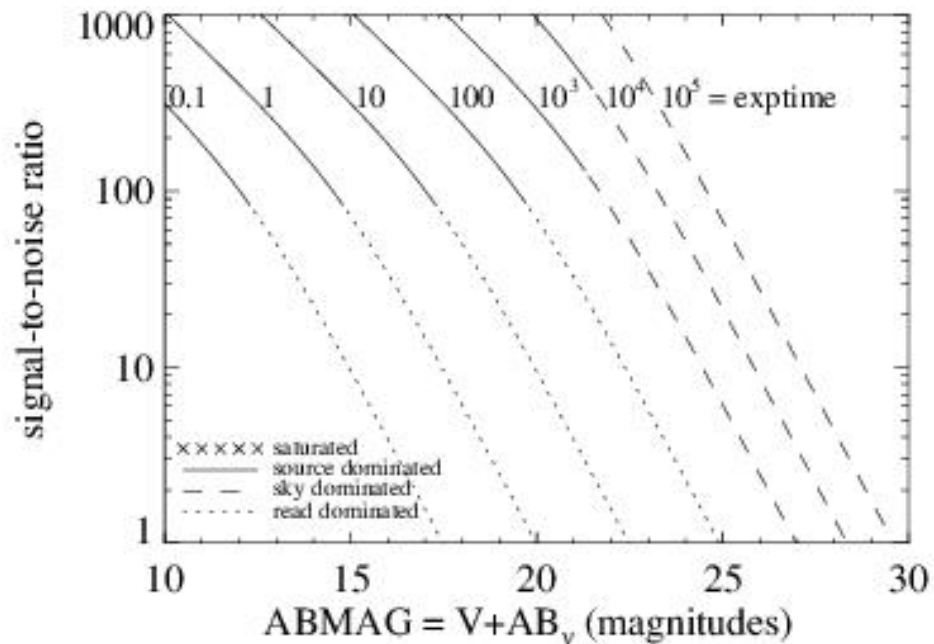


Figure A.117: Extended source S/N vs. $V+AB_V$ for the F814W filter, assuming high sky backgrounds and a source uniformly filling a 1 arcsec^2 aperture.



UVIS F845M

Description

11% passband filter.

Figure A.118: Integrated system throughput for F845M.

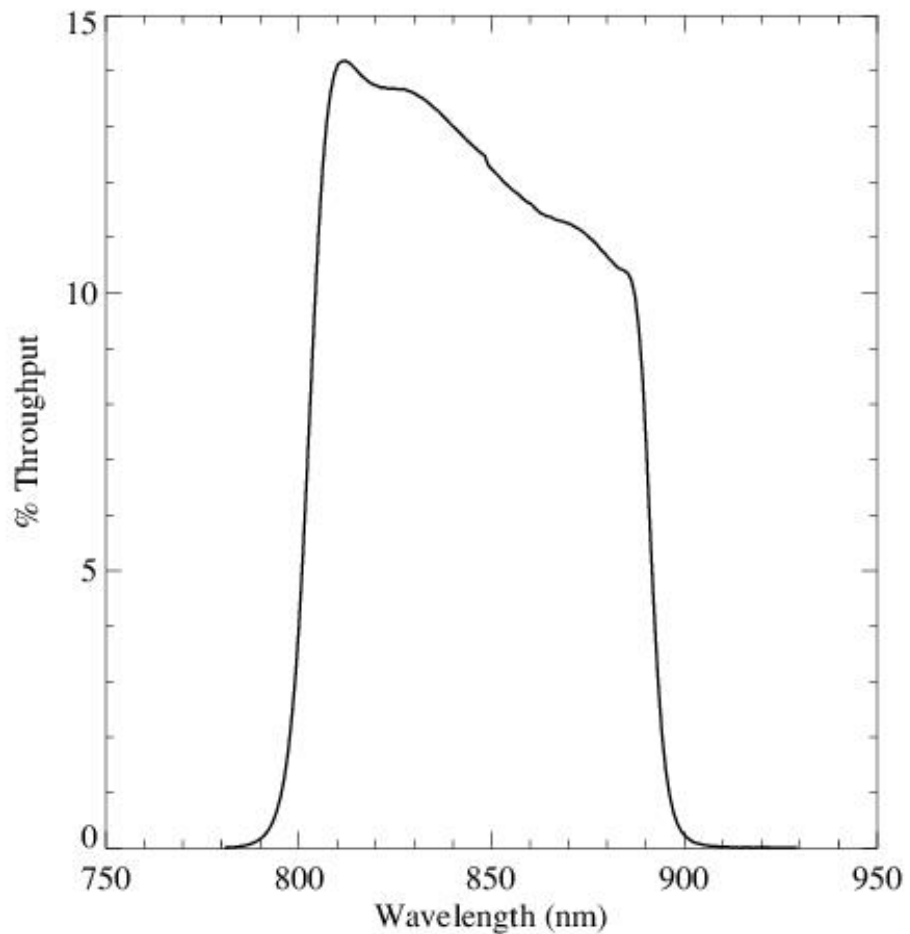


Figure A.119: Point source S/N vs. $V+AB_v$ for the F845M filter, assuming high sky backgrounds and a 5×5 pixel aperture.

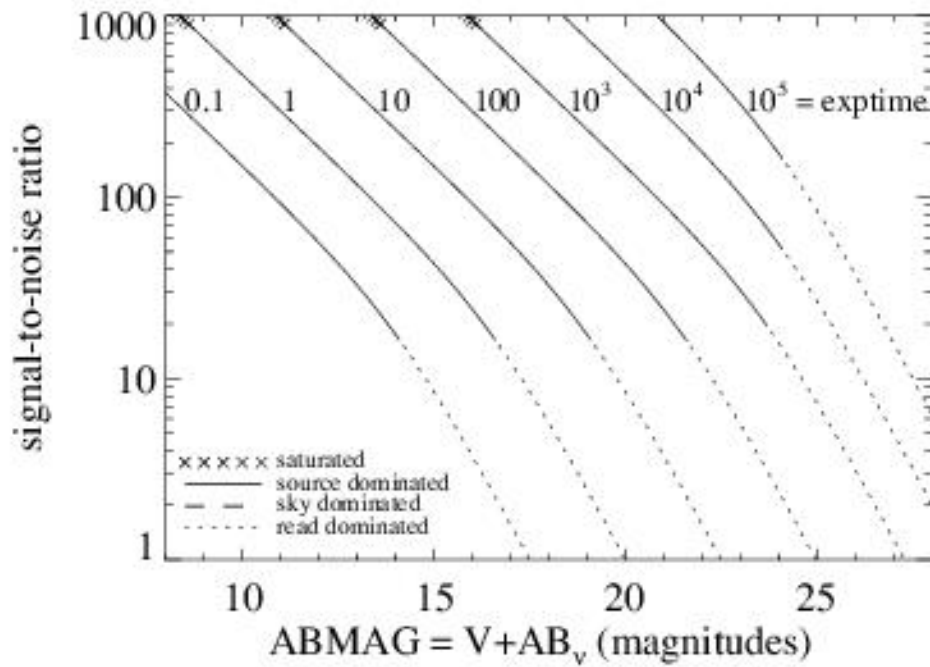
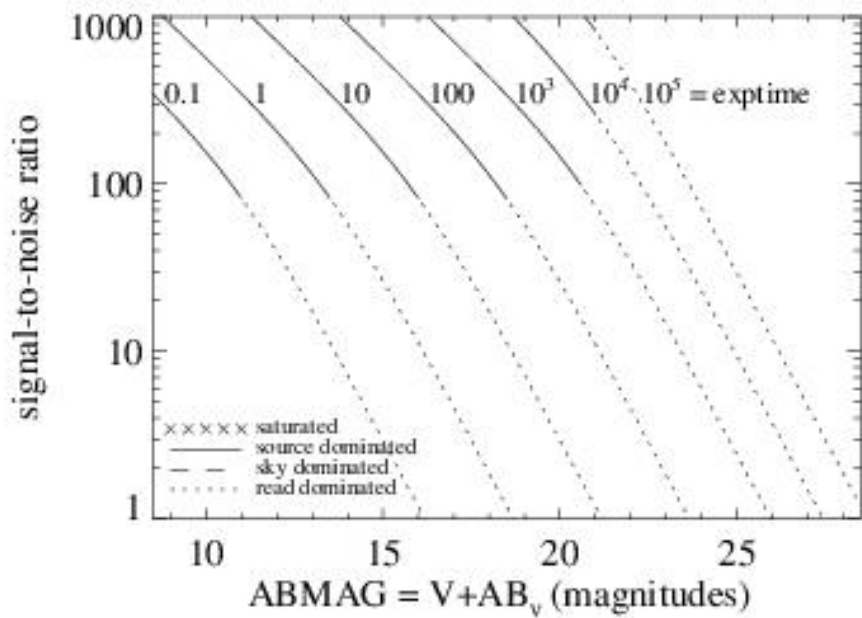


Figure A.120: Extended source S/N vs. $V+AB_V$ for the F845M filter, assuming high sky backgrounds and a source uniformly filling a 1 arcsec^2 aperture.



UVIS F850LP

Description

Sloan Digital Sky Survey z' filter.

Figure A.121: Integrated system throughput for F850LP.

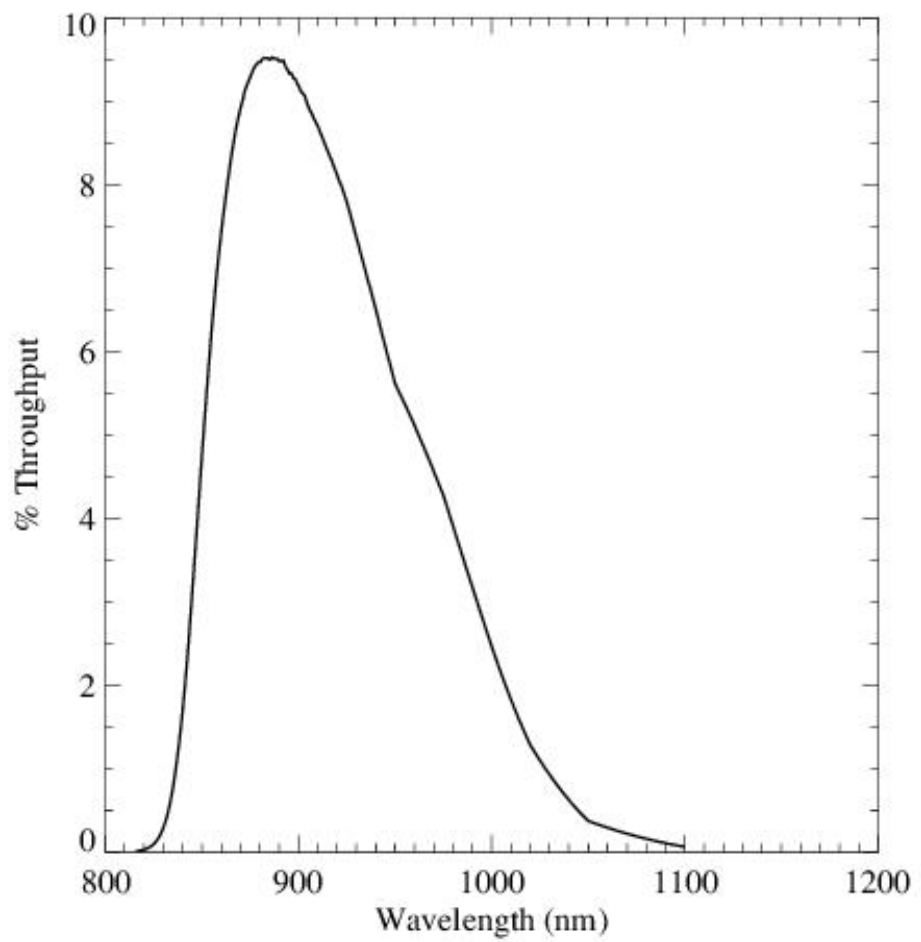


Figure A.122: Point source S/N vs. $V+AB_v$ for the F850LP filter. Top curves are for low sky; bottom curves are for average sky.

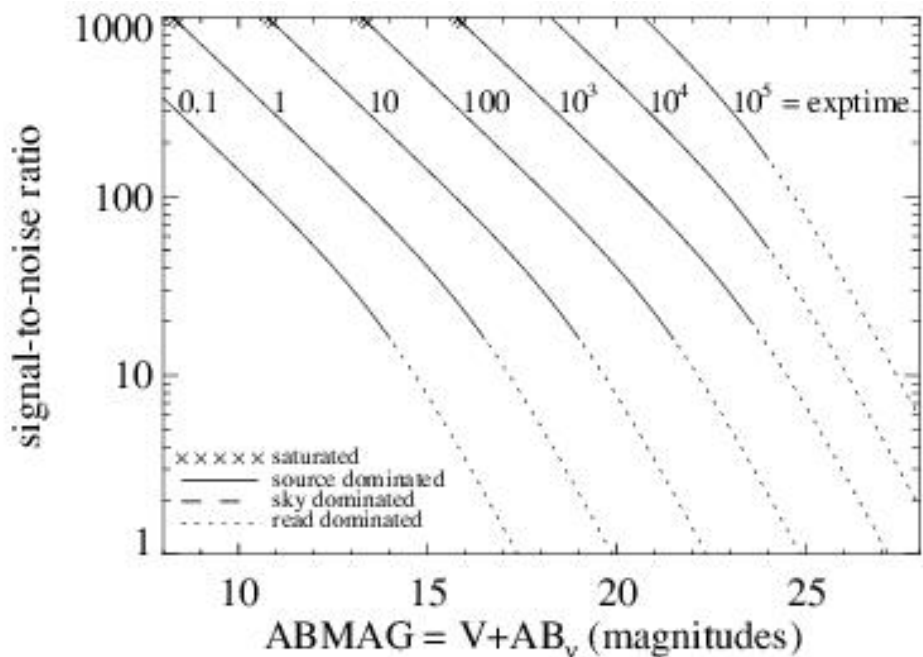
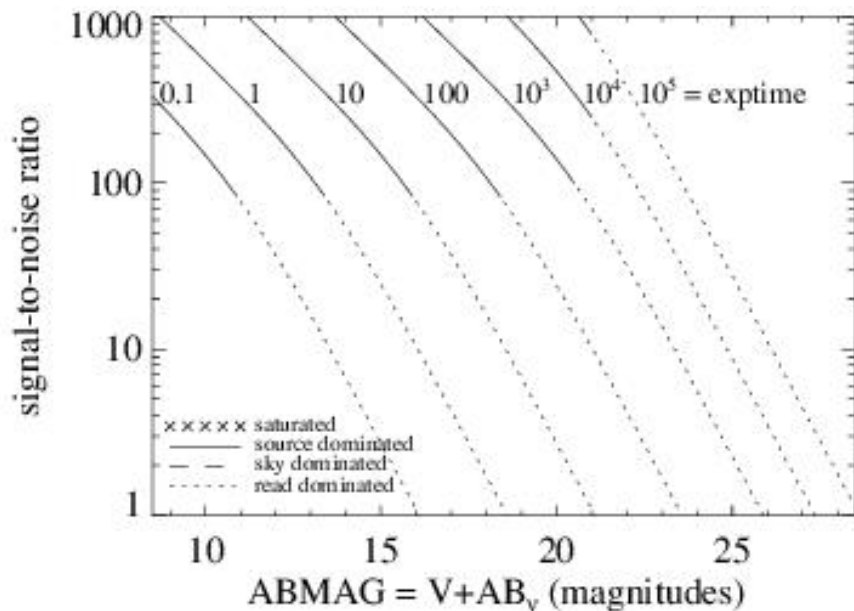


Figure A.123: Extended source S/N vs. $V+AB_v$ for the F850LP filter, assuming high sky backgrounds and a source uniformly filling a 1 arcsec^2 aperture.



UVIS F953N

Description

[S III] 9532 filter.

Figure A.124: Integrated system throughput for F953N.

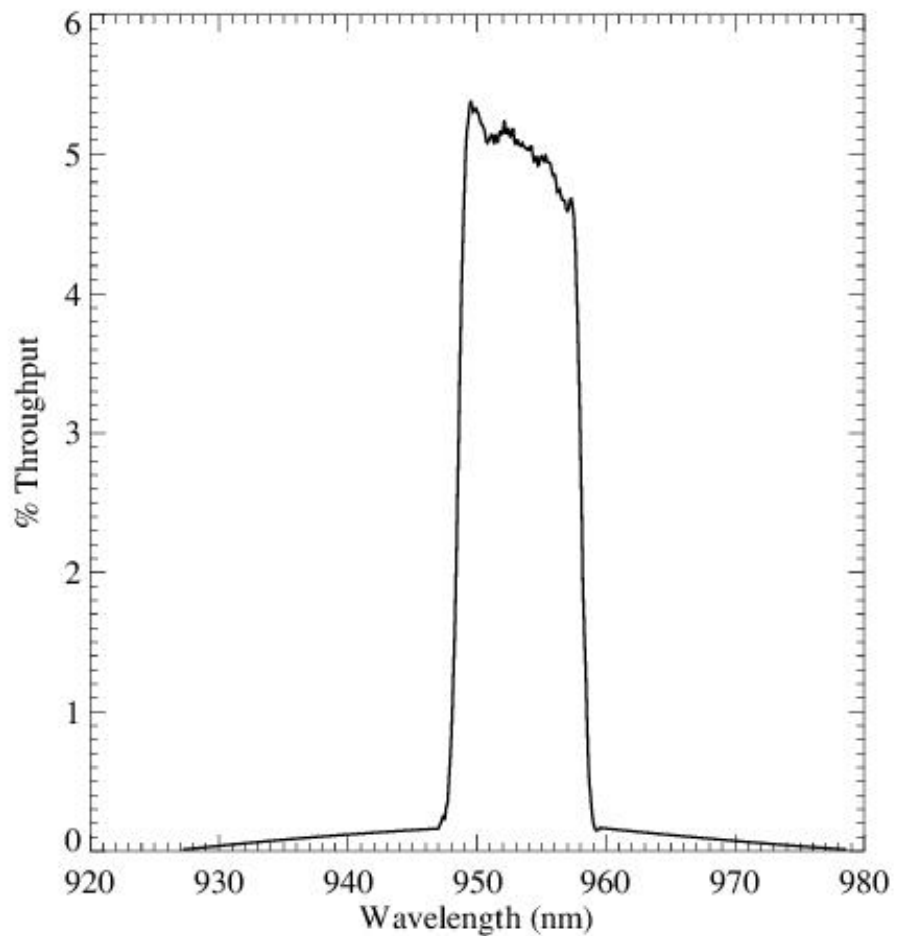


Figure A.125: Point source S/N vs. $V+AB_v$ for the F953N filter, assuming high sky backgrounds and a 5×5 pixel aperture.

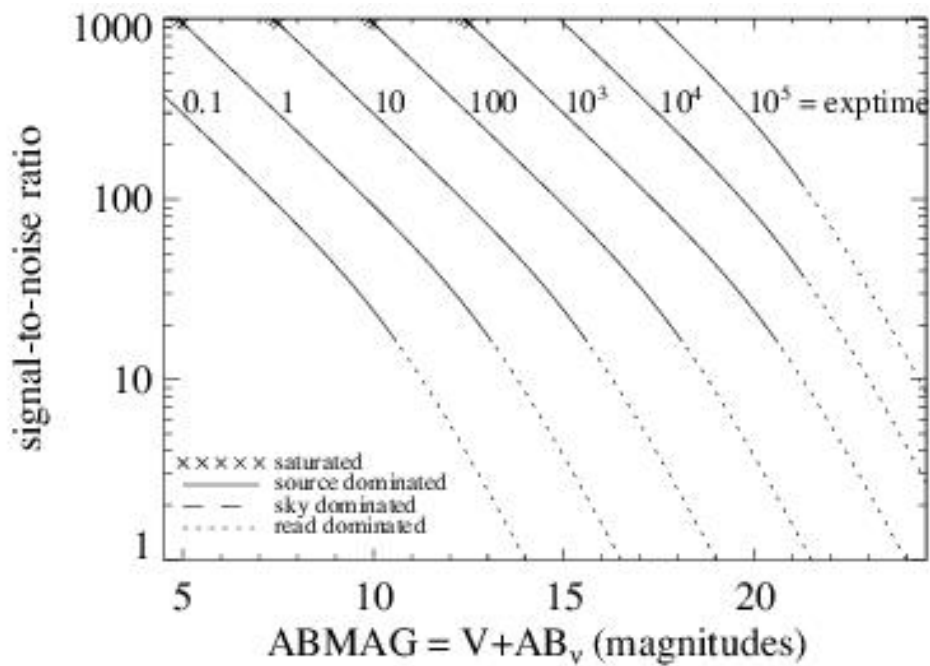
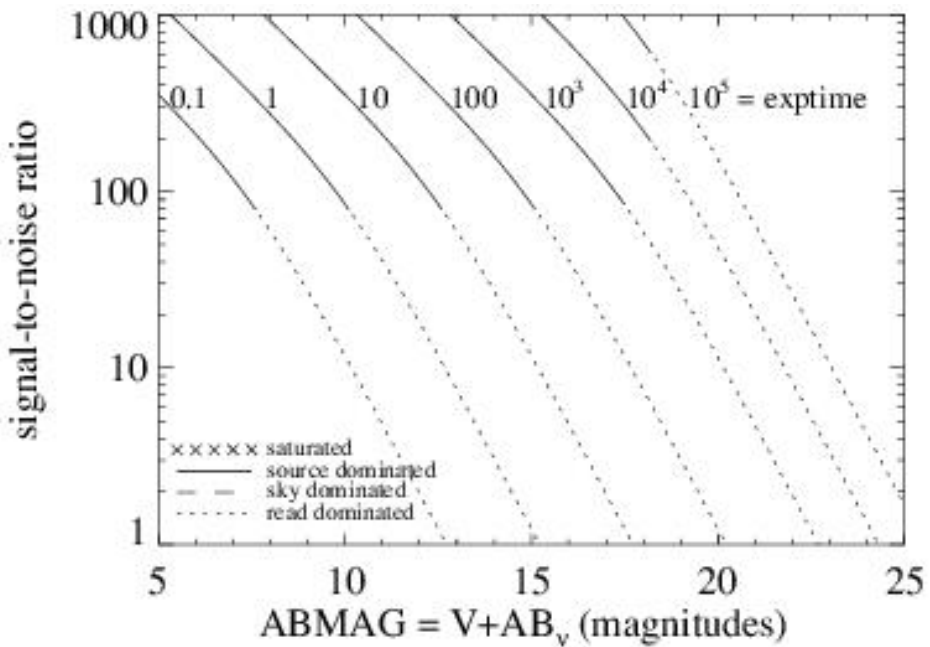


Figure A.126: Extended source S/N vs. $V+AB_V$ for the F953N filter, assuming high sky backgrounds and a source uniformly filling a 1 arcsec^2 aperture.



UVIS FQ232N

Description

C II] 2326 filter.

Figure A.127: Integrated system throughput for FQ232N.

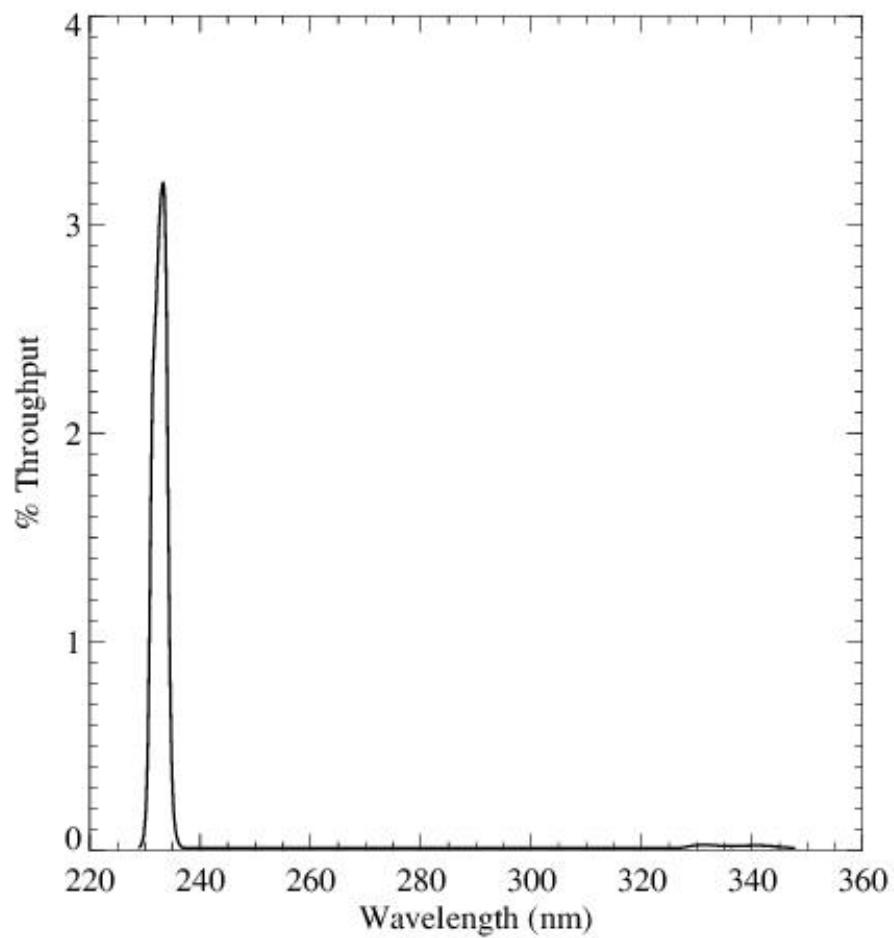


Figure A.128: Point source S/N vs. $V+AB_V$ for the FQ232N filter, assuming high sky backgrounds and a 5×5 pixel aperture.

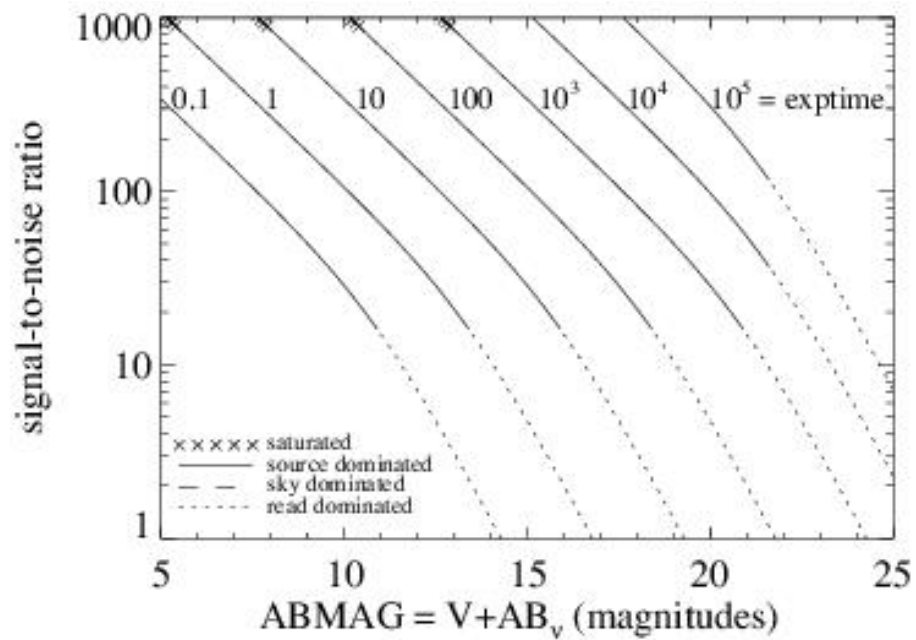
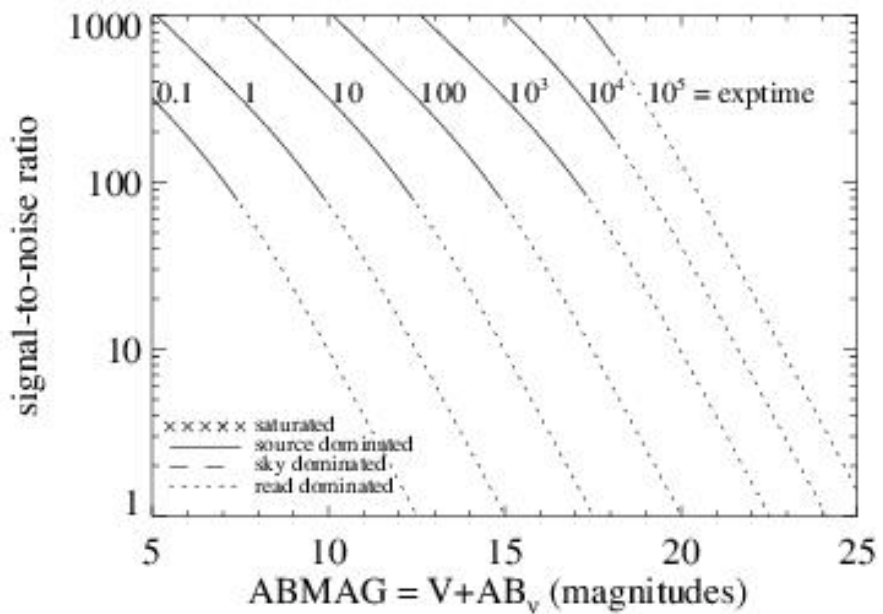


Figure A.129: Extended source S/N vs. $V+AB_v$ for the FQ232N filter, assuming high sky backgrounds and a source uniformly filling a 1 arcsec^2 aperture.



UVIS FQ243N

Description

[Ne IV] 2425 filter.

Figure A.130: Integrated system throughput for FQ243N.

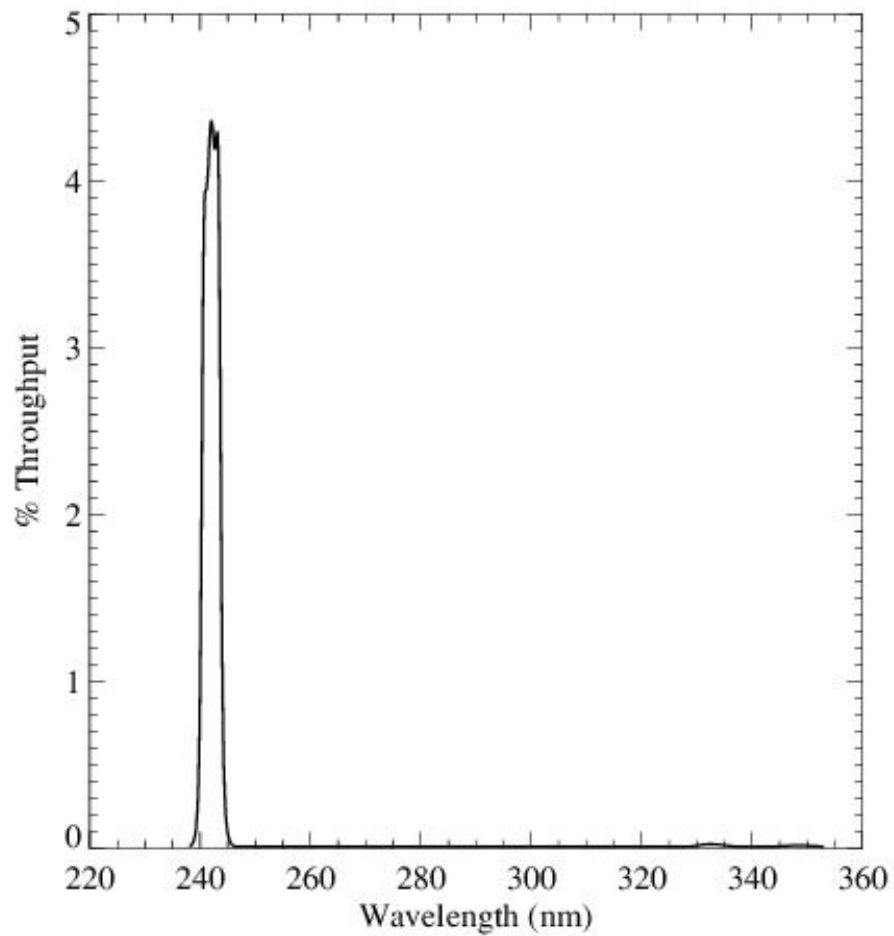


Figure A.131: Point source S/N vs. $V+AB_V$ for the FQ243N filter, assuming high sky backgrounds and a 5×5 pixel aperture.

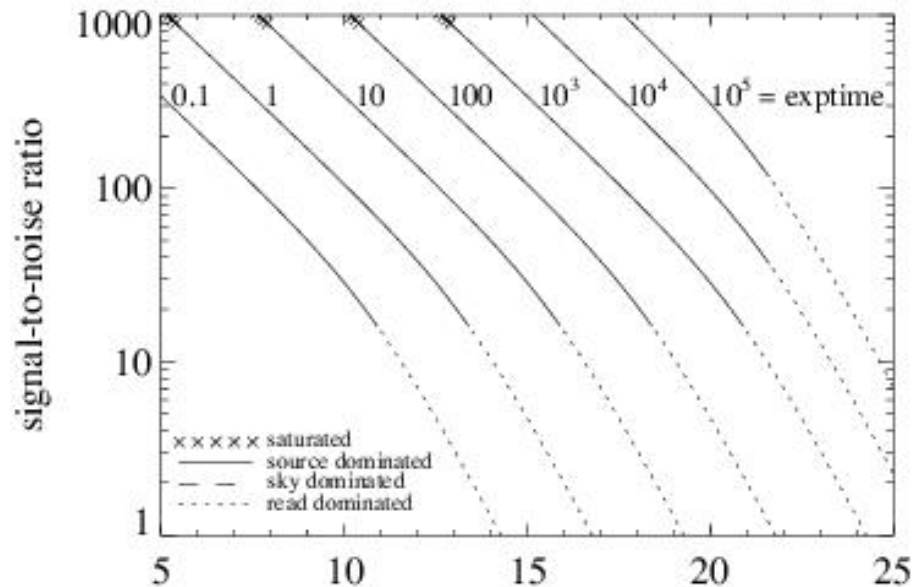
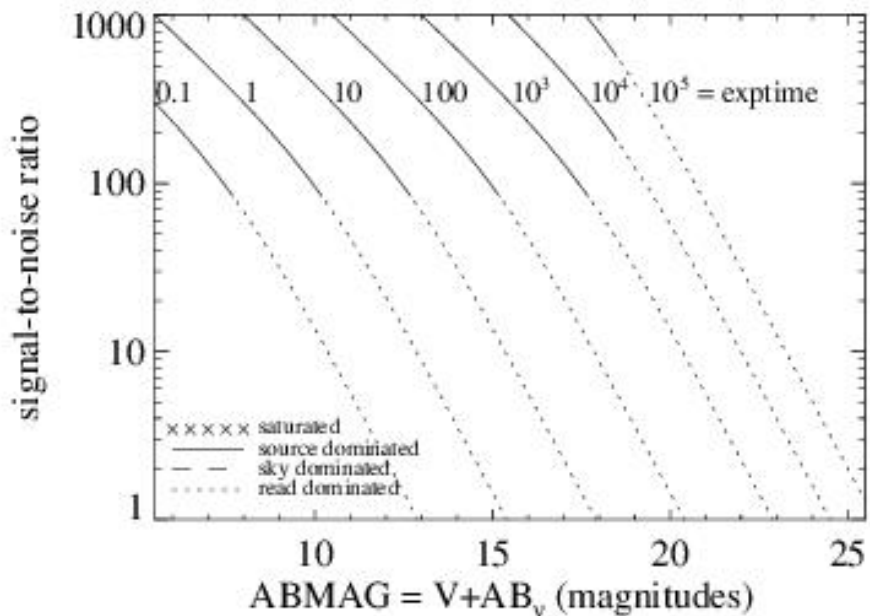


Figure A.132: Extended source S/N vs. $V+AB_v$ for the FQ243N filter, assuming high sky backgrounds and a source uniformly filling a 1 arcsec^2 aperture.



UVIS FQ378N

Description
z ([O II] 3726) filter.

Figure A.133: Integrated system throughput for FQ378N.

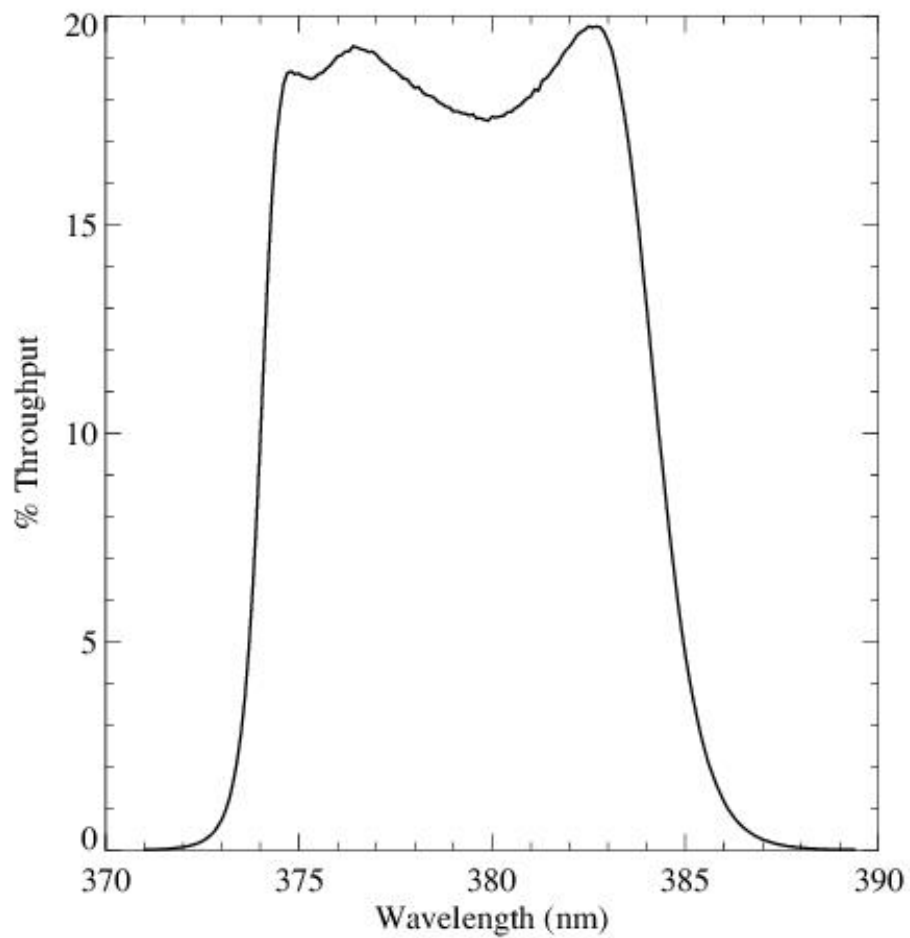


Figure A.134: Point source S/N vs. $V+AB_V$ for the FQ378N filter, assuming high sky backgrounds and a 5×5 pixel aperture.

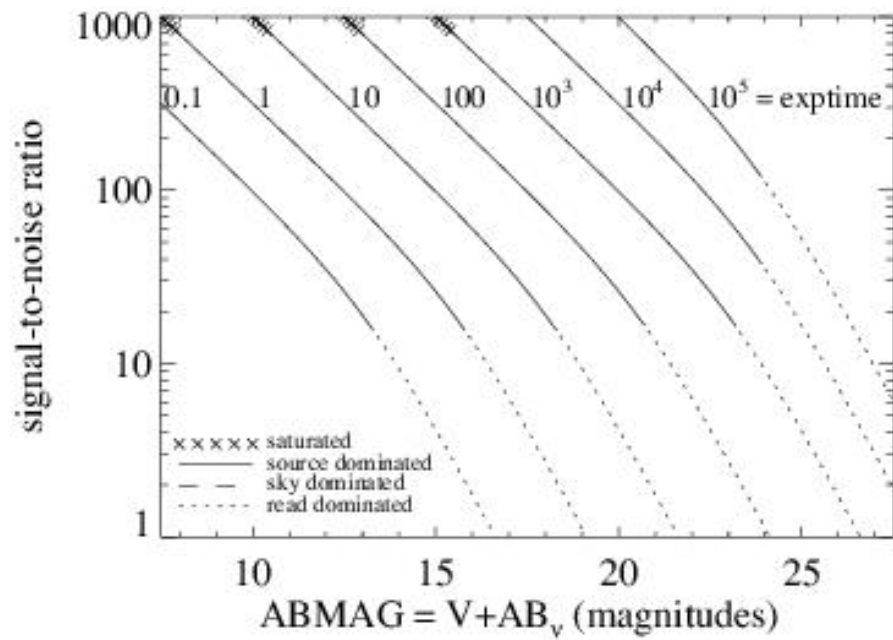
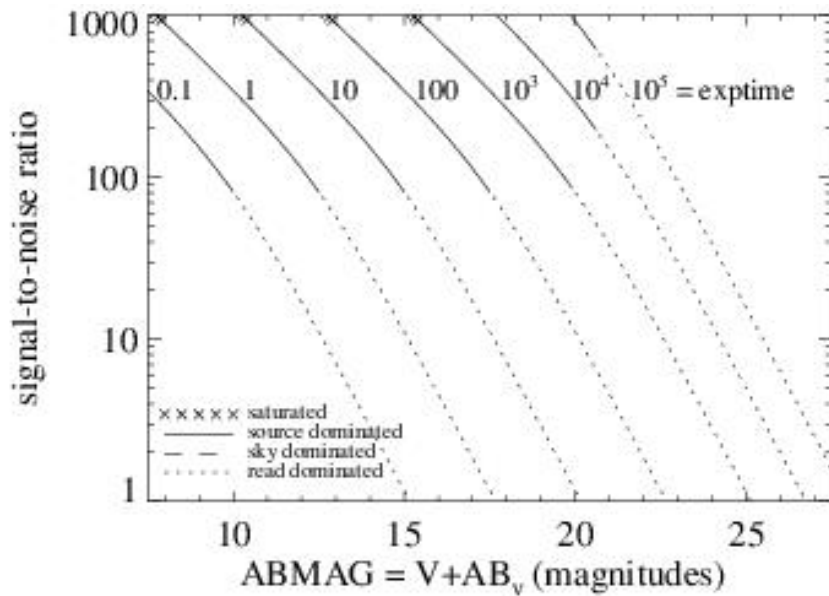


Figure A.135: Extended source S/N vs. $V+AB_v$ for the FQ378N filter, assuming high sky backgrounds and a source uniformly filling a 1 arcsec^2 aperture.



UVIS FQ387N

Description

[Ne III] 3868 filter.

Figure A.136: Integrated system throughput for FQ387N.

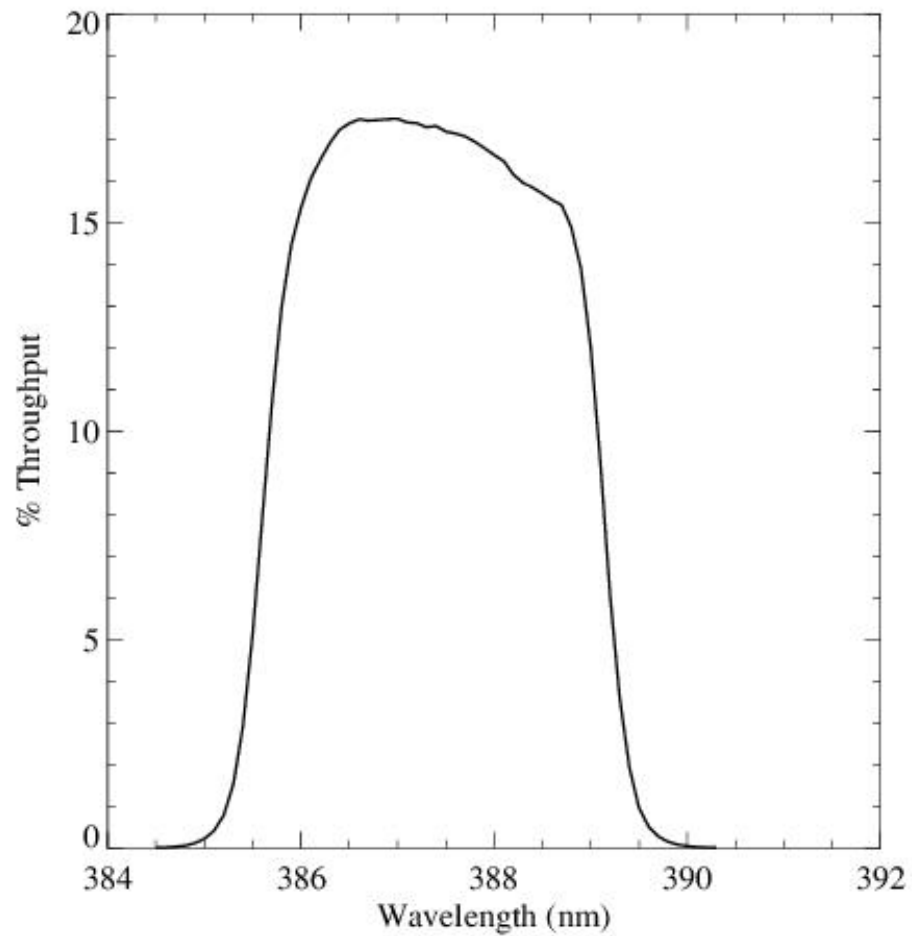


Figure A.137: Point source S/N vs. $V+AB_v$ for the FQ387N filter, assuming high sky backgrounds and a 5×5 pixel aperture.

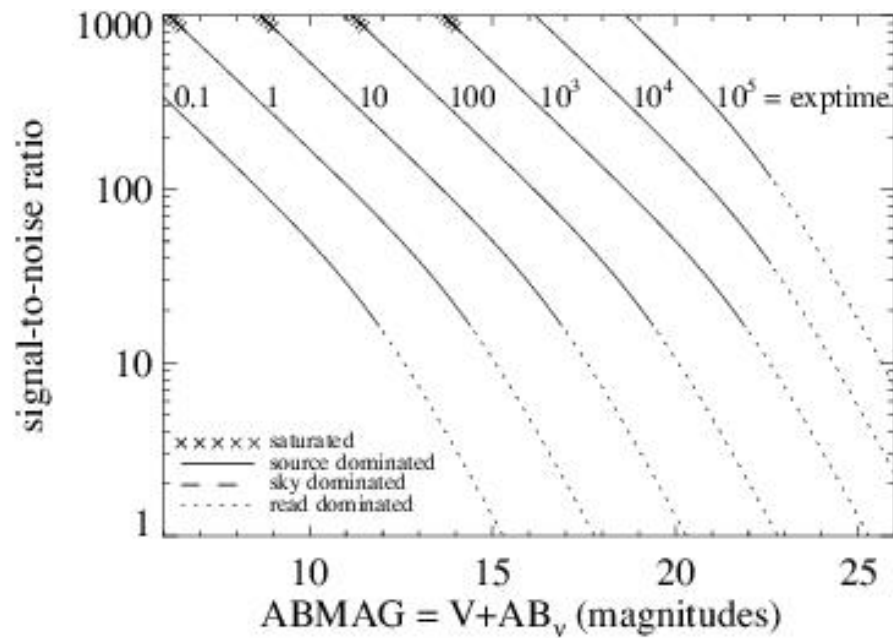
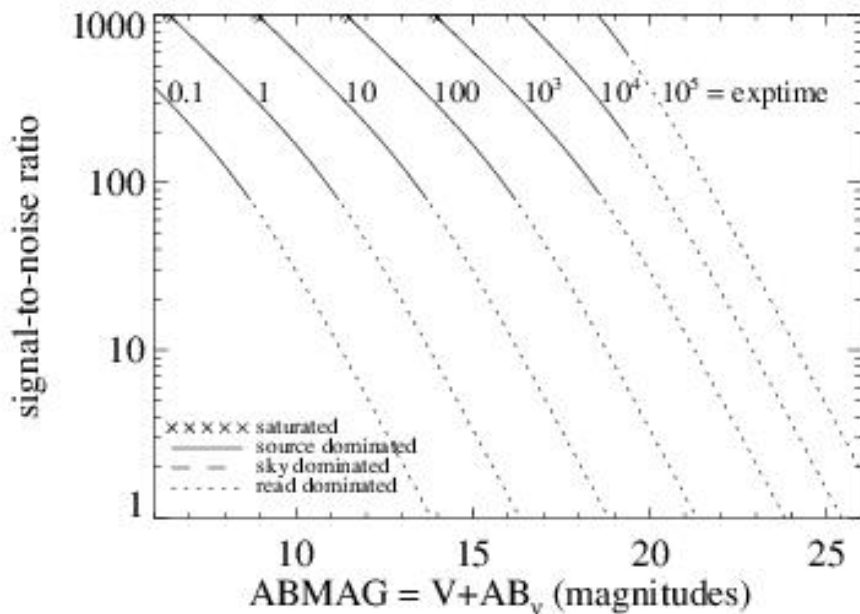


Figure A.138: Extended source S/N vs. $V+AB_v$ for the FQ387N filter, assuming high sky backgrounds and a source uniformly filling a 1 arcsec^2 aperture.



UVIS FQ422M

Description

Blue continuum filter.

Figure A.139: Integrated system throughput for FQ422M.

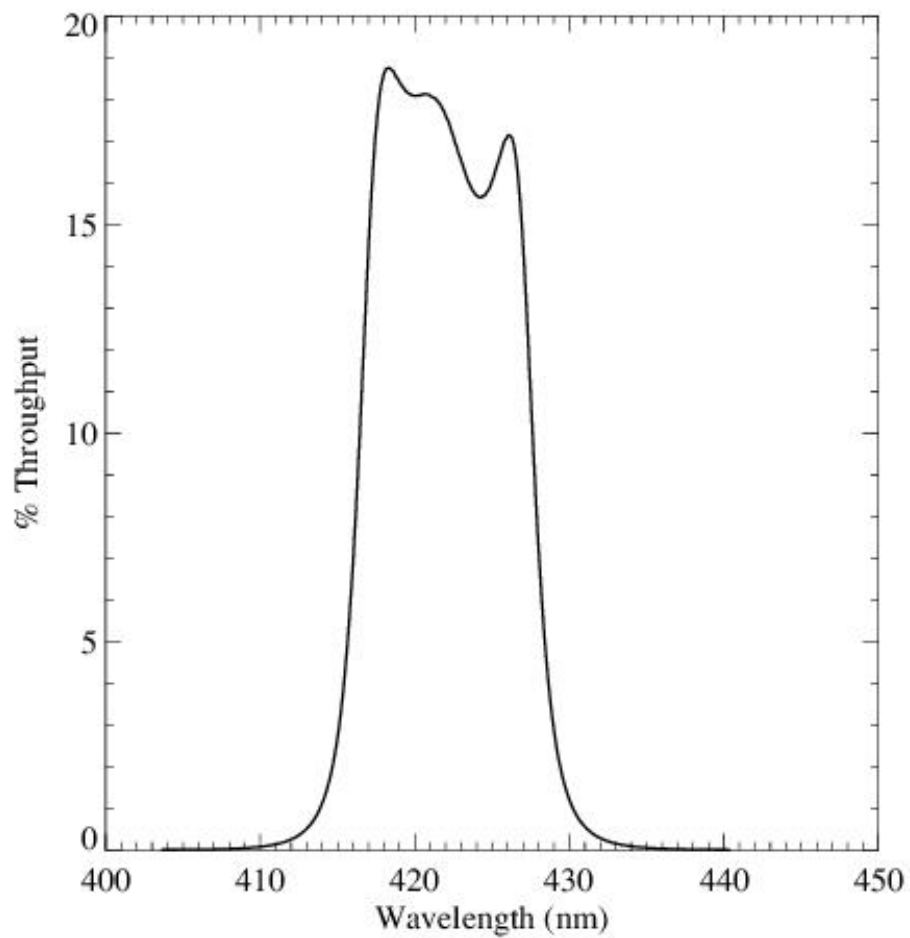


Figure A.140: Point source S/N vs. $V+AB_V$ for the FQ422M filter, assuming high sky backgrounds and a 5×5 pixel aperture.

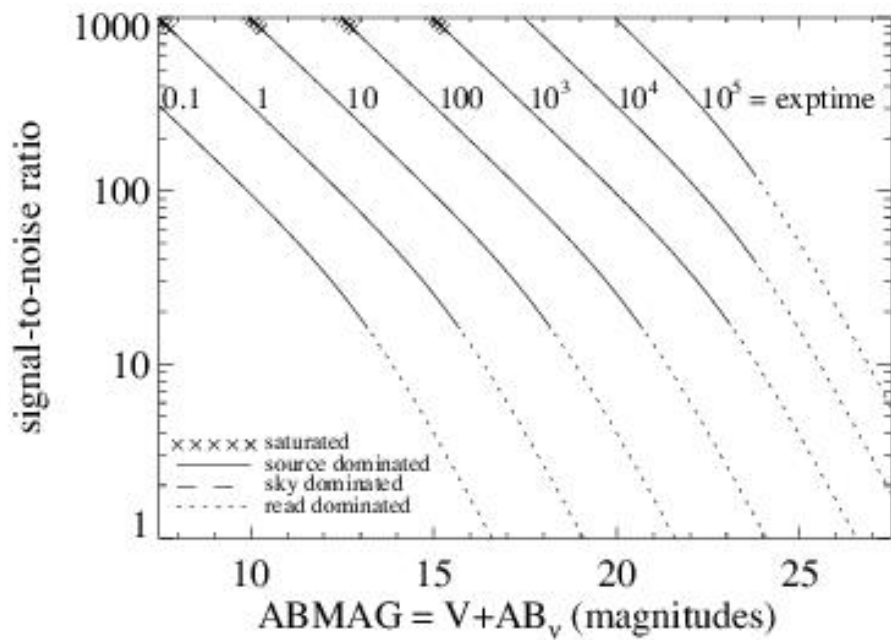
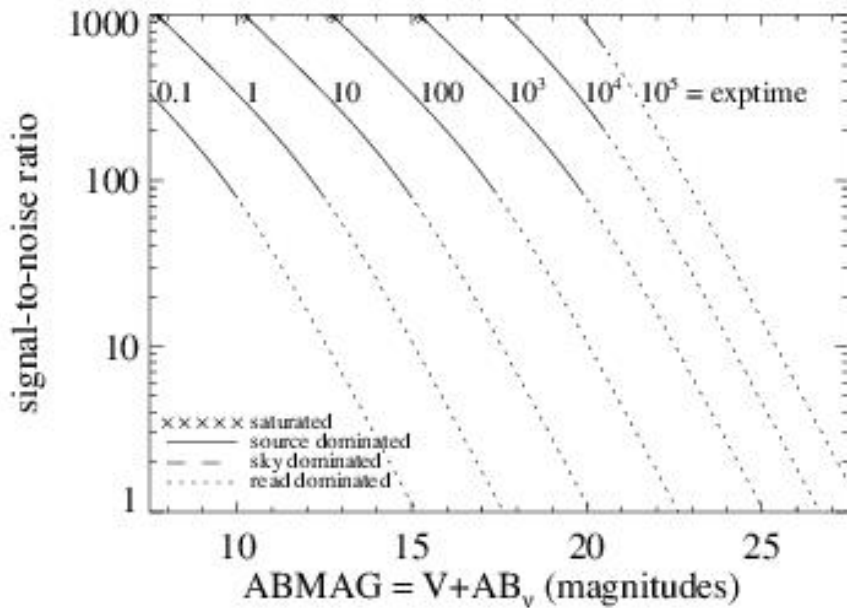


Figure A.141: Extended source S/N vs. $V+AB_v$ for the FQ422M filter, assuming high sky backgrounds and a source uniformly filling a 1 arcsec^2 aperture.



UVIS FQ436N

Description

H γ 4340 + [O III] 4363 filter.

Figure A.142: Integrated system throughput for FQ436N.

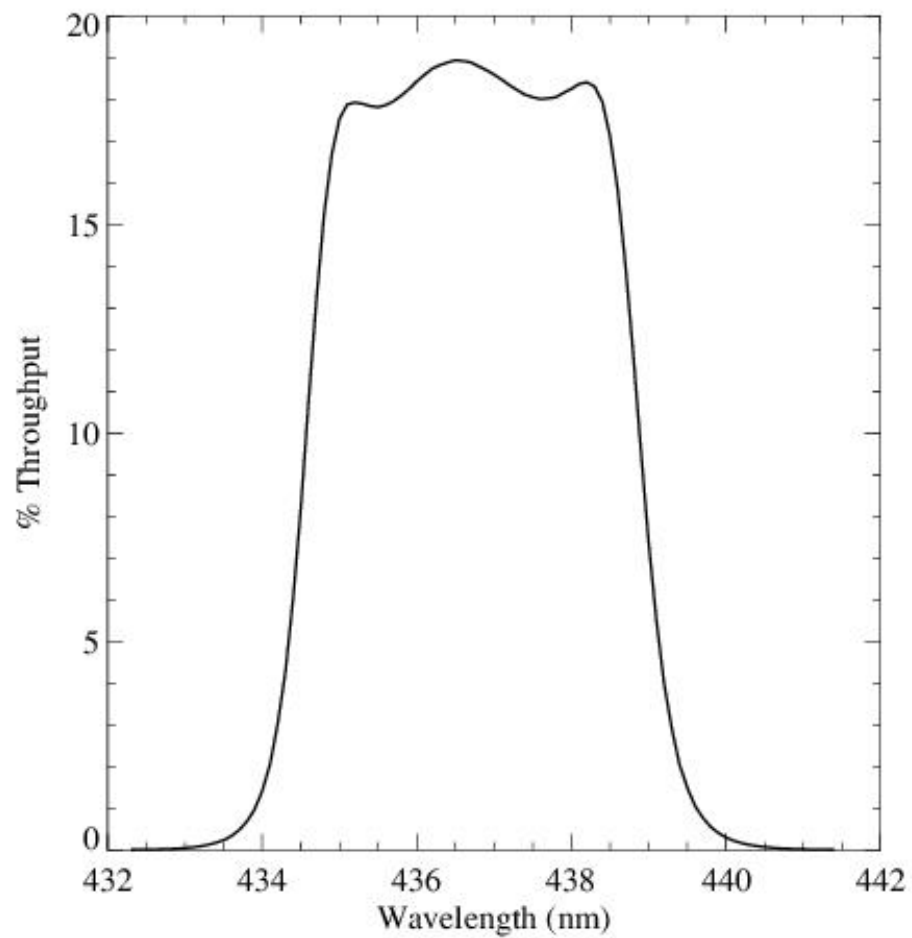


Figure A.143: Point source S/N vs. $V+AB_v$ for the FQ436N filter, assuming high sky backgrounds and a 5×5 pixel aperture.

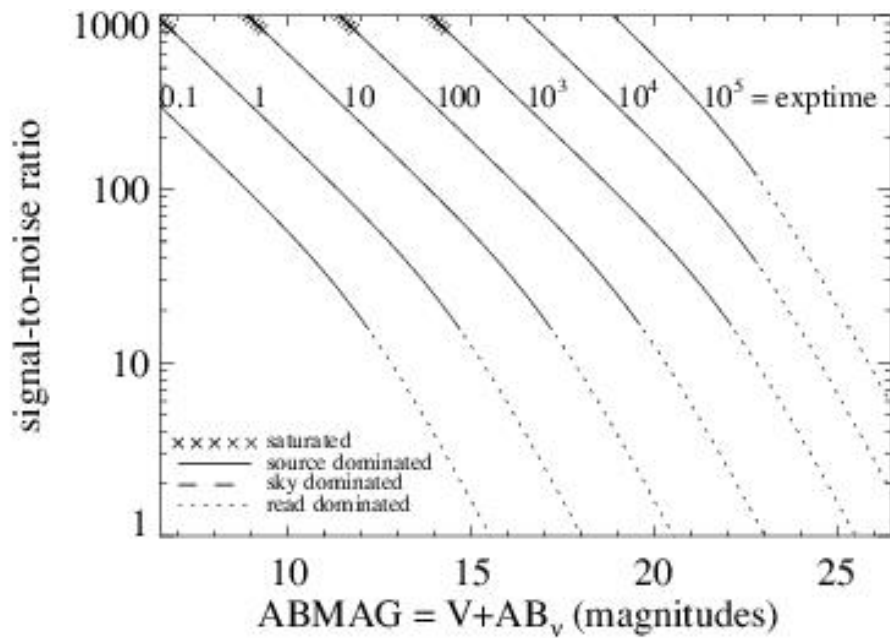
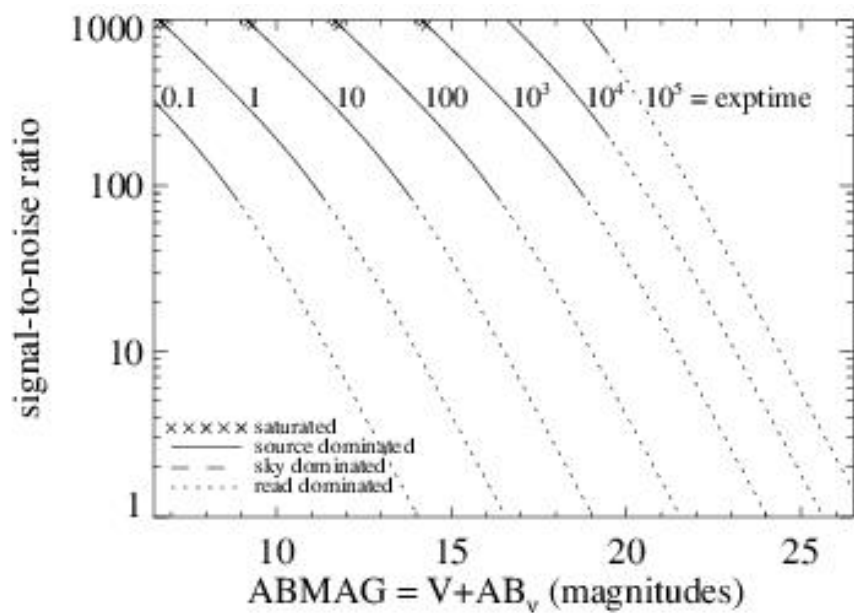


Figure A.144: Extended source S/N vs. $V+AB_v$ for the FQ436N filter, assuming high sky backgrounds and a source uniformly filling a 1 arcsec^2 aperture.



UVIS FQ437N

Description

[O III] 4363 filter.

Figure A.145: Integrated system throughput for FQ437N.

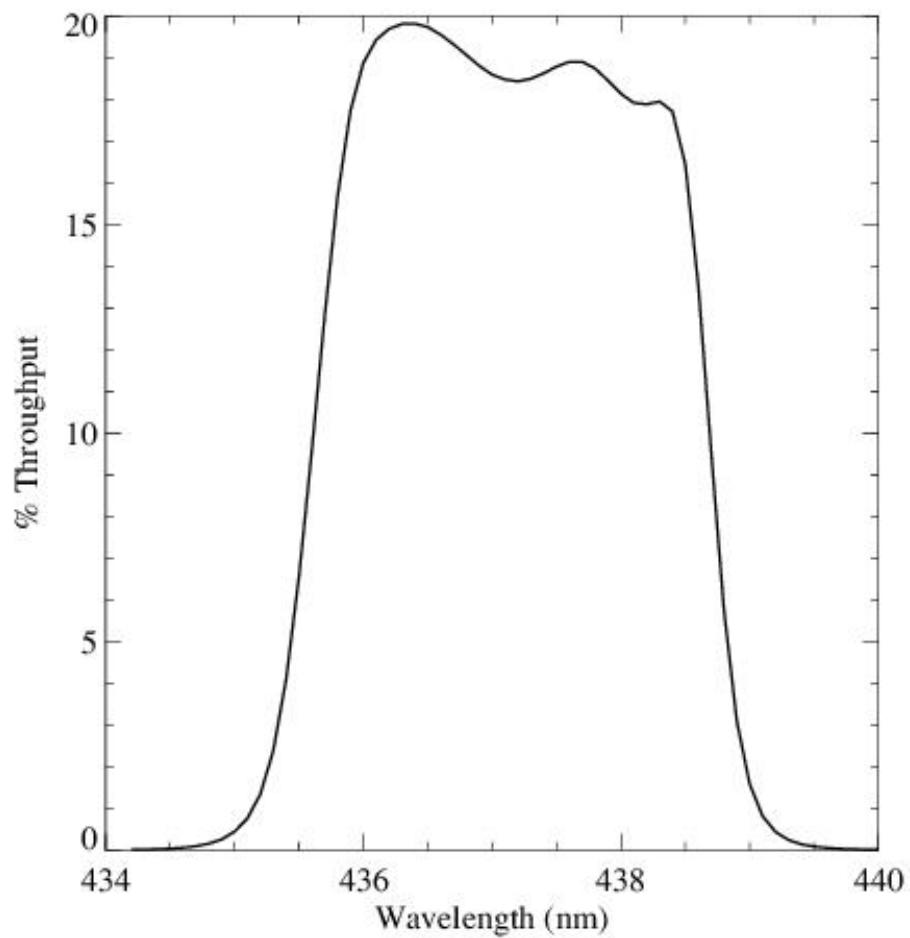


Figure A.146: Point source S/N vs. $V+AB_v$ for the FQ437N filter, assuming high sky backgrounds and a 5×5 pixel aperture.

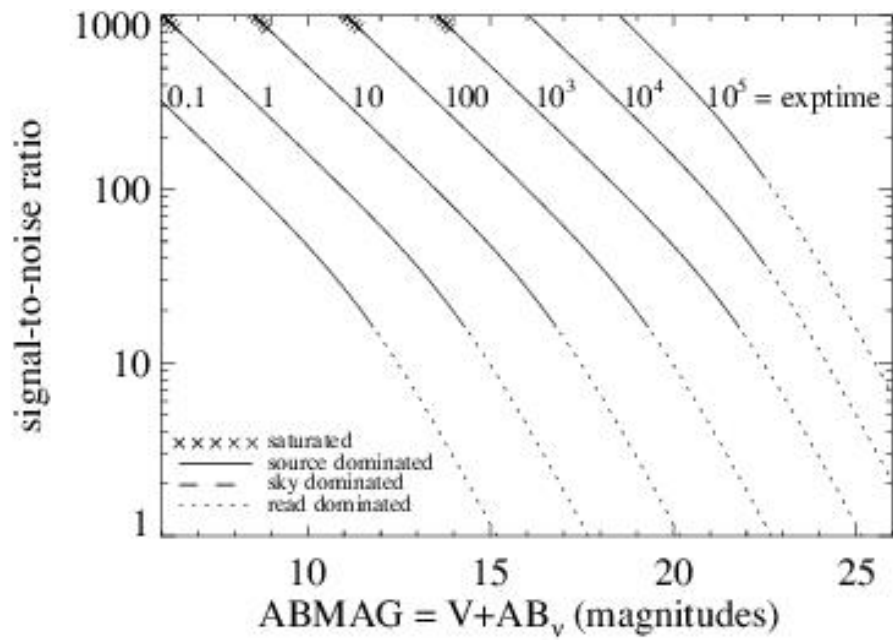
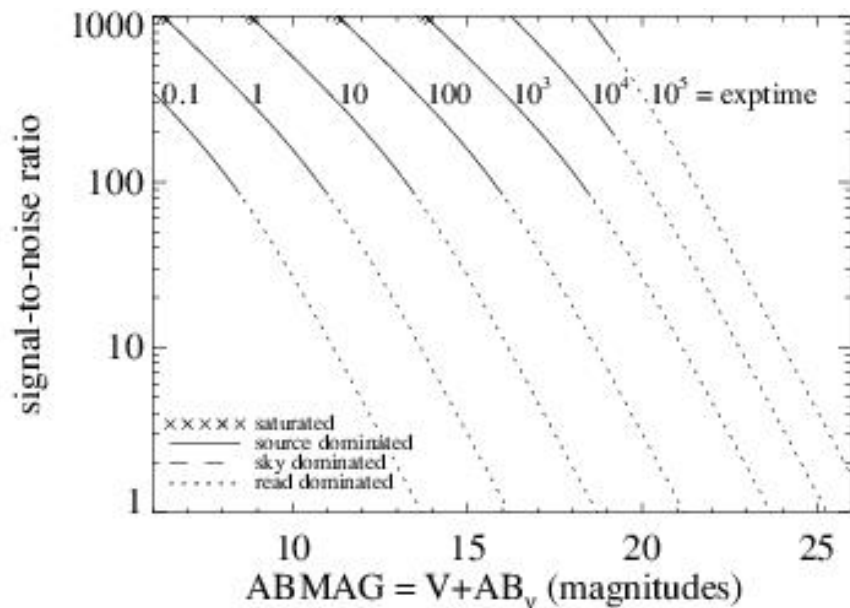


Figure A.147: Extended source S/N vs. $V+AB_v$ for the FQ437N filter, assuming high sky backgrounds and a source uniformly filling a 1 arcsec^2 aperture.



UVIS FQ492N

Description

$z(\text{H}\beta)$ filter.

Figure A.148: Integrated system throughput for FQ492N.

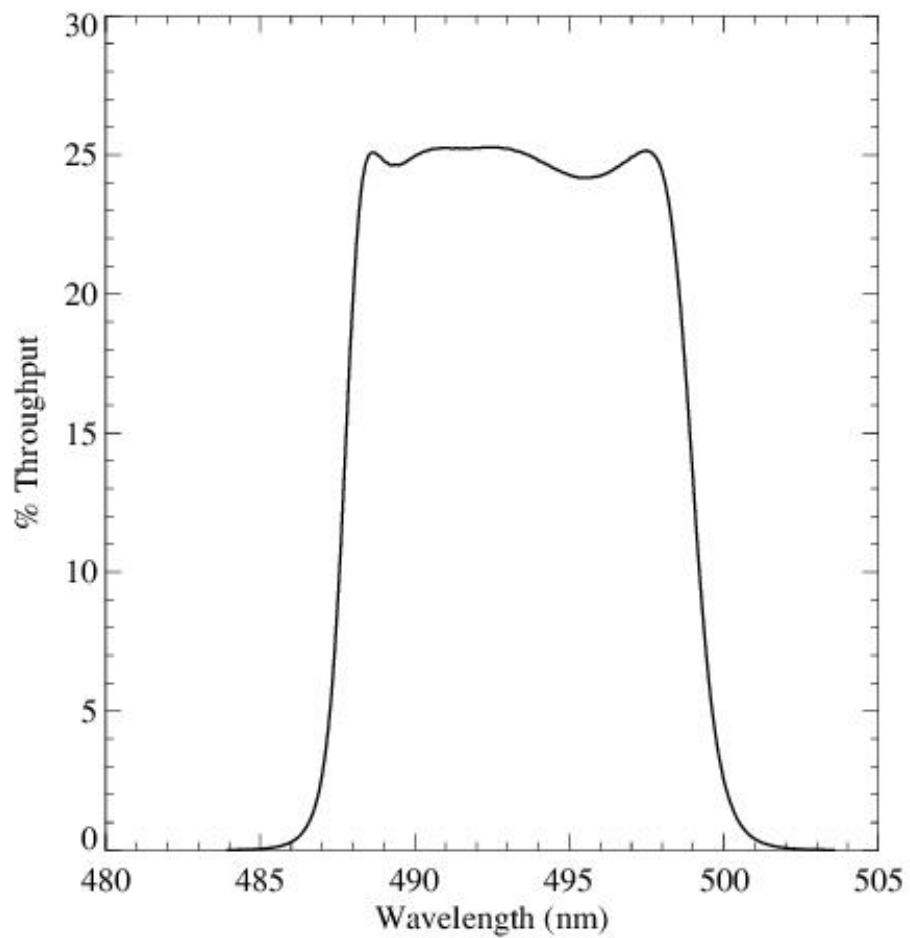


Figure A.149: Point source S/N vs. $V+AB_v$ for the FQ492N filter, assuming high sky backgrounds and a 5×5 pixel aperture.

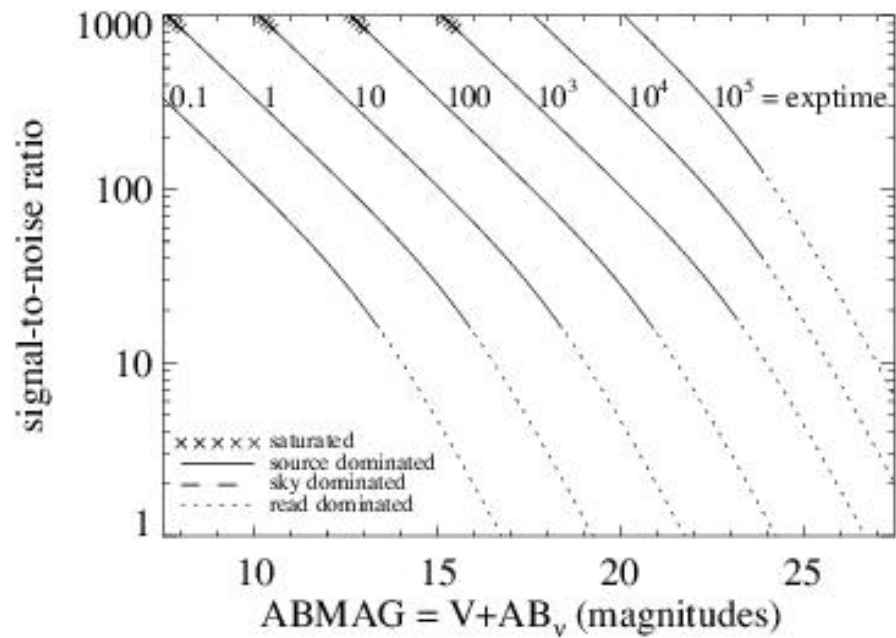
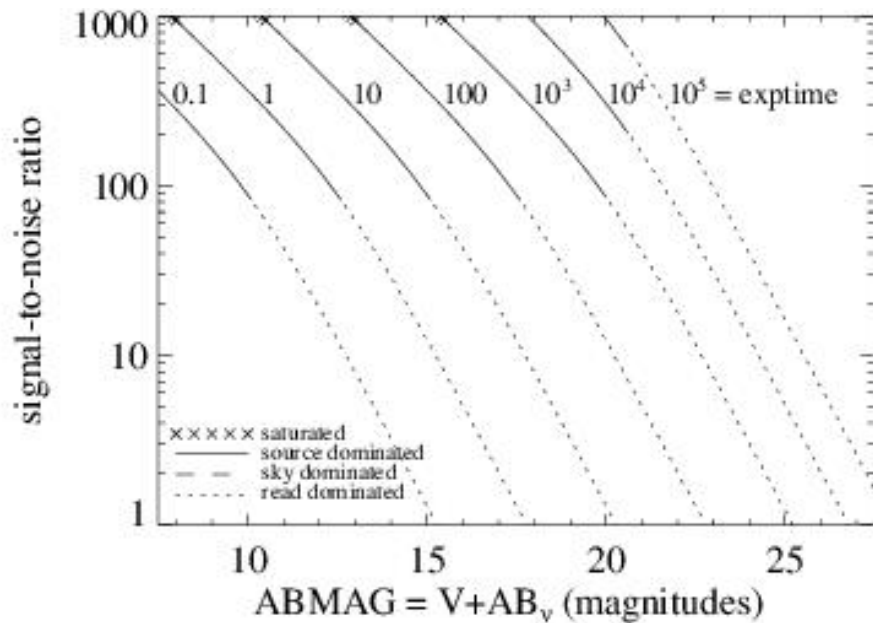


Figure A.150: Extended source S/N vs. $V+AB_V$ for the FQ492N filter, assuming high sky backgrounds and a source uniformly filling a 1 arcsec^2 aperture.



UVIS FQ508N

Description
z ([O III] 5007) filter.

Figure A.151: Integrated system throughput for FQ508N.

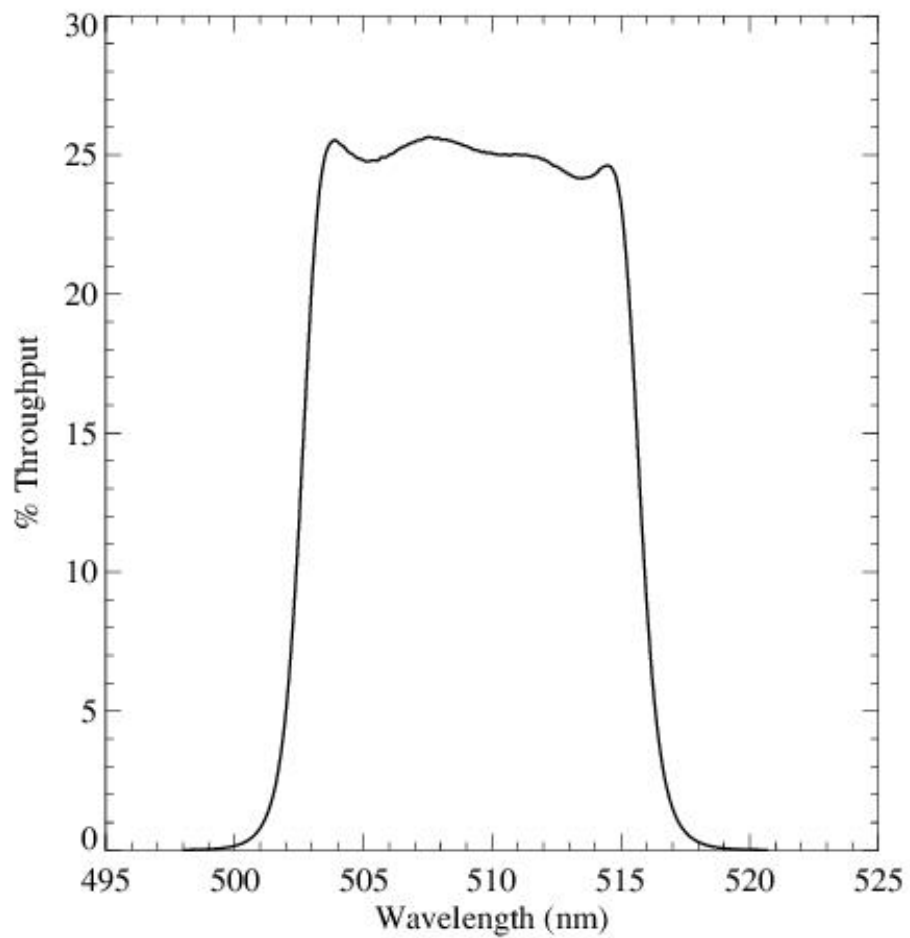


Figure A.152: Point source S/N vs. $V+AB_V$ for the FQ508N filter, assuming high sky backgrounds and a 5×5 pixel aperture.

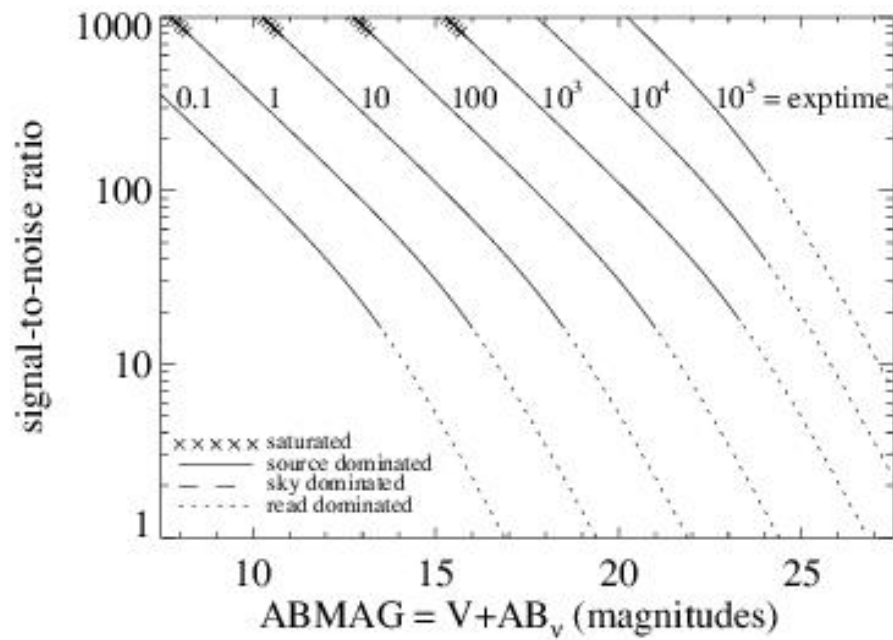
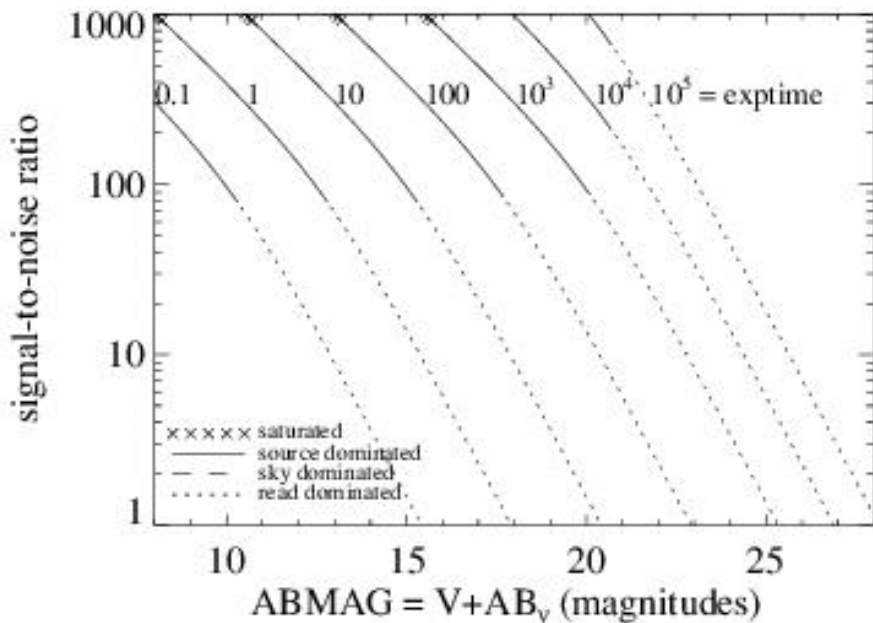


Figure A.153: Extended source S/N vs. $V+AB_V$ for the FQ508N filter, assuming high sky backgrounds and a source uniformly filling a 1 arcsec^2 aperture.



UVIS FQ575N

Description

[N II] 5754 filter.

Figure A.154: Integrated system throughput for FQ575N.

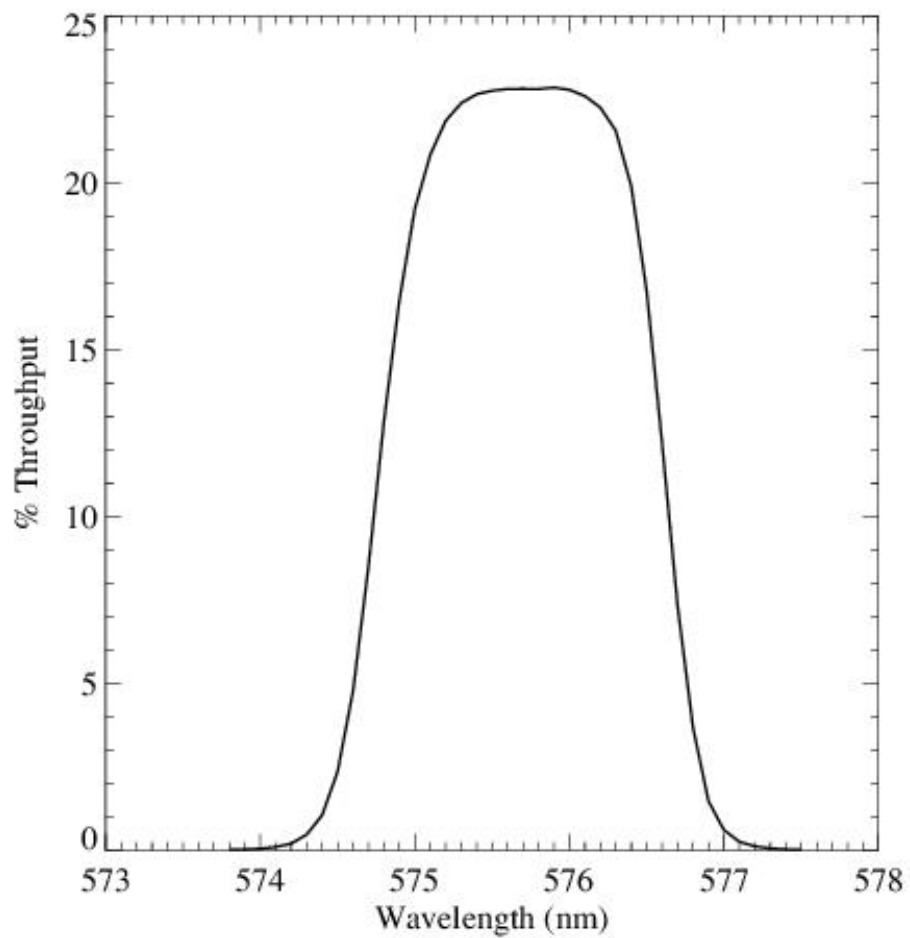


Figure A.155: Point source S/N vs. $V+AB_v$ for the FQ575N filter, assuming high sky backgrounds and a 5×5 pixel aperture.

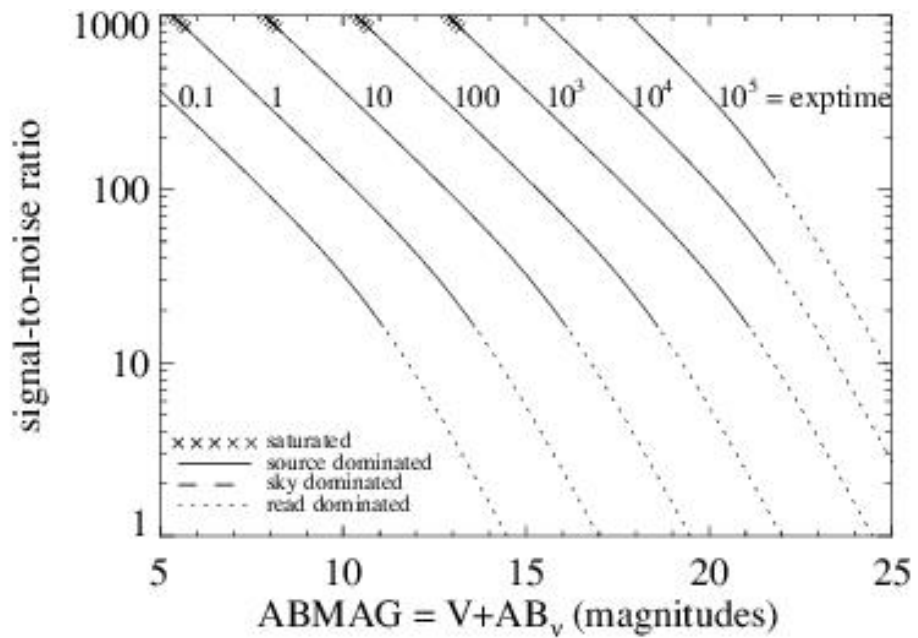
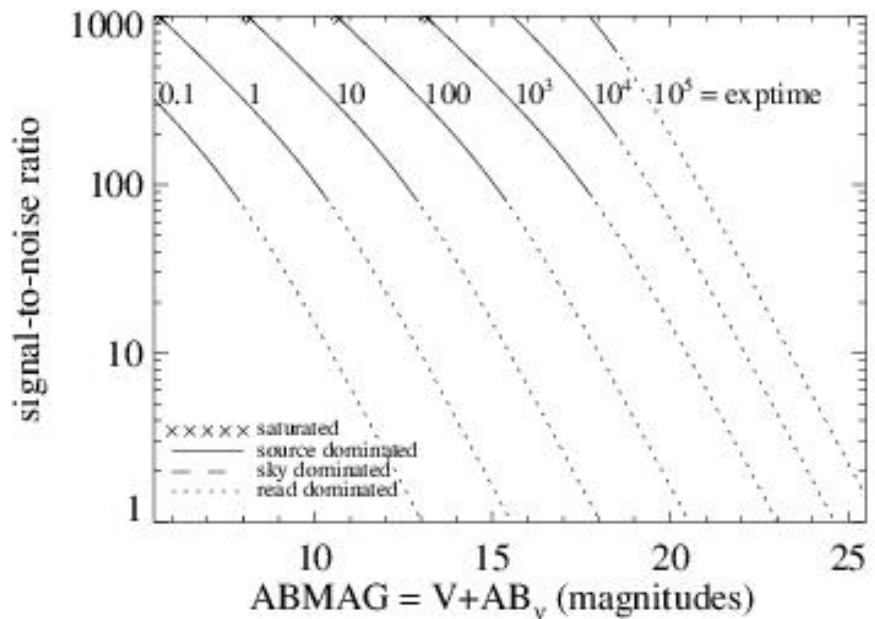


Figure A.156: Extended source S/N vs. $V+AB_V$ for the FQ575N filter, assuming high sky backgrounds and a source uniformly filling a 1 arcsec^2 aperture.



UVIS FQ619N

Description

CH₄ 6194 filter.

Figure A.157: Integrated system throughput for FQ619N.

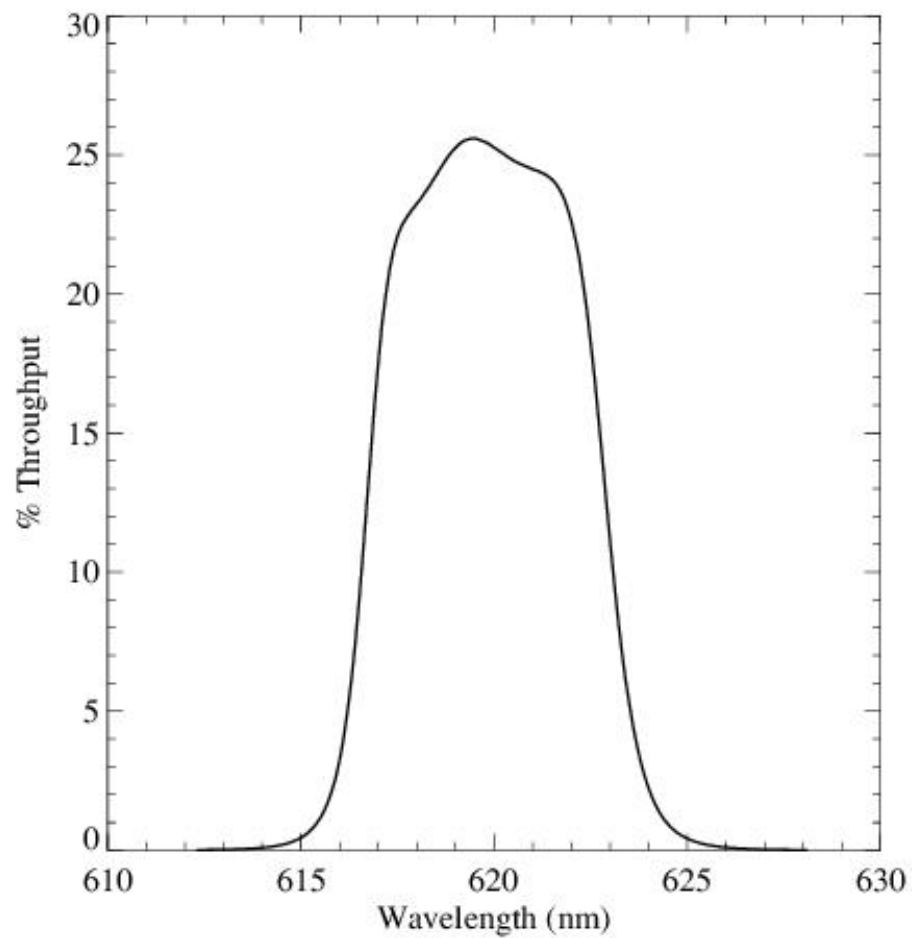


Figure A.158: Point source S/N vs. $V+AB_v$ for the FQ619N filter, assuming high sky backgrounds and a 5×5 pixel aperture.

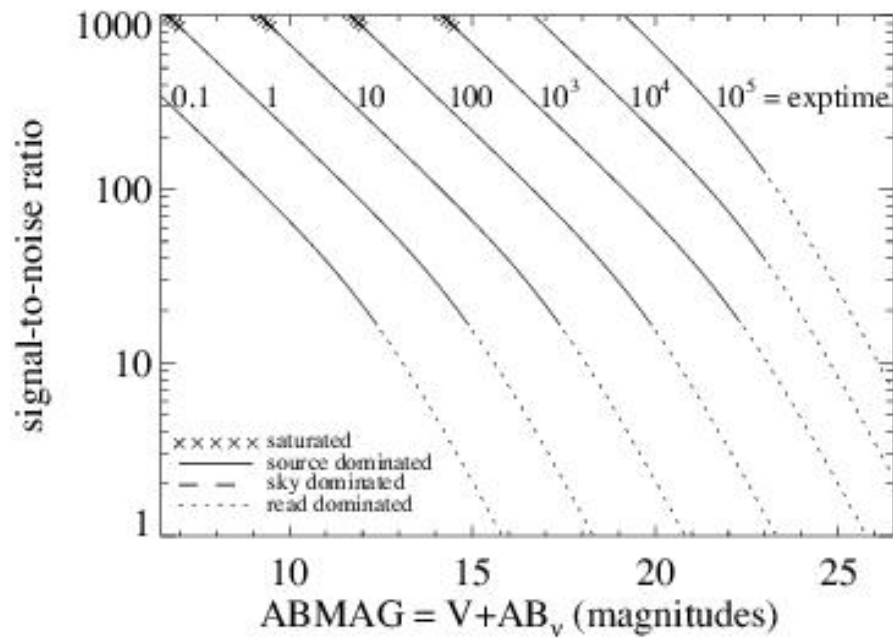
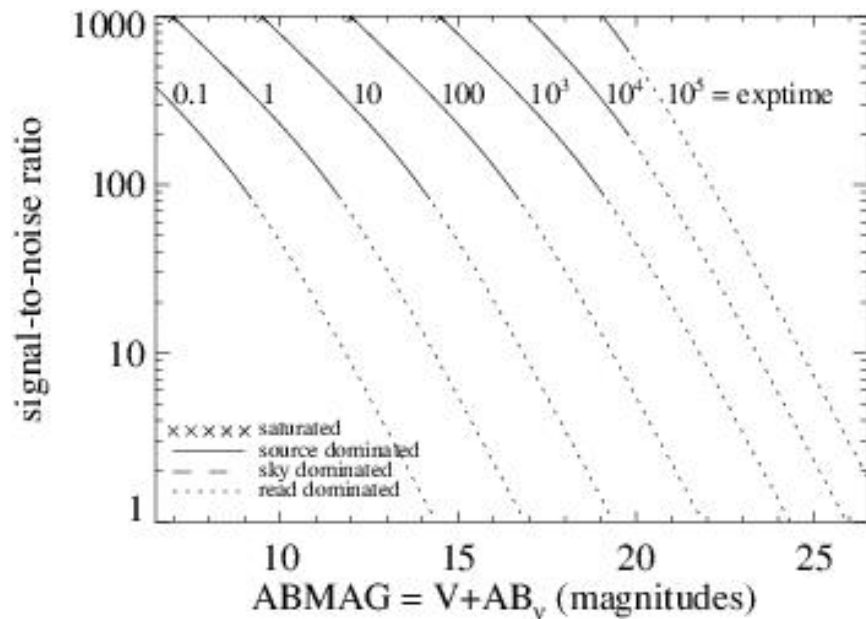


Figure A.159: Extended source S/N vs. $V+AB_v$ for the FQ619N filter, assuming high sky backgrounds and a source uniformly filling a 1 arcsec^2 aperture.



UVIS FQ634N

Description

6194 continuum filter.

Figure A.160: Integrated system throughput for FQ634N.

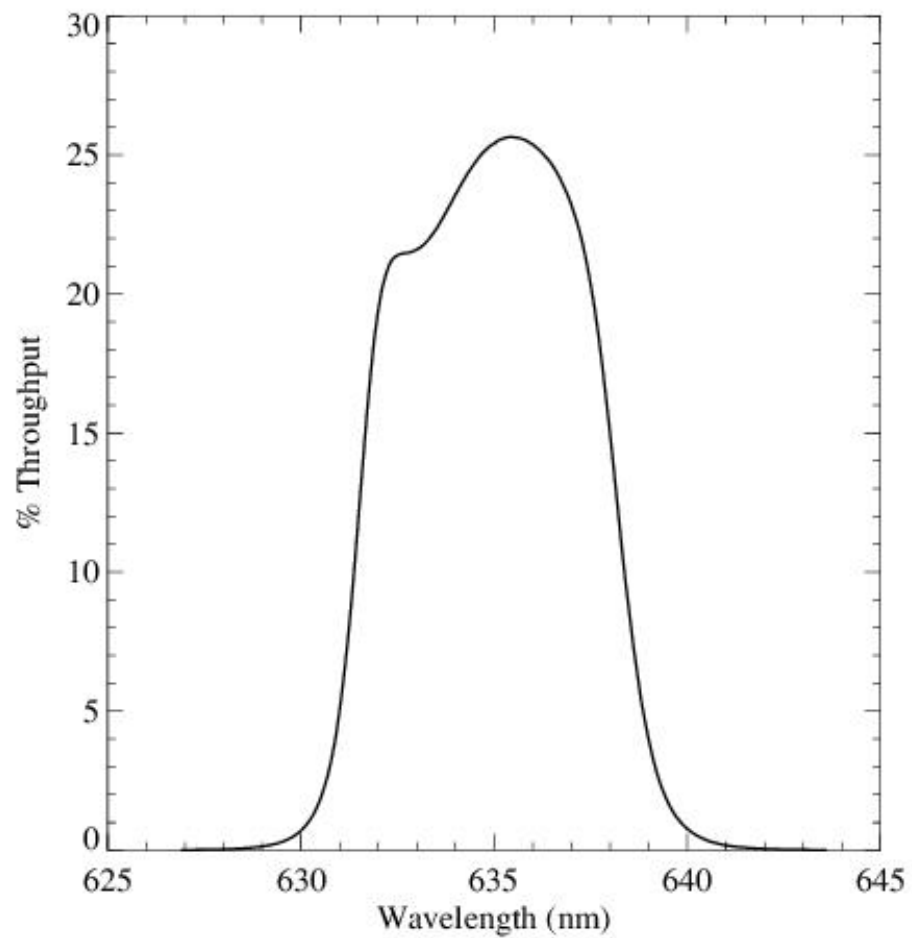


Figure A.161: Point source S/N vs. $V+AB_v$ for the FQ634N filter, assuming high sky backgrounds and a 5×5 pixel aperture.

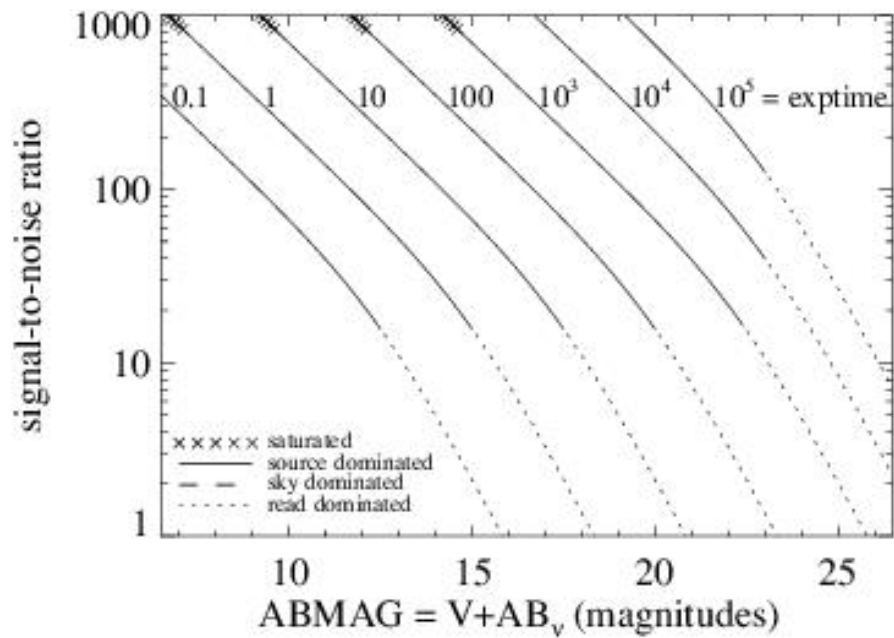
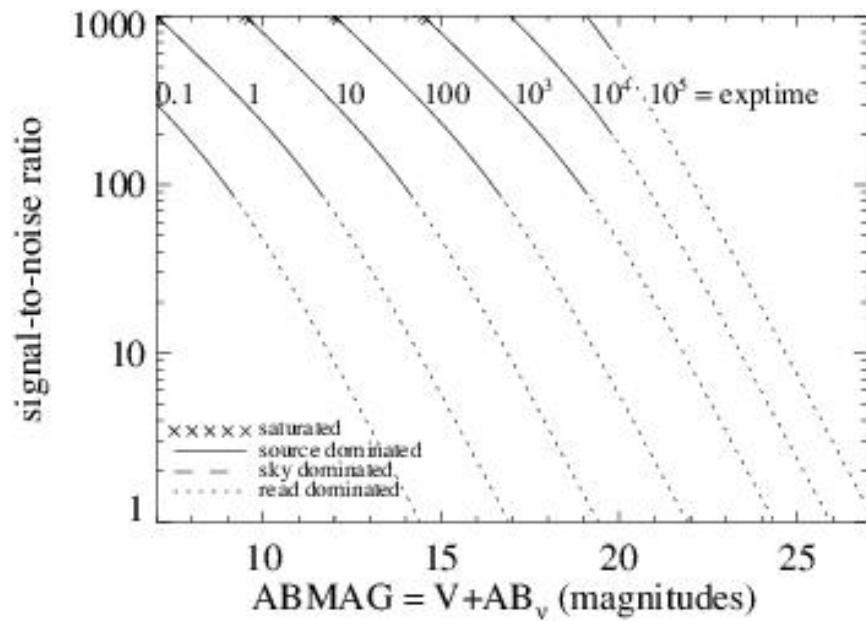


Figure A.162: Extended source S/N vs. $V+AB_v$ for the FQ634N filter, assuming high sky backgrounds and a source uniformly filling a 1 arcsec^2 aperture.



UVIS FQ672N

Description

[S II] 6717 filter.

Figure A.163: Integrated system throughput for FQ672N.

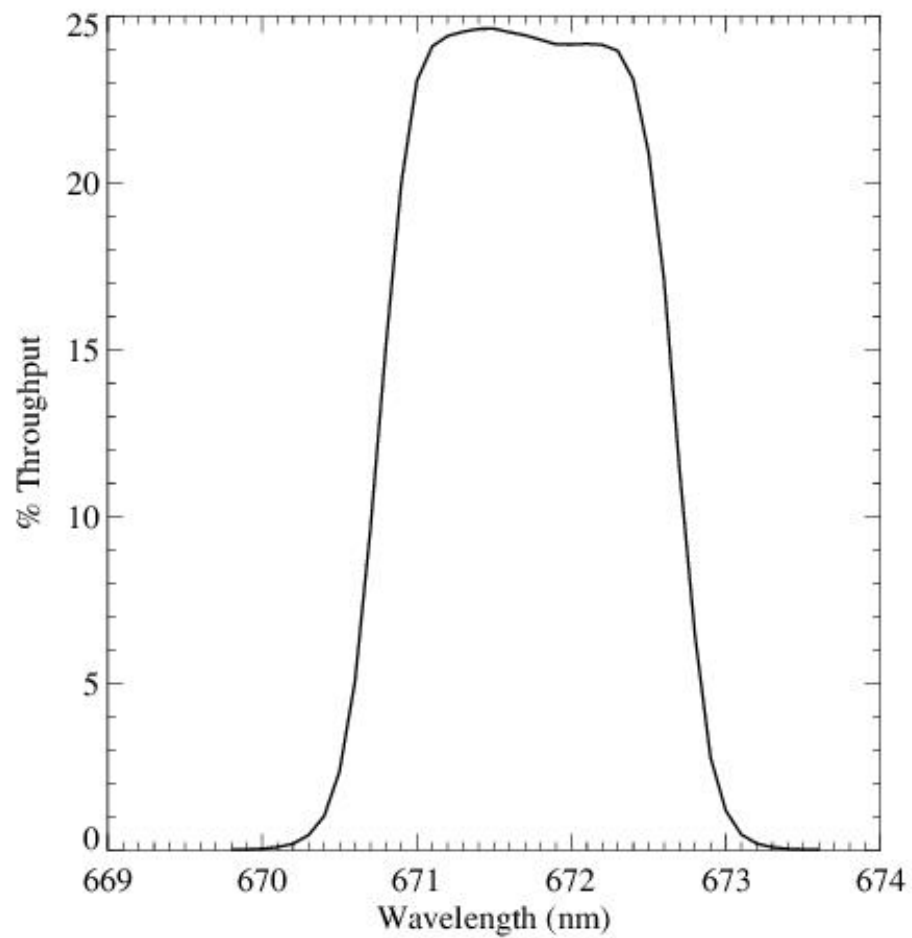


Figure A.164: Point source S/N vs. $V+AB_v$ for the FQ672N filter, assuming high sky backgrounds and a 5×5 pixel aperture.

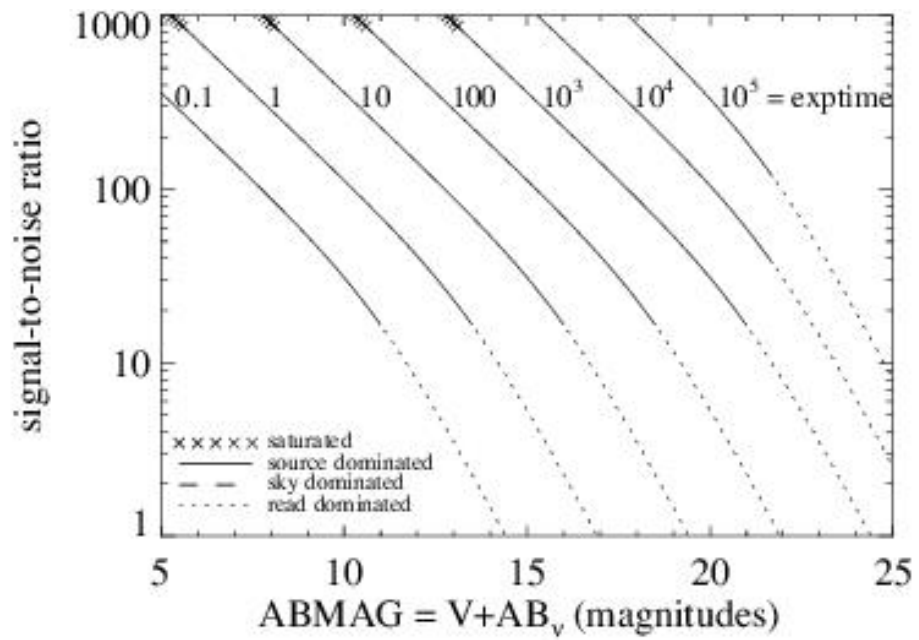
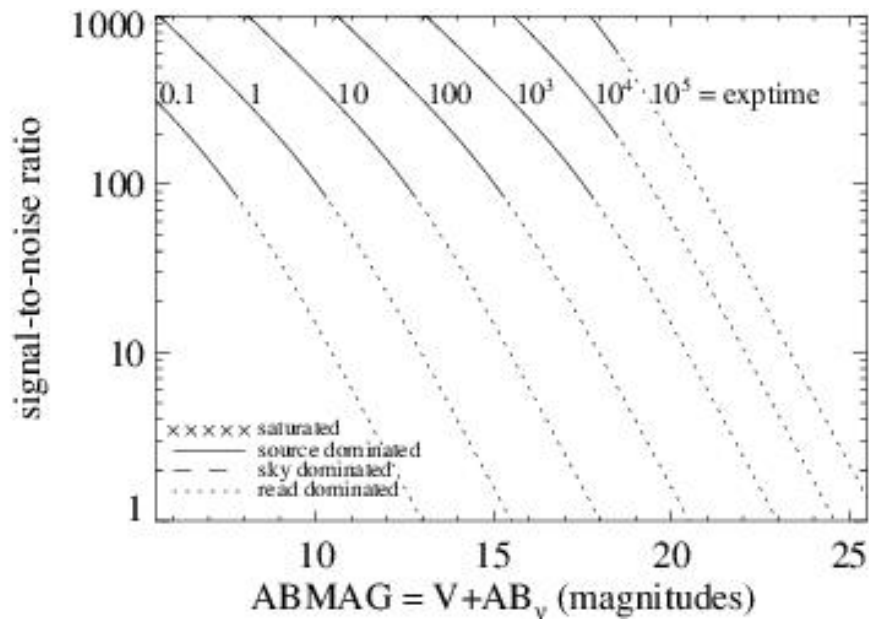


Figure A.165: Extended source S/N vs. $V+AB_v$ for the FQ672N filter, assuming high sky backgrounds and a source uniformly filling a 1 arcsec^2 aperture.



UVIS FQ674N

Description

[S II] 6731 filter.

Figure A.166: Integrated system throughput for FQ674N.

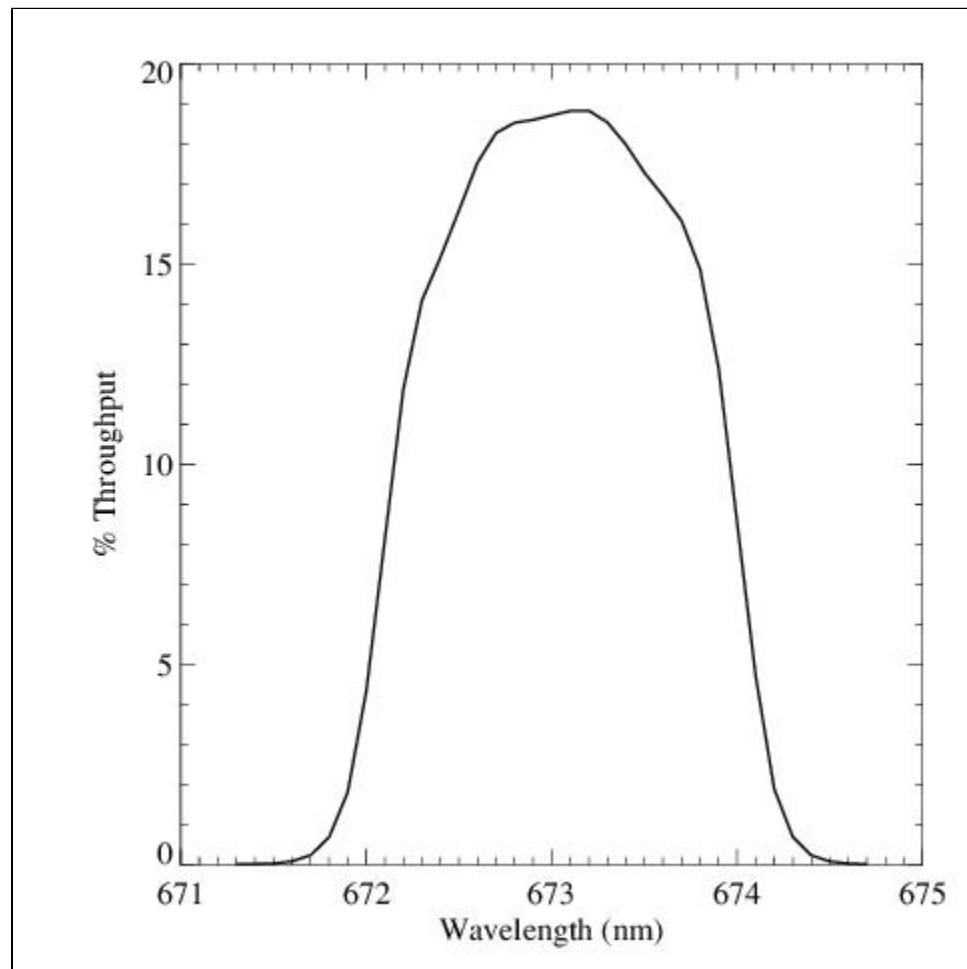


Figure A.167: Point source S/N vs. $V+AB_v$ for the FQ674N filter, assuming high sky backgrounds and a 5×5 pixel aperture.

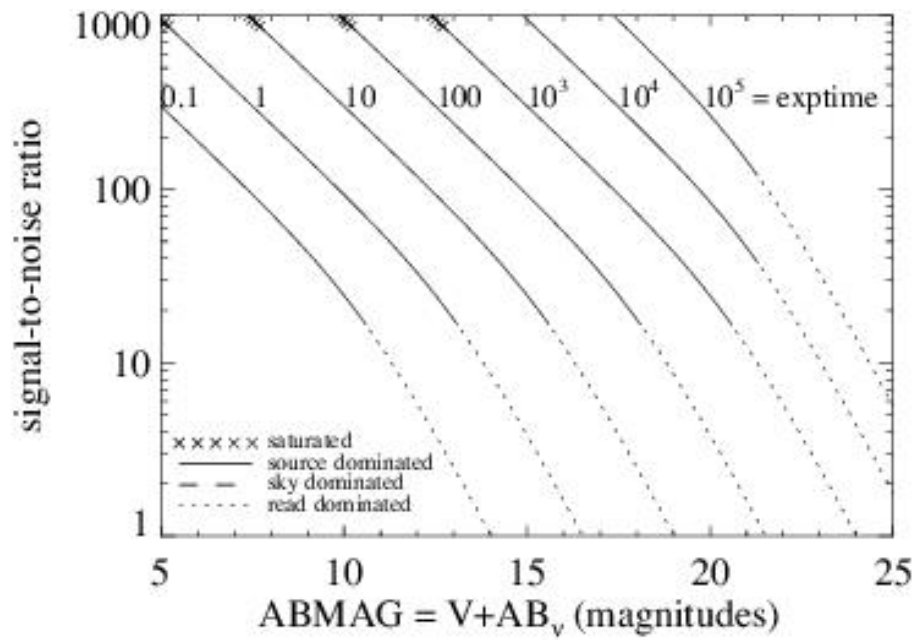
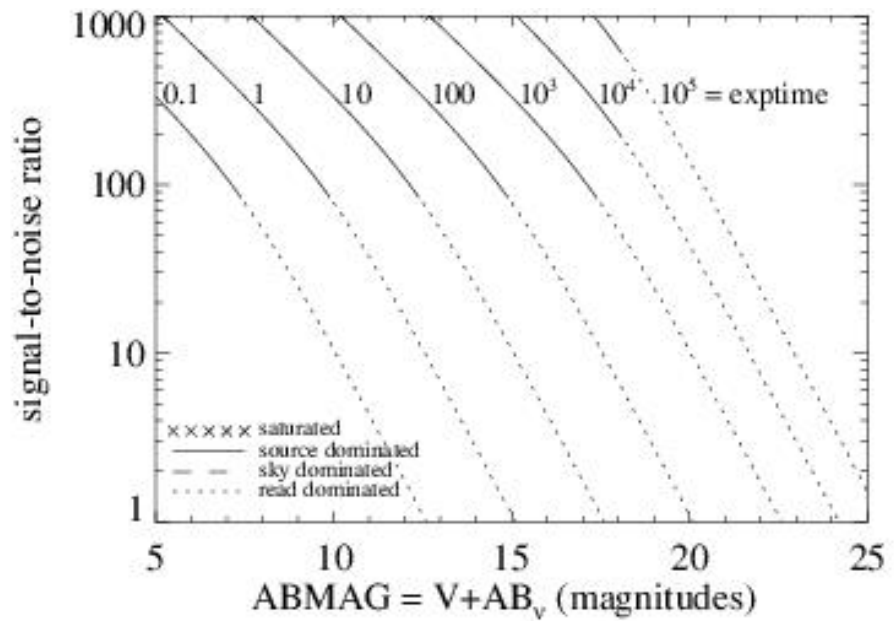


Figure A.168: Extended source S/N vs. $V+AB_v$ for the FQ674N filter, assuming high sky backgrounds and a source uniformly filling a 1 arcsec^2 aperture.



UVIS FQ727N

Description

CH₄ 7270 filter.

Figure A.169: Integrated system throughput for FQ727N.

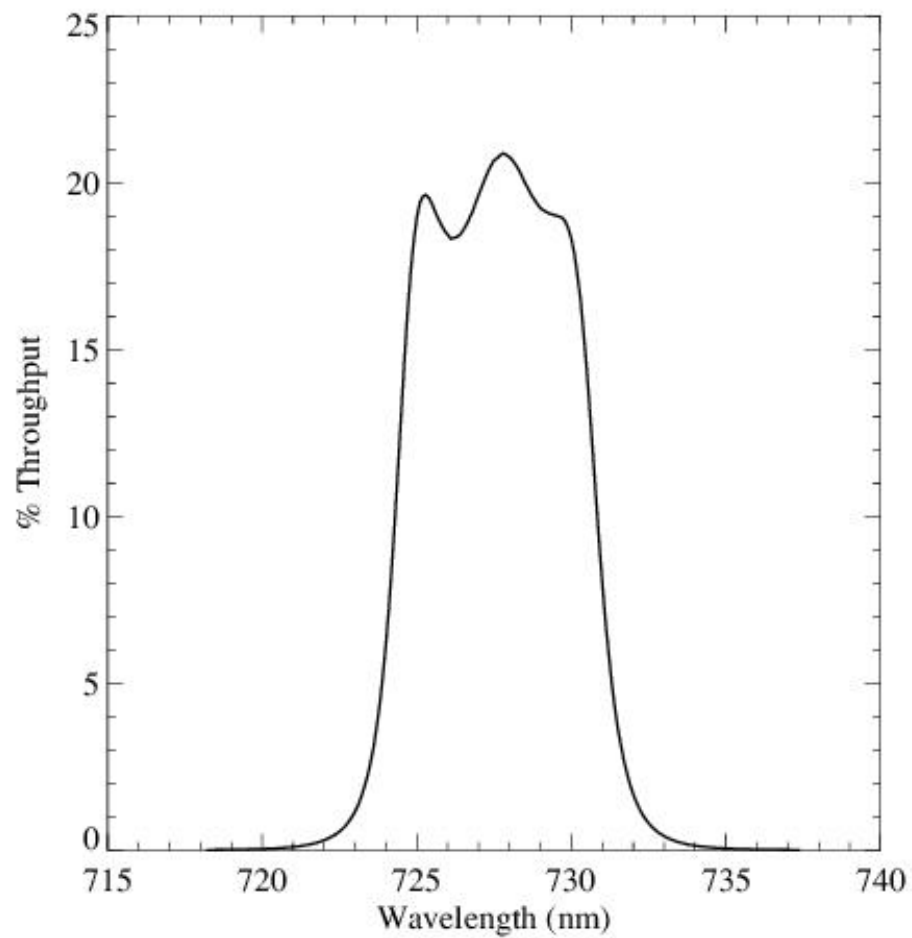


Figure A.170: Point source S/N vs. $V+AB_v$ for the FQ727N filter, assuming high sky backgrounds and a 5×5 pixel aperture.

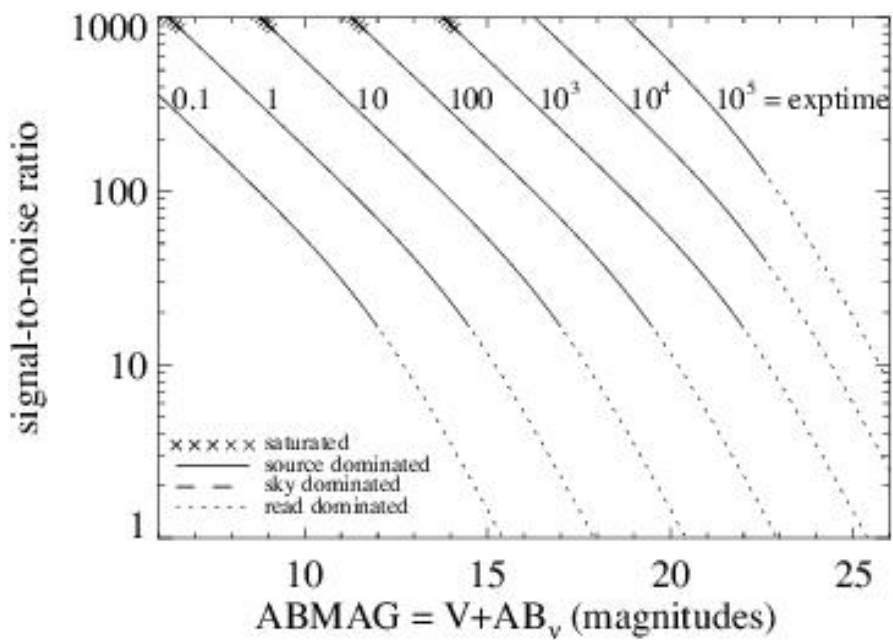
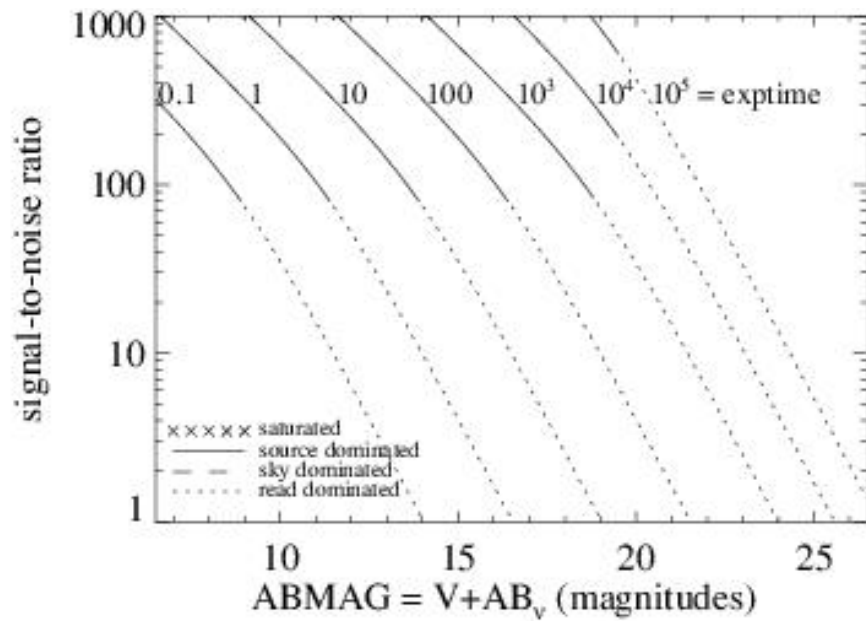


Figure A.171: Extended source S/N vs. $V+AB_v$ for the FQ727N filter, assuming high sky backgrounds and a source uniformly filling a 1 arcsec^2 aperture.



UVIS FQ750N

Description

7270 continuum filter.

Figure A.172: Integrated system throughput for FQ750N.

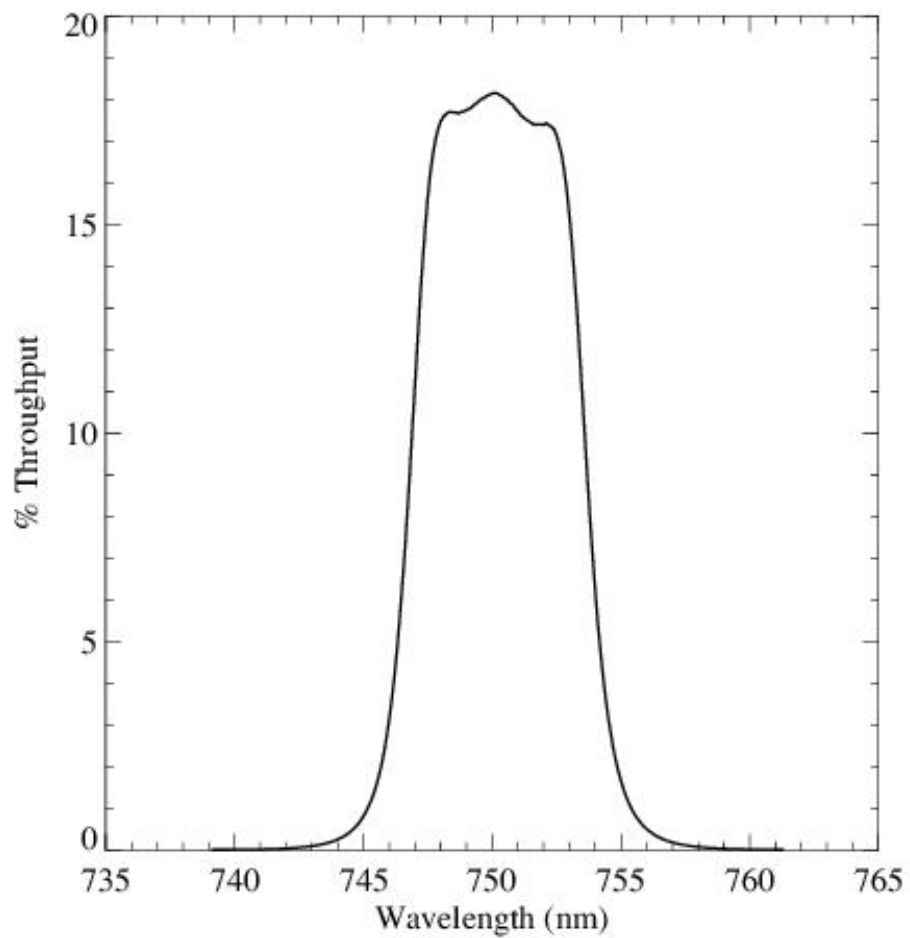


Figure A.173: Point source S/N vs. $V+AB_v$ for the FQ750N filter, assuming high sky backgrounds and a 5×5 pixel aperture.

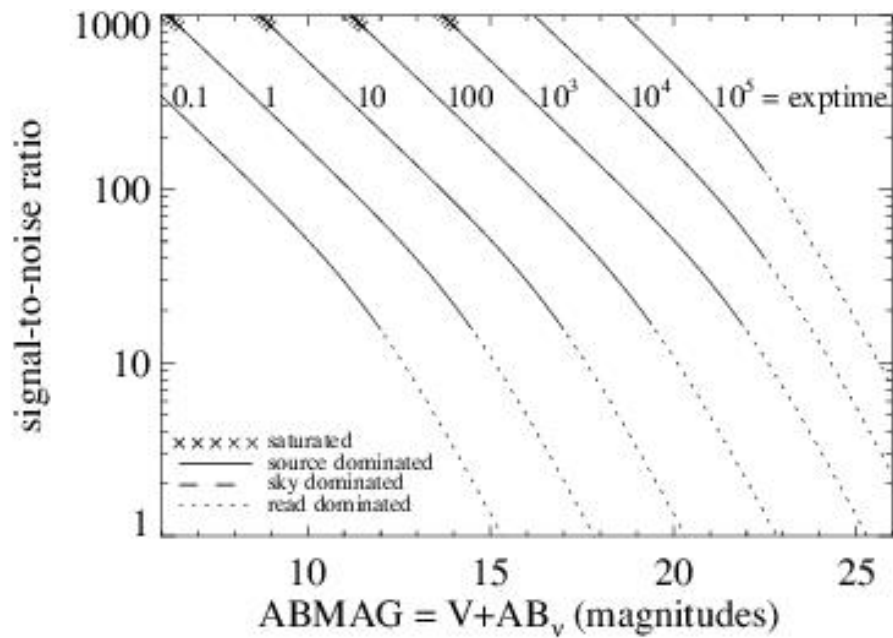
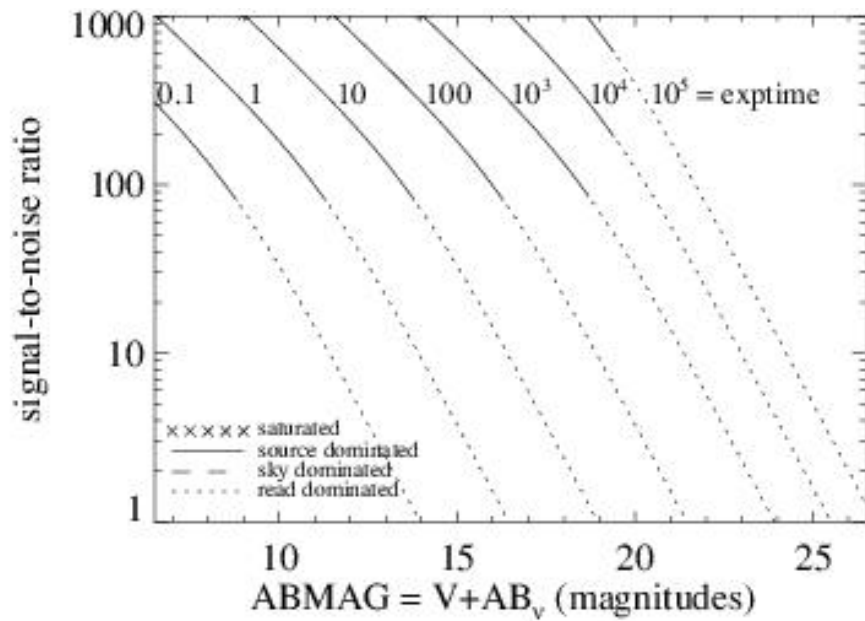


Figure A.174: Extended source S/N vs. $V+AB_v$ for the FQ750N filter, assuming high sky backgrounds and a source uniformly filling a 1 arcsec^2 aperture.



UVIS FQ889N

Description

CH₄ 25 km-agt filter.

Figure A.175: Integrated system throughput for FQ889N.

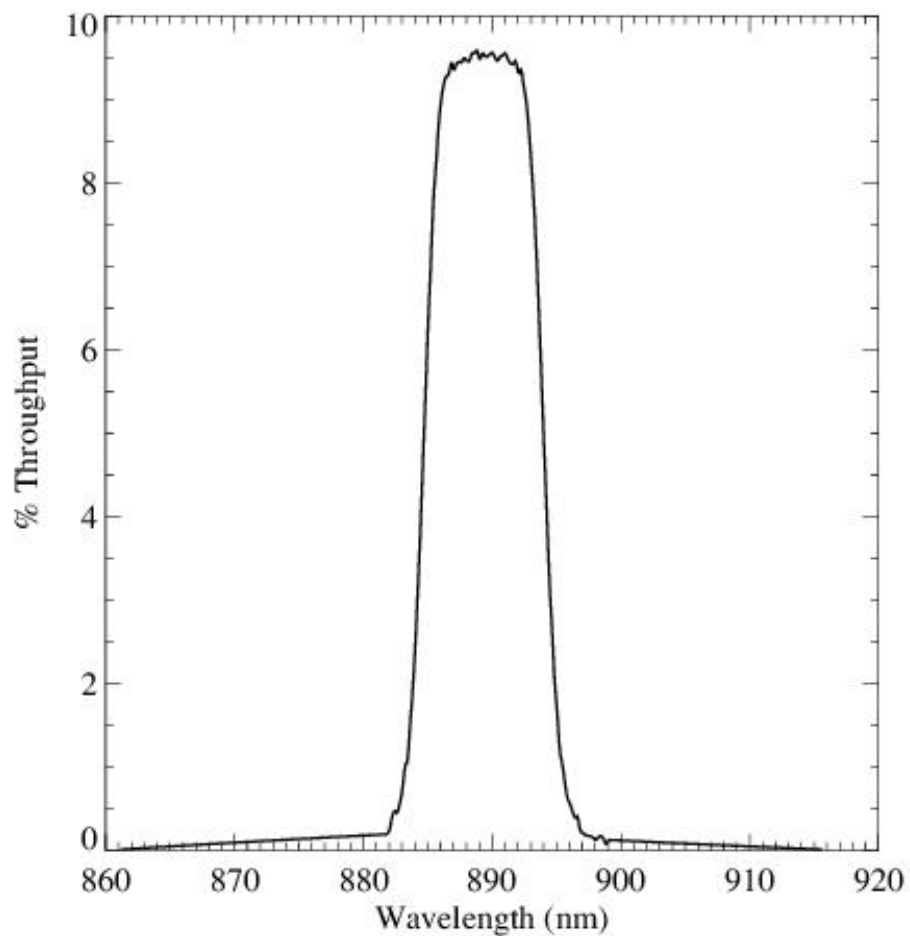


Figure A.176: Point source S/N vs. $V+AB_v$ for the FQ889N filter, assuming high sky backgrounds and a 5×5 pixel aperture.

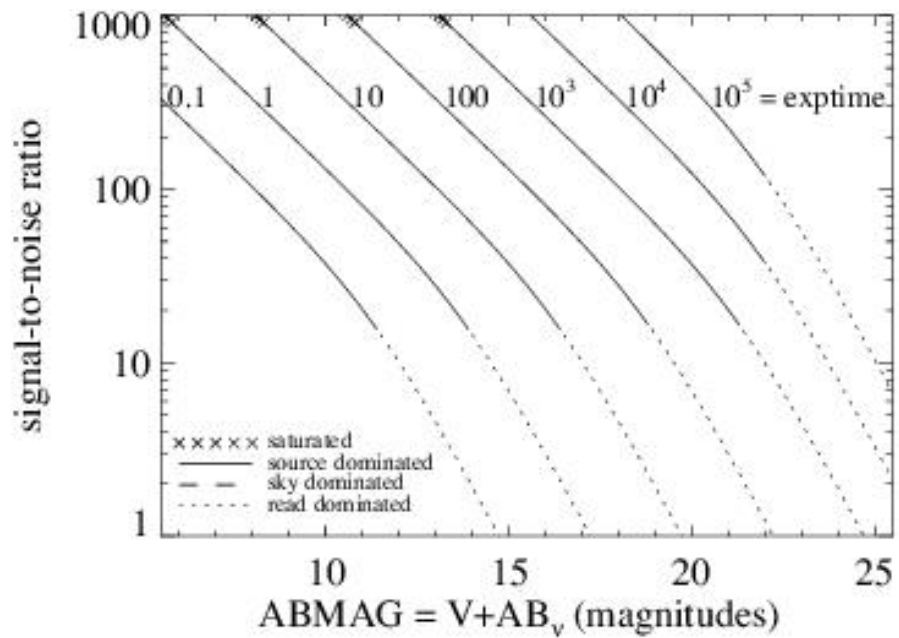
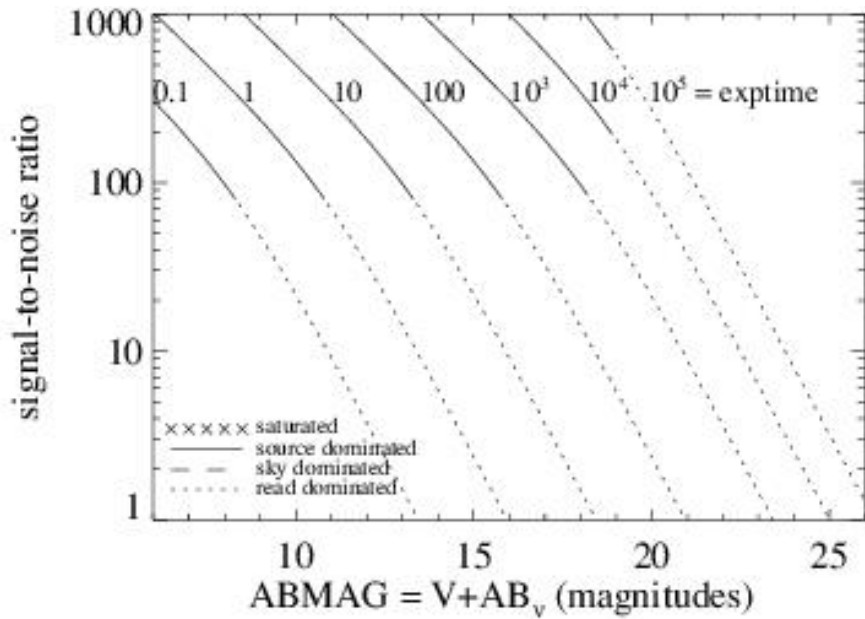


Figure A.177: Extended source S/N vs. $V+AB_v$ for the FQ889N filter, assuming high sky backgrounds and a source uniformly filling a 1 arcsec^2 aperture.



UVIS FQ906N

Description

CH₄ 2.5 km-agt filter.

Figure A.178: Integrated system throughput for FQ906N.

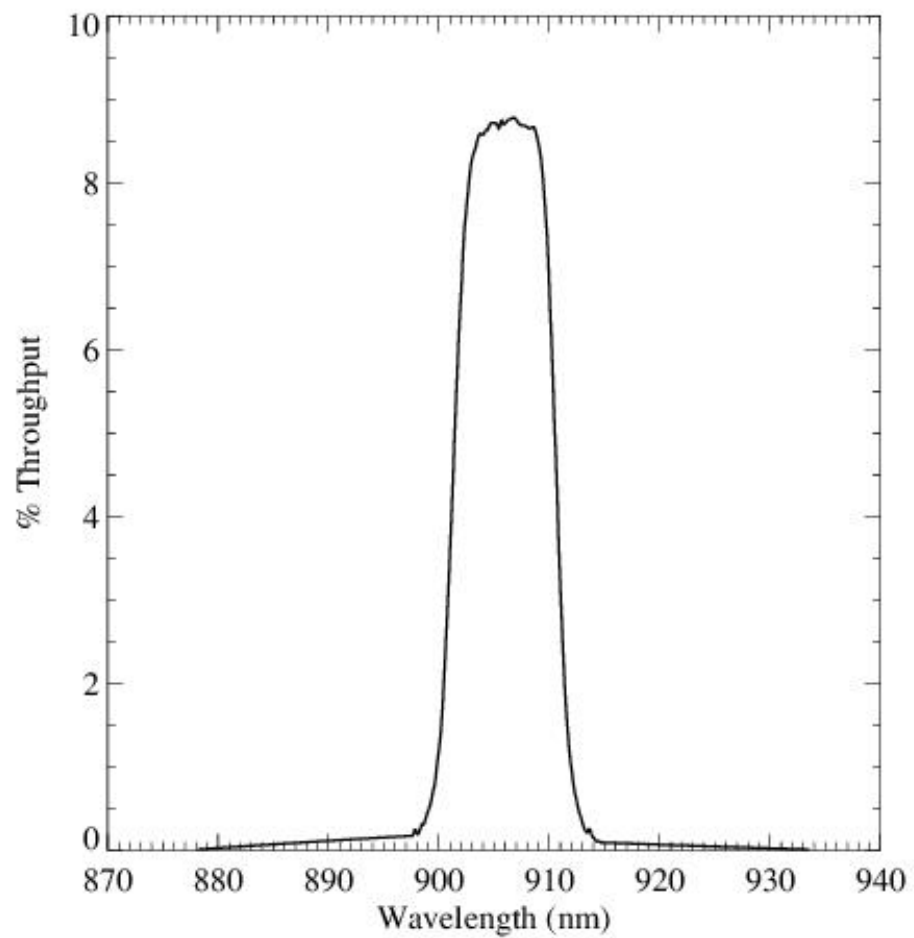


Figure A.179: Point source S/N vs. $V+AB_v$ for the FQ906N filter, assuming high sky backgrounds and a 5×5 pixel aperture.

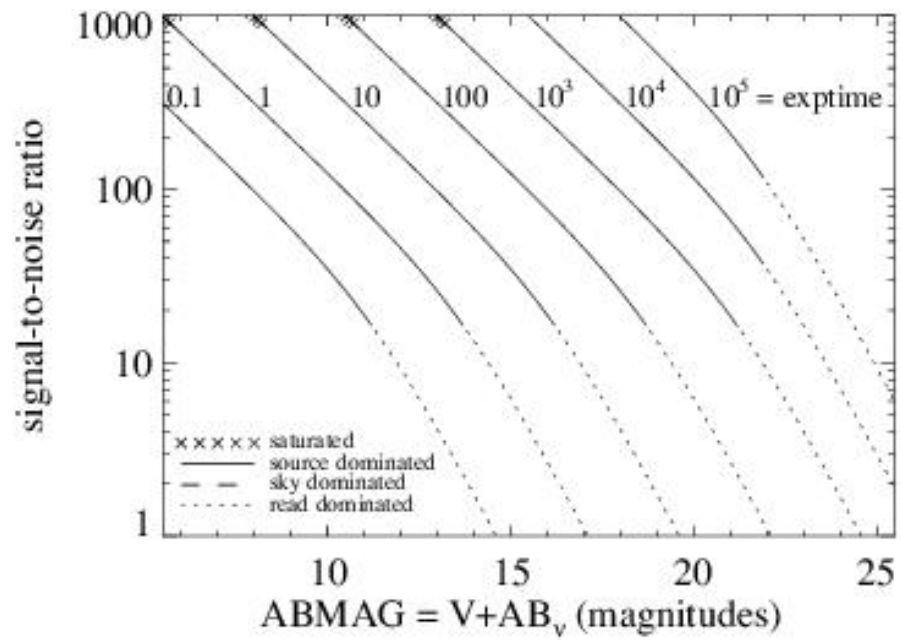
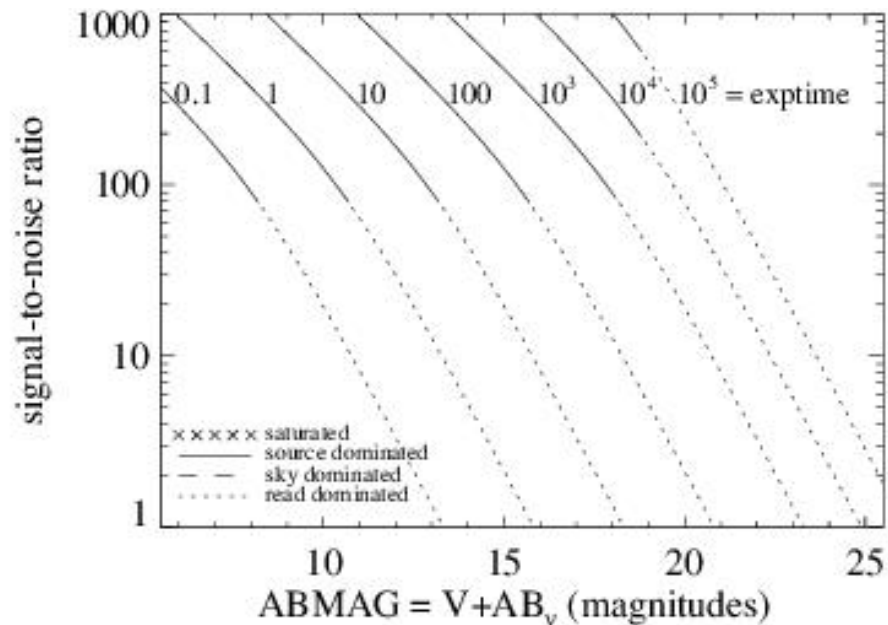


Figure A.180: Extended source S/N vs. $V+AB_v$ for the FQ906N filter, assuming high sky backgrounds and a source uniformly filling a 1 arcsec^2 aperture.



UVIS FQ924N

Description

CH₄ 0.25 km-agt filter.

Figure A.181: Integrated system throughput for FQ924N.

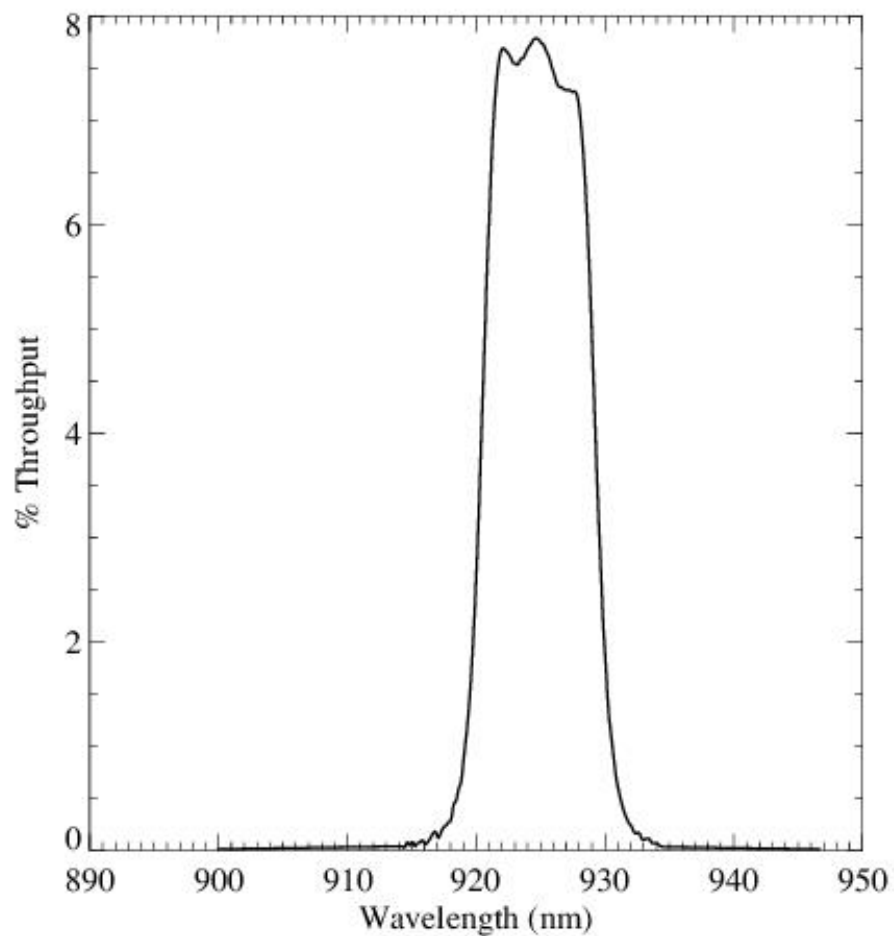


Figure A.182: Point source S/N vs. $V+AB_v$ for the FQ924N filter, assuming high sky backgrounds and a 5×5 pixel aperture.

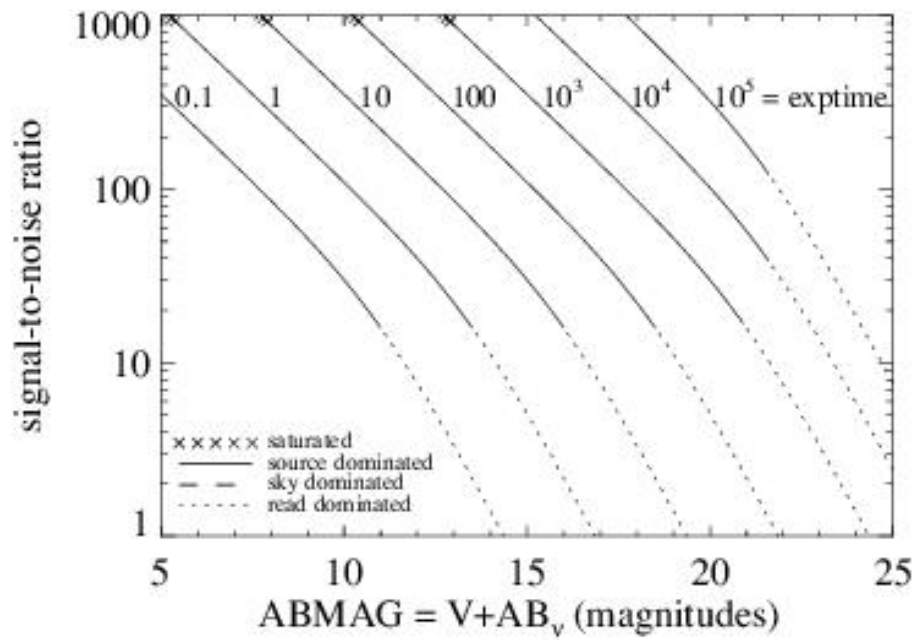
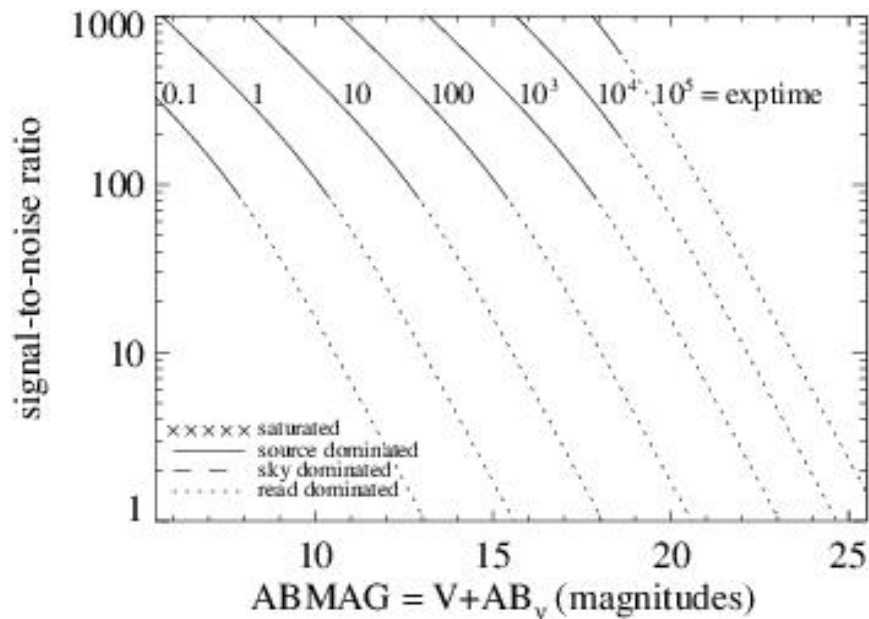


Figure A.183: Extended source S/N vs. $V+AB_v$ for the FQ924N filter, assuming high sky backgrounds and a source uniformly filling a 1 arcsec^2 aperture.



UVIS FQ937N

Description

CH₄ 0.025 km-agt filter.

Figure A.184: Integrated system throughput for FQ937N.

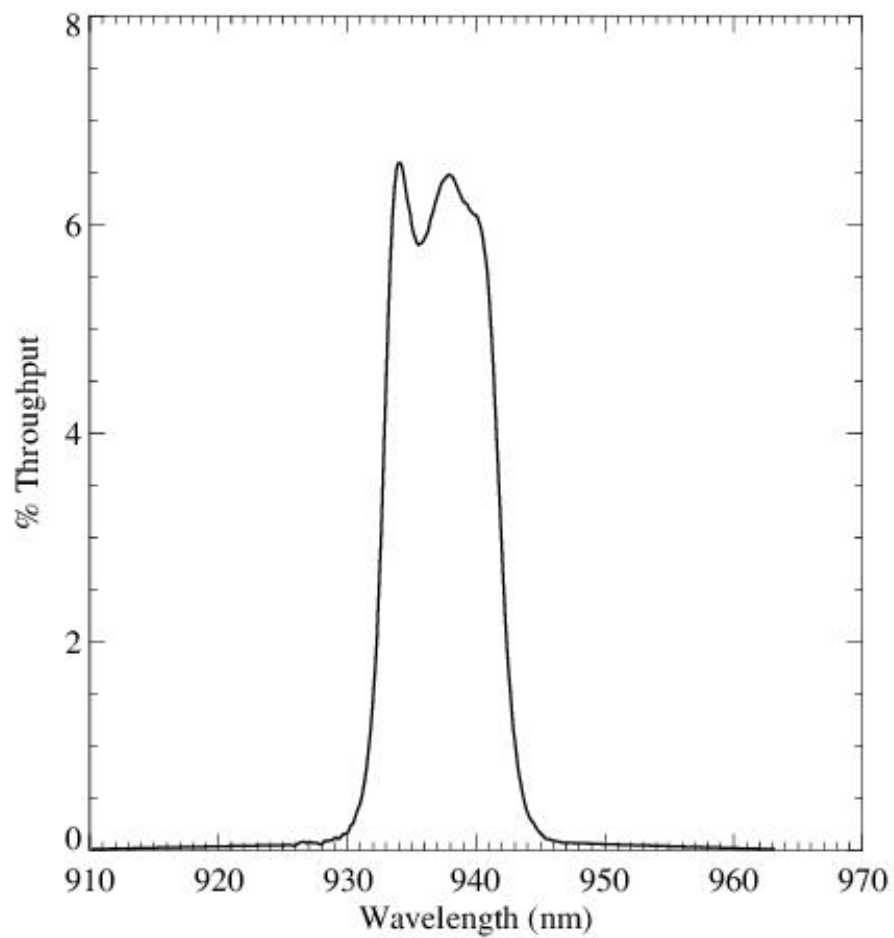


Figure A.185: Point source S/N vs. $V+AB_v$ for the FQ937N filter, assuming high sky backgrounds and a 5×5 pixel aperture.

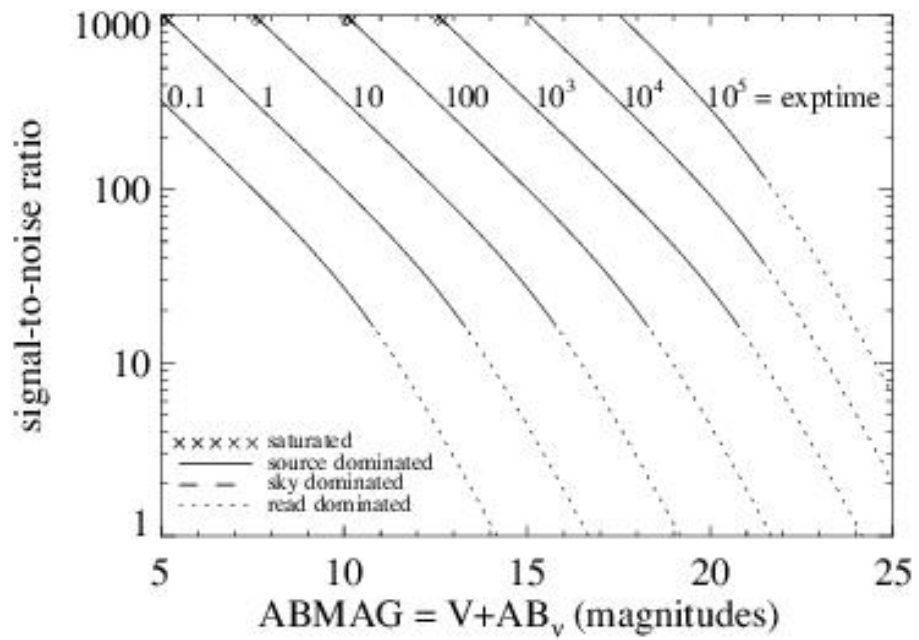


Figure A.186: Extended source S/N vs. $V+AB_V$ for the FQ937N filter, assuming high sky backgrounds and a source uniformly filling a 1 arcsec^2 aperture.

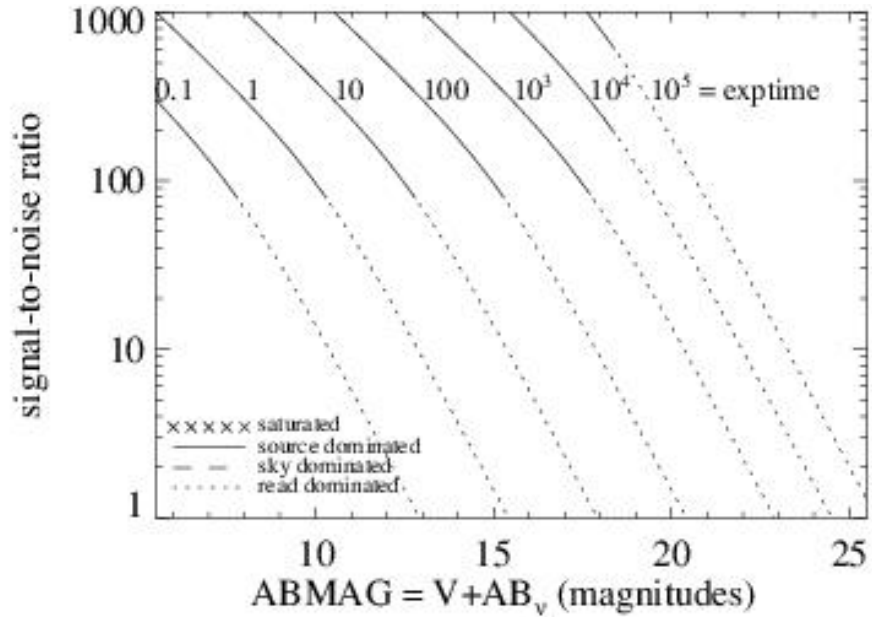


Table A.1: Color corrections AB_V to go from Johnson V magnitude to AB magnitude for WFC3 as a function of stellar effective temperature.

				Teff				
Mode	2500K	5000K	7500K	10000K	15000K	20000K	30000K	50000K
UVIS/F200LP	-2.22	0.45	0.48	0.40	0.08	-0.12	-0.40	-0.57
UVIS/F218W	7.21	7.82	2.95	1.51	0.09	-0.53	-1.22	-1.55
UVIS/F225W	6.07	7.22	2.84	1.51	0.12	-0.49	-1.15	-1.46
UVIS/F275W	7.30	5.30	2.27	1.35	0.10	-0.42	-0.96	-1.24
UVIS/F280N	3.29	4.49	2.50	1.44	0.13	-0.40	-0.90	-1.17
UVIS/F300X	5.96	4.05	1.98	1.26	0.10	-0.39	-0.91	-1.19
UVIS/F336W	4.98	2.71	1.31	1.00	0.10	-0.26	-0.64	-0.86
UVIS/F343N	4.74	2.62	1.24	0.97	0.11	-0.24	-0.60	-0.82
UVIS/F350LP	-2.64	0.07	0.18	0.18	0.09	0.04	-0.02	-0.07

UVIS/F373N	7.03	2.53	1.10	0.94	0.21	-0.09	-0.43	-0.65
UVIS/F390M	4.25	2.08	0.67	0.25	-0.20	-0.33	-0.48	-0.60
UVIS/F390W	3.80	1.63	0.59	0.26	-0.14	-0.29	-0.47	-0.60
UVIS/F395N	3.91	1.92	0.67	0.15	-0.27	-0.37	-0.49	-0.58
UVIS/F410M	2.96	1.16	0.29	-0.10	-0.32	-0.39	-0.46	-0.52
UVIS/F438W	2.28	0.86	0.18	-0.12	-0.28	-0.33	-0.39	-0.43
UVIS/F467M	1.74	0.34	0.02	-0.15	-0.22	-0.24	-0.26	-0.27
UVIS/F469N	1.64	0.33	0.03	-0.14	-0.21	-0.24	-0.26	-0.26
UVIS/F475W	1.23	0.44	0.09	-0.07	-0.17	-0.20	-0.24	-0.26
UVIS/F475X	0.61	0.35	0.12	-0.01	-0.12	-0.15	-0.19	-0.23
UVIS/F487N	1.47	0.29	0.20	0.28	0.06	-0.02	-0.11	-0.17
UVIS/F502N	2.32	0.32	0.02	-0.07	-0.11	-0.12	-0.14	-0.15
UVIS/FQ508N	1.07	0.32	0.01	-0.06	-0.08	-0.10	-0.11	-0.12
UVIS/F547M	0.08	0.03	0.02	0.01	0.01	0.01	0.01	0.02
UVIS/F555W	0.15	0.09	0.03	-0.01	-0.03	-0.04	-0.05	-0.06
UVIS/F600LP	-3.71	-0.42	0.09	0.34	0.47	0.52	0.57	0.60
UVIS/F606W	-0.83	-0.11	0.04	0.10	0.12	0.12	0.13	0.13
UVIS/F621M	-1.23	-0.26	0.03	0.16	0.22	0.25	0.27	0.28
UVIS/F625W	-1.17	-0.25	0.04	0.16	0.22	0.24	0.26	0.27
UVIS/F631N	-0.33	-0.28	0.03	0.17	0.24	0.27	0.30	0.31
UVIS/F645N	-2.20	-0.29	0.04	0.20	0.28	0.31	0.35	0.35
UVIS/F656N	-1.99	-0.26	0.36	0.63	0.56	0.54	0.52	0.45
UVIS/F657N	-2.31	-0.31	0.14	0.37	0.39	0.41	0.42	0.41
UVIS/F658N	-2.04	-0.31	0.18	0.42	0.42	0.43	0.44	0.41
UVIS/F665N	-1.30	-0.35	0.06	0.26	0.34	0.38	0.42	0.42
UVIS/F673N	-0.69	-0.37	0.04	0.24	0.35	0.39	0.44	0.45
UVIS/F680N	-1.61	-0.38	0.05	0.26	0.38	0.42	0.47	0.48
UVIS/F689M	-1.69	-0.37	0.06	0.28	0.39	0.43	0.47	0.48
UVIS/F763M	-3.09	-0.45	0.09	0.37	0.53	0.59	0.65	0.69

UVIS/F775W	-3.60	-0.45	0.09	0.38	0.54	0.59	0.65	0.70
UVIS/F814W	-4.14	-0.48	0.12	0.43	0.60	0.67	0.74	0.79
UVIS/F845M	-4.56	-0.51	0.16	0.51	0.70	0.77	0.84	0.91
UVIS/F850LP	-5.03	-0.56	0.21	0.56	0.79	0.89	0.98	1.06
UVIS/F953N	-5.52	-0.59	0.27	0.68	0.91	1.00	1.10	1.16
UVIS/FQ232N	2.15	4.54	2.68	1.53	0.20	-0.43	-1.12	-1.46
UVIS/FQ243N	2.84	5.10	2.76	1.52	0.18	-0.44	-1.11	-1.40
UVIS/FQ378N	4.90	2.32	0.86	0.61	0.01	-0.20	-0.44	-0.62
UVIS/FQ387N	6.34	2.42	0.61	0.25	-0.21	-0.34	-0.49	-0.61
UVIS/FQ422M	5.05	1.17	0.18	-0.22	-0.36	-0.41	-0.46	-0.48
UVIS/FQ436N	2.64	0.84	0.23	0.08	-0.16	-0.24	-0.31	-0.39
UVIS/FQ437N	2.59	0.83	0.18	0.00	-0.21	-0.28	-0.34	-0.40
UVIS/FQ492N	0.91	0.27	0.04	-0.02	-0.10	-0.13	-0.16	-0.17
UVIS/FQ575N	-0.58	-0.18	0.01	0.07	0.10	0.11	0.13	0.13
UVIS/FQ619N	0.72	-0.25	0.03	0.15	0.22	0.24	0.27	0.27
UVIS/FQ634N	-0.96	-0.28	0.03	0.18	0.26	0.29	0.32	0.32
UVIS/FQ672N	-0.77	-0.35	0.04	0.23	0.34	0.38	0.42	0.44
UVIS/FQ674N	-0.39	-0.37	0.04	0.24	0.35	0.39	0.43	0.44
UVIS/FQ727N	-2.81	-0.41	0.07	0.32	0.46	0.52	0.57	0.60
UVIS/FQ750N	-3.06	-0.44	0.08	0.36	0.51	0.57	0.63	0.66
UVIS/FQ889N	-4.98	-0.55	0.20	0.57	0.78	0.86	0.95	1.01
UVIS/FQ906N	-5.15	-0.56	0.21	0.57	0.79	0.88	0.98	1.05
UVIS/FQ924N	-4.89	-0.57	0.26	0.66	0.87	0.95	1.04	1.10
UVIS/FQ937N	-5.19	-0.58	0.19	0.48	0.77	0.89	1.01	1.11
IR/F098M	-5.40	-0.60	0.25	0.60	0.88	1.00	1.12	1.21
IR/F105W	-5.68	-0.62	0.31	0.69	0.98	1.11	1.24	1.34
IR/F110W	-5.77	-0.64	0.39	0.80	1.12	1.25	1.39	1.49
IR/F125W	-5.91	-0.67	0.48	0.94	1.28	1.43	1.58	1.69
IR/F126N	-5.99	-0.67	0.49	0.96	1.31	1.46	1.61	1.72

IR/F127M	-6.04	-0.67	0.52	1.01	1.35	1.49	1.65	1.75
IR/F128N	-6.08	-0.67	0.59	1.11	1.41	1.55	1.69	1.78
IR/F130N	-6.13	-0.68	0.53	1.02	1.37	1.52	1.68	1.79
IR/F132N	-6.04	-0.67	0.54	1.03	1.39	1.55	1.71	1.82
IR/F139M	-5.64	-0.69	0.60	1.11	1.49	1.64	1.81	1.92
IR/F140W	-5.89	-0.69	0.61	1.12	1.49	1.64	1.80	1.92
IR/F153M	-6.03	-0.71	0.73	1.29	1.69	1.85	2.02	2.14
IR/F160W	-6.05	-0.70	0.74	1.30	1.69	1.85	2.02	2.15
IR/F164N	-6.39	-0.70	0.84	1.42	1.82	1.99	2.16	2.28
IR/F167N	-6.32	-0.69	0.84	1.41	1.83	2.00	2.18	2.31

Table A.2: Color corrections AB_V to go from Johnson V magnitude to AB magnitude for WFC3 as a function of age in an instantaneous burst population.

Mode	Age				
	10 Gyr	1 Gyr	100 Myr	10 Myr	1 Myr
UVIS/F200LP	0.38	0.48	0.29	0.02	-0.48
UVIS/F218W	6.11	3.89	1.06	0.15	-1.22
UVIS/F225W	5.83	3.76	1.03	0.16	-1.15
UVIS/F275W	4.75	3.14	0.93	0.19	-0.97
UVIS/F280N	4.32	3.03	0.89	0.21	-0.92
UVIS/F300X	3.95	2.80	0.89	0.20	-0.94
UVIS/F336W	2.69	1.98	0.77	0.27	-0.67
UVIS/F343N	2.55	1.89	0.76	0.28	-0.63
UVIS/F350LP	-0.09	0.04	0.06	-0.06	-0.04
UVIS/F373N	2.28	1.57	0.66	0.34	-0.49
UVIS/F390M	2.03	1.12	0.22	0.14	-0.50
UVIS/F390W	1.63	1.00	0.27	0.15	-0.50

UVIS/F395N	1.88	1.03	0.14	0.11	-0.49
UVIS/F410M	1.23	0.64	0.02	0.02	-0.47
UVIS/F438W	0.90	0.48	0.01	0.02	-0.39
UVIS/F467M	0.44	0.22	-0.03	-0.01	-0.26
UVIS/F469N	0.46	0.23	-0.02	-0.01	-0.25
UVIS/F475W	0.48	0.27	0.02	0.04	-0.23
UVIS/F475X	0.38	0.24	0.03	0.03	-0.20
UVIS/F487N	0.36	0.27	0.12	0.10	-0.14
UVIS/F502N	0.33	0.17	0.02	0.08	-0.12
UVIS/F547M	0.04	0.03	0.03	0.03	0.02
UVIS/F555W	0.11	0.07	0.02	0.01	-0.05
UVIS/F600LP	-0.72	-0.38	-0.04	-0.27	0.54
UVIS/F606W	-0.17	-0.08	0.01	-0.04	0.13
UVIS/F621M	-0.33	-0.18	0.00	-0.10	0.26
UVIS/F625W	-0.33	-0.18	-0.00	-0.10	0.26
UVIS/F631N	-0.34	-0.19	0.00	-0.10	0.29
UVIS/F645N	-0.43	-0.23	-0.02	-0.15	0.33
UVIS/F656N	-0.45	-0.18	0.06	-0.16	0.37
UVIS/F657N	-0.47	-0.22	0.00	-0.18	0.37
UVIS/F658N	-0.47	-0.22	0.00	-0.18	0.37
UVIS/F665N	-0.48	-0.26	-0.03	-0.18	0.39
UVIS/F673N	-0.49	-0.28	-0.02	-0.15	0.42
UVIS/F680N	-0.54	-0.30	-0.02	-0.17	0.45
UVIS/F689M	-0.53	-0.29	-0.02	-0.18	0.45
UVIS/F763M	-0.77	-0.40	-0.05	-0.32	0.64
UVIS/F775W	-0.78	-0.41	-0.05	-0.31	0.64
UVIS/F814W	-0.89	-0.47	-0.07	-0.36	0.71
UVIS/F845M	-1.00	-0.53	-0.09	-0.41	0.82

UVIS/F850LP	-1.18	-0.65	-0.13	-0.47	0.96
UVIS/F953N	-1.27	-0.71	-0.12	-0.50	1.06
UVIS/FQ232N	4.48	3.43	1.03	0.17	-1.14
UVIS/FQ243N	4.88	3.62	0.98	0.14	-1.10
UVIS/FQ378N	2.24	1.37	0.42	0.22	-0.51
UVIS/FQ387N	2.27	1.16	0.23	0.14	-0.51
UVIS/FQ422M	1.16	0.55	-0.03	0.01	-0.44
UVIS/FQ436N	0.86	0.49	0.04	0.05	-0.36
UVIS/FQ437N	0.86	0.46	0.00	0.03	-0.37
UVIS/FQ492N	0.31	0.17	0.01	0.05	-0.15
UVIS/FQ508N	0.31	0.17	0.04	0.12	-0.09
UVIS/FQ575N	-0.18	-0.08	0.00	-0.06	0.12
UVIS/FQ619N	-0.28	-0.16	0.02	-0.06	0.26
UVIS/FQ634N	-0.37	-0.21	-0.01	-0.12	0.30
UVIS/FQ672N	-0.47	-0.27	-0.02	-0.16	0.40
UVIS/FQ674N	-0.48	-0.27	-0.02	-0.16	0.41
UVIS/FQ727N	-0.65	-0.34	-0.01	-0.26	0.56
UVIS/FQ750N	-0.81	-0.43	-0.07	-0.33	0.61
UVIS/FQ889N	-1.12	-0.61	-0.14	-0.46	0.91
UVIS/FQ906N	-1.22	-0.68	-0.15	-0.49	0.94
UVIS/FQ924N	-1.21	-0.65	-0.12	-0.48	1.00
UVIS/FQ937N	-1.16	-0.65	-0.11	-0.47	1.00
IR/F098M	-1.35	-0.74	-0.15	-0.51	1.10
IR/F105W	-1.39	-0.74	-0.14	-0.54	1.22
IR/F110W	-1.38	-0.70	-0.11	-0.57	1.36
IR/F125W	-1.39	-0.67	-0.08	-0.60	1.57
IR/F126N	-1.37	-0.64	-0.07	-0.62	1.60
IR/F127M	-1.38	-0.64	-0.07	-0.62	1.62

IR/F128N	-1.39	-0.64	-0.07	-0.63	1.64
IR/F130N	-1.40	-0.65	-0.07	-0.63	1.66
IR/F132N	-1.40	-0.64	-0.07	-0.62	1.69
IR/F139M	-1.37	-0.62	-0.05	-0.60	1.78
IR/F140W	-1.41	-0.65	-0.06	-0.64	1.77
IR/F153M	-1.49	-0.69	-0.07	-0.70	1.98
IR/F160W	-1.49	-0.68	-0.07	-0.70	1.97
IR/F164N	-1.59	-0.75	-0.11	-0.79	2.10
IR/F167N	-1.58	-0.74	-0.10	-0.78	2.13

Table A.3: Color corrections AB_V to go from Johnson V magnitude to AB magnitude for WFC3 as a function of age in a population with constant star formation.

Mode	Age				
	10 Gyr	1 Gyr	100 Myr	10 Myr	1 Myr
UVIS/F200LP	0.31	0.24	0.03	-0.15	-0.48
UVIS/F218W	1.39	0.79	0.08	-0.48	-1.22
UVIS/F225W	1.39	0.79	0.09	-0.44	-1.15
UVIS/F275W	1.35	0.78	0.12	-0.36	-0.97
UVIS/F280N	1.34	0.77	0.14	-0.33	-0.92
UVIS/F300X	1.31	0.76	0.13	-0.34	-0.93
UVIS/F336W	1.15	0.71	0.19	-0.21	-0.66
UVIS/F343N	1.13	0.71	0.20	-0.18	-0.62
UVIS/F350LP	0.00	0.03	-0.01	-0.01	-0.04
UVIS/F373N	1.04	0.66	0.24	-0.11	-0.49
UVIS/F390M	0.67	0.28	-0.00	-0.25	-0.50
UVIS/F390W	0.64	0.30	0.03	-0.23	-0.49
UVIS/F395N	0.60	0.21	-0.04	-0.27	-0.49

UVIS/F410M	0.37	0.07	-0.11	-0.30	-0.47
UVIS/F438W	0.29	0.05	-0.09	-0.25	-0.39
UVIS/F467M	0.14	-0.00	-0.08	-0.18	-0.26
UVIS/F469N	0.15	0.00	-0.07	-0.17	-0.25
UVIS/F475W	0.18	0.04	-0.03	-0.14	-0.23
UVIS/F475X	0.16	0.05	-0.02	-0.11	-0.20
UVIS/F487N	0.21	0.14	0.05	-0.05	-0.14
UVIS/F502N	0.13	0.04	0.01	-0.06	-0.13
UVIS/F547M	0.03	0.03	0.03	0.03	0.02
UVIS/F555W	0.05	0.02	-0.00	-0.03	-0.05
UVIS/F600LP	-0.36	-0.13	-0.05	0.22	0.54
UVIS/F606W	-0.06	-0.00	0.01	0.07	0.13
UVIS/F621M	-0.14	-0.03	0.01	0.13	0.26
UVIS/F625W	-0.14	-0.03	0.01	0.12	0.26
UVIS/F631N	-0.15	-0.03	0.02	0.14	0.29
UVIS/F645N	-0.19	-0.05	-0.01	0.15	0.33
UVIS/F656N	-0.16	0.01	0.02	0.19	0.37
UVIS/F657N	-0.20	-0.04	-0.01	0.16	0.37
UVIS/F658N	-0.20	-0.04	-0.02	0.16	0.37
UVIS/F665N	-0.23	-0.07	-0.02	0.16	0.39
UVIS/F673N	-0.23	-0.06	0.01	0.19	0.42
UVIS/F680N	-0.26	-0.07	0.00	0.20	0.45
UVIS/F689M	-0.25	-0.07	-0.01	0.20	0.45
UVIS/F763M	-0.39	-0.13	-0.06	0.25	0.64
UVIS/F775W	-0.39	-0.14	-0.06	0.25	0.64
UVIS/F814W	-0.46	-0.18	-0.08	0.26	0.71
UVIS/F845M	-0.53	-0.22	-0.12	0.28	0.82
UVIS/F850LP	-0.66	-0.31	-0.14	0.30	0.96

UVIS/F953N	-0.72	-0.34	-0.15	0.32	1.06
UVIS/FQ232N	1.37	0.79	0.10	-0.43	-1.14
UVIS/FQ243N	1.37	0.78	0.08	-0.43	-1.10
UVIS/FQ378N	0.85	0.46	0.10	-0.20	-0.50
UVIS/FQ387N	0.70	0.29	0.01	-0.25	-0.51
UVIS/FQ422M	0.32	0.02	-0.12	-0.30	-0.44
UVIS/FQ436N	0.31	0.08	-0.06	-0.22	-0.37
UVIS/FQ437N	0.28	0.05	-0.09	-0.24	-0.38
UVIS/FQ492N	0.12	0.03	-0.01	-0.09	-0.15
UVIS/FQ508N	0.14	0.06	0.04	-0.03	-0.09
UVIS/FQ575N	-0.07	-0.01	-0.00	0.06	0.13
UVIS/FQ619N	-0.12	-0.01	0.03	0.14	0.26
UVIS/FQ634N	-0.17	-0.04	0.00	0.14	0.30
UVIS/FQ672N	-0.22	-0.06	-0.00	0.18	0.40
UVIS/FQ674N	-0.22	-0.06	0.00	0.19	0.41
UVIS/FQ727N	-0.31	-0.09	-0.03	0.23	0.56
UVIS/FQ750N	-0.42	-0.16	-0.08	0.23	0.61
UVIS/FQ889N	-0.62	-0.28	-0.15	0.28	0.91
UVIS/FQ906N	-0.69	-0.34	-0.17	0.27	0.94
UVIS/FQ924N	-0.67	-0.30	-0.14	0.31	1.00
UVIS/FQ937N	-0.65	-0.30	-0.14	0.31	0.99
IR/F098M	-0.76	-0.37	-0.16	0.33	1.10
IR/F105W	-0.78	-0.37	-0.17	0.36	1.22
IR/F110W	-0.76	-0.33	-0.17	0.39	1.36
IR/F125W	-0.74	-0.30	-0.17	0.44	1.57
IR/F126N	-0.73	-0.29	-0.18	0.45	1.60
IR/F127M	-0.73	-0.29	-0.18	0.45	1.62
IR/F128N	-0.74	-0.29	-0.18	0.45	1.64

IR/F130N	-0.74	-0.29	-0.18	0.46	1.66
IR/F132N	-0.74	-0.28	-0.17	0.47	1.69
IR/F139M	-0.71	-0.25	-0.14	0.49	1.78
IR/F140W	-0.75	-0.28	-0.17	0.47	1.77
IR/F153M	-0.81	-0.32	-0.20	0.47	1.97
IR/F160W	-0.80	-0.32	-0.21	0.46	1.97
IR/F164N	-0.88	-0.39	-0.27	0.43	2.10
IR/F167N	-0.88	-0.38	-0.26	0.44	2.13

IR F098M

Description

Blue grism reference filter.

Figure A.187: Integrated system throughput for F098M.

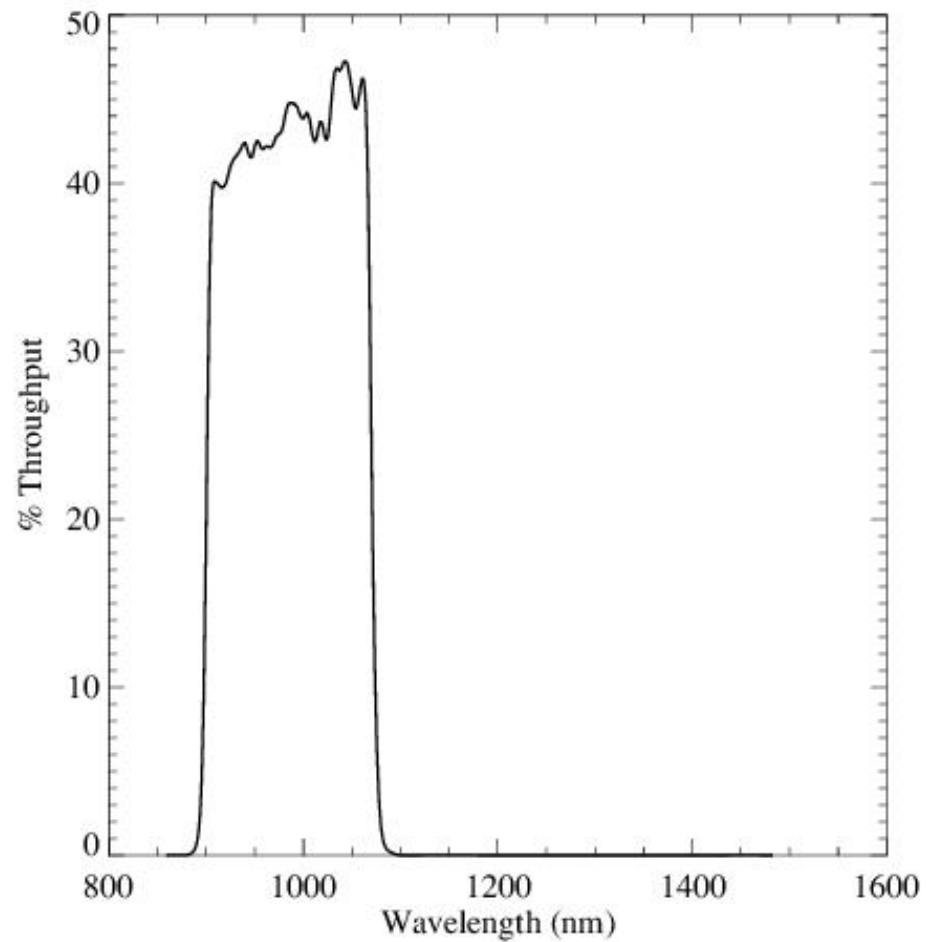


Figure A.188: Point source S/N vs. $V+AB_v$ for the F098M filter, assuming high sky backgrounds and a 3×3 pixel aperture.

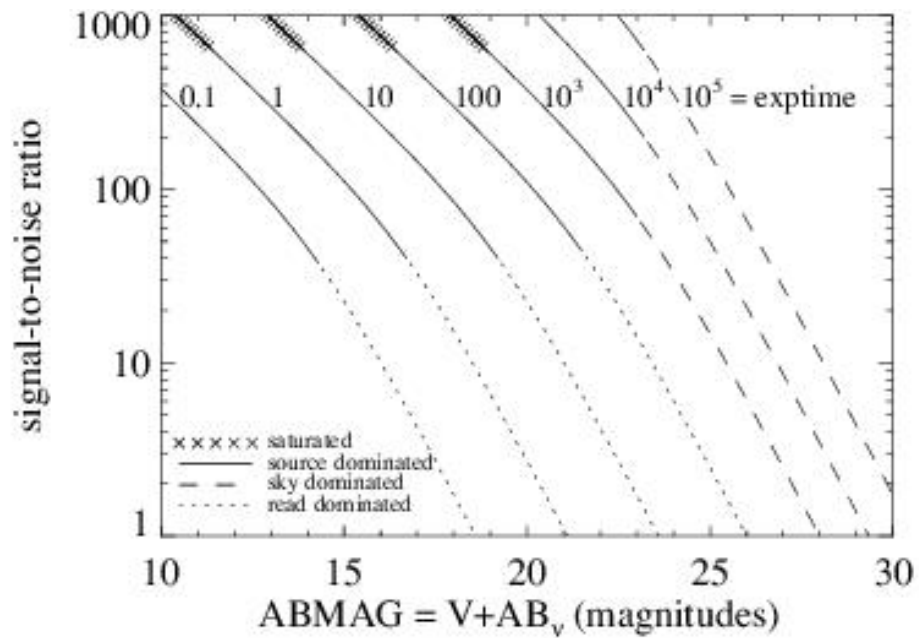
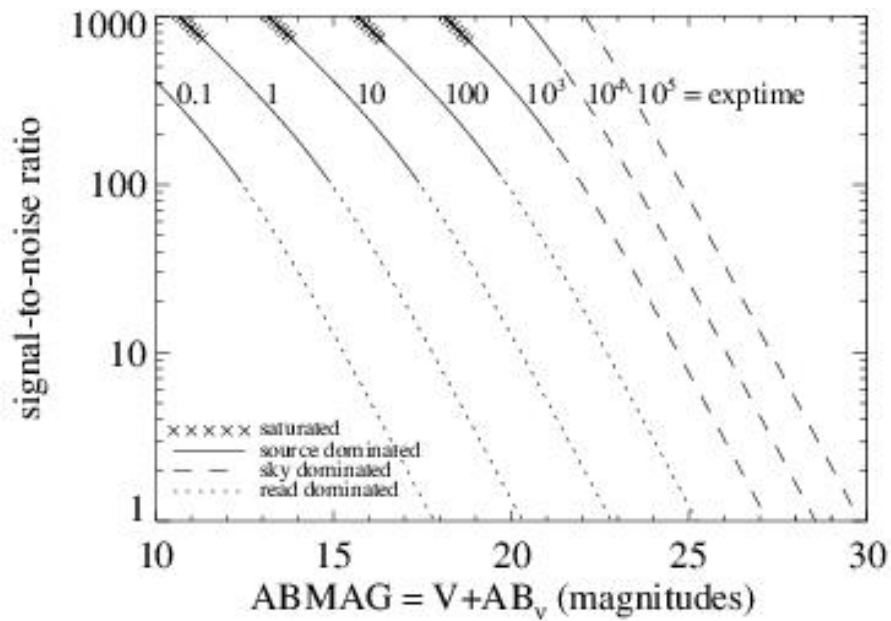


Figure A.189: Extended source S/N vs. $V+AB_v$ for the F098M filter, assuming high sky backgrounds and a source uniformly filling a 1 arcsec^2 aperture.



IR F105W

Description

Wide Yfilter.

Figure A.190: Integrated system throughput for F105W.

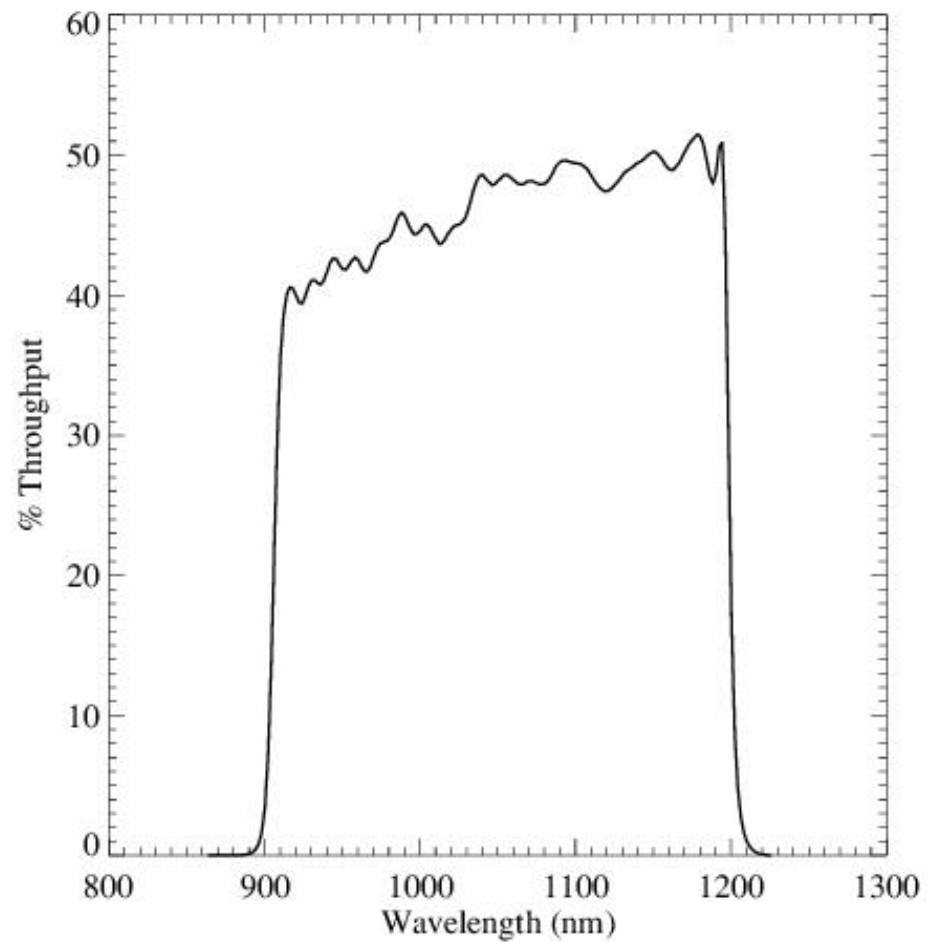


Figure A.191: Point source S/N vs. $V+AB_v$ for the F105W filter, assuming high sky backgrounds and a 3×3 pixel aperture.

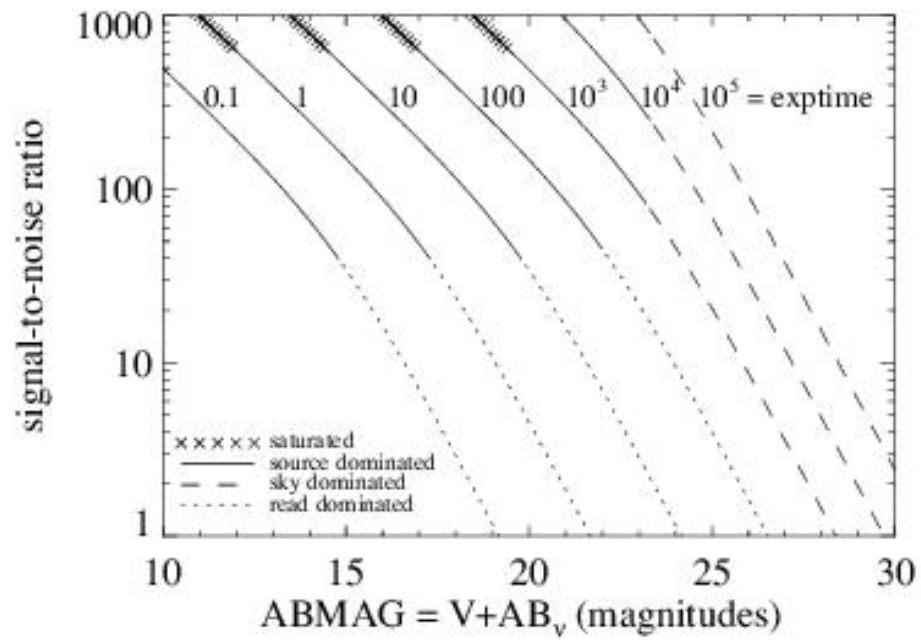
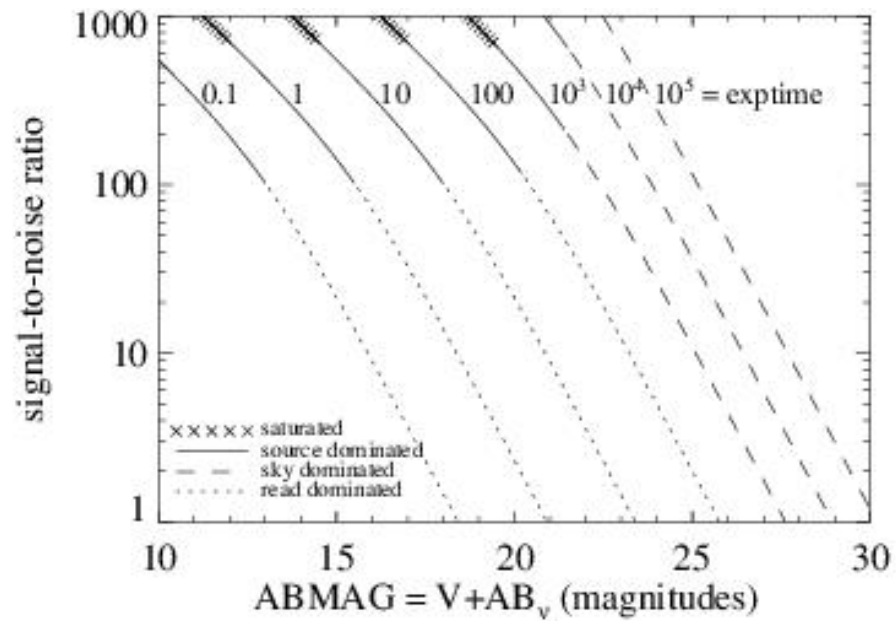


Figure A.192: Extended source S/N vs. $V+AB_v$ for the F105W filter, assuming high sky backgrounds and a source uniformly filling a 1 arcsec^2 aperture.



IR F110W

Description

Wide YJ filter.

Figure A.193: Integrated system throughput for F110W.

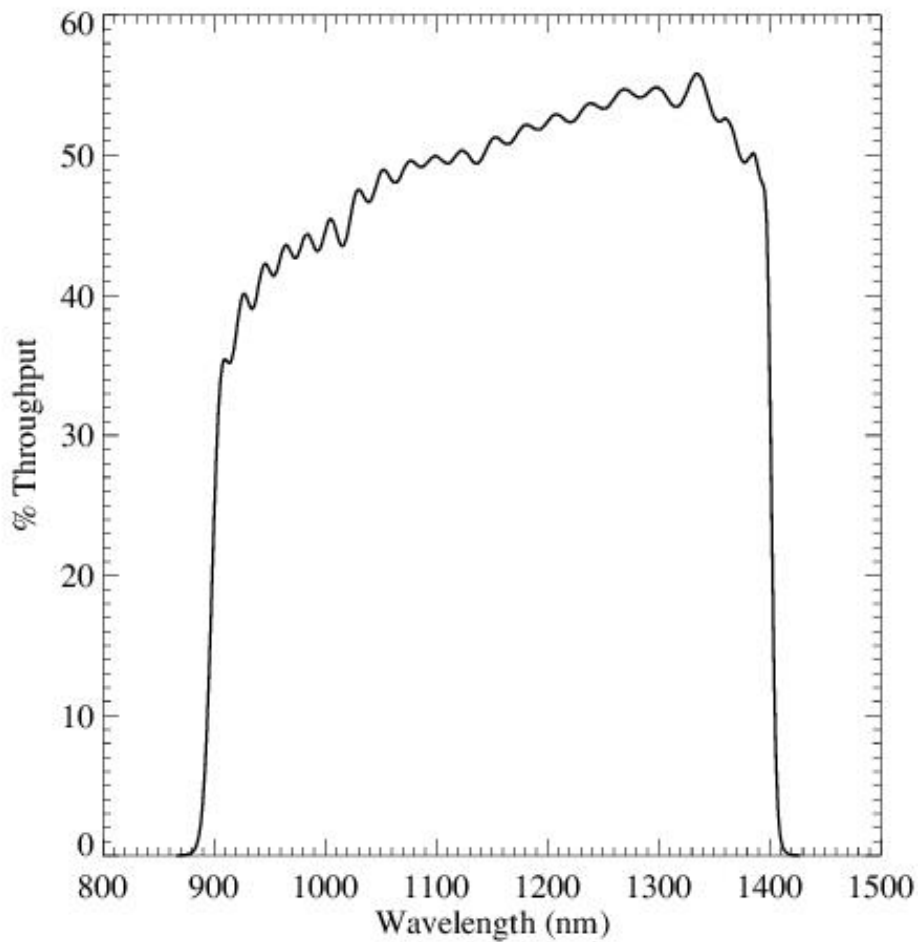


Figure A.194: Point source S/N vs. $V+AB_v$ for the F110W filter, assuming high sky backgrounds and a 3×3 pixel aperture.

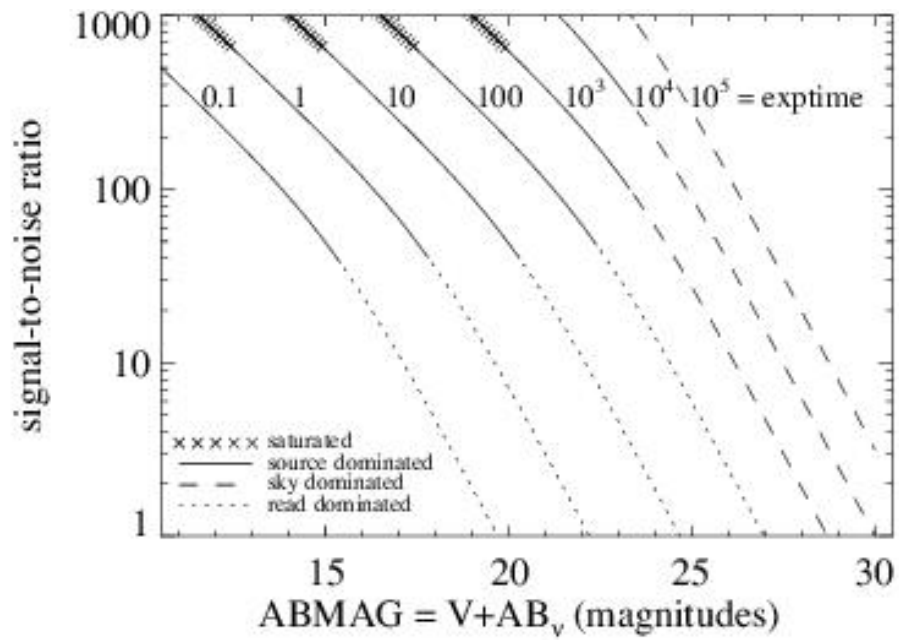
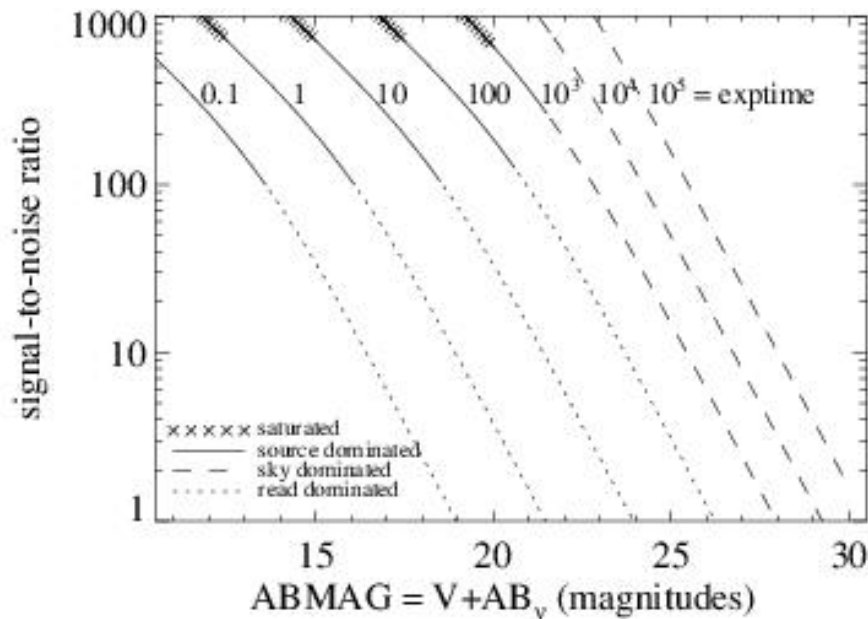


Figure A.195: Extended source S/N vs. $V+AB_V$ for the F110W filter, assuming high sky backgrounds and a source uniformly filling a 1 arcsec^2 aperture.



IR F125W

Description

Wide *J* filter.

Figure A.196: Integrated system throughput for F125W.

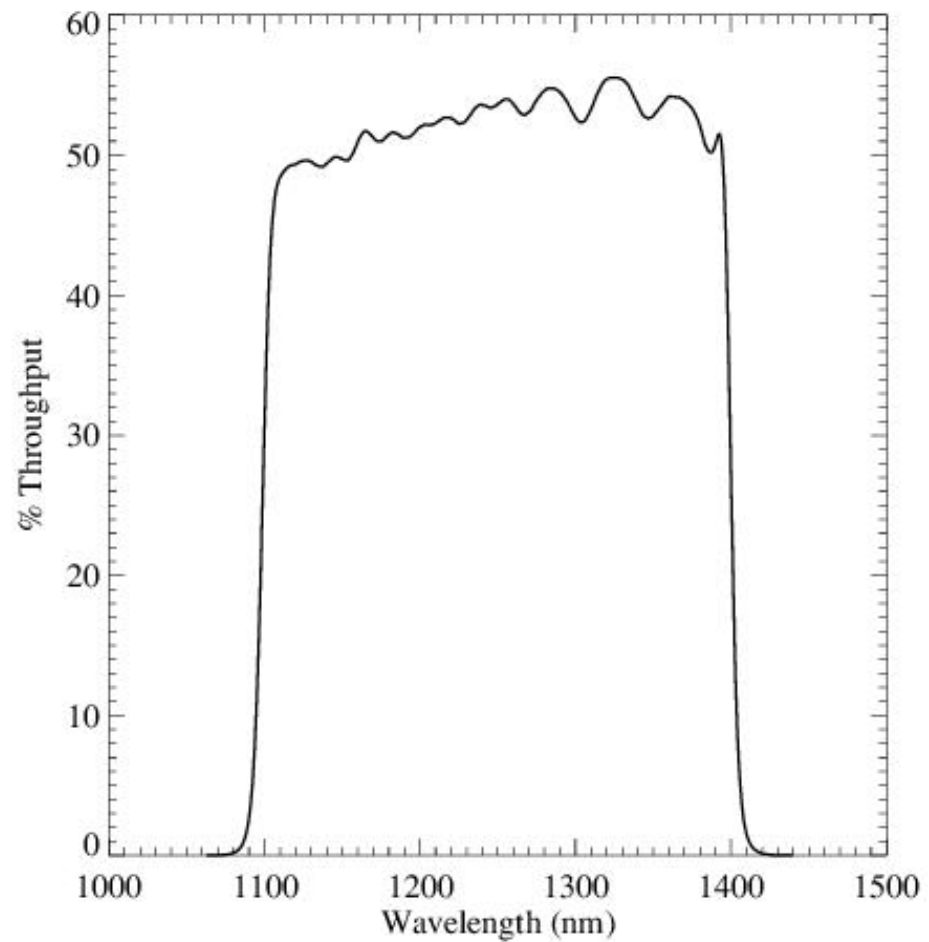


Figure A.197: Point source S/N vs. $V+AB_v$ for the F125W filter, assuming high sky backgrounds and a 3×3 pixel aperture.

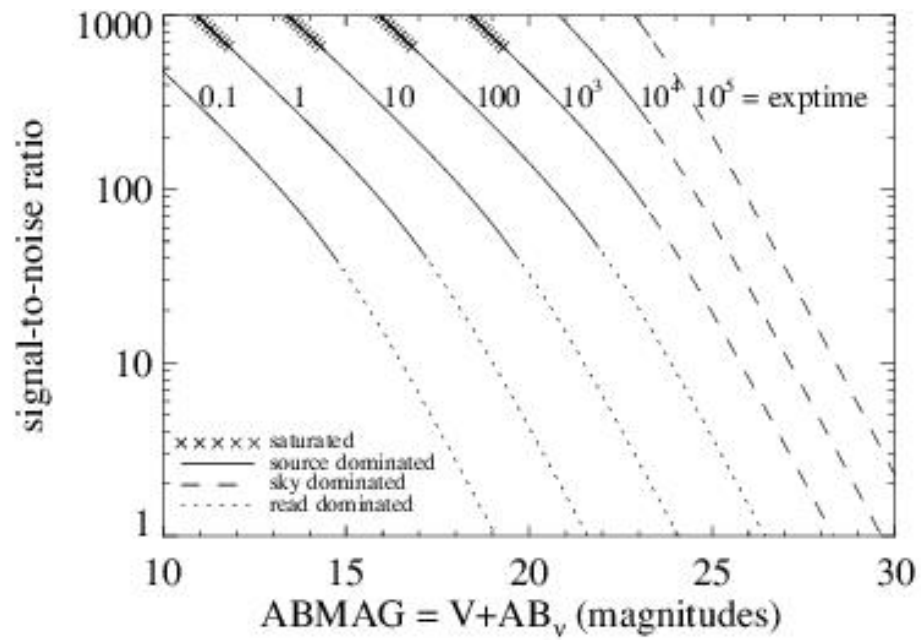
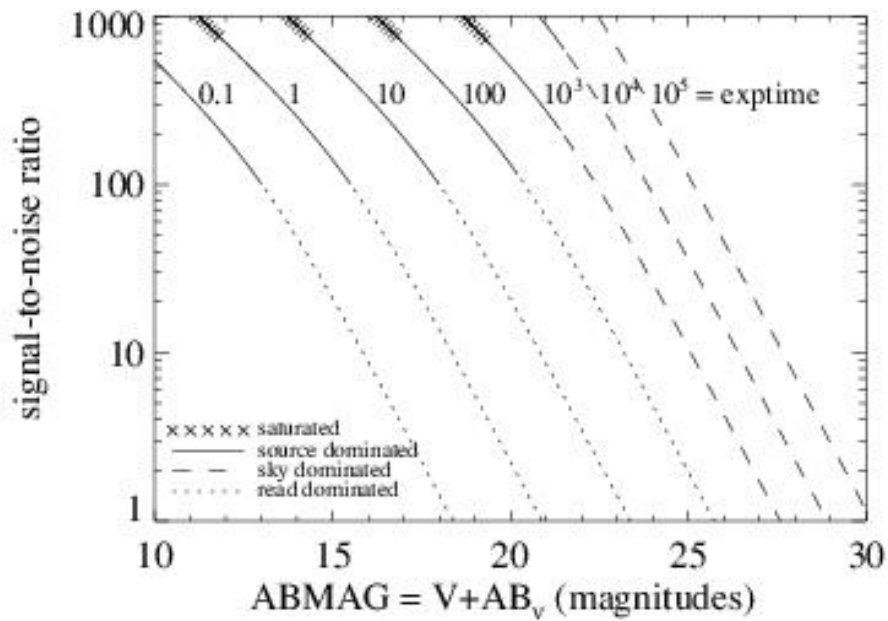


Figure A.198: Extended source S/N vs. $V+AB_V$ for the F125W filter, assuming high sky backgrounds and a source uniformly filling a 1 arcsec^2 aperture.



IR F126N

Description
[Fe II] filter.

Figure A.199: Integrated system throughput for F126N.

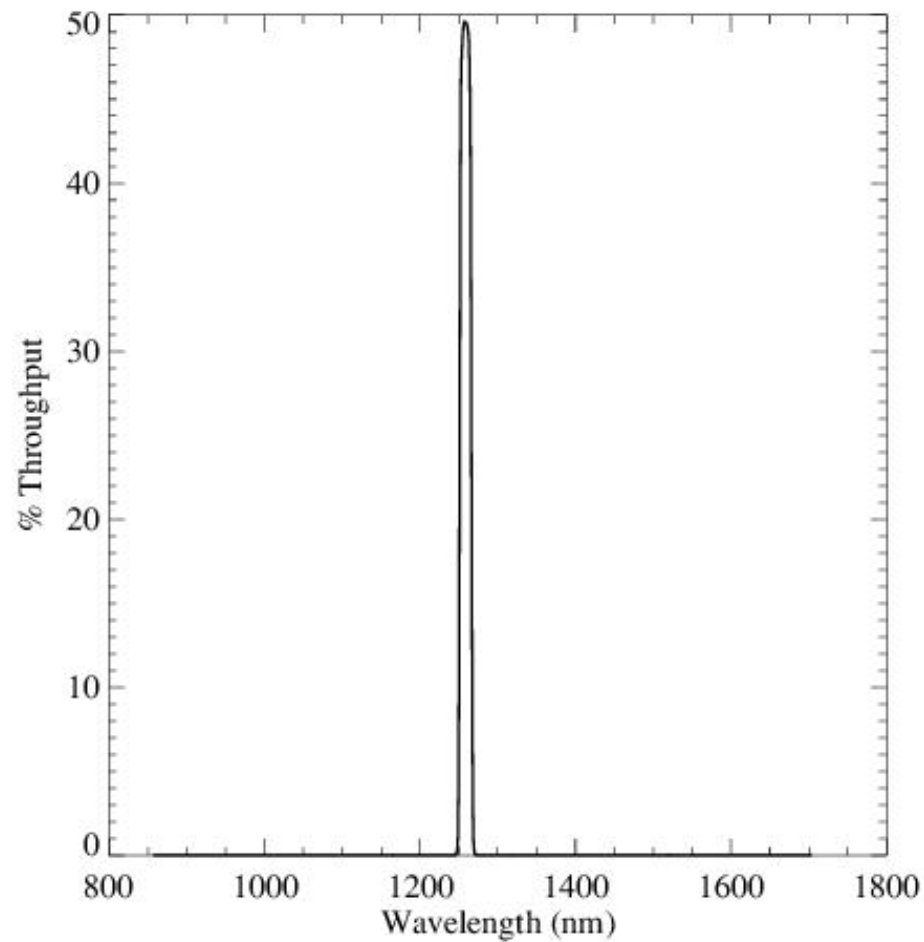


Figure A.200: Point source S/N vs. $V+AB_v$ for the F126N filter, assuming high sky backgrounds and a 3×3 pixel aperture.

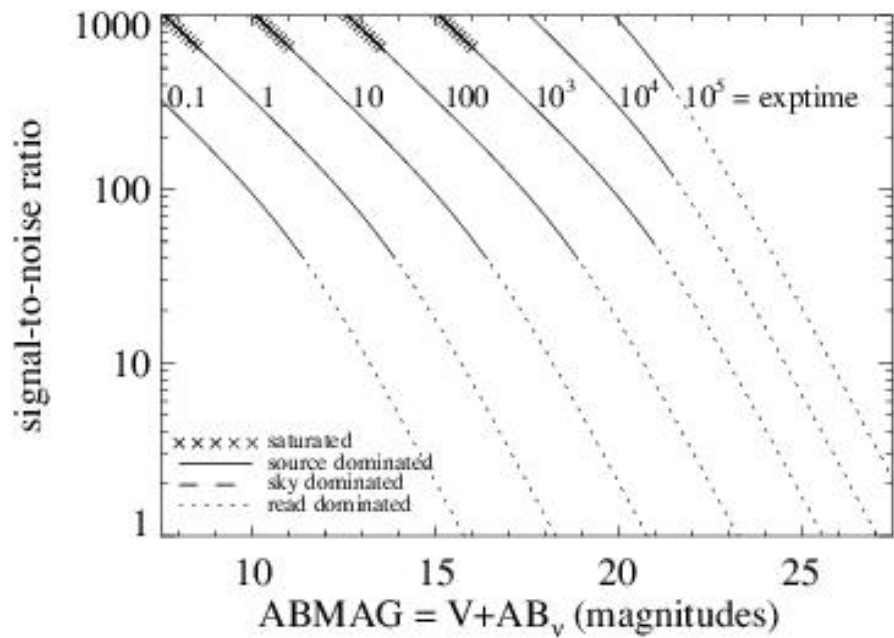
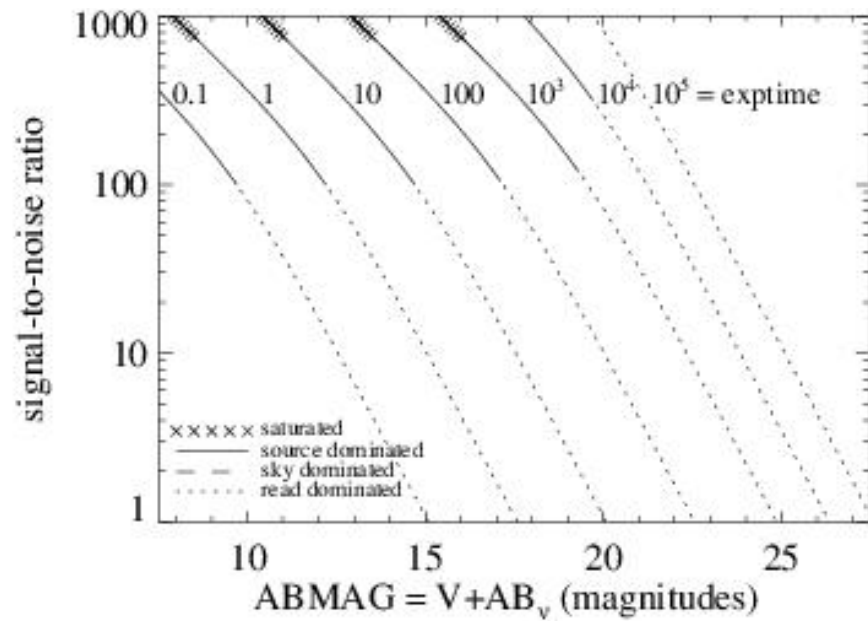


Figure A.201: Extended source S/N vs. $V+AB_v$ for the F126N filter, assuming high sky backgrounds and a source uniformly filling a 1 arcsec^2 aperture.



IR F127M

Description

H₂O/CH₄ continuum filter.

Figure A.202: Integrated system throughput for F127M.

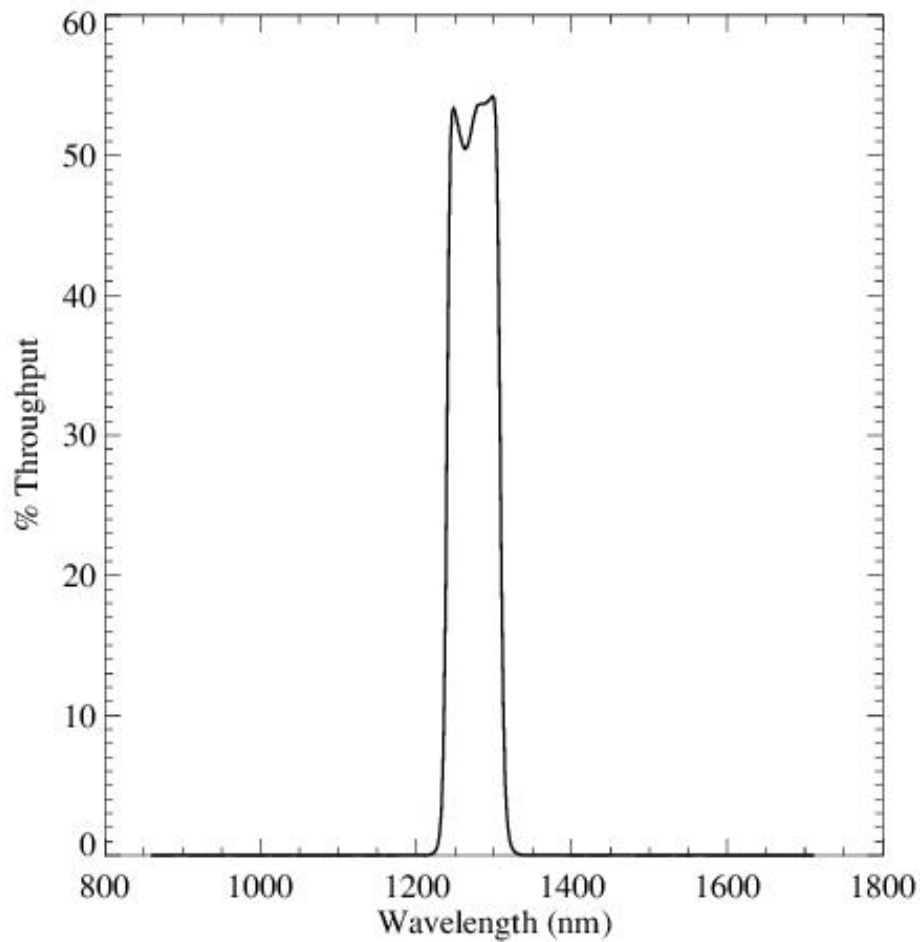


Figure A.203: Point source S/N vs. $V+AB_v$ for the F127M filter, assuming high sky backgrounds and a 3×3 pixel aperture.

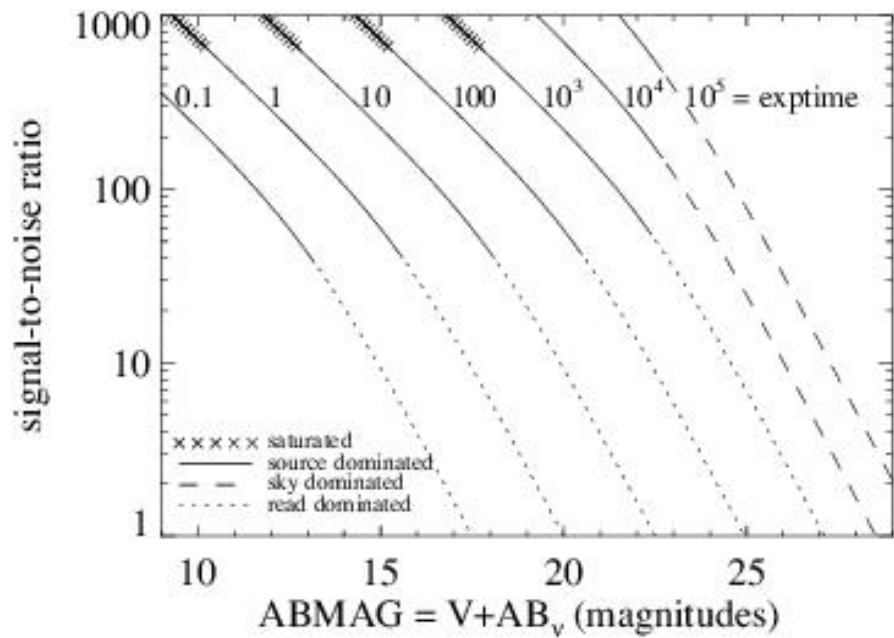
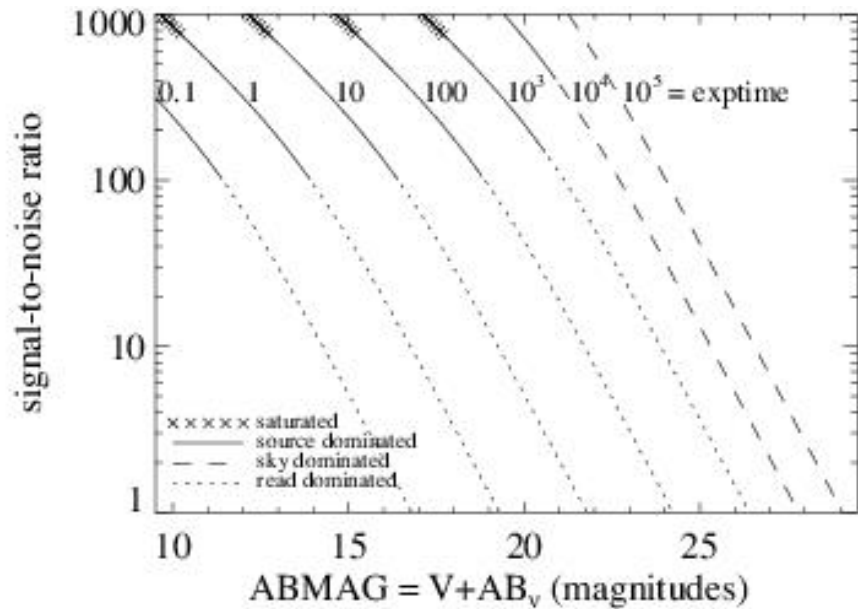


Figure A.204: Extended source S/N vs. $V+AB_v$ for the F127M filter, assuming high sky backgrounds and a source uniformly filling a 1 arcsec^2 aperture.



IR F128N

Description

Paschen β filter.

Figure A.205: Integrated system throughput for F128N.

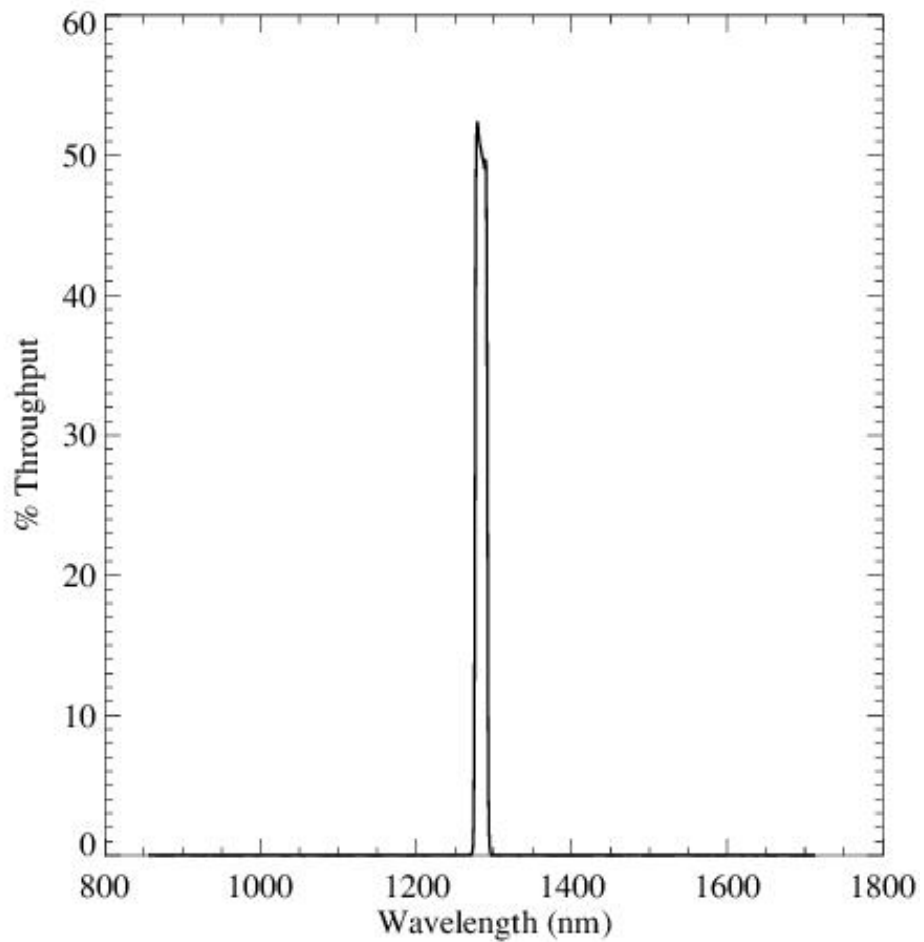


Figure A.206: Point source S/N vs. $V+AB_v$ for the F128N filter, assuming high sky backgrounds and a 3×3 pixel aperture.

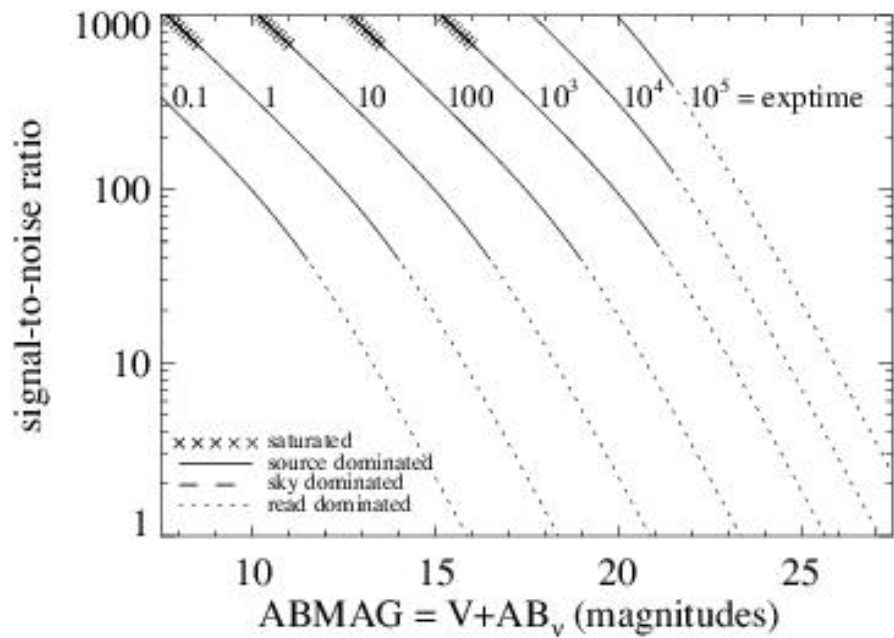
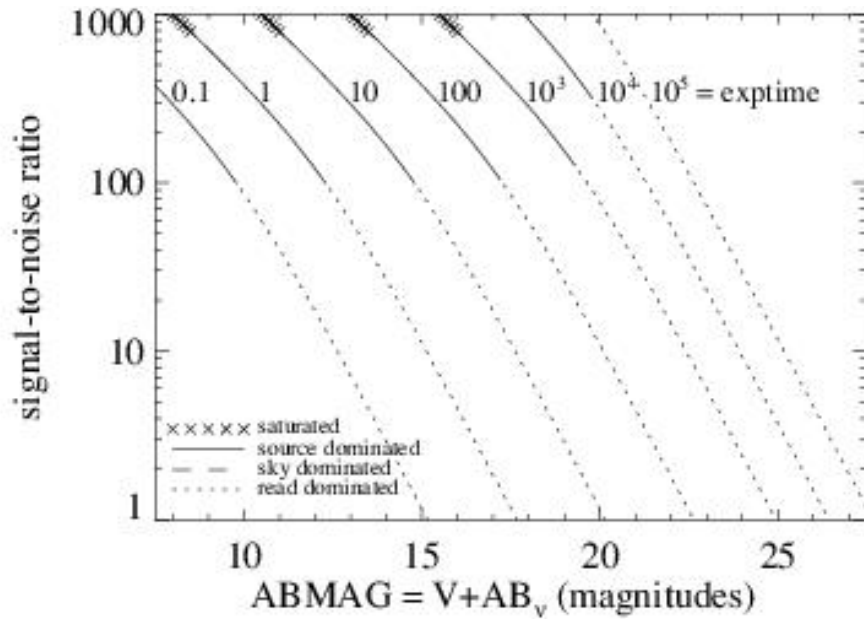


Figure A.207: Extended source S/N vs. $V+AB_v$ for the F128N filter, assuming high sky backgrounds and a source uniformly filling a 1 arcsec^2 aperture.



IR F130N

Description

Paschen β continuum filter.

Figure A.208: Integrated system throughput for F130N.

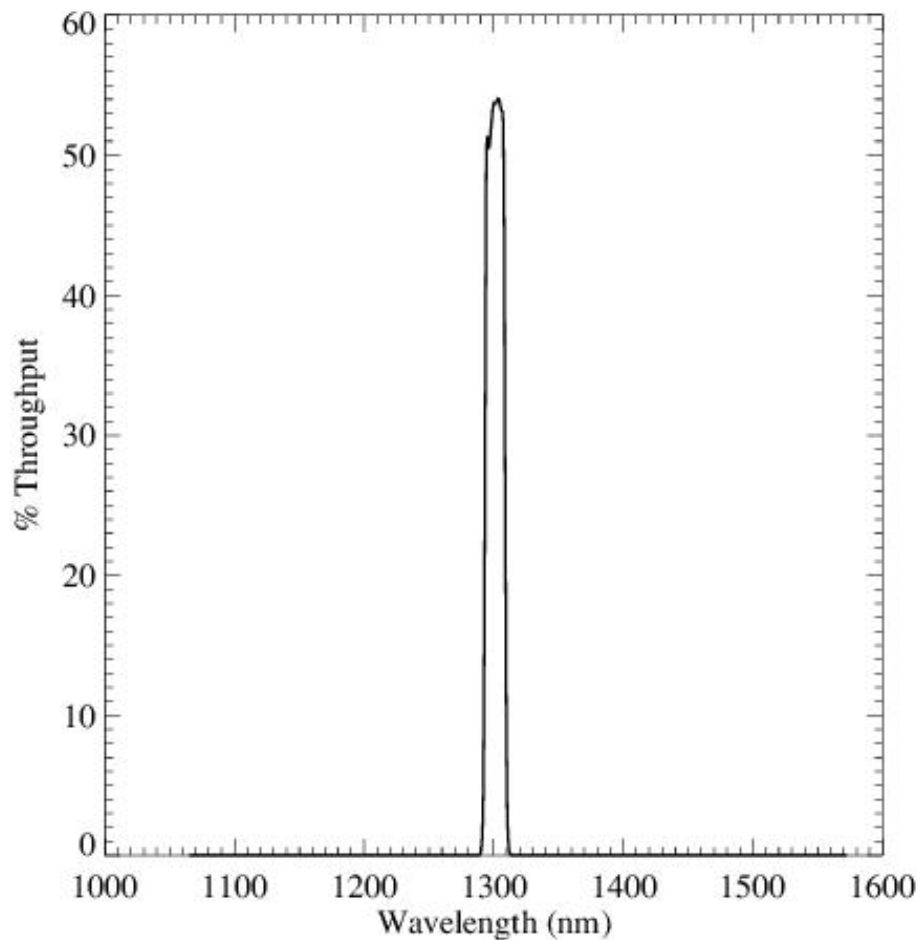


Figure A.209: Point source S/N vs. $V+AB_v$ for the F130N filter, assuming high sky backgrounds and a 3×3 pixel aperture.

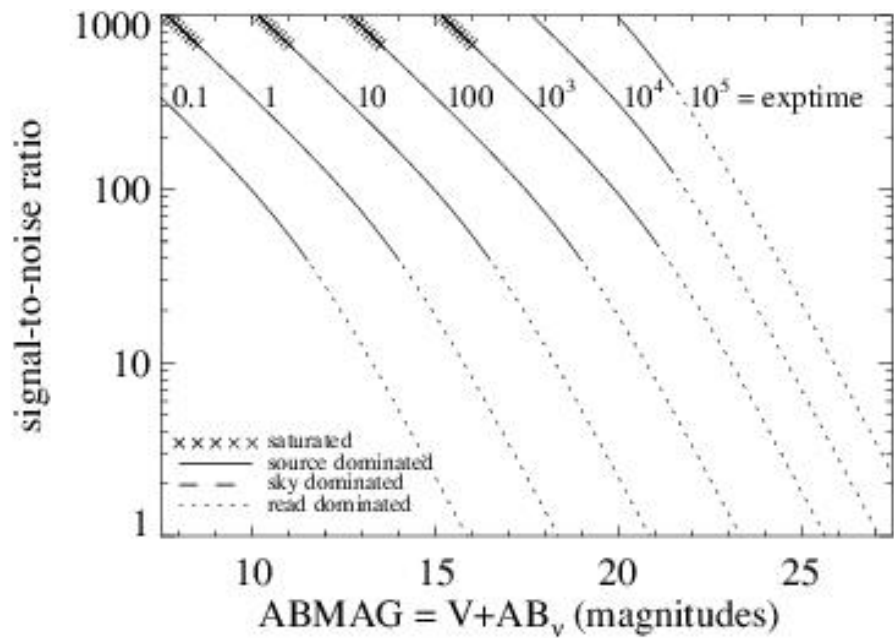
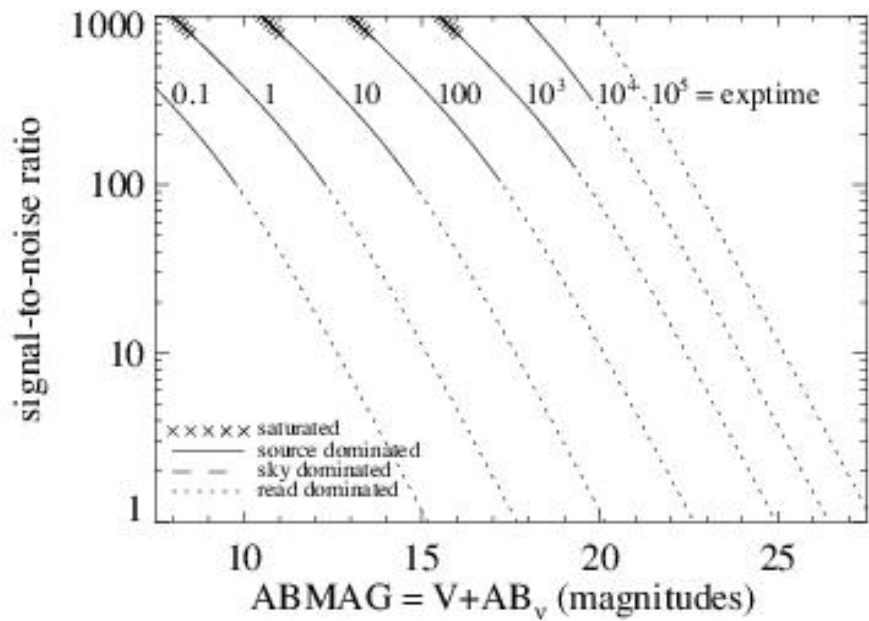


Figure A.210: Extended source S/N vs. $V+AB_v$ for the F130N filter, assuming high sky backgrounds and a source uniformly filling a 1 arcsec^2 aperture.



IR F132N

Description

Paschen β (redshifted) filter.

Figure A.211: Integrated system throughput for F132N.

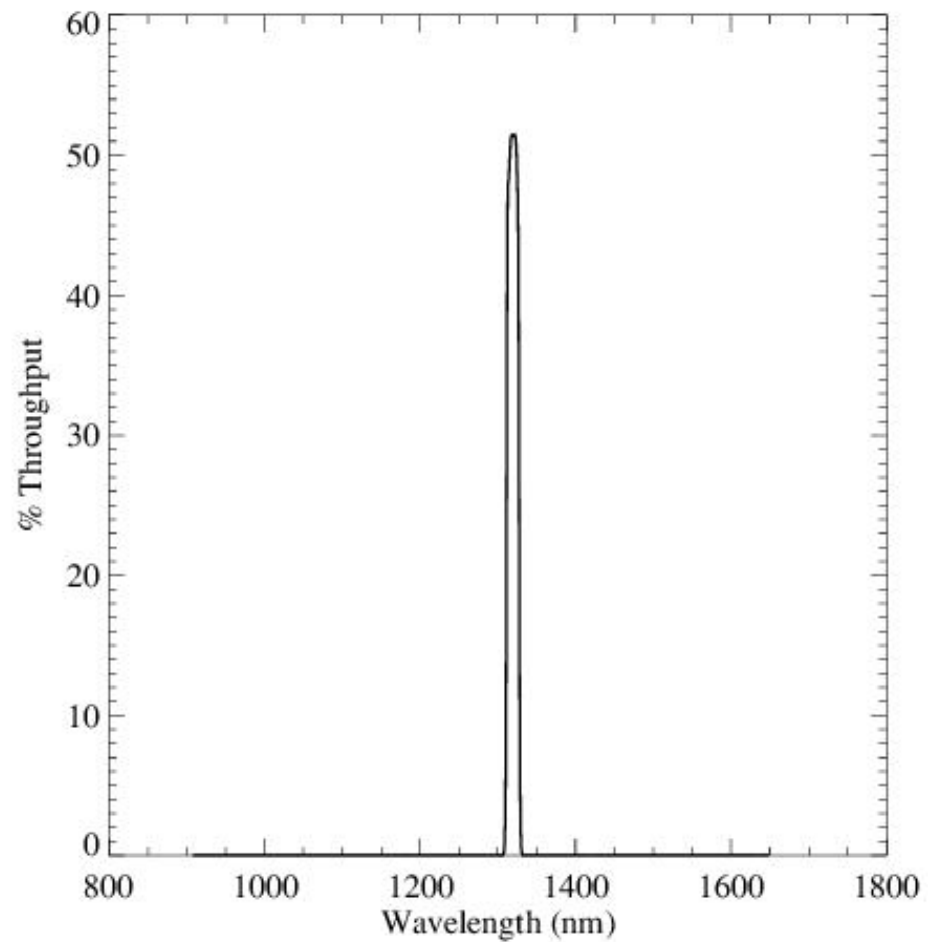


Figure A.212: Point source S/N vs. $V+AB_v$ for the F132N filter, assuming high sky backgrounds and a 3×3 pixel aperture.

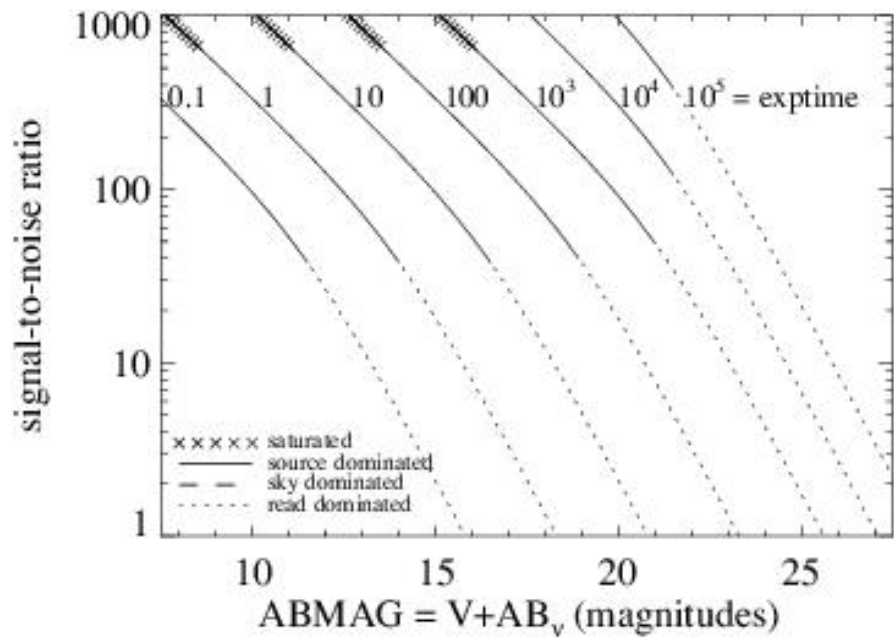
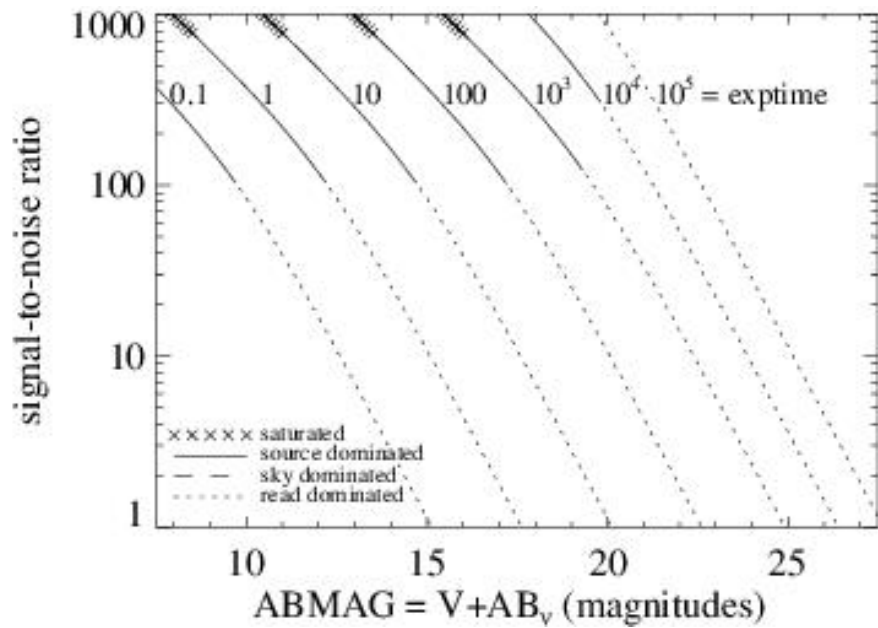


Figure A.213: Extended source S/N vs. $V+AB_V$ for the F132N filter, assuming high sky backgrounds and a source uniformly filling a 1 arcsec^2 aperture.



IR F139M

Description

$\text{H}_2\text{O}/\text{CH}_4$ line filter.

Figure A.214: Integrated system throughput for F139M.

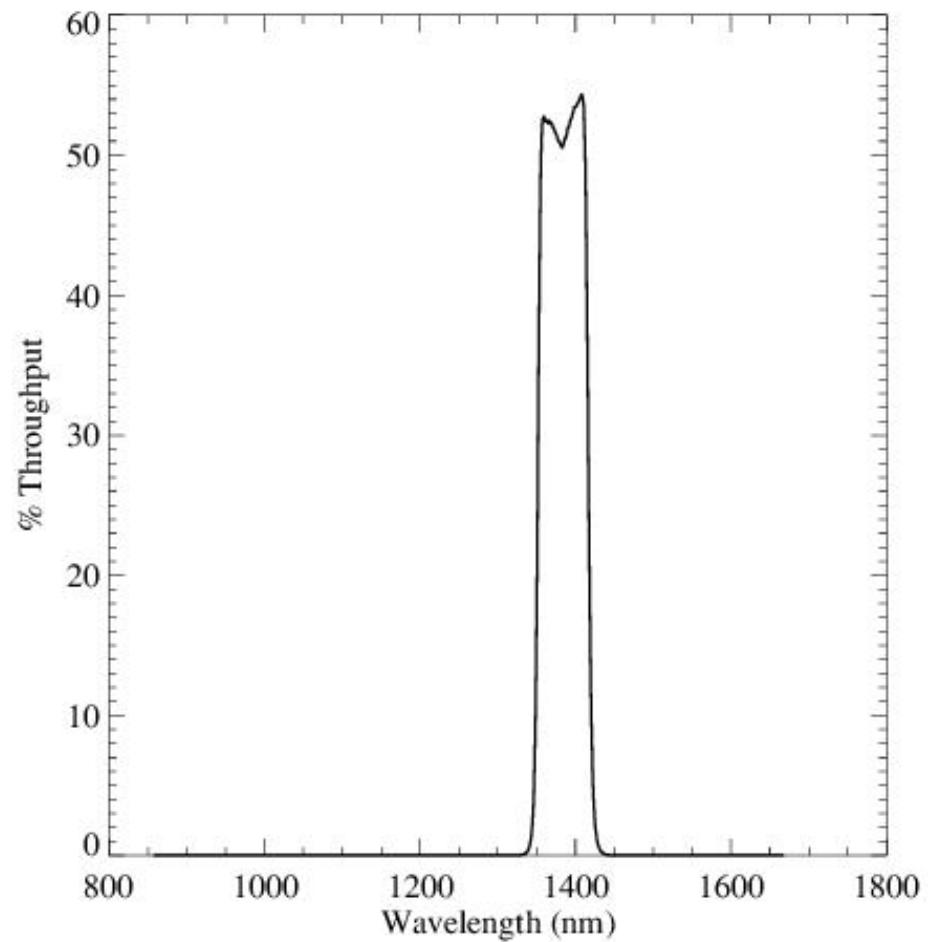


Figure A.215: Point source S/N vs. $V+AB_v$ for the F139M filter, assuming high sky backgrounds and a 3×3 pixel aperture.

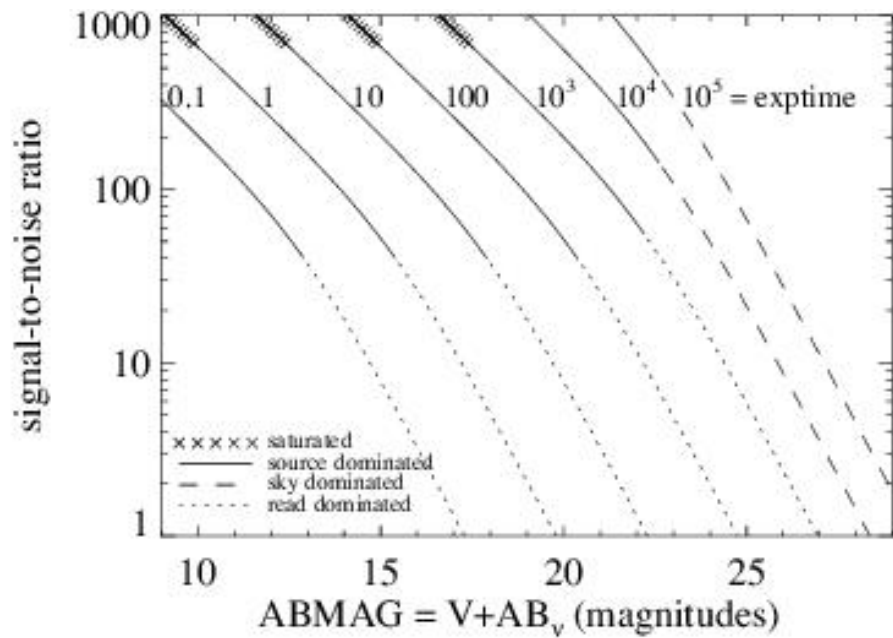
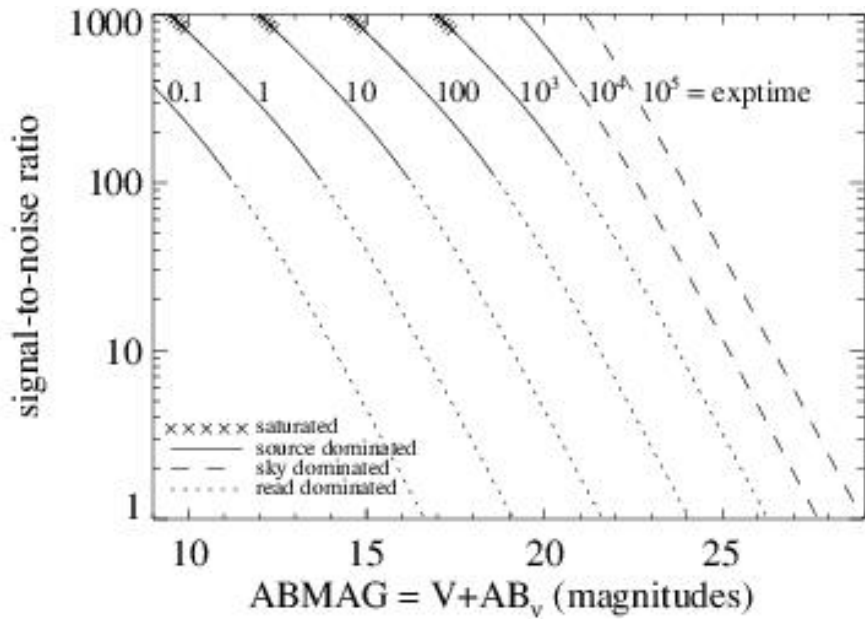


Figure A.216: Extended source S/N vs. $V+AB_v$ for the F139M filter, assuming high sky backgrounds and a source uniformly filling a 1 arcsec^2 aperture.



IR F140W

Description

Wide *JH* gap; red grism reference filter.

Figure A.217: Integrated system throughput for F140W.

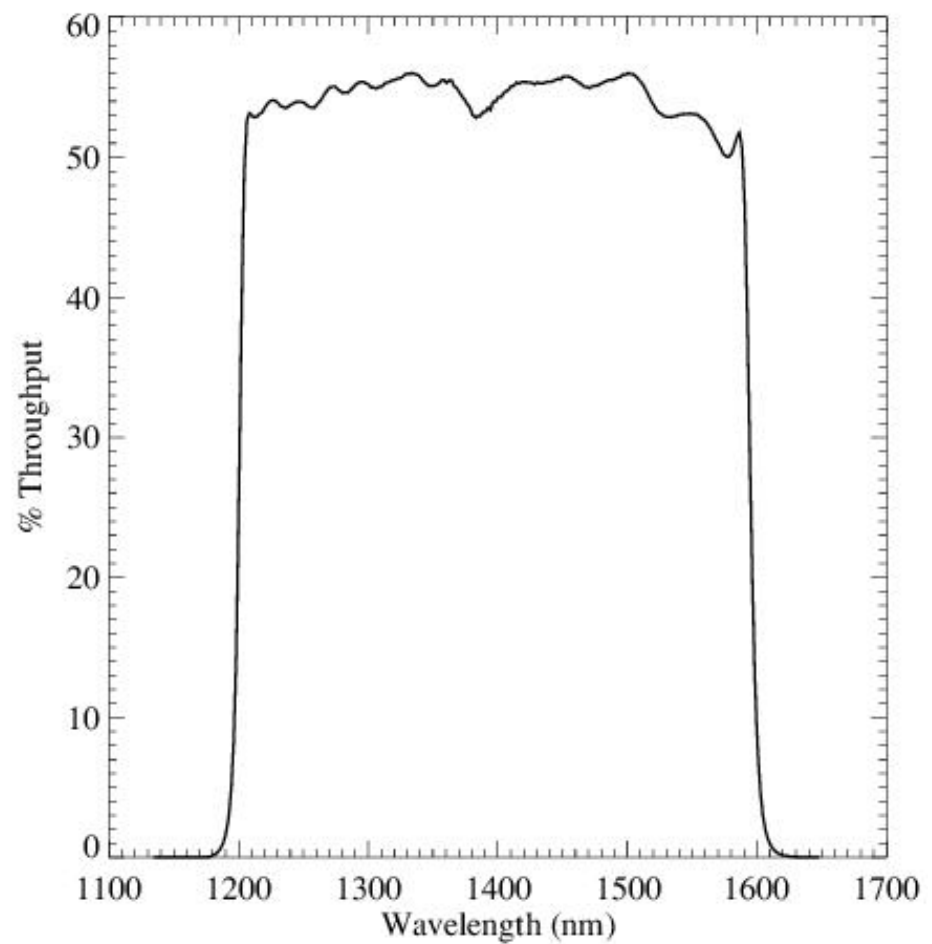


Figure A.218: Point source S/N vs. $V+AB_v$ for the F140W filter, assuming high sky backgrounds and a 3×3 pixel aperture.

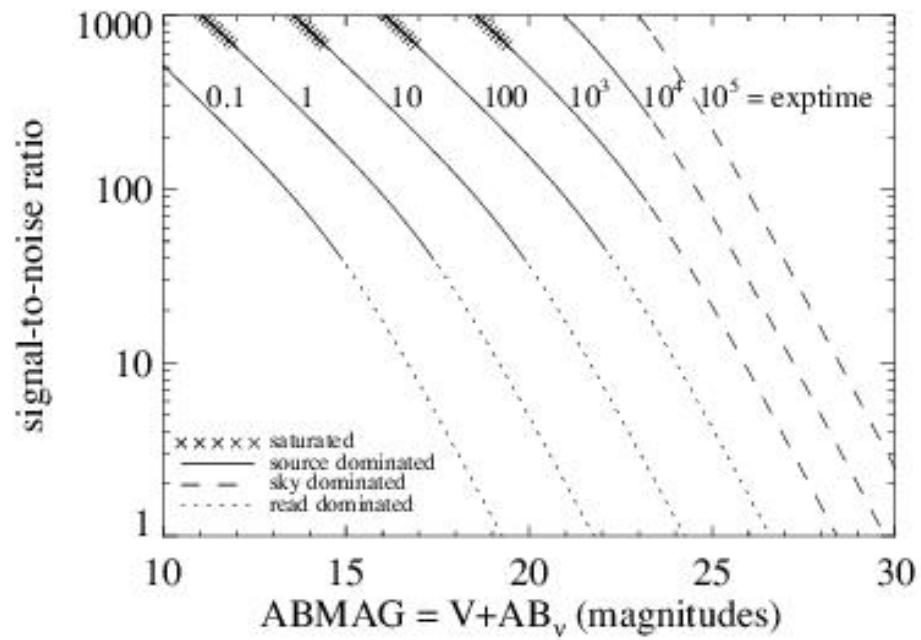
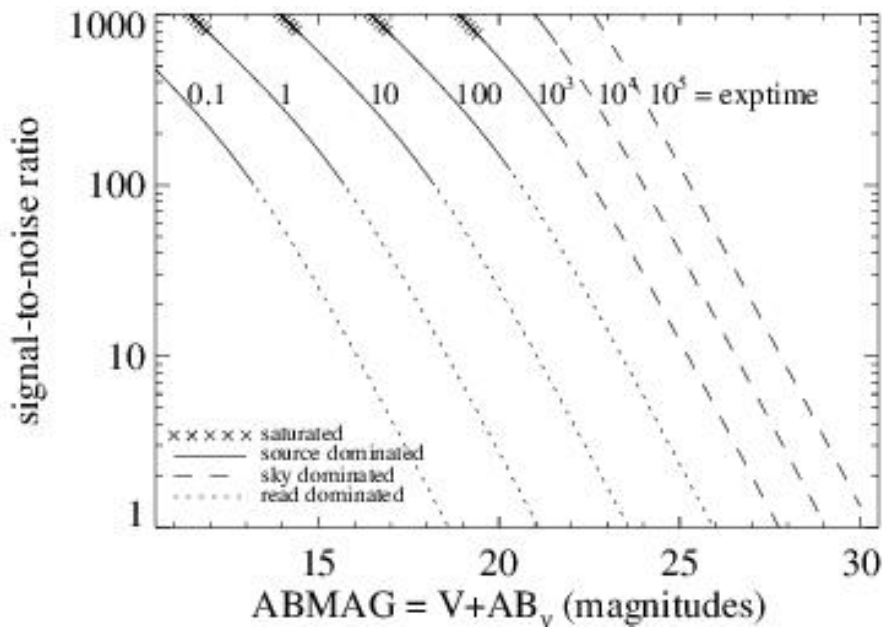


Figure A.219: Extended source S/N vs. $V+AB_v$ for the F140W filter, assuming high sky backgrounds and a source uniformly filling a 1 arcsec^2 aperture.



IR F153M

Description

H₂O and NH₃ filter.

Figure A.220: Integrated system throughput for F153M.

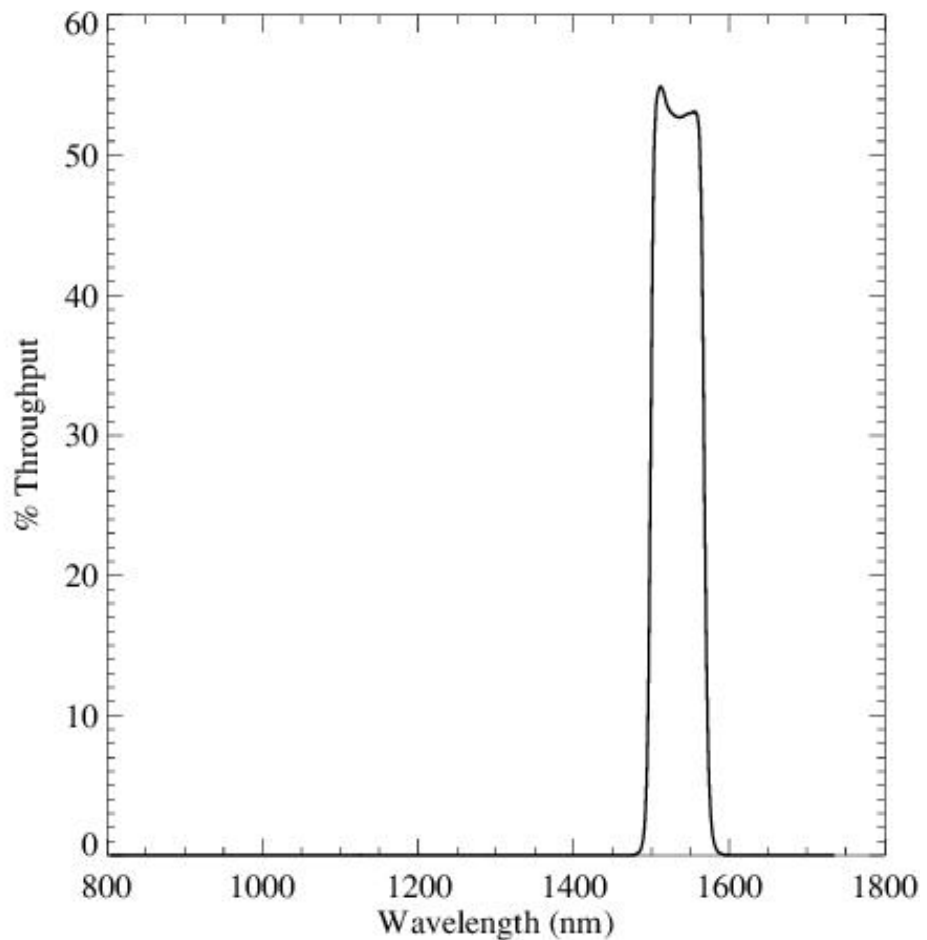


Figure A.221: Point source S/N vs. $V+AB_v$ for the F153M filter, assuming high sky backgrounds and a 3×3 pixel aperture.

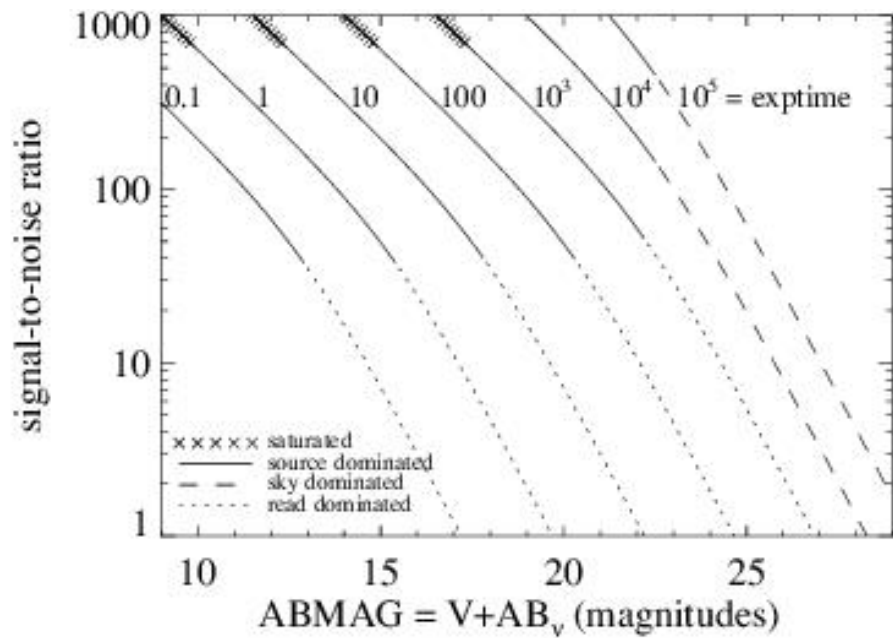
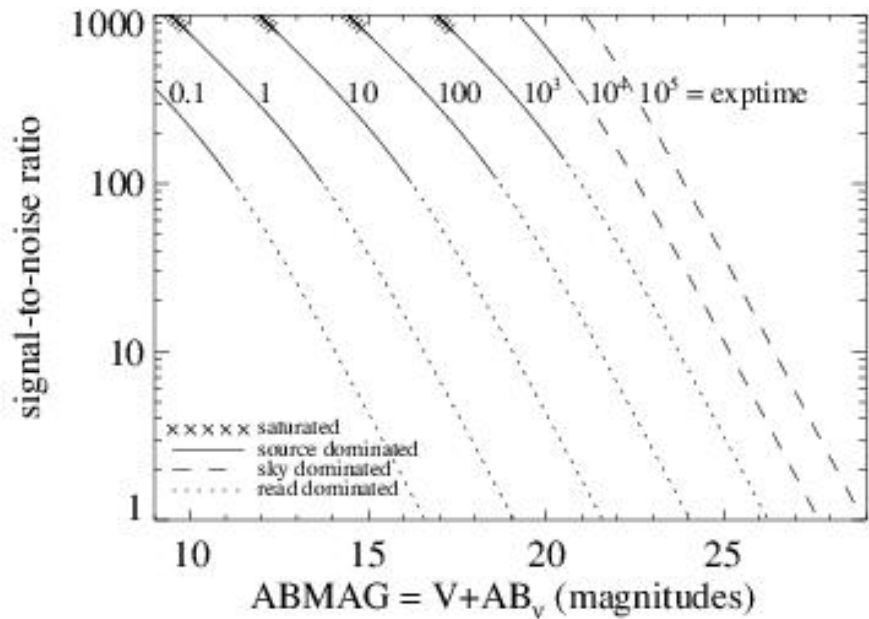


Figure A.222: Extended source S/N vs. $V+AB_v$ for the F153M filter, assuming high sky backgrounds and a source uniformly filling a 1 arcsec² aperture.



IR F160W

Description
WFC3 *H* filter.

Figure A.223: Integrated system throughput for F160W.

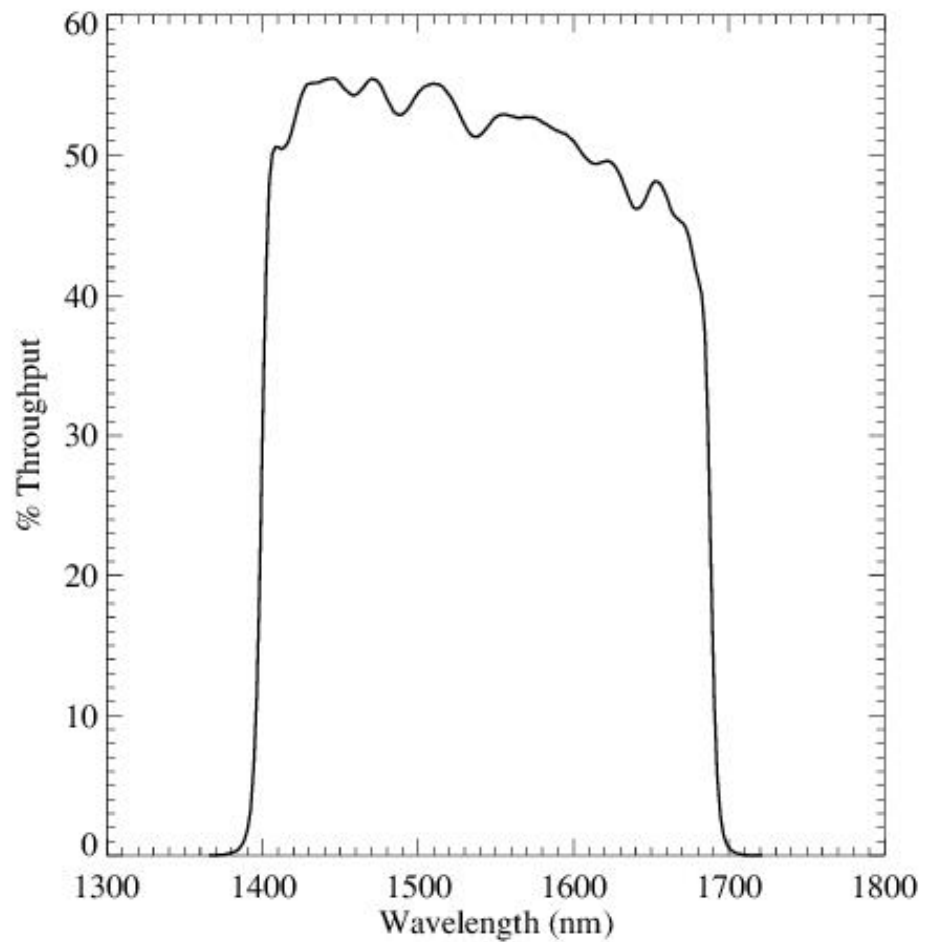


Figure A.224: Point source S/N vs. $V+AB_v$ for the F160W filter, assuming high sky backgrounds and a 3×3 pixel aperture.

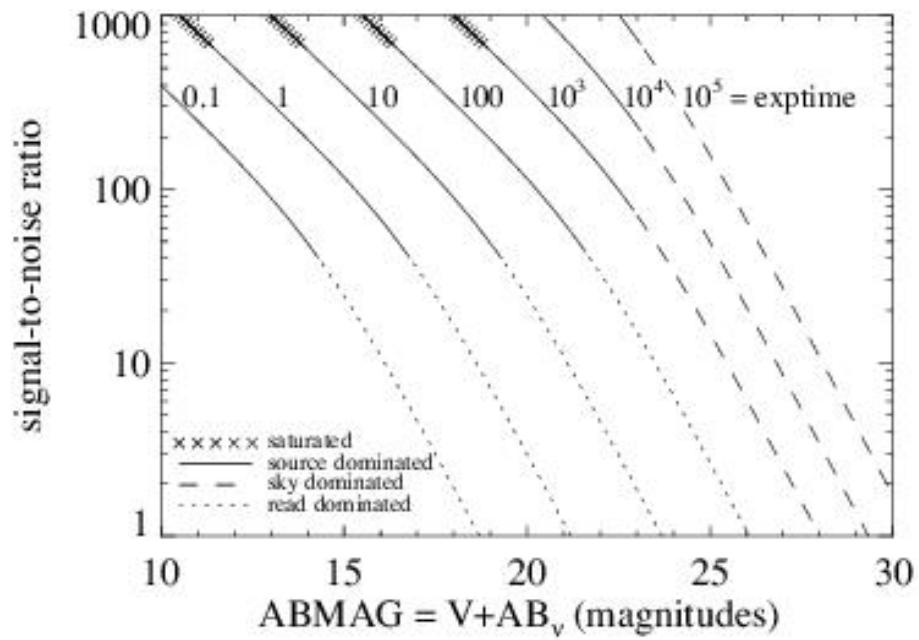
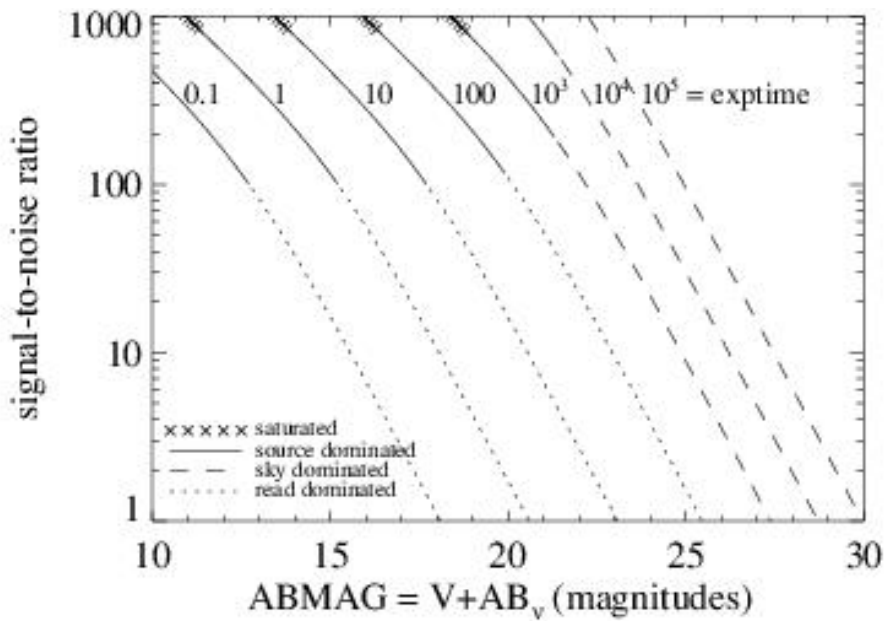


Figure A.225: Extended source S/N vs. $V+AB_v$ for the F160W filter, assuming high sky backgrounds and a source uniformly filling a 1 arcsec^2 aperture.



IR F164N

Description
[Fe II] filter.

Figure A.226: Integrated system throughput for F164N.

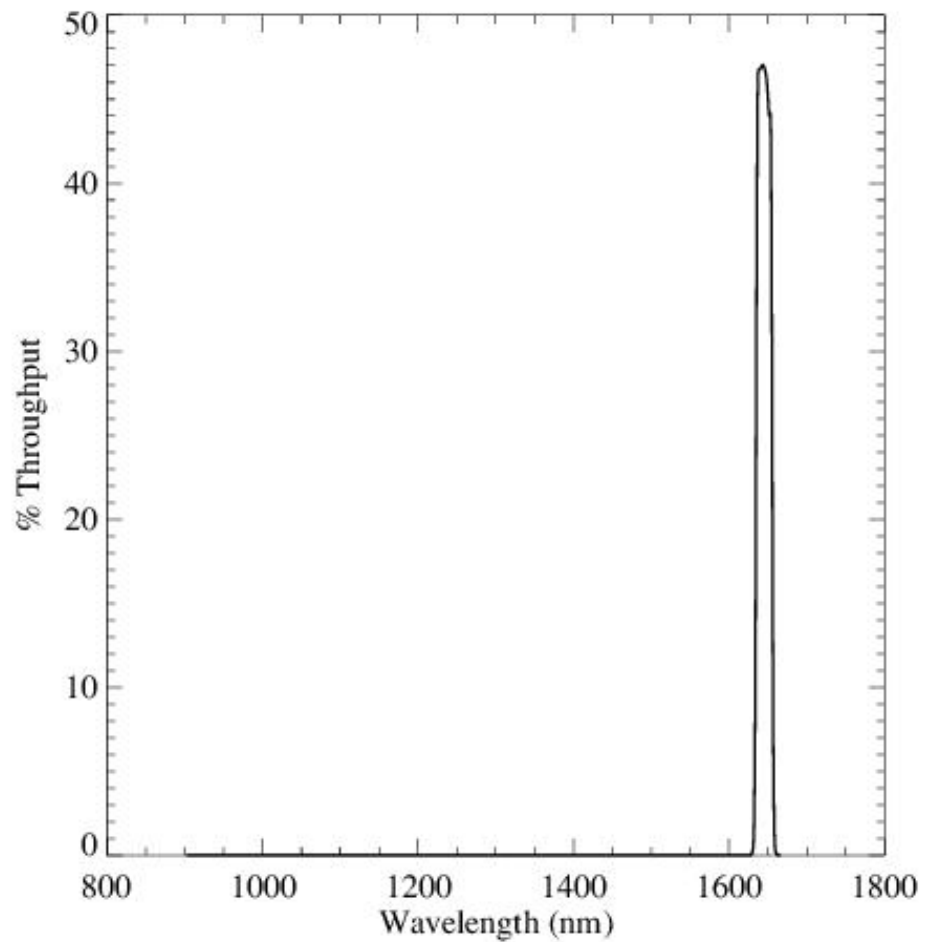


Figure A.227: Point source S/N vs. $V+AB_v$ for the F164N filter, assuming high sky backgrounds and a 3×3 pixel aperture.

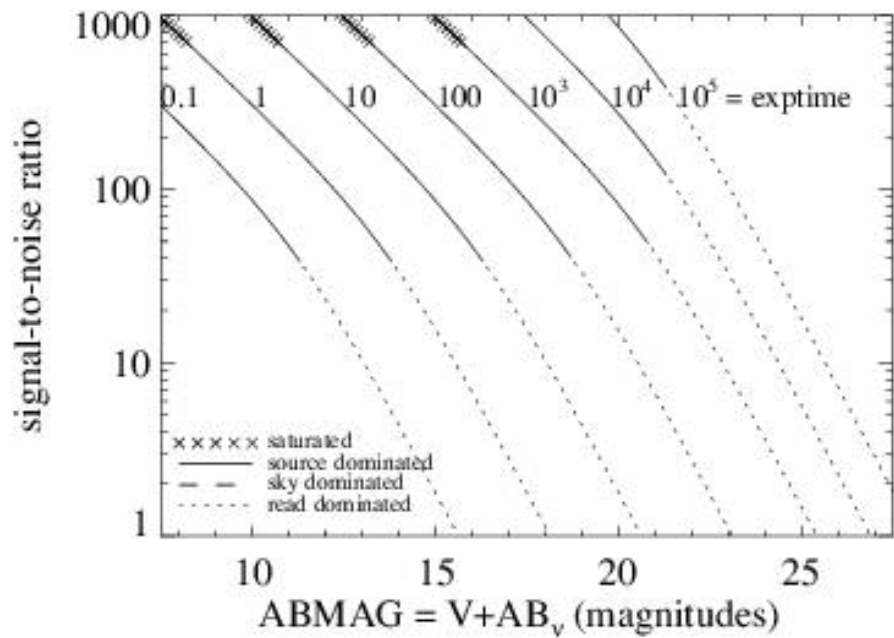
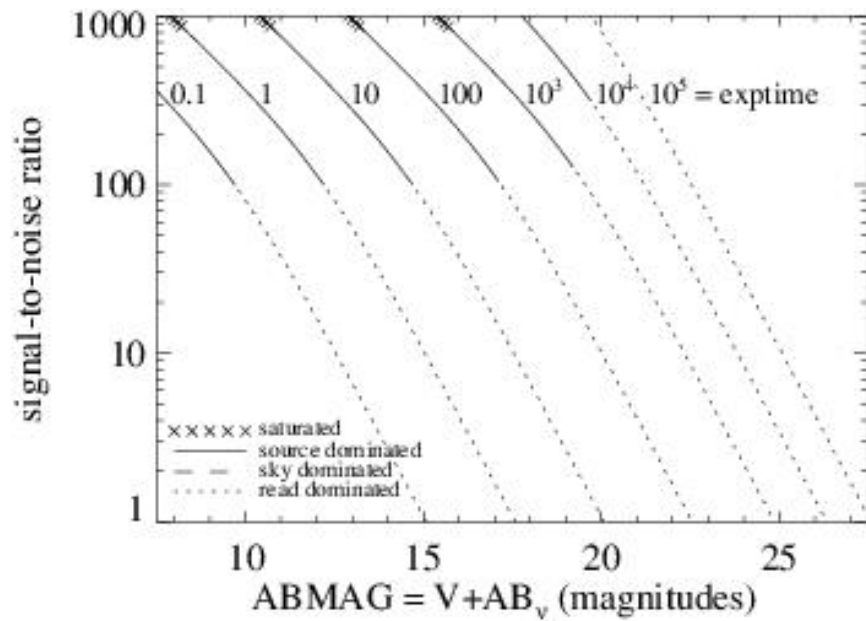


Figure A.228: Extended source S/N vs. $V+AB_v$ for the F164N filter, assuming high sky backgrounds and a source uniformly filling a 1 arcsec^2 aperture.



IR F167N

Description

[Fe II] continuum filter.

Figure A.229: Integrated system throughput for F167N.

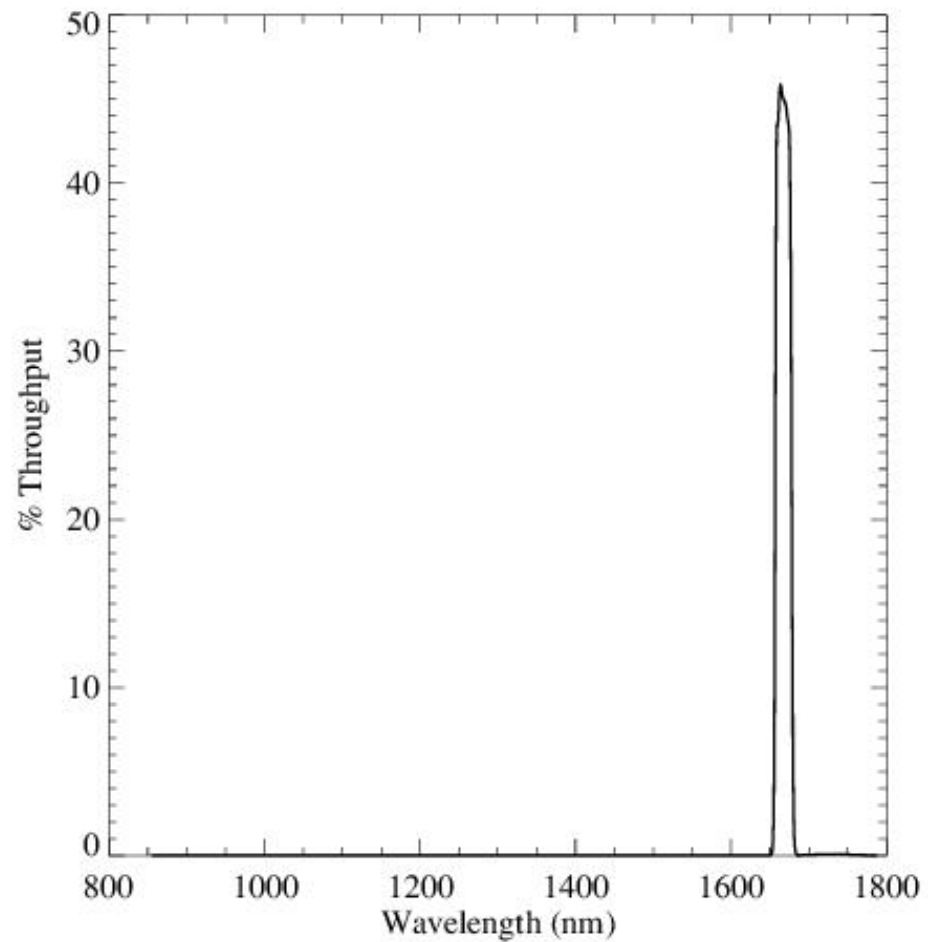


Figure A.230: Point source S/N vs. $V+AB_v$ for the F167N filter, assuming high sky backgrounds and a 3×3 pixel aperture.

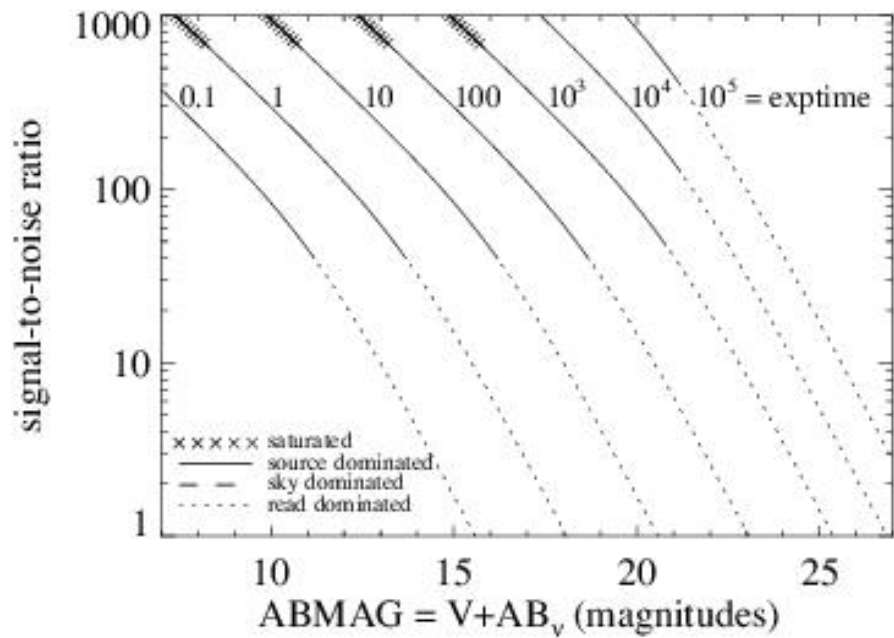


Figure A.231: Extended source S/N vs. $V+AB_V$ for the F167N filter, assuming high sky backgrounds and a source uniformly filling a 1 arcsec^2 aperture.

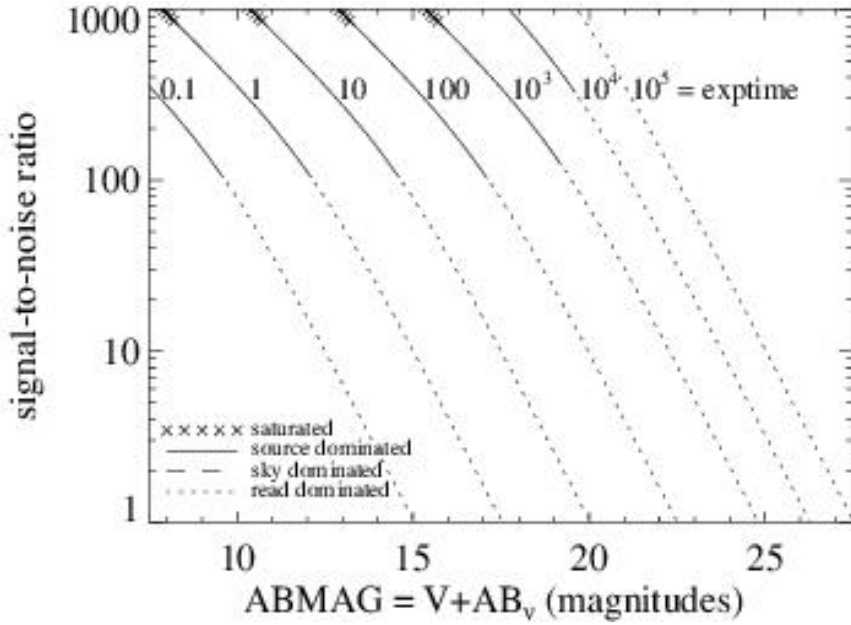


Table A.1: Color corrections AB_V to go from Johnson V magnitude to AB magnitude for WFC3 as a function of stellar effective temperature.

				T_{eff}				
Mode	2500K	5000K	7500K	10000K	15000K	20000K	30000K	50000K
UVIS/F200LP	-2.22	0.45	0.48	0.40	0.08	-0.12	-0.40	-0.57
UVIS/F218W	7.21	7.82	2.95	1.51	0.09	-0.53	-1.22	-1.55
UVIS/F225W	6.07	7.22	2.84	1.51	0.12	-0.49	-1.15	-1.46
UVIS/F275W	7.30	5.30	2.27	1.35	0.10	-0.42	-0.96	-1.24
UVIS/F280N	3.29	4.49	2.50	1.44	0.13	-0.40	-0.90	-1.17
UVIS/F300X	5.96	4.05	1.98	1.26	0.10	-0.39	-0.91	-1.19
UVIS/F336W	4.98	2.71	1.31	1.00	0.10	-0.26	-0.64	-0.86
UVIS/F343N	4.74	2.62	1.24	0.97	0.11	-0.24	-0.60	-0.82
UVIS/F350LP	-2.64	0.07	0.18	0.18	0.09	0.04	-0.02	-0.07

UVIS/F373N	7.03	2.53	1.10	0.94	0.21	-0.09	-0.43	-0.65
UVIS/F390M	4.25	2.08	0.67	0.25	-0.20	-0.33	-0.48	-0.60
UVIS/F390W	3.80	1.63	0.59	0.26	-0.14	-0.29	-0.47	-0.60
UVIS/F395N	3.91	1.92	0.67	0.15	-0.27	-0.37	-0.49	-0.58
UVIS/F410M	2.96	1.16	0.29	-0.10	-0.32	-0.39	-0.46	-0.52
UVIS/F438W	2.28	0.86	0.18	-0.12	-0.28	-0.33	-0.39	-0.43
UVIS/F467M	1.74	0.34	0.02	-0.15	-0.22	-0.24	-0.26	-0.27
UVIS/F469N	1.64	0.33	0.03	-0.14	-0.21	-0.24	-0.26	-0.26
UVIS/F475W	1.23	0.44	0.09	-0.07	-0.17	-0.20	-0.24	-0.26
UVIS/F475X	0.61	0.35	0.12	-0.01	-0.12	-0.15	-0.19	-0.23
UVIS/F487N	1.47	0.29	0.20	0.28	0.06	-0.02	-0.11	-0.17
UVIS/F502N	2.32	0.32	0.02	-0.07	-0.11	-0.12	-0.14	-0.15
UVIS/FQ508N	1.07	0.32	0.01	-0.06	-0.08	-0.10	-0.11	-0.12
UVIS/F547M	0.08	0.03	0.02	0.01	0.01	0.01	0.01	0.02
UVIS/F555W	0.15	0.09	0.03	-0.01	-0.03	-0.04	-0.05	-0.06
UVIS/F600LP	-3.71	-0.42	0.09	0.34	0.47	0.52	0.57	0.60
UVIS/F606W	-0.83	-0.11	0.04	0.10	0.12	0.12	0.13	0.13
UVIS/F621M	-1.23	-0.26	0.03	0.16	0.22	0.25	0.27	0.28
UVIS/F625W	-1.17	-0.25	0.04	0.16	0.22	0.24	0.26	0.27
UVIS/F631N	-0.33	-0.28	0.03	0.17	0.24	0.27	0.30	0.31
UVIS/F645N	-2.20	-0.29	0.04	0.20	0.28	0.31	0.35	0.35
UVIS/F656N	-1.99	-0.26	0.36	0.63	0.56	0.54	0.52	0.45
UVIS/F657N	-2.31	-0.31	0.14	0.37	0.39	0.41	0.42	0.41
UVIS/F658N	-2.04	-0.31	0.18	0.42	0.42	0.43	0.44	0.41
UVIS/F665N	-1.30	-0.35	0.06	0.26	0.34	0.38	0.42	0.42
UVIS/F673N	-0.69	-0.37	0.04	0.24	0.35	0.39	0.44	0.45
UVIS/F680N	-1.61	-0.38	0.05	0.26	0.38	0.42	0.47	0.48
UVIS/F689M	-1.69	-0.37	0.06	0.28	0.39	0.43	0.47	0.48
UVIS/F763M	-3.09	-0.45	0.09	0.37	0.53	0.59	0.65	0.69

UVIS/F775W	-3.60	-0.45	0.09	0.38	0.54	0.59	0.65	0.70
UVIS/F814W	-4.14	-0.48	0.12	0.43	0.60	0.67	0.74	0.79
UVIS/F845M	-4.56	-0.51	0.16	0.51	0.70	0.77	0.84	0.91
UVIS/F850LP	-5.03	-0.56	0.21	0.56	0.79	0.89	0.98	1.06
UVIS/F953N	-5.52	-0.59	0.27	0.68	0.91	1.00	1.10	1.16
UVIS/FQ232N	2.15	4.54	2.68	1.53	0.20	-0.43	-1.12	-1.46
UVIS/FQ243N	2.84	5.10	2.76	1.52	0.18	-0.44	-1.11	-1.40
UVIS/FQ378N	4.90	2.32	0.86	0.61	0.01	-0.20	-0.44	-0.62
UVIS/FQ387N	6.34	2.42	0.61	0.25	-0.21	-0.34	-0.49	-0.61
UVIS/FQ422M	5.05	1.17	0.18	-0.22	-0.36	-0.41	-0.46	-0.48
UVIS/FQ436N	2.64	0.84	0.23	0.08	-0.16	-0.24	-0.31	-0.39
UVIS/FQ437N	2.59	0.83	0.18	0.00	-0.21	-0.28	-0.34	-0.40
UVIS/FQ492N	0.91	0.27	0.04	-0.02	-0.10	-0.13	-0.16	-0.17
UVIS/FQ575N	-0.58	-0.18	0.01	0.07	0.10	0.11	0.13	0.13
UVIS/FQ619N	0.72	-0.25	0.03	0.15	0.22	0.24	0.27	0.27
UVIS/FQ634N	-0.96	-0.28	0.03	0.18	0.26	0.29	0.32	0.32
UVIS/FQ672N	-0.77	-0.35	0.04	0.23	0.34	0.38	0.42	0.44
UVIS/FQ674N	-0.39	-0.37	0.04	0.24	0.35	0.39	0.43	0.44
UVIS/FQ727N	-2.81	-0.41	0.07	0.32	0.46	0.52	0.57	0.60
UVIS/FQ750N	-3.06	-0.44	0.08	0.36	0.51	0.57	0.63	0.66
UVIS/FQ889N	-4.98	-0.55	0.20	0.57	0.78	0.86	0.95	1.01
UVIS/FQ906N	-5.15	-0.56	0.21	0.57	0.79	0.88	0.98	1.05
UVIS/FQ924N	-4.89	-0.57	0.26	0.66	0.87	0.95	1.04	1.10
UVIS/FQ937N	-5.19	-0.58	0.19	0.48	0.77	0.89	1.01	1.11
IR/F098M	-5.40	-0.60	0.25	0.60	0.88	1.00	1.12	1.21
IR/F105W	-5.68	-0.62	0.31	0.69	0.98	1.11	1.24	1.34
IR/F110W	-5.77	-0.64	0.39	0.80	1.12	1.25	1.39	1.49
IR/F125W	-5.91	-0.67	0.48	0.94	1.28	1.43	1.58	1.69
IR/F126N	-5.99	-0.67	0.49	0.96	1.31	1.46	1.61	1.72

IR/F127M	-6.04	-0.67	0.52	1.01	1.35	1.49	1.65	1.75
IR/F128N	-6.08	-0.67	0.59	1.11	1.41	1.55	1.69	1.78
IR/F130N	-6.13	-0.68	0.53	1.02	1.37	1.52	1.68	1.79
IR/F132N	-6.04	-0.67	0.54	1.03	1.39	1.55	1.71	1.82
IR/F139M	-5.64	-0.69	0.60	1.11	1.49	1.64	1.81	1.92
IR/F140W	-5.89	-0.69	0.61	1.12	1.49	1.64	1.80	1.92
IR/F153M	-6.03	-0.71	0.73	1.29	1.69	1.85	2.02	2.14
IR/F160W	-6.05	-0.70	0.74	1.30	1.69	1.85	2.02	2.15
IR/F164N	-6.39	-0.70	0.84	1.42	1.82	1.99	2.16	2.28
IR/F167N	-6.32	-0.69	0.84	1.41	1.83	2.00	2.18	2.31

Table A.2: Color corrections AB_V to go from Johnson V magnitude to AB magnitude for WFC3 as a function of age in an instantaneous burst population.

Mode	Age				
	10 Gyr	1 Gyr	100 Myr	10 Myr	1 Myr
UVIS/F200LP	0.38	0.48	0.29	0.02	-0.48
UVIS/F218W	6.11	3.89	1.06	0.15	-1.22
UVIS/F225W	5.83	3.76	1.03	0.16	-1.15
UVIS/F275W	4.75	3.14	0.93	0.19	-0.97
UVIS/F280N	4.32	3.03	0.89	0.21	-0.92
UVIS/F300X	3.95	2.80	0.89	0.20	-0.94
UVIS/F336W	2.69	1.98	0.77	0.27	-0.67
UVIS/F343N	2.55	1.89	0.76	0.28	-0.63
UVIS/F350LP	-0.09	0.04	0.06	-0.06	-0.04
UVIS/F373N	2.28	1.57	0.66	0.34	-0.49
UVIS/F390M	2.03	1.12	0.22	0.14	-0.50
UVIS/F390W	1.63	1.00	0.27	0.15	-0.50

UVIS/F395N	1.88	1.03	0.14	0.11	-0.49
UVIS/F410M	1.23	0.64	0.02	0.02	-0.47
UVIS/F438W	0.90	0.48	0.01	0.02	-0.39
UVIS/F467M	0.44	0.22	-0.03	-0.01	-0.26
UVIS/F469N	0.46	0.23	-0.02	-0.01	-0.25
UVIS/F475W	0.48	0.27	0.02	0.04	-0.23
UVIS/F475X	0.38	0.24	0.03	0.03	-0.20
UVIS/F487N	0.36	0.27	0.12	0.10	-0.14
UVIS/F502N	0.33	0.17	0.02	0.08	-0.12
UVIS/F547M	0.04	0.03	0.03	0.03	0.02
UVIS/F555W	0.11	0.07	0.02	0.01	-0.05
UVIS/F600LP	-0.72	-0.38	-0.04	-0.27	0.54
UVIS/F606W	-0.17	-0.08	0.01	-0.04	0.13
UVIS/F621M	-0.33	-0.18	0.00	-0.10	0.26
UVIS/F625W	-0.33	-0.18	-0.00	-0.10	0.26
UVIS/F631N	-0.34	-0.19	0.00	-0.10	0.29
UVIS/F645N	-0.43	-0.23	-0.02	-0.15	0.33
UVIS/F656N	-0.45	-0.18	0.06	-0.16	0.37
UVIS/F657N	-0.47	-0.22	0.00	-0.18	0.37
UVIS/F658N	-0.47	-0.22	0.00	-0.18	0.37
UVIS/F665N	-0.48	-0.26	-0.03	-0.18	0.39
UVIS/F673N	-0.49	-0.28	-0.02	-0.15	0.42
UVIS/F680N	-0.54	-0.30	-0.02	-0.17	0.45
UVIS/F689M	-0.53	-0.29	-0.02	-0.18	0.45
UVIS/F763M	-0.77	-0.40	-0.05	-0.32	0.64
UVIS/F775W	-0.78	-0.41	-0.05	-0.31	0.64
UVIS/F814W	-0.89	-0.47	-0.07	-0.36	0.71
UVIS/F845M	-1.00	-0.53	-0.09	-0.41	0.82

UVIS/F850LP	-1.18	-0.65	-0.13	-0.47	0.96
UVIS/F953N	-1.27	-0.71	-0.12	-0.50	1.06
UVIS/FQ232N	4.48	3.43	1.03	0.17	-1.14
UVIS/FQ243N	4.88	3.62	0.98	0.14	-1.10
UVIS/FQ378N	2.24	1.37	0.42	0.22	-0.51
UVIS/FQ387N	2.27	1.16	0.23	0.14	-0.51
UVIS/FQ422M	1.16	0.55	-0.03	0.01	-0.44
UVIS/FQ436N	0.86	0.49	0.04	0.05	-0.36
UVIS/FQ437N	0.86	0.46	0.00	0.03	-0.37
UVIS/FQ492N	0.31	0.17	0.01	0.05	-0.15
UVIS/FQ508N	0.31	0.17	0.04	0.12	-0.09
UVIS/FQ575N	-0.18	-0.08	0.00	-0.06	0.12
UVIS/FQ619N	-0.28	-0.16	0.02	-0.06	0.26
UVIS/FQ634N	-0.37	-0.21	-0.01	-0.12	0.30
UVIS/FQ672N	-0.47	-0.27	-0.02	-0.16	0.40
UVIS/FQ674N	-0.48	-0.27	-0.02	-0.16	0.41
UVIS/FQ727N	-0.65	-0.34	-0.01	-0.26	0.56
UVIS/FQ750N	-0.81	-0.43	-0.07	-0.33	0.61
UVIS/FQ889N	-1.12	-0.61	-0.14	-0.46	0.91
UVIS/FQ906N	-1.22	-0.68	-0.15	-0.49	0.94
UVIS/FQ924N	-1.21	-0.65	-0.12	-0.48	1.00
UVIS/FQ937N	-1.16	-0.65	-0.11	-0.47	1.00
IR/F098M	-1.35	-0.74	-0.15	-0.51	1.10
IR/F105W	-1.39	-0.74	-0.14	-0.54	1.22
IR/F110W	-1.38	-0.70	-0.11	-0.57	1.36
IR/F125W	-1.39	-0.67	-0.08	-0.60	1.57
IR/F126N	-1.37	-0.64	-0.07	-0.62	1.60
IR/F127M	-1.38	-0.64	-0.07	-0.62	1.62

IR/F128N	-1.39	-0.64	-0.07	-0.63	1.64
IR/F130N	-1.40	-0.65	-0.07	-0.63	1.66
IR/F132N	-1.40	-0.64	-0.07	-0.62	1.69
IR/F139M	-1.37	-0.62	-0.05	-0.60	1.78
IR/F140W	-1.41	-0.65	-0.06	-0.64	1.77
IR/F153M	-1.49	-0.69	-0.07	-0.70	1.98
IR/F160W	-1.49	-0.68	-0.07	-0.70	1.97
IR/F164N	-1.59	-0.75	-0.11	-0.79	2.10
IR/F167N	-1.58	-0.74	-0.10	-0.78	2.13

Table A.3: Color corrections AB_V to go from Johnson V magnitude to AB magnitude for WFC3 as a function of age in a population with constant star formation.

Mode	Age				
	10 Gyr	1 Gyr	100 Myr	10 Myr	1 Myr
UVIS/F200LP	0.31	0.24	0.03	-0.15	-0.48
UVIS/F218W	1.39	0.79	0.08	-0.48	-1.22
UVIS/F225W	1.39	0.79	0.09	-0.44	-1.15
UVIS/F275W	1.35	0.78	0.12	-0.36	-0.97
UVIS/F280N	1.34	0.77	0.14	-0.33	-0.92
UVIS/F300X	1.31	0.76	0.13	-0.34	-0.93
UVIS/F336W	1.15	0.71	0.19	-0.21	-0.66
UVIS/F343N	1.13	0.71	0.20	-0.18	-0.62
UVIS/F350LP	0.00	0.03	-0.01	-0.01	-0.04
UVIS/F373N	1.04	0.66	0.24	-0.11	-0.49
UVIS/F390M	0.67	0.28	-0.00	-0.25	-0.50
UVIS/F390W	0.64	0.30	0.03	-0.23	-0.49
UVIS/F395N	0.60	0.21	-0.04	-0.27	-0.49

UVIS/F410M	0.37	0.07	-0.11	-0.30	-0.47
UVIS/F438W	0.29	0.05	-0.09	-0.25	-0.39
UVIS/F467M	0.14	-0.00	-0.08	-0.18	-0.26
UVIS/F469N	0.15	0.00	-0.07	-0.17	-0.25
UVIS/F475W	0.18	0.04	-0.03	-0.14	-0.23
UVIS/F475X	0.16	0.05	-0.02	-0.11	-0.20
UVIS/F487N	0.21	0.14	0.05	-0.05	-0.14
UVIS/F502N	0.13	0.04	0.01	-0.06	-0.13
UVIS/F547M	0.03	0.03	0.03	0.03	0.02
UVIS/F555W	0.05	0.02	-0.00	-0.03	-0.05
UVIS/F600LP	-0.36	-0.13	-0.05	0.22	0.54
UVIS/F606W	-0.06	-0.00	0.01	0.07	0.13
UVIS/F621M	-0.14	-0.03	0.01	0.13	0.26
UVIS/F625W	-0.14	-0.03	0.01	0.12	0.26
UVIS/F631N	-0.15	-0.03	0.02	0.14	0.29
UVIS/F645N	-0.19	-0.05	-0.01	0.15	0.33
UVIS/F656N	-0.16	0.01	0.02	0.19	0.37
UVIS/F657N	-0.20	-0.04	-0.01	0.16	0.37
UVIS/F658N	-0.20	-0.04	-0.02	0.16	0.37
UVIS/F665N	-0.23	-0.07	-0.02	0.16	0.39
UVIS/F673N	-0.23	-0.06	0.01	0.19	0.42
UVIS/F680N	-0.26	-0.07	0.00	0.20	0.45
UVIS/F689M	-0.25	-0.07	-0.01	0.20	0.45
UVIS/F763M	-0.39	-0.13	-0.06	0.25	0.64
UVIS/F775W	-0.39	-0.14	-0.06	0.25	0.64
UVIS/F814W	-0.46	-0.18	-0.08	0.26	0.71
UVIS/F845M	-0.53	-0.22	-0.12	0.28	0.82
UVIS/F850LP	-0.66	-0.31	-0.14	0.30	0.96

UVIS/F953N	-0.72	-0.34	-0.15	0.32	1.06
UVIS/FQ232N	1.37	0.79	0.10	-0.43	-1.14
UVIS/FQ243N	1.37	0.78	0.08	-0.43	-1.10
UVIS/FQ378N	0.85	0.46	0.10	-0.20	-0.50
UVIS/FQ387N	0.70	0.29	0.01	-0.25	-0.51
UVIS/FQ422M	0.32	0.02	-0.12	-0.30	-0.44
UVIS/FQ436N	0.31	0.08	-0.06	-0.22	-0.37
UVIS/FQ437N	0.28	0.05	-0.09	-0.24	-0.38
UVIS/FQ492N	0.12	0.03	-0.01	-0.09	-0.15
UVIS/FQ508N	0.14	0.06	0.04	-0.03	-0.09
UVIS/FQ575N	-0.07	-0.01	-0.00	0.06	0.13
UVIS/FQ619N	-0.12	-0.01	0.03	0.14	0.26
UVIS/FQ634N	-0.17	-0.04	0.00	0.14	0.30
UVIS/FQ672N	-0.22	-0.06	-0.00	0.18	0.40
UVIS/FQ674N	-0.22	-0.06	0.00	0.19	0.41
UVIS/FQ727N	-0.31	-0.09	-0.03	0.23	0.56
UVIS/FQ750N	-0.42	-0.16	-0.08	0.23	0.61
UVIS/FQ889N	-0.62	-0.28	-0.15	0.28	0.91
UVIS/FQ906N	-0.69	-0.34	-0.17	0.27	0.94
UVIS/FQ924N	-0.67	-0.30	-0.14	0.31	1.00
UVIS/FQ937N	-0.65	-0.30	-0.14	0.31	0.99
IR/F098M	-0.76	-0.37	-0.16	0.33	1.10
IR/F105W	-0.78	-0.37	-0.17	0.36	1.22
IR/F110W	-0.76	-0.33	-0.17	0.39	1.36
IR/F125W	-0.74	-0.30	-0.17	0.44	1.57
IR/F126N	-0.73	-0.29	-0.18	0.45	1.60
IR/F127M	-0.73	-0.29	-0.18	0.45	1.62
IR/F128N	-0.74	-0.29	-0.18	0.45	1.64

IR/F130N	-0.74	-0.29	-0.18	0.46	1.66
IR/F132N	-0.74	-0.28	-0.17	0.47	1.69
IR/F139M	-0.71	-0.25	-0.14	0.49	1.78
IR/F140W	-0.75	-0.28	-0.17	0.47	1.77
IR/F153M	-0.81	-0.32	-0.20	0.47	1.97
IR/F160W	-0.80	-0.32	-0.21	0.46	1.97
IR/F164N	-0.88	-0.39	-0.27	0.43	2.10
IR/F167N	-0.88	-0.38	-0.26	0.44	2.13

Appendix B: Geometric Distortion

Appendix Contents

- [B.1 Overview](#)
- [B.2 UVIS Channel](#)
- [B.3 IR Channel](#)
- [B.4 IR Summary](#)

B.1 Overview

WFC3 images exhibit significant geometric distortion, similar to that seen in ACS images. The required folding, with powered optics, of the light paths in both channels to fit within the instrument's optical-bench envelope results in substantial tilts of the focal surfaces with respect to the chief rays. The WFC3 UVIS detector is tilted at $\sim 21^\circ$ about one of its diagonals, producing a rhomboidal elongation of $\sim 7\%$. The IR detector has a $\sim 24^\circ$ tilt about its x-axis, creating a rectangular elongation of $\sim 10\%$.

If these were the only distortions they would not present much difficulty: their impacts on photometry, mosaicking, or dithering could be computed simply. More problematic, however, is the variation of plate scale across each detector. For the WFC3 UVIS and IR channels, this variation in plate scale amounts to a change of 3.5% in x and y, and 2% in x and 6% in y, respectively, over the full field. Hence the area on the sky covered by a pixel varies, by about 7% for the UVIS channel and about 8% for the IR channel. Allowance for this change in plate scale must be made in photometric reductions of WFC3 data that have not been corrected for distortion. Further details are available in [WFC3 ISR 2010-08](#) and at the pixel area map section of the WFC3 website: <http://www.stsci.edu/hst/instrumentation/wfc3/data-analysis/pixel-area-maps>

Dithering and mosaicking are complicated by the fact that an integer pixel shift near the center of the detector translates into a non-integer displacement for pixels in other locations. Even this is not a fundamental difficulty, but implies some computational complexity in registering and correcting images. All of these considerations make it necessary to obtain accurate measurements of the distortions. The orientations of the WFC3 detector edges for both detectors are at approximately 45° with respect to the V2 and V3 coordinate axes of the telescope. [Figure 2.2](#) shows the WFC3 apertures in the telescope's V2,V3 reference frame. For a telescope roll angle of zero this would correspond to an on-sky view with the V3 axis aligned with north and the V2 axis with east. See Section 6.2.2 of the [Phase II Proposal Instructions](#), which gives detailed information on the relationship between detector coordinates, spacecraft coordinates, and ORIENT.

The first on-orbit measurements of the geometric distortion for the WFC3 detectors were made during SMOV (Servicing Mission Observatory Verification). Astrometric fields in 47 Tuc (NGC 104) and the LMC were observed with multiple offsets in programs 11444 (UVIS, filter F606W) and 11445 (IR, filter F160W). Geometric distortion solutions were derived from this data ([WFC3 ISR 2009-33](#), [WFC3 ISR 2009-34](#)) and entered into IDCTAB files to support the use of MultiDrizzle to produce distortion-corrected images. (MultiDrizzle has since been replaced by [DrizzlePac](#).) In the initial IDCTAB files, the solutions for filters F606W and F160W were applied to all UVIS and IR filters, respectively. Because there are small filter-dependent differences in distortion, exposures made with other filters during SMOV and in subsequent calibration programs observing Omega Centauri have been used to derive improved solutions for the more commonly used filters ([WFC3 ISR 2012-07](#), [WFC3 ISR 2018-10](#)). The distortion has been found to be stable over two years ([WFC3 ISR 2012-03](#)). The relative displacement of stars in exposures made with different filters due to non-coplanarity of the filters is ~ 0.02 arcsec in most cases ([WFC3 ISR 2010-12](#), [WFC3 ISR 2012-01](#).) Astrometric accuracy of the WFC3/UVIS distortion solutions has been improved by incorporating correction for the lithographic mask pattern of the detector ([WFC3 ISR 2013-14](#)). Further work on the lithographic mask pattern and filter-dependent fine scale structure has reduced astrometric errors to the level of ~ 1 mas for many of the UVIS filters ([WFC3 ISR 2014-12](#)). The WFC3/UVIS distortion solution for F606W was found to be time-independent and accurate to ± 2 mas over 5 years using a standard astrometric catalog of the central region of Omega Centauri created from exposures made at different centerings and roll angles ([WFC3 ISR 2015-02](#)). Furthermore, the stability and time-independence of the WFC3/UVIS distortion solution for F606W was confirmed again, this time over a 10 year period, through a study that compared F606W images corrected with the current geometric solutions to the Gaia DR2 source catalogue in the central region of Omega Centauri ([WFC3 ISR 2019-09](#)).

Delivered IDCTABs with distortion solutions for WFC3/IR filters and WFC3/UVIS filters, and a WFC3/UVIS IDCTAB in preparation, are listed in Table B.1. Any IR filter or UVIS filter not listed in the delivered IDCTABs is still using the solution derived for F160W and F606W, respectively. All UVIS filters listed in the table have accompanying NPOLFILE (Non-polynomial Offset) reference files available. The NPOLFILE reference files are the 2-D look-up-tables of the filter-dependent fine scale distortion (see [WFC3 ISR 2014-12](#), [WFC3 ISR 2018-10](#)).

Table B.1: IDCTAB (Instrument Distortion Correction file) deliveries for the IR and UVIS filters

WFC3 Channel Updated	Name of IDCTAB Reference File	Date of Delivery	Filters updated (Later files include filters calibrated previously)
IR (current available version)	w3m18525i_idc.fits	Mar 2012	F105W, F110W, F125W, F140W, F098M, F139M, F153M
UVIS	yas1621ai_idc.fits	Oct 2014	F350LP, F850LP, F225W, F275W, F336W, F390W, F438W, F475W, F555W, F606W, F775W, F814W, F390M, F621M, F953N
UVIS	1cl1823gi_idc.fits	Dec 2017	F390M, F547M, F763M, F845M
UVIS (current available version)	2731450pi_idc.fits	July 2018	F475W, F475X, F600LP, F280N, F343N, F373N, F395N, F469N, F487N, F502N, F631N, F645N, F656N, F658N, F665N, F680N

B.2 UVIS Channel

[Figure B.1](#) illustrates the shape of the UVIS channel field of view as projected onto the sky. As noted above, its rhomboidal shape is due primarily to the diagonal tilt of the CCD focal plane with respect to the chief ray (see the schematic mechanical drawing of the instrument in [Figure 2.1](#)). The angle between the x- and y-axes is $\sim 86.1^\circ$. The field diagonals are tilted slightly from the V2 and V3 axes. There is a ~ 1.2 arcsec gap between the two CCD chips. The crosses in the diagram indicate where points in the image would be located without non-linear distortion, and the vectors, scaled up by a factor of 10, indicate the actual locations of the points on the sky, including the non-linear distortion components.

The corner displacements are about 30 pixels, corresponding to 1.3 arcsec. The principal effect is the diagonal variation of scale. At the center of UVIS1 (CCD Chip 1), the scale in the x-direction is 0.0396 arcsec/pixel, and 0.0393 arcsec/pixel in the y-direction. For UVIS2 (CCD Chip 2), these scales are 0.0400 arcsec/pixel, and 0.0398 arcsec/pixel, respectively. Between the corner of the UVIS image nearest to Amp A and the diagonally opposite corner near Amp D, the overall scale increases by 3.5%. UVIS1 forms a slightly distorted rectangle 162×81 arcsec in size, while UVIS2 subtends 164×81 arcsec.

The resulting variation of the projected pixel area on the sky requires corrections to photometry of point sources using images that have not been distortion-corrected. A contour plot of relative pixel size across the UVIS image, normalized at the photometric reference pixel, is shown in [Figure B.2](#). The ratio of maximum to minimum pixel area over the detector is 1.074.

See <http://www.stsci.edu/hst/instrumentation/wfc3/data-analysis/pixel-area-maps> for a FITS file of the pixel area map and a discussion of its normalization and application for photometry.

Figure B.1: Linear components (crosses) and non-linear components (vectors, magnified by 10) of geometric distortion on the WFC3/UVIS detector.

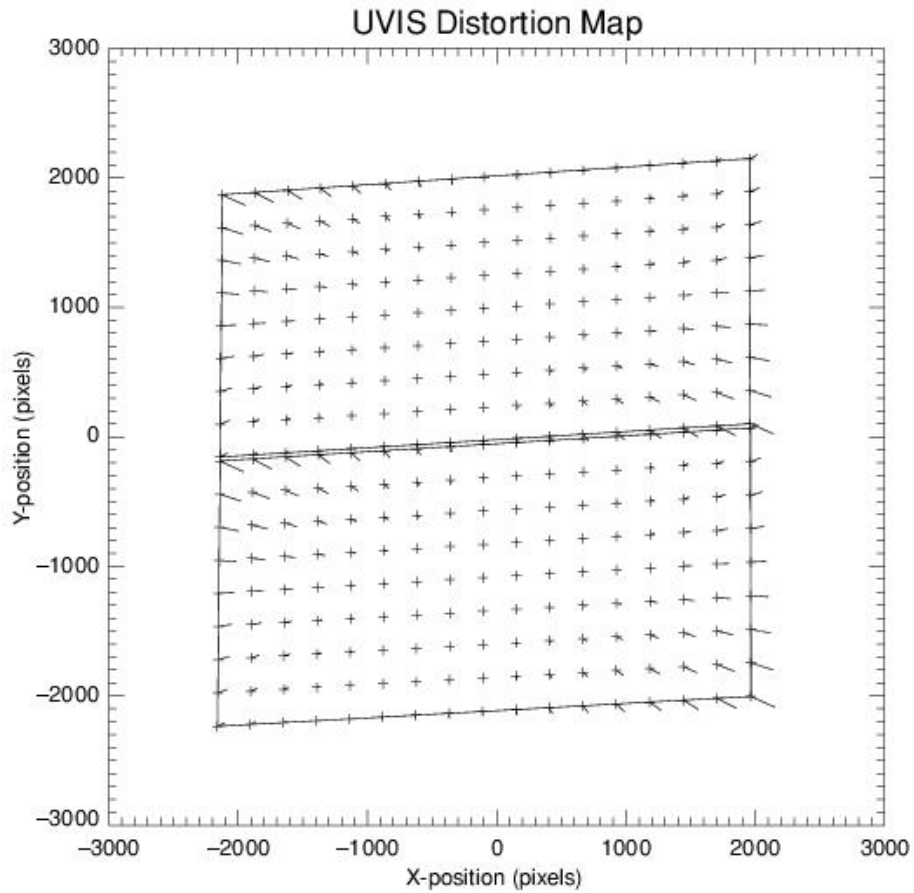
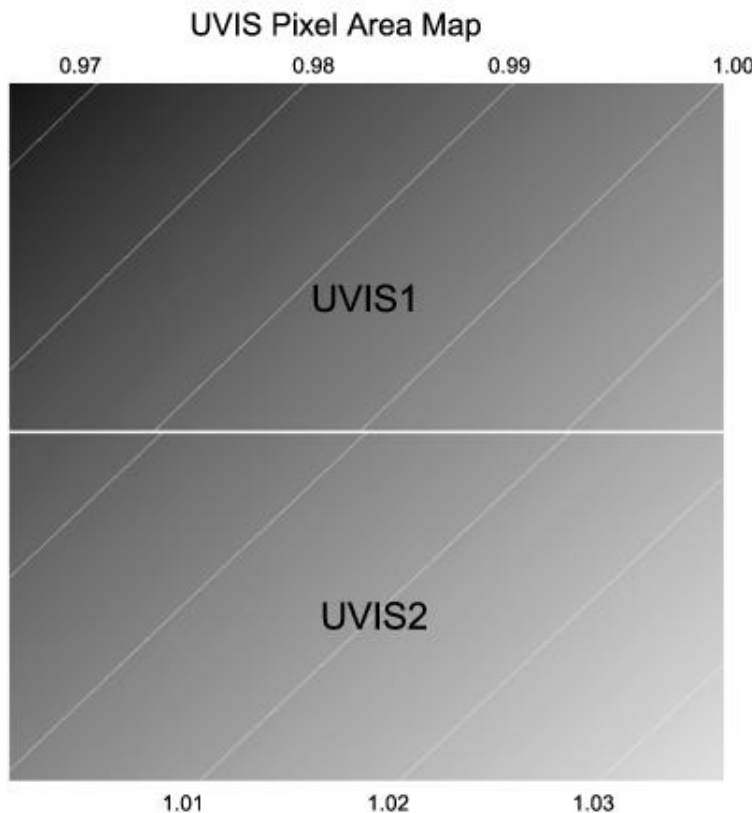


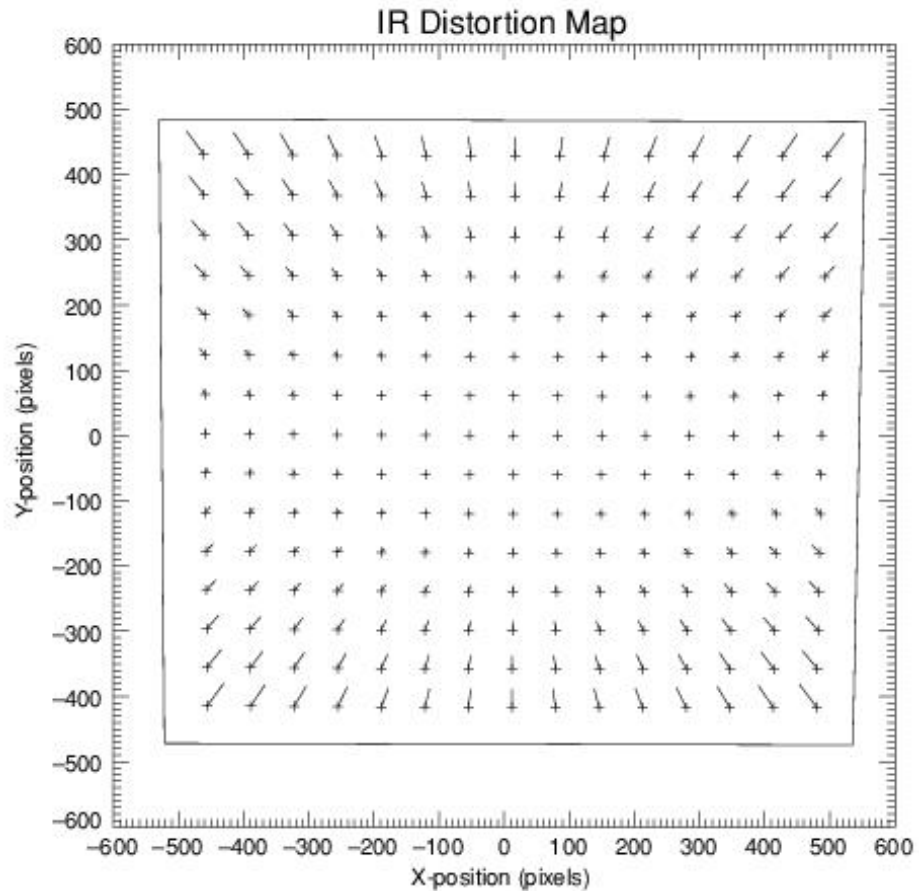
Figure B.2: Variation of the effective pixel area with position on the UVIS detector. Darker shading indicates pixels with smaller area. Contours are drawn at 1% increments.



B.3 IR Channel

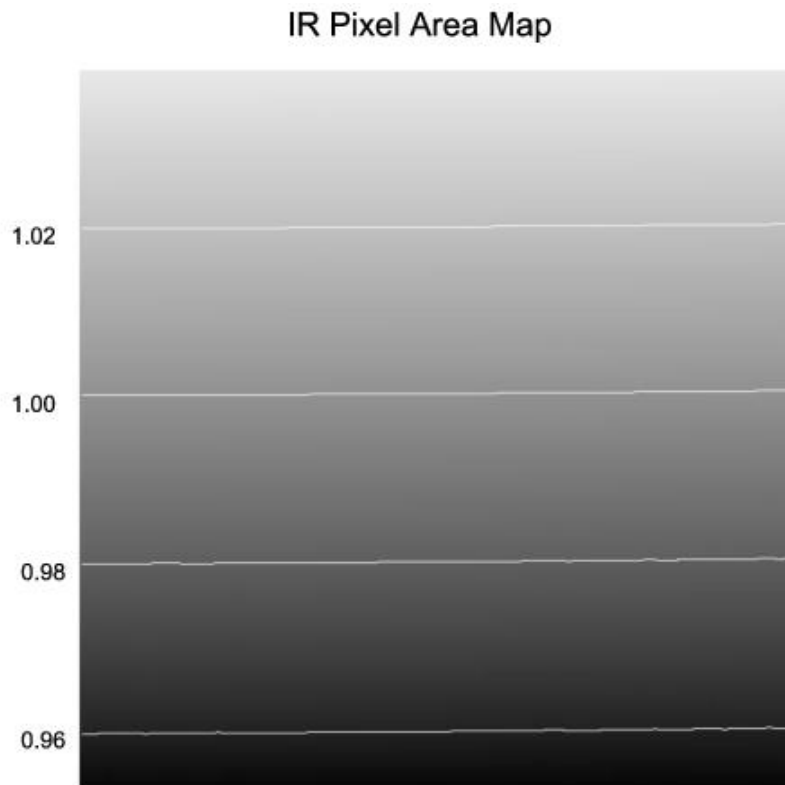
The IR detector field of view is nominally concentric with the UVIS field, but subtends a somewhat smaller area on the sky, 136×123 arcsec. The detector tilt is about the x-axis (AXIS1 in [Figure 7.1](#)), so the projected aperture shape is nearly a rectangle, with the angle between the x- and y-axes on the sky nearly 90° , as shown by the outline in [Figure B.3](#). At field center, the x- and y-scales are 0.135 and 0.121 arcsec/pixel, respectively. A vector plot of the deviation from linearity is given in [Figure B.3](#). The deviations have been magnified by a factor of 10, as in [Figure B.1](#). The largest deviation is 10 pixels, corresponding to about 1.4 arcsec.

Figure B.3: Linear components (crosses) and non-linear components (vectors, magnified by 10) of the geometric distortion on the WFC3/IR detector.



A map of the variation of pixel area across the IR detector to be used for correction of point-source photometry from images that have not been distortion-corrected (see <http://www.stsci.edu/hst/instrumentation/wfc3/data-analysis/pixel-area-maps>) is shown in Figure B.4. The ratio of maximum to minimum pixel area is 1.090.

Figure B.4: Variation of the effective pixel area with position on the IR detector. Darker shading indicates pixels with smaller area. Contours are drawn at 2% increments.



B.4 IR Summary

Images produced by both WFC3 channels are affected by considerable geometric distortion, dominated by a linear anamorphism introduced by the tilt of the image surface with respect to the chief ray. This is compounded by non-linear terms that produce changes across the field of view in both plate scale and area subtended by the pixels. Distortion solutions derived from data taken during SMOV with UVIS filter F606W and IR filter F160W are presented here. They have been entered into IDCTAB files to support the use of MultiDrizzle to produce distortion-corrected images. (MultiDrizzle has since been replaced by [DrizzlePac](#).) The corresponding pixel area maps, also presented here, have been made available for photometric calibration.

Appendix C: Dithering and Mosaicking

Appendix Contents

- [C.1 Why Mosaicking and Dithering are Needed](#)
- [C.2 WFC3 Patterns](#)

C.1 Why Mosaicking and Dithering are Needed

The sizes of telescope pointing offsets between successive exposures can be very different, depending on whether the purpose is “mosaicking” or “dithering.” Mosaicking is done with the aim of increasing the area of sky covered by a particular set of exposures, usually with the goal of providing a seamless joining of contiguous frames. The angular offsets used when mosaicking are generally large, up to the size of the field of view. Only programs observing targets larger than the field of view of the detector need to use mosaicked exposures.

Dithering generally involves much smaller telescope offsets, often on the order of a few pixels in size. Most imaging programs are advised to use dithering for several reasons, including:

- removal of hot pixels and other detector blemishes ([Section 6.11.2](#))
- improving sampling of the PSF ([Sections 6.12.1](#) and [7.10.1](#))
- improving photometric accuracy by averaging over flat-fielding errors ([Sections 5.4.3](#), [5.7.4](#), and [6.12.1](#))
- bridging over the gap between the chips in the UVIS channel ([Section 5.2.2](#)).

Dithered and mosaicked exposures can be combined using software included in *DrizzlePac*. Several documents provide examples of how to use this software. [WFC3 ISR 2014-23](#) describes the procedure by which the individual images in the Frontier Fields program have been aligned using galaxies and provides the FORTRAN source code `hst2galign` that accomplishes the alignment. (Further uses of `hst2galign` involving PSF-fitting and faint source location and photometry are discussed in [WFC3 ISR 2014-24](#).) [WFC3 ISR 2015-04](#) describes a methodology for optimizing the parameter `pixfrac` and shows the results of tests conducted for the Frontier Fields program. [WFC3 ISR 2015-09](#) shows how mosaic alignment can be achieved in a single step in *DrizzlePac* 2.0 by building up an expanded reference catalog, using the WFC3 observations of the Eagle Nebula (M16) as an example.

Note that it is sometimes necessary to use software like that in DrizzlePac to combine even CR-SPLIT or repeat exposures, when pointing drift causes slight misalignment of exposures and differences in how PSFs are pixilated, or when gradual changes in focus over the course of an orbit produce changes in the observed PSF.

In some programs, especially those observing time-variable phenomena, combining dithered exposures to correct for cosmic rays and transient bad pixels may be scientifically infeasible. In such cases, single-image based methods must be used. These methods use statistical properties of cosmic-ray brightness or sharpness to identify and interpolate across cosmic rays. Single-image cosmic ray rejection schemes are not available through the standard WFC3 calibration pipeline.

C.2 WFC3 Patterns

A number of different types of patterns are available to support dithered and mosaicked WFC3 observations. The pre-defined patterns that have been implemented in APT are described in the [Phase II Proposal Instructions](#), which are updated when the selection of a new cycle of proposals is announced. The WFC3 patterns in effect in APT at the time of publication of this Handbook are summarized here.

WFC3 dither patterns designed to subsample pixels can optionally be selected as secondary patterns when WFC3 patterns with larger steps are selected as primary patterns. WFC3 patterns can also be added as secondary patterns to any of the generic pattern types (BOX, LINE, SPIRAL). When combining patterns, the smaller dither pattern should be the secondary pattern to minimize the time spent moving the telescope. Due to geometric distortion ([Appendix B](#)), a large mosaic step shifts some objects by an integer number of rows (or columns), and others by an integer plus some fraction of a pixel. The PSF is thus not evenly sampled in the overlap region of the two exposures, so a PSF-sampling dither should be added if spatial resolution is important.

Sets of exposures with offsets executed using patterns or POS TARGs are associated and combined automatically during [calwf3](#) pipeline processing, as long as the same guide stars have been used for all exposures. Pointings must be contained within a diameter ~130 arcsec or less (depending on the availability of guide stars in the region) to use the same guide stars. Note that the rms pointing repeatability is significantly less accurate if different guide stars are used for some exposures. (See Appendix B of the [DrizzlePac Handbook](#).)

The names and purposes of the patterns in effect in APT at the time of publication are given in Table C.1. (The initially adopted names of patterns have been preserved for continuity, although they do not always correspond to the distinction between dither steps and mosaic steps outlined above.) The small BOX dither patterns are designed to optimally sample the PSF when 4 steps are used. Since time constraints do not always permit visits to be broken into multiples of 4 steps, LINE dither patterns that optimally sample the PSF in 2 or 3 steps are also given. The BOX and LINE dither patterns are illustrated in [WFC3 ISR 2010-09](#). For a full discussion and illustrations of patterns that optimally sample the PSF for different numbers of steps, see Section C.2 of the [DrizzlePac Handbook](#).) Note that PSF sampling generally produces a more significant improvement for IR images than for UVIS images (see [Section 6.6.1](#) and [Section 7.6.1](#)) The remainder of the patterns in Table C.1 are special-purpose mosaic patterns that are expected to be commonly needed. We have not defined patterns to deal with specific features in flats—notably, the circular dead spot on the IR detector ([WFC3 ISR 2008-08](#)) and the UVIS “droplets” ([WFC3 ISR 2008-10](#)). However, patterns that can be used to mitigate the effects of these artifacts are discussed in [WFC3 ISR 2010-09](#).

Table C.1: Dithering and Mosaicking Patterns for WFC3.

Pattern Name	Description
WFC3 IR Patterns	
WFC3-IR-DITHER-BLOB	Dithers over “blobs” (Section 7.9.6)
WFC3-IR-DITHER-BOX-MIN	Provides optimal 4-step sampling of the PSF.

WFC3-IR-DITHER-BOX-UVIS	Produces an IR mosaic (despite the name) covering approximately the same area as the UVIS-CENTER aperture.
WFC3-IR-DITHER-LINE	Provides optimal 2-step sampling of the PSF.
WFC3-IR-DITHER-LINE-3PT	Provides optimal 3-step sampling of the PSF
WFC3 UVIS Patterns	
WFC3-UVIS-DITHER-BOX	Provides optimal 4-step sampling of the PSF; produces spacings of >1 column for removal of hot columns
WFC3-UVIS-DITHER-LINE	Provides optimal 2-step sampling of the PSF; produces spacings of >1 column for removal of hot columns
WFC3-UVIS-DITHER-LINE-3PT	Provides optimal 3-step sampling of the PSF; produces spacings of >1 column for removal of hot columns
WFC3-UVIS-GAP-LINE	Dithers over the interchip gap
WFC3-UVIS-MOS-BOX-LRG	Produces a mosaic that can generally be executed with a single set of guide stars.
WFC3-UVIS-MOS-DITH-LINE	Combines a primary gap-stepping pattern with an optional dither at each primary position.
WFC3-UVIS-MOSAIC-LINE	For full-frame UVIS with ACS/WFC in parallel; steps the gap on both detectors.

The default specifications of the patterns are summarized in Table C.2. The equivalent POS TARG moves are summarized in Table C.3, along with the approximate number of pixels corresponding to these moves. The number of pixels was computed using only the linear distortion terms with coefficients measured at the center of each detector. This is an excellent approximation for small moves and for objects that remain in the central region of the detector. (See [Figure B.1](#) and [B.3](#) in [Appendix B](#).)

Note that you can easily scale up the patterns in APT to make them larger; e.g., multiply the Point Spacing and Line Spacing of patterns with half-pixel sampling (WFC3-IR-DITHER-BOX-MIN, WFC3-IR-DITHER-LINE, WFC3-UVIS-DITHER-BOX, WFC3-UVIS-DITHER-LINE) by an odd number to preserve the half-pixel sampling. (This is equivalent to multiplying the POS TARGs and steps in pixels by that number.) You may want to do this, for example, to move a saturated persistence-generating core of a target by a greater distance than the minimal default distance. Be aware, however, that larger steps result in larger variations in sub-pixel sampling of the PSF over the face of the detector due to non-linear geometric distortion. See [WFC3 ISR 2016-14](#).

Table C.2: Default values of the parameters that define the WFC3 convenience patterns

Pattern	No. of Points	Point Spacing (arcsec)	Line Spacing (arcsec)	Pattern Orient (degrees)	Angle between Sides (degrees)	Center Pattern

WFC3-IR-DITHER-BLOB	2	5.183		41.859		yes
WFC3-IR-DITHER-BOX-MIN	4	0.572	0.365	18.528	74.653	no
WFC3-IR-DITHER-BOX-UVIS	4	23.020	35.212	0.713	89.287	yes
WFC3-IR-DITHER-LINE	2	0.636		41.788		no
WFC3-IR-DITHER-LINE-3PT	3	0.605		41.788		no
WFC3-UVIS-DITHER-BOX	4	0.173	0.112	23.884	81.785	no
WFC3-UVIS-DITHER-LINE	2	0.145		46.840		no
WFC3-UVIS-DITHER-LINE-3PT	3	0.135		46.840		no
WFC3-UVIS-GAP-LINE	2	2.414		85.759		yes
WFC3-UVIS-MOS-BOX-LRG	4	79.400	77.500	5.550	95.300	yes
WFC3-UVIS-MOS-DITH-LINE						
primary pattern	3	2.400		85.754		yes
secondary pattern	2	0.119		33.606		no
WFC3-UVIS-MOSAIC-LINE	2	3.264		63.697		no

Table C.3: Steps in arcsec in the POS TARG frame and in detector pixels for the WFC3 convenience patterns.

Pattern Name	POS TARG X (arcsec)	POS TARG Y (arcsec)	x (pixels)	y (pixels)
WFC3-IR-DITHER-BLOB	-1.930 1.930	-1.729 1.729	-14.25 14.25	-14.25 14.25

WFC3-IR-DITHER-BOX-MIN	0.000 0.542 0.339 -0.203	0.000 0.182 0.485 0.303	0.0 4.0 2.5 -1.5	0.0 1.5 4.0 2.5
WFC3-IR-DITHER-BOX-UVIS	-11.071 11.947 11.071 -11.947	-17.744 -17.457 17.744 17.457	-81.7 88.2 81.7 -88.2	-146.5 -144.2 146.5 144.2
WFC3-IR-DITHER-LINE	0.000 0.474	0.000 0.424	0.0 3.5	0.0 3.5
WFC3-IR-DITHER-LINE-3PT	0.000 0.451 0.902	0.000 0.403 0.806	0.00 3.33 6.67	0.00 3.33 6.67
WFC3-UVIS-DITHER-BOX	0.000 0.158 0.099 -0.060	0.000 0.070 0.165 0.095	0.0 4.0 2.5 -1.5	0.0 1.5 4.0 2.5
WFC3-UVIS-DITHER-LINE	0.000 0.099	0.000 0.106	0.0 2.5	0.0 2.5
WFC3-UVIS-DITHER-LINE-3PT	0.000 0.092 0.185	0.000 0.098 0.197	0.00 2.33 4.67	0.00 2.33 4.67
WFC3-UVIS-GAP-LINE	-0.089 0.089	-1.203 1.203	-2.25 2.25	-30.25 30.25
WFC3-UVIS-MOS-BOX-LRG	-39.611 39.611 39.611 -39.611	-42.120 -36.860 42.120 36.860	-1000.0 1000.0 1000.0 -1000.0	-997.0 -1001.0 997.0 1001.0
WFC3-UVIS-MOS-DITH-LINE	-0.178 -0.079 0.000 0.099 0.178 0.277	-2.393 -2.328 0.000 0.066 2.393 2.459	-4.5 -2.0 0.0 2.5 4.5 7.0	-60.2 -58.7 0.0 1.5 60.2 61.7
WFC3-UVIS-MOSAIC-LINE	0.000 1.446	0.000 2.926	0.0 36.5	0.0 71.5

For the IR detector, the linear relation between POS TARGs and pixels is simply

$$\text{POS TARG X} = a_{11} * x$$

$$\text{POS TARG Y} = b_{10} * y$$

where $a_{11} \sim 0.1355$ arcsec/pixel and $b_{10} \sim 0.1211$ arcsec/pixel near the center of the detector. For the UVIS detector, there is a cross-term that takes into account the fact that the projected axes are not perpendicular:

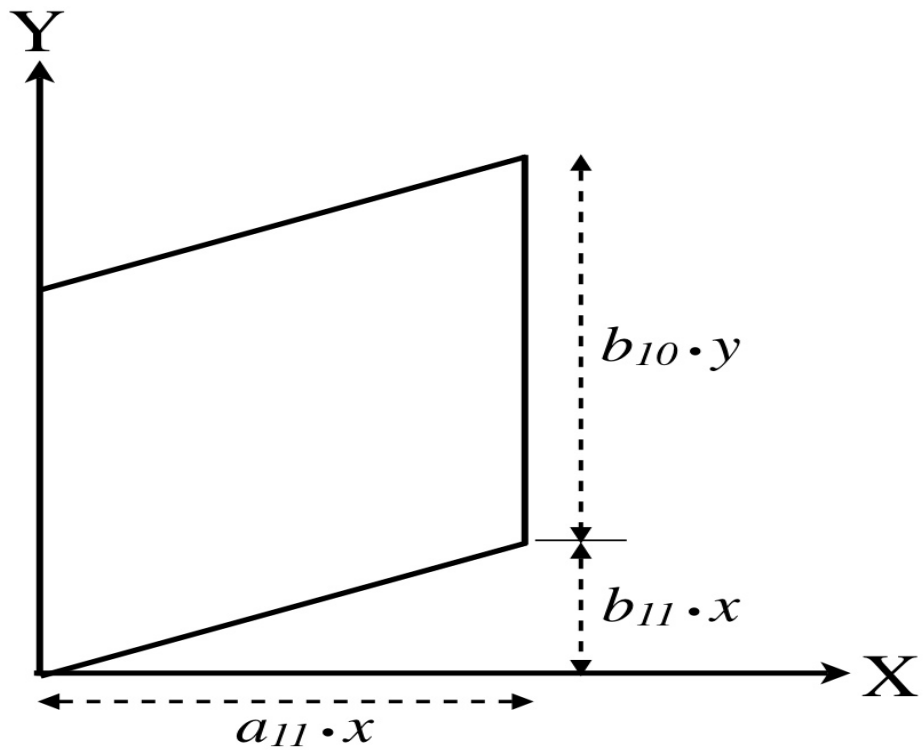
$$\text{POS TARG X} = a_{11} * x$$

$$\text{POS TARG Y} = b_{11} * x + b_{10} * y$$

where $a_{11} \sim 0.0396$ arcsec/pixel, $b_{11} \sim 0.0027$ arcsec/pixel, and $b_{10} \sim 0.0395$ arcsec/pixel near the center of the detector. This relationship is illustrated in Figure C.1.

The values of these coefficients were derived using optical models and apply to the centers of the detectors. On-orbit geometric distortion solutions give marginally different coefficients ([WFC3 ISR 2010-09](#)). The corresponding changes in pixel steps in small dithers are insignificant. The corresponding changes in pixel steps in large dithers or mosaic steps are inconsequential, since non-linear distortion makes the step size in pixels variable over the detector.

Figure C.1: Transformation between image x,y coordinates (in pixel units) and X,Y coordinates (in arcsec) in the POS TARG frame. See also [Figure 6.1](#).



Appendix D: Bright-Object Constraints and Image Persistence

Appendix Contents

- [D.1 UVIS Channel](#)
- [D.2 IR Channel](#)

D.1 UVIS Channel

The UVIS channel's CCDs have no bright-object constraints. Overexposures on very bright targets do not have any adverse health and safety issues, nor should they affect subsequent exposures. As for any CCD, there can be some bleeding into adjacent rows and columns surrounding the bright object. This however is generally quite modest assuming the bright object is not itself the science target. From a scientific perspective, the largest problem with bright targets in the field is likely to arise from window or filter ghosts (See [Section 6.5.3](#)).

D.2 IR Channel

The IR channel likewise has no bright-object constraints that are imposed due to instrument safety concerns. However, as discussed in [Section 5.7.9](#) and [Section 7.9.4](#), observers should bear in mind that there is a potential for image-persistence effects that could compromise observations made immediately following an exposure on a bright target. Such observations contain “afterglow” images at the location of the overexposed object, which gradually fades away over an interval of several hours.

Observers are not expected to be able to mitigate the effects of persistence from previous visits of other investigators. The Institute is minimizing the effects of persistence due to other observers as part of scheduling. We also provide estimates of the amount of persistence expected due to earlier exposures through MAST (as described in the [WFC3 Data Handbook](#)). These estimates allow the user to exclude regions of images that are affected by persistence and in some cases to subtract the persistence from an image.

Observers are responsible for assuring that persistence within a visit is not harmful to the science requirements of their own observations. Persistence is primarily a function of fluence, the total number of electrons accumulated by a pixel in an exposure. Very little persistence is observed when the fluence is less than about 35,000 electrons. The best way to avoid persistence effects is to adopt an observing strategy that keeps fluence levels below 35,000 electrons. Therefore, an observing strategy involving a larger number of shorter exposures will result in less persistence than one with fewer longer exposures.

The WFC IR channel has a field of view seven times larger than NICMOS Camera 3 and also has higher sensitivity. This combination means that for WFC3/IR images it is often impossible to avoid saturating some portions of the image, especially since one is also constrained by the total volume of data that can be accumulated. In many cases this will not matter from a science perspective. For example, if your observing strategy involves small dithers and there are a few bright stars in the field, then persistence from earlier images will appear in the wings of the PSF of the bright star. Even if you have large dithers, you will probably not find persistence to be a major problem in the analysis, as long as you are willing to treat pixels with significant persistence as bad pixels.

Nevertheless, if you are planning a sequence of IR observations that may contain severely overexposed images, you may wish to estimate the degree of overexposure. Examples of types of observations for which this is commonly a problem are observations of regions in the Galactic plane or the LMC with large numbers of fairly bright stars, such as eta Car or 30 Dor. Significant amounts of persistence have also been observed in certain instances from globular clusters and nearby elliptical galaxies.

An IR observer might expect that the Two Micron All Sky Survey (2MASS) would be the appropriate catalog for examining the frequency of WFC3/IR saturation, but in fact the 2MASS catalog is generally not deep enough for this purpose. Although the depth of the survey varies across the sky, the faint limit is typically near 15th mag in J, H, and Ks (the formal Level 1 requirements on limiting magnitudes of the 2MASS catalog are J = 15.8, H = 15.1, and Ks = 14.3). Stars near this faint limit saturate the WFC3/IR detector in a relatively short time in both the medium and broad band filters. The STScI Guide Star Catalog (GSC), currently at version 2.3, generally goes much fainter (down to 22nd mag in V), but the extrapolation from the optical into the infrared depends on the accuracy of the spectral type implied by the optical colors and the assumed extinction (a large source of systematic errors along sightlines of high extinction).

As described in [Chapter 9](#), the WFC3 [Exposure Time Calculator \(ETC\)](#) can be used to estimate the count rate in the central pixel for a given astronomical source. (Note that it is the rate for the central pixel and not the total count rate in an aperture that matters.) However, as a rough guideline, below we present tables of the count rates for two cases: a “hot star” with spectral type O3V, Teff = 45,000 K, [Fe/H] = 0, and log g = 4.0; and a “cool star” with spectral type M5V, Teff = 3500 K, [Fe/H] = 0, and log g = 5.0.

Tables D.1, D.2, D.3, and D.4 give the results for the cases where one normalizes to Johnson *J*, *K*, *V*, and Bessel *H*, as stated in the table captions. In each case a magnitude of 15 in the respective bandpass is assumed. The count rates are given in e⁻/s for the central pixel of a star centered in a WFC3/IR pixel. These tables give the most reliable results when normalizing to a ground-based bandpass that overlaps with the WFC3 bandpass, regardless of the assumed spectral energy distribution. However, when normalizing to Johnson *V*, one must know the underlying spectral energy distribution to high accuracy in order to predict the count rate in the WFC3/IR bandpasses.

The Bright Object Tool (BOT) in the [Astronomer’s Proposal Tool \(APT\)](#) can provide a list of saturated objects for a potential WFC3/IR observation, given a Phase II proposal. Because the 2MASS survey is sufficiently deep for objects that would severely oversaturate the detector (by more than a factor of 100), the BOT uses 2MASS data where they are available, and the GSC2 where no 2MASS data are available. To use this feature, display a visit with the Aladin tool, loading the DSS image. Then, click on the BOT button in the main tool bar, which will bring up the Bright Object Tool. At this point you press the “Update 2MASS Display” button and stars likely to cause persistence problems are indicated in the Aladin Window, and can be looked at individually there, or shown as a list with the “Get Details...” button. The tool lists stars with different levels of saturation, computed using the time between pixel resets, which can be significantly longer than the exposure time for subarray exposures ([WFC3 ISR 2011-09](#)). One should probably be more concerned with the numbers of stars listed as saturated and their locations than with the crude categorization by saturation level, but keep in mind that extremely bright stars saturate not only the central pixel, but also pixels in the PSF wings.

One should be aware that neither the BOT nor other estimates based on star catalogs provide good information about persistence due to diffuse sources, e.g., a bright and extended galaxy nucleus. For that one can use the ETC, if one has an estimate of the surface brightness of the source.

The best strategy to reduce the effects of persistence is to reduce the exposure times. Two exposures of 350 seconds (SPARS25 with 15 full-frame readouts) will result in less persistence than one exposure of 700 seconds (SPARS50 with 15 full-frame readouts). If one cannot get short enough exposures (or enough readouts) with the full array and the science target does not fill all of the field, one should consider using sub-arrays. (See [Section 7.7.4](#).)

A second possibility if the program involves images that go to different depths is to place shallower exposures at the beginning of an orbit and deeper exposures at the end of an orbit. For example, if one is planning three 500 second exposures with a narrow band filter and one 500 second exposure through a broad band filter, one should almost always put the broad band filter last.

If neither of these strategies solves the problem, then one needs to very carefully examine dither patterns, and decide what is most important to the observing program. Sometimes, if persistence is isolated to one portion of the image, a line dither in the appropriate direction can limit the damage effects of persistence. Small dither patterns tend to keep bad pixels confined to small regions within the point spread function of the stars that cause persistence. On the other hand, these dither patterns do not cover enough area to step over IR blobs. (See [Section 7.9.6](#).) In some cases, one simply needs to decide which of these two problems it is more important to mitigate as part of planning an observation. An observer who cannot determine the best strategy for a program should consult the Contact Scientist for that program for advice.

Table D.1: Count Rates (e⁻/s) for source with J=15 renormalized to Johnson/J.

WFC3 IR filter	Cool star ¹	Hot star ¹
F098M	2542.9	1876.2
F105W	4541.3	3572.4
F110W	7610.7	6754.8
F125W	4570.8	4484.4
F126N	226.4	215.0
F127M	1108.7	1068.2
F128N	244.9	238.8
F130N	246.9	243.5
F132N	235.2	240.0
F139M	790.2	1030.2
F140W	5136.5	6336.3
F153M	749.4	1144.6
F160W	3021.0	4527.5
F164N	204.0	301.0
F167N	197.4	295.3

¹ Cool star has spectral type M5V; hot star has spectral type O3V. See text for full definition.

Table D.2: Count Rates (e⁻/s) for source with H=15 renormalized to Bessell/H.

WFC3 IR filter	Cool star ¹	Hot star ¹
F098M	1540.5	5141.9
F105W	2751.2	7706.9
F110W	4610.7	10850.3
F125W	2769.1	4982.5
F126N	137.2	226.2

F127M	671.7	1065.4
F128N	148.3	229.7
F130N	149.6	224.8
F132N	142.5	210.3
F139M	478.7	744.7
F140W	3111.8	4652.4
F153M	454.0	554.7
F160W	1830.2	2202.0
F164N	123.6	112.3
F167N	119.6	104.0

¹ Cool star has spectral type M5V; hot star has spectral type O3V. See text for full definition.

Table D.3: Count Rates (e^-/s) for source with K=15 renormalized to Johnson/K.

WFC3 IR filter	Cool star ¹	Hot star ¹
F098M	1402.6	5684.4
F105W	2504.9	8520.0
F110W	4197.8	11995.0
F125W	2521.2	5508.2
F126N	124.9	250.1
F127M	611.5	1177.8
F128N	135.1	253.9
F130N	136.2	248.5
F132N	129.7	232.4
F139M	435.9	823.3
F140W	2833.2	5143.2
F153M	413.3	613.2

F160W	1666.3	2434.3
F164N	112.5	124.0
F167N	108.9	115.0

¹Cool star has spectral type M5V; hot star has spectral type O3V. See text for full definition.

Table D.4: Count Rates (e⁻/s) for source with V=15 renormalized to Johnson/V.

WFC3 IR filter	Cool star ¹	Hot star ¹
F098M	52334.0	2291.8
F105W	93463.6	3435.0
F110W	156631.7	4836.1
F125W	94070.7	2220.8
F126N	4660.4	100.8
F127M	22818.0	474.8
F128N	5039.4	102.4
F130N	5081.7	100.2
F132N	4840.2	93.7
F139M	16262.9	331.9
F140W	105713.1	2073.6
F153M	15422.3	247.1
F160W	62174.0	981.5
F164N	4197.5	50.0
F167N	4062.2	46.4

¹Cool star has spectral type M5V; hot star has spectral type O3V. See text for full definition.

Appendix E: Reduction and Calibration of WFC3 Data

Appendix Contents

- [E.1 The STScI Reduction and Calibration Pipeline](#)
- [E.2 The SMOV Calibration Plan](#)
- [E.3 The Cycle 17 Calibration Plan](#)
- [E.4 The Cycle 18 Calibration Plan](#)
- [E.5 The Cycle 19 Calibration Plan](#)
- [E.6 The Cycle 20 Calibration Plan](#)
- [E.7 The Cycle 21 Calibration Plan](#)
- [E.8 The Cycle 22 Calibration Plan](#)
- [E.9 The Cycle 23 Calibration Plan](#)
- [E.10 The Cycle 24 Calibration Plan](#)
- [E.11 The Cycle 25 Calibration Plan](#)
- [E.12 The Cycle 26 Calibration Plan](#)
- [E.13 The Cycle 27 Calibration Plan](#)

E.1 The STScI Reduction and Calibration Pipeline

In this appendix, we summarize the basic reductions and calibrations that are performed in the STScI WFC3 pipeline. The material in this appendix is intended to provide only enough background to develop robust observing proposals. The [WFC3 Data Handbook](#) provides more detailed information needed for analyzing your data.

In February 2016, the pipeline began to process WFC3/UVIS data with [*calwf3*](#) version 3.3, which incorporates two fundamental changes to the way exposures are calibrated and corrected. First, [*calwf3*](#) applies pixel-based CTE (Charge Transfer Efficiency) corrections. ([*Calwf3*](#) version 3.4, which added CTE corrections for subarray apertures, became operational in October 2016.) Second, photometric calibrations are determined and applied independently for each CCD chip. See [WFC3 Space Telescope Analysis Newsletter issue 22](#) for a summary of the changes underlying and included in [*calwf3*](#) version 3.3. [WFC3 ISR 2016-01](#) and [WFC3 ISR 2016-02](#) provide a reference guide and cookbook for [*calwf3*](#) version 3.3, respectively. [WFC3 ISR 2016-03](#) provides chip-dependent inverse sensitivities. [WFC3 ISR 2016-04](#) describes the creation of chip-dependent flat fields, which included a correction for the effect of the crosshatch pattern in the UV filters on sensitivity calibrations, based on analysis presented in [WFC3 ISR 2015-18](#) and described in [Section 5.4.3](#). [WFC3 ISR 2016-07](#) documents the changes in WFC3/UVIS component files used by SYNPHOT and PYSYNPHOT to simulate HST photometric measurements.

Science data taken by WFC3 are received from the Space Telescope Data Capture Facility and sent to the STScI OPUS pipeline, where the data are unpacked, keyword values are extracted from the telemetry stream, and the science data reformatted and repackaged into raw (uncalibrated) FITS files by the generic conversion process. All WFC3 science data products are two-dimensional images that are stored in FITS image-extension files. Like ACS and STIS images, WFC3 UVIS channel exposures are stored as triplets of FITS image extensions, consisting of science (SCI), error (ERR), and data quality (DQ) arrays. There is one triplet of image extensions for each CCD chip used in an exposure. Full-frame exposures, using both chips, therefore have two triplets of SCI, ERR, and DQ extensions in a single FITS file. UVIS subarray exposures, which use only one CCD chip, have a single triplet of extensions in their FITS files.

WFC3 IR channel exposures use the NICMOS file structure, which are quintuplets of FITS image extensions, consisting of science (SCI), error (ERR), data quality (DQ), number of samples (SAMP), and integration time (TIME) arrays. There is one quintuplet of extensions for each of the non-destructive detector readouts that make up an IR exposure. Using the maximum number of readouts (16) in an IR exposure therefore results in a single FITS file containing a total of 80 image extensions.

The raw, uncalibrated FITS files are processed through [*calwf3*](#), the software task that calibrates the data for individual exposures, producing calibrated FITS files. Exposures that are obtained as part of an associated set, such as dithered images, have [*calwf3*](#) calibration applied to the individual exposures before being processed as a set for the purpose of image combination. All calibrated images will be processed further with the STScI [AstroDrizzle](#) software, for the purpose of removing geometric distortions from individual exposures and for combining associated exposures.

The FITS file name suffixes given to WFC3 raw and calibrated data products are described in [Table E.1](#) and closely mimic the suffixes used by ACS and NICMOS. The initial input files to [*calwf3*](#) are the raw (RAW) files from generic conversion and the association (ASN) table, if applicable, for the complete observation set. Most WFC3/UVIS RAW images first go through

pixel-based CTE correction, producing a temporary, CTE-corrected RAW file with the suffix “RAC_TMP”. The RAC_TMP and original RAW files have the same calibration steps applied, producing two sets of final calibrated products (one uncorrected and one corrected for CTE). For WFC3/UVIS images, a temporary file, with the suffix “BLV_TMP” (BLC_TMP for CTE products), is created by *calwf3* once bias levels have been subtracted and the overscan regions trimmed. This file is renamed using the “FLT” (“FLC” for CTE products) suffix after the remaining standard calibrations (dark subtraction, flat fielding, etc.) have been completed. For exposures taken as part of a UVIS CR-SPLIT or REPEAT-OBS set, a parallel set of processing is performed, using the BLV_TMP/BLC_TMP files as input to an image combination and cosmic ray rejection routine. The resulting CR-combined image, with a temporary file name suffix of “CRJ_TMP” (“CRC_TMP” for CTE products), then receives the remaining standard calibrations, after which it is renamed using the “CRJ” (“CRC” for CTE products) suffix.

Table E.1: WFC3 File Name Suffixes.

File Suffix	Description	Units
_RAW (_RAC_TMP)	Raw data (with CTE correction)	DN
_ASN	Association file for observation set	
_SPT	Telemetry and engineering data	
_TRL	Trailer file with processing log	
_BLV_TMP (_BLC_TMP)	Bias subtracted individual UVIS exposure (with CTE correction)	DN
_CRJ_TMP (_CRC_TMP)	Uncalibrated, CR-rejected combined UVIS image (with CTE correction)	DN
_IMA	Calibrated intermediate IR exposure	e ⁻ /s
_FLT (_FLC)	Calibrated individual exposure (with CTE correction)	e ⁻ (UVIS) e ⁻ /s (IR)
_CRJ (_CRC)	Calibrated, CR-rejected, combined UVIS image (with CTE correction)	e ⁻
_DRZ	Calibrated, geometrically-corrected, dither-combined image	e ⁻ /s

Processing of WFC3/IR exposures results in an intermediate MULTIACCUM (IMA) file, which is a file that has had all calibrations applied (dark subtraction, linearity correction, flat fielding, etc.) to all of the individual readouts of the IR exposure. A final step in *calwf3* processing of WFC3/IR exposures produces a combined image from the individual readouts, which is stored in an FLT output product file.

The UVIS processing portion of ***calwf3*** is based on ***calacs*** calibrations of ACS/WFC CCD images, while the ***calwf3*** IR processing is very similar to ***calnica*** processing of NICMOS images. ***Calwf3*** performs the following basic science data calibrations:

- Pixel-based CTE correction (UVIS only)
- Bad pixel flagging
- Bias level subtraction (UVIS); Reference pixel subtraction (IR)
- Bias image subtraction (UVIS); Zero-read subtraction (IR)
- Dark current subtraction
- Post-Flash subtraction
- Non-linearity correction
- Flat-field correction and gain calibration
- Shutter shading correction (UVIS only)
- Up-the-ramp fitting (IR only)
- Photometric calibration
- CR-SPLIT/REPEAT-OBS image combination

As noted in the list above, the details of some calibration steps differ for UVIS and IR exposures, while others do not apply at all. The process of bias subtraction, in particular, differs for UVIS and IR exposures. The UVIS channel CCDs include regions of overscan, which are used for measuring and subtracting the overall bias level from each CCD exposure. A bias reference image is also subtracted from each science exposure to remove spatial variations in the bias. For IR exposures, the reference pixels located around the perimeter of the detector are used to track and remove changes in the overall bias level between readouts, while the image from the initial (“zeroth”) readout of the exposure is subtracted from all subsequent readouts to remove spatial bias structure.

UVIS shutter shading correction is in principle only necessary for very short duration exposures. Note, however, that testing has shown that the shading amounts to only a 0.2-0.3% variation across the field and therefore this step is normally not applied.

Up-the-ramp fitting is applied to IR exposures to determine a final signal rate for each pixel in the image. This process not only determines the best-fit rate from the individual readouts of the exposure, but also detects and removes effects due to cosmic-ray hits. This process is also capable of recovering a useful signal for pixels that go into saturation during the exposure by using only the non-saturated readouts to compute the fit.

WFC3 grism observations are handled in a special way by the pipeline. Grism observations require a special flat-fielding procedure, where the flat-field value for each pixel is based on the wavelength of the detected signal. ***Calwf3*** processing of grism images therefore uses an “identity” flat-field reference image (an image filled with values of 1.0 at each pixel), which allows for the gain calibration part of the flat-fielding step to still be applied without actually flat-fielding the science image. A separate software package, aXe, which was developed at ST-ECF and previously used for processing NICMOS and ACS spectral observations, is used to extract and calibrate one-dimensional spectra from WFC3 grism exposures (see [Section 8.5](#)). The aXe software is available in STSDAS via PyRAF. The aXe software is used to locate and extract spectra of individual sources from calibrated images and performs wavelength calibration, background subtraction, flat fielding, and absolute flux calibration for the extracted spectra.

Table E.2 shows the values assigned to pixels in the DQ arrays of calibrated images, which indicate anomalous conditions and are frequently used in downstream processes to reject a pixel value. If more than one data quality condition applies to a pixel, the sum of the values is used. Note that some flag values have different meanings for UVIS and IR images.

Table E.2: WFC3 Data Quality Flags.

FLAG Value	Data Quality Condition	
	UVIS	IR
0	OK	OK
1	Reed-Solomon decoding error	Reed-Solomon decoding error
2	Data replaced by fill value	Data replaced by fill value
4	Bad detector pixel	Bad detector pixel
8	(unused)	Unstable in zero-read
16	Hot pixel	Hot pixel
32	CTE tail	Unstable photometric response
64	Warm pixel	(Obsolete: Warm pixel)
128	Bad pixel in bias	Bad reference pixel
256	Full-well saturation	Full-well saturation
512	Bad or uncertain flat value	Bad or uncertain flat value
1024	Charge trap	(unused)
2048	A-to-D saturation	Signal in zero-read
4096	Cosmic ray detected by AstroDrizzle	Cosmic ray detected by AstroDrizzle
8192	Cosmic ray detected during CR-SPLIT or REPEAT-OBS combination	Cosmic ray detected during up-the-ramp fitting
16384	Pixel affected by ghost or crosstalk (not used)	Pixel affected by crosstalk (not used)

E.2 The SMOV Calibration Plan

The Servicing Mission Observatory Verification (SMOV) plan for WFC3 was executed following its successful installation in HST in May, 2009. The calibration plan consisted of engineering, alignment, and calibration activities whose principal goal was to verify that the instrument would be ready for science at the beginning of Cycle 17 in August, 2009. WFC3's SMOV activities began on 25 May 2009 with the Activation Test. The first set of SMOV imaging data were acquired on 11 June 2009, and the last in the first week of September. Because of the short duration, only a critical subset of WFC3's imaging and spectroscopic modes were calibrated. All of the 44 activities are presented in Table E.3. The proposals and observation dates can be viewed by entering the Proposal ID into the [HST Program Information webpage](#). Most of these activities have an associated Instrument Science Report, published in 2009 with the proposal number in the title, and are available on the WFC3 website at: <http://www.stsci.edu/hst/wfc3/documents/ISRs/>.

Table E.3: SMOV4 Calibration Programs.

Proposal ID	Title
11454	Activation Test
11357	Memory Test
11358	Sci Data Buffer Test
N/A	UVIS CCD Cooldown
N/A	IR Detector Cooldown
11419	UVIS Det Functional
11420	IR Det Functional
11421	CSM Test
11422	UVIS SOFA Test
11529	UVIS Spare Tungsten Lamp
11423	IR FSM Test
11543	IR Spare Tungsten Lamp
11424	UVIS Initial Alignment
11425	IR Initial Alignment
11426	UVIS Contam Monitor
11427	UVIS Shutter Test
11428	D2 Cal Lamp Test

N/A	UVIS TEC Performance
N/A	IR TEC Performance
11431	UVIS Hot Pixel Anneal
11432	UVIS Int Flats
11433	IR Int Flats
11434	UVIS Fine Alignment
11435	IR Fine Alignment
11436	UVIS Image Quality
11437	IR Image Quality
11438	UVIS PSF Wings
11439	IR PSF Wings
11549	UVIS & IR Pointing Stability
11442	FGS-UVIS Update
11443	FGS-IR Update
11444	UVIS Plate Scale
11445	IR Plate Scale
11446	UVIS Dark, Noise, Backgnd
11447	IR Dark, Noise, Backgnd
11448	UVIS SAA Passage
11449	IR SAA Passage
11450	UVIS Phot Zero Points
11451	IR Phot Zero Points
11452	UVIS Flat Field Uniformity
11453	IR Flat Field Uniformity
11552	IR Grisms
11798	UVIS PSF Core Modulation
11808	UVIS Bowtie Monitor

E.3 The Cycle 17 Calibration Plan

The Cycle 17 calibration plan was executed from August 2009 through November 2010. The calibration programs comprising this plan are listed in Table E.4. The proposals and observation dates can be viewed by entering the Proposal ID into the [HST Program Information webpage](#). The initial plan provided improved photometric, spectroscopic, flat field, and geometric distortion values and additional on-orbit detector characterization. Supplemental programs, beginning with proposal ID 12087, were introduced mid-cycle to provide data needed to improve calibration in specific areas and to characterize problems or anomalies.

The results of these calibration programs have been documented in Instrument Science Reports on the WFC3 website at: <http://www.stsci.edu/hst/instrumentation/wfc3/documentation/instrument-science-reports-isrs>.

The overall Cycle 17 calibration plan is discussed in [WFC3 ISR 2009-08](#), with more details available concerning the photometric calibration of WFC3 ([WFC3 ISR 2009-05](#)) and the detector monitoring campaign ([WFC3 ISR 2009-07](#)). Galactic cluster observations are a cornerstone of the Cycle 17 calibration effort ([WFC3 ISR 2009-06](#)).

Table E.4: Cycle 17 Calibration Programs.

Proposal ID	Title
11903	UVIS Zero Points
11904	UVIS Droplets
11905	UVIS CCD Daily Monitor
11906	UVIS CCD Gain
11907	UVIS Contamination Monitor
11908	Bowtie Monitor
11909	UVIS Hot Pixel Anneal
11911	UVIS L-Flats & Geometric Distortion
11912	UVIS Internal Flats
11913	IR Filter Wedge Check
11914	UVIS Earth Flats

11915	IR Internal Flats
11916	IR Intrapixel Sensitivity
11917	IR Earth Flats
11918	UVIS Image Quality
11919	UVIS PSF Wings
11920	IR Image Quality
11921	IR PSF Wings
11922	UVIS Fringing
11923	UVIS Filter Wedge Check
11924	UVIS CTE Monitoring
11925	UVIS Linearity
11926	IR Zero Points
11927	IR Persistence
11928	IR L-Flats and Geometric Distortion
11929	IR Dark Monitor
11930	IR Gain
11931	IR Count Linearity
11932	IR Stray Light
11933	IR Rate-Dependent Non-Linearity
11934	UVIS G280 Flux Calibration
11935	UVIS G280 Wavelength Calibration
11936	IR Grism Flux Calibration
11937	IR Grism Wavelength Calibration
11938	UVIS Stray Light
12087	WFC3 IR subarray anomaly
12088	Tungsten lamp warm-up time
12089	Persistence - Part 2

12090	WFC3/UVIS Photometric Calibration - The Spatial Stability of the Detector
12091	WFC3/UVIS Fringe Calibration - Part 2
12092	UVIS Stray Light Characterization
12093	IR non-linearity calibration using subarrays
12094	WFC3/UVIS image skew
12325	Photometry with Spatial Scans

E.4 The Cycle 18 Calibration Plan

The Cycle 18 calibration plan is summarized in [WFC3 ISR 2011-14](#). It was executed from October 2010 through September 2011. The calibration programs comprising this plan are listed in Table E.5. The proposals and observation dates can be viewed by entering the Proposal ID into the [HST Program Information webpage](#). The Cycle 18 plan provides less frequent monitoring of characteristics that were demonstrated to be stable during Cycle 17. It places increased emphasis on characterizing IR persistence, measuring UVIS and IR flat fields, calibrating the IR grism, monitoring CTE on the UVIS detector, and quantifying the ability to do high contrast imaging on both detectors. It tests CTE mitigation procedures and the performance of spatial scans for high S/N IR observations.

The results of these calibration programs have been documented in Instrument Science Reports on the WFC3 website at: <http://www.stsci.edu/hst/instrumentation/wfc3/documentation/instrument-science-reports-isrs>.

Table E.5: Cycle 18 Calibration Programs

Proposal ID	Title
12333	UVIS&IR Zeropoint Stability Monitor
12334	UVIS & IR Photometric Calibration
12335	IR Color Transformation with asterisms
12336	Scan Enabled Photometry
12337	UVIS Flat Field Stability
12338	IR Flat Field Stability Monitor
12339	UVIS L-Flat Correction
12340	IR L-Flat Correction
12341	IR Blob Photometry Test
12342	UVIS Darks and Bias Monitor
12343	UVIS Anneal
12344	UVIS Bowtie Monitor
12345	UVIS Long Darks Test
12346	UVIS CCD Gain Stability Test
12347	UVIS Internal CTE Monitor: EPER
12348	UVIS Charge Injection Test

12349	IR Dark Monitor
12350	IR Gain Monitor
12351	IR Persistence Experiments
12352	IR Non-linearity (full frame & subarrays)
12353	UVIS & IR Geometric Distortion Corrections
12354	High Contrast Imaging
12355	IR Grism Wavelength and LSF Calibration
12356	IR Grism Wavelength Calibration Stability Test
12357	IR Grism Flux Calibration Monitor
12358	IR Grism L-flat Correction and Independent 2-D Wavelength Solution
12359	UVIS Grism Wavelength Calibration
12379	UVIS CTE Monitor: Star Clusters

E.5 The Cycle 19 Calibration Plan

The Cycle 19 calibration plan was executed from October 2011 through October 2012. It is discussed in [WFC3 ISR 2012-04](#).

The calibration programs comprising this plan are listed in Table E.6. The proposals and observation dates can be viewed by entering the Proposal ID into the [HST Program Information webpage](#).

The Cycle 19 calibration plan was designed to:

- continue to maintain and update the standard reference files (biases, darks, IR non-linearity, UVIS and IR geometric distortion table)
- monitor the pixel-to-pixel response of both channels and the hysteresis (QE) offset
- validate the temporal and spatial photometric performance of the WFC3 channels
- characterize and model the persistence effects in the IR detector and verify the temporal behavior
- characterize and model the charge transfer efficiency (CTE) in the UVIS channel, including analysis and calibration of the post-flash option
- improve the wavelength and flux calibration over the whole detector for all the WFC3 grisms
- validate in-flight correction of the flat fields
- improve the accuracy of the absolute photometric calibration

The results of these calibration programs are being documented in Instrument Science Reports on the WFC3 website at:
<http://www.stsci.edu/hst/instrumentation/wfc3/documentation/instrument-science-reports-isrs>

Table E.6: Cycle 19 Calibration Programs

Proposal ID	Title
12687	UVIS Anneal
12688	UVIS Bowtie Monitor
12689	UVIS CCD Daily Monitor
12690	UVIS CCD Gain Stability
12691	UVIS CTI Monitor (EPER)
12692	UVIS CTE Monitor (Star Clusters)
12693	UVIS Charge Injection
12694	IR Persistence Strength
12695	IR Dark Monitor
12696	IR Linearity Monitor
12697	IR Gain Monitor

12698	WFC3 Contamination & Stability Monitor
12699	WFC3 Photometric Calibration & Calibration Flux Ladder
12700	Extending the Range & Precision of the Count Rate non Linearity
12701	WFC3 PSF Wings
12702	IR Grisms: Flux/Trace Calibration & Stability
12703	IR Grisms: Wavelength Calibration & Stability
12704	UVIS Grism: Flux Calibration
12705	UVIS Grism: Wavelength Calibration & Stability
12706	UVIS Flare Wavelength Dependence
12707	UVIS Spatial Sensitivity
12708	IR Spatial Sensitivity
12709	UVIS & IR Moonlit Flats
12710	UVIS Bright Earth Flats
12711	UVIS Internal Flats
12712	IR Internal Flats
12713	Spatial Scanned L-flat Validation Pathfinder
12714	UVIS & IR Geometric Distortion
12784	Characterization of UVIS Traps Via Charge-Injected Biases
12794	Repeatability of High Precision Photometry and Astrometry in Spatially Scanned UVIS Data
12798	Bias, Dark, and Charge Injection (CI) for UVIS Binned mode
12802	WFC3 Post-Flash Characterization
12803	Guard Darks
12808	Characterization of UVIS Pixel-to-Pixel QE Variations Via Internal Flats
13068	WFC3 Blob Monitor Using Dark-Earth IR Flats
13069	WFC3 UVIS Post-Flash Calibration
13103	WFC3/UVIS Anneal
13104	UVIS Bowtie Monitor

E.6 The Cycle 20 Calibration Plan

The Cycle 20 calibration plan is summarized in [WFC3 ISR 2013-05](#). It was executed from November 2012 through October 2013.

The calibration programs comprising this plan are listed in Table E.7. The proposals and observation dates can be viewed by entering the Proposal ID into the [HST Program Information webpage](#).

The Cycle 20 calibration plan was designed to:

- continue to maintain and update the standard reference files (biases, darks, linearity, CTE traps)
- continue to monitor the instrument (throughput, gain, hysteresis, bad/hot pixels, filter transmission, IR blobs, grism calibration, CTE decline, stability of post-flash)
- improve photometric precision (CTE correction, IR flat fields, dynamic range)
- improve astrometric precision (spatial scans, DGEO files)
- enhance UV calibration (flat fields, post-flash and CTE correction)
- improve our understanding of IR persistence, IR blobs and the CSM, anomalous QE in CCD pixels

The results of these calibration programs will be documented in Instrument Science Reports on the WFC3 website at:
<http://www.stsci.edu/hst/instrumentation/wfc3/documentation/instrument-science-reports-isrs>

Table E.7: Cycle 20 Calibration Programs

Proposal ID	Title
13071	UVIS Anneal
13072	UVIS Bowtie Monitor
13073	UVIS CCD Daily Monitor A
13074	UVIS CCD Daily Monitor B
13075	UVIS CCD Daily Monitor C
13076	UVIS CCD Daily Monitor D
13077	IR Dark Monitor
13078	UVIS Post-Flash Monitor
13079	IR Linearity Monitor
13080	IR Gain Monitor

13081	Guard Dark for MCT Programs
13082	UVIS CTI Monitor (E珀ER)
13083	UVIS CTE Monitor (star clusters)
13084	Characterization of UVIS Traps with CI
13085	Line 10 CI Bias
13086	IR Persistence Behaviors as Function of Saturation Time
13087	IR Persistence Model Tests
13088	WFC3 Contamination & Stability Monitor
13089	WFC3 UVIS & IR Photometry
13090	UVIS Grism: Flux Calibration
13091	UVIS Grism: Wavelength Calibration
13092	IR Grisms: Flux Calibration
13093	IR Grisms: Wavelength Calibration
13094	IR Grism -1 Order Calibration
13095	UVIS L-Flat via Spatial Scans
13096	UVIS Flat Field Validation
13097	UVIS Internal Flats
13098	IR Internal Flats
13099	IR Earth Flats
13100	UVIS & IR Geometric Distortion
13101	High Precision Astrometry
13168	UVIS CCD Gain Stability
13169	CCD Anomalous QE pixels
13499	WFC3 Blob Monitor Using Dark-Earth IR Flats

E.7 The Cycle 21 Calibration Plan

The Cycle 21 calibration plan is summarized in [WFC3 ISR 2014-07](#). It was executed from November 2013 through October 2014.

The calibration programs comprising this plan are listed in Table E.8. The proposals and observation dates can be viewed by entering the Proposal ID into the [HST Program Information webpage](#).

The Cycle 21 calibration plan was designed to:

- continue to maintain and update the standard reference files (biases, darks, linearity, CTE traps)
- continue to monitor the instrument (throughput, gain, hysteresis, bad/hot pixels, filter transmission, IR blobs, grism calibration, CTE decline, stability of post-flash)
- improve photometric precision (CTE correction, IR flat fields, dynamic range, IR persistence)
- improve astrometric precision (spatial scans, DGEO files)
- enhance UV calibration (flat fields, post-flash and CTE correction)
- improve our understanding of IR persistence, IR blobs and the CSM, anomalous QE in CCD pixels

The results of these calibration programs will be documented in Instrument Science Reports on the WFC3 website at:
<http://www.stsci.edu/hst/instrumentation/wfc3/documentation/instrument-science-reports-isrs>

Table E.8: Cycle 21 Calibration Programs

Proposal ID	Title
13554	UVIS anneal
13555	UVIS bowtie monitor
13556	UVIS CCD daily monitor A
13557	UVIS CCD daily monitor B
13558	UVIS CCD daily monitor C
13559	UVIS CCD un-flashed monitor
13560	UVIS post-flash monitor
13561	UVIS CCD gain stability
13562	IR dark monitor
13563	IR linearity monitor
13564	IR gain monitor
13565	UVIS CTI monitor (EPER)

13566	UVIS CTE monitor (star cluster)
13567	CTE characterization with post-flashed darks
13568	Characterization of the charge-level dependence of CTE losses
13569	Characterization of UVIS traps with CI
13570	UVIS & IR geometric distortion
13571	High precision astrometry
13572	IR persistence model tests
13573	Trapping mitigation in spatial scan observations of exosolar planets
13574	WFC3 contamination & stability monitor
13575	WFC3 UVIS & IR photometry
13576	IR grisms: cross check sensitivity function of hot and cool stars
13577	UVIS grisms: flux calibration
13578	UVIS grisms: wavelength calibration
13579	IR grisms: flux calibration
13580	IR grisms: wavelength calibration
13581	IR grisms: sky characterization
13582	Calibration of the IR grism wavelength ZPs
13583	UV flats spatial scan
13584	UV flat field validation
13585	CCD anomalous QE pixels
13586	UVIS internal flats
13587	IR internal flats
13588	CSM monitor with earth flats
13624	Monitoring Persistence after scanned grism observations
13625	Characterizing persistence following scanned grism observations
13627	Timing verification for spatial scan observations

E.8 The Cycle 22 Calibration Plan

The Cycle 22 calibration plan is summarized in [WFC3 ISR 2015-07](#). It was executed from November 2014 through October 2015.

The calibration programs comprising this plan are listed in Table E.9. The proposals and observation dates can be viewed by entering the Proposal ID into the [HST Program Information webpage](#).

The Cycle 22 calibration plan was designed to:

- maintain and update the standard reference files (biases, darks, linearity CTE traps, UVIS anomalous QE pixels)
- monitor the health of the instrument (throughput, gain, hysteresis, bad/hot pixels, wavelength and flux stability of grisms; filter transmission, number of IR blobs, CTE decline, stability of the post-flash LED, state of the CSM)
- improve astrometric precision (in narrow and medium band filters, and with spatial scan)
- improve the characterization of persistence in IR observations

The results of these calibration programs will be documented in Instrument Science Reports on the WFC3 website at:
<http://www.stsci.edu/hst/instrumentation/wfc3/documentation/instrument-science-reports-isrs>

Table E.9: Cycle 22 Calibration Programs

Proposal ID	Title
14000	UVIS Anneal
14001	UVIS Bowtie Monitor
14002	UVIS Daily Monitor A
14003	UVIS Daily Monitor B
14004	UVIS Daily Monitor C
14005	UVIS Unflashed Monitor
14006	UVIS Post-Flash Monitor
14007	UVIS CCD Gain Stability
14008	IR Dark Monitor
14009	IR Linearity Monitor
14010	IR Gain Monitor
14011	UVIS CTI Monitor (EPER)
14012	UVIS CTE Monitor (Star cluster)

14013	UVIS CTE in subarrays
14014	UVIS Traps with CI
14015	Refining IR Persistence Model
14016	Short term IR Persistence
14017	Persistence after Worst Actors
14018	UVIS Contam Monitor
14019	UVIS Shutter Characterization
14020	Photometric Repeatability
14021	UVIS & IR Photometry Zero Points
14022	IR Observations of Red CALSPEC Stars
14023	IR Grism wavelength Calibration stability
14024	IR Grisms flux and trace calibration stability
14025	UVIS Grism wavelength Calibration stability
14026	UVIS Grisms flux and trace calibration stability
14027	UVIS Pixel variations via int-flat monitor
14028	UVIS Internal Flats
14029	IR Internal Flats
14030	CSM monitor Earth Flats
14031	Astrometric Validation of UVIS Filters
13929	High precision calibration of UVIS Geometric distortion

E.9 The Cycle 23 Calibration Plan

The Cycle 23 calibration plan is being executed from October 2015 through October 2016.

The calibration programs comprising this plan are listed in Table E.10. The proposals and observation dates can be viewed by entering the Proposal ID into the [HST Program Information webpage](#).

The Cycle 23 calibration plan was designed to:

- maintain and update the standard reference files (biases, darks, linearity, CTE traps, UVIS anomalous QE pixels, post-flash)
- monitor the health of the instrument (throughput, gain, hysteresis, bad/hot pixels, wavelength and flux stability of grisms; filter transmission, number of IR blobs, CTE decline, stability of the post-flash LED, state of the CSM)
- improve astrometric precision (in narrow and medium band filters, and with spatial scan)
- improve the characterization of persistence in IR observations

The results of these calibration programs will be documented in Instrument Science Reports on the WFC3 website at:
<http://www.stsci.edu/hst/instrumentation/wfc3/documentation/instrument-science-reports-isrs>

Table E.10: Cycle 23 Calibration Programs

Proposal ID	Title
14366	UVIS Anneal
14367	UVIS Bowtie Monitor
14368	UVIS Daily Monitor A
14369	UVIS Daily Monitor B
14370	UVIS Daily Monitor C
14371	UVIS Unflashed Monitor
14372	UVIS Post-Flash Monitor
14373	UVIS CCD Gain Stability
14374	IR Dark Monitor
14375	IR Linearity Monitor
14376	IR Gain Monitor
14377	UVIS CTI Monitor (EPER)
14378	UVIS CTE Monitor (Star cluster)

14379	UVIS Traps with CI
14380	IR Persistence: Amplitude Variations
14381	IR Persistence: Improve the Position Dependent Model
14382	UVIS Contamination and Stability Monitor
14383	UVIS Shutter Characterization
14384	UVIS & IR Photometry Zero Points
14385	IR Grisms: Wavelength Calibration
14386	IR Grisms: Trace and Flux Calibration
14387	UVIS Grism Wavelength Calibration Stability
14388	-1st Order Grism Calibration in IR Grisms
14389	UVIS Pixel Variations Via Int-flat Monitor
14390	UVIS Internal Flats
14391	IR Internal Flats
14392	CSM monitor Earth Flats
14393	Astrometric Calibration of All Remaining UVIS Filters
14394	Time Dependence of X-CTE & Astrometry

E.10 The Cycle 24 Calibration Plan

The Cycle 24 calibration plan is being executed from November 2016 through October 2017. The individual programs are listed in Table E.11 and are described in more detail on the [WFC3 Calibration Plan webpage](#). Following the link to Cycle 24 Calibration, a similar table may be found with direct links to the phase II programs and observation dates. This information may alternately be accessed via the [HST Program Information webpage](#) by entering the Proposal ID.

The [WFC3 Cycle 24 webpage](#) also links to a PDF presentation summarizing WFC3 usage in the latest cycle and comparing the current plan with the prior cycle. This document contains more details on the calibration justification and in many cases includes supporting figures with the latest results from regular monitoring.

The Cycle 24 calibration plan was designed to:

- maintain and update the standard reference files (biases, darks, linearity, CTE traps, UVIS anomalous QE pixels, post-flash)
- monitor the health of the instrument (throughput, gain, hysteresis, bad/hot pixels, sink pixels, CTE decline, stability of the post-flash LED, filter transmission, wavelength and flux stability of grisms, number of IR blobs, state of the CSM)
- test the precision of the IR count rate non-linearity correction for faint targets and determine whether a wavelength-dependent correction is required
- improve the precision of the UVIS contamination monitor by making use of spatially scanned observations of photometric standards
- re-evaluate the 2013 UVIS pixel-based CTE model and verify that the recommended post-flash level has not changed

The results of these calibration programs will be documented in Instrument Science Reports on the WFC3 website at:
<http://www.stsci.edu/hst/wfc3/documents/ISRs/>

Table E.11: Cycle 24 Calibration Programs

Proposal ID	Title
14529	UVIS Anneal
14530	UVIS Bowtie Monitor
14531	UVIS Daily Monitor A
14532	UVIS Daily Monitor B
14533	UVIS Daily Monitor C
14534	UVIS Unflashed Monitor
14535	UVIS Post-Flash Monitor
14536	UVIS CCD Gain Stability

14537	IR Dark Monitor
14538	IR Linearity Monitor
14539	IR Gain Monitor
14540	UVIS CTI Monitor (EPER)
14541	UVIS CTE Monitor (Star cluster)
14542	UVIS Traps with CI
14815	UVIS Contamination and Stability Monitor
14543	IR Grisms: Wavelength Calibration
14544	IR Grisms: Trace and Flux Calibration
14545	UVIS Grism Wavelength Calibration Stability
14546	UVIS Pixel-to-Pixel QE Variations Via Internal Flats
14547	UVIS Internal Flats
14548	IR Internal Flats
14549	CSM monitor Earth Flats
14550	WFC3 Astrometric Scale Monitoring
14868 ¹	Improved Precision, Wavelength Dependence of the IR Count Rate Non-Linearity
14870 ¹	IR Zeropoint Linearity
14871 ¹	Improving the CALSPEC model for GRW+70D5824
14878 ¹	UVIS Contamination Using Spatial Scans
14879 ¹	UVIS Sink Pixel Map Update
14880 ¹	UVIS CTE Model Re-characterization
14881 ¹	UVIS CTE Pixel-Based Model Evaluation
14882	UVIS Shutter Monitoring
14883	WFC3 UVIS & IR Photometry

¹New programs this cycle; others are routine monitors.

E.11 The Cycle 25 Calibration Plan

The Cycle 25 calibration plan is being executed from November 2017 through October 2018. The individual programs are listed in Table E.12 and are described in more detail on the [WFC3 Calibration Plan webpage](#). Following the link to Cycle 25 Calibration, a similar table may be found with direct links to the phase II programs and observation dates. This information may alternately be accessed via the [HST Program Information webpage](#) by entering the Proposal ID.

The [WFC3 Cycle 25 webpage](#) also links to a PDF presentation summarizing WFC3 usage in the latest cycle and comparing the current plan with the prior cycle. This document contains more details on the calibration justification and in many cases includes supporting figures with the latest results from regular monitoring.

The Cycle 25 calibration plan was designed to:

- maintain and update the standard reference files (biases, darks, linearity, CTE traps, UVIS anomalous QE pixels, post-flash)
- monitor the health of the instrument (throughput, gain, hysteresis, bad/hot pixels, sink pixels, CTE decline, stability of the post-flash LED, filter transmission, wavelength and flux stability of grisms, number of IR blobs, state of the CSM)
- improve the precision of the UVIS contamination monitor by using spatially scanned observations of photometric standards
- quantify color terms for the UVIS filters and recheck the photometric calibration at the center of the detector
- test a strategy to mitigate IR persistence using the calibration lamps to fill charge traps prior to obtaining science observations

The results of these calibration programs will be documented in Instrument Science Reports on the WFC3 website at:
<http://www.stsci.edu/hst/instrumentation/wfc3/documentation/instrument-science-reports-isrs>

Table E.12: Cycle 25 Calibration Programs.

Program ID	Title
14978	WFC3 UVIS Anneal
14979	WFC3 UVIS Bowtie Monitor
14980	WFC3 UVIS CCD Daily Monitor (darks & biases) (Part 1)
14981	WFC3 UVIS CCD Daily Monitor (darks & biases) (Part 2)
14982	WFC3 UVIS CCD Daily Monitor (darks & biases) (Part 3)
14983	WFC3 UVIS CCD Un-flashed Monitor
14984	WFC3 UVIS Post-flash Monitor
14985	WFC3 UVIS CCD Gain Stability
14986	WFC3 IR Dark Monitor

14987	WFC3 IR Linearity Monitor
14988	WFC3 IR Gain Monitor
14989	WFC3 UVIS CTI monitor (EPER)
14990	WFC3 UVIS CTE monitor (star cluster)
14991	WFC3 Characterization of UVIS traps with CI
14992	WFC3 UVIS & IR photometry
14993	WFC3 IR grisms wavelength calibration
14994	WFC3 IR grisms flux/trace calibration
14995	WFC3 UVIS grism wavelength calibration
14996	WFC3 UVIS Pixel-to-Pixel QE Variations via Internal Flats
14997	WFC3 UVIS Internal Flats
14998	WFC3 IR Internal Flats
14999	WFC3 CSM monitor with Earth Flats
15000	WFC3 Astrometric scale monitoring
15397	UVIS shutter monitoring
15398	UVIS contamination monitor (staring and scans)
15399 ¹	UVIS Supplemental Photometry: Color Terms & Revisiting M512
15400 ¹	Mitigating Persistence for Time-Series Observations

¹New programs this cycle; others are routine monitors.

E.12 The Cycle 26 Calibration Plan

The Cycle 26 calibration plan is being executed from November 2018 through October 2019. The individual programs are listed in Table E.13 and are described in more detail on the [WFC3 Calibration Plan webpage](#). Following the link to Cycle 26 Calibration, a similar table may be found with direct links to the phase II programs and observation dates. This information may alternately be accessed via the [HST Program Information webpage](#) by entering the Proposal ID.

The [WFC3 Cycle 26 webpage](#) also links to a PDF presentation summarizing WFC3 usage in the latest cycle and comparing the current plan with the prior cycle. This document contains more details on the calibration justification and in many cases includes supporting figures with the latest results from regular monitoring.

The Cycle 26 calibration plan was designed to:

- Maintain and update the standard reference files (biases, darks, linearity, CTE traps, UVIS anomalous QE pixels, post-flash)
- Monitor the health of the instrument (throughput, gain, hysteresis, bad/hot pixels, sink pixels, CTE decline, stability of the post-flash LED, filter transmission, state of the CSM, number of IR blobs, wavelength and flux stability of the grisms)
- Support new initiatives and obtain supplemental (non-routine) calibration data

In this cycle, two new calibration programs will supplement the standard monitoring data. These programs (15585, 15581) were designed to:

- Cross-calibrate the HST focus values derived from the OTA Focus monitor (based on UVIS/F410M observations) with the focus values derived empirically from the WFC3/UVIS PSF database, which has many more F606W observations
- Characterize the decay of IR persistence at short time-scales ($t < 300$ sec), where the observed residual signal deviates from the current power-law model

The results of these calibration programs will be documented in Instrument Science Reports on the WFC3 website at:
<http://www.stsci.edu/hst/instrumentation/wfc3/documentation/instrument-science-reports-isrs>

Table E.13: The Cycle 26 Calibration Programs

Program ID	Title
15567	WFC3 UVIS Anneal
15568	WFC3 UVIS Bowtie Monitor
15569	WFC3 UVIS CCD Daily Monitor (Darks and Biases) Part 1
15570	WFC3 UVIS CCD Daily Monitor (Darks and Biases) Part 2
15571	WFC3 UVIS CCD Daily Monitor (Darks and Biases) Part 3
15572	WFC3 UVIS CCD Unflashed (CTE) Monitor

15573	WFC3 UVIS Post-flash Monitor
15574	WFC3 UVIS CCD Gain Stability
15575	WFC3 UVIS CTI Monitor (EPER)
15576	WFC3 UVIS CTE Monitor (star cluster)
15577	WFC3 Characterization of UVIS traps with Charge Injection
15578	WFC3 IR Dark Monitor
15579	WFC3 IR Linearity Monitor
15580	WFC3 IR Gain Monitor
15581	WFC3 Short-term IR Persistence
15582	WFC3 UVIS & IR Photometry
15583	WFC3 UVIS Contamination Monitor (staring and scans)
15584	WFC3 UVIS Shutter Monitoring
15585	WFC3 Focus Cross-Calibration
15586	WFC3 IR Grism Wavelength Calibration
15587	WFC3 IR Grism Flux/trace Calibration
15588	WFC3 UVIS Grism Wavelength Calibration
15589	WFC3 UVIS Pixel-to-Pixel QE Variations via Internal Flats
15590	WFC3 UVIS Internal Flats
15591	WFC3 IR Internal Flats
15592	WFC3 CSM Monitor with Earth Flats
15593	WFC3 Astrometric Scale Monitoring

E.13 The Cycle 27 Calibration Plan

The Cycle 27 calibration plan is being executed from November 2019 through October 2020. The individual programs are listed in Table E.14 and are described in more detail on the [WFC3 Calibration Plan webpage](#). Following the link to Cycle 27 Calibration, a similar table may be found with direct links to the phase II programs and observation dates. This information may alternately be accessed via the [HST Program Information webpage](#) by entering the Proposal ID.

The [WFC3 Cycle 27 webpage](#) also links to a PDF presentation summarizing WFC3 usage in the latest cycle and comparing the current plan with the prior cycle. This document contains more details on the calibration justification and in many cases includes supporting figures with the latest results from regular monitoring.

The Cycle 27 calibration plan was designed to:

- Maintain and update the standard reference files (biases, darks, linearity, CTE traps, UVIS anomalous QE pixels, post-flash)
- Monitor the health of the instrument (throughput, gain, hysteresis, bad/hot pixels, sink pixels, CTE decline, stability of the post-flash LED, filter transmission, state of the CSM, number of IR blobs, wavelength and flux stability of the grisms)
- Support new initiatives and obtain supplemental (non-routine) calibration data

In this cycle, two standard monitoring programs have been restructured from Cycle 26. These programs (16021, 16030) were designed to:

- Quantify losses in the UVIS sensitivity using spatial scans (previously called 'UVIS Contamination Monitor')
- Monitor the 'UVIS and IR Photometric Calibration' via staring mode observations of HST standards

Five new calibration programs will supplement the standard monitoring. These programs (16020, 16022, 16023, 16029, 16031) were designed to:

- Measure the stability of the tungsten lamp output immediately after turn-on
- Refine the UVIS grism wavelength calibration across the entire detector with better 2D sampling
- Finalize the flux calibration of the UVIS grism with similar spatial sampling as for the wavelength calibration
- Recheck the optimal UVIS background level to mitigate CTE losses
- Check for time dependent sensitivity in the IR detector grisms and filters

The results of these calibration programs will be documented in Instrument Science Reports on the WFC3 website at:
<http://www.stsci.edu/hst/instrumentation/wfc3/documentation/instrument-science-reports-isrs>

Table E.14: The Cycle 27 Calibration Programs

Program ID	Title
15712	WFC3 UVIS Anneal
15713	WFC3 UVIS Bowtie Monitor
15714	WFC3 UVIS CCD Daily Monitor (Darks and Biases) Part 1

15715	WFC3 UVIS CCD Daily Monitor (Darks and Biases) Part 2
15716	WFC3 UVIS CCD Daily Monitor (Darks and Biases) Part 3
15717	WFC3 UVIS CCD Unflashed (CTE) Monitor
15718	WFC3 UVIS Post-flash Monitor
15719	WFC3 UVIS CCD Gain Stability
15720	WFC3 UVIS CTI Monitor (EPER)
15721	WFC3 UVIS CTE Monitor (star cluster)
15722	WFC3 Characterization of UVIS traps with Charge Injection
15723	WFC3 IR Dark Monitor
15724	WFC3 IR Linearity Monitor
15725	WFC3 IR Gain Monitor
15726	WFC3 UVIS Shutter Monitoring
15727	WFC3 IR Grism Wavelength Calibration
15728	WFC3 IR Grism Flux/trace Calibration
15729	WFC3 UVIS Pixel-to-Pixel QE Variations via Internal Flats
15730	WFC3 UVIS Internal Flats
15731	WFC3 IR Internal Flats
15732	WFC3 CSM Monitor with Earth Flats
15733	WFC3 Astrometric Scale Monitoring
16020	WFC3 Tungsten Lamp Warmup
16021	WFC3 UVIS Time Dependent Sensitivity
16022	WFC3 UVIS Grism Wavelength Calibration
16023	WFC3 UVIS Grism Flux Calibration
16029	WFC3 UVIS Background Check
16030	WFC3 UVIS & IR Photometry Monitor
16031	IR Time Dependent Sensitivity

Glossary

The following terms and acronyms are used in this Handbook.

ADU	Analog-to -digital Unit
ADC	Analog to digital Converter
ABMAG	$-2.5 \log (F_v) - 48.60$ where F_v is the flux from the source in $\text{erg cm}^{-2} \text{ sec}^{-1} \text{ Hz}^{-1}$
AB_v	Correction to ABMAG to account for the fact that the source spectrum is not constant in F_v ($\text{ABMAG}=V+\text{AB}_v$)
ACS	Advanced Camera for Surveys
APT	Astronomer's Proposal Tool
aXe	Spectroscopic Data Extraction Software
BOP	Bright Object Protection
calwf3	WFC3 calibration pipeline software
CCD	Charge Coupled Device. Solid-state, photon counting device
CDS	Correlated Double Sampling
COS	Cosmic Origins Spectrograph
CP	Call for Proposals
CR	Cosmic ray
CR-SPLIT	Division of a CCD exposure into shorter exposures to be used for cosmic ray rejection
CSM	Channel select mechanism
CTE	Charge Transfer Efficiency
CVZ	Continuous Viewing Zone
DCL	Detector Characterization Laboratory at NASA GSFC
DN	Data Number
DQ	Data Quality
EE	Encircled energy
ETC	Exposure Time Calculator. ETCs are Web-based tools which can be accessed through the WFC3 webpages .

FET	Field-effect Transistor
FGS	Fine Guidance Sensors
FITS	Flexible Image Transport System.
FOV	Field of View
FPA	Focal-Plane Array
FSM	Filter select mechanism
FWHM	Full width at half maximum
GO	General Observer
GSC	Guide Star Catalog
GSFC	NASA's Goddard Space Flight Center
Help Desk	Facility for getting help on <i>HST</i> related topics: http://hsthelp.stsci.edu or help@stsci.edu .
HRC	High Resolution Channel of ACS (non-operational)
HST	Hubble Space Telescope
IPT	Integrated Product Team
IR	Infrared
IRAF	Image Reduction and Analysis System. The environment in which -STSDAS operates.
ISR	Instrument Science Report
K	Degree Kelvin
MBE	Molecular-beam Epitaxial
MPP	Multi Pinned Phased, a CCD mode that reduces dark current rate
MTF	Modulation Transfer Function
MUX	Multiplexer
NICMOS	Near-Infrared Camera and Multi-Object Spectrograph
NUV	Near ultraviolet (~2000–4000 Å)
OTA	Optical Telescope Assembly
PASP	Publications of the Astronomical Society of the Pacific

Phase I	A proposal for observing time on <i>HST</i>
Phase II	An approved <i>HST</i> proposal; includes precise detail of how program is to be executed
PI	Principal investigator
POM	Pick-off Mirror
PRF	Pixel Response Function
PSF	Point-spread function
PyRAF	version of IRAF implemented in the Python language
QE	Quantum efficiency
ramp	A sequence of non-destructive readouts comprising a single IR exposure
rms	Root mean square
SAA	South Atlantic anomaly
SBC	Solar-Blind Channel of ACS
SDSS	Sloan Digital Sky Survey
SED	Spectral-energy Distribution
SIAF	Science Instrument Aperture File
SM4	Servicing Mission 4
SMOV	Servicing Mission Observatory Verification
S/N	Servicing Mission Observatory Verification
SOFA	Selectable Optical Filter Assembly
SOC	Scientific Oversight Committee
ST-ECF	Space Telescope European Coordinating Facility
STIS	Space Telescope Imaging Spectrograph
STScI	Space Telescope Science Institute
STSDAS	Space Telescope Science Data Analysis System. The complete suite of IRAF data analysis and calibration routines used to process <i>HST</i> data.
synphot	Synthetic Photometry software package: https://synphot.readthedocs.io/en/latest/

TAC	Telescope Allocation Committee
TEC	Thermal Electric Coolers
UV	Ultraviolet
UVIS	Ultraviolet and Visual (CCD channel of WFC3)
WFC	Wide-Field Channel of ACS
WFC3	Wide Field Camera 3
WF/PC-1	Wide Field Planetary Camera-1. Original on-axis HST camera
WFPC2	Wide Field Planetary Camera-2. Replacement for WF/PC installed during first servicing mission of December 1993.